REPORT DOCUMENTATION PAGE

Form Approved

OMB No. 0704-0188

The public reporting burden for this collection of information is estimated to average 1 hour per response, including the time for reviewing instructions, searching existing data sources, gathering and maintaining the data needed, and completing and reviewing the collection of information. Send comments regarding this burden estimate or any other aspect of this collection of information, including suggestions for reducing the burden, to Department of Defense, Washington Headquarters Services, Directorate for Information Operations and Reports (0704-0188), 1215 Jefferson Davis Highway, Suite 1204, Arlington, VA 22202-4302. Respondents should be aware that notwithstanding any other provision of law, no person shall be subject to any penalty for failing to comply with a collection of information if it does not display a currently valid OMB control number.

PLEASE DO NOT RETURN YOUR FORM TO THE ABOVE ADDRESS.

1. REPORT DATE *(DD-MM-YYYY)*	2. REPORT TYPE	3. DATES COVERED *(From - To)*
10-04-2001	Conference Proceedings	23 Oct-26 Oct 2000

4. TITLE AND SUBTITLE

International Conference On Adaptive Structures & Technologies (ICAST)

5a. CONTRACT NUMBER

F6256200M9208

5b. GRANT NUMBER

5c. PROGRAM ELEMENT NUMBER

6. AUTHOR(S)

Conference Committee

5d. PROJECT NUMBER

5e. TASK NUMBER

5f. WORK UNIT NUMBER

7. PERFORMING ORGANIZATION NAME(S) AND ADDRESS(ES)

Nagoya University
Department of Aerospace Engineering
Chikusa, Nagoya 464-8603
Japan

8. PERFORMING ORGANIZATION REPORT NUMBER

N/A

9. SPONSORING/MONITORING AGENCY NAME(S) AND ADDRESS(ES)

AOARD
UNIT 45002
APO AP 96337-5002

10. SPONSOR/MONITOR'S ACRONYM(S)

AOARD

11. SPONSOR/MONITOR'S REPORT NUMBER(S)

CSP-001021

12. DISTRIBUTUION/AVAILABILITY STATEMENT

Approved for public release; distribution is unlimited.

13 SUPPLEMENTARY NOTES

14. ABSTRACT

This is an interdisciplinary conference. Topics include active materials, actuator & sensor technologies, active vibration control, microsystems, and active/adaptive structures.

15. SUBJECT TERMS

Microsystems, Aerospace Materials, Active Control, Intelligent Materials, Intelligent Systems, Materials, Adaptive Systems

16. SECURITY CLASSIFICATION OF:			17. LIMITATION OF ABSTRACT	18. Number of pages	19a. NAME OF RESPONSIBLE PERSON
a. REPORT	b. ABSTRACT	c. THIS PAGE			Brett J. Pokines, Ph.D.
U	U	U	UU	501	19b. TELEPHONE NUMBER *(Include area code)* +81-3-5410-4409

Standard Form 298 (Rev. 8/98)
Prescribed by ANSI Std. Z39.18

ELEVENTH INTERNATIONAL CONFERENCE ON ADAPTIVE STRUCTURES AND TECHNOLOGIES

NEW ERA, NEW AREAS, AND NEW DIRECTIONS

October 23–26, 2000
Nagoya, Japan

Edited by

YUJI MATSUZAKI
TADASHIGE IKEDA
VIJAYAN BABURAJ

TECHNOMIC
PUBLISHING CO., INC.
LANCASTER • BASEL

DISTRIBUTION STATEMENT A
Approved for Public Release
Distribution Unlimited

20010417 043

Eleventh International Conference on Adaptive Structures and Technologies

a**TECHNOMIC**®publication

Technomic Publishing Company, Inc.
851 New Holland Avenue, Box 3535
Lancaster, Pennsylvania 17604 U.S.A.

Copyright © 2001 by Technomic Publishing Company, Inc.
All rights reserved

No part of this publication may be reproduced, stored in a
retrieval system, or transmitted, in any form or by any means,
electronic, mechanical, photocopying, recording, or otherwise,
without the prior written permission of the publisher.

Printed in the United States of America
10 9 8 7 6 5 4 3 2 1

Main entry under title:
Eleventh International Conference on Adaptive Structures and Technologies

A Technomic Publishing Company book
Bibliography: p.

ISSN No. 1068-0578
ISBN No. 1-58716-103-6

HOW TO ORDER THIS BOOK

BY PHONE: 800-233-9936 or 717-291-5609, 8AM–5PM Eastern Time

BY FAX: 717-295-4538

BY MAIL: Order Department
Technomic Publishing Company, Inc.
851 New Holland Avenue, Box 3535
Lancaster, PA 17604, U.S.A.

BY CREDIT CARD: American Express, VISA, MasterCard

BY WWW SITE: http://www.techpub.com

PERMISSION TO PHOTOCOPY—POLICY STATEMENT

Authorization to photocopy items for internal or personal use, or the internal or personal use of specific clients, is granted by Technomic Publishing Co., Inc. provided that the base fee of US $5.00 per copy, plus US $.25 per page is paid directly to Copyright Clearance Center, 222 Rosewood Drive, Danvers, MA 01923, USA. For those organizations that have been granted a photocopy license by CCC, a separate system of payment has been arranged. The fee code for users of the Transactional Reporting Service is 1-58716/01 $5.00 + $.25.

Contents

Preface ix

International Organizing Committee, Local Committee, Participating Organizations, Sponsors and Financial Support for Asian Young Researchers xi

COMPLEX SYSTEMS AND DESIGN

Decentralized Vibration Control and Coupled Aeroservoelastic Simulation of Helicopter Rotor Blades with Adaptive Airfoils 3
Peter Konstanzer, *DaimlerChrysler Research and Technology, FTK/A, 70546 Stuttgart, Germany*
Boris Grohmann, *EADS Deutschland GmbH, Industrial Researach and Technology*
Bernd Kröplin, *Institute of Statics and Dynamics of Aerospace Structures, Stuttgart University*

Performance Comparison between Piezoelectric and Elastomeric Lag Dampers on Ground Resonance Stability of Helicopter 10
Seung Jo Kim, C. Y. Yun, *Department of Aerospace Engineering, Seoul National University, Seoul 151-742, Korea*

Simultaneous Optimum Design of Structural and Control Systems for Truss Structure 19
Yukio Tada, *Faculty of Engineering, Kobe University, Rokkodai, Nada, Kobe 657-8501, Japan*
Hidekazu Yuasa, *Power Tool Products Division, Matsushita Electric Works, Ltd., 33 Okamachi, Hikone, Shiga 522-8520, Japan*

Combined Design of Structural and Control Systems with Consideration of the Location of Sensor/Actuator. 27
Yukio Tada, *Department of Computer and Systems Engineering, Kobe University, 1-1 Rokkodai, Nada, Kobe 657-8501, Japan*
Jun Yamazaki, *Division of Computer and Systems Engineering, Graduate School of Science and Technology, Kobe University, 1-1 Rokkodai, Nada, Kobe 657-8501, Japan*

Material Structure Design of Stress-Dependent Adaptive Stiffness 35
Masao Tanaka, Masahiro Todoh, Kazushige Oki, Akihisa Naomi, *Division of Mechanical Science, Department of Systems and Human Science, Graduate School of Engineering Science, Osaka University, 1-3 Machikaneyama, Toyonaka, Osaka 560-8531, Japan*

Experimental Verification of Flat Sound Radiator by Pattern Optimization of Piezofilm Actuator . . . 43
Jin Yeon Cho, *Department of Aerospace Engineering, Inha University, Inchon, Korea*
Sung Lee, Joon-Seok Hwang, Seung Jo Kim, *Department of Aerospace Engineering, Seoul National University, Seoul 151-742, Korea*

Vibration Mode Reconstruction of a Thin Plate by Using Shaped PVDF Sensors 50
Katsuyoshi Nagayasu, Takuro Hayashi, Norio Uchida, Hiroaki Nakamura, Hiroshi Takahashi, *Toshiba Corp., R&D Center, 1 Komukai Toshiba-cho, Saiwai-ku, Kawasaki 212-8582, Japan*

DAMPING AND SMART MATERIALS

Quasi-Steady Bingham Biplastic Analysis of ER/MR Dampers 61
Glen A. Dimock, Norman M. Wereley, *Smart Structures Laboratory, Alfred Gessow Rotorcraft Center, Department of Aerospace Engineering, University of Maryland, College Park MD 20742, USA*

Dynamic Characteristics and Semi-Active Control of a Smart Composite Plate with ER Fluid 73
Ki-Dae Cho, Do-Hyung Kim, Won-Ho Shin, In Lee, *Division of Aerospace Engineering,*

Department of Mechanical Engineering, Korea Advanced Institute of Science and Technology, 373-1 Kusong-Dong, Yusong-Gu, Taejon 305-701, Korea

Orientation of Magnetic Field on the Sensing and Actuating Performance of an MR-Fluid Filled Cantilever Beam 81
Y. S. Jeng, C. S. Yeh, C. K. Lee, *Institute of Applied Mechanics, National Taiwan University, Taipei 10764, Taiwan, ROC*
K. C. Chen, *Department of Civil Engineering, National Chi Nan University, 1-6 Tieh-Shan Rd., Pu Li, Nantou, Taiwan, ROC*

Smart Material Based Actuation 89
Ephrahim Garcia, *DARPA, USA*
Janet Sater, *Institute for Defense Analyses, USA*
Gregory Fischer, *Strategic Analysis, Inc. USA*

Good Choice of Hybrid Piezoelectric Damping Configuration Based on Control Power Requirement—Series Type versus Separated Type 100
Kazuhiko Adachi, Yoshifumi Awakua, Takuzo Iwatsubo, *Department of Mechanical Engineering, Faculty of Engineering, Kobe University, Rokkodai-cho 1-1, Nada-ku, Kobe 657-8501, Japan*

Mechanical Property of Metallic Closed Cellular Materials Containing Polymer for Smart Structures 108
S. Kishimoto, N. Shinya, *National Research Institute for Metals, 1-2-1 Sengen, Tsukuba, Ibaraki 305-0047, Japan*

MODELING

Shape Control with Karhunen-Loève-Decomposition 119
Weihua Zhang, Bernd Michaelis, *Institute for Electronics, Signal Processing and Communications (IESK), Otto-von-Guericke-University Magdeburg, P.O. Box 4120, D-39016 Magdeburg, Germany*

Experimental Flutter Control of a Cantilevered Plate Using Piezoelectric Actuation and Modern Control Theory 127
Jae-Hung Han, Jong-Heung Park, *Electronics and Telecommunications Research Institute, 161 Kajong-dong, Yusong-gu, Taejon, Korea*
Junji Tani, Jinhao Qiu, *Institute of Fluid Science, Tohoku University, Katahira 2-1-1, Sendai, Japan*
In Lee, *Department of Aerospace Engineering, Korea Advanced Institute of Science and Technology, Science Town, Taejon, Korea*

Robust Fault Detection for Smart Structure Control Systems 134
Hiroshi Okubo, Yuki Tai, Eiichi Muramatsu, Hiroshi Tokutake, *Osaka Prefecture University, 1-1 Gakuen-cho, Sakai, Osaka 599-8531, Japan*

Modeling and Analysis of Elliptical Piezoelectric Laminates with Clamped Boundary 142
S.-W. Ricky Lee, H. L. Wong, *Department of Mechanical Engineering, HKUST, Clear Water Bay, Hong Kong*

Structural Vibration Suppression in Linear Feedback Control with Adaptive Gyroscopic Damper System 150
Atsuo Kobori, Satoru Ozawa, Hiroshi Furuya, *Department of Built Environment, Tokyo Institute of Technology, 4259 Nagatsuta, Midori-ku, Yokohama 226-8502, Japan*

A Simple Finite Element for Sandwich Shells of Revolution with Piezoelectric Transverse Shear Actuator 158
Ayech Benjeddou, Valérie Gorge, Roger Ohayon, *Structural Mechanics and Coupled Systems Laboratory, CNAM, 2 rue Conté, 75003 Paris, France*

TRANSDUCERS

Miniature Free Fall Sensors 169
C. K. Lee, Y. H. Hsu, *Institute of Applied Mechanics, National Taiwan University, Taipei 10764, Taiwan, ROC*

Design and Testing Methodologies of Rotational Accelerometers: A Smart Structure Perspective . . . 177
Y. H. Hsu, C. K. Lee, *Institute of Applied Mechanics, National Taiwan University, Taipei 10764, Taiwan, ROC*

Development of a Soft Tribo-Sensor for Monitoring Skin Conditions 185
M. Tanaka, H. Ichinose, S. Chonan, *Department of Mechatronics and Precision Engineering, Tohoku University, Sendai 980-8579, Japan*

K. Numagami, *Department of Dermatology, Tohoku University School of Medicine, Sendai 980-8574*, Japan
Z. W. Jiang, *Department of Mechanical Engineering, Yamaguchi University, Ube 755-8611, Japan*

Angular Piezoelectric Actuators for Dynamic Applications 193
Marc E. Regelbrugge, *Rhombus Consultants Group, Inc., 2565 Leghorn Street, Mountain View, CA 94043, USA*

A Self-Sensing Actuator Using Piezoelectric Films with Different Thickness for Vibration Control of Curved Structures (Proposition of Principal Concepts and Applications to Cantilever and Circular Ring) 200
Tsutomu Nishigaki, Mitsuru Endo, *Department of Mechanical Sciences and Engineering, Tokyo Institute of Technology, 2-12-1, O-okayama, Meguro-ku, Tokyo 152-8552, Japan*

Variable Frequency Flexural Piezoelectric Transducers for High Power Linear Chirp Transmission 208
Julien E. Bernard, George A. Lesieutre, *Penn State University, 229 Hammond, University Park, PA 16802, USA*

ADAPTIVE SPACE STRUCTURES

Soft Docking of Variable Geometry Truss with Redundant DOF by Impedance Control Considering Joint Frictions 219
Kei Senda, Shinsuke Nishimoto, *Osaka Prefecture University, 1-1 Gakuen-cho, Sakai, Osaka 599-8531, Japan*
Yoshisada Murotsu, *Osaka Prefectural College of Technology, Japan*

Design of Statically Indeterminate Geometry Adaptive Truss with Wire Member Actuators 227
Kazuyuki Hanahara, Yukio Tada, *Department of Computer and Systems Engineering, Faculty of Engineering, Kobe University, 1-1 Rokkodai, Nada, Kobe 657-8501, Japan*

Optimum Posture Determination of Adaptive Structure by Immune Algorithm 235
Yukio Tada, Yasumasa Oda, *Department of Computer and Systems Engineering, Faculty of Engineering, Kobe University, 1-1 Rokkodai, Nada, Kobe 657-8501, Japan*

Decentralized Static Shape Control of Large-Scaled Geometry Adaptive Truss by Two-Person Game Approach 243
Masao Tanaka, Noriyo Ichinose, *Division of Mechanical Science, Department of Systems and Human Science, Graduate School of Engineering Science, Osaka University, 1-3 Machikaneyama, Toyonaka, Osaka 560-8531, Japan*

Concepts of Redundant Space Structures Using Multi-Cellular Inflatable Elements 251
Hiraku Sakamoto, Kosei Ishimura, M. C. Natori, Ken Higuchi, *Institute of Space and Astronautical Science, Space Structures Laboratory, 3-1-1 Yoshinodai, Sagamihara, Kanagawa 229-8510, Japan*
Hiraku Sakamoto, Kosei Ishimura, *Department of Aeronautics and Astronautics, The University of Tokyo, Japan*

HEALTH MONITORING

Improved Surface Treatment of SMA Foils and Damage Suppression of SMA-Foil Embedded CFRP Laminates 261
Toshimichi Ogisu, Norio Ando, Junji Takaki, *Fuji Heavy Industries Ltd., Utsunomiya Plant, Aerospace Division, 1-1-11 Yonan, Utsunomiya-city, Tochigi Prefecture 320-8564, Japan*
Tomonaga Okabe, Nobuo Takeda, *Graduate School of Frontier Sciences, The University of Tokyo, c/o Komaba Open Laboratory (KOL), The University of Tokyo, 4-6-1 Komaba, Meguro-ku, Tokyo 153-8904, Japan*

Development of Structural Health Monitoring Systems for Smart Composite Structure Systems . . . 269
Nobuo Takeda, *Department of Advanced Energy, Graduate School of Frontier Sciences and Department of Aeronautics and Astronautics, School of Engineering, The University of Tokyo, 7-3-1 Hongo, Bunkyo-ku, Tokyo 113-8656, Japan*

A Wireless Transmission System for Monitoring Cable Tension of Cable-Stayed Bridges Using PVDF Piezoelectric Films 277
W. H. Liao, D. H. Wang, *Smart Materials and Structures Lab, Department of Automation and Computer-Aided Engineering, The Chinese University of Hong Kong, N.T., Hong Kong*

Impedance-Based Monitoring of Stress in Thin Structural Members 285
Masato Abe, *Department of Civil Engineering, The University of Tokyo, Tokyo 113-8656, Japan*
Gyuhae Park, Daniel J. Inman, *Center for Intelligent Material Systems and Structures, Virginia Polytechnic Institute and State University, Blacksburg, VA 24061-0261, USA*

Simultaneous Measurement of Strain and Temperature of Structures Using Fiber Optic Sensor 293
Hyun-Kyu Kang, Chi-Young Ryu, Chang-Sun Hong, Chun-Gon Kim, *Division of Aerospace Engineering, Korea Advanced Institute of Science and Technology, 373-1, Kusong-dong, Yusong-gu, Taejon 305-338, Korea*

Impact Damage Monitoring of Composite Panels by Embedded Small-Diameter Optical Fibers 301
Hiroaki Tsutsui, Akio Kawamata, Tomio Sanda, *Kawasaki Heavy Industries Ltd., 1 Kawasaki-cho, Kakamigahara City, Gifu-Prefecture 504-8710, Japan*
Nobuo Takeda, *The University of Tokyo, 4-6-1 Komaba, Meguro-ku, Tokyo 153-8904, Japan*

Simultaneous Health Monitoring and Control of Panels 309
Daniel J. Inman, Thomas Hegewald, *Center for Intelligent Material Systems and Structures, Department of Mechanical Engineering, MC 0261, Virginia Tech, Blacksburg, VA 24051, USA*

SHAPE MEMORY MATERIALS

Passive Damping Augmentation of a Vibrating Beam Using Pseudoelastic Shape Memory Alloy Wires 319
Farhan Gandhi, Gautier Chapuis, *Department of Aerospace Engineering, The Pennsylvania State University, 233 Hammond Building, University Park, PA 16802, USA*

Damping with Shape Memory Alloys for Structural Systems 336
Christian Boller, *EADS Military Aircraft, P.O. Box 80 11 60, 81663 Munich, Germany*
Peter Konstanzer, *DaimlerChrysler AG, Research and Technology, P.O. Box 80 04 65, 81663 Munich, Germany*
Yuji Matsuzaki, Tadashige Ikeda, *Department of Aerospace Engineering, Nagoya University, Chikusa, Nagoya 464-8603, Japan*

Stress-Strain Relationship of Pseudoelastic Transformation of Shape Memory Alloys during Loading Cycles 344
Hisashi Naito, Ken Funami, Junpei Sato, Yuji Matsuzaki, Tadashige Ikeda, *Department of Aerospace Engineering, Nagoya University, Chikusa, Nagoya 464-8603, Japan*

Behaviors of the Superelastic SMA Columns under Compressive Loading-Unloading Cycles 351
Muhammad Ashiqur Rahman, Jinhao Qiu, Junji Tani, *Institute of Fluid Science, Tohoku University, Katahira 2-1-1, Aoba-ku, Sendai-shi 980-8577, Japan*

Superelastic Properties of TiNi Shape Memory Alloy under Various Loading Conditions 359
Jian-ming Gong, *Department of Mechanical Engineering, Nanjing University of Chemical Technology, Nanjing 21009, China*
Hisaaki Tobushi, Kazuyuki Takata, Kayo Okumura, *Department of Mechanical Engineering, Aichi Institute of Technology, 1247 Yachigusa, Yagusa-cho, Toyota 470-0392, Japan*

Stress-Induced Martensitic Transformation Behavior and Lateral Strain of TiNi Shape Memory Alloy 367
Hisaaki Tobushi, Kayo Okumura, Masato Endo, *Aichi Institute of Technology, 1247 Yachigusa, Yagusa-cho, Toyota 470-0392, Japan*
Kazuyuki Takata, *Elastomix Co., Ltd., Shinkawa 1-17-25, Chuo-ku, Tokyo 104-0033, Japan*

Thermomechanical Properties of Polyurethane-Shape Memory Polymer Foam 375
Hisaaki Tobushi, Kayo Okumura, Masato Endo, *Aichi Institute of Technology, 1247 Yachigusa, Yagusa-cho, Toyota 470-0392, Japan*
Syunichi Hayashi, *Mitsubishi Heavy Industries, Ltd., 1 Takamichi, Iwatsuka-cho, Nakamura-ku, Nagoya 453-8515, Japan*

Two-Way Shape Memory Behavior Obtained by Combined Loading Training 382
Masataka Tokuda, Souichi Sugino, Tadashi Inaba, *Department of Mechanical Engineering, Mie University, Kamihama 1515, Tsu 514-8507, Japan*

SIGNAL PROCESSING AND COMPOSITES

Wavelet Damage Detection Algorithm for Smart Structures 393
Katharine J. Jones, *Department of Mathematics, Rice University, 6100 Main St., Houston, TX 77005, USA*

Real-Time Estimation of Multi-Modal Frequencies for Smart Structures **401**
Keun-Ho Rew, Sunmin Kim, In Lee, Youngjin Park, *Department of Mechanical Engineering, KAIST, Taejon, Korea*

Simultaneous Monitoring of Impact Locations and Damages Using Neural Networks and Wavelet Analysis **409**
Dae-Un Sung, Chun-Gon Kim, Chang-Sun Hong, *Korea Advanced Institute of Science and Technology (KAIST), 373-1 Kusong-dong, Yusong-gu, Taejon 305-701, Korea*

Specific Damping Capacity of Multiphase Unidirectional Hybrid Fiber Composites **417**
Vijayan Baburaj, *Micro System Engineering Department, Nagoya University, Chikusa-ku, Nagoya 464-8603, Japan*
Yuji Matsuzaki, Nae Florin Andrei, Tadashige Ikeda, *Aerospace Engineering Department, Nagoya University, Chikusa-ku, Nagoya 464-8603, Japan*

Optimal Sensor Location for Damage Detection Using Mutual Information **428**
Wan M. Said, Wieslaw J. Staszewski, *Department of Mechanical Engineering, Sheffield University, Mappin Street, Sheffield S1 3JD, UK*

GENERAL

Brief Overview of the Physical Basis for the "Active Materials" Concept **439**
P. F. Gobin, J. C. Baboux, L. Goujon, *GEMPPM UMR 5510 INSA de Lyon 69621 Villeurbanne, France*
M. Salvia, *Laboratoire IFOS UMR, 5621 Ecole Centrale de Lyon, 69131 Ecully, France*

Study on Adaptive Control Strategies for Smart Structure Vibration Suppression **447**
Kougen Ma, Jörg Melcher, Hans Peter Monner, *Institute of Structural Mechanics, German Aerospace Center (DLR), Lilienthalplatz 7, 38108, Braunschweig, Germany*

Recent Progress on the Development of a Smart Rotor System **455**
Inderjit Chopra, *Alfred Gessow Rotorcraft Center, Department of Aerospace Engineering, University of Maryland, College Park, MD 20742, USA*

Author Index *501*

Preface

The Eleventh International Conference on Adaptive Structures and Technologies (11th ICAST) was held under the theme of "New Era, New Areas, and New Directions" on October 23–26, 2000 in Nagoya, which was also the venue of the second conference held in 1991. The ICAST has entered into the second decade in this symbolic year 2000. During the past ten years, the ICAST has been established as a major international conference in the fields of active materials, structures and systems.

The objective of the 11th ICAST was to extend a further promotion of scientific research, innovative exchanges and beneficial interactions among the global communities associated with this leading research field. In this regard, a Special Lecture on Intelligent Fibers, an emerging topic in Japan, and Evening Special Talks on R&D Projects in USA and Europe were presented. In addition to Oral Presentations, we included a Seminar Session chaired by Moderators to highlight some selected topics of current importance. The Seminar Presentations consisted of pre-conference exchanges between Moderators and presenters, a preparatory meeting held before the Seminar Session, short Oral Presentations, Poster Presentations and Moderators' Summary Presentations on their topics at a Round Talk Session held on the final day. At the Round Talk Session, Invited Talks on R&D Status in Hong Kong, Korea and Taiwan were also followed by a one-hour Free Discussion on future collaborations between industry and academia, and at international levels on this topic, focussing on application-oriented programs.

We hope the 11th ICAST will be memorable as another great success and enjoyment to all participants both technically and socially. Finally, we would like to express our sincere thanks to Mr. Toshiyuki Sasaki and students of the Structural Mechanics Laboratory, Nagoya University for their valuable contribution to the organization of the 11th ICAST.

Yuji Matsuzaki
Tadashige Ikeda
Vijayan Baburaj

INTERNATIONAL ORGANIZING COMMITTEE

Y. Matsuzaki (Chair), *Nagoya University, Japan*
V. Baburaj, *Nagoya University, Japan*
P. M. Bainum, *Howard University, USA*
R. Barboni, *University of Rome, Italy*
E. J. Breitbach, *German Aerospace Center, Germany*
M. Bernadou, *Pôle Universitaire Léonard de Vinci and INRIA, France*
G. P. Carman, *University of California at Los Angeles, USA*
S. Chonan, *Tohoku University, Japan*
I. Chopra, *University of Maryland, USA*
L. E. Cross, *The Pennsylvania State University, USA*
T. Fujita, *University of Tokyo, Japan*
E. Garcia, *DARPA Defense Sciences Office, USA*
P. Gaudenzi, *University of Rome, Italy*
P.-F. Gobin, *National Institute of Applied Sciences of Lyon (INSA), France*
N. W. Hagood, *Massachusetts Institute of Technology, USA*
H. Hanselka, *Otto-von-Guericke-Universität Magdeburg, Germany*
A. Hariz, *University of South Australia, Australia*
D. J. Inman, *Virginia Polytechnic Institute and State University, USA*
S. J. Kim, *Seoul National University, Korea*
C. K. Lee, *National Taiwan University, Taiwan*
I. Lee, *Korea Advanced Institute of Science and Technology, Korea*
W. H. Liao, *Chinese University of Hong Kong, China*
D. Martinez, *Sandia National Laboratory, USA*
K. Miura, *University of Tokyo and Institute of Space and Astronautical Science, Japan*
Y. Murotsu, *Osaka Prefectural College of Technology, Japan*
M. C. Natori, *Institute of Space and Astronautical Science, Japan*
R. Ohayon, *Conservatoire National des Arts et Métiers, France*
M. Regelbrugge, *Rhombus Consultants Group, Inc., USA*
S. W. Ricky Lee, *Hong Kong University of Science and Technology, China*
C. A. Rogers, *University of South Carolina, USA*
C. Starvrinidis, *ESTEC European Space Agency, The Netherlands*
N. Takeda, *University of Tokyo, Japan*
J. Tani, *Tohoku University, Japan*
B. K. Wada, Retired, *Jet Propulsion Laboratory, USA*
T. Weller, *Israel Institute of Technology, Israel*

LOCAL COMMITTEE

Y. Matsuzaki (Chair), *Nagoya University, Japan*
V. Baburaj, *Nagoya University, Japan*
T. Fukuda, *Nagoya University, Japan*
T. Ikeda, *Nagoya University, Japan*
K. Ikuta, *Nagoya University, Japan*
N. Nakayama, *Kawasaki Heavy Industries, Ltd., Japan*
H. Otaki, *Mitsubishi Heavy Industries, Ltd., Japan*
H. Tobushi, *Aichi Institute of Technology, Japan*
M. Tokuda, *Mie University, Japan*

PARTICIPATING ORGANIZATIONS

Nagoya Industrial Science Research Institute
The Japanese Society for Aeronautical and Space Sciences
The Japanese Society of Mechanical Engineers
The Society of Japanese Aerospace Companies
The American Astronautical Society
The American Institute of Aeronautics and Astronautics
The American Society of Civil Engineers
Associazione Italiana di Aeronautica e Astronautica
Deutsche Gesellschaft für Luft- und Raumfahrt
The Royal Aeronautical Society

SPONSORS

Central Japan Railway Company
Chubu Center for Space Industry, Science and Technology
Daiko Foundation
Fuji Ceramics Corporation
Honda Motor Co., Ltd.
Inoue Foundation for Science
Ishikawajima-Harima Heavy Industries Co., Ltd.
Kawasaki Heavy Industries, Ltd.
Matsushita Inter-Techno Co., Ltd.
Mitsubishi Heavy Industries, Ltd.
Nagoya University Foundation
Toyota Motor Corporation

FINANCIAL SUPPORT FOR ASIAN YOUNG RESEARCHERS

U.S. Air Force Research Laboratory, Asian Office of Aerospace Research and Development

Complex Systems and Design

DECENTRALIZED VIBRATION CONTROL AND COUPLED AEROSERVOELASTIC SIMULATION OF HELICOPTER ROTOR BLADES WITH ADAPTIVE AIRFOILS

Peter Konstanzer,[1] Boris Grohmann,[2] Bernd Kröplin[3]

ABSTRACT

Helicopter rotor blades with adaptive airfoils are investigated considering discrete trailing edge flaps as well as continuous shape adaptation. First, a method for lagging mode stability augmentation is proposed demonstrating the potential of using discrete flaps. In the second part, we discuss continuous shape adaptation in order to overcome the disadvantages of discrete flaps.

INTRODUCTION

In helicopters, a high vibration level of the airframe occurs due to higher harmonic aerodynamic loads acting on the rotor blades. However, when the airfoil shape is adaptive, the aerodynamic loads can be affected to reduce vibration and moreover, the airfoil shape can be adjusted to the periodically changing flow conditions to increase aerodynamic efficiency. Adaptation of the airfoil shape may be achieved by discrete trailing edge flaps or continuously by a variation of the airfoil camber and bending of smart tabs. For vibration reduction applying feedback [4], stability augmentation of the lagging modes becomes indispensible. This is discussed first for rotors with discrete trailing edge flaps. The disadvantages of a discrete flap, such as kinks of the airfoil contour and concentrated masses, may be overcome by continuous shape adaptation, investigated in the second part.

DECENTRALIZED STABILITY AUGMENTATION

A method for lagging mode stability augmentation for helicopter rotors based on decentralized control is proposed. Since helicopter rotors consist of N rotor blades, the application of decentralized controllers to each rotor blade intuitively appears to be a natural approach, see Fig. 1. Furthermore, since all blades may be assumed to be identical, there is no reason for the individual blade controllers to be non-identical. This introduces a further conceptual simplification into the control system. Second, the interactions of the rotor blades with the vortices generated by the preceding blades – the blade-vortex interactions – introduce uncertainties in the interconnection of the rotor blade subsystems. Decentralized control [9] inherently provides robustness with respect to this type of uncertainty.

[1]Corresponding author. Current Affiliation: DaimlerChrysler Research and Technology, FTK/A, 70546 Stuttgart, Germany. Email: peter@konstanzer.com

[2]Current Affiliation: EADS Deutschland GmbH, Industrial Research and Technology.

[3]Institute of Statics and Dynamics of Aerospace Structures, Stuttgart University.

The aeroservoelastic behavior of active helicopter rotors about the trim state can be described by a linear time-periodic LTP system [3]

$$\dot{\tilde{x}} = A(\psi)\tilde{x} + B(\psi)\tilde{u}, \qquad \tilde{y} = C(\psi)\tilde{x} \tag{1}$$

with periodic system matrices $A(\psi) = A(\psi+2\pi), B(\psi) = B(\psi+2\pi), C(\psi) = C(\psi+2\pi)$. The vectors $\tilde{x} = [\tilde{x}_1, \ldots, \tilde{x}_N]^T, \tilde{u} = [\tilde{u}_1, \ldots, \tilde{u}_N]^T, \tilde{y} = [\tilde{y}_1, \ldots, \tilde{y}_N]^T$ denote state, input and output vector of the N individual blades. The LTP system can be approximated by a linear time-invariant LTI system applying the multiblade coordinate MBC transformation [3], subsequent expansion of the system matrices in Fourier series, and neglecting the periodic coefficients. This yields an approximation in terms of an LTI system in MBC

$$\dot{x} = Ax + Bu, \qquad y = Cx \tag{2}$$

which represents the periodic system characteristics about the trim state. The state vector x consists of the collective x_0, cyclic x_{1c}, x_{1s} and differential form x_2 of the rotor state. Similar for the input vector u and the output vector y. Figure 1 compares an LTI system in multiblade coordinates MBC and an LTI system in individual blade coordinates IBC with the exact LTP system. It is observed that the response of the LTP

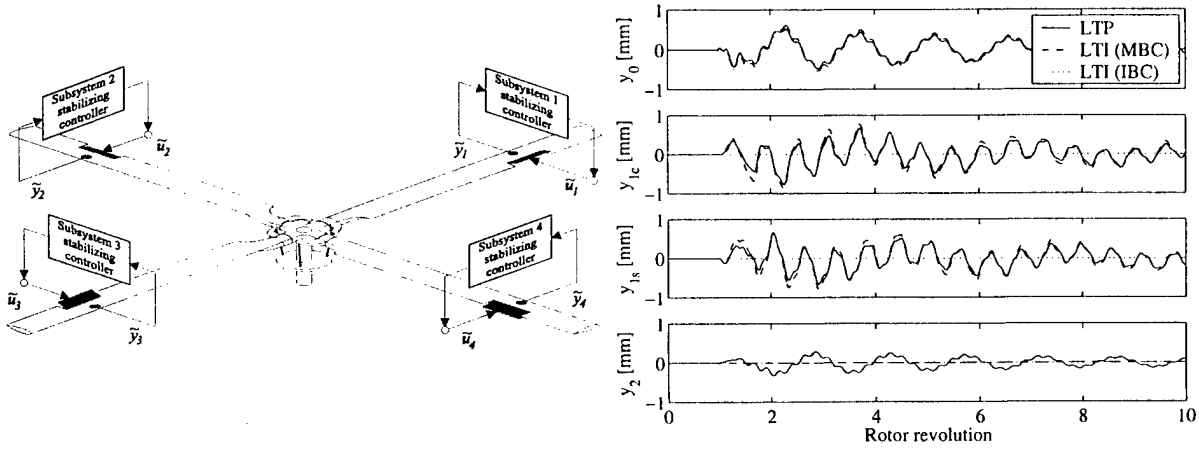


Figure 1: Decentralized control and response due to a collective impulse input $u_0(t) = \delta(t-T)$

system due to a collective impulse input $u_0(t) = \delta(t-T)$ is approximated with sufficient accuracy for the collective output y_0 by both LTI systems. The response of the cyclic outputs y_{1c}, y_{1s} is captured by the LTI system in MBC only whereas in IBC this interconnection does not appear at all. The interconnection of non-differential (e.g. collective) and differential form is neither represented by the LTI system in IBC nor by the LTI system in MBC. This can be observed from the response of the differential output y_2. Thus, for a constant coefficient approximation of an LTP system, the MBC transformation recovers some of the periodic system characteristics, but a considerable error in the interconnection of differential and non-differential form is inevitable. Therefore, when designing a controller based on an LTI system in MBC, robustness with respect to uncertainties in this interconnection is essential. The subsequently proposed design method will inherently provide this robustness.

Let the plant (rotor) consist of N interconnected subsystems (blades) and consider N individual subsystem (blade) controllers. These controllers may be constructed from a generalized second-order filter

$$F(s) \;=\; k\frac{s^2/\omega_z^2 + 2\zeta_z s/\omega_z + 1}{s^2/\omega_p^2 + 2\zeta_p s/\omega_p + 1} \tag{3}$$

where the coefficients $k, \zeta_z, \zeta_p, \omega_z, \omega_p$ specify various filters with different gain-phase characteristics such as lowpass, highpass, bandpass, or nonminimum-phase allpass filter [13]. Based on these basic filters, a

frequency-shaped subsystem controller can be constructed by simple series connection, e.g. a bandpass and a nonminimum-phase allpass filter may be combined to target a certain mode and provide the proper phase characteristics. Since the subsystems are identical, there is no reason for the subsystem controllers to be non-identical. After transforming the individual subsystem controllers into MBC, the overall stabilizing controller for $N = 4$ rotor blades is given by

$$\dot{x}_s = \underbrace{\begin{bmatrix} \hat{A}_s & 0 & 0 & 0 \\ 0 & \hat{A}_s & -\Omega I & 0 \\ 0 & \Omega I & \hat{A}_s & 0 \\ 0 & 0 & 0 & \hat{A}_s \end{bmatrix}}_{A_s} x_s + \underbrace{\begin{bmatrix} \hat{B}_s & 0 & 0 & 0 \\ 0 & \hat{B}_s & 0 & 0 \\ 0 & 0 & \hat{B}_s & 0 \\ 0 & 0 & 0 & \hat{B}_s \end{bmatrix}}_{B_s} y \tag{4}$$

$$u = \underbrace{\begin{bmatrix} \hat{C}_s & 0 & 0 & 0 \\ 0 & \hat{C}_s & 0 & 0 \\ 0 & 0 & \hat{C}_s & 0 \\ 0 & 0 & 0 & \hat{C}_s \end{bmatrix}}_{C_s} x_s + \underbrace{\begin{bmatrix} \hat{D}_s & 0 & 0 & 0 \\ 0 & \hat{D}_s & 0 & 0 \\ 0 & 0 & \hat{D}_s & 0 \\ 0 & 0 & 0 & \hat{D}_s \end{bmatrix}}_{D_s} y \tag{5}$$

where Ω denotes the rotor speed and $\hat{A}_s, \hat{B}_s, \hat{C}_s, \hat{D}_s$ the system matrices of the 4 identical subsystem controllers constructed from the generalized second-order filter. Defining $u_s := \dot{x}_s, y_s := x_s$, we obtain an expanded system consisting of plant and stabilizing controller

$$\underbrace{\begin{bmatrix} \dot{x} \\ \dot{x}_s \end{bmatrix}}_{\dot{x}_e} = \underbrace{\begin{bmatrix} A & 0 \\ 0 & 0 \end{bmatrix}}_{A_e} \underbrace{\begin{bmatrix} x \\ x_s \end{bmatrix}}_{x_e} + \underbrace{\begin{bmatrix} 0 & B \\ I & 0 \end{bmatrix}}_{B_e} \underbrace{\begin{bmatrix} u_s \\ u \end{bmatrix}}_{u_e} \tag{6}$$

$$\underbrace{\begin{bmatrix} y_s \\ y \end{bmatrix}}_{y_e} = \underbrace{\begin{bmatrix} 0 & I \\ C & 0 \end{bmatrix}}_{C_e} \underbrace{\begin{bmatrix} x \\ x_s \end{bmatrix}}_{x_e} \quad \text{and} \quad \underbrace{\begin{bmatrix} u_s \\ u \end{bmatrix}}_{u_e} = \underbrace{\begin{bmatrix} A_s & B_s \\ C_s & D_s \end{bmatrix}}_{K} \underbrace{\begin{bmatrix} y_s \\ y \end{bmatrix}}_{y_e} \tag{7}$$

where all unknown parameters are contained in the static output feedback matrix K of which the structure depends on the choice of the subsystem controllers. The structure is given by the arbitrary feedback structure formulation defined as

$$K = K_p + \sum_{i=1}^{m} t_i \, k^T \, U_i \tag{8}$$

where K_p denotes the matrix of prescribed coefficients, k the vector of feedback parameters to be designed, and t_i and U_i are vectors and matrices, respectively, which determine the entry of the feedback parameters k into the gain matrix K. The remaining static output feedback problem [10] is to find a static output feedback matrix K of arbitrarily specified structure. Decentralized optimal output feedback DOOF may be applied to find a matrix K which minimizes an infinite horizon quadratic performance index of the type

$$J = \frac{1}{2} \int_0^\infty (x_e^T \, Q \, x_e + u_e^T \, R \, u_e) \, dt \tag{9}$$

where Q and R are symmetric positive semidefinite weighting matrices.

A lagging mode stability augmentation system is designed for a Bo105 helicopter rotor in forward flight with trailing edge flaps located at 65% radial station [4]. The lagwise displacement signals at the radial station of the flaps are assumed to be amenable for measurement. The subsystem controllers consist of a fixed bandpass and two nonminimum-phase allpass filters of which the parameters are calculated by DOOF with an additional constraint on the allowable pole region as indicated in Fig. 2. As shown in Tab. 1, active damping enhancement of about 600% is achieved for the 1st as well as the 2nd lagging

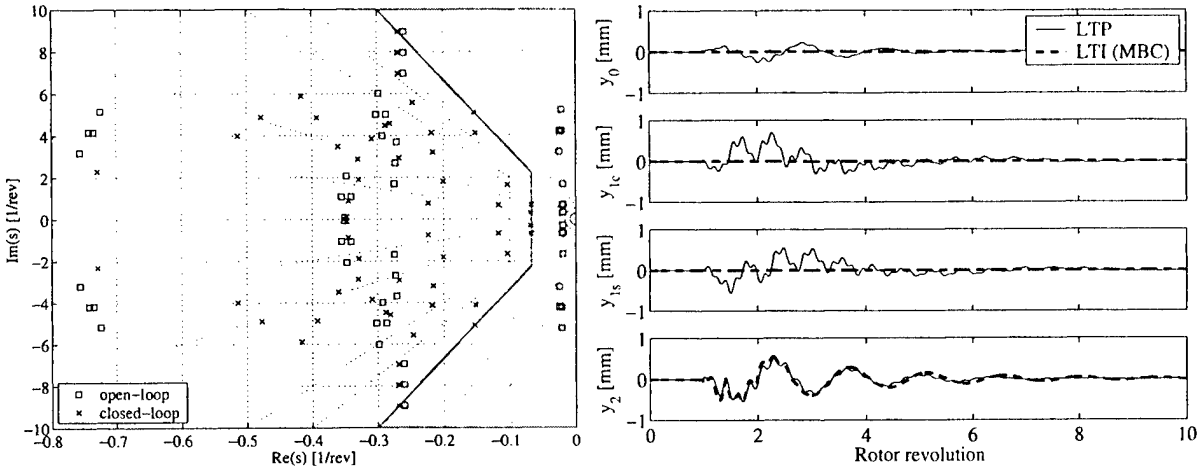


Figure 2: Pole map and closed-loop system response due to a differential impulse input

mode. Robustness with respect to uncertainties in the interconnections is shown by the closed-loop system response due to a differential impulse input $u_2(t) = \delta(t - T)$ shown in Fig. 2. Although the LTI design model does not generate any response in the non-differential outputs y_0, y_{1c}, y_{1s} the controller applied to the time-periodic plant provides excellent regulation in the non-differential as well as the differential outputs.

Table 1: Controller parameters and critical damping

	controller parameters					critical damping	
	ζ_1	ζ_2	$\omega_1[1/s]$	$\omega_2[1/s]$	k	1st lag	2nd lag
uncontrolled	–	–	–	–	–	1 - 5 %	0.5 - 1 %
controlled	0.92	1.17	90.4	112.2	-9695	6 - 20%	3 - 6 %

AEROSERVOELASTIC DESIGN OF ACTIVE CAMBER ROTOR (ACR)

The investigation on decentralized vibration control employs the concept of a smart trailing edge flap with discrete piezo actuators which has been investigated in the framework of RACT (Rotor Active Control Technology), see Geissler *et al* [1] and Schimke *et al* [6]. In the following, the structural concept for a smart helicopter rotor with active material components integrated in and distributed across the host structure resulting in continuous shape adaptation is discussed.

Aeroelastically Unbalanced Concept. Due to the integration of the active material into the host structure, a balanced design between the conflicting basic functionalities *dynamic shape adaptation* and *load carrying capability* is necessary to guarantee the efficiency of actuation. This is attempted by the concept

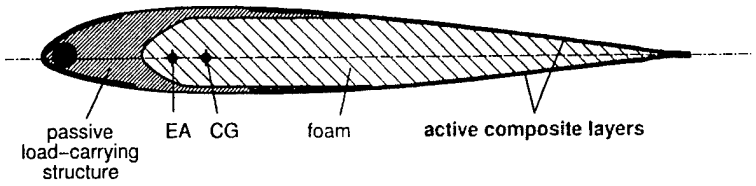


Figure 3: Smart Airfoil

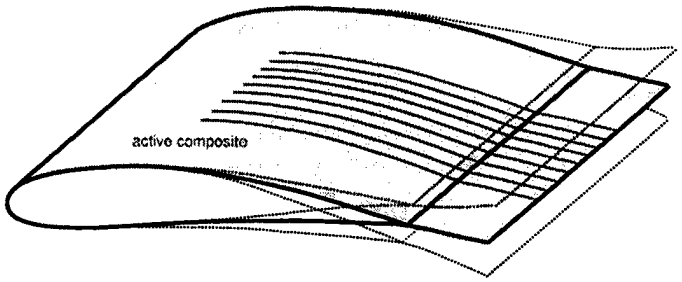


Figure 4: Active Camber Rotor (ACR) with smart tab actuated in bending

depicted in Figure 3. The stiff, passive nose structure, reaching up to approximately 30-40% of the chord, supplies bending and torsion stiffness and carries the centrifugal loads. The flexible trailing edge area is responsible for dynamic shape adaptation by opposite chord-wise strain actuation of the upper and lower active composite layers. These layers may consist of thin piezoceramic plates actuated in 31-mode via standard electrodes, in 33-mode via interdigitated electrodes or piezoceramic fibers. The foam core must be very flexible to avoid losses or it may even be replaced by a different type of supporting skeleton that prevents the active composite layers from buckling. Displacement amplification increases with decreasing airfoil thickness ratio. Note that the trailing edge structure still has to carry local (aerodynamic) loads. Since the smart airfoil concept depicted in Figure 3 has limited authority, it may be combined with a smart tab actuated in bending, see Figure 4.

Coupled Multiphysics Simulation. The contradictory design paradigms "*as stiff as necessary to carry loads*" and "*as flexible as possible for shape adaptation*" of smart aeroservoelastic structures are the basic motivation for the development of the coupled aeroservoelastic simulation described in the following. See Grohmann [2] for details on the formulation.

Electromechanics. The smart composite structure including piezoceramic layers is modeled by curved shell elements employing classical laminate theory. Two different models of the active material are used. First, its effect is modeled by equivalent actuator loads. Second, a coupled electromechanical model for actuation in 31-mode based on linear piezoelectricity is employed. Due to the different characteristic time scales, the electric field is treated as quasi-steady.

Aeroelasticity. The two-dimensional Euler equations are employed for compressible and inviscid aerodynamics. A representative blade segment at 85% of the rotor diameter is investigated. The varying flow conditions during one revolution of the rotor blades in forward flight are simulated by oscillatory mesh motion in streamwise direction. Concerning fluid-structure interaction, the displacements of the structure are considered as deformation of the fluid domain and the aerodynamic pressure acts as load on the structure. This leads to momentum and energy transfer at the fluid-structure interface. For the correct coupled response, conservation of mass, momentum and energy at the interface is essential.

Stabilized Space-Time Finite Element Discretization. The time-discontinuous Galerkin method yields implicit, unconditionally stable time discretization, see Wallmersperger *et al* [12]. The deformation of the fluid domain is modeled by a space-time isoparametric approach for the geometry of the fluid elements, see Tezduyar *et al* [11]. Stabilization of the convective term of the fluid equations is attained by means of the Galerkin/least squares approach which yields the required "upwinding" and high frequency/short wave length filtering property. In order to obtain monotonic solutions at shocks and to satisfy entropy stability, i.e. the second law of thermodynamics, nonlinear higher order discontinuity capturing operators are

employed, see Shakib [8]. The stabilized space-time finite element discretization yields accurate, locally conservative and stable discretization for electromechanics, transonic aerodynamics and fluid-structure interaction.

Solution procedure. In the case of the linear model for piezoelectricity, it is possible to eliminate the electric field of the smart composite by static condensation and the structure is written in terms of mechanical displacement unknowns only. In aeroelasticity, staggered solution procedures for fluid-structure interaction are very popular. However, potential deficiencies concerning conservation and stability are well known, see Piperno *et al* [5]. For this reason, an efficient and reliable block iterative solver based on a coupled Newton-Raphson formulation for fluid-structure interaction including deformation of the fluid mesh is formulated. It does not degrade conservation, stability and accuracy of the underlying finite element discretization.

Aerodynamic Effectiveness of Smart Airfoil. Results of quasi-steady numerical simulations are presented for transonic flow around a NACA23010 airfoil at an angle of attack $\alpha = 0$ and a Mach number $M = 0.74$. This corresponds to forward flight conditions of the advancing blade at a radial station of 85%. Consider the smart airfoil according to Fig. 3 with the upper and lower active composite layers contracting and expanding, respectively. Table 2 shows a comparison of the change of the angle of attack $\Delta\alpha$, lift C_l and moment coefficient C_m for different values of equivalent free actuator strain ϵ. It is seen that significant actuation is required for aerodynamic effectiveness.

Comparison of Smart Airfoil, Smart Tab and Discrete Trailing Edge Flap. For a discrete trailing edge flap $\lambda_F = c_F/c$ where c_F and c are the chord of the flap and the total chord of the wing section, respectively. According to Schlichting *et al* [7], a large $\lambda_F \to 1$ and small flap $\lambda_F \to 0$ behave like a direct lift and servo flap, respectively. In Figure 5 it is also seen, that the variable camber of the smart airfoil according to Figure 3 behaves like a direct lift flap where $\lambda_C = c_C/c$ and c_C is the chord length of the flexible part of the airfoil. For the smart tab according to Figure 4 we employ $\lambda_T = c_T/c$ where c_T and c are the chord of the tab itself and the chord of the plain airfoil without tab, respectively. The tab bending actuation leads to a servo effect, slightly depending on λ_T. Both concepts may be combined to tailor the aerodynamic characteristics for specific needs.

TABLE 2. Influence of equivalent free actuator strain ϵ on angle of attack $\Delta\alpha$, lift C_l and moment C_m coefficient

ϵ	$\Delta\alpha$	C_l	Cm
0.00%	0.00	0.18	−0.016
0.15%	−0.58	−0.01	0.003
0.25%	−0.96	−0.14	0.015
0.35%	−1.35	−0.27	0.028

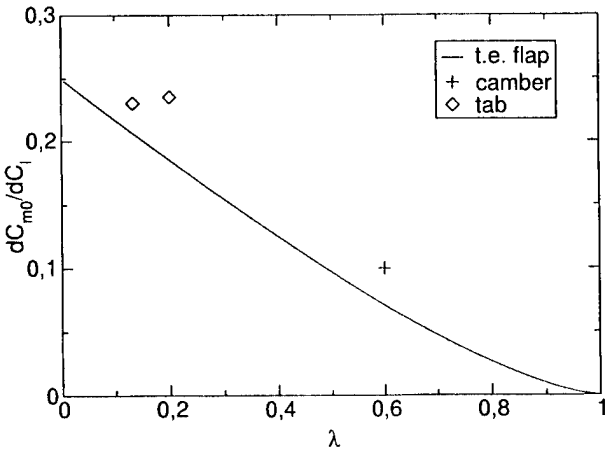


Figure 5. Comparison of trailing edge flap, variable camber of smart airfoil and smart tab

CONCLUSIONS

A method for lagging mode stability augmentation for active helicopter rotors based on decentralized control has been proposed. Active damping enhancement of about 600% has been achieved while providing robust performance when applying the controller to the time-periodic plant. Moreover, the derived decentralized controller consisting of N identical subsystem controllers is conceptually simple, permitting a certain degree of tuning during experiments.

Furthermore, an Active Camber Rotor (ACR) with distributed active material components and continuous shape adaptation has been proposed. Because it is an aeroelastically unbalanced concept, aeroservoelastic design turns out to be essential. For this reason, multiphysics simulation for coupled electromechanics and aeroelasticity of the smart composite structure including piezoceramic layers in inviscid, transonic flow has been developed based on stabilized space-time finite elements. Numerical simulations have been presented demonstrating the aerodynamic effectiveness of shape adaptation and comparing the ACR to a discrete trailing edge flap.

REFERENCES

[1] W. Geissler, H. Sobieczky, and H. Vollmers. Numerical study of the unsteady flow on a pitching airfoil with oscillating flap. In *24th European Rotorcraft Forum*, Marseilles, France, 15th-17th September 1998.

[2] B. A. Grohmann. *Stabilized Space-Time Finite Elements for Transonic Aeroelasticity.* PhD thesis, Universitt Stuttgart, June 2000. submitted.

[3] W. Johnson. *Helicopter Theory.* Dover Publications Inc., 1980.

[4] P. Konstanzer and B.-H. Kröplin. Performance considerations in the control of helicopter vibration. In *SPIE Proceedings of Smart Structures and Materials 1999: Mathematics and Control in Smart Structures*, volume 3667, 1999.

[5] S. Piperno and C. Farhat. Energy based design and analysis of staggered solvers for nonlinear transient aeroelastic problems. In *Structures, Structural Dynamics and Materials Conference.* AIAA/ASME/ASCE/AHS/ASC, April 2000. Atlanta, Georgia, AIAA-2000-1447.

[6] D. Schimke, P. Jänker, V. Wendt, and B. Junker. Wind tunnel evaluation of a full scale piezoelectric flap control unit. In *24th European Rotorcraft Forum*, 1998.

[7] H. Schlichting and E. Truckenbrodt. *Aerodynamik des Flugzeuges.* Springer Verlag, 1969.

[8] F. Shakib. *Finite Element Analysis of the compressible Euler and Navier-Stokes equations.* PhD thesis, Stanford University, 1988.

[9] D. Siljak. *The Control Handbook*, chapter Decentralized Control, pages 779 – 793. CRC Press, 1996.

[10] V. Syrmos, C. Abdallah, P. Dorato, and K. Grigoriadis. Static output feedback – a survey. *Automatica*, 33(2):125 – 137, 1997.

[11] T. E. Tezduyar, M. Behr, and J. Liou. A new strategy for finite element computations involving moving boundaries and interfaces – The deforming-spatial-domain/space-time procedure: I. The concept and the preliminary numerical tests. *Comput. Methods Appl. Mech. Engrg.*, 94:339–351, 1992.

[12] T. Wallmersperger, B. A. Grohmann, and B.-H. Kröplin. Time-discontinuous stabilized space-time finite elements for PDEs of first- and second-order in time. In *European Conference on Computational Mechanics ECCM '99*, München, Germany, 1999. GACM.

[13] B. Wie and K.-W. Byun. New generalized structural filtering concept for active vibration control synthesis. *Journal of Guidance, Control, and Dynamics*, 12:147 – 154, 1989.

PERFORMANCE COMPARISON BETWEEN PIEZOELECTRIC AND ELASTOMERIC LAG DAMPERS ON GROUND RESONANCE STABILITY OF HELICOPTER

Seung Jo Kim, Chol Yong Yun

ABSTRACT

In this study, a piezoelectric lag damper using damping characteristics of piezoelectric ceramics is proposed for alleviating ground resonance instability. The piezoelectric passive damper consists of the piezoelectric elements and electrical circuits such as a resistor and inductor in series. For the piezoelectric bonded to the rotor flexures, piezoelectric strain energy is converted to electrical energy and dissipated through an electrical network. Performance comparison between piezoelectric and elastomeric lag dampers on ground resonance instability is made. In the comparison, fan plot and modal damping with respect to rotating speed are presented.

INTRODUCTION

Since the hingeless and the bearingless main rotors of helicopter are usually as a soft-inplane rotor, it is susceptible to aeromechanical instabilities, such as ground and air resonance. These dynamic instabilities are generally caused by coupling of blade regressing lag mode and fuselage motions. The instabilities appear when the rotating lag frequency is less than 1/rev, as is typical for articulated and soft-inplane hingeless and bearingless rotors. To alleviate these instabilities, most rotors need to be equipped with lag dampers. In conventional hingeless rotors, the elastomeric lag dampers are used. Elastomeric damper is nonlinear and highly dependent on frequency, temperature and loading conditions such as preload and excitation amplitudes. The lag instability of helicopter rotors occurs at the natural frequency, usually 0.6 ~ 0.7/rev, of lag motion and the 1/rev frequency. Under these conditions, the damping in elastomer has been shown to degrade substantially at low amplitudes, thus causing undesirable limit cycle oscillation.

S.J. Kim, Professor, Department of Aerospace Engineering, Seoul National University, Seoul, 151-742, Korea

C.Y. Yun, Graduate Research Assistant, Seoul National University, Department of Aerospace Engineering, Seoul, 151-742, Korea

We propose a new lag damper using piezoelectric damping characteristics. The characteristics of the piezoelectric material are to transform mechanical vibration energy to electrical energy. The transformed electrical energy can be dissipated into the heat energy by shunt circuits. The piezoelectric passive damper consists of the piezoelectric element and electrical networks such as a resistor and inductor in series. In the case of the piezoelectric bonded to the structures such as a rotor flexures, piezoelectric strain energy is converted to electrical energy and dissipated through a electrical network. For the oscillating lag motion of blade, the current alternates direction and varies with the lag mode frequency. The inductor coupled with the inherent capacitance of piezoceramic makes the large current induced in the circuit, and the resistor dissipates the converted electrical energy into heat energy to increase damping in blades. While not addressed in this paper, the piezoelectic damper can work effectively for lag motions that occur at multiple frequencies simultaneously since single piezoelectric patch can suppress the multiple modes only by changing the number of electrical resonances.

Performance comparison between piezoelectric and elastomeric lag dampers on ground resonance is presented. For the comparison, fan plot and modal damping with respect to rotating speed are presented. The effect of the piezoelectric damper on ground resonance stability is investigated using the classical four-degree-of-freedom model of Coleman and Feingold. In addition to the cyclic lag and the x-and y-hub motion equations, the piezoelectric damper equation needs to be solved simultaneously. For a four-bladed rotor, the four damper equations are transformed to the non-rotating-frame to yield a collective, differential and two cyclic damper equations. Only the cyclic damper equations need to be included for stability calculations since the collective and differential lag motions do not couple with hub motions.

PIEZOELECTRIC PASSIVE DAMPER

The linear constitutive equations for piezoelectric materials, simplified for one-dimensional transverse loading are

$$\begin{Bmatrix} E \\ T \end{Bmatrix} = \begin{bmatrix} \varepsilon^T & -h_{31} \\ -h_{31} & c^D \end{bmatrix} \begin{Bmatrix} D \\ S \end{Bmatrix} \tag{1}$$

where D is electrical charge density, S is mechanical strain, E is electrical field, and T is mechanical stress. h_{31} and ε^T are piezoelectric constants, and c^D is young's modulus. In the single-degree-of-freedom setting, the constitutive equations of the piezoelectric material can be written

$$\begin{Bmatrix} V \\ M_P \end{Bmatrix} = \begin{bmatrix} 1/C_P^S & -H \\ -H & K_P \end{bmatrix} \begin{Bmatrix} q \\ \varsigma \end{Bmatrix} \tag{2}$$

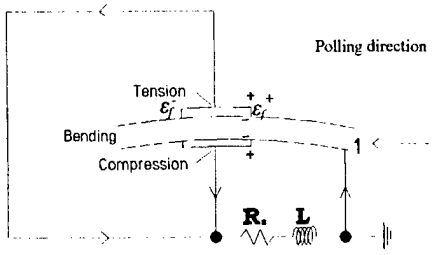


Figure 1. The piezoelectric damper

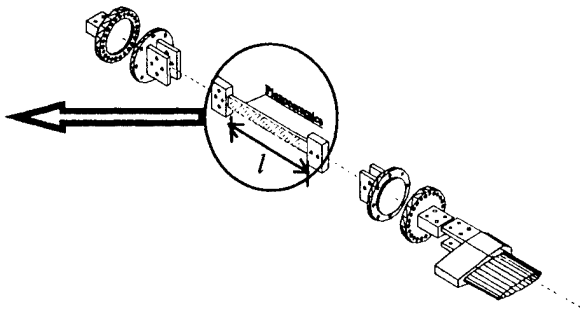


Figure 2. The rotor blade with piezoelectric damper.

C_P^S is the capacitance of the piezoelectrics under constant strain, K_P is the stiffness of the piezoelectric material, and H is the electro-mechanical coupling. q and ζ which are generalized coordinates are charge and lag angle displacements of the piezoelectric, respectively. And V and M_P are voltage appearing across the material and moment applied to flexure by the piezoelectric, respectively. Schematic drawings of the piezoelectric damper attached to a rotor flexure of hingeless helicopter are shown in Figure 1 and 2.

For the perfect bonding, the moment applied to flexure by piezoelectric is equal to (ref.5)

$$M_P = \frac{E_f t_f^2 b}{E_f / E_P + 6}\{\varepsilon_f^+ + \varepsilon_f^- - 2\frac{h_{31}}{E_P lb} q\} = K_P \varsigma - Hq \tag{3}$$

where E_f and E_P are young's Modula of the flexure and the piezoelectric, respectively. t_f is thickness of the flexure, b is width, and l is length of the piezoelectric. Flexure surface strains, ε_f^+ and ε_f^-, are proportional to lag angle ζ and the piezoelectric stiffness K_P is small compared to blade flexure stiffness and is added to blade lag hinge spring stiffness. The electro-mechanical coupling H depends on the material properties of flexure and the piezoelectric, but is independent of strains. H is equal to

$$H = \frac{2(E_f / E_P) t_f^2}{(E_f / E_P + 6) l} h_{31} \tag{4}$$

The ground resonance instabilities of articulated and hingeless rotor blades can be studied by retaining only the lead-lag degree of freedom. The blade is assumed rigid and undergoes a single degree of motion in the plane of rotation. It has a hinge offset at a distance e from the rotating axis. The simple configuration represents an articulated blade with lag hinge and can be an approximate representation for a hingeless blade with a possible leaf spring at the hinge. Considering moment equilibrium for inertial force, centrifugal force, aerodynamic force, hinge spring moment, and piezoelectric force moment about the lag hinge, the blade lag equation in the rotating frame can be written as

$$\overset{**}{\varsigma} + \nu_\varsigma^2 \varsigma - \frac{H}{I_\varsigma \Omega^2} q = M_{aero} \tag{5}$$

where "Star(*)" above a symbol represents derivatives with respect to rotor azimuth and

ν_ζ is non-dimensional lag frequency in terms of rotational speed Ω.

The shunted piezoelectric with inductance L and resistance R in series can be modeled as the electric circuit which consists of the voltage source $H\zeta$ which is induced by mechanical deformation, inherent capacitor C_P^S, the resistor, and inductor. From the Kirchhoff's voltage law, the piezoelectric circuit equation can be written as

$$L\ddot{q} + R\dot{q} + \frac{1}{C_P^S}q - H\zeta = 0 \tag{6}$$

The electrodes of piezoelectric material as a capacitor can be resonant with properly selected inductor and the accumulated energy is dissipated through the resistor. The mechanical vibration energy is transformed into the electric energy by the piezoelectric and this is dissipated through the resistor into heat energy. Thus the vibration can be damped.

For simplification, non-dimensional parameters are introduced as follows:

electrical resonance $\omega_e = 1/\sqrt{L \cdot C_P^S}$, rotating lag frequency $\omega_b = \Omega\nu_\zeta$

tuning ratio $\delta = \omega_e / \omega_b$, damping parameter $r = R \cdot C_P^S \cdot \omega_b$

non-dimensional charge $\bar{q} = \frac{H}{I_\zeta \Omega^2} q$, non-dimension H $\eta = \frac{H}{\sqrt{I_\zeta \Omega^2 \nu_\zeta^2}\sqrt{1/C_P^S}}$

Using the non-dimensional parameters, the blade lag-piezoelectric equations of motion in the rotating frame can be rewritten as

$$\begin{aligned} &\overset{**}{\zeta} + \nu_\zeta^2 \zeta - \bar{q} = \bar{f} \\ &\overset{**}{\bar{q}} + r\delta^2 \nu_\zeta \overset{*}{\bar{q}} + \nu_\zeta^2 \delta^2 \bar{q} - (\nu_\zeta^2 \delta\eta)^2 \zeta = 0 \end{aligned} \tag{7}$$

The tuning parameter δ reflects the frequency to which the electrical circuit is tuned, while the r parameter is an expression for the damping in the shunt circuit. When the electrical resonance frequency is tuned to rotating lag frequency, the damping is maximized. If frequency and damping of the blade lag-piezoelectric system are plotted as a function of parameter r at the fixed δ, it can be observed that the frequency remains a constant at low r value and gradually shifts to a higher value as the r is increased. It is also observed that maximum damping exists at the r value which is 0.2245 in the case.

ELASTOMERIC DAMPER

The elastomeric damper model developed in Ref. 7 is adopted. The model consists of a nonlinear spring, S1, in series with a linear Kelvin chain. The spring S1 was softening in nature to represents the instantaneous force/displacement behavior of an elastomer, and was described by

$$\zeta_{S1} = f(D) = sign(D)(c_1 |D| + c_2 |D|^2 + c_3 |D|^3 + c_4 |D|^4) \tag{8}$$

where D is the force and ζ_{S1} is the displacement in S1. The damper nonlinear differential equation is

$$K_2\varsigma + C\dot{\varsigma} = K_2 f(D) + C\frac{df}{dD}\dot{D} + D \tag{9}$$

where ζ is the lag displacement at the lag hinge, and K_2 and C are the stiffness and damping of the linear spring S2 and the linear dashpot D_2, respectively. The system parameter c_1, c_2, c_3, c_4, K_2, and C are identified using amplitude-dependent complex modulus data.

GROUND RESONANCE

In order to clearly identify the effects of the damper, a simplified mathematical model of the helicopter is considered for the numerical studies in this paper. The rigid fuselage undergoes x- and y-hub motion, and the rigid blades undergo lag motions. For ground resonance studies, the effects of aerodynamics, which are known to be small, are neglected. The mathematical model to be used in the analysis is shown in Figure 3. In the figure, only a typical blade is shown. Each blade has a rotating spring k_ς and piezoelectric or elastomeric damper which act about the lag hinge. C_ς is viscous damping in the rotating frame. x_h and y_h are inplane longitudinal and lateral hub motion, respectively. The effect of the piezoelectric damper on ground resonance stability is investigated using the classical four-degree-of-freedom model of Coleman and Feingold. In addition to the cyclic lag and the x-and y-hub motion equations, the piezoelectric damper equation needs to be solved simultaneously. For a four-bladed rotor, the four damper equations are transformed to the non-rotating-frame to yield a collective, differential and two cyclic damper equations. Only the cyclic damper equations need to be included for stability calculations since the collective and differential lag motions do not couple with hub motions. The non-dimensionalized cyclic lag and cyclic damper-force equations along with x-and y-hub motion equations, are expressed as

$$\mathbf{M}\ddot{\mathbf{X}} + \mathbf{C}\dot{\mathbf{X}} + \mathbf{K}\mathbf{X} = 0 \tag{10}$$

where state vector $\mathbf{X} = [\varsigma_{1c} \quad \varsigma_{1s} \quad \bar{x}_h \quad \bar{y}_h \quad \bar{q}_{1c} \quad \bar{q}_{1s}]^T$,

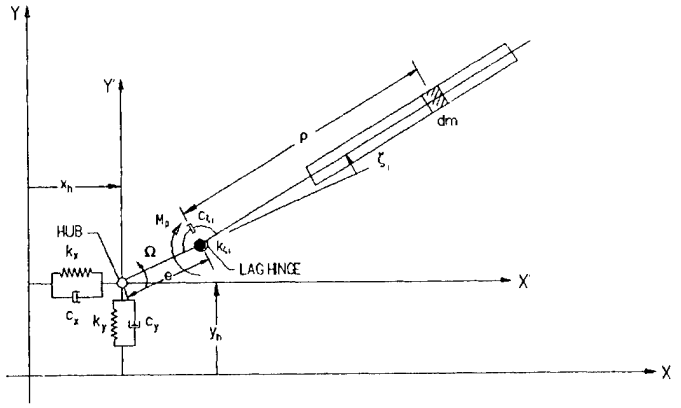


Figure 3. Ground resonance model including piezoelectric damper

$$\mathbf{M}=\begin{bmatrix} 1 & 0 & 0 & -S_\zeta^* & 0 & 0 \\ 0 & 1 & S_\zeta^* & 0 & 0 & 0 \\ 0 & \dfrac{S_\zeta^*}{2M_x^*} & 1 & 0 & 0 & 0 \\ -\dfrac{S_\zeta^*}{2M_x^*} & 0 & 0 & 1 & 0 & 0 \\ 0 & 0 & 0 & 0 & 1 & 0 \\ 0 & 0 & 0 & 0 & 0 & 1 \end{bmatrix}, \quad \mathbf{C}=\begin{bmatrix} C_\zeta^* & 2 & 0 & 0 & 0 & 0 \\ -2 & C_\zeta^* & 0 & 0 & 0 & 0 \\ 0 & 0 & C_x^* & 0 & 0 & 0 \\ 0 & 0 & 0 & C_y^* & 0 & 0 \\ 0 & 0 & 0 & 0 & r\delta^2\nu_\zeta & 2 \\ 0 & 0 & 0 & 0 & -2 & r\delta^2\nu_\zeta \end{bmatrix}$$

$$\mathbf{K}=\begin{bmatrix} \nu_\zeta^2-1 & C_\zeta^* & 0 & 0 & -1 & 0 \\ -C_\zeta^* & \nu_\zeta^2-1 & 0 & 0 & 0 & -1 \\ 0 & 0 & \omega_x^2/\Omega^2 & 0 & 0 & 0 \\ 0 & 0 & 0 & \omega_y^2/\Omega^2 & 0 & 0 \\ -(\nu_\zeta^2\delta\eta)^2 & 0 & 0 & 0 & \nu_\zeta^2\delta^2-1 & r\delta^2\nu_\zeta \\ 0 & -(\nu_\zeta^2\delta\eta)^2 & 0 & 0 & -r\delta^2\nu_\zeta & \nu_\zeta^2\delta^2-1 \end{bmatrix}$$

In the above equations, the hub displacement $\bar{x}_h$ and $\bar{y}_h$ are also non-dimensional with respect to rotor radius R. The governing equations are six second order differential equations. The ground resonance characteristics of a helicopter with the piezoelectric damper can be determined by carrying out the eigenvalue analysis of these equations. The blade, fuselage and damper properties used for calculations are given in table 1.

No. of Blade	4	Hub spring, K_v	1240481.8 N/m
Blade mass	94.9 kg	Fuselage support frequency w_x	12.148 rad/s
Blade mass moment S_ζ*	1.5	Fuselage support frequency w_y	18.402 rad/s
Lag hinge offset, e	0.3048	Piezoelectric tuning ratio, δ	1.0
Blade lag frequency	0.6/rev	Piezoelectric damping parameter	0.225
Hub mass, M_x	8026.6 kg	Blade structural damping ration	0.413
Hub mass, M_y	3283.6 kg	Support damping ratio, C_x	0.146
Hub spring, K_x	1240481.8 N/m	Support damping ratio, C_v	0.0964

Table 1. Blade-fuselage-piezoelectric damper properties.

RESULTS

The effect of the piezoelectric damper on ground resonance stability is investigated, with comparing to elastomeric lag dampers. For the comparison, fan plot and modal damping with respect to rotating speed are presented. Figure 4 shows the Coleman diagram for a soft-inplane hingeless rotor helicopter with piezoelectric damper. The non-dimensional lag frequency at the operating speed is ν_ζ = 0.6/rev. It is observed that the regressive and progressive lag frequencies are slightly higher than the baseline

frequencies since the piezoelectric material is stiffer near the optimum resistance and inductance. The diagram shows that the coalescence of the regressive lag mode with the fuselage modes is weaker due to the presence of the piezoelectric damper. Figure 5 shows modal damping of piezoelectric and elastomeric dampers for the case of no blade structural damping and no support damping. The piezoelectric damper has more stable effect than elastomeric damper, but instability of piezoelectric damper spreads over a larger range of rotor speed. The regressive and progressive lag modes are stable for all range of rotor speed. Figure 6 shows modal damping with the inclusion of blade damping in addition to the each damper. The rotating-frame lag damping ratio is 0.0413. As seen in the figure, the instability tendency of both dampers is similar. The instability remains in the fuselage modes since support is not damped. The modal damping shown in figure 7 is for the case of blade damping and support damping. The viscous damping ratio in the x-and y-fuselage modes is taken as 0.146 and 0.0964, respectively. The effect of piezoelectric damper is similar to that of elastomeric damper. With the inclusion of adequate support damping, the rotor becomes stable for the complete range of rotor speed.

CONCLUSION

The effect of piezoelectric damper on ground resonance is investigated with comparing to elastomeric damper. For the analysis of ground resonance, the blade lag-piezoelectric equations of motion in the rotating frame are transformed to the non-rotating-frame. In addition to fuselage motions, the six differential equations are solved simultaneously through eigenvalue analysis to examine the ground resonance stability characteristics of piezoelectric damper. The investigation is made for the three cases of blade and support damping. For the case of low blade structural damping, the piezoelectric damper has more strong stabilizing effects on the weakly damped lag mode than elastomeric damper. As the inherent damping becomes small, the benefits of the piezoelectric damper increase. Considering the structural damping effect of blade and no support damping, as with the elastomeric damper, the piezoelectric damper lowers the magnitude of the ground resonance instability. With the inclusion of adequate support damping, the piezoelectric damper eliminates the instability.

ACKNOWLEDGEMENT

The research was supported in part by a grant from the BK-21 Program for Mechanical and Aerospace Engineering Research at Seoul National University.

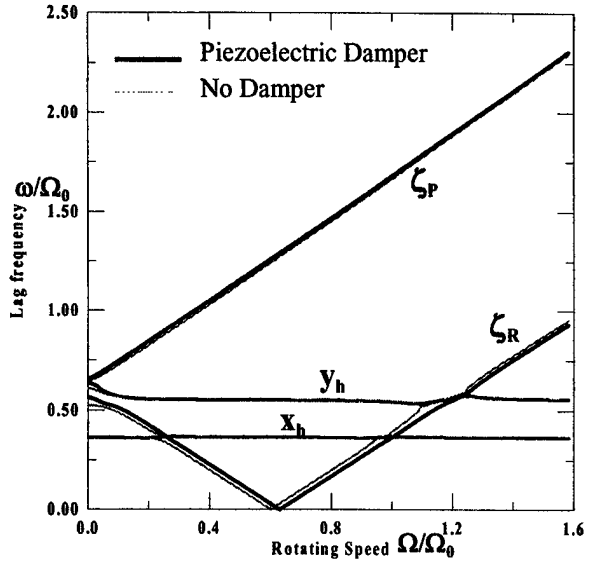


Figure 4. Coleman diagram for piezoelectric damper(no support damping and no blade damping)

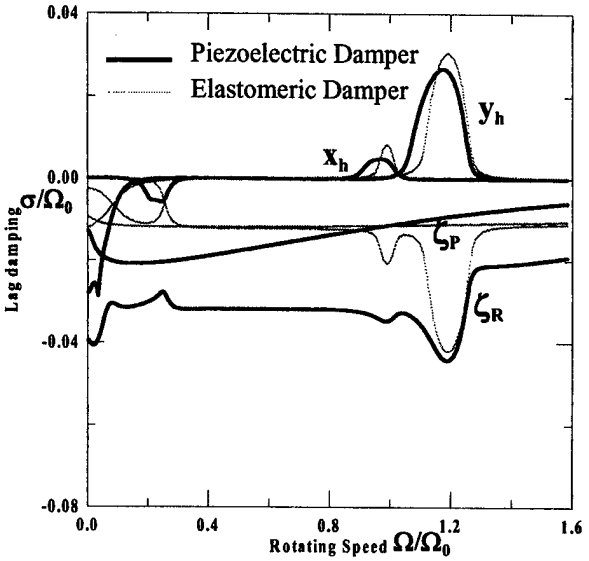


Figure 5. Modal damping for both dampers(no blade structural damping and no support damping)

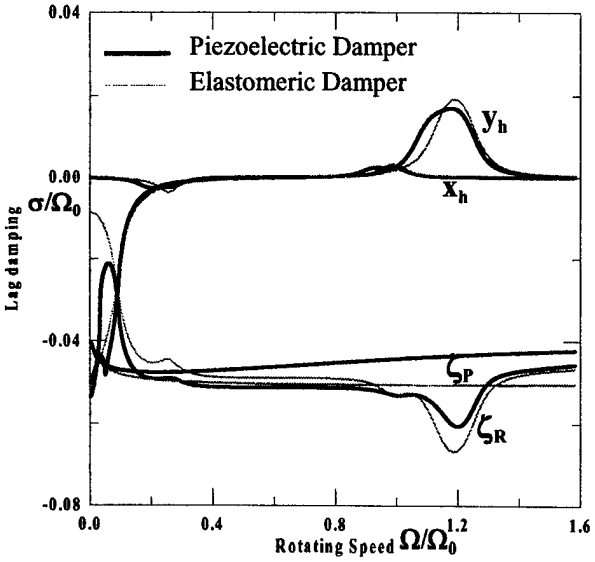


Figure 6. Modal damping for both dampers(blade damping and no support damping)

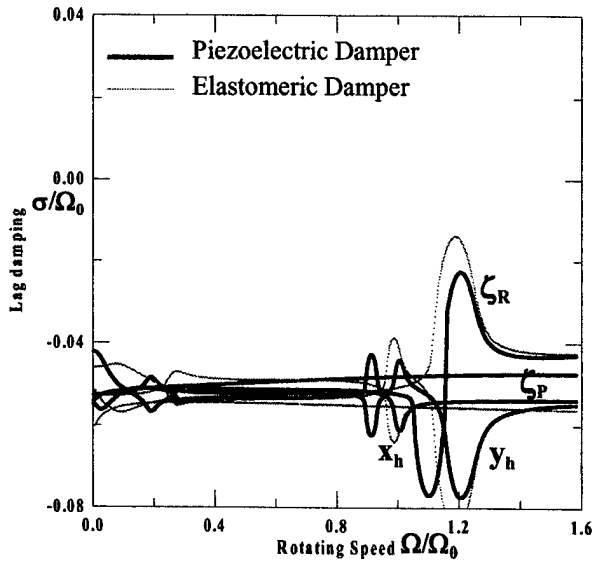


Figure 7. Modal damping for both dampers(blade damping and support damping)

References

1. Robert A. Ormiston,"Investigations of Hingeless Rotor Stability." *Vertica*, Vol. 7, No. 2, pp. 143-181, 1983.
2. Robert A. Ormiston, "The Challenge of the Damperless Rotor" *Preceedings of the 22nd European Rotorcraft Forum*, September 17-17, 1996.
3. N. W. Hagood and E. F. von Flotow, "Damping of Structural Vibrations with Piezoelectric Materials and Passive Electrical Networks", *Journal of Sound and Vibration*, Vol. 146, No. 2, pp. 243-268, 1991.
4. J. J. Hollkamp, "Multimode Passive Vibration Suppression with Piezoelectric Materials and Resonant Shunts", *Journal of Intelligent Material Systems and Structures*, Vol. 5, pp. 49-57, January 1994.
5. Crawly E. F. and DeLuis J, "Use of Piezoelectric Actuators as Elements of Intelligent Structures", *AIAA Journal*, Vol. 25, No. 10, pp. 1373-1385, 1987.
6. S. J. Kim, C. H. Han, and C. Y. Yun, "Improvement of aeroelastic stability of hingeless helicopter rotor blade by passive piezoelectric damping", *Proceedings of SPIE*, Vol. 1991, pp. 1552-1561, 1999.
7. Gandhi, F., and Chopra, I., "An Analytical Model for a Nonlinear Elastomeric Lag Damper and its Effect on Aeromechanical Stability in Hover", *Journal of the American Helicopter Society*, Vol.39, No.4, Oct 1994, pp. 59-69.
8. McGuire, D.P., "The Application of Elastomeric Lead-Lag Dampers to Helicopter Rotors", Lord Library No. LL2133,1976.

SIMULTANEOUS OPTIMUM DESIGN OF STRUCTURAL AND CONTROL SYSTEMS FOR TRUSS STRUCTURE

Yukio Tada, Hidekazu Yuasa

ABSTRACT

This paper proposes an optimum design problem of structural and control systems, taking a 2-D truss structure as an example. The structure is supposed to be subjected to initial static loads and disturbances. The structure is controlled by an output feedback H_∞ controller to suppress the effect of the disturbances. The design variables are the cross sectional areas of truss members. The structural objective function is the structural weight. As the control objective, we consider two types of performance indices. The first function is the H_∞ norm, that is, the performance index for disturbance suppression. The second one is the energy of the response related to the initial state, which is derived from the time integration of the quadratic form of the state in the closed-loop system. Through numerical examples, an advantage of the simultaneous optimum design of structural and control systems is shown.

INTRODUCTION

Conventionally, structural design problems that take into account vibration and methods for control are researched separately. Recently, however, in the area of large scale space structure and electronic devices which must satisfy severe specifications, noting the close relationship between structural and control systems, the necessity of design concept that emphasizes the simultaneous design of both systems has been recognized and many studies have been published [1]~[3]. In the design of structures, it is important to perform the optimization taking factors on the structural strength such as stress and strain into consideration. It holds also in the simultaneous design. However, it is difficult to predict behaviors of variables such as the maximum stress during transient response in time and space. We think that it is possible to consider the structural strength such as strain energy and kinetic energy by evaluating the integral

Yukio Tada, Faculty of Engineering, Kobe University, Rokkodai, Nada, Kobe 657-8501 Japan
Hidekazu Yuasa, Power Tool Products Division, Matsushita Electric Works, Ltd., 33 Okamachi, Hikone, Shiga 522-8520 Japan

of quadratic of states during the observatory time. By the minimization of this integral, we can reduce the average magnitude of response and constraints such as stress one are considered by operating other constraint (for example, constraint on the structural weight).

In this paper, a two-dimensional truss structure is treated as a design object, which begins to vibrate from the deformed state due to static loads (initial loads) and is also subjected to continuous disturbances. First, the design object is represented by FEM and a reduced model obtained by the use of the modal transformation is adopted as a control object. As the error due to the reduction of modes is regarded as additive one, we design H_∞ controller by output feedback in order to obtain robust stability.

The objective function in the optimization is the structural weight for the structural system. For the control system, H_∞ norm of the transfer function from disturbance to controlled output is adopted as the evaluating factor in order to reduce the influence of disturbances. In addition, for the evaluation of structural strength, the integral of quadratic forms of state variables is also considered. This multi-objective problem is solved by the formulation based on both ε -constraint method and weighting method. The optimization of the obtained function is performed by the complex method.

TRUSS STRUCTURE AND ITS CONTROL PROBLEM

System Modeling

Through the modeling by Finite-Element-Method, the equation of motion of the object structure is described by the following one with n degrees of freedom

$$M_s\ddot{q} + D_s\dot{q} + K_s q = L_1 w + L_2 u \tag{1}$$

where M_s, D_s and K_s are the stiffness matrix, mass matrix and damping matrix, respectively and q $\in R^n$, w and u are displacement vector, disturbance input and control input, respectively. As it is impossible to control all vibration modes, the system freedom is reduced by the modal transformation as

$$q = \Phi\xi \quad , \quad \Phi^T M_s \Phi = I_r \tag{2}$$

where $\Phi \in R^{nxr}$ is the matrix of eigenmodes of the system and r is the adopted degrees of freedom. After the modal transformation, the state equation of the control object is given as

$$\begin{cases} \dot{x}_s = A_s x_s + B_{1s} w + B_{2s} u \\ z_s = C_{1s} x_s + D_{12s} u \\ y = C_{2s} x_s + D_{21s} w \end{cases} \quad , \quad x_s = \begin{bmatrix} \xi \\ \dot{\xi} \end{bmatrix} \tag{3}$$

where the observed output is defined by the original system state added by an infinitesimal disturbance and as the controlled output, we adopt

$$z_s = \begin{bmatrix} \omega_1 \xi_1 & \cdots & \omega_r \xi_r & \dot{\xi}^T & u^T \end{bmatrix}^T \tag{4}$$

for evaluating structural responses as undermentioned, where ω_i is the i-th eigen angular frequency.

H_∞ Control Problem

In the H_∞ control problem, such a controller is considered that stabilizes the closed loop system and by which the H_∞ norm of the closed loop transfer function from disturbance input w to controlled output z, $G_{zw}(s)$, satisfies the following condition

$$J_n = \|G_{zw}(s)\|_\infty < \gamma \tag{5}$$

for a small positive γ [4]. The smaller J_n (or γ) is, the more we can suppress the influence of the disturbances.

In this study, for the elevation of control performance and in order to obtain a design which is robust for the modeling errors, we introduce two weighting functions $W_1(s)$ and $W_2(s)$; $W_1(s)$ is applied to the transfer function from disturbance to controlled output y and which has a large gain in the region of low frequency. And $W_2(s)$ is applied to the transfer function from disturbance to control input and has a large gain in the region of high frequency. The latter is introduced for the suppression of the spillover due to ignored modes. Moreover, we assume that the disturbance affects the system in low frequency area and introduce a weighting function W_F as a filter that has a large gain in the region of low frequency.

Considering these terms, H_∞ control problem with frequency-weights is expressed as the problem that searches for a controller which satisfies

$$\left\| \begin{matrix} T_{z_s w} \\ W_1 T_{yw} \\ W_2 T_{uw} \end{matrix} \right\|_\infty < \gamma \quad . \tag{6}$$

From Eqs.(3) and(6), the state equation of the closed loop is expressed as

$$\begin{cases} \dot{\tilde{x}} = \tilde{A}\tilde{x} + \tilde{B}w \\ z = \tilde{C}\tilde{x} \end{cases}, \quad \tilde{x} = \begin{bmatrix} x \\ \hat{x} \end{bmatrix} \tag{7}$$

where x is the combined state of control object and weighting functions and $\hat{x}$ is the estimated value from the observer in output feedback control. In the above equations, coefficients are given by Riccati solution matrices, X and Y, and the following Riccati equation holds

$$\tilde{A}^T P + P\tilde{A} + \frac{1}{\gamma^2} P\tilde{B}\tilde{B}^T P + \tilde{C}^T \tilde{C} = 0 \quad . \tag{8}$$

$$P = \begin{bmatrix} \gamma^2 Y^{-1} & -(\gamma^2 Y^{-1} - X) \\ -(\gamma^2 Y^{-1} - X) & \gamma^2 Y^{-1} - X \end{bmatrix} \tag{9}$$

Objective Functions

In this paper, we consider following three items; the structural weight W for the weight minimization, H_∞ norm J_n for the suppression of the influence of disturbances and an integral of quadratic forms of the state $\tilde{x}$ for the minimization of structural responses. As to the third item, if we adopt weighing matrix Q as $Q = \tilde{C}^T\tilde{C}$, the integral is resolved as

$$J_{e1} = \int_0^\infty \tilde{x}^T Q\tilde{x}dt = \int_0^\infty \tilde{x}^T\tilde{C}^T\tilde{C}\tilde{x}dt = \int_0^\infty {z_1}^T z_1 dt + \int_0^\infty {z_2}^T z_2 dt + \int_0^\infty \{q^T K_s q + \dot{q}^T M_s \dot{q} + u^T u\}dt \quad (10)$$

from the definition of the controlled output, Eq.(4), where z_1 and z_2 are outputs of weighting functions, W_1 and W_2, respectively. The third integral in the last equation represents the strain energy, kinetic energy and control cost. Therefore, J_{e1} can be regarded as a function that includes the evaluation of structural strength.

On the other hand, from the specification of H_∞ control, Eq.(5), we can obtain the relation

$$J_{e1} = \int_0^\infty \tilde{x}^T Q\tilde{x}dt = \int_0^\infty \tilde{x}^T\tilde{C}^T\tilde{C}\tilde{x}dt \le \gamma^2 \int_0^\infty w^T w dt + \tilde{x}_0{}^T P\tilde{x}_0 \quad . \quad (11)$$

The first term of the right hand side is given by disturbances and the second term

$$J_{e2} = \tilde{x}_0{}^T P\tilde{x}_0 \quad (12)$$

is related to the initial state of the system, $\tilde{x}_0$. By making J_{e2} smaller, we can reduce J_{e1}. Then, instead of J_{e1}, we adopt J_{e2} as the objective function for the structural strength.

In this paper, we assume that the truss begins to vibrate when it is subjected to initial static loads. Then, $q_0 = K_s^{-1}p_0$. Assume that it is impossible to know the initial loads definitely but we can know it by probabilistic low as

$$p_0 = p_0' + \psi, \qquad E[p_0] = E[p_0'] = p_0', \qquad E[\psi] = 0 \quad . \quad (13)$$

where p_0' is the expected initial load and Ψ is a random variable whose mean is zero. The notation $E[\ ]$ represents the operation for calculating the average value of its argument. The covariance matrix of the initial load is

$$Cov(p_0, {p_0}^T) = E[(p_0 - p_0')(p_0 - p_0')^T] = E[\psi\psi^T] \quad . \quad (14)$$

As the initial value of the modal coordinate is given from the displacement vector q_0, the initial state of the system is expressed as the function of the initial load p_0 as

$$x_{s0} = \begin{bmatrix} \xi_0 \\ 0 \end{bmatrix} = \begin{bmatrix} \Phi^{-1} q_0 \\ 0 \end{bmatrix} = \begin{bmatrix} \Phi^T M_s q_0 \\ 0 \end{bmatrix} = \begin{bmatrix} \Phi^T M_s K_s{}^{-1} p_0 \\ 0 \end{bmatrix} = \begin{bmatrix} S p_0 \\ 0 \end{bmatrix} \quad . \quad (15)$$

When the initial load p_0 is a random variable, its response J_{e2} also must be considered as a random variable. Therefore, we consider the expected value of response, J_{e2}, $J_e = E[J_{e2}]$, as the object function of the control system instead of J_{e2} and we call it initial-state-energy.

$$J_e = E[J_{e2}] = E[\tilde{x}_0{}^T P \tilde{x}_0] = \gamma^2 trace\left(\begin{bmatrix} SE[\psi\psi^T]S^T & 0 \\ 0 & 0 \end{bmatrix} Y^{-1} \right) + \begin{bmatrix} (Sp_0')^T & 0 \end{bmatrix} X \begin{bmatrix} Sp_0' \\ 0 \end{bmatrix} \quad (16)$$

FORMULATION OF OPTIMIZATION PROBLEM

For solving the present three-objective problem, we use the ε -constraint method and weighting method. That is, by restricting the structural weight to given specified value, we search for the optimum cross sectional areas of truss members that minimize the weighted sum of both objective functions from the control system. The problem is formulated as follows

$$\min_a J(a) = s\frac{J_n(a)}{J_{n0}} + t\frac{J_e(a)}{J_{e0}} \qquad (s+t=1) \quad (17)$$

$$\text{s.t.} \quad J_m = W(a) = \sum_{i=1}^{n_O} \rho_i l_i a_i = W_c \quad (18)$$

where a_i, l_i and ρ_i are the cross sectional area, length and density of the i - th member of truss, a is a set of design variables (cross sectional areas) and W_c is a specified value for structural weight constraint. J_{n0} and J_{e0} are H_∞ norm and initial-state-energy of the initial truss which has members of uniform cross section, respectively, and s and t are weightings for respective objective functions. In addition to Eq.(18), we introduce the side constraint for limiting maximum and minimum sizes of cross sectional areas. As a method for optimization, we use the complex method [5].

DESIGN EXAMPLE

Design Object

The design object in this paper is a 2-dimensional truss as shown in Figure1. This truss has a non-dimensional sizes (length of long members is 2.0 and that of short members is 0.2) and material characteristics (density is 1.0) and the weight of the initial truss is 30.8. The displacement of the truss is constrained at nodes 10 to 13. Sensors and actuators are located at the central node (node 7) in x and y directions and sensors can measure the displacements of node 7. As to the structural design, since it is not always proper to vary member sizes independently, we take into consideration the structural symmetry and treat only 7 design variables (cross sectional areas). The initial static loads are applied at nodes 6,7 and 8 with their means p_o' = [0, $\cdots$,0,[1,-2,1,-2,1,-2],0,$\cdots$,0]^T. These loads are independent with each other and their covariance matrix is given by $Cov(p_0, p_0{}^T)$ = $diag$[0,$\cdots$,0,[1,1,1,1,1,1],0,$\cdots$,0]x10^{-2}. Moreover, continuous disturbances act at node 7. In the control design, we deal with only first two modes. The characteristic of the damping is assumed as D_s = 0.001 x M_s + 0.001 x K_s.

Relation Between Structural Weight And H_∞ Norm

Setting the weightings s and t in Eq.(17) as $s = 1.0$ and $t = 0.0$, that is, when we consider only the H_∞ norm as the objective function from the control system, we solve the optimization problem for several values of the constraint, specified structural weight W_c. Figure 2 shows the relation between the specified value of the structural weight, W_c, and the minimum of the H_∞ norm obtained. The point "a" corresponds to "Design a" which was obtained by designing only the control system with the γ -iteration method for the initial truss. By optimizing the member sizes we can reduce H_∞ norm and obtain "Design b" (the point "b") with the same structural weight as the initial truss. Moreover, the effectiveness of the simultaneous design is observed in Figure 2. For example, in "Design c", we can make the structural weight smaller by keeping the value of H_∞ norm small as "Design b". Thus, by the simultaneous optimization, we can make both structural weight and H_∞ norm smaller than the controller-only design.

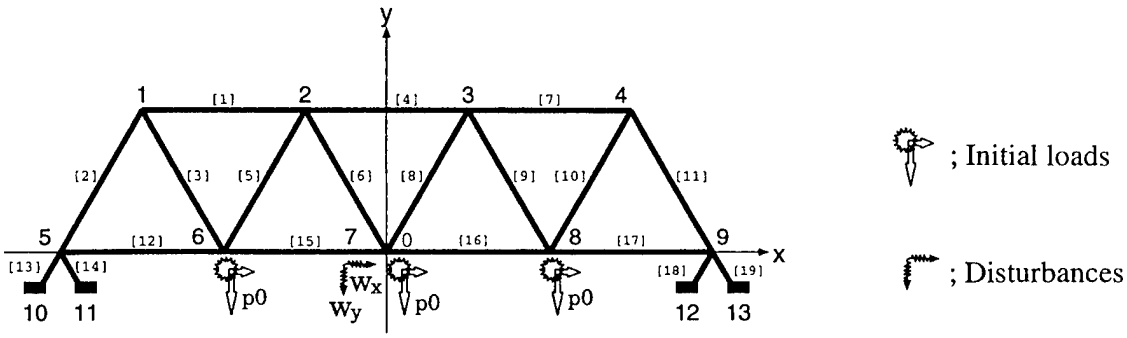


Figure 1. 2-D truss structure

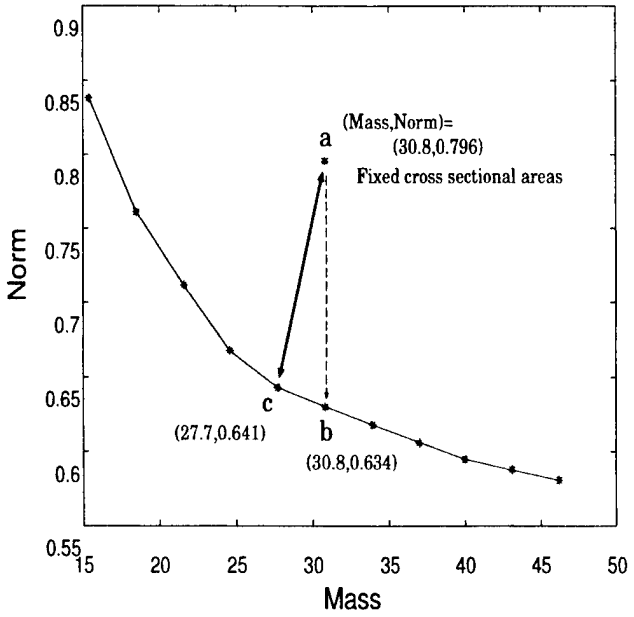


Figure 2. Pareto optimality of two objectives for structural weight and H_∞ norm

Relation Between H_∞ Norm And Initial-State-Energy

Next, we solve the optimization problem, Eqs.(17) and (18) by varying the weightings s and t with constraining the structural weight to that of the initial truss. In Figure 3, the initial-state-energy and H_∞ norm are plotted at the minimum of the combined objective function J for several sets of weightings s and t. It is observed from Figure 3 that the two objective functions about the control system conflict with each other and it is impossible to minimize both functions at the same time. Among Pareto optimum solutions in Figure 3, we select two designs "b" and "d" and compare them. Though the difference in H_∞ norm for "Design d" and "Design b" is small, "Design d" which is obtained considering not only H_∞ norm but also the initial-state-energy has a smaller initial-state-energy than "Design b" which is obtained considering only H_∞ norm. Examples of initial responses in displacement and in stress are shown in Figures 4 and 5, respectively. In these figures, solid lines show responses in controlled cases and broken lines are cases without control. Figure 4 shows the displacement in y direction at node 7 and Figure 5 shows the stress of the member [15]. It is observed from Figure 4 that as both designs have almost near values of H_∞ norm, both trusses satisfy near specification for disturbance suppression and vibrations attenuate with similar manners. On the other hand, in the response of stress, Figure 5, the attenuation of stress is comparatively more earlier in "Design d" which takes into consideration the initial-state-energy than in "Design b". From these, it can be said that "Design d" is a good one which can reduce both H_∞ norm and the initial-state-energy.

CONCLUSION

In this paper, we show the effectiveness of simultaneous optimization of structural system

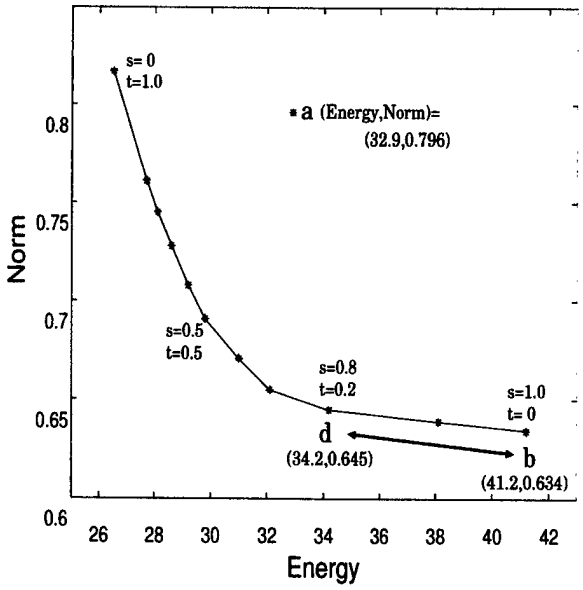
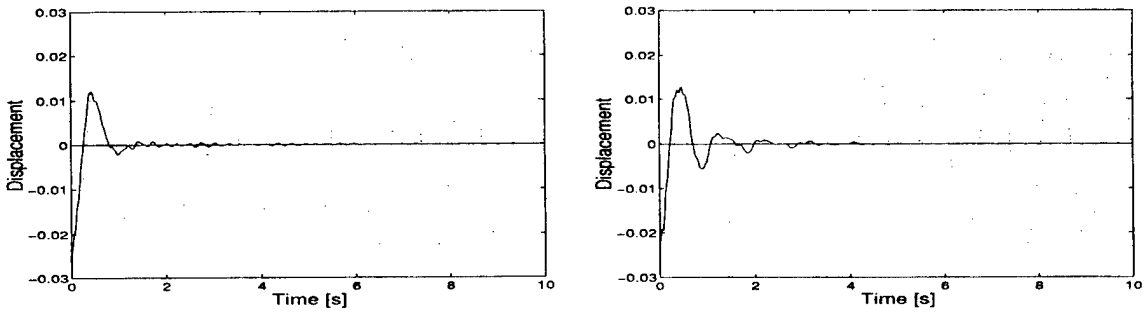
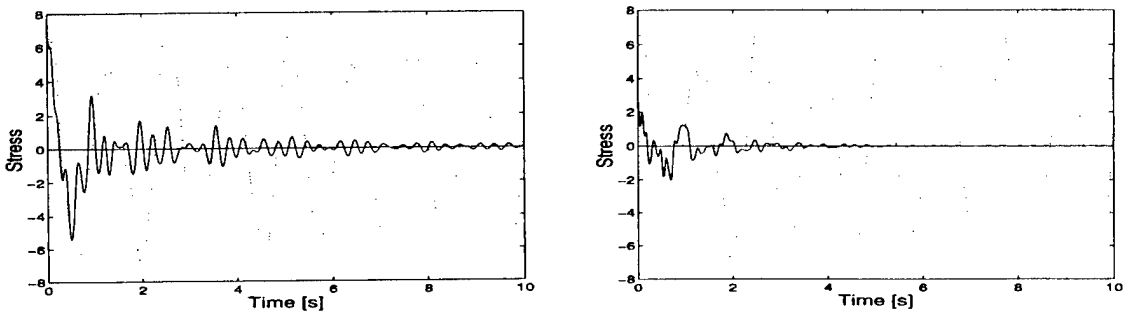


Figure 3. Pareto optimality of two objectives for H_∞ norm and initial-state-energy



(a) Design b ($s = 1.0$, $t = 0.0$) (b) Design d ($s = 0.8$, $t = 0.2$)

Figure 4. Comparison of initial responses in displacement



(a) Design b ($s = 1.0$, $t = 0.0$) (b) Design d ($s = 0.8$, $t = 0.2$)

Figure 5. Comparison of initial responses in stress

and control one through the design of 2-dimensional truss. The formulated problem is a multi-purpose one and from the consideration of Pareto optima, the followings are concluded; 1. We can make both structural weight and H_∞ norm more smaller than control-only design. 2. By selecting proper weightings, we can obtain strong truss with good control performance.

REFERENCES

1. Khot, N.S., 1991. "Combined Design of Structural and Control System", in *Computational Mechanics '91*, ICES Publications, pp.490-496.
2. Iwatsubo, T., Kawamura, S. and Adachi, K. 1993. "Research Trends and Future Subjects on Simultaneous Optimum Design of Structural and Control Systems for Mechanical Structure", *Trans. Jpn. Soc. Mech. Eng.* (in Japanese), 59 (559), C, pp.631-637.
3. Kajiwara, I., Tsujioka, K. and Ngamatsu, A. 1994. "Approach for Simultaneous Optimization of a Structure and Control System", *AIAA J.*, 32 (4), pp.866-873.
4. Mita, T. 1994. *H_∞ Control* (in Japanese). Shoukoudou.
5. Box, M.J. 1965. "A New Method of Constrained Optimization and a Comparison with Other Methods", *Computer J.*, 8, p.42.

COMBINED DESIGN OF STRUCTURAL AND CONTROL SYSTEMS WITH CONSIDERATION OF THE LOCATION OF SENSOR/ACTUATOR

Yukio Tada, Jun Yamazaki

ABSTRACT

In this paper, a problem of combined design of the structural system and the control one is proposed. One problem is treated that determines structural specification to aim the minimum weight design and to control vibration when we suppose that disturbance acts on the structure. As design variables of structural system, we adopt cross sectional areas of base and vertical members. In addition, we adopt the location of sensor/actuator as a design variable of control system. We adopt structural weight as structural objective function and H_∞ norm of the transfer function from disturbance input to controlled output as control objective function. We seek the solution of this optimum design problem by using weighting method and simplex method for this multi-purpose problem. From the result of a numerical example, the effectiveness of combined design and considering the location of sensor/actuator is shown.

INTRODUCTION

In design of controlled structures, the problem of structural design considering vibration and the problem about active control have been researched separately[1-3]. However, designs of large scale structures like space structures need the consideration not only of safety but also of light weight. To achieve the design purpose of such light weight causes the problem whether it is possible to satisfy the constraint about safety and vibration control. Thus, there is a close relationship between the structural system and the control one

Yukio. Tada, Department of Computer and Systems Engineering, Kobe University, 1-1 Rokkodai, Nada, Kobe 657-8501 Japan

Jun. Yamazaki, Div. of Computer and Systems Eng., Graduate School of Science and Technology, Kobe University, 1-1 Rokkodai, Nada, Kobe 657-8501 Japan

and the combined design that designs the structural system and control one as one system becomes necessary. Moreover, as large scale structures also have large degrees of freedom, the location of sensor/actuator naturally has large degrees of freedom. Therefore, it is important to consider the location of sensor/actuator for better control.

DESIGN OF STRUCTURAL AND CONTROL SYSTEMS

Modeling

The equation of motion of the truss structure modeled by finite element method is shown as

$$M_s\ddot{q} + D_s\dot{q} + K_s q = L_1 w + L_2 u \tag{1}$$

where M_s, D_s and K_s are the mass matrix, damping matrix, and stiffness matrix, respectively. q is a displacement, w is a disturbance input, u is a control input, L_1 is an arrange matrix of disturbance input and L_2 is an arrange matrix of control input. It is actually impossible to control all degrees of freedom in designing large scale structures. Then, we lower dimensions of the system by using modal transformation. In other words, we transform the displacement vector q into the vector ξ of mode coordinate as

$$q = \Phi\xi \tag{2}$$

where $\Phi \in R^{n\times r}$ is the mode eigen-matrix of the system and r is the number of adopted modes. Then, the state equation of the system can be expressed as

$$\begin{cases} \dot{\eta} = A\eta + B_1 w + B_2 u \\ z = C_1\eta + D_{12}u \\ y = C_2\eta + D_{21}w \end{cases} \tag{3}$$

$$\eta = \begin{bmatrix} \xi \\ \dot{\xi} \end{bmatrix}, \; A = \begin{bmatrix} 0 & I_r \\ -\Omega^2 & -\Lambda \end{bmatrix}, \; B_1 = \begin{bmatrix} 0 \\ \Phi^T L_1 \end{bmatrix}, \; B_2 = \begin{bmatrix} 0 \\ \Phi^T L_2 \end{bmatrix}$$

$$\Omega^2 = \Phi^T K \Phi = diag(\omega_1^2, \omega_2^2, \cdots, \omega_r^2), \; \Lambda = \Phi^T D_m \Phi$$

where z and y are a controlled output and an observed output, respectively. Ω^2 is the eigenvalue matrix and w_i is the ith eigen angular frequency.

Design of Control System

The present study accepts the H_∞ control theory[4-5] as control design to suppress

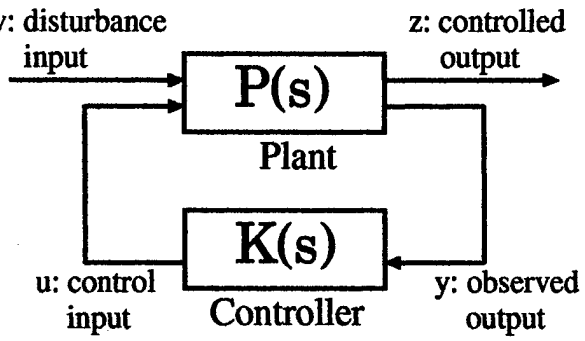


Figure 1. H_∞ control system

vibration due to disturbance. First, H_∞ norm for a stable transfer function from the disturbance input to the controlled output, $G(s)$, is defined as

$$\|G(s)\|_\infty = \sup_\omega \sigma_{max} G(j\omega) \tag{4}$$

where $\sigma_{max} G(j\omega)$ is the maximum singular value of $G(j\omega)$. In H_∞ control theory, the problem to determine the controller which satisfies next two conditions is considered. First, the closed-loop system from the disturbance input w to the controlled output z is stable. Second, H_∞ norm satisfies the following inequality,

$$G = \|G_{zw}(s)\|_\infty < \gamma \tag{5}$$

where γ is a positive constant and the smaller it is, the more the system can reduce the influence of disturbance.

In addition, the state of the system cannot always be measurable. Then, we use H_∞ control theory by output feedback. Figure 1 shows a diagram of the H_∞ control system.

FORMULATION OF DESIGN PROBLEM

In this study, we use cross sectional areas which are concerned with lightening and stiffness of the structural system as design variables of structural system. But, for reduction of computational complexity, we adopt cross sectional areas of base and vertical members as design variables because we think that the influence of disturbance on them is big. In addtion, we think that it is important to take account of the number and location of sensor/actuator. Then, we adopt the location of sensor/actuator as design variables of control system. But as premises, we assume that following conditions are satisfied. First, only one sensor/actuator is used. Second, sensor/actuator is arranged at collocation.

Definition of Objective Function

First, we adopt structural weight W as the structural objective function J_m. Here, in order to normalize, we divide this by the weight of the initial structure that has uniform cross sectional areas, W_0.

$$J_m = \frac{W}{W_0} \tag{6}$$

$$W = \sum_{i=1}^{n} \rho_i l_i a_i \tag{7}$$

where ρ_i, l_i and a_i are density, length and cross sectional area of the ith member, respectively.

Next, we adopt H_∞ norm of the transfer function from disturbance to controlled output, G, as the objective function of control system. Similary, in order to normalize, we divide this by H_∞ norm of the initial structure when sensor/actuator is arranged in y-direction at node 49, G_0.

$$J_n = \frac{G}{G_0} \tag{8}$$

Multi-Purpose Problem

The solution of the design problem that minimizes the structural objective function is not always identical with one that minimizes the objective function of control system. Usually, the minimization of respective functions may conflict. Thus, the design problem becomes a multi-purpose optimization one. Then, in this study, we transform structural and control objective functions into a single-purpose problem by using weighting method. In this method, minimization of a weighed sum of two objective functions, $J(a,b)$, is considerd, as

$$\min_{a,b} \quad J(a,b) = w_m J_m(a) + w_n J_n(a,b) \tag{9}$$

$$s.t. \quad w_m + w_n = 1 \tag{10}$$

$$a_{min} \leq \quad a \quad \leq a_{max} \tag{11}$$

where a is a set of design variables from cross sectional areas and b is a design variable which represents the location of sensor/actuator. w_m and w_n are weightings for respective objective functions. a_{max} and a_{min} are specified maximum and minimum values of cross sectional areas, respectively.

Optimum Design Method

Using the objective function and constraint formulated, we search for the optimum

solution by simplex method[6]. As a characteristic in this study, from a point of view that we take account of the location of sensor/actuator, we use the following simplex method.

We think that the most suitable location of sensor/actuator should exist in each candidate structure. In this study, we define the most suitable location as the location where H_∞ norm becomes minimum. In other words, First, we assume design variables of cross sectional areas. Next, for the obtained structure, we search for the optimum location of sensor/actuator by changing their location in turn. That is, once cross sectional areas are determined, a design point in simplex space has its own optimum sensor/actuator location.

By using this method, we regard design variables as only cross sectional areas whose sets have respective optimum sensor/actuator locations. Then, the objective function of control system and the weighted objective function can be regarded as functions in cross sectional areas only, that is, $J_n(a, b(a))$ and $J(a, b(a))$.

DESIGN EXAMPLE

Design Object

The design object of this paper is a three-dimensional truss structure as shown in Figure 2. Nodes $1 \sim 8$ are fixed in all x, y and z directions. Disturbances act in y direction at nodes 49 and 50. To arrange sensor/actuator at all nodes in this structure is

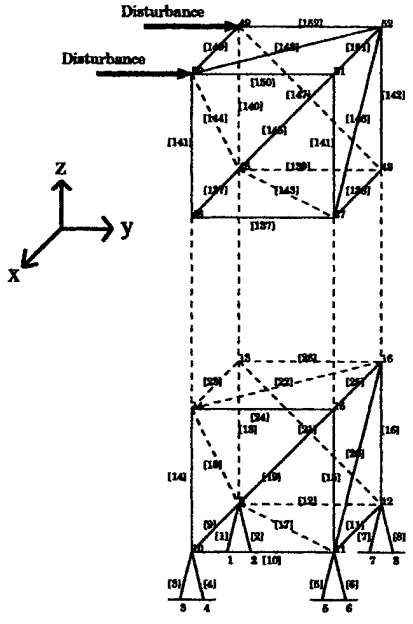


Figure 2. 3-D truss structure

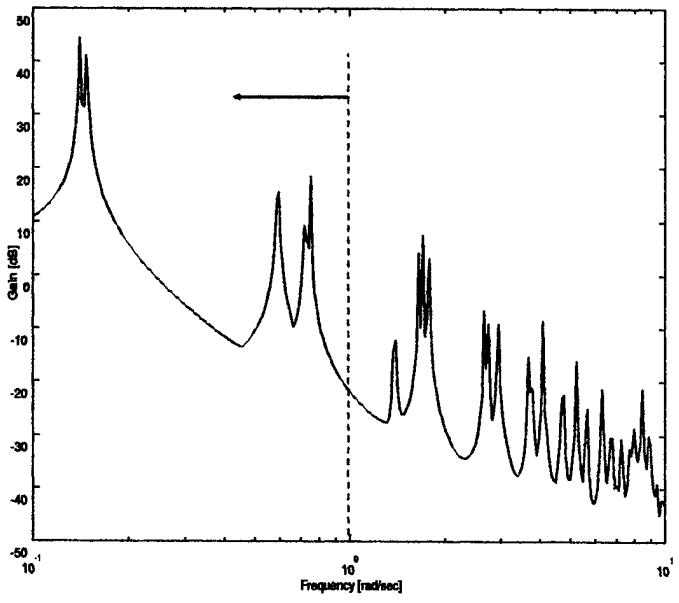


Figure 3. Frequency characteristic of the Initial-Structure

not practical. Then, we arrange only one sensor/actuator in one of x, y and z directions at a node from 9 to 52, and at collocation. The sensor can measure displacement in an arranged direction and at an arranged node, and the actuator can supply the control input in the arranged direction at the arranged node. Here, we call the structure with uniform initial cross sectional areas Initial-Structure, as mentioned before.

Figure 3 shows frequency characteristics in the Initial-Structure. From the figure, we think that first 5 modes are dominant in vibration. Then, we adopt first 5 modes in modal analysis.

Design Example

First, we perform Control-Only Design that designs the control system for given Initial-Structure with considering the location of sensor/actuator. Next, we perform the combined design whose weighting coefficients in the weighting method are $w_m = 0.4$ and $w_n = 0.6$, respectively. Table 1 shows the comparison of results of structural weight and H_∞ norm and Table 2 shows the most suitable location of sensor/actuator in each

TABLE 1. Comparison of two designs

	structural weight	H_∞ norm
Control-Only Design	1696.5	68.52
Combined Design	1656.4	17.71

TABLE 2. Optimum sensor/actuator location

	Node number	Direction
Control-Only Design	52	y
Combined Design	52	y

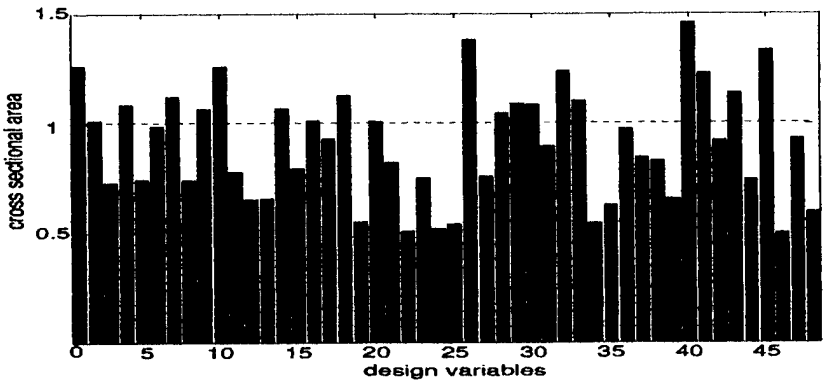


Figure 4. Distribution of cross sectional areas

designed structure. Figure 4 shows the distribution of obtained cross sectional areas that are design variables of structural system.

It is found from Table 1 that both structural weight and H_∞ norm are reduced by the combined design as compared with Control-Only Design. Then, the effectiveness of the combined design is shown.

Next, we examine the effectiveness of considering the location of sensor/actuator. Node 52 is the most suitable location of sensor/actuator in optimized structure. Here, in order

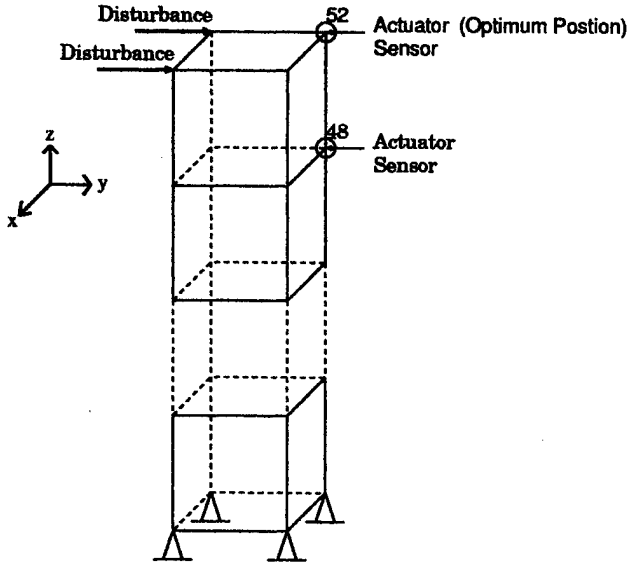


Figure 5. Location of sensor/actuator

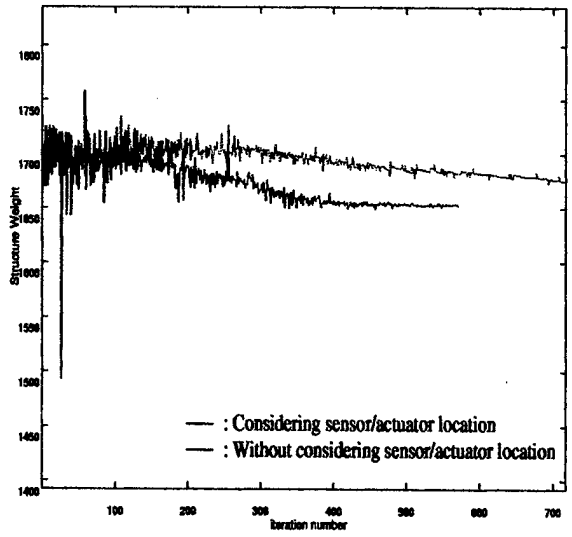


Figure 6. Behaviors of the structural weight

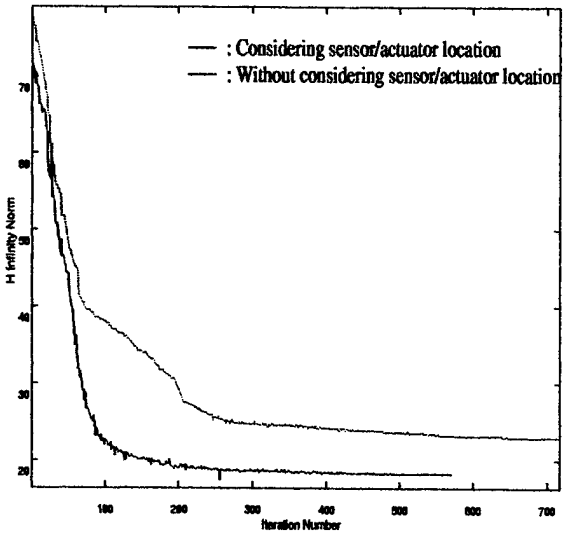


Figure 7. Behaviors of H_∞ norm

to examine the effectiveness of considering the location of sensor/actuator on design, we arrange sensor/actuator in y-direction at node 48 as shown in Figure 5 and we perform the combined design on only cross sectional areas without considering the location of sensor/actuator. And then, we compare these two designs. Figures 6 and 7 show the behaviors of structural weight and H_∞ norm, respectively. From these results, clear differences in both structural weight and H_∞ norm are found. Therefore, the effectiveness of considering the location of sensor/actuator is shown.

CONCLUSION

This study dealed with the combined design of structural and control systems instead of the design from only one side of structural or control system for the three-dimensional truss structure. We think that the location of sensor/actuator affects the control system deeply when we control the structure. Then, we suggest a combined design method with considering the location of sensor/actuator, premising that only one sensor/actuator is arranged at collocation. From numerical results, we can find that both of the structural weight and H_∞ norm are reduced by the combined design. Then, the effectiveness of Combined Design is shown. Moreover, we show the effectiveness of considering the location of sensor/actuator.

REFERENCES

1. Iwatsubo, T., Kawamura, S., and Adachi, K. 1993. "Research Trends and Future Subjects on Simultaneous Optimum Design of Structural and Control Systems for Mechanical Structure (in Japanese)," *Trans. Jap. Soc. Mech. Eng.*, 59(559), pp.631-637.

2. Kajiwara, I., Tsujioka, K., and Nagamatsu, A. 1994. "Approach for Simultaneous Optimization of a Structure and Control System," *AIAA Journal*, 32(4), pp.866-873.

3. Khot, N. S. 1991. "Combined Optimum Design of Structural and Control System," *Computational Mechanics '91-Theory and Applications-*, pp490-496.

4. Doyle, J. C., Francis, B. A., and Tannenbaum, A. R. 1989. "State-Space Solutions to Standard H_2 and H_∞ Control Problems," *IEEE Trans.*, 34(8), pp831-847.

5. Tada, Y., Ikeda, M., Kan, S., and Terao, H. 1998. "Optimum Design of Structures with Disturbunce Suppression by H_∞ Control (Output Feedback Case)," *JSME International Journal, Series C*, 41(4), pp.759-765.

6. Box, M. J., Davis, D., and Swann, W. H. 1969. "Non-linear optimization techniques," *Imperial Chemical Industries Ltd.*

MATERIAL STRUCTURE DESIGN OF STRESS-DEPENDENT ADAPTIVE STIFFNESS

Masao Tanaka,[1] Masahiro Todoh,[2] Kazushige Oki,[3] Akihisa Naomi[3]

ABSTRACT

Use of functional material is a primitive and most promising approach to the functional structural system, e.g. adaptive/smart structures. It, however, is not always necessary for a certain aspect of such structural function. This study proposes a material structure design approach to the stress-dependent anisotropic adaptive stiffness by using the conventional linear elastic material of isotropy. The structural design problem has been formulated for the material structure consist of mesoscopic unit cells and solved by using the simple isotropic material with penalization (SIMP) method for the topology design and the traction method for the geometry design for microstructure of the unit cell. The effectiveness of the proposed idea has been examined through numerical studies in two-dimensional cases.

INTRODUCTION

The internal structure of material plays the critical role in the designed material characteristics in the traditional and smart composite materials [1]. Such a material structural design is also expected to work as a key feature in the design of adaptive mechanical systems. In fact, the structure-mechanism intersection has been an important category in the adaptive structure studies, and the conventional material, for example, has been used to realize a micro-mechanism [2] by choosing the structural topology and geometry appropriately. The use of functional material is straightforward to evolute them to more adaptive/smart ones, for instance, microelectromechanical systems (MEMS) [3] and microactuators [4]. Although the functional material has the capability to adjust the material structural characteristics directly, a certain aspect of such adjustment could be realized only by using the elastic behaviour of the material itself. That is, elastic deformation at the microstructure in the material structural system may cause the topological change of the microstrucre followed by the alteration of the material characteristics in accordance with the increase/decrease of deformation. This is the concept of stress-dependent adaptive stiffness.

This article discusses the concept of the stress-dependent anisotropic adaptive stiffness by using very standard passive linear elastic material of isotropy, and the structural design problem

[1]Professor, [2]Research Associate, [3]Graduate Student, Division of Mechanical Science, Department of Systems and Human Science, Graduate School of Engineering Science, Osaka University, 1-3 Machikaneyama, Toyonaka, Osaka 560-8531, Japan

is formulated for structural topology and geometry in the mesoscopic unit cell.

STRESS-DEPENDENT ADAPTIVE STIFFNESS

Basic Concept

The concept of stress-dependent anisotropic adaptive stiffness has two aspects: anisotropic mechanical properties made of isotropic material and stress-dependent adaptive stiffness of piecewise linear elasticity made of linear elastic material. The first aspect is coming from the idea of inverse homogenization for the materials with prescribed constitutive parameters [5]. The second aspect is related to the variable stiffness, that is the piecewise-linear constitutive characteristics, by incorporating the topology change due to the transition between the opening and the closure at the internal gap in the structure [6]. The stress-dependent adaptive stiffness as the macroscopic material system is, thus, expected to be realized by means of the structural topology and geometry design of the microstructure in the mesoscopic unit cell.

Homogenization

Consider the macroscopic material structural system that is made of mesoscopic unit cells arranged periodically and uniformly. The size of unit cell, ϵ is much smaller than that of the whole macroscopic structure, d. Within the mesoscopic unit cell, the material distribution is not uniform exhibiting some internal microscopic structure. Figure 1 illustrates the hierarchy of such a material system. The homogenization technique is a standard tool to characterize the macroscopic properties of such a macroscopic material structural system in general [5].

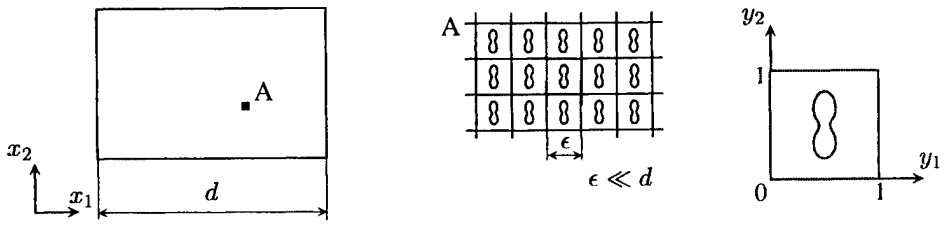
In the two-dimensional elasticity, the macroscopic material properties is characterized in terms of constitutive equation relating the macroscopic strain tensor ϵ_{kl} to the stress tensor σ_{ij}

$$\sigma_{ij} = E^H_{ijkl}\epsilon_{kl} \tag{1}$$

where E^H_{ijkl} is a tensor of material constants. In the context of the homogenization technique, the macroscopic constitutive parameters is written as

$$E^H_{ijkl}(\chi^{ij}_p, \chi^{kl}_p) = \frac{1}{|Y|}\int_Y E_{pqrs}\left(\epsilon^{0(ij)}_{rs} - \frac{\partial \chi^{ij}_r}{\partial y_s}\right)\left(\epsilon^{0(kl)}_{pq} - \frac{\partial \chi^{kl}_p}{\partial y_q}\right)dY \tag{2}$$

The characteristic displacement χ^{kl}_p of the unit cell is the weak form solution to the base cell



(a) Macroscopicstructure material system (b) Mesoscopic unit cells (c) Microstructure of unit cell

Figure 1. Hierarchy of materail structure system.

under the periodic boundary conditions subject to three independent cases of macroscopic strain $\epsilon_{pq}^{0(kl)}(k,l=1,2,p,q=1,2)$:

$$\int_Y E_{ijpq}\frac{\partial \chi_p^{kl}}{\partial y_q}\frac{\partial v_i}{\partial y_j}dY = \int_Y E_{ijkl}\frac{\partial v_i}{\partial y_j}dY \tag{3}$$

$$\epsilon_{pq}^{0(kl)} = \begin{cases} 1 & \text{for} \quad k=p, l=q \\ 0 & \text{for} \quad others \end{cases} \tag{4}$$

where the periodic boundary condition is imposed by the direct method [7] considering a bisymmetric unit cell with respect to two orthogonal axes of symmetry.

Stress-Dependent Switching

The stress-dependent change of macroscopic material properties is introduced by the context of the topological change of the microstructure in the unit cell. Consider a certain internal boundary of the microstructure of unit cell that is expected to alter its status form/to the opening to/from the closure due to the change of macroscopic stress σ_{ij} applied. Figure 2 illustrates the schema of this status change in the unit cell. An internal boundary Γ_c in the unit cell is open so far as the macroscopic stress σ_{ij} is smaller than the threshold σ_{ij}^*, on which it starts to close contacting a part of the boundary to some other part of the boundary. When the macroscopic stress increases beyond the threshold, the topology of the microstructure of the unit cell is changed and the macroscopic material properties become different from that before the internal boundary closure. The gap zero slit perpendicular to the direction of the stress applied gives the most simple situation in which the macroscopic elastic modulus in tension is smaller than that in compression due to the slit gap opening by tension.

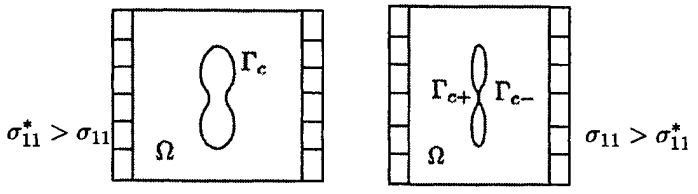
In order to describe the change of microscopic structural topology, the proportional loading is considered for the macroscopic stress, that is, $\sigma_{ij} = \beta\sigma_{ij}^0$, where σ_{ij}^0 is the reference. Denoting the displacement at the material point x_i in the microstructure by u_i^0 under the reference stress σ_{ij}^0, the over-loading beyond the threshold stress, that is not known yet, gives the the numerical overlapping, $\Omega'(\beta)$

$$\Omega'(\beta) = \{X_i \mid X_i = x_i + \beta u_i^0(x_j),\ x_i \in \Omega\} \tag{5}$$

and the loading coefficient β^* at the threshold stress is defined as

$$\beta^* = \max\left(\arg\min_{\beta} \int_{\hat{\Omega}(\beta)} d\Omega\right) \tag{6}$$

$$\hat{\Omega}(\beta) = \{X_i \in \Omega'(\beta) \mid X_i = Y_i, Y_i \in \Omega'(\beta)\} \tag{7}$$



(a) $\beta < \beta^*$ (b) $\beta > \beta^*$

Figure 2. Topological change of microstructure in unit cell.

Two parts on the inner boundary Γ_c is then defined for the inner boundary condition for the closed status. That is, Γ_{c+} and Γ_{c-} are distinguished as

$$\begin{aligned} &\Gamma_{c+} \subset \Gamma_c,\ \Gamma_{c-} \subset \Gamma_c \\ &\Gamma_{c-} = \{y_i \mid y_i \in \Gamma_c,\ y_i \notin \Gamma_{c+},\ \exists x_i \in \Gamma_{c+},\ y_i + \beta^* u_i^0(y_j) = x_i + \beta^* u_i^0(x_j)\} \\ &\Gamma_{c+} \cap \Gamma_{c-} = \phi \end{aligned} \tag{8}$$

and the fixed contact condition is assumed for them as

$$\beta^*(u_i^0(y_j) - u_i^0(x_j)) = (x_i - y_i) \quad x_i \in \Gamma_{c+},\ y_i \in \Gamma_{c-},\ \beta \geq \beta^* \tag{9}$$

beyond the threshold stress. In the case of most simple zero-gap slit perpendicular to the direction of stress, the threshold stress is characterized by $\beta^* = 0$.

PROBLEM FORMULATION

Topology Design

The topology design is the first half of the microstructural design for stress-dependent adaptive stiffness. The problem is written as the volume minimization of the unit cell under the constraints of prescribed macroscopic material properties by means of homogenization for both sides of stress threshold prescribed. The volume fraction ρ is the design variable in the context of the SIMP method for topology design, and the problem is described as follows:

$$\begin{aligned} &\text{minimize} && \int_\Omega \rho d\Omega \\ &\text{with respect to} && \rho(\mathbf{x}) \\ &\text{subject to} && \rho_{\min} \leq \rho \leq \rho\max \\ & && \max\left(\arg\min_\beta \int_{\hat{\Omega}(\beta)} d\Omega\right) = \beta^* \\ & && E_{ijkl}^{H(m)}(\chi_p^{ij(m)}, \chi_p^{kl(m)}) = E_{ijkl}^{*(m)} \\ & && a(\chi_j^{st(m)}, v_i^{(m)}) = L^{st}(v_i^{(m)}) \quad \forall v_i^{(m)} \in U_0^{st} \\ & && \beta^*(\chi_i^{st(0)}(y_j) - \chi_i^{st(0)}(x_j)) = (x_i - y_i) \quad x_i \in \Gamma_{c-}, y_i \in \Gamma_{c+},\ \beta \geq \beta^* \\ & && \qquad\qquad\qquad\qquad\qquad\qquad (s,t = 1,2) \end{aligned} \tag{10}$$

where the superscript in parentheses distinguishes $\beta < \beta^*$ with $m = 1$ and $\beta \geq \beta^*$ with $m = 0$, and the asterisk denotes the values prescribed. A penalty is imposed on the intermediate volume fraction apart from its lower limit ρ_{min} and upper limit ρ_{max}, because this is beneficial to make the obtained structural topology more distinguishable. In the formulation of Eq.(10), the bilinear form $a(\chi_j^{kl(m)}, v_i^{(m)})$ denotes the variational strain energy with respect to the topology with internal boundary status (m), and the linear form $L^{kl}(v_i^{(m)})$ stands for the variational potential under the loading condition described by $\epsilon_{pq}^{0(kl)}$, where the virtual displacement v_i^m is taken from the set of admissible one U_0^{kl}. The constraints of this minimization problem are treated by means of the Lagrangean multiplier method and the penalty method. The problem is discretized based on the boxel finite element approximation, and is solved by using the standard sequential linear programming supported by the moving limits strategy for the stability of the convergence process [8][9].

Geometry Design

The gray-valued distribution, the result of the topology design, is then simplified to the binary-valued material distribution of full or null volume fraction by the image-based technique and used for the start of geometry design problem, in which the geometrical configuration of the microstructure of unit cell is detailed. In the geometry design, the microstructure is made of full volume fraction part only and its contour is determined by the volume minimization problem

$$
\begin{array}{ll}
\text{minimize} & \displaystyle\int_{\Omega} d\Omega \\
\text{with respect to} & \Omega \\
\text{subject to} & \max\left(\arg\min_{\beta} \displaystyle\int_{\hat{\Omega}(\beta)} d\Omega\right) = \beta^* \\
& E_{ijkl}^{H(m)}(\chi_p^{ij(m)}, \chi_p^{kl(m)}) = E_{ijkl}^{*(m)} \\
& a(\chi_j^{st(m)}, v_i^{(m)}) = L^{st}(v_i^{(m)}) \quad \forall v_i^{(m)} \in U_0^{st} \\
& \beta^*(\chi_i^{st(0)}(y_j) - \chi_i^{st(0)}(x_j)) = (x_i - y_i) \quad x_i \in \Gamma_{c-}, y_i \in \Gamma_{c+}, \ \beta \geq \beta^* \\
& \qquad\qquad\qquad\qquad\qquad\qquad\qquad\qquad (s,t = 1,2)
\end{array}
\tag{11}
$$

In this study, the traction method [10] is recruited to solve this problem. The shape gradient is derived by means of the material derivative and used as the boundary traction. The treatment of the constraints is identical to that used at the topology design. This method enables us to reduce the objective function maintaining the smoothness of the contour boundary of the structure.

NUMERICAL CASE STUDIES

This section illustrates a couple of case studies for unit cells with zero gap slit. Figure 3 shows the initial configuration for the topology design. The isotropic linear material used has Young's modulus of $E = 210\ GPa$ and Poisson's ratioof $\nu = 0.3$. Following cases assume the orthotropic symmetry for a unit cell.

Heterogeneous Tensile/Compressive Stiffness

The first case is devoted for a heterogeneous tensile/compressive stiffness in which the tensile stiffness is smaller than the compressive one (Table 1). The internal boundary assumed is of

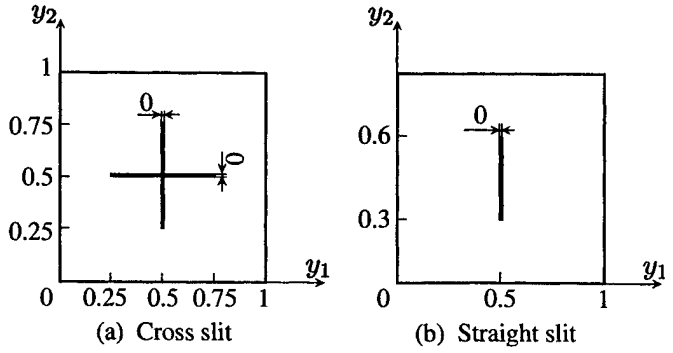


Figure 3. Unit cell with zero-gap slit.

Figure 3(a). The optimal topology obtained is shown in Figure 4(b) resulting the prescribed heterogeneous stiffness with the error smaler than 1.0 % error. This gray scaled topology is converted into binary one of Figure 4(c) with the threshold of 0.45, and the contours are used to make the initial (Figure 4(d)) for the geometry design. The optimal geometry shown in Figure 4(e) has the prescribed tensile/compressive stiffness with 1.5 % error at maximum as listed in Table 1. Figures 4(f) and (g) illustrate the deformation under the uni-axial tensile and compressive stresses in y_1 direction demonstrating the opening and closing of gap-zero slit colinear to y_2 axis. It is confirmed that the internal boundary in a unit cell works as a switching mechanism for the adaptive stiffness dependent on the working stress.

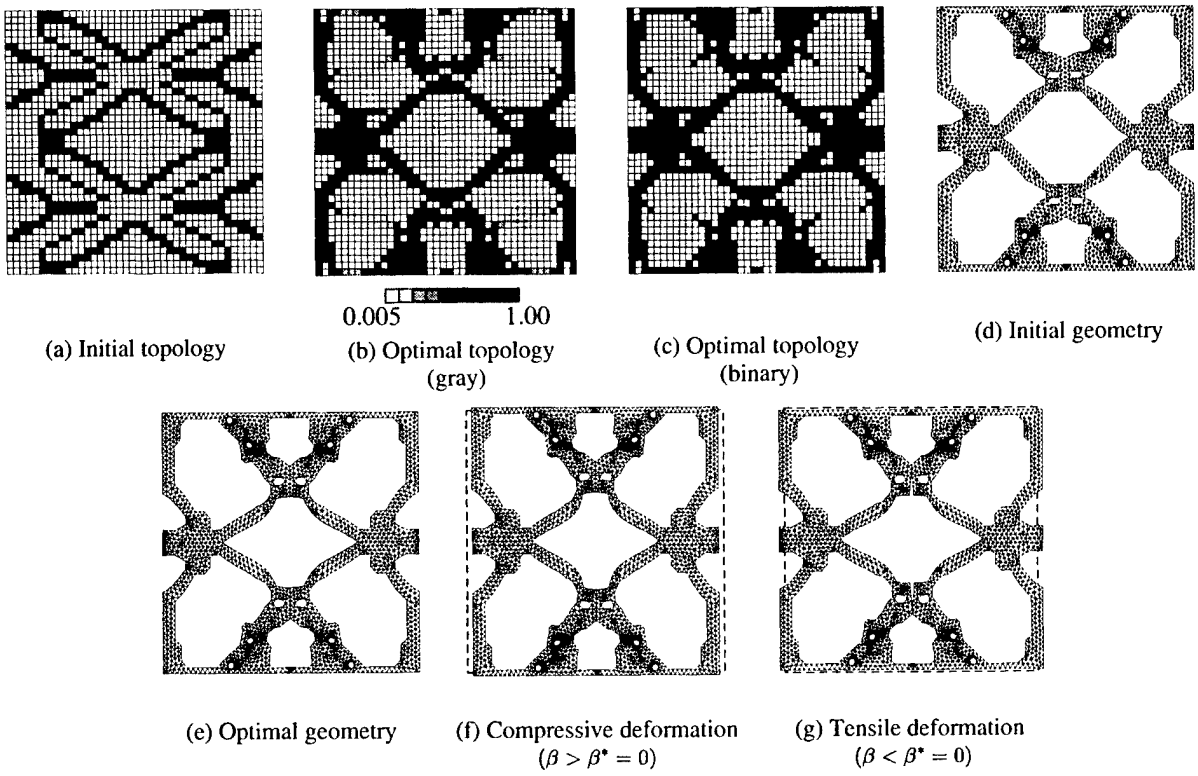


Figure 4. Microstructural topology and geometry for heterogeneous tensile / compressive stiffness.

Table 1. Structural volume and homogenized material parameters for heterogeneous tensile/compressive stiffness [GPa]

		Volume	$E^{(0)}_{1111}$	$E^{(0)}_{2222}$	$E^{(1)}_{1111}$	$E^{(1)}_{2222}$
	Target		25.0	25.0	20.0	20.0
Topology	Initial	1.00	9.45	3.99	5.40	4.47
	Optimal(gray)	0.41	25.0	24.8	19.9	20.2
	Optimal(binary)	0.44	27.0	23.5	20.4	17.8
Geometory	Initial	0.42	27.7	26.8	20.6	19.7
	Optimum	0.39	25.1	25.0	19.7	19.9

Positive/Negative Poisson's Ratio

The second case is provided for a positive/negative Poisson's Ratio in which the Poisson's Ratio is negative under compression (Table 2). The inner boundary assumed is of Figure 3(b) at the initial. The optimal topology obtained is shown in Figure 5(b) resulting the prescribed tensor of material constants with the error smaller than 0.01 %. This gray scale topology is converted into binary one of Figure 5(c) with the threshold of 0.3, and the contours are used to make the initial shape (Figure 5(d)) for geometry design by paying attention to the region of medium volume fraction. The obtained geometry shown in Figure 5(e) realizes the prescribed material property under compression with several percent errors. The property, however, under tension is not satisfactory because of the difficulty of appropriate estimation of initial contour

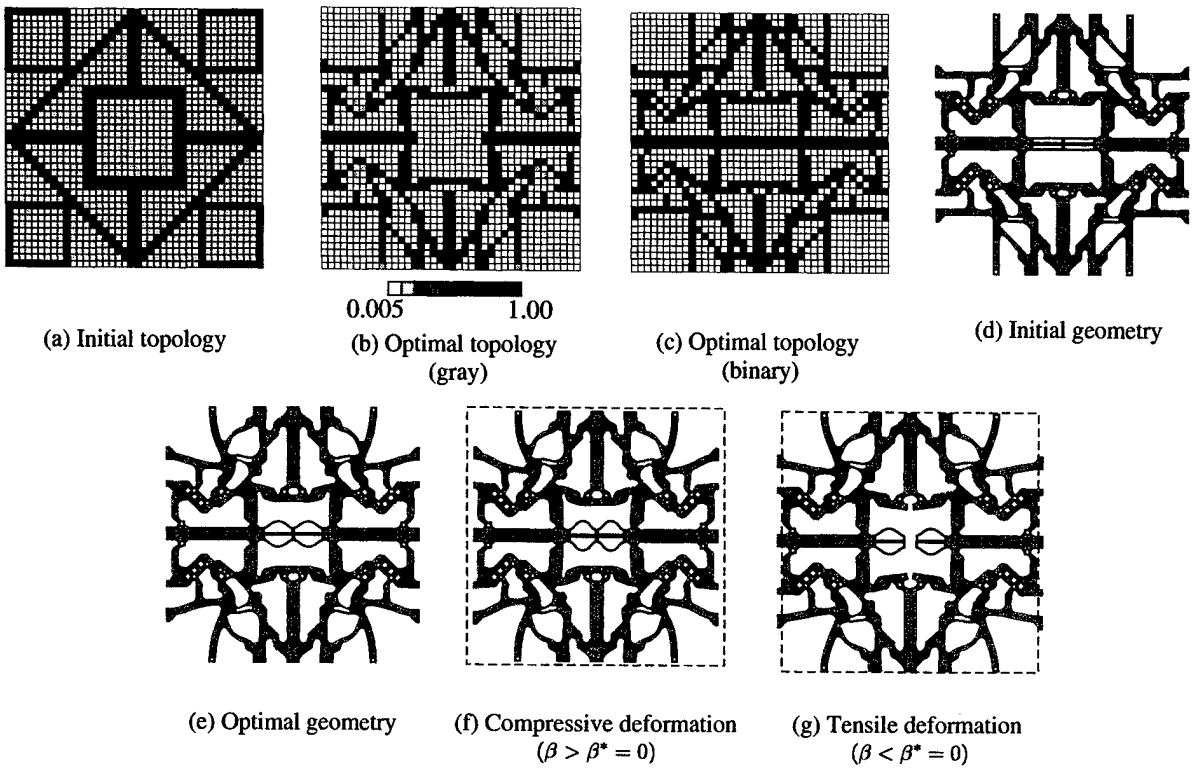


Figure 5. Microstructural topology and geometry for positive / negative Poisson's Ratio.

Table 2. Structural volume and homogenized material parameters for positive/negative Poisson's ratio [GPa]

		Volume	$E^{(0)}_{1111}$	$E^{(0)}_{2222}$	$E^{(0)}_{1122}$	$E^{(1)}_{1111}$	$E^{(1)}_{2222}$	$E^{(1)}_{1122}$
	Target		10.0	10.0	-1.00	5.00	5.00	0.50
Topology	Initial	1.00	40.8	40.8	11.5	34.0	40.7	11.0
	Optimal(gray)	0.37	10.0	10.0	-1.00	5.00	5.00	0.50
	Optimal(binary)	0.36	18.5	29.0	-1.79	9.50	20.4	7.08
Geometory	Initial	0.37	13.1	10.2	-1.07	6.22	7.70	0.84
	Optimal	0.36	10.7	10.4	-1.05	5.17	7.81	0.79

at the region of medium volume fraction in Figure 5(b). In spite of this difficulty, the material property of positive/negative Poisson's ratio is realized in the context of the topology design for quantitatively and in the geometry design qualitatively.

CONCLUSION

In this article, the concept of stress-dependent adaptive stiffness is proposed for the macroscopic material structural system. The topological change of microstructure in the unit cell is introduced by utilizing the open/close transition at the internal boundary of microstructure. This enables us to realize the stress-dependent alternation of macroscopic material characteristics, evaluated by means of homogenization. The topology and geometry design problems are formulated under the constraints of constitutive parameters before and after the threshold stress prescribed. They are solved by the pair of the SIMP method and the traction method, and the effectiveness of the proposed approach has been demonstrated through numerical cases. These suggest us an alternative towards adaptive structural/material systems, although further consideration is expected for the internal boundary assignment for the topology design and the initial contour determination for the geometry design.

REFERENCES

[1] Sigmund, O. and Torquato, S., 1999, "Design of smart composite materials using topology optimization," *Smart Materials and Structures*, pp.365–379.

[2] Kikuchi, N., Nishiwaki, S., Fonseca, J. S. O. and Silva, E. C. N., 1998, "Design optimization method for compliant mechanisms and material microstructure," *Computer Methods in Applied Mechanics and Engineering*, Vol.151, pp.401–417.

[3] Sigmund, O., 1998, "Topology optimization in multiphysics problems," *American Institute of Aeronautics and Astronautics, AIAA-98-4905*, pp.1942–1500.

[4] Silva, E., Ono, J, S. and Kikuchi, N., 1997, "Optimal design of piezoelectric microstructure," *Computational mechanics*, Vol.19, pp.397–410.

[5] Sigmund, O., 1994, "Materials with prescribed constitutive parameters: An inverse homogenization problem," *Internal Journal of Solids and Structures*, Vol.31, No.17, pp.2313–2329.

[6] Tanaka, M. and Oki, K., 1999, "Shape design of bilinear stiffness structure," *Jpn. Soc. Mech. Eng. Design & Systems Conference*, No.99-27, pp.346–348(in Japanese).

[7] Hassani, B., 1996, "A direct method to derive the boundary conditions of the homogenization equation for symmetric cells," *Communications in Numerical Methods in Engineering*, Vol.12, pp.185–196.

[8] Sigmund, O., 1997, "On the design of compliant mechanisms using topology optimization," *Mechanics of structures and machines*, Vol.25, No.4, pp.493–524.

[9] Petersson, J. and Sigmund, O., 1998, "Slope topology optimization," *Internatinal Journal for Numerical Methods in Engineering*, Vol.41, pp.1417–1434.

[10] Azegami, H., 1994, "Solution to Domain Optimization Problems," *Trans. Jpn. Soc Mech. Eng*, Series A, Vol.60, No.574, pp.1479–1485(in Japanese).

EXPERIMENTAL VERIFICATION OF FLAT SOUND RADIATOR BY PATTERN OPTIMIZATION OF PIEZOFILM ACTUATOR

Jin Yeon Cho, Sung Lee, Joon-Seok Hwang, Seung Jo Kim

ABSTRACT

In this study, experimental verification of performance of flat sound radiator has been conducted. The piezofilm (PVDF) actuator has been designed to prevent the distortion of sound and make the frequency response of radiated sound to be flat. The electrode pattern of piezofilm actuator is optimized to satisfy the design objective. The formulation of design method is based on the coupled finite element and boundary element method and electrode pattern is optimized by genetic algorithm. The flat sound radiator with optimized piezofilm actuator has been manufactured. The sound pressure level at the distance of 50cm is measured using microphone and compared with the result of numerical simulation.

INTRODUCTION

Moving coil type drivers are widely used for the driving unit of typical loudspeaker. But the size of conventional driving unit has some restrictions on the configuration of loudspeaker. Therefore loudspeakers will be thick and heavy. In the previous work, we proposed the design method of flat sound radiator, whose shape is much thinner than those of conventional loudspeakers[1]. Piezofilm(PVDF) had been adopted for the driving unit of the diaphragm of flat sound radiator. Piezofilm is widely used for the actuator in the field of the vibration control and noise control of structure. Good mechanical properties such as flexibility, easiness to cut or shape into complex

J.Y. Cho, Assistant professor, Department of Aerospace Engineering, Inha University, Inchon, Korea
L. Sung, Graduate Research Assistant, Department of Aerospace Engineering, Seoul National University, Seoul, 151-742, Korea
J.S. Hwang, Graduate Research Assistant, Seoul National University, Department of Aerospace Engineering, Seoul, 151-742, Korea
S.J. Kim, Professor, Department of Aerospace Engineering, Seoul National University, Seoul, 151-742, Korea

configurations and light-weight make the piezofilm more useful in the field of distributed actuator system. By the change of the paradigm of driving unit, the shape of sound radiator could be made thin enough. The flat sound radiator has been designed to make the frequency response of radiated sound flat and the design objective could be fulfilled by adjusting modal characteristics of piezofilm actuator by optimizing electrode pattern of piezofilm actuator. The numerical simulation showed that the frequency response of sound radiated from the designed flat sound radiator has been made flat in the frequency range of interest.

In this study, the performance of flat sound radiator has been verified by experiment. The electrode pattern of piezofilm actuator has been optimized. The flat sound radiator with optimized piezofilm actuator has been manufactured. The sound pressure level is measured by using microphone and compared with numerical simulation.

In the first section, the numerical modeling is explained briefly. The second section shows the optimization procedures and the third section shows the design results and numerical simulation. The experimental results are shown in the last section.

NUMERICAL MODELING

Finite Element Analysis of Vibrating Plate

The vibration of diaphragm is considered to be the vibration of thin plate. The finite element method is used to model the vibration of the plate with piezofilm actuator. Nine-node Reissner-Mindlin plate elements with classical lamination theory[2] and first-order shear deformation theory[3] have been used in the finite element formulation. The electrode of piezofilm in one element is divided into 4 segments (Fig. 2). The actuation force of i-th element is obtained by assembling the actuation forces of each segment of piezofilm in i-th element. The actuation force of the j-th segment in i-th element ($\mathbf{F}_{aj}^{(i)}$) is as follows.

$$\mathbf{F}_{aj}^{(i)} = \int_{V_j} \frac{\mathbf{B}_I^T \mathbf{e}}{t_j} dV_j \tag{1}$$

where, $\mathbf{B}_I$ is inplane strain-displacement interpolation matrix, $\mathbf{e}$ is piezoelectric constants vector and V_j and t_j is the volume and the thickness of j-th segment.

The actuation force of i-th element is obtained by summing the actuation forces of each segment.

$$\mathbf{F}_a^{(i)} = \sum_j^4 \mathbf{S}(i,j)\mathbf{F}_{aj}^{(i)} \tag{2}$$

where, $\mathbf{S}(i,j)$ is defined as follows,

$$\mathbf{S}(i,j) = \begin{cases} 1, & \text{if j-th electrode segment is } on \\ 0, & \text{if j-th electrode segment is } off \end{cases}$$

$\mathbf{S}$ determines the electrode patterns of piezofilm and is used as the present design

variables. *On* means that the piezoelectricity is active and *off* means that the piezoelectricity will be deactivated by removing the electrode from piezofilm.

Global actuation force vector is summed over all the elements and obtained as follows,

$$\mathbf{F}_a = \sum_{i}^{N_e} \mathbf{F}_a^{(i)} \tag{3}$$

As a result, the equation of motion of the vibrating plate including piezofilm actuator is,

$$\mathbf{M\ddot{u}} + \mathbf{Ku} = \mathbf{F}_a V_a \tag{4}$$

where, V_a is the actuating voltage applied to the piezofilm actuator. Structural damping is neglected in this study.

Equation of the Acoustic System

The acoustic pressure in acoustic domain induced by vibrating plate can be facilitated by introducing potential function, φ, which satisfies the following equation [4].

$$\left[\nabla^2 + k^2\right]\varphi(x,y,z,\omega) = 0 \tag{5}$$

subject to the boundary conditions

$$\frac{\partial \varphi}{\partial z} = \begin{cases} (-i\omega)\, w(x,y,\omega), & x \in A \\ 0 & otherwise \end{cases} \tag{6}$$

where A is the plate surface area, k is wave number and ω is frequency. The potential function can be obtained by introducing the Green's function

$$\varphi(x,y,z,\omega) = \int_A G(x,y,z|x',y',0)(-i\omega)w(x',y',\omega)dx'dy' \tag{7}$$

The quantity G in Eq. (7) is the Green's function, which is given by

$$G(x,y,z|x',y',0) = -\frac{e^{ikR}}{2\pi R} \tag{8}$$

where R is defined as follows:

$$R = \sqrt{(x-x')^2 + (y-y')^2 + z^2} \tag{9}$$

The radiated acoustic pressure in the frequency domain can now be written as

$$p(x,y,z,\omega) = i\omega\rho\varphi(x, y, z, \omega) \tag{10}$$

where ρ is the fluid density, p, φ are the acoustic pressure, and the potential function,

respectively, in the frequency domain.

When Eq. (10) along with the condition (6) is discretized using the boundary element method, we obtain the matrix equation as

$$\mathbf{p} = \mathbf{G}\,\mathbf{v}_n \tag{11}$$

where $\mathbf{p}$ and $\mathbf{v}_n$ are the vectors containing the acoustic pressure and the normal velocity at nodal points, respectively. A four-node quadrilateral element is used for the discretization. The transformation method, which divides the quadrilateral element domain into two triangular domains, is used for the singular integration in the diagonal term of the matrix $\mathbf{G}$[5].

DESIGN OPTIMIZATION PROCEDURES OF PIEZOFILM ACTUATOR

Modal Coordinate Transformation of the Equation of Motion

Eq. (4) is transformed by using the following modal coordinate transformation

$$\mathbf{u} = \boldsymbol{\Phi}\boldsymbol{\eta} \tag{12}$$

where, $\boldsymbol{\Phi}$ is modal matrix containing eigenvectors and $\boldsymbol{\eta}$ is modal coordinate vector. The eigenvectors are normalized as follows,

$$\boldsymbol{\Phi}^T\mathbf{M}\boldsymbol{\Phi} = \mathbf{I}, \quad \boldsymbol{\Phi}^T\mathbf{K}\boldsymbol{\Phi} = \boldsymbol{\Lambda} \tag{13}$$

where, $\mathbf{I}$ is identity matrix and $\boldsymbol{\Lambda}$ is diagonal matrix of eigenvalues.

Substituting Eq. (12) into Eq. (4) and pre-multiplying $\boldsymbol{\Phi}^T$, the equation of motion by modal coordinate transformation can be written as

$$\ddot{\boldsymbol{\eta}} + \boldsymbol{\Lambda}\boldsymbol{\eta} = \boldsymbol{\Phi}^T\mathbf{F}_a V_a \tag{14}$$

In the above equation, $\boldsymbol{\Phi}^T\mathbf{F}_a$ is defined as modal actuating force per unit voltage. $\boldsymbol{\Phi}^T\mathbf{F}_a$ can be considered as the degree of contribution of total actuating force ($\mathbf{F}_a$) to the specific modal characteristics. So, the radiated sound from vibrating structures is adjusted by controlling the modal forces according to the design objective.

Design of Piezofilm Actuator

The design optimization problem is described as optimizing modal actuating force $\boldsymbol{\Phi}^T\mathbf{F}_a$ such that the frequency response of sound is to be flat within the interested frequency band. To obtain flat frequency response, unwanted peak in the frequency response should be suppressed. Therefore, modal forces for the unwanted modes are to be minimized. And, modal forces of certain modes are to be enhanced for better performance. As a result, the performance index of the design optimization problem is as follows,

$$\text{Maximize} : \mathrm{J} = \min\left(\left|\boldsymbol{\Phi}_W{}^T\mathbf{F}_a\right|\right) - \max\left(\left|\boldsymbol{\Phi}_U{}^T\mathbf{F}_a\right|\right) \tag{15}$$

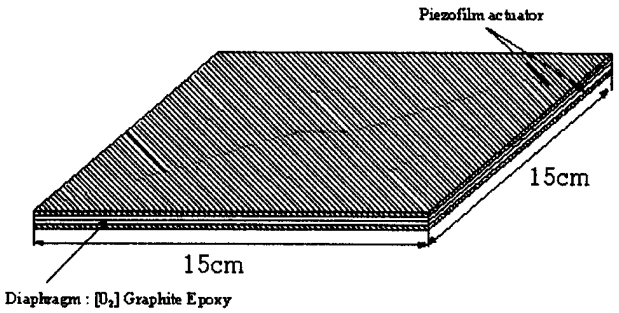


Figure 1. The configuration of flat sound radiator

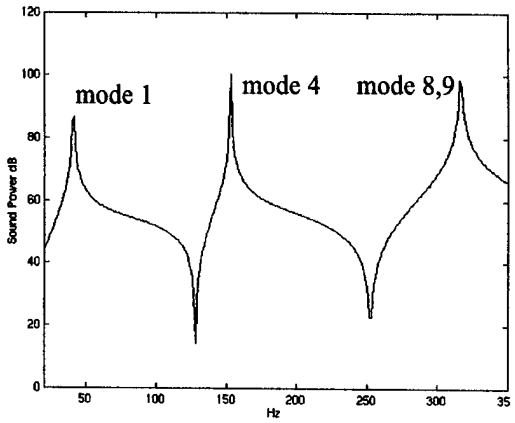


Figure 2. Frequency response in the case of the piezofilm actuator with fully covered electrode

Where, $\Phi_W{}^T, \Phi_U{}^T$ is eigen matrix of wanted modes and unwanted modes, respectively. Genetic algorithm is utilized as an optimization scheme[6]. The piezofilm actuators bonded on both the top and bottom side have the same design with opposite poling direction. So, one of the two piezofilm is involved in the optimization procedures. The electrode of piezofilm is divided into many segments in regular size. In this study, the number of electrode segment of one piezofilm is 12×12=144.

DESIGN RESULTS AND NUMERICAL SIMULATION

Simply supported 15 cm×15 cm $[0_2]$ Graphite/Epoxy laminated composite is used for the diaphragm. Piezofilm actuator is bonded on both the top and bottom side of the diaphragm. The configuration of flat sound radiator is shown in Figure 1. Voltage applied to the piezofilm actuator is ± 100 V. Frequency response is calculated in the range of 100-300Hz. Sound pressure level is calculated and scaled as dB scale with reference value of 2×10^{-5} Pa. The flat sound radiator has been designed through the

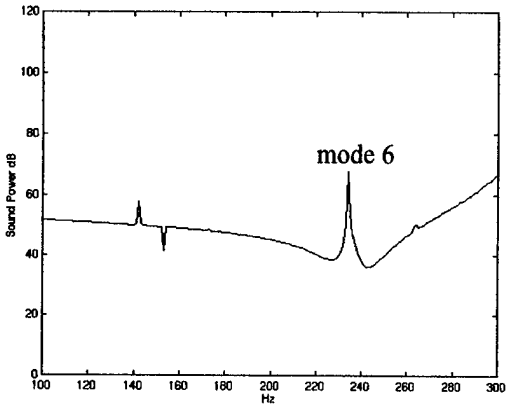


Figure 3 Frequency response by the designed actuator (mode 1 wanted, mode 4 unwanted)

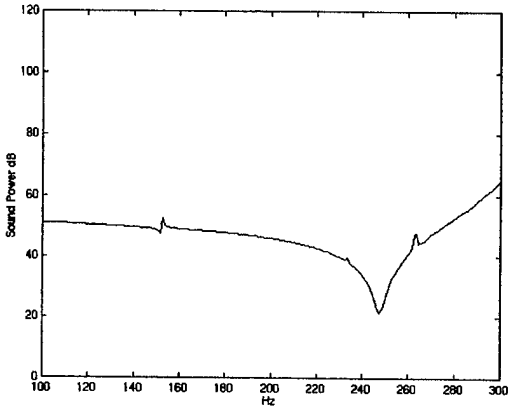


Figure 4 Frequency response by the designed actuator (mode 1 wanted, mode 4,6 unwanted)

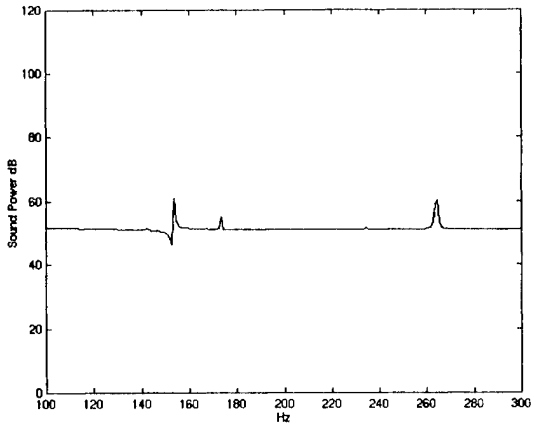


Figure 5. Frequency response by the optimal piezofilm actuator (mode 1 wanted, mode 4,6,8 unwanted)

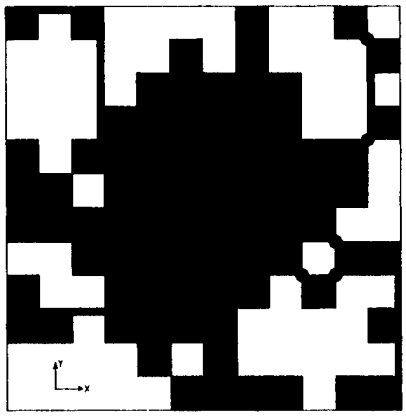


Figure 6. The optimal electrode pattern of piezofilm actuator

procedures described in the previous work by optimization of the electrode pattern of piezofilm[1]. Figure 2 shows the frequency response of sound radiated from flat sound radiator with the piezofilm actuator of fully covered electrode. At first, design optimization is performed considering mode 1 as wanted mode to be maximized, and mode 4 as unwanted mode to be minimized. Figure 3 shows the frequency response of designed flat sound radiator. As shown in Figure 3, the peak value due to mode 4 is suppressed. And mode 6, which is not excited by the fully covered actuator, should be included in the unwanted modes. The design optimization is proceeded again considering mode 1 as wanted mode and mode 4,6 as unwanted modes. Figure 4 shows the frequency response for the second design. It is noted that the valley in the 245 Hz has emerged by the effect of modes beyond 300 Hz. Therefore in the next design step, mode 8,9 would be included in the unwanted modes. After the third optimization process, we could obtain flat frequency response in the interested frequency range (Figure 5). Figure 6 depicts the corresponding electrode pattern of piezofilm actuator.

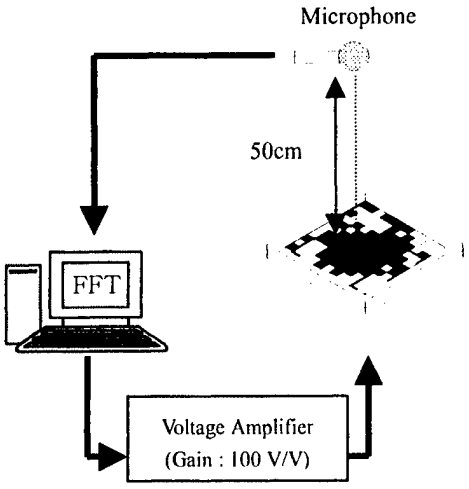


Figure 7 Configuration of Experimental Instrument

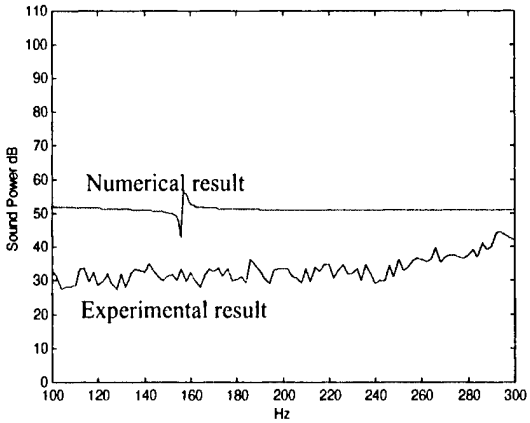


Figure 8 Comparison between experimental and numerical simulation

EXPERIMENT

Flat sound radiator with designed piezofilm actuator has been manufactured. The composite plate is made by stacking prepregs and cured by hot press. The electrode pattern is implemented by removing the electrode in the white region in Figure 6 by chemical etching process. The piezofilm actuators are bonded on the composite plate using epoxy adhesive. The experimental setup is shown in Figure 7. The sound pressure level is measured at the distance of 50 cm above the flat sound radiator. Signal generator is used for the sine sweep and the high voltage amplifier is used to drive the piezofilm actuators. The gain of high voltage amplifier is 100V/V. Figure 8 shows the measured sound pressure level. Sound pressure level in the frequency range of 200~300 is about 35~45dB.

CONCLUSION

In this study, experimental verification of the performance of the flat sound radiator is performed. For the design of flat sound radiator, piezofilm (PVDF) actuators are used for the driving unit. Composite plate, which is efficient sound radiating material, is used as the diaphragm. Piezofilm actuators are designed through the design process proposed in the previous work. For the experiment, flat sound radiator with optimized piezofilm actuators is manufactured. The frequency response of sound pressure level at the distance of 50 cm is measured and compare with the result of numerical simulation. The sound pressure level in the frequency range of 200Hz~300Hz is about 35~45dB. Until now, sound pressure level is not high enough to compete with commercial loudspeaker. Efforts for the enlargement of sound pressure level are needed. The layup and geometry of composite plate should be investigated. And multi-layered piezofilm actuator can raise the sound pressure level. The refinement of electrode pattern will be also investigated for the full utilization of the anisotropy of piezofilm.

References

1. Kim, S.J. and Hwang, J.S., "Design of Flat Sound Radiator by Pattern Optimization of Piezofilm Actuator" , 10th ICAST, Paris, France, October, 1999
2. Jones, R. M., *Mechanics of Composite Materials*, Scipta Book Co., 1975
3. Ochoa, O. O. and Reddy, J. N., *Finite Element of Composite Laminates*, Kluwer Academic Pub. 1992
4. Wu, S. F., and Maestrello, L., "Responses of Finite Baffled Plate to Turbulent Flow Excitations", *AIAA Journal*, Vol.33, No.1, 1995, pp 13-19
5. Hall, W. S., *The Boundary Element Method*, Boston:Kluwer Academic Publishers, 1993
6. Goldberg, D. E., *Genetic Algorithm in Search, Optimization & Machine Learning*, Addison-Wesley, 1989

VIBRATION MODE RECONSTRUCTION OF A THIN PLATE BY USING SHAPED PVDF SENSORS

Katsuyoshi Nagayasu, Takuro Hayashi, Norio Uchida, Hiroaki Nakamura, Hiroshi Takahashi

INTRODUCTION

This study aims to establish basic techniques for detecting vibration of flexible structures by using distributed sensors. It is important to establish measuring methods using distributed sensors. This paper shows the sensor shapes and the measuring methods for vibration distribution of a thin plate by using long span PVDF (polyvinylidene fluoride) sensors as distributed sensors. The methods are evaluated by the comparison between experimental results and calculational prediction based on our theory.

In a previous study[1], we show the experimental results were in good agreement qualitatively with the values obtained by theoretical calculation. In the present study, we performed precise simulations and experiments, and we obtained quantitatively good agreement between experiments and theoretical calculations. We also predicted the errors in the case of omitting higher-order mode of PVDF shapes.

THE THEORY OF VIBRATION MEASUREMENT BY SHAPED PVDF SENSORS[1]

Deduction of displacement distributions

The method makes use of the fact that, in theory, any wave can be developed to the sum of Fourier series. A number of PVDF films cut to Fourier series shapes are used so that each PVDF film can output th e corresponding Fourier coefficient. PVDF films cut to Fourier series shapes are affixed to the same position. This approach is illustrated in Fig. 1. Film length direction is defined as x direction. Obviously, x-direction strain is a second-order derivative of displacement $z(x,y)$ with respect to x. As PVDF film output is integrated x-direction strains

Toshiba Corp., R&D Center, 1 Komukai Toshiba-cho, Saiwai-ku, Kawasaki, 212-8582, Japan.

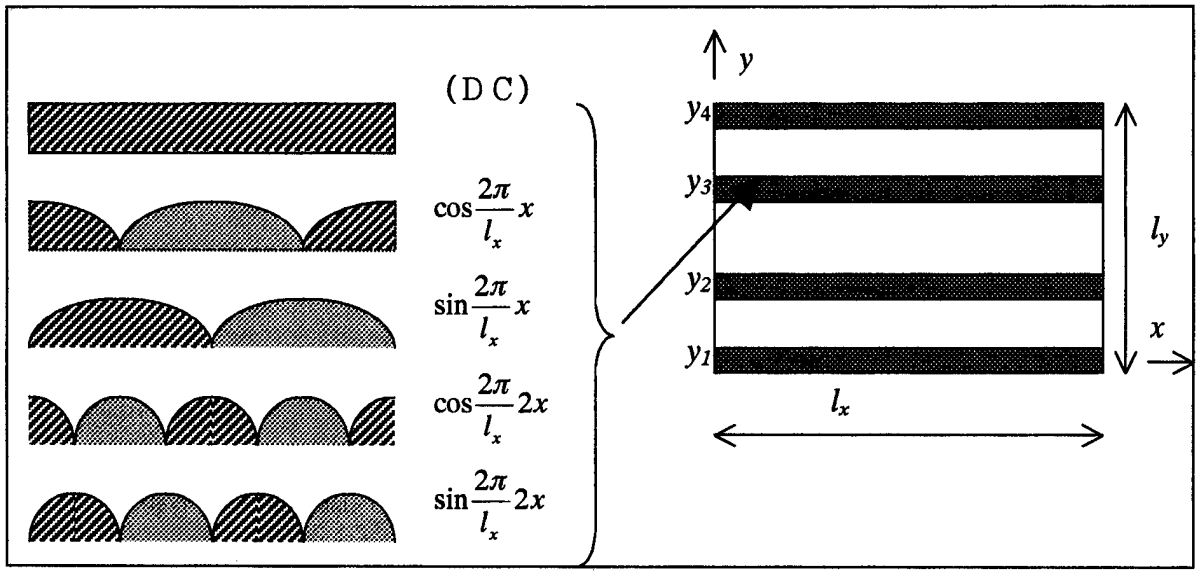


Fig.1 Fourier series affixed patterns

along the film length multiplied coefficient corresponding to the film width, each output of the films is as follows:

$$f_m(t,y)=\int_0^{l_x}\frac{\partial^2 z(x,y)}{\partial x^2}e^{-jk_m x}dx \qquad \cdots\cdots\cdots\cdots\cdots\cdots\cdots\cdots\cdots\cdots\cdots\cdots\cdots\cdots\cdots\cdots\cdots\cdots \quad (1)$$

where, $f_m(t,y)$ is m-th sensor output,

$z(x,y)$ is displacement at x, y position, and so $\partial^2 z(x,y)/\partial x^2$ represents x-direction strain at x, y position,

l_x is sensor length,

$k_m = 2\pi m/l_x$, which represents wave number.

Calculating transfer functions between each output at given frequency ω, we can obtain the spatial Fourier transferred values at y_1, y_2, y_3 and y_4 positions. Multiplying constants, $1/k_m^2$, to every component and inverse Fourier transformed, the displacement distributions on the surfaces are deduced.

The Fourier series shape affixing method is similar to the eigenmode affixing method[2] in that the films are cut to specific shapes. However, the eigenmode affixing method can only detect specific shape plates, for example, that all ends are supported ends, because it is necessary to know the vibration modes of the plate in advance. On the other hand, the Fourier series shape affixing method has a merit in that the object shapes do not restrict it in theory.

Mode reconstruction method

Here we discuss the theory of the mode reconstruction method. Cutting the PVDF sensors to the strain function shapes, we intend to detect the spatial filtering values of the strains. In this study, the plate is a cantilever, so considering second-order terms the strain distribution is expressed as follows:

Outputs of the PVDF sensors shaped $\cos(\pi x/2L)$, $\cos(3\pi x/2L)$ are

$$\int_0^L \cos(\frac{\pi}{2L}x)\varepsilon(x,t)dx \cong \int_0^L \cos(\frac{\pi}{2L}x)\frac{\partial^2 y}{\partial x^2}dx = \frac{L}{2}p_1(t)$$
$$\int_0^L \cos(\frac{3\pi}{2L}x)\varepsilon(x,t)dx \cong \int_0^L \cos(\frac{3\pi}{2L}x)\frac{\partial^2 y}{\partial x^2}dx = \frac{L}{2}p_2(t) \quad \cdots\cdots\cdots\cdots\cdots\cdots\cdots\cdots\cdots\cdots \quad (2)$$

So we can detect $p_1(t)$, $p_2(t)$. If we multiply $p_1(t)$, $p_2(t)$ by $\cos(\pi x/2L)$, $\cos(3\pi x/2L)$ and sum up, we can deduce spatial distribution of strain $\varepsilon(x,t)$ and its time variance. In order to deduce the displacement distribution, the strain distributions are integrated by x in two times.

$$y = \iint[\frac{\partial^2 y}{\partial x^2}dx]dx = -(\frac{2L}{\pi})^2\cos(\frac{\pi}{2L}x)p_1(t) - (\frac{2L}{3\pi})^2\cos(\frac{3\pi}{2L}x)p_2(t) + c(t)x + d(t) \quad \cdots \quad (3)$$

The boundary conditions are 0 displacement and 0 inclination at x=0. Given that

$c(t)$=0 and

$$d(t) = (\frac{2L}{\pi})^2 p_1(t) + (\frac{2L}{3\pi})^2 p_2(t), \quad \cdots\cdots\cdots\cdots\cdots\cdots\cdots\cdots\cdots\cdots\cdots\cdots\cdots\cdots \quad (4)$$

displacement distributions are deduced as the next equation.

$$y(x,t) = -(\frac{2L}{\pi})^2[\cos(\frac{\pi}{2L}x) - 1]p_1(t) - (\frac{2L}{3\pi})^2[\cos(\frac{3\pi}{2L}x) - 1]p_2(t) \quad \cdots\cdots\cdots\cdots \quad (5)$$

In other words, by using spatial filters, $\cos(\pi x/2L)$, $\cos(3\pi x/2L)$, outputs of $p_1(t)$, $p_2(t)$ are deduced. Then, these outputs are multiplied by second-order integration of the spatial filters, $-(\frac{2L}{\pi})^2\cos(\frac{\pi}{2L}x), -(\frac{2L}{3\pi})^2\cos(\frac{3\pi}{2L}x)$, and the multiplied results are summed up. Next, by using the boundary conditions such that the displacements are always zero at the fixed ends, the constant terms are determined. In consequence, the spatial distributions and the time variations of the displacements are deduced.

COMPARISON OF VIBRATION MEASURED BY POINT SENSORS AND BY PVDF DISTRIBUTED SENSORS

Vibration measurement by laser point sensors

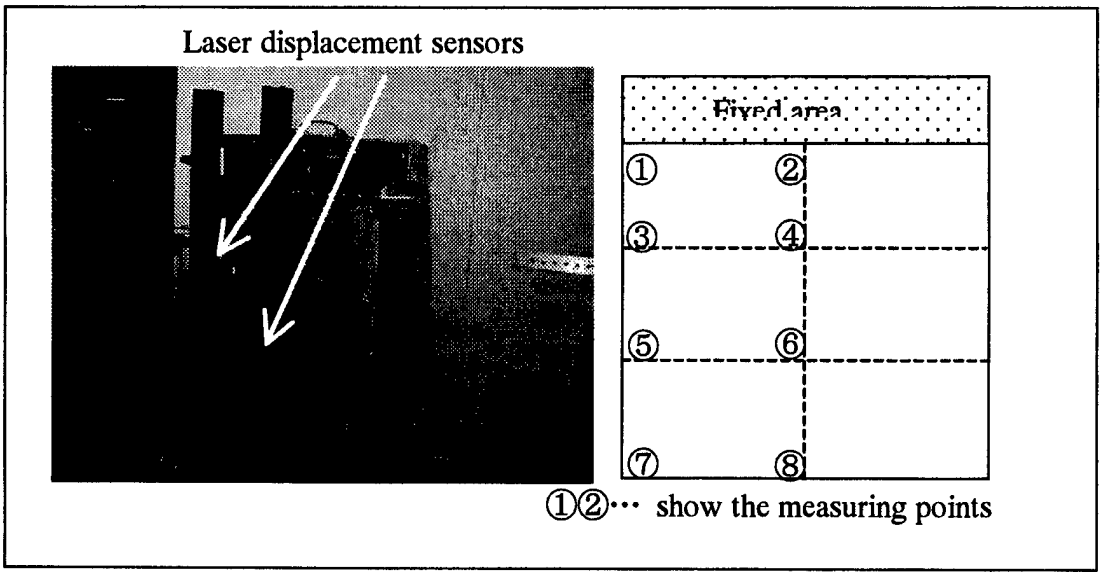


Fig.2 Arrangement of laser sensors

In order to verify the theory, the results obtained by PVDF sensors as distributed sensors were compared with the displacements measured by laser sensors applied as point sensors. If the values obtained by both types of sensor were to agree, it would confirm the accuracy of the PVDF distributed sensor measurements. Fig. 2 shows arrangement of laser point sensors on the experimental equipment. The measuring method is as follows:

At first, excite the vibration of the thin plate using an impulse hummer, and then detect the response of the plate. The laser sensor values are divided by a value from a load cell on the impulse hummer. This makes frequency transfer functions, and then it is possible to detected the vibration distribution.

Vibration measurement by PVDF distributed sensors

Fig. 3 illustrates the affixing positions and the shapes of the PVDF sensors for vibration measurement of the plate.

Results obtained by the laser point sensors and by the PVDF sensors are shown in Table 1. The both results were quantitatively in excellent agreement, and so the accuracy of the PVDF distributed sensor measurements was verified.

MODE COMPARISON BETWEEN BY EXPERIMENT BASED ON OUR THEORY AND BY CALCULATION

In order to confirm the validity of our theory, the Fourier series shape affixing method, we

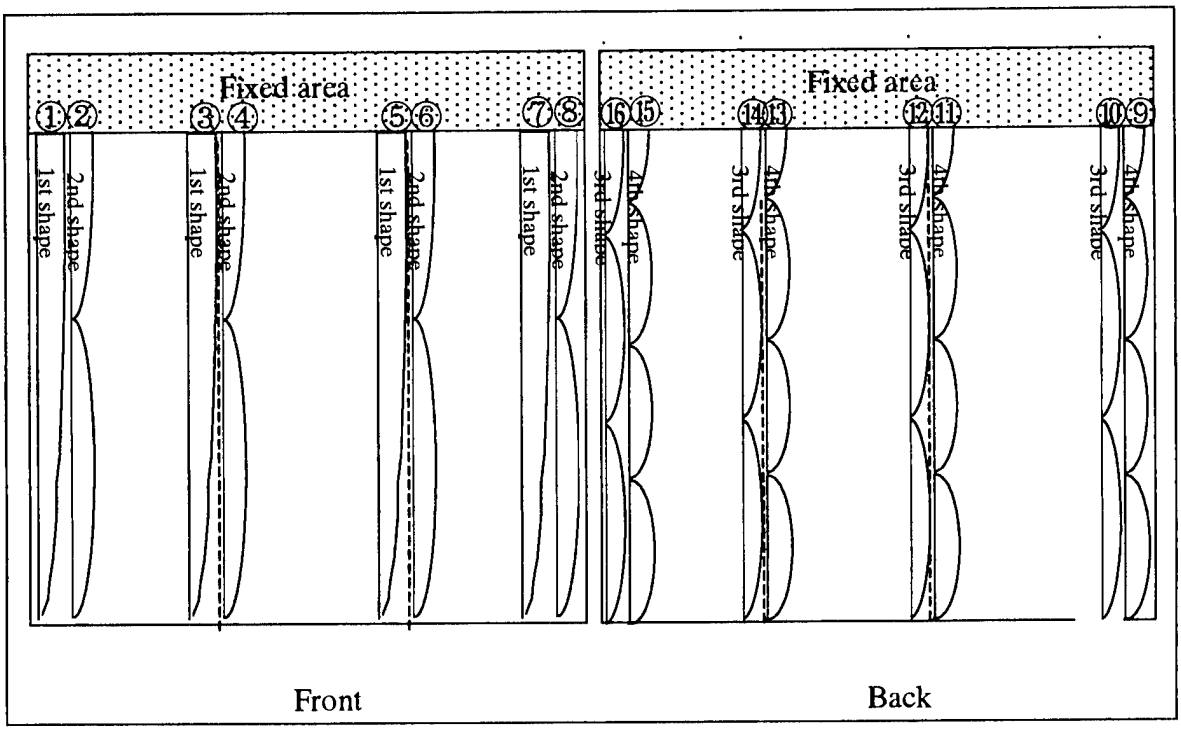


Fig.3 Affixing positions and shapes of PVDF

TABLE 1. Vibration obtained by laser and by PVDF

Sensor Types	Measuring Points	Frequency[Hz]	Ratio of Amplitude (Left Side / Center)	Phase[deg]
Laser	Center	2.88	0.940	-2.24
	Left Side	2.88		-2.30
PVDF	Center	2.88	0.977	-2.07
	Left Side	2.88		-2.10

performed the following procedures and compared the results. If the modes reconstructed by means of the experiment based on our theory were to be in good agreement with the mode obtained by calculation, the validity of our theory would be confirmed.

(1) Determine the vibration modes by the direct outputs from NASTRAN

(2) Reconstruction using strains calculated by NASTRAN (Reconstructed vibration modes based on the theory of the Fourier series shape affixing method)

(3) Reconstruction using PVDF outputs (Reconstructed vibration modes based on the theory of the Fourier series shape affixing method)

Vibration modes by the direct outputs from NASTRAN

In order to confirm the accuracy of the Fourier series shape affixing method, the vibration

modes of the direct numerical predictions of NASTRAN, which is a finite element method software, were applied.

The modes of the direct outputs from NASTRAN are shown in Fig.4(a).

Reconstructed vibration modes based on the Fourier series shape affixing method

The data detected by PVDF indicate the amplitude and the phase at each measuring point. These show peak values, and so time variances cannot be detected. The phases indicate vibration direction and simplify the direction to the sign that shows the same or the opposite direction. If the vibration varies by the time of the same function without depending on the measuring points, the vibration $p(t)$ can be expressed as the following equation.

$$p(t) = p_0 \sin(t) \quad \cdots\cdots\cdots\cdots\cdots\cdots\cdots\cdots\cdots\cdots\cdots\cdots\cdots\cdots\cdots\cdots\cdots\cdots\cdots\cdots \quad (6)$$

where p_0 = deduced vibration amplitude * sign determined by the phase

For example, the method of drawing modes by the 1st- and the 2nd-order shapes of PVDF affixed at four separated points, i=1~4, is illustrated. We can deduce $p_{1i}(t)$ (where i=1~4) from the values of the 1st order shape and $p_{2i}(t)$ (where i=1~4) from the values of the 2nd order shape using Eq.(5). For drawing animations, we normalize the amplitudes. Using normalized values, reconstructed vibration at the i-th position is expressed as the next equation.

$$y_i(x,t) = (\frac{2L}{\pi})^2[\cos(\frac{\pi}{2L}x) - 1]p_{1i}(t) - (\frac{2L}{3\pi})^2[\cos(\frac{3\pi}{2L}x) - 1]p_{2i}(t) \quad \cdots\cdots\cdots\cdots\cdots (7)$$

We draw the vibration mode shapes using equations of this type.

Reconstructing the modes, we use strain distributions both calculated by NASTRAN and detected by PVDF. Reconstructed modes obtained by calculated strain distributions are shown in Fig.4(b) and reconstructed modes obtained by PVDF outputs are shown in Fig.4(c).

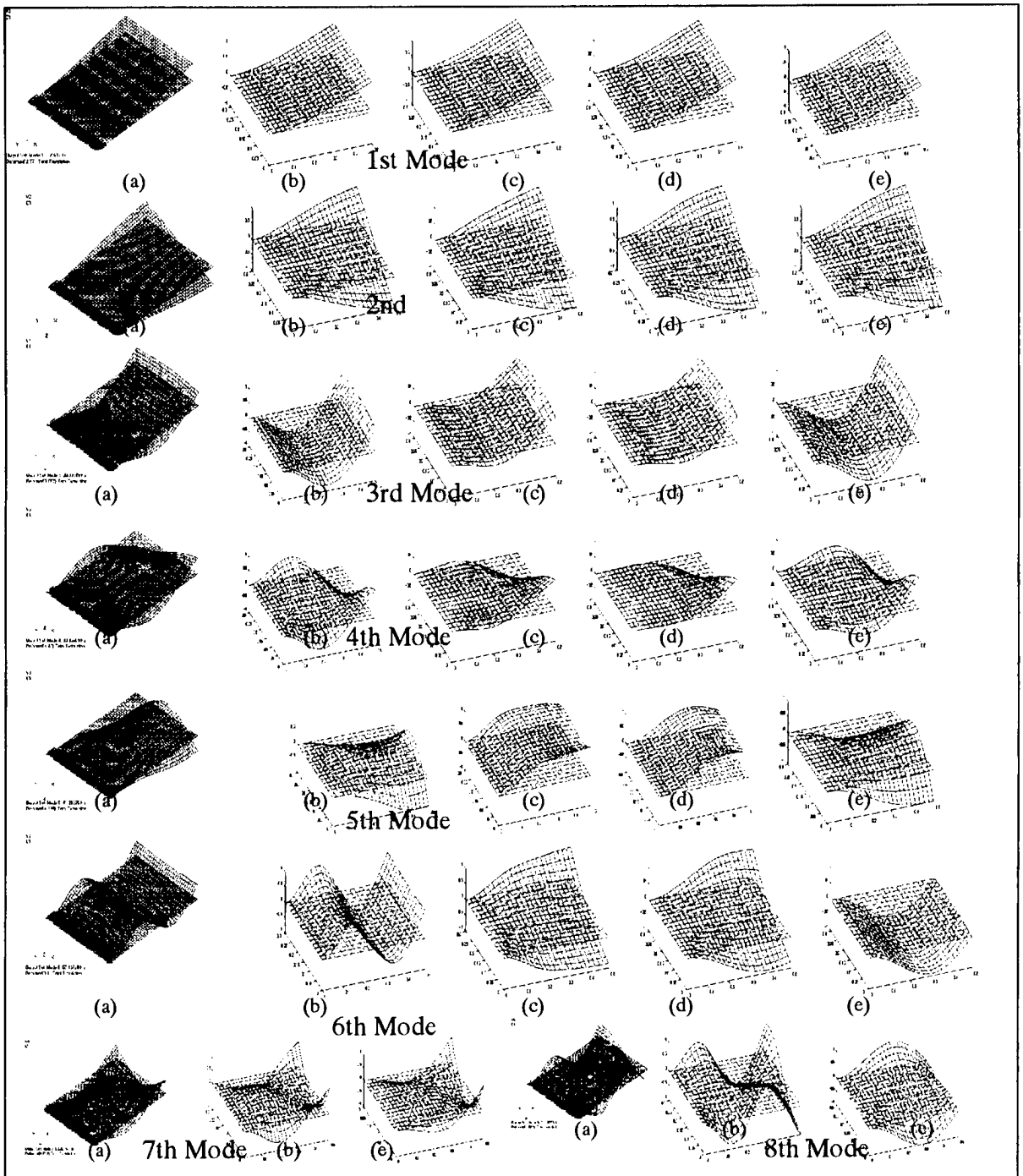
The results (1st to 8th vibration modes) shown in Fig.4(a)-(c) are summarized as follows:

(1) From the 1st to the 8th all vibration modes of the results of "the direct output from NASTRAN" and of "the reconstructed vibration modes, based on our theory, by using predicted strains output from NASTRAN" were quantitatively in good agreement.

(2) In the range from the 1st to the 4th modes, the results obtained by PVDF and the direct output from NASTRAN were quantitatively in good agreement.

ERROR IN CASE OF OMITTING HIGHER-ORDER PVDF SHAPES

In order to estimate the errors in the case of omitting the 3rd- and the higher-order shapes



(a) Modes of Direct outputs from NASTRAN (b) Modes by calculated strain distribution (c) Modes by PVDF outputs (d) Modes by using measured outputs from only 1st and 2nd PVDF shapes (e) Modes by using calculated strains of only 1st and 2nd PVDF shapes

Fig.4 Vibration modes

of PVDF, the experimental results were compared with the estimations based on the calculations by NASTRAN.

Shown in Fig.4(d) and (e) are reconstructed vibration modes from which higher-order PVDF shapes are omitted. Measured outputs were used in (d), and calculated strains were used in (e). The figures show the following results. If only the 1st- and the 2nd-order shape sensors are used, which means that the 3rd- and the higher-order shapes are omitted, then the accuracies are affected in the 4th and the higher vibration modes of reconstruction from the PVDF output, and in the 6th and the higher vibration modes of reconstruction from the strains calculated by NASTRAN.

CONCLUSIONS

We developed a novel vibration measurement method using distributed sensors for detecting vibration of flexible structures. In this study, being performed precise simulations and experiments, we obtained quantitatively good agreements between experiments and theoretical calculations. The errors in the case of omitting higher order PVDF shapes are also predicted.

Both experimentally and theoretically, we have confirmed the efficacy of the method based on our theory, namely the Fourier series shape affixing method, in which PVDF sensors are used and strain distributions are multiplied by weights and integrated.

ACKNOWLEDGEMENT

This work is supported by the New Energy and Industrial Technology Development Organization (NEDO) of Japan as part of the research and development on smart materials and structure systems.

REFERENCES

1. Nagayasu, K., N. Uchida, T. Hayashi and H. Takahashi. 2000. "Vibration Distribution Reconstruction and Control of a Thin Plate by Using Distributed PVDF Sensors Affixed to the Plate," *Smart Structures and Materials 2000: Mathematics and Control in Smart Structures, Proceedings of SPIE*, 3984, pp. 576-586.
2. Tanaka, N., Y. Kikushima, and Y. Fergusson. 1998. "One-dimensional distributed modal sensors and active modal control for planar structures," *J. of Acoust. Soci. of Am.* 104(1), pp. 217-225.

Damping and Smart Materials

QUASI-STEADY BINGHAM BIPLASTIC ANALYSIS OF ER/MR DAMPERS[1]

Glen A. Dimock,[2] Norman M. Wereley[3]

Abstract

Magnetorheological (MR) fluids are characterized by dynamic yield stress with the application of a magnetic field. The Bingham plastic model has proven useful in modeling MR fluid properties, as in flow mode dampers. However, certain MR fluids can exhibit shear thinning behavior, wherein the fluid's apparent plastic viscosity decreases at high strain rates. The Bingham plastic model does not account for such behavior, resulting in over-prediction of equivalent viscous damping. This paper proposes a Bingham biplastic model to account for shear thinning or shear thickening. This approach assumes a bilinear post-yield viscosity, with a critical strain rate specifying the region of high strain rate flow. Furthermore, the model introduces non-dimensional terms to account for the additional parameters associated with shear thinning and thickening. A comparison is made between Bingham plastic and Bingham biplastic force responses to sinusoidal input, and equivalent viscous damping is examined with respect to nondimensional parameters.

1 Introduction

Magnetorheological (MR) fluids, characterized by a dynamic yield stress in the presence of a magnetic field, have been proposed for a wide variety of shock absorber applications to achieve semi-active damping. These fluids are known to exhibit a number of nonlinear phenomena, such as shear thinning. This effect has traditionally been modeled with power-law or exponential functions (Wang et al, 1999, and Wolff et al, 1998). Shear thinning in MR fluids refers to the reduction in apparent viscosity at high strain rates (Jolly et al, 1999). In order to develop an accurate model for use in MR damper design, it is important to understand all significant fluid properties, including shear thinning.

The Bingham plastic model has been successfully used in previous studies to model rheological fluids (Kamath, 1996). This model considers a fluid with a dynamic yield stress, beyond which a linear plastic viscosity is observed. When applied to flow between two parallel plates, the Bingham plastic model predicts a region of fluid that does not shear, having not reached the dynamic yield stress. Approaching the walls, the fluid shear rate increases as the shear stress increases. For high rod velocity and small gap size, this shear rate can reach values known to cause shear thinning. The Bingham plastic model predicts a constant plastic viscosity for all shear rates, but this assumption can be inaccurate at high shear rates.

This paper proposes a modified Bingham plastic model to account for shear thinning. Rather than fit an exponential curve to the post-yield viscosity, the Bingham biplastic approach considers biplastic post-yield behavior. This approach, while clearly a simplification, may be accurate enough to model MR fluid in most situations. Furthermore, the resulting model is simple enough to readily compare to the Bingham plastic case. For the new model, two parameters are added to the Bingham plastic model. Shear thinning is assumed to occur at a fixed *critical strain rate*, after which the fluid exhibits a *high strain rate*

[1]Presented at the International Conference on Adaptive Structures, 23–26 October 2000, Nagoya, Japan.
[2]Smart Structures Laboratory, Alfred Gessow Rotorcraft Center, Dept. of Aerospace Engineering, University of Maryland, College Park, MD 20742, USA.
[3]Smart Structures Laboratory, Alfred Gessow Rotorcraft Center, Dept. of Aerospace Engineering, University of Maryland, College Park MD 20742, USA. Tel: 301-405-1927. Fax: 301-314-9001. E-mail: wereley@eng.umd.edu

viscosity, and both of these parameters are assumed to be independent of field or strain rate. The new parameters are nondimensionalized for comparison to the Bingham plastic model. Finally, the Bingham biplastic relations are shown to reduce down to Bingham plastic equivalents when limiting cases suggest Bingham plastic flow.

2 Flow mode damper analysis

2.1 Flow mode damper description

Figure 1 depicts a magnetorheological damper operating in the flow mode. A force F is applied to the damper shaft, resulting in a pressure differential ΔP across the piston head. As a result, fluid flows through the annulus, resulting in shaft motion of velocity V_0. Solving for force equilibrium on a fluid element, we obtain the general differential equation of motion and make several simplifications. First, we assume a uniform axial pressure gradient and consider a pressure drop per unit length, $\frac{-\Delta P}{L}$. Secondly, if the gap thickness, d, is very small in comparison to the overall annulus diameter, r, then the gap may be approximated by two parallel plates. Finally, the assumption of steady flow eliminates the acceleration terms. Therefore, the simplified governing equation for plane Poiseuille flow is

$$\frac{d\tau}{dy} = \frac{\Delta P}{L} \tag{1}$$

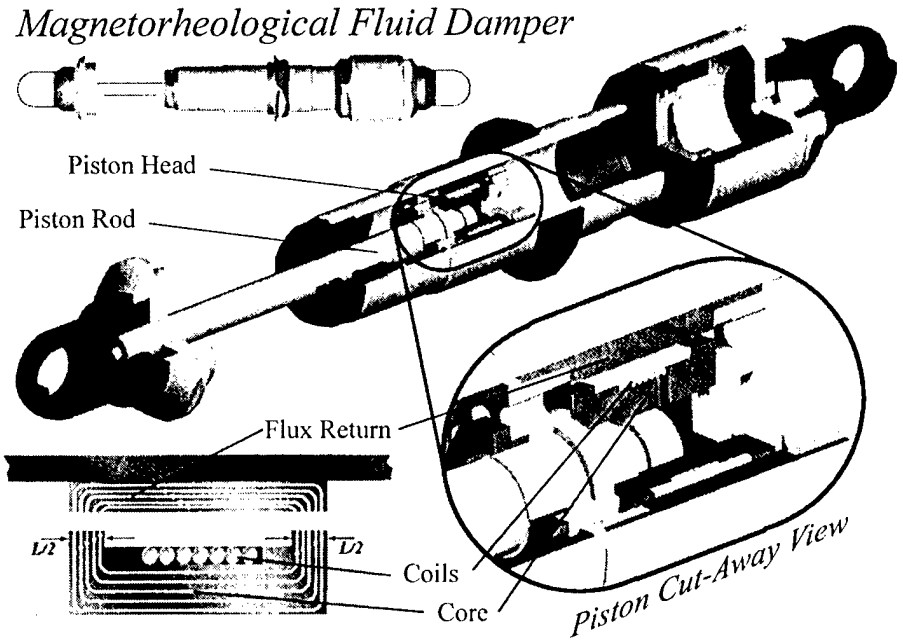


Figure 1: Typical magnetorheological damper

2.2 Newtonian flow

For incompressible fluids, the Newtonian shear mechanism is

$$\tau = \mu \frac{du}{dy} \tag{2}$$

Differentiating Eq. 2 with respect to y and substituting the result into governing Eq. 1 gives the relation

$$\mu \frac{d^2u}{dy^2} = \frac{\Delta P}{L} \tag{3}$$

Integrating Eq. 3 twice with respect to y and applying the velocity boundary conditions, $u(0) = 0$ and $u(d) = 0$, gives the Newtonian velocity profile

$$u(y) = \frac{\Delta P}{2\mu L}\left(y^2 - dy\right) \tag{4}$$

Integrating governing Eq. 1 and applying the shear stress boundary condition, $\tau\left(\frac{d}{2}\right) = 0$, gives the shear stress profile between parallel plates

$$\tau(y) = \frac{\Delta P}{2L}(2y - d) \tag{5}$$

Integrating the velocity profile across the gap yields the total volume flux through the annulus

$$Q = b\int_0^d u(y)dy = -\frac{bd^3\Delta P}{12\mu L} \tag{6}$$

Noting that $Q = A_p v_0$, and that $\Delta P = -\frac{F}{A_p}$, Eq. 6 can be expressed as

$$F = Cv_0 \tag{7}$$

Where the Newtonian viscous damping, C, is given by

$$C = \frac{12A_p^2\mu L}{bd^3} \tag{8}$$

2.3 Bingham plastic flow

A Bingham plastic material is characterized by a dynamic yield stress. Shearing does not occur until the local shear stress, τ, exceeds the dynamic yield stress, τ_y. At the onset of shearing, the fluid exhibits a plastic viscosity, μ, and behaves like a Newtonian fluid. Therefore, the post-yield shear stress can be expressed as

$$\tau = \tau_y \text{sign}\left(\frac{du}{dy}\right) + \mu\frac{du}{dy} \tag{9}$$

Thus, a Newtonian fluid can be viewed as a Bingham plastic material with a dynamic yield stress of zero (Fig. 2). For an MR fluid, the dynamic yield stress can be approximated by a quadratic function of the magnetic field. In the presence of a field, the fluid particles are aligned perpendicular to the field (Fig. 2). Thus, the fluid becomes more rigid and develops a yield stress.

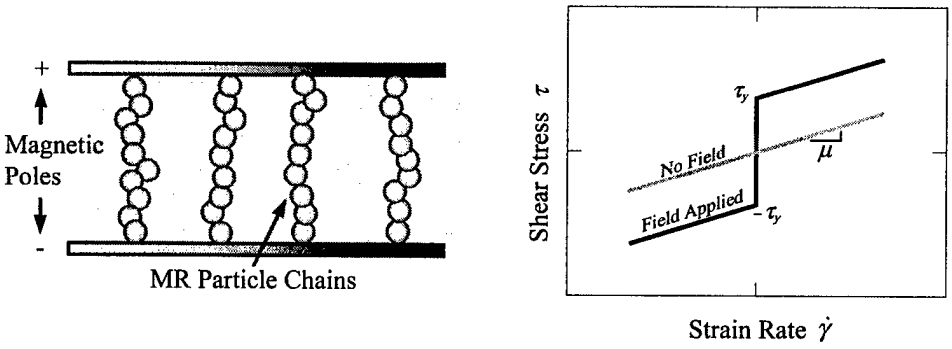


Figure 2: MR particle chains and Bingham plastic shear stress vs. strain rate

The velocity profile for Bingham plastic flow between parallel plates is given by Wereley and Pang (1998). Three distinct flow regions (Fig. 3) are given as

$$\begin{aligned} u_1(y) &= \frac{\Delta P}{2\mu L}\left[\left(y^2 - (d-\delta)\,y\right)\right] \\ u_2(y) &= -\frac{\Delta P}{8\mu L}(d-\delta)^2 \\ u_3(y) &= \frac{\Delta P}{2\mu L}\left[\left(y^2 - (d+\delta)\,y + d\delta\right)\right] \end{aligned} \tag{10}$$

Region 2, the plug region, is characterized by a shear stress less than the fluid yield stress τ_y, and therefore zero strain rate. This width of the pre-yield region is denoted by the plug thickness, δ, which is nondimensionalized with respect to the gap width as

$$\bar{\delta} = \frac{2L\tau_y}{d\Delta P} \tag{11}$$

The total Bingham plastic volume flux is

$$Q = \frac{bd^3\Delta P}{12\mu L}\left(1-\bar{\delta}\right)^2\left(1+\frac{\bar{\delta}}{2}\right) \tag{12}$$

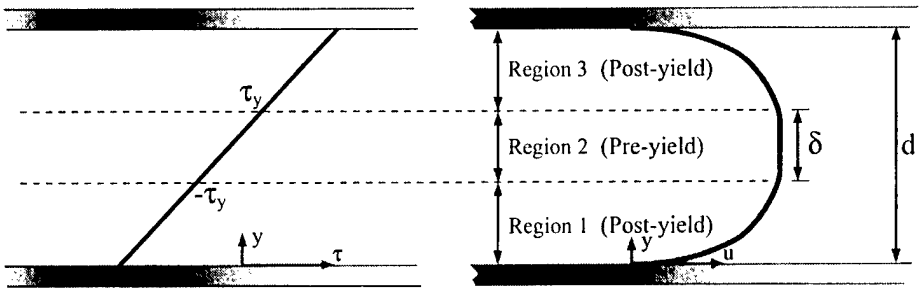


Figure 3: Parallel plate Bingham plastic shear stress and velocity profiles

2.4 Bingham biplastic flow

Shear thinning refers to the decrease of apparent viscosity at high strain rates and is an important characteristic of MR fluids, as shown in Fig. 4 (Jolly et al, 1999). To account for this behavior, we will consider a bingham biplastic material with two distinct, linear post-yield viscosities. A critical strain rate, $\dot{\gamma}_t$, marks the boundary between the low strain rate viscosity, μ_0, and the high strain rate viscosity, μ_1. Figure 5 shows the effects of shear thinning and shear thickening in this analysis.

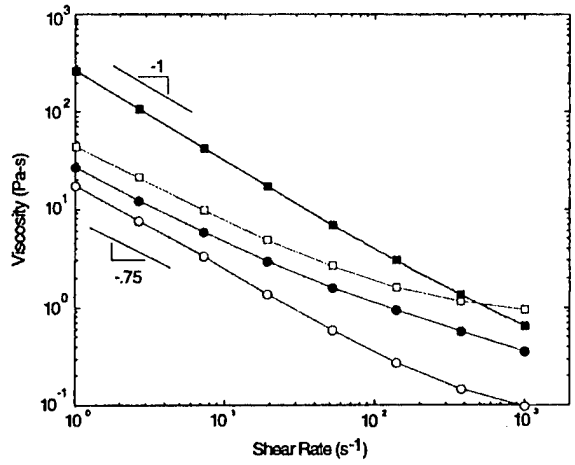


Figure 4: Viscosity as a function of shear rate at 25° for MRX-126PD(○), MRX-242AS (●), MRX-140ND (□), and MRX-336AG (■). Figure provided courtesy of Dr. Mark Jolly (Lord Corporation).

By calculating force equilibrium across the gap, we obtain shear stress in terms of pressure drop, ΔP, as

$$\tau = \frac{y\Delta P}{L} \tag{13}$$

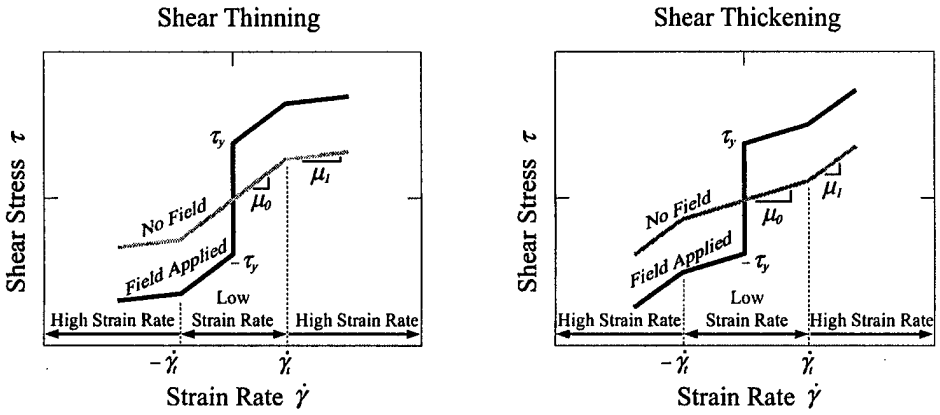


Figure 5: Bingham biplastic shear stress vs. strain rate for shear thinning and shear thickening

This expression is useful when calculating the velocity profile

By inspection of Fig. 5, the shear stress can also be written in terms of the Bingham biplastic fluid parameters as

$$\tau = \begin{cases} \tau_y \text{sign}\left(\frac{du}{dy}\right) + \mu \frac{du}{dy} & \text{if} \quad \frac{du}{dy} < \dot{\gamma}_t \\ \tau_y \text{sign}\left(\frac{du}{dy}\right) + \mu_0 \dot{\gamma}_t + \mu_1 \left(\frac{du}{dy} - \dot{\gamma}_t\right) & \text{if} \quad \frac{du}{dy} > \dot{\gamma}_t \end{cases} \tag{14}$$

Note that the high strain rate equation collapses down to the Bingham plastic case for equal low and high strain rate viscosities, μ_0 and μ_1. Also, this analysis is general enough to account for shear thickening, where $\mu_1 > \mu_0$.

Bingham biplastic flow consists of three regions, each symmetric about the gap-center axis (Fig. 6). Region 1, the pre-yield region, is identical to the Bingham plastic pre-yield plug, where the local shear stress has not yet exceeded the dynamic yield stress. Region 2, the post-yield, low strain rate region, consists of fluid that has yielded but has not reached the critical strain rate, $\dot{\gamma}_t$, or the onset of shear thinning or thickening. Region 3, the post-yield, high strain rate region, contains fluid exhibiting shear thinning or thickening behavior at high strain rates. The velocity profile is obtained by summing forces and applying the appropriate boundary conditions in each region.

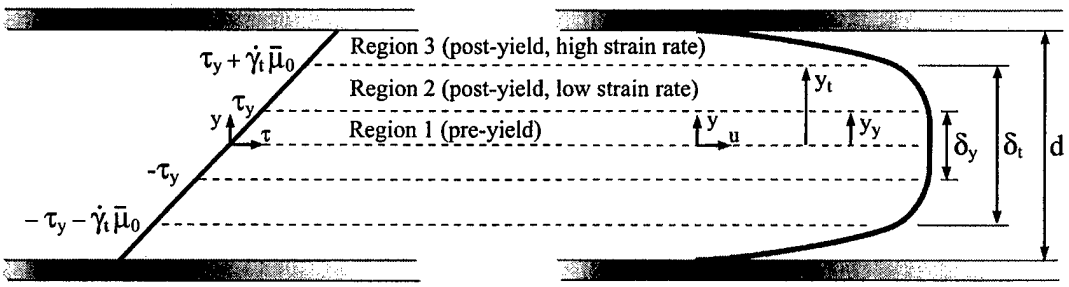


Figure 6: Bingham biplastic shear stress and velocity profiles

In calculating the velocity profile, y is chosen to originate at the gap center, and the flow is examined on only one side of the gap. Because the velocity profile is symmetric about the gap-central axis in a parallel plate analysis, the resulting volume flux equations are doubled to obtain total volume flux. Note that this approach is a change from the original Bingham plastic analysis, where the y axis was measured from one side of the gap (Wereley and Pang, 1998).

Force equilibrium yields distances y_y and y_t, which define the flow regions as below

$$y_y = \frac{\delta_y}{2} = \frac{\tau_y L}{\Delta P} \tag{15}$$

$$y_t = \frac{\delta_t}{2} = \frac{\dot{\gamma}_t \mu_0 L}{\Delta P} + \frac{\tau_y L}{\Delta P} \tag{16}$$

It can be noted that y_t does not depend on the high strain rate viscosity viscosity, μ_1, and that this value approaches y_y as critical strain rate $\dot{\gamma}_t$ approaches zero.

Note that δ_y is equivalent to the Bingham plastic plug thickness, δ, and δ_t represents the low strain rate region. These parameters are nondimensionalized with respect to the gap width as

$$\bar{\delta}_y = \frac{2\tau_y L}{d\Delta P} \tag{17}$$

$$\bar{\delta}_t = \frac{2\dot{\gamma}\mu_0 L}{d\Delta P} + \frac{2\tau_y L}{d\Delta P} \tag{18}$$

2.4.1 Region 3 (post-yield, high strain rate)

The boundary condition for region 3 dictates zero flow at the walls

$$u_3\left(\frac{d}{2}\right) = 0 \tag{19}$$

In this region, Eq. 14 gives the shear stress as

$$\tau = \tau_y + \mu_0\dot{\gamma}_t + \mu_1\left(\frac{du}{dy} - \dot{\gamma}_t\right) \tag{20}$$

The velocity profile in region 3 is obtained by integrating Eq. 20 across the region and substituting Eq. 13 for τ. Applying the aforementioned boundary condition gives

$$u_3(y) = \left(\frac{2y-d}{2\mu_1}\right)\left(\frac{\Delta P}{4L}(2y+d) - \tau_y - \dot{\gamma}_t(\mu_0 - \mu_1)\right) \tag{21}$$

2.4.2 Region 2 (post-yield, low strain rate)

In region 2, the boundary condition requires flow continuity between regions 2 and 3: $u_2(y_t) = u_3(y_t)$ Because region 2 does not experience shear thinning, Eq. 14 gives the shear stress here as

$$\tau = \tau_y \text{sign}\left(\frac{du}{dy}\right) + \mu_0\frac{du}{dy} \tag{22}$$

Noting that the shear stress in region 2 corresponds to that of a Bingham plastic material.

The region 2 velocity profile is calculated by integrating Eq. 22 across the region and applying the flow-continuity boundary condition. Eq. 15 and Eq. 16 define the locations of regions 2 and 3, and we obtain

$$u_2(y) = \frac{1}{\mu_0}\left(\frac{y\Delta P}{2L} - \tau_y\right) + \frac{1}{\mu_1}\left[-\dot{\gamma}_t(\mu_0 - \mu_1)\left(\frac{\dot{\gamma}_t L\mu_0}{2\Delta P} + \frac{\tau_y L}{\Delta P} - \frac{d}{2}\right) + \frac{d}{2}\left(\tau_y - \frac{d\Delta P}{4L}\right) + \frac{\tau_y^2 L}{2\Delta P}(\bar{\mu} - 1)\right] \tag{23}$$

where the viscosity ratio, $\bar{\mu}$, is defined as

$$\bar{\mu} = \frac{\mu_1}{\mu_0} \tag{24}$$

2.4.3 Region 1 (pre-yield)

In region 1, the fluid flows with a uniform velocity, because the local shear stress throughout this region has not reached the yield stress necessary for shearing. Thus, given the boundary condition of flow continuity between regions 1 and 2, the pre-yield plug velocity may be found by substituting Eq. 15 into Eq. 23 to give

$$u_1(y) = \frac{-\tau_y^2 L}{2\mu_0\Delta P} + \frac{1}{\mu_1}\left[-\dot{\gamma}_t(\mu_0 - \mu_1)\left(\frac{\dot{\gamma}_t L\mu_0}{2\Delta P} + \frac{\tau_y L}{\Delta P} - \frac{d}{2}\right) + \frac{d}{2}\left(\tau_y - \frac{d\Delta P}{4L}\right) + \frac{\tau_y^2 L}{2\Delta P}(\bar{\mu} - 1)\right] \tag{25}$$

2.4.4 Flow rate

Total flow rate will be examined in terms of the flow properties, $\bar{\delta}_y$ and $\bar{\delta}_t$. These properties, in turn, depend on fluid parameters and applied pressure differential. Therefore, with knowledge of the fluid properties and damper geometry, flow rate can be predicted in terms of applied force.

The velocity profile is related to the flow properties by substituting Eqs. 15 and 16 into the velocity profile relations to obtain

$$\begin{aligned} u_1(y) &= -\frac{\Delta P}{8L}\left[\frac{(\delta_t-d)^2}{\mu_1}+\frac{(\delta_y-\delta_t)(\delta_y+\delta_t-2d)}{\mu_0}\right] \\ u_2(y) &= -\frac{\Delta P}{8L}\left[\frac{(\delta_t-d)^2}{\mu_1}-\frac{4y(y-\delta_y)+2d(\delta_y-\delta_t)+\delta_t^2}{\mu_0}\right] \\ u_3(y) &= -\frac{\Delta P}{8L}\left[\frac{(d-2y)(2y+d-2\delta_t)}{\mu_1}+\frac{2(d-2y)(\delta_t-\delta_y)}{\mu_0}\right] \end{aligned} \tag{26}$$

Integrating the velocity profile across each region gives the flow rate in that region. Each region exists twice in the symmetrical gap, so the results are doubled to yield total flow.

$$\begin{aligned} Q_1 &= 2b\int_0^{y_y} u_1(y)\,dy = -\frac{bd^3\Delta P}{8L}\left[\frac{\bar{\delta}_y(\bar{\delta}_t-1)^2}{\mu_1}+\frac{\bar{\delta}_y^2(\bar{\delta}_y-2)-\bar{\delta}_y\bar{\delta}_t(\bar{\delta}_t-2)}{\mu_0}\right] \\ Q_2 &= 2b\int_{y_y}^{y_t} u_2(y)\,dy = -\frac{bd^3\Delta P}{8L}\left[\frac{(\bar{\delta}_t-2)(\bar{\delta}_t^2-\bar{\delta}_t\bar{\delta}_y)+\bar{\delta}_t-\bar{\delta}_y}{\mu_1}-\frac{2\left(2\bar{\delta}_t^3+\bar{\delta}_y^3-3\bar{\delta}_y\bar{\delta}_t^2-3(\bar{\delta}_y-\bar{\delta}_t)^2\right)}{3\mu_0}\right] \\ Q_3 &= 2b\int_{y_t}^{\frac{d}{2}} u_3(y)\,dy = -\frac{bd^3\Delta P}{4L}\left[\frac{(\bar{\delta}_t-1)^3}{3\mu_1}+\frac{\bar{\delta}_t(\bar{\delta}_t-2)(1-\bar{\delta}_y+\bar{\delta}_t-\bar{\delta}_y)}{2\mu_0}\right] \end{aligned} \tag{27}$$

The total volume flux is then

$$Q=\frac{bd^3\Delta P}{12\mu_0 L}\left[(1-\bar{\delta}_y)^2\left(1+\frac{\bar{\delta}_y}{2}\right)-(1-\bar{\delta}_t)^2\left(1+\frac{\bar{\delta}_t}{2}\right)\left(1-\frac{1}{\bar{\mu}}\right)\right] \tag{28}$$

The velocity profile in the case of shear thinning is plotted as a function of field and viscosity ratio, $\bar{\mu}$, in Fig. 7. Note the effects of these parameters on the size of the pre-yield region, δ_y, and the location of the extent of shear thinning, the region outside δ_t. Increasing field widens the pre-yield region, δ_y, and a higher critical strain rate increases the size of low strain rate region, δ_t.

3 Constant velocity input

For flow mode damper analysis, it is useful to consider force response for a given velocity. For Bingham plastic flow, this response depends on plastic viscosity, μ, yield stress, τ_y, and the damper geometry. However, in the event of shear thinning, several new parameters must be considered. The high strain rate behavior depends both on critical strain rate, $\dot{\gamma}_t$, and on the high strain rate viscosity, μ_1.

By noting that $Q = A_p v_0$ and that $\Delta P = \frac{F}{A_p}$, Eq. 28 can be manipulated to give a polynomial expression for applied force F with respect to rod velocity v_0

$$F^3\left(\frac{bd^3}{12\mu_1 A_p^2 L}\right)+F^2\left[v_0+\left(\frac{bd^3\dot{\gamma}_t}{4A_p}\right)\left(1-\frac{1}{\bar{\mu}}\right)\right]-\left(\frac{bA_pL^2}{3\mu_0}\right)\left[(\dot{\gamma}_t\mu_0-\tau_y)^3\left(1-\frac{1}{\bar{\mu}}\right)-\tau_y^3\right]=0 \tag{29}$$

The roots of this polynomial are solved numerically, and the single valid root is determined. For a Bingham plastic material, the fluid yield stress causes a yield force in the damper, and the post-yield plastic viscosity causes nearly linear post-yield damping. Shear thinning modifies this profile, due to a bilinear post-yield viscosity, characterized by a critical strain rate. Fig. 8 compares these effects to Newtonian (zero yield stress) and Bingham plastic flow, respectively. Both plots show the effects of low and high critical strain rate, $\dot{\gamma}_t$, as well as low and high values of high strain rate viscosity, μ_1, which correspond to shear thinning and shear thickening, respectively.

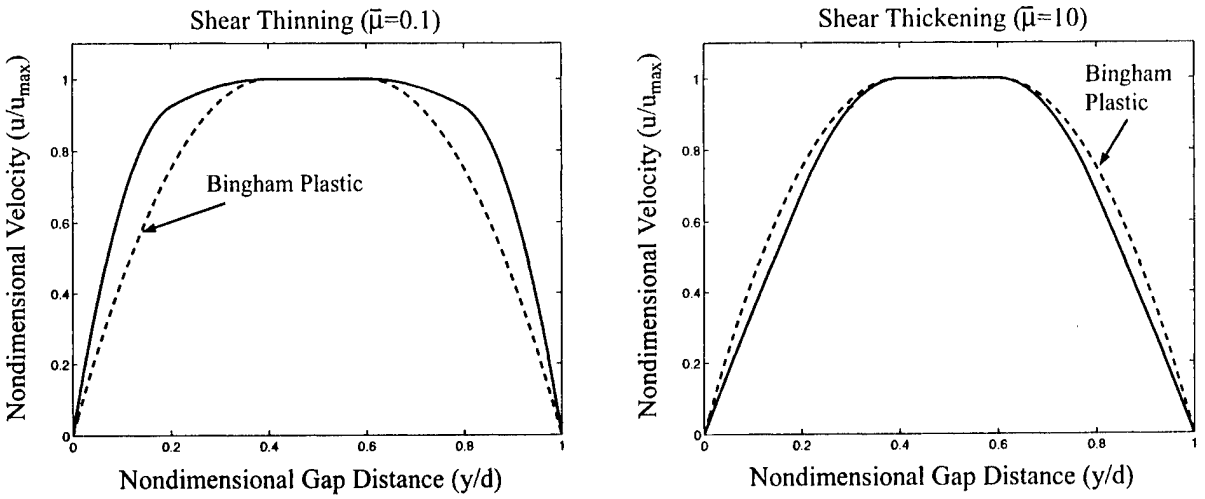


Figure 7: The velocity profile of a Bingham biplastic material with shear thinning and thickening is compared to that of a Bingham plastic material

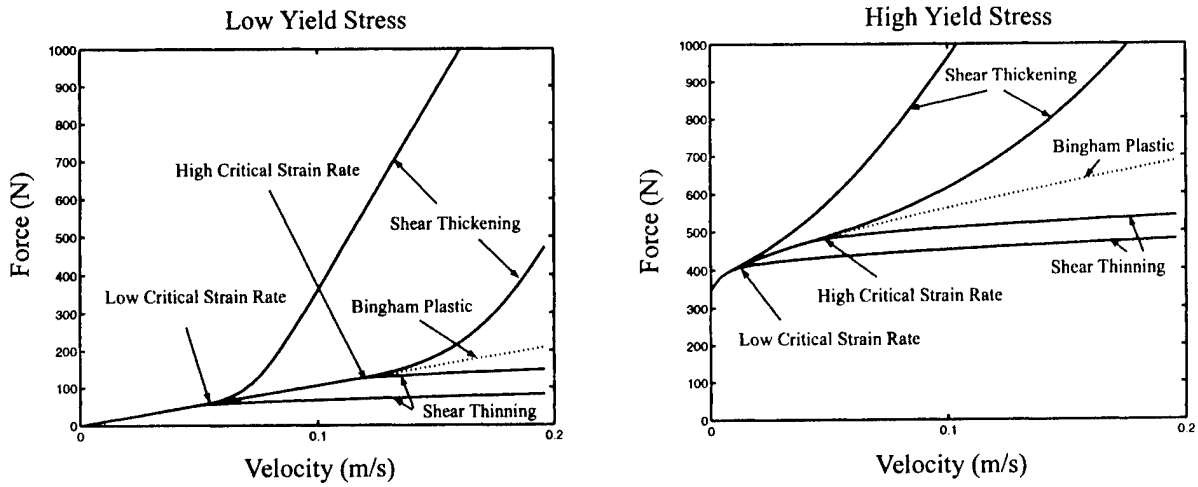


Figure 8: Force vs. Velocity for varying yield force, critical strain rate, and viscosity ratio

4 Nondimensional analysis

For damper sizing purposes, we examine equivalent viscous damping, C_{eq}, in nondimensional terms, with and without shear thinning or thickening. The equivalent viscous damping is nondimensionalized with respect to Newtonian damping, C_n, and special considerations are made for shear thinning. The nondimensional damping term is compared to various nondimensionalized flow properties as follows.

4.1 Bingham plastic flow

Noting that $Q = A_p v_0$, and that $\Delta P = -\frac{F}{A_p}$, Eq. 12 can be expressed as

$$F = C_{eq} v_0 \tag{30}$$

where C_{eq} represents the equivalent viscous damping for a Bingham plastic flow. The ratio of C_{eq} to the Newtonian damping constant, C, is

$$\frac{C_{eq}}{C} = \frac{1}{(1-\bar{\delta})^2\left(1+\frac{\bar{\delta}}{2}\right)} \tag{31}$$

The damping coefficient $\frac{C_{eq}}{C}$ indicates the dynamic range of the damper because it is the ratio of the field dependent damping to the zero field damping. Note that as the strain rate becomes very high or the applied magnetic field becomes very low, the nondimensional plug thickness approaches zero, and the damper exhibits a dynamic range of 1. In this case, the damper behaves as a passive viscous damper. Similarly, at low strain rates or high applied magnetic fields, the plug thickness increases, giving the damper a high dynamic range.

4.2 Bingham biplastic flow with Newtonian normalization

To determine the Bingham biplastic damping coefficient, an appropriate value of C must be chosen for the normalization. In the Bingham plastic case, C_{eq} is simply normalized with respect to Newtonian damping, C, which also corresponds to the zero-field Bingham plastic case. If we normalize Bingham biplastic damping, $C_{eq,t}$, with respect to Newtonian damping as illustrated in Fig. 9, we obtain the relation

$$\frac{C_{eq,t}}{C} = \frac{1}{(1-\bar{\delta}_y)^2\left(1+\frac{\bar{\delta}_y}{2}\right) - (1-\bar{\delta}_t)^2\left(1+\frac{\bar{\delta}_t}{2}\right)\left(1-\frac{1}{\bar{\mu}}\right)} \tag{32}$$

where Newtonian damping, C, is given by Eq. 8, and we have set the Newtonian viscosity equal to the low strain rate viscosity, μ_0. Note that this normalization is ineffective at high strain rates, where it indicates an unrealistic dynamic range for the damper. As the strain rate gets very large ($\bar{\delta}_y \to 0$), the damper should exhibit pure viscous damping, with a damping coefficient of 1. However, because this normalization does not allow for shear thinning in the Newtonian damping value, $C_{eq,t}$ does not approach C at high strain rates.

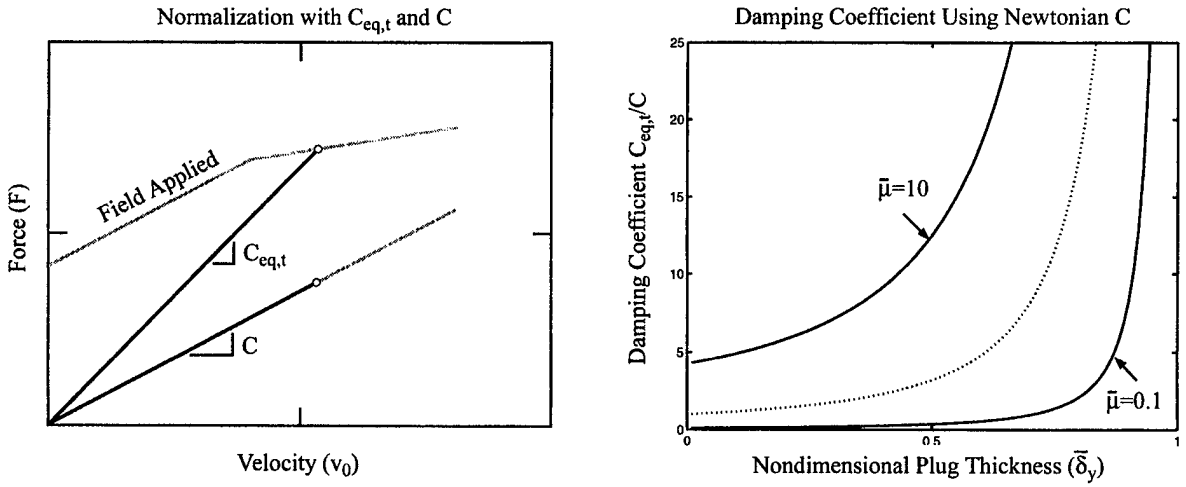


Figure 9: Normalization with respect to Newtonian damping C

4.3 Bingham biplastic flow with zero-field damper normalization

Bingham biplastic damping, $C_{eq,t}$, is more appropriately normalized with respect to the zero-field biplastic case, C_t, which is defined as

$$C_t = C_{eq,t} \quad \text{as} \quad \bar{\delta}_y \to 0 \tag{33}$$

This normalization accurately predicts the damper's dynamic range at all strain rates, as illustrated in Fig. 10.

When $C_{eq,t}$ is compared to the equivalent zero-field case with shear thinning, C_t, the damping coefficient becomes

$$\frac{C_{eq,t}}{C_t} = \frac{1-\left(1-\bar{\delta}_t\right)^2\left(1+\frac{\bar{\delta}_t}{2}\right)\left(1-\frac{1}{\bar{\mu}}\right)}{\left(1-\bar{\delta}_y\right)^2\left(1+\frac{\bar{\delta}_y}{2}\right)-\left(1-\bar{\delta}_t\right)^2\left(1+\frac{\bar{\delta}_t}{2}\right)\left(1-\frac{1}{\bar{\mu}}\right)} \tag{34}$$

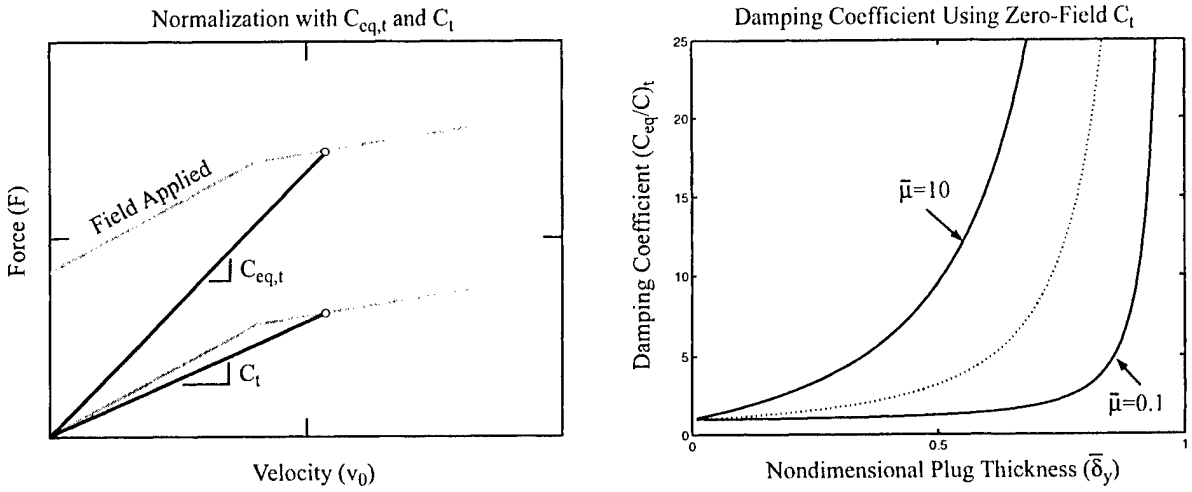


Figure 10: Normalization with respect to zero-field damping with shear thinning C_t

4.4 Variation of biplastic parameters

Bingham biplastic flow depends on two additional nondimensional parameters. First, the ratio of low and high strain rate viscosity is defined by the viscosity ratio, $\bar{\mu}$. Secondly, critical strain rate, $\dot{\gamma}$, will be nondimensionalized with a new parameter, $\bar{\epsilon}$.

From Eq. 17, it can be seen that the size of the low strain rate region depends on critical strain rate but not on the high strain rate viscosity. Therefore, a nondimensional term including δ_t will provide information about $\dot{\gamma}_t$ independently of $\bar{\mu}$. We define a ratio, $\bar{\epsilon}$, as

$$\bar{\epsilon} = \frac{1-\bar{\delta}_t}{1-\bar{\delta}_y} \tag{35}$$

where $\bar{\epsilon}$ represents the extent of shear thinning or thickening in the gap, which is the ratio of fluid exhibiting shear thinning to the total amount of post-yield fluid. When $\bar{\epsilon}$ approaches 1, all post-yield fluid is undergoing shear thinning. Similarly, as $\bar{\epsilon}$ approaches 0, no fluid exhibits shear thinning. It is important to use $\bar{\epsilon}$ instead of $\bar{\delta}_t$ when nondimensionalizing the damper properties, because $\bar{\delta}_t$ can never be smaller than $\bar{\delta}_y$; shear thinning does not apply within the pre-yield region. This would restrict the scope of the nondimensional analysis. Therefore, $\bar{\delta}_t$ is incorporated into a parameter that can vary independently of $\bar{\delta}_y$.

By substituting Eq. 35 into Eqs. 32 and 34, the damping ratios can be expressed in terms of $\bar{\epsilon}$ as

$$\frac{C_{eq,t}}{C} = \frac{1}{\left(1-\bar{\delta}_y\right)^2\left(1+\frac{\bar{\delta}_y}{2}-\bar{\epsilon}^2\left(\frac{3}{2}-\frac{\bar{\epsilon}}{2}\left(1-\bar{\delta}_y\right)\right)\right)\left(1-\frac{1}{\bar{\mu}}\right)} \tag{36}$$

$$\frac{C_{eq,t}}{C_t} = \frac{1-\bar{\epsilon}^2\left(1-\bar{\delta}_y\right)^2\left(\frac{3}{2}-\frac{\bar{\epsilon}}{2}\left(1-\bar{\delta}_y\right)\right)\left(1-\frac{1}{\bar{\mu}}\right)}{\left(1-\bar{\delta}_y\right)^2\left(1+\frac{\bar{\delta}_y}{2}-\bar{\epsilon}^2\left(\frac{3}{2}-\frac{\bar{\epsilon}}{2}\left(1-\bar{\delta}_y\right)\right)\right)\left(1-\frac{1}{\bar{\mu}}\right)} \tag{37}$$

Given these relations, shear thinning behavior may be compared to Bingham plastic behavior, which is represented on all plots by a dashed line. Fig. 11 shows variation in viscosity ratio, $\bar{\mu}$ for low and high values of the shear thinning ratio, $\bar{\epsilon}$. This plot uses the $\left(\frac{C_{eq}}{C}\right)_t$ normalization and demonstrates the effect of shear thinning extent on damping coefficient. As would be expected, shear thinning and thickening are more noticeable at high values of $\bar{\epsilon}$, where they seriously affect the dynamic range of the damper. Note that shear thinning lowers the damping coefficient, while shear thickening raises the damping coefficient.

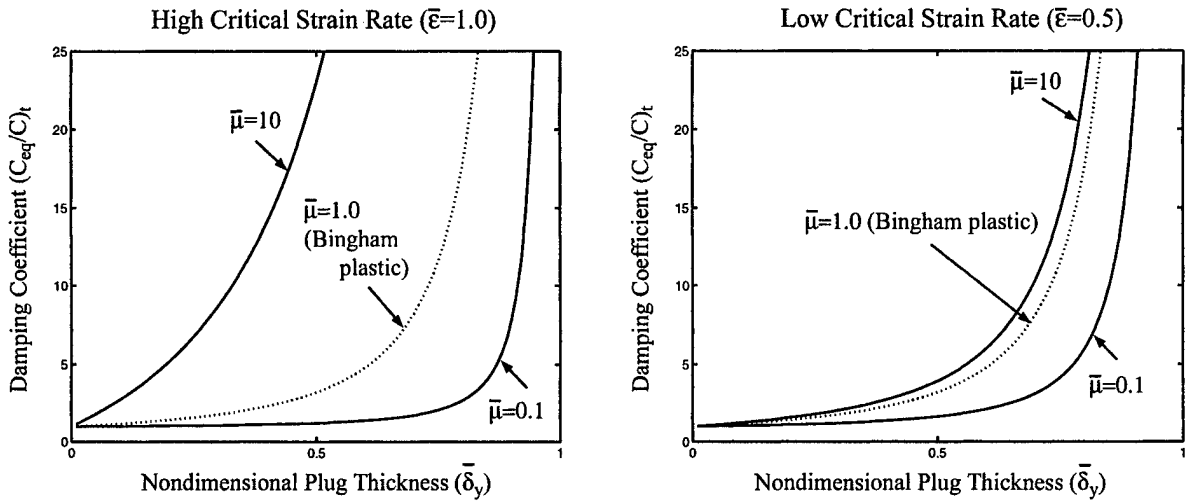


Figure 11: $\left(\frac{C_{eq}}{C}\right)_t$ vs. $\bar{\delta}_y$ for varying $\bar{\epsilon}$ and $\bar{\mu}$

5 Limiting cases

The shear thinning relations can be shown to collapse down to equivalent Bingham plastic equations in various limiting cases.

5.1 Extreme strain rates

When the strain rate, $\frac{du}{dy}$, has not yet reached the critical strain rate, $\dot{\gamma}_t$, the fluid exhibits only two velocity profile regions. Here, $\bar{\delta}_t = 1$, and all the region 3 terms in the shear thinning equations approach zero. Therefore, these equations collapse down to Bingham plastic equivalents. Indeed, it can be seen from Fig. 5 that the fluid behaves as a Bingham plastic material at low strain rates.

When the strain rate is small, it may be seen from Eq. 17 that δ_t approaches δ_y. In this case, the fluid is dominated by shear thinning, as region 2 disappears. Similar to the low strain rate case, high strain rates result in a Bingham plastic material, where $\bar{\delta}_t = \bar{\delta}_y$. Again, the shear thinning equations collapse down to Bingham plastic equivalents, where the fluid exhibits a plastic viscosity μ_1.

5.2 Colinear post-yield viscosities

When the low strain rate viscosity, μ_0, approaches the high strain rate viscosity, μ_1, Eq. 24 demonstrates that the viscosity ratio, $\bar{\mu}$, approaches 1. Furthermore, it can be shown that all of the Bingham biplastic relations collapse down to equivalent Bingham plastic equations with viscosity $\mu_0 = \mu_1$.

6 Conclusions

MR fluids have been successfully modeled with the Bingham plastic model, but these fluids are known to exhibit shear thinning. In this analysis, the Bingham plastic model is extended to account for shear

thinning or thickening, which is the respective decrease or increase of viscosity at high strain rates. Shear thinning or thickening over a given strain rate range is approximated by low and high strain rate regions, each of which is characterized by a unique linear plastic viscosity. A critical strain rate divides the two regions.

Nondimensional parameters are introduced to account for the ratio of low and high strain rate viscosity, as well as critical strain rate. When coupled with Bingham plastic nondimensional parameters, these relationships show the expected effects of shear thinning or thickening on MR damper performance. The damping coefficient indicates the dynamic range of the damper and is compared to the Bingham plastic case. With shear thinning, we observe that the damper exhibits a lower dynamic range and must be operated at higher magnetic fields or lower speeds to achieve a given damping ratio. The opposite is true of shear thickening.

Acknowledgements

Research support was provided under a grant by the U.S. Army Research Office Young Investigator Program, contract no. 38856-EG-YIP. Laboratory equipment was provided under a grant by the FY96 Defense University Research Instrumentation Program (DURIP), contract no. DAAH-0496-10301. For both grants, Dr. Gary Anderson served as technical monitor.

References

[1] M. Jolly, J. Bender and J. Carlson (1999). "Properties and applications of commercial magnetorheological fluids," *Journal of Intelligent Material Systems and Structures,* Vol. 10, No. 1, pp. 5–13.

[2] G. Kamath, M. Hurt and N. Wereley (1996). "Analysis and Testing of Bingham Plastic Behavior in Semi-Active Electrorheological Fluid Dampers," *Smart Materials and Structures,* Vol. 5, No. 5, pp. 576–590.

[3] X. Wang and F. Gordaninejad (2000). "Controllable fluid dampers in flow mode using Herschel-Bulkley model," *7th Annual SPIE Symposium on Smart Structures and Materials, Conference on Damping and Isolation,* Newport Beach, CA, 5-9 March, Paper No. 3989-23.

[4] N. Wereley and L. Pang (1998). "Nondimensional analysis of semi-active electrorheological and megnetorheological dampers using approximate parallel plate models," *Smart Materials and Structures,* Vol. 7, pp. 732–743.

[5] C. Wolff-Jesse and G. Fees (1998). "Examination of flow behaviour of electrorheological fluids in the flow mode," *Journal of Systems and Control Engineering,* Vol. 212, No. 13, pp. 159–173.

DYNAMIC CHARACTERISTICS AND SEMI-ACTIVE CONTROL OF A SMART COMPOSITE PLATE WITH ER FLUID

Ki-Dae-Cho, Do-Hyung Kim, Won-Ho Shin, In Lee

ABSTRACT

In this research, a smart structure with multi-electrode configuration is proposed, which contains ER fluid. Multi-electrode configuration gives the structure a capability to change their modal characteristics effectively. The proposed configuration also provides the effective vibration control performance with the reduced power consumption in the smart structures. A finite element model has been developed for the analysis of a smart composite plate under fully and partially applied electric fields. The numerical results of the composite plate with ER fluid are compared with experimental results. The performance and energy consumption of the control system are investigated experimentally for various applied areas of electric field by applying a semi-active control law to the vibrating composite plate.

INTRODUCTION

Many experimental and theoretical studies for smart structures constructed with ER fluid have been performed out since the controllability of the rheological property by the applied electric field was first discovered by Winslow in 1949. Gandhi et al.[1] suggested a possibility of using the ER fluid to suppress deflections of the ER fluid-based structures by avoiding resonance situation. Choi et al.[2] also studied the vibration characteristics of an ER beam. Several researchers introduced the conventional sandwich beam theories[3,4] to formulate an analytical model for the ER fluid-filled structures. Coulter et al.[5] examined the applicability of two theoretical structural theories, the RKU model[3] and the Mead & Markus model[4] developed for polymer-based beam structures, to ER-based-beam structures. Rahn et al.[6] introduced results from sandwich beams to analyze the ER beam but experimental implementation for realizing an active vibration control was not accomplished. Choi et al.[7] used a finite element model based on three-layer model like the approach by Mead[4] to predict field-dependent modal characteristics of an ER fluid-based plate with four partitioned electrodes. Also, experimental implementation was accomplished.

Researches on the dynamic model and vibration control of ER fluid-filled plate structures

Division of Aerospace Engineering, Department of Mechanical Engineering, Korea Advanced Institute of Science and Technology, 373-1 Kusong-Dong, Yusong-Gu, Taejon, 305-701, KOREA.

with refined multi-electrode configuration are considerably rare. Most of previous works have used conductive face plate or simple partition of aluminum foil tape as electrode and the three-layer model. In this study, the effects of fully and partially applied electric field of the multi-electrode on the vibration characteristics of the multi-layer composite plate with embedded ER fluid are investigated through finite element analysis and experiments. Also, a simple semi-active control is carried out.

FINITE ELEMENT FORMULATION

Based on the layerwise plate theory[8], the displacement fields (u,v,w) for a two-dimensional element i, of which the area is defined as Ω_i, can be expressed by introducing the piecewise interpolation function, $\Phi^J(z)$.

$$u=\sum_{J=1}^{N_i}U^J(x,y,t)\Phi^J(z),\quad v=\sum_{J=1}^{N_i}V^J(x,y,t)\Phi^J(z),\quad w=W(x,y,t) \tag{1}$$

Here (U^J,V^J,W) are undetermined coefficients for in-plane displacements; N_i is the number of degrees of freedom for the in-plane displacement through the thickness for element i. The linear strain-displacement relation is adopted and constitutive equations of the k-th layer can be written as

$$\{\sigma\}_k=[\overline{C}]\{\varepsilon\}_k \tag{2}$$

where $[\overline{C}]$ is the transformed reduced stiffness matrix. The constitutive equation in the geometric x-y-z coordinate system can be obtained by the proper co-ordinate transformation.

In order to derive the equation of motion for the ER fluid-based laminated plate, Hamilton's principle was applied. Combination of Equations (1), (2), strain-displacement relationship and integration through-the-thickness of the ER fluid-based laminated plate provides the following equation of motion.

$$\int_0^T\iint_{\Omega_i}\Big[\delta\mathbf{e}^T\mathbf{A}_S\mathbf{e}+\sum_J^{N_i}\{\delta\mathbf{e}^T\mathbf{B}_S^J\mathbf{e}_S^J+\delta\mathbf{e}_S^{JT}\mathbf{B}_S^J\mathbf{e}\}+\sum_J^{N_i}\sum_K^{N_t}\{\delta\mathbf{e}^{JT}\mathbf{D}^{JK}\mathbf{e}^K+\delta\mathbf{e}_S^{JT}\mathbf{D}_S^{JK}\mathbf{e}_S^K\}$$
$$+I^0\delta W\ddot{W}+\sum_J^{N_i}\sum_K^{N_t}\delta\mathbf{d}^{JT}\mathbf{I}^{JK}\ddot{\mathbf{d}}^K\Big]dAdt=0 \tag{3}$$

where δ and $\ddot{(\,)}$ mean the variational operator and the second differentiation with respect to time, respectively, and the subscript S denotes transverse shear properties, and other symbols can be referred to reference 9.

Introducing Lagrangian shape functions, the finite element formulation of the ER fluid-based laminated plate in sinusoidal motion gives the equation of motion in the form of a standard eigenvalue problem for free vibration analysis:

$$(\mathbf{K}-\omega^2\mathbf{M})\mathbf{u}=\mathbf{0} \tag{4}$$

where $\mathbf{M}$ and $\mathbf{K}$ are the global mass and stiffness matrices, respectively; $\mathbf{u}$ is the nodal displacement vector of the whole system and ω is the natural frequency.

The modal damping based on the modal strain energy method of the ER fluid-based laminated plate is defined as :

$$\eta = \frac{1}{2\pi}\frac{\Delta E}{E} \tag{5}$$

where ΔE is the energy dissipated per cycle and E is the maximum strain energy. The dissipated energy can be expressed as:

$$\Delta E_e = \frac{1}{2}\int_{\Omega}\left[\mathbf{e}^T\hat{\mathbf{A}}_S\mathbf{e} + \sum_{J}^{N_i}\{\mathbf{e}^T\hat{\mathbf{B}}_S^J\mathbf{e}_S^J + \mathbf{e}_S^{JT}\hat{\mathbf{B}}_S^J\mathbf{e}\} + \sum_{J}^{N_i}\sum_{K}^{N_i}\{\mathbf{e}^{JT}\hat{\mathbf{D}}^{JK}\mathbf{e}^K + \mathbf{e}_S^{JT}\hat{\mathbf{D}}_S^{JK}\mathbf{e}_S^K\}\right]dA \tag{6}$$

Since $\hat{\mathbf{A}}_S$, $\hat{\mathbf{B}}_S^J$, $\hat{\mathbf{D}}^{JK}$ and $\hat{\mathbf{D}}_S^{JK}$ are well documented in reference 9, the details are omitted here. The dissipated energy can be obtained by the introduction of Lagrangian shape functions as follows:

$$\Delta E = \sum_{e=1}^{Ne}\Delta E_e = \frac{1}{2}\mathbf{u}^T\mathbf{K}_d\mathbf{u} \tag{7}$$

where $\mathbf{K}_d$ is referred to as the damped stiffness matrix. In the computation of stiffness matrix, the reduced integration is used for the terms related with shear dissipation energy.

Therefore, the loss factor for each mode based on the MSE can be computed as

$$\eta_i = \frac{1}{2\pi}\frac{\Delta E_i}{E_i} = \frac{1}{2\pi}\frac{\phi_i^T\mathbf{K}_d\phi_i}{\phi_i^T\mathbf{K}\phi_i} \tag{8}$$

where ϕ_i is the i th modal vector obtained from the free vibration analysis.

FABRICATION OF SMART COMPOSITE PLATE

The proposed ER fluid-based smart plate was fabricated by sandwiching an ER fluid between two face plates and sealing with a silicone rubber. The face plate consists of a glass/epoxy laminate with the lay-ups of $[0]_{4T}$ as a host structural member and a copper clad laminate as an electrode. A copper clad laminate is in the form that one side of a glass/epoxy woven laminate is coated with very thin copper layer. The copper clad laminate used in the lower face plate serves as an electrode of common electric field. The copper clad laminate used in the upper face plate has a multi-electrode configuration to provide different positive electric fields to the ER fluid domain independently. The printed circuit technology was used to make this configuration. First, the negative image of the multi-electrode configuration designed in full scale is printed on a negative film as shown in Fig.1. Then, a photosensitizer is applied over the entire surface of a copper clad laminate and dried in a temperature-controlled oven. After being exposed to light through the negative image, the copper clad laminate is developed to leave a protective coating on the multi-electrode configuration. Exposed area is chemically etched out and ferric chloride is used as the etch. Consequently, it changes the surface of a copper clad laminate into the multi-electrode configuration where the copper layer is partitioned into 5×3 segments. This procedure is illustrated in Fig.2. Each face plate was prepared by joining each electrode sheet made applying printed circuit technology to a glass/epoxy laminate with cyanoacrylate adhesive.

The silicone rubber strips which serve as the electrical insulators between the two face plates were lined up along the free edges of the upper face plate. At the clamped end of the smart plate, a glass/epoxy pad was bonded as the mid-layer to provide both the insulation and the rigidity against the clamping force. The lower face plate was bonded to the silicone rubber strips with liquid silicone adhesive (Loctite LC-1524). After this hollow sandwich plate was exposed to room temperature, it was filled with ER fluid. Piezoceramic actuator was bonded to the surface of the upper face plate to obtain steady state responses. The smart plate constructed is presented in Fig. 3.

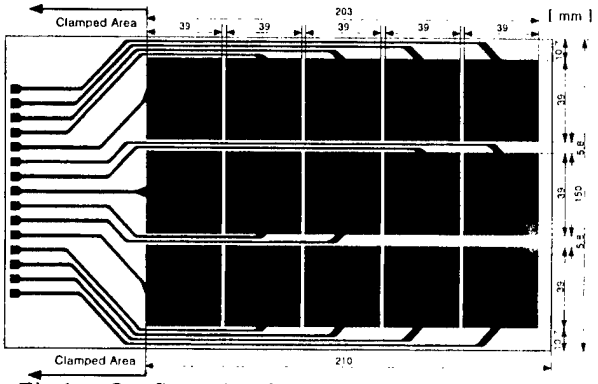


Fig 1. Configuration for positive multi-electrode.

DYNAMIC CHARACTERISTICS

Experimental Implementation

Fig. 4 presents an experimental apparatus to investigate the dynamic characteristics for the smart plate. The cantilevered plate was clamped in the fixture. Each electrode terminal in the upper face plate was wired to a switch in such a way that each can be connected separately to the positive potential, while the common electrode in the lower face plate was connected to the negative potential of a high voltage electric power supply (Matsusada, HEOPS-5B6).

The characteristics of a smart plate can be obtained by modal testing techniques. In this study the actuation force can be given both by the impact hammer (PCB 086B01) and by the bonded piezoelectric actuator. As a measuring device, a laser displacement meter (Keyence LB-1001) was used. The output from the impact hammer and the laser sensor were connected to a FFT analyzer (HP 3567A) to measure the frequency response function. The frequency response functions were then transferred to the STAR modal software system, and they were curve fitted using a polynomial function to obtain the natural frequencies and damping ratios. The bonded

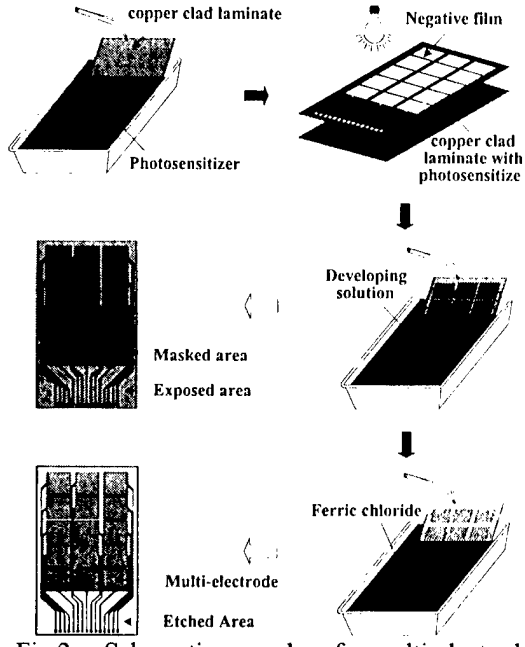


Fig 2. Schematic procedure for multi-electrode shaping.

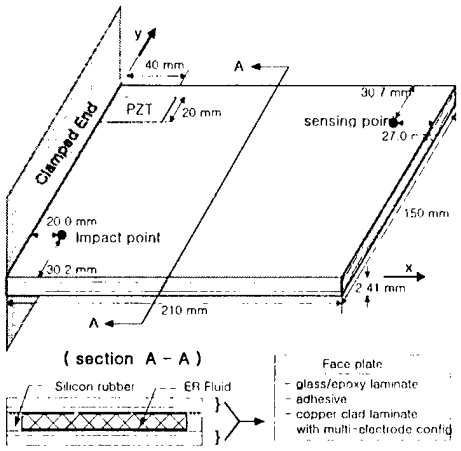


Fig 3. Configurations for cantilevered ER plate.

piezoelectric actuator was used to apply steady state responses in the time domain under forced excitation.

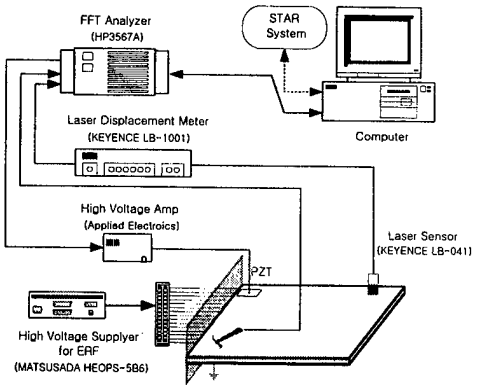


Fig 4. Experimental setup.

Indentification of Dynamic Characteristics

The smart composite plate has total dimensions of $210\times150\times2.41\,mm^3$. In the analysis, four node isoparametric elements with 11 by 10 mesh are used. Each electrode segment was typically modeled using four plate elements, which provides the sufficient resolution of shear in the ER fluid. For the finite element model depicted in Fig. 5, the smart plate was treated as three sublaminates. The individual layer in the face plate has not the degrees of freedom, that is, 2×4 degrees of freedom per node was used to describe the variable in-plane displacement through the thickness. Table I gives the material properties of the face plate and sealing layer. In the analysis, the effect of sealing layer on dynamic properties of the smart plate was considered. The ER fluid used in this study is TX-ER8 of Nippon Shokubai. The rotary oscillation test with ARES rheometer (Rheometric Scientific Inc) was undertaken to extract the field-dependent complex shear modulus of the ER fluid. The measured vlaues were obtained from ER fluid placed in circular parallel plate fixtures with the diameter of 25 mm, maintaining the gap between the fixtures to be 0.5 mm, under constant electric field. Fig. 6 illustrates the measured storage shear modulus and shear loss factor of the employed ER fluid which are a function of the applied electric field as well as the shear strain rate. Becaues the actual strain experienced by an ER fluid layer in a smart plate is very small, average values to the extent of a strain rate of $0.05\,s^{-1}$ were used in the analysis. The variation of ER property with respect to the frequency was neglected.

Table II presents a comparison of the numerical predictions and experimental results of the fundamental mode for various areas subject to electric filed of 1 kV/mm. The predicted fundamental frequencies and loss factors are in a good agreement with the expeimental results except for the case of 80 % area ratio.

Steady state response in the time domain of the smart plate were measured experimentally by forced vibration tests with both different intensities and areas of electric field applied to an ER Fluid. Figure 7 presents the measured

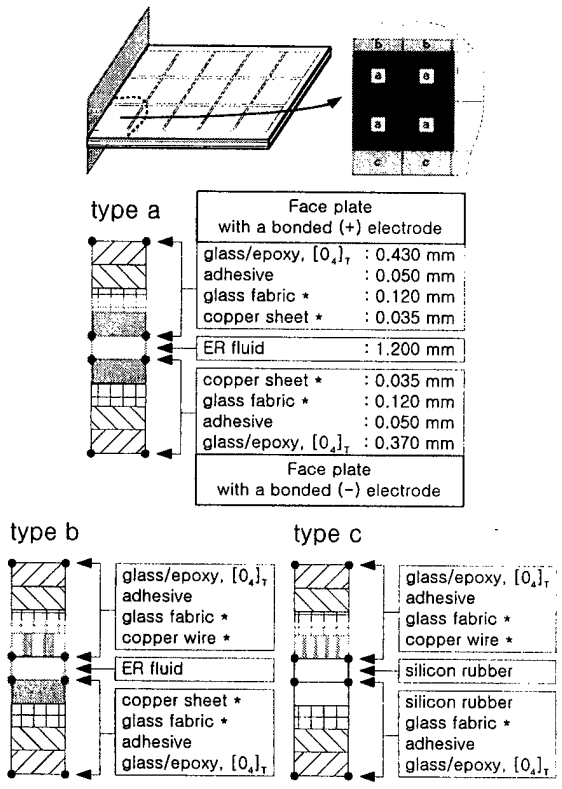
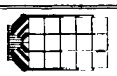
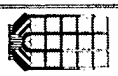
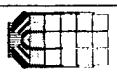
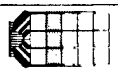
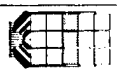
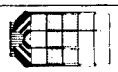
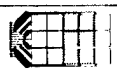
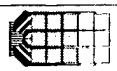
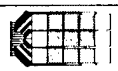
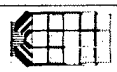
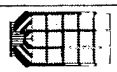


Fig 5. Finite element model with three sub-laminates through the thickness.
(* : the components of copper clad laminate)

Table I. Material properties of the face plate and silicone rubber.

	Face plate				Silicone rubber
	Glass/ epoxy	Adhesive	Electrode sheet		
			Glass/fabric	Copper	
E_L (Gpa)	43.5	1.78	19.6	120	4.47e-4
E_T (Gpa)	5.0	1.78	19.6	120	4.47e-4
G_{LT} (Gpa)	5.0	0.69	4.5	44	1.5e-4
ν_{LT}	0.25	0.3	0.17	0.35	0.49
$\rho\ (kg/m^3)$	1980	1050	1994	8980	1500
η_{mn} (%)	0.524	0.782	0.804	0.518	11.3
η_{ms} (%)	0.572	0.782	1.441	0.518	11.3

Table II. Fundamental frequencies and loss factors for various areas subject to electric field of 1 kV/mm.

Electric field pattern*						
Exp. : freq. (Hz) L.F. (%)	10.75	4.07	14.68	21.88	11.61	9.28
FEM : freq. (Hz) L.F. (%)	10.60	4.39	15.09	18.59	12.19	11.31
Electric field pattern*						
Exp. : freq. (Hz) L.F. (%)	11.16	4.96	11.51	10.64	11.75	11.44
FEM : freq. (Hz) L.F. (%)	10.73	5.26	11.38	8.75	12.05	11.62
Electric field pattern*						
Exp. : freq. (Hz) L.F. (%)	11.84	11.00	12.40	14.50	12.58	14.08
FEM : freq. (Hz) L.F. (%)	11.49	9.24	12.73	14.16	13.42	15.29
Electric field pattern*						
Exp. : freq. (Hz) L.F. (%)	12.92	15.74	13.94	18.50	13.21	15.86
FEM : freq. (Hz) L.F. (%)	12.84	14.56	14.09	17.62	13.89	15.56
Electric field pattern*						
Exp. : freq. (Hz) L.F. (%)	14.12	26.68	13.48	11.96	14.34	17.62
FEM : freq. (Hz) L.F. (%)	14.22	18.08	14.95	18.08	14.02	16.11

* : The shaded region indicates applied electric field.

responses under the fundamental mode excitation. For each applied area of electric field shown in Figure 7, the comparison of the relative suppressed amplitudes and consumed powers is given in Figure 8. In this plot, the consumed power is normalized with respect to that of full area subject to the electric field of 3 kV/mm. It is shown that for the multi-electrode configuration utilized, the suppressed amplitude of a smart plate is more dependent on the location and area ratio of the applied electric field than on the electric field strength.

SEMI-ACTIVE CONTROL

Semi-Active methods in terms of reliability, stability, simplicity and relative cost have the advantage in suppressing unexpected vibration of the system. Accordingly, a simple semi-active control scheme has been applied. The signal from the laser sensor is fed back into the computer through the DSP board to provide the information on excitation disturbances.

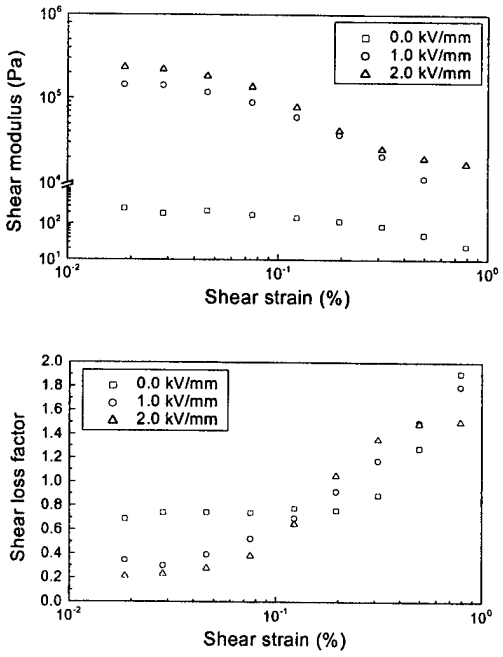


Fig 6. Field-dependent complex shear modulus of the ER fluid.

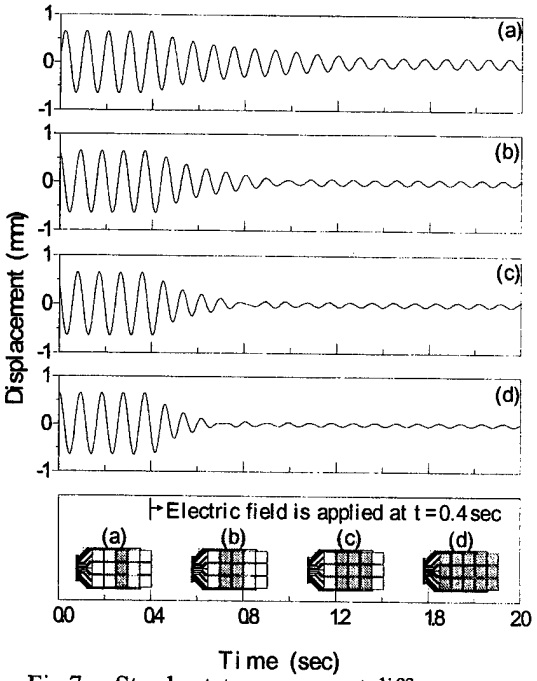


Fig 7. Steady state response at different electric field pattern (E = 2kV/mm).

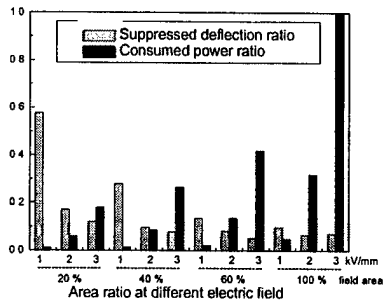


Fig 8. Comparison of suppressed deflection and consumed power ratio.

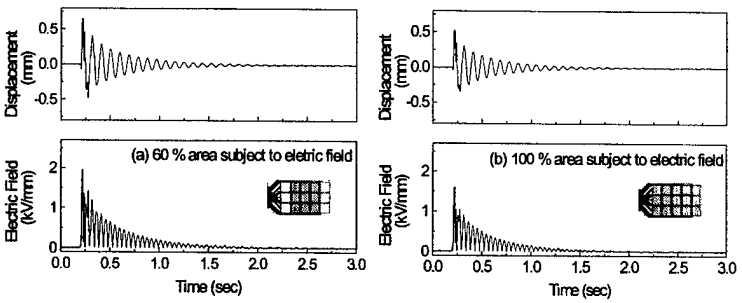


Fig 9. Transient response with deflection feedback control (K=0.72).

Depending on the information from the feedback sensor signal, the control voltages for the ER fluid are determined in the computer through the deflection feedback controller given by MATLAB/Simulink model. Through the formulation of semi-active control schemes and experimental implementation on the condition of full and partial electric field, both the depressed vibration level and control energy required to suppress the external disturbances were evaluated under the impulse loading. The time response for the semi-active control with 0.72 gain is presented in Fig. 9. Table Ⅲ presents a comparison of the control performance and consumed energy for three gains. It is shown that the use of partially electric field is better for energy efficiency.

Table Ⅲ. Consumed energy and amplitude ratio under impulse excitation of different field patterns.

Vibration Control Law		Consumed Energy (*mJ*)		Amplitude Ratio	
		60 %*	100 %*	60 %*	100 %*
Deflection feedback	K = 0.48	2.190	5.144	0.1358	0.1201
	K = 0.72	7.820	10.130	0.0908	0.0817
	K = 0.96	12.865	23.097	0.0633	0.0534

* : Field energizing area ratio.

CONCLUSIONS

The finite element model for suppressing the vibration of the multi-layer composite plate containing ER fluid has been developed and the effectiveness of the proposed multi-electrode configuration has been verified. The study shows that the vibration response characteristics of smart structure can be tuned by tailoring the applied field in order to obtain the desired performance characteristics with respect to energy consumption. It can be concluded that if the electric field is concentrated at the partial area of the high shear deformation of ER fluid, it is more efficient than applying electric field to full area.

ACKNOWLOGEMENT

This study has been supported by a grant from the National Research Program of the Ministry of Science and Technology, Korea. The authors gratefully acknowledge this support.

REFERENCES

1. Gandhi, M.V., Thompson, B.S., and Choi, S.B., "A new generation of innovative ultra-advanced intelligent composite mateials featuring electro-rheological fluids: An experimental investigtion," *Journal of Composite Materials,* Vol. 23, 1989, pp. 1232-1255.
2. Choi, Y., Sprecher, F. and Conrad, H., "Vibration characteristics of composite beam containing an electrorheological fluid," *Journal of Intelligen Material Systems and Structures*, Vol. 1, 1990, pp. 91-104.
3. Ross, D., E.E. Ungar and E. M. Kerwin, "Damping of plate flexural vibrations by means of viscoelastic lamina," Structural Damping, Section 3, J.E. Ruzicka, ed., ASME.
4. Mead, D.J. and S. Markus, "The forced vibration of a three-layer, damped sandwich beam with aritrary boundary conditons," *Journal of Sound and Vibration*, Vol. 10, 1969, pp. 163-175.
5. M. Yalcintas and Coulter, J.P., "Electrorheological material based adaptive beams subjected to various boundary conditions," *Journal of Intelligen Material Systems and Structures*, Vol. 6, 1995, pp. 700-717.
6. C. D. Rahn and S. Joshi, "Modeling and control of an electrorheological sandwich beam," ASME *Journal of Vibration and Acoustics*, Vol. 120, 1998, pp. 221-227.
7. S. B. Choi, Y. K. Park, and S. B. Jung, "Modal Characteristics of a flexible plate filled with electrorheological fluids, " AIAA *Journal of Aircraft*, Vol. 36, 1999, pp. 458-464.
8. Reddy, J.N., "A generalization of two-dimensional theories of laminated composite plates," Communications in Applied Numerical Methods, Vol. 3, 1987, pp. 173-180.
9. Cho, K.D., Han, J.H. and Lee, I., "Vibration and damping analysis of laminated plates with fully and partially covered damping layers," to appear in *Journal of Reinforced Plastics and Composites*, 2000.

ORIENTATION OF MAGNETIC FIELD ON THE SENSING AND ACTUATING PERFORMANCE OF AN MR-FLUID FILLED CANTILEVER BEAM

Y. S. Jeng,* C. S. Yeh,* C. K. Lee,* K. C. Chen**

ABSTRACT

Reduction of structure vibration plays an ever more important role as structures are becoming ever more complex. The vibration of a magnetorheological fluid filled sandwich beam was investigated to examine the possibility of reducing or eliminating the vibrations by using an externally applied magnetic field. It was identified that the vibration behaviors of this sandwich beam can be changed significantly with different external magnetic fields. In addition, the effect on the damping and stiffness properties of this sandwich beam by the direction of the externally applied magnetic field was also detailed. A composite beam theory was used to optimize the effective properties of the test specimen. Experimental data obtained was found to agree well with the theoretical predictions. In addition, the potential of using the MR fluid within the cantilever beam as the sensing mechanism was also evaluated experimentally.

1. INTRODUCTION

This paper attempts to address the interaction between a structure and the Magneto-rheological (MR) fluid filled within from a fundamental perspective, i.e., the material magnetization perspective and the mechanical modeling perspective. The test bed deployed is a cantilever beam. The MR-fluid will be filled into the center portion of the cantilever beam and magnetic fields along the horizontal and the vertical axes will be applied to evaluate the stiffness and damping performance of this MR-fluid cantilever beam.

It is well known that MR fluid is made from suspending magnetic particles in a fluid. Due to its ability to react rapidly to the externally applied magnetic field and can even change from liquid phase to solid phase when the externally applied field is large enough; it has certainly attracted a lot of attentions within the intelligent structure research circles[1][2]. The properties of magnetic materials will be reviewed first to emphasize the factors that may influence the effect of magnetization, which includes field strength, field orientations, and the shape of the materials, etc. The basic understandings generated will then be used to understand the behavior of the MR-fluid filled sandwich cantilever beam. Borrowing from

* Institute of Applied Mechanics, National Taiwan University, Taipei 10764, Taiwan, R.O.C.

** Department of Civil Engineering, National Chi Nan University, 1-6, Tieh-Shan Rd., Pu Li, Nantou, Taiwan, R.O.C.

fundamental understandings of magnetic materials, examine the MR-fluid filled test bed by using the easy and the hard axes relative the externally applied magnetic field will be shown to be an effective model of examining the behaviors of the MR fluid filled structures. Armed with this perspective, the most effective direction to apply the magnetic field for the simple test bed will thus be examined. In addition, the possibility of using MR fluid as a sensing mechanism will also be examined. Following the same hard and easy axes perspective, the magnetic fields generated by the vibration of the MR fluid filled structure will be measured along the two axes, the horizontal and the vertical axes. Due to the reciprocal relationship of the magnetic field, it is expected that the direction that makes MR fluid filled structure easy to be magnetized will be the axis that is easier to induce the magnetic field under vibration.

It will be shown that by applying the magnetic field along the so called easy axis of the MR-filled test bed, the magnetic particles of the MR-fluid can align to the least energy state in order to counter the external disturbances. That is, the above-mentioned perspective can be used to optimize the stiffness and the damping performance of the test bed. In addition, a simple beam model will be used to examine the performance of the MR-fluid filled cantilever beam. Two simple understandings can be generated from this mechanical perspective that can clearly demonstrate the effect of the orientation of the externally applied magnetic field. As magnetic particles align to the magnetic field direction, which in turn increase the stiffness and damping of the sandwich structure, coupling this understanding with the simple beam model can certainly demonstrate the effect of placing and aligning the externally applied magnetic field. It will be shown that applying magnetic field along the horizontal axis is more efficient than applying the magnetic field along the vertical axis in terms of counteracting the external disturbances that induce bending vibrations of the MR-fluid filled cantilever beam.

2. THE TEST BED

To facilitate the relevance of the modeling and the underlying structure application perspective, the schematic of the test bed is first shown in Fig. 1. Two polyurethane (PU) blocks were used to create the test bed. The first block was machined to 120 mm long, 20 mm wide, and 2 mm thick and the second block was machined to 120 mm long, 20 mm wide, and 2 mm thick. A cavity of 110 mm long, 10 mm wide, and 4 mm thick was then machined out of the first block. A silicon-oil based magneto-rheological fluids[3] were used to fill in the cavity. The two PU blocks were then glued to form the sandwich beam and served as the test bed used for this study. A polyvinylidene fluoride (PVF_2) was cut to a triangular shape (see Fig. 2) and then glued to the top surface of the beam to serve as the sensor for measuring the tip displacement of the test bed [4].

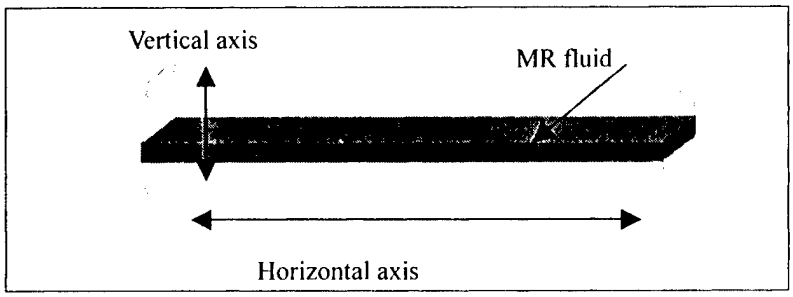


Figure 1. The schematic of the MR filled test bed

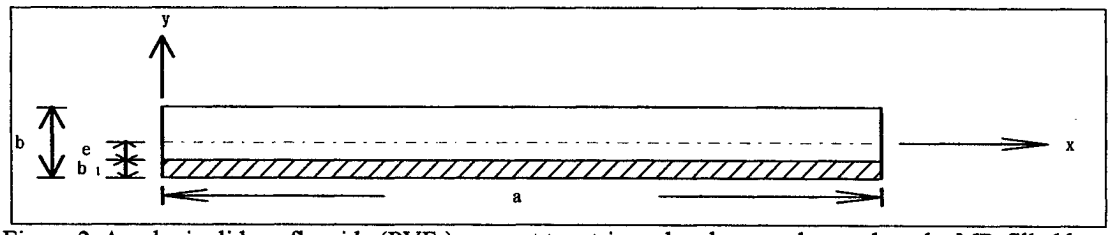


Figure 2. A polyvinylidene fluoride (PVF_2) was cut to a triangular shape and pasted on the MR-filled beam.

The schematic of the test setup used to examine the vibration behavior of the test bed is shown in Fig. 3. Two homemade electromagnets were designed and built to vary both the strength and the orientations of the externally applied magnetic fields.

The first electromagnet was made from a horseshoe shaped ferromagnetic material and by winding 3000 turns of wires onto the ferromagnetic material. The opening of the horseshoe shape is large than the thickness of the test bed so that magnetic field generated by the electromagnet can be applied to the test bed along the vertical axis. The width of the horseshoe shaped electromagnet is long enough to cover the entire length of the cantilever beam in order to make sure uniform magnetic field can be applied throughout the test bed. The wire diameter is 0.55 mm. While examining the possibility of using the MR fluid as the sensor within the test bed, this first electromagnet was used to measure the magnetic field along the vertical axis. More specifically, the test bed, i.e., the MR fluid filled cantilever beam, is being placed within the horseshoe opening and is driven by the shaker. While the test bed is oscillating, the first electromagnet was used as the coil magnetic sensor to measure the magnetic field induced by the MR fluid along the vertical axis. The change of the magnetic field was picked up by the electromagnet and is converted into current by the electromagnet coil. The acceleration induced by the shaker was measured by using a piezoelectric based accelerometer, which is PCB309A made by PCB Corporation of USA and has an acceleration sensitivity of 10mV/g. The frequency response of the MR fluid based sensor was measured by using a dynamic signal analyzer, which is HP 35665A from Hewlett Packard Corp. For the case that the MR fluid was used as the actuator to influence the dynamic behavior of the test bed, the first electromagnet was used to apply the magnetic field along the vertical axis to control the stiffness and damping of the test bed at different frequencies. By sending current from 0 to 2A into the wire of the first electromagnet, the induced magnetic field along the vertical axis, which is the hard axis of the test bed relative to the external magnetic field, can vary from 0 to 0.33 Tesla (T).

On the other hand, the second electromagnet was made from an iron tube and by winding approximate 2000 turns of wires onto the iron tube, i.e., the wire wounding is in cylindrical form and can induce magnetic field along the horizontal axis of the test bed. The wire diameter is also 0.55 mm. While exploring the possibility of using the MR fluid as the sensor in the test bed, the second tube shaped electromagnet was used as the coil magnetic sensor to measure the magnetic field along the horizontal axis of the test bed. Again, the change of the magnetic field will appear as current on the tube shaped electromagnet. By varying the input current from 0 to 2A into the wire of the second electromagnet, the induced magnetic field along the horizontal axis, i.e., the easy axis, can vary from 0 to 0.11 Tesla (T).

In summary, no matter the MR fluid was used as the sensing or actuating mechanisms, the orientation of the magnetic fields were sensed or exerted by using the two above-mentioned homemade electromagnets.

3. THE BEAM MODEL

The governing equation of a composite beam can be shown[5][6][7][8] to be

$$E_c I_c \frac{\partial^4 w_t(x,t)}{\partial x^4} + \rho_c A_0 \frac{\partial^2 w_t(x,t)}{\partial t^2} = 0 \tag{1}$$

where $w_t(x,t)$ is the absolute transverse deformation of the beam, $E_c I_c$ is the effective flexural rigidity, ρ_c is the effective beam density which takes into both the density and the PU material into account, and A_0 is the transverse cross-sectional area. Decompose the deformation of the beam $w_t(x,t)$ into

$$w_t(x,t) = w(x,t) + w_g(t) \tag{2}$$

where $w(x,t)$ is the transverse deformation of the beam and $w_g(t)$ is the deformation along the horizontal direction induced by the vibration shaker (Fig. 3). Substituting Eq. (2) into Eq. (1) yields

$$E_c I_c \frac{\partial^4 w(x,t)}{\partial x^4} + \rho_c A_0 \frac{\partial^2 w(x,t)}{\partial t^2} = -\rho_c A_0 \ddot{w}_g(t) \tag{3}$$

Performing modal expansion to the transverse deformation leads to[9]

$$w(x,t) = \sum_{i=1}^{\infty} A_i(t)\Phi_i(x) \tag{4}$$

where $A_i(t)$ is the i_{th} modal coordinates, $\Phi_i(x)$ is the i_{th} mode shape. Furthermore, the clamp-free boundary conditions used is

$$\Phi(0) = 0, \Phi'(0) = 0, \Phi''(a) = 0, \Phi'''(a) = 0 \tag{5}$$

where a is the length of the cantilever beam, $x=0$ is the fixed end, and $x=a$ is the free end.

Substituting Eq. (4) into Eq. (3) and utilizing the boundary conditions n in Eq. (5) yields the mode shape of the cantilever sandwich beam

$$\Phi_i(x) = (\cos k_i x - \cosh k_i x) + R_i(\sin k_i x - \sinh k_i x) \tag{6}$$

where $K_1 a = 1.875$, $R_1 = -0.7341$, $K_2 a = 4.694$, $R_2 = -1.0185$, $K_3 a = 7.855$, $R_3 = -0.9992$, $K_4 a = 10.996$, $R_4 = -1.0000^+$, and $K_i a \approx (2i-1)\pi/2$, and $R_i \approx -1.0000^-$. The virtual work done by the external magnetic field can be shown to be

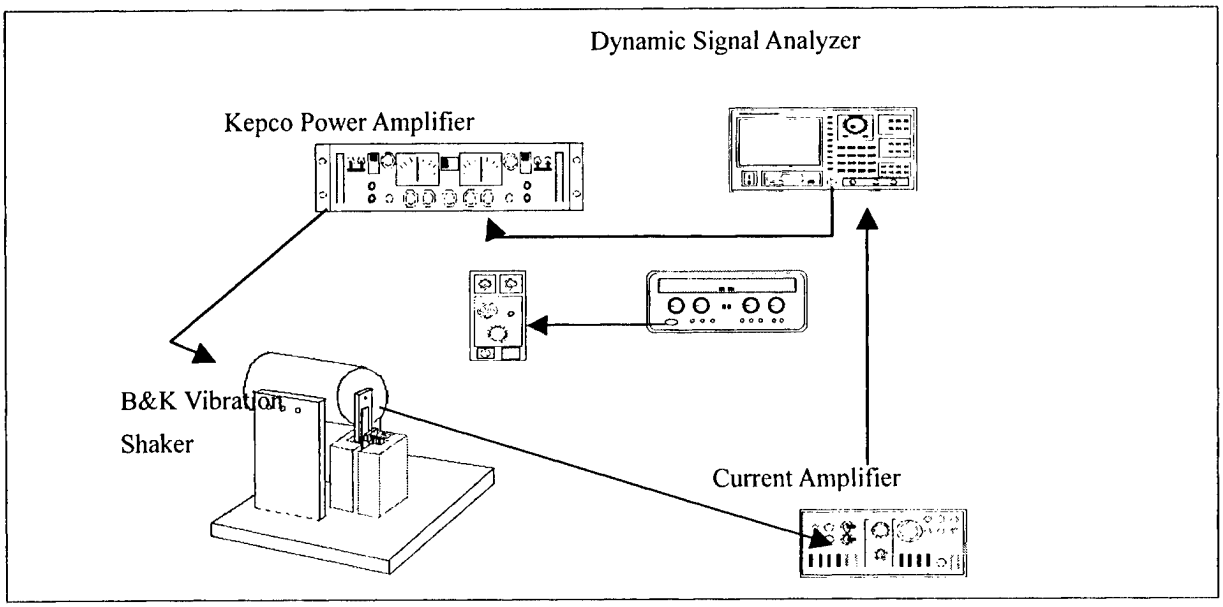


Figure 3. The experimental setup

$$\delta W_E(t) = \int_0^a \left[-\rho_c A_0 \ddot{w}(x,t)\right]\delta\left[w(x,t)\right]dx + \int_0^a \left[-\rho_c A_0 \ddot{w}_g(t)\right]\delta\left[w(x,t)\right]dx$$

$$= \sum_{i=1}^{\infty}\left\{-\rho_c A_0 \ddot{A}_i(t)\left[\int_0^a \Phi_i^2(x)dx\right]\delta A_i - \rho_c A_0 \ddot{w}_g(t)\left[\int_0^a \Phi_i(x)dx\right]\delta A_i\right\} \quad (7)$$

The virtual work done by the internal work is

$$\delta W_I(t) = \int_0^a M(x,t)\delta\left[w(x,t)\right]'' dx \quad (8)$$

Assuming that stresses within the MR-fluid behave like a damping material, i.e., it is proportion to the strain speed, the stress-strain can then be shown to be[10]

$$\sigma = E_c\left[\varepsilon + a_1\dot{\varepsilon}\right] \quad (9)$$

where E_c is the Young's modulus, and a_1 is the damping constant. Taking Eq. (9) into considerations, the moment equation can be rewritten as follows:

$$M(x,t) = E_c I_c\left[w''(x,t) + a_1\dot{w}''(x,t)\right]\delta W_I(t) = \int_0^a E_c I_c\left[w''(x,t) + a_1\dot{w}''(x,t)\right]\delta\left[w(x,t)\right]'' dx$$

$$= \sum_{i=1}^{\infty}\left\{E_c I_c A_i(t) + a_1 E_c I_c \dot{A}_i(t)\left[\int_0^a (\Phi_i''(x))^2 dx\right]\right\}\delta A_i + a_1 E_c I_c \dot{A}_i(t)\left[\int_0^a (\Phi_i''(x))^2 dx\right]\delta A_i \quad (10)$$

From virtual-work principle that

$$\delta W_E(t) = \delta W_I(t) \quad (11)$$

and that δA_i is arbitrary yields that

$$M_i\ddot{A}_i(t) + C_i\dot{A}_i(t) + K_i A_i(t) = P_i(t) \quad (12)$$

where $M_i = \rho_c A_0\left[\int_0^a \Phi_i^2(x)dx\right]$ $C_i = a_1 E_c I_c\left[\int_0^a (\Phi_i''(x))^2 dx\right]$ $K_i = E_c I_c\left[\int_0^a (\Phi_i''(x))^2 dx\right]$ $P_i = -\rho_c A_0\left[\int_0^a \Phi_i(x)dx\right]$, and $i = 1, 2, \ldots, \infty$. The nature frequency of the beam can be calculated to be

$$\omega_i = \sqrt{\frac{K_i}{M_i}} = \sqrt{\frac{E_c I_c\left[\int_0^a (\Phi_i''(x))^2 dx\right]}{\rho_c A_0\left[\int_0^a \Phi_i^2(x)dx\right]}} \quad (13)$$

where $i=1,2,\ldots..,\infty$, and

$$E_c I_c = \rho_c A_0 \frac{\int_0^a (\Phi_i(x))^2 dx}{\int_0^a (\Phi_i''(x))^2 dx}\cdot\omega_i^2 \quad (14)$$

Considering the magnetic field parameters, Eq. (14) can be rewritten to

$$E_c I_c(B_j) = \rho_c A_0 \frac{\int_0^a (\Phi_i(x))^2 dx}{\int_0^a (\Phi_i''(x))^2 dx}\cdot\omega_i^2(B_j) \quad (15)$$

where $i=1, 2, .., \infty$, and $j= 1, 2, .., N$.

4. EXPERIMENTAL RESULTS

First, the potential of using the MR fluid as the sensor for smart structure applications was evaluated. Driving the test bed (Fig. 1) by the shaker shown in Fig. 3, the magnetic field generated by the MR fluid was measured by using the two electromagnets along the two axes respectively. The experimental results were shown in Fig. 4, where the input channel, i.e., the denominator of the frequency response curves[11] shown in Fig. 4, is the acceleration output from an accelerometer mounted on top of the shaker. The output channel, i.e., the numerator of the frequency response curves shown in Fig. 4, is the voltage generated by

flowing the current generated by the electromagnet coil, which picks up the MR fluid induced magnetic field, through the input channel of the dynamic signal analyzer. The input impedance of the dynamic signal analyzer as set at $1M\Omega$. It is clear from the data shown in Fig. 4 that magnetic particles contained within the MR fluid could induce magnetic field when subjected to external vibration. Comparing the data shown in Fig. 4 and the resonant frequency data shown in Figs. 5, 6 indicates that at the resonant condition of the test bed, the magnetic field along the vertical axis is reduced and the magnetic field along the horizontal axis remains approximately the same. This phenomenon can potentially be further explored to examine or to implement the MR fluid based sensing mechanism.

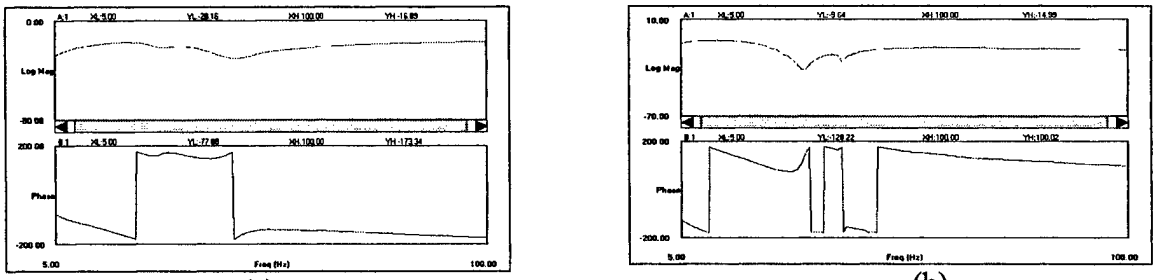
To verify the influence of the externally applied magnetic field, the vibration behavior of the test bed was measured by using a triangular shaped PVF_2 sensor, as tip displacement is directly proportional to the charge generated from the sensor. A charge amplifier with variable gain adjustment capabilities was thus used to convert the charge signal generated to voltage signal in order to facilitate the signal measurement during the experiments.

Considering the case that the external magnetic field was applied along vertical axis first. It is clear from Fig. 5(a) that the first resonant mode is 21.16Hz and 74.76dB when there is no external magnetic field applied. The first resonant mode changed to 20.44Hz and 73.71dB when 12 volts or 0.24 Amp was sent to the electromagnet (Fig. 5(b)), which corresponds to magnetic field strength of 0.0396 Tesla. In addition, when 0.132 Tesla magnetic field was applied through the electromagnet, the first resonant mode was further moved to 24Hz and 61.83 dB as shown in Fig. 5(c). Comparing the data obtained for 0 Tesla and 0.132 Tesla magnetic field strength, the damping and stiffness improvement is clear. However, comparing the data shown in Figs. (a) and (b), which corresponds to 0 and 0.0396 Tesla magnetic field strength, the damping and stiffness improvement is not significant or even in contradiction with the trend shown between Figs. (a) and (c). This somewhat trend reversal behavior is in agreement with some previous findings when electro-rheological (ER) fluid was involved, where the Young's modulus of a ER fluid filled cantilever beam was found to reduce when the externally applied electric field is low [12]. In addition, that same report also indicates that the Young's modulus of the ER fluid filled cantilever beam was found to increase significantly when enough field strength is applied. Combining these two results seems to indicate the both MR and ER fluid will possess some sort of threshold and nonlinear behavior when different field strengths are applied.

Placing the test bed into the second electromagnet in order to apply the magnetic field along the horizontal axis leads to the experimental data shown in Fig. 6. Due to the experimental configuration, the length of the cantilever beam has to be clamped slightly shorter than the previous case. In addition, the gain on the charge amplifier used to interface the PVF2 sensor was also changed to accommodate different signal strength. Nevertheless, this length change will not influence the understanding generated from the preliminary test data as different magnetic field strength can still be compared to each other. The data shown in Fig. 6(a) indicates the test bed has first mode resonant at 21.39Hz and 71.95dB when there is no externally applied magnetic field. When 16 volts was applied to the second electromagnet, which corresponds to 0.48 Amp input current and in turn generate 0.0172 Tesla, the data shown in Fig. 6(b) indicates that the first mode is resonant at 21.39Hz and 70.05dB. The data shown in Fig. 6(c) was obtained when 0.0216Tesla external magnetic field was applied to the horizontal axis of the MR fluid filled cantilever beam, which indicates that the first mode becomes resonant at 22.34Hz and 68.42dB.

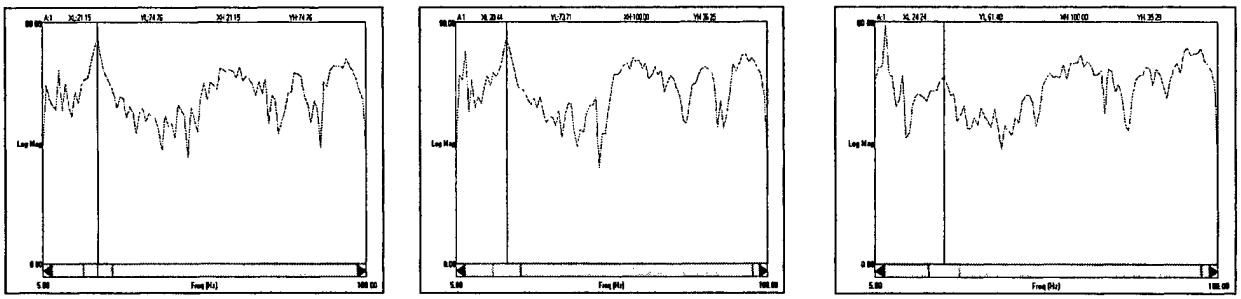
Comparing the two sets of data shown in Figs. 5 and 6, the significance of the orientation

of the externally applied magnetic field is significant. For example, comparing the data shown in Figs. 6(a, b) and 5(b), even where the magnetic field strength applied to case shown in Fig. 6(b) is lower than that of the case shown in Fig. 5(b), no stiffness and damping behavior reversal discussed above was found. In addition, even though the magnetic field strength applied along the horizontal axis is much smaller than the cases when the magnetic field was applied along the vertical axis, the improvement of the damping and stiffness along the horizontal axis, i.e., the easy axis, is far more significant.



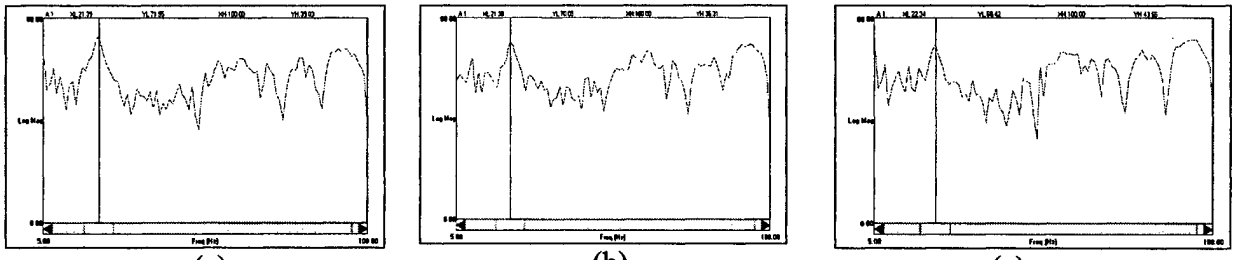
(a) (b)

Figure. 4 Sensor response of the MR fluids along the horizontal axis (a) and along the vertical axis (b) when the test bed was driven by the shaker. Note that the horizontal axis is the easy axis and the vertical axis is the hard axis.



(a) (b) (c)

Figure 5. Frequency respones of the test bed when the external magnetic field is applied along the vertical axis, where the applied magnetic field strengths 0 (a), 0.0396 (b), and 0.132 (c) Teslas.



(a) (b) (c)

Figure 6. Frequency respones of the test bed when the external magnetic field is applied along the horizontal axis, where the applied magnetic field strengths are 0 (a), 0.0172 (b), and 0.0216 (c) Teslas.

5.CONCLUSION

The possibility to adopt MR fluid for smart structure application has been explored and demonstrated. Even though the investigation is still at its infant stage, the results obtained were encouraging nevertheless. The investigation also demonstrates that the perspective related to traditional magnetic material, i.e., the easy and the hard axes concept could be adopted to examine the behavior of the MR fluid. The preliminary data obtained clearly indicates that the orientations of the so called easy and hard axes of the MR fluid filled cantilever beam are in agreement with that of a cantilever beam completely made of solid ferromagnetic materials. This finding can be used to facilitate the understanding and design of various MR fluid filled composite structures and thus can potentially be used for various smart structure configurations as well as applications.

Taking the discussions on magnetic hard and easy axis, the MR fluid filled test bed were found to be an effective vehicle to evaluate the sensing and actuating capabilities of the MR fluid. It was found that magnetic field could be induced when the MR fluid was driven to oscillations. In addition, the dynamic properties of MR fluid filled cantilever beam were also found to change significantly when external magnetic field was applied. It was also identified that externally applied magnetic field strength will have much stronger effect on the dynamic properties of the MR fluid filled beam when the field was applied along the easy axis, which is the horizontal axis of the test bed.

6.REFERENCES

1. O. Volkova, S. Cutillas, P. Carletto, G. Bossis, A. Cebers, and A. Meunier, "Flow-induced Structures in Magneto-rheological Suspensions," *Journal of Magnetism and Magnetic Materials*, 201, 66-69,1999.
2. C. S. Yeh, K. C. Chen, "A Thermodynamic Model For Magnetorheological Fluids," *Continuum Mech. Thermodynamic*, 9:273-291, 1997.
3. Y. Choi, A. F. Sprecher, and H. Onrad, "Vibration Characteristics of a Composite Beam Containing an Electrorheological Fluid," *Journal of Intelligent Material and Structures*, 1:91-104, 1990.
4. C. K. Lee, "Theory of Laminated Piezoelectric Plates for the Design of Distributed Sensors/Actuators: Part I. Governing Equations and Reciprocal Relationships," *The Journal of Acoustical Society of America*, 87:1144-1158, 1990.
5. S. B. Choi, Y. K. Park, and C. C. Cheong, "Active Vibration Control of Intelligent Composite Laminate Structures Incorporating an Electro-Rheological Fluid", *Journal of Intelligent Material and Structures*, 7:411-419, 1996.
6. S. B. Choi, Y. K. Park, and J. D. Kim, "Vibration Characteristics of Hollow Cantilevered Beams Containing an Electro-Rheological Fluid," *International Journal of Mechanical Sciences*, 35(9):757-768, 1993.
7. G. Haiqing, and L. M. King, "Vibration Characteristics of Sandwich Beams Partially and Fully Treated with Electro-Rheological Fluid," *Journal of Intelligent Material and Structures*, 8:401-413, 1997.
8. C. Y. Lee, "Finite Element Formulation of a Sandwich Beam with Embedded Electro-Rheological Fluids," *Journal of Intelligent Material and Structures*, 6:718-728, 1995.
9. R. D. Blevins, *Formulas for Natural Frequency and Mode Shape*, Krieger, New York, USA, 1985.
10. R. W. Clough, and J. Penzien, *Dynamics of Structures*, McGraw-Hill, New York, USA, 1993.
11. N. S. Nise, "Frequency Response Techniques," chap. 10, *Control Systems Engineering*, The Benjammin/Cumming Publishing Company, Inc., USA, 1995.
12. C. D. Berg, L. F. Evans, and P. R. Kermode, "Composite Structure Analysis of A Hollow Cantilever Beam Filled With Electrorheological Fluid," *Journal of Intelligent Material Systems and Structure*, 7:494-502, 1996.

SMART MATERIAL BASED ACTUATION

Ephrahim Garcia,[1] Janet Sater,[2] Gregory Fischer[3]

ABSTRACT

The Defense Advanced Research Projects Agency (DARPA) currently supports several programs with a focus on smart materials and structures. Two of these—the Smart Materials and Structures Demonstration Program and the Compact Hybrid Actuators Program (CHAP)—will be described and reviewed. The Smart Materials and Structures Demonstration projects aim to show the value of smart materials-based actuation systems in realistic applications. The CHAP effort focuses on the development of new types of useful electro-mechanical and chemo-mechanical actuators that exceed the specific power and power density of traditional electromagnetic and hydraulic-based actuation systems by a factor of ten for a range of applications. This paper outlines the expected capabilities, significant technical challenges, and performance advantages foreseen in successful development and transition of the technologies targeted for exploration.

INTRODUCTION

The term "smart materials" has been applied to a broad range of materials that have one or more physical properties that can be varied with some input. By using these materials, a device that once consisted of separate structural, sensing, and actuation components can now exist as a single component. For some applications, a smart material-based device can be substituted for existing components, reducing overall size and complexity. Smart materials have also opened the door for the development of many novel sensors, actuators, and structural components not previously possible.

Recent progress in developing improved actuation materials, including electroactive ceramics, magnetostrictive alloys, shape memory alloys (SMAs), and magnetic shape memory alloys is notable. DARPA initiated a number of new programs to develop higher authority actuator materials—including SMAs, single crystal electro-active ceramics, piezoelectric fibers, and injection-molded piezoelectric ceramics—as a direct result of input from end users who were experiencing problems with existing "smart" actuator materials and devices.

[1]DARPA, USA.
[2]Institute for Defense Analyses, USA.
[3]Strategic Analysis, Inc., USA.

Actuators-General Concerns

Desirable features for actuators include: consistent and predictable device-to-device and cycle-to-cycle response, shape uniformity and extreme mechanical tolerances (especially surface parallelness and flatness in electro-active ceramics), low or predictable hysteresis, low creep, large force/load-carrying capability, high frequency response, linearity in displacement with respect to input, capacitive in nature, durability and reliability over time, including aging and environmental effects, and suitable size and weight characteristics (application-dependent need). Current smart material-based actuators exhibit some, but not all, of these characteristics [1-7]. While there has been significant emphasis on developing smart materials there has, in general, been much less effort focused on developing devices that take full advantage of their unique properties. A number of studies have been carried out to characterize smart materials and smart material driven devices. The relevant properties investigated were primarily the electrical and mechanical fatigue characteristics, [4, 5] and the power and energy characteristics [8] of available actuator devices in order to determine their suitability for particular applications. The programs that are described herein represent a shift in the classic smart materials research paradigm desribed above, and instead emphasize the development of devices which will advance and expand the arenas within which smart materials can provide novel solutions and significantly increase the amount of work smart materials can deliver to a system.

The fact that performance capabilities of currently "available" actuators are still orders of magnitude from the levels needed in order to realize applications for large structures like aircraft wings will be addressed, to some degree, in the following section describing the DARPA Smart Materials and Structures Demonstrations. A new DARPA program, to be described later, will focus on innovative compact hybrid actuation schemes that address integrated electronics and power issues.

SMART MATERIALS AND STRUCTURES DEMONSTRATIONS PROGRAM

The primary focus of the DARPA Smart Materials and Structures Demonstrations projects has been to apply existing smart materials in an appropriate device form to reduce noise and vibration and to achieve aerodynamic and hydrodynamic flow control in a variety of structures—basically to create paradigm shifts for the design of undersea vehicles, helicopter rotor blades, aircraft wings, and engine inlets. Examples of these devices include small, high bandwidth devices for acoustic signature reduction; small, powerful actuators capable of fitting into the confined interior space of a rotating helicopter rotor blade for noise reduction; and flexible skins with embedded SMA wires that permit continuous control surface shape changes for improved aerodynamic performance. Expected performance benefits are quantified and technical issues, especially those related to the smart materials and devices—are identified and will be noted in the text.

Torpedo Quieting Demonstration

Building on the successes of a previous effort, the Composite Smart Materials program (CSM), a team headed by the Lockheed Martin Missiles and Space Advanced Technology Center, undertook an effort called the Smart Sleeve Demonstration System (S^2DS) in the fall of 1998. This effort is leveraging technology developments from the CSM program in order to provide significant underwater silencing improvements in a system that is considerably smaller and less expensive to produce than the arrays produced in the previous research program. Accordingly the goals of the S^2DS were established to be as follows: up to a 10 dB reduction in self noise generated by turbulent boundary layer induced flow noise, a significant cost reduction relative to the CSM third iteration array, and a 50 to 75% reduction in the thickness of the discrete actuator/sensor/electronics package to approximately 51 to 24 millimeters [9]. In order to test the effectiveness of the developed control system and hardware in a realistic configuration, the hull of a Mk 48 torpedo was chosen by the Lockheed team to be the primary test structure for S^2DS. The Mk 48 torpedo in its original configuration or its advanced ADCAP configuration is currently in service aboard every U.S. submarine.

The program to date has proceeded from a requirements and design phase, through a single channel closed loop test of the system on the torpedo hull, and to its final phase, which included outfitting and instrumentation of a multi-channel, full sleeve for underwater testing. The hull section used for underwater testing houses six distinct entities of the system: a Tubulent Boundary Layer (TBL) – like noise source, 60 reference sensors which are circumferentially arranged, 12 error sensors, two staggered rings comprised of 36 actuators, a digital control system, and a signal monitoring system. Single channel tests show levels of attenuation on the order of 18dB in selectable frequency band windows

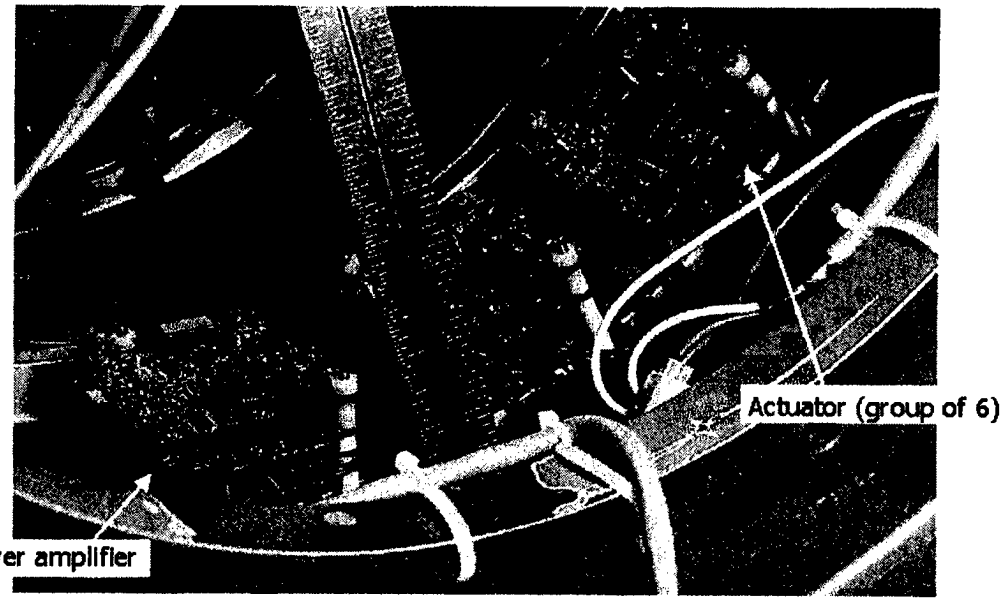


Figure 1. View of the inside of the S^2DS MK 48 hull test section showing a portion of the integrated actuator and power amplifier array

across the TBL noise. The underwater testing and data analysis of the multi-channel smart sleeve will be completed by October 1, 2000; as noted the preliminary data suggests significant quieting capability across all frequencies of interest in a package that is economical in terms of volume and cost. [10]

Smart Rotor Demonstrations

The aerodynamics of rotating blades are quite complex. The aerodynamic environment varies with blade position around the azimuth and leads to sub-optimal performance throughout much of the flight envelope. One particular issue, blade vortex interaction (BVI) noise is caused by the wake from the previous helicopter blade meeting the leading edge of the next blade. Vibrations also increase when blades are out of track. Blade-tracking adjustments, required to account for slight physical differences between the helicopter blades, are done infrequently because of the high cost, significant set-up time, and subsequent maintenance. Active, real-time blade tracking adjustments can produce large savings in maintenance costs and significant reductions in system down time.

The Smart Rotor Program is now in Phase II of its DARPA funded research effort and is being managed by the Boeing Company in Philadelphia, Pennsylvania. Two technologies have emerged as candidates for achieving practical individual blade control (IBC). The first approach utilizes trailing edge flaps which extend from 74 to 92 percent blade span, and the other approach employs an active fiber composite that is embedded in the blade structure to achieve dynamic blade twisting. [11,12] The trailing edge flaps are actuated by mechanically amplified piezolectric actuators installed inside the blade spar and are capable of moving the flaps ±3° from the centerline of the chord [13]. This active flap will provide the modification of aerodynamic forces required to affect helicopter performance and will reduce cockpit vibrations by 80 to 90 percent and provide 5 to 10 dB reduction in BVI noise. A unique X-frame actuator concept [14-16], developed by MIT, was selected for the final demonstration articles. Preliminary blade production was initiated during Summer 2000 with an expected completion date of December 2000. The full-scale, 5-bladed MD-900 rotor is expected to be whirl tower tested in February 2001 and flight

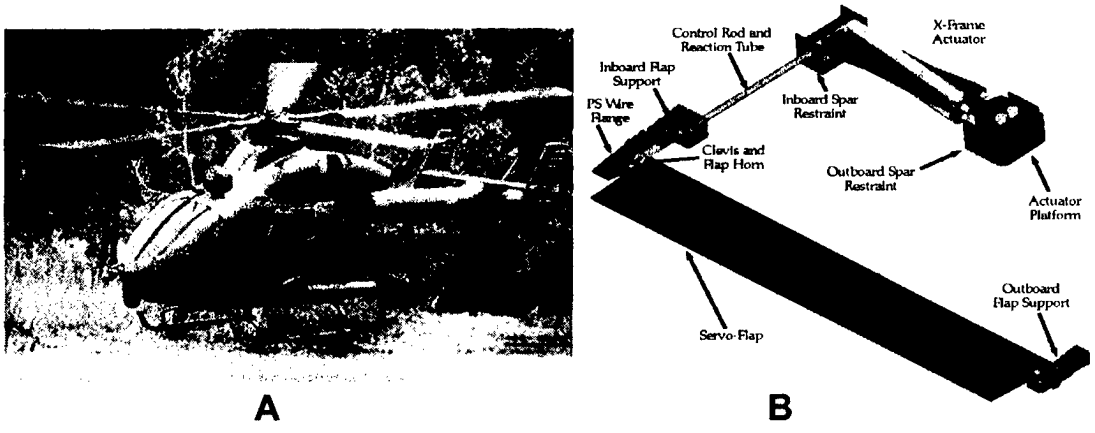


Figure 2. a) MD 900 Explorer is the platform to be outfitted with active trailing flaps and test flown in the spring of 2001 b) schematic of the actuator and flap configuration that is embedded in the composite blade

tested in late spring of 2001 on an MD-900 Explorer which is a twin engine, 6,000-pound helicopter with a 34-foot, all-composite main rotor.

Active fiber composite (AFC) research is being pursued at MIT concurrently to this Phase II flight demonstration task. The major focus of this parallel task is to demonstrate the benefits of an active twist rotor system via a test of a Mach-scale rotor, complete with predictions and extrapolation to a full-scale rotor. In the AFC rotor blade concept AFC plies are oriented at $\pm 45^{\circ}$ within the primary structure of the blade to generate dynamic blade twisting. Analytical studies indicate that twist amplitudes of 1 to 2° over a relatively wide frequency bandwidth are possible using the strain actuation capabilities of the AFC plies. System studies indicate that this magnitude of twist actuation authority should be possible at full scale, with only modest increases in blade weight and, possibly, relatively low levels of power consumption. An active fiber IBC system would allow for elimination of the swashplate, swashplate actuators, rotor blade torque tubes, and lag dampers, a very significant step forward for improving helicopter performance: e.g., an 85-percent range increase is predicted by combining advanced rotor technologies with on-blade flight control for a UH-60 baseline system [17]. The final demonstration in this task is expected to be a hover test of a Mach-scale rotor in December 2000.

Smart Wing Demonstration

The DARPA Smart Wing program is investigating techniques for wing twisting and camber control using smart structures [18]. This contract was awarded to Northrop Grumman for Phase I (September 1994) and Phase II (August 1998) research efforts.[1] The overall objective of this program is to design, develop, and demonstrate the use of smart materials and structures to improve the aerodynamic performance of military aircraft,

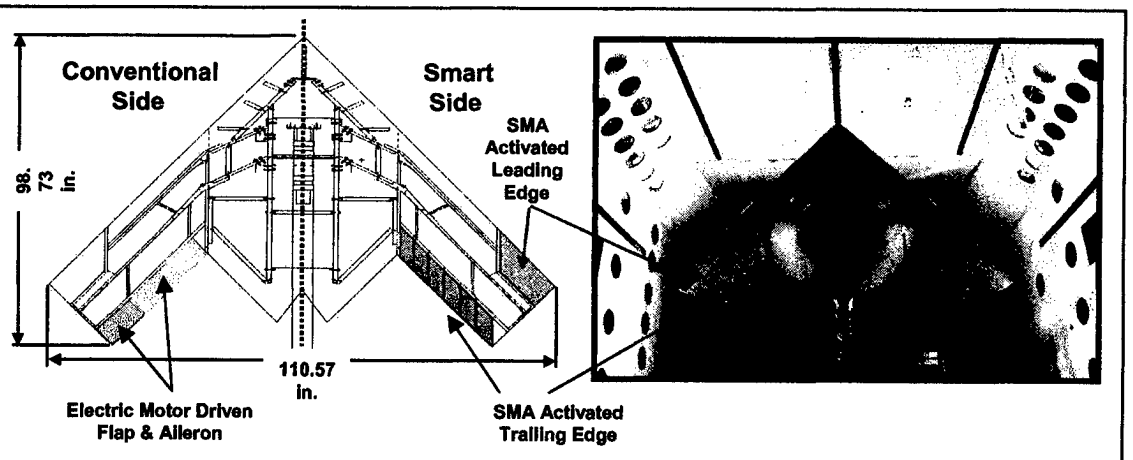


Figure 3. UCAV schematic and 30% scale model on the NASA Langley Research Center TDT

[1] Other members of the large team of researchers involved in the program have included Lockheed Martin Astronautics, Lockheed Martin Control Systems, Naval Research Laboratory (NRL), Mission Research Corporation, Rockwell Science Center, Fiber & Sensor Technologies, Etrema Products, SRI International, University of California at Los Angeles, Georgia Institute of Technology, and the University of Texas at Arlington. Wind tunnel testing for the program is provided by NASA-Langley's TDT [84]. The Air Force Research Laboratory currently manages the program.

including improvements in lift-to-drag (L/D) ratio, maneuver capabilities, and aeroelastic effects [19]. Estimated performance improvements for fighter aircraft include an 8-percent increase in allowable take-off gross weight, 30-percent increase in weapons payload, and a 10 to 15 percent increase in maneuver rates. Performance improvements for unmanned vehicles could be significantly greater. The approach includes designing, fabricating, and testing scaled semi-span and full-span wind-tunnel models; addressing power, reliability, packaging, and system integration issues; and laying the ground work for technology transition in a potential follow-on program.

During Phase I of the program, a 16 percent scaled semi-span model of the F/A-18 aircraft was designed and fabricated, incorporating three key features: hingeless, smoothly contoured, trailing edge control surfaces; variable spanwise wing twist; and fiber optic strain and pressure transducers [18]. On this "smart" model, the hingeless aileron and flap were actuated using agonist/antagonist SMA tendons [20] and wing twist was accomplished by using two SMA-actuated torque tubes.

The first wind-tunnel test in Phase I took place in May 1996. During this test, 1.25° of twist was achieved using the SMA torque tubes, resulting in approximately an 8 percent improvement in rolling moment. The hingeless control surfaces deployed up to 10°, provided between an 8 and 18 percent increase in rolling moment and approximately an 8 percent increase in lift [21]. The actuator scale-up results from these Phase I tests indicate that torque requirements for a full-size fighter aircraft wing twisting are so large that they are beyond the capability of present-day smart actuation materials. Results also identified a key limitation in the Phase 1 effort as being the low bandwidth of the SMA actuated control surfaces. Phase II of the Smart Wing program has further matured the technologies developed in Phase I and is investigating new actuation concepts—e.g., hybrid piezoelectric devices [22] and piezoelectric motors—to address the bandwidth limitations. The test structure is a 30% scale Unmanned Combat Air Vehicle (UCAV) design: the full-span model has a 10-foot wing span with a 12-foot length and weighs close to 500 pounds; it is fully instrumented to measure strains, pressure, force, deflection, and acceleration. Expected performance benefits for this type of vehicle using these "Smart Wing" technologies include reduced turn radius, increased range, improved survivability, and increased sorties. Data from the first wind tunnel tests in air and heavy gas in the NASA-Langley TDT, completed in March 2000, is currently being analyzed. A second wind-tunnel test, tentatively planned for February 2001, will focus specifically on the actuator bandwidth issue.

Smart Aircraft and Marine Propulsion System demonstration (SAMPSON)

The inlet system of jet-powered aircraft pre-conditions the air entering the engine. Jet engines require air to enter the engine at approximately Mach 0.5 or less. Because of the wide range of Mach speeds, altitude, angle-of-attack, angle-of-slip, and engine airflow conditions, a fixed geometry inlet cannot provide ideal performance under all conditions. At low speeds, having large inlets with very blunt lips is desirable. This allows the high airflow associated with take-off conditions to be drawn into the inlet without flow separation. At subsonic cruise, sharp inlet lips are desirable because they produce less drag. Sharp inlets

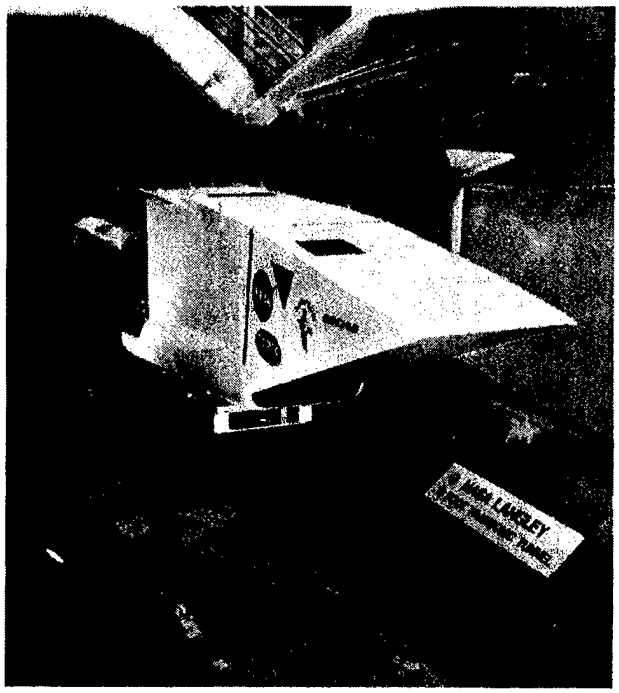


Figure 4. Sampson F-15 adaptive inlet being installed in the NASA Langley high speed wind tunnel.

also reduce radar cross-section (RCS). At supersonic conditions, the losses caused by rapidly decelerating the flow from supersonic to subsonic result in substantial losses in pressure and thrust. To overcome these limitations, variable geometry inlets have been used. The variable geometry inlets used on the F-15, for example, improve performance over a range of conditions, but their mechanical complexity adds weight and cost to the aircraft.

The DARPA-sponsored SAMPSON program[2] is focused on both aircraft and undersea vehicle applications, with a specific interest in shape and flow control approaches for inlets. Objectives for the aircraft portion of SAMPSON include designing, fabricating, and demonstrating a full-scale adaptive inlet for a tactical F-15 Eagle aircraft, with a particular focus on validating control of inlet geometry and internal flows [23]. Potential benefits include improved range—20 percent for tactical aircraft—and maneuverability, flutter and buffet control, and reduced signature. Important core technology efforts [24] are addressing needs for quasi-static shape control for inlet shaping, leading edge lip deflection, and leading edge blunting via compliant surfaces actuated with SMAs. Piezoelectric motor concepts are being evaluated for high rate motion of the leading edge

[2] Team members include Boeing-St. Louis (formerly McDonnell Douglas), Lockheed Martin Astronautics, Georgia Institute of Technology, NRL, Electric Boat Corporation, BBN (now GTE), and PSU's Applied Research Laboratory (ARL) and Center for Acoustics and Vibration. This program is managed jointly by NASA-Langley and ONR. Wind tunnel testing of the full-scale aircraft inlet will be performed at NASA-Langley facilities.

lip for blunting. As part of the first wind tunnel test program, an agonist/antagonist SMA actuator system was used to rotate the cowl about a pivot point to vary capture area, similar to the way the current inlet operates. The forces to achieve the necessary stroke (about 6 in.) are quite large, on the order of 20,000 lb. The advantage of using SMAs in this way is their integration into the structure, which eliminates the need for a separate subsystem (e.g., hydraulics) to run it. The first wind tunnel test of the full-scale section was completed in April 2000. This first test established test procedures, verified aerodynamic loads, and demonstrated cowl actuation. A second wind tunnel test is planned for November 2000; the cowl actuation concept will be refined and other innovative concepts for lip deflection, lip blunting, and wall shaping will be demonstrated in this test.

COMPACT HYBRID ACTUATORS PROGRAM

DARPA awarded several research efforts beginning in July of 2000—the Compact Hybrid Actuator Program and several related SBIR topics, which focused on the development of new types of electro-mechanical and chemo-mechanical actuators that take advantage of the high energy density of smart material transduction elements and the novel and efficient energy conversion of hydrocarbon fuels. The goal is the creation of useful devices that exceed the specific power and power density of traditional electromagnetic- and hydraulic-based actuation systems by a factor of ten. These technologies include smart material-driven hydraulic systems, duty-cycle combustion systems, mechanically-amplified systems, the control and drive electronics associated with these systems (which are typically addressed apart from the device [25]), as well as development efforts for magnetic shape memory alloys. These compact hybrid actuators can potentially supplant traditional actuation systems while reducing the overall power and space consumed, thus the interest in applications requiring distributed actuator systems such as adaptive airframes and robotic locomotion.

As outlined in Table 1, the Compact Hybrid Actuator Program currently has eleven research efforts underway that address the following four categories: materials development, smart material driven fluidic devices, combustion driven devices, and mechanically amplified devices. The organization serving as the principal investigators is identified as well as a brief desription of the system under development and its driving element. Preliminary data from these efforts is expected in the first quarter of 2001.

TABLE 1. COMPACT HYBRID ACTUATOR PROGRAM SUMMARY

Device Classification	Lead Performer	Driving element	Research/Device Description
1. Materials Development	Mide Technology Corporation	Ferro Magnetic Shape Memory Alloy (FSMA)	Study to characterize the frequency performance and fatique properties of FSMA
	University of Washington	FSMA Fe-Pd-Pt	Development of long stroke (10 cm) and large force (150N) ferromagnetic polycrystal Fe-Pd Material
2. Smart Material Driven Fluidic Devices	Active Control eXperts	FSMA	FSMA driven mechanical amplification mechanism driving a piston with PZT actuated valves
	Active Signals Technologies	TERFENOL	Terfenol powered solid state pump with active check valves
	Concepts ETI	PZT	PZT driven peristaltic pump
	CSA Engineering	PZT	PZT driven diaphragm with active spool valve
	HRL Laboratories	SMA	Thin film SMA diaphragm pump
3. Combustion Driven Devices	Sarcos Research Corporation	JP-8	.7mm diameter linear combustion chambers in arrays to produce a high enegy working fluid
4. Mechanically Amplified Devices	Burleigh Instruments	PZT	Inchworm motor that utilizes a novel ratcheting system and PZT drivers
	Penn State Center for Acoustics and Vibrations	PZT	PZT ceramic drive elements used with a mchanical rectification device to produce rotary motion
	University of Michigan	PZT	Development of a new family of high stroke large bandwidth actuators with compliant transmission elements

REFERENCES

1. Ikegami, R, Wilson, D.G, and Laakso, J.H, "Advanced Composites with Embedded Sensors and Actuators (ACESA), Final Report AL-TR-90-022, Astronautics Laboratory/Air Force Space Technology Center, June 1990, 111 pages.
2. Bronowicki, A.J., Mendenhall, T.L., and Manning, R.M., "Advanced Composites with Embedded Sensors and Actuators (ACESA), Final Report AL-TR-89-086, Astronautics Laboratory/Air Force Space Technology Center, April 1990, 150 pages.
3. Bronowicki, A.J., Betros, R.S., Dvorsky, G.R., Wyse, R.E., Innis, J.W., and Kuritz, S.P., "Advanced Composites with Embedded Sensors and Actuators (ACESA)," Phase III-V Final Report, PL-TR-93-3017, Phillips Laboratory Space & Missiles Directorate, Kirtland AFB, November 1993, 72 pages.
4. Mitrovic, M., Carman, G.P., and Straub, F., "Response of Piezoelectric Stack Actuators Under Combined Electro-Mechanical Loadin," *International Journal of Solids and Structures* to be published in 2000.
5. Mitrovic, M., Carman, G.P., and Straub, F., "Durability Characterization of Piezoelectric Stack Actuators Under Combined Electro-Mechanical Loading," *Proceedings of the 41st Structures, Structural Dynamics and Materials Conference*, Paper AIAA-2000-1500, AIAA, Reston, VA, April 2000.
6. Huber, J.E., Fleck, N.A., and Ashby, M.F., "The Selection of Mechanical Actuators Based on Performance Indices," *Proeedings of the Royal Society of London*, Volume A 453, Royal Society of London, London, 1997, pp. 2185-2205.
7. West, J., "Basics of Actuator Technology," *Lasers & Optronics*, September 1993, pp. 21-22.
8. Giurgiutiu, V., and Rogers, C.A., "Power and Energy Characteristics of Solid-State Induced-Strain Actuators for Static and Dynamic Applications," *Journal of Intelligent Material Systems and Structures*, Vol. 8, September 1997, pp. 738-750.
9. Winzer, Stephen R.,"S2D Quarterly Technical Report," CDRL A001, Quarterly Report, July 2000.
10. Winzer, Stephen R.,"S2D Quarterly Technical Report," CDRL A001, Quarterly Report, March 2000.
11. Derham, R.C., and Hagood, N.W., "Rotor Design Using Smart Materials to Actively Twist Blades," *Proceedings of the American Helicopter Society 52nd Annual Forum*, Vol. 2, American Helicopter Society, Alexandria, VA, 1996, pp. 1242-1252.
12. Straub, F.K., and King, R.J., "Application of Smart Materials to Control of a Helicopter Rotor," *Industrial and Commercial Applications of Smart Structures Technologies*, Vol. 2721, Society of PhotoOptical Instrumentation Engineers (SPIE), Bellingham, WA, 1996, pp. 66-76.
13. Anand, V., Domzalski, D., Hassan, A., Kennedy, D., Ngo, H., and Straub, F., "Smart Materials Actuatoed Rotor Technology—SMART", *Proceedings of the 41st Structures, Structural Dynamics, and Materials Conference*, AIAA 2000-1715, AIAA, Reston, VA, 2000.
14. Prechtl, E.F., and Hall, S.R., "An X-Frame Actuator Servo-Flap Actuation System for Rotor Control," *Smart Structures and Integrated Systems*, SPIE 3329-33, Vol. 3329, Society of PhotoOptical Instrumentation Engineers (SPIE), Bellingham, WA, 1998.
15. Hall, S.R., and Prechtl, E.F., "Preliminary testing of a Mach-Scaled Active Rotor Blade with a Trailing Edge Servo-Flap," *Smart Structures and Integrated Systems*, Vol. 3668, Society of PhotoOptical Instrumentation Engineers (SPIE), Bellingham, WA, 1999, pp. 14-21.
16. Prechtl, E.F., and Hall, S.R., "Design of a high efficiency, large stroke, electromechanical actuator," *Smart Materials and Structures*, Vol. 8, 1999, pp. 13-30.
17. Ormiston, R.A., "Smart Materials and Structures for Rotor Dynamics Applications," *Proceedings of the 4th ARO Workshop on Smart Structures*, Pennsylvania State University, State College, PA, August 16-18, 1999.
18. Kudva, J.N., Martin, C.A., Scherer, L.B., Jardine, A.P., McGowan, A.R., Lake, R.C., Sendeckyj, G., and Sanders, B., "Overview of the DARPA/AAFRL/NASA Smart Wing Program," *Industrial and Commercial Applications of Smart Structures Technologies*, SPIE 3674-28, Vol. 3674, Society of PhotoOptical Instrumentation Engineers (SPIE), Bellingham, WA, pp. 230-236.
19. Kudva, J., Appa, K., Martin, C., Jardine, P., Sendeckyj, G., Harris, T., McGowan, A., and Lake, R., "Design, Fabrication and Testing of the DARPA/WL Smart Wing Wind-Tunnel Model", *Proceedings of the 38th Structures, Structural Dynamics, and Materials Conference and Adaptive Structures Forum*, AIAA-97-1198, AIAA, Reston, VA, 1997.
20. Martin, C., Bartley-Cho, J., Flanagan, J., and Carpenter, B.F., "Design and Fabrication of Smart Wing Wind Tunnel Model and SMA Control Surfaces," *Industrial and Commercial Applications of Smart Structures Technologies*, SPIE 3674-28, Vol. 3674, Society of PhotoOptical Instrumentation Engineers (SPIE), Bellingham, WA, 1999, pp. 237-248.

21. Scherer, L.B., Martin, C.A., Appa, K., Kudva, J., and West, M.N., "Smart Wing Wind-Tunnel Test Results", *Industrial and Commercial Applications of Smart Structures Technologies*, Paper 3044-05, Vol. 3044, Society of PhotoOptical Instrumentation Engineers (SPIE), Bellingham, WA, 1997.
22. Lynch, C., Piezoelectric Hydraulic Pump Design," *Proceedings of the 41st Structures, Structural Dynamics, and Materials Conference*, AIAA 2000-1789, AIAA, Reston, VA, 2000.
23. Hopkins, M.A., Dunne, J.P., Baumann, E.W., and White, E.V., "Adaptive Fighter Engine Inlet," *Proceedings of the 40th Structures, Structural Dynamics, and Materials Conference*, AIAA-99-1512, AIAA, Reston, VA, 1999.
24. Dunne, J., Hopkins, M., Pitt, D., White, E., and Garcia. E., "Load Development in Adaptive Fighter Inlet," *Proceedings of the 41st Structures, Structural Dynamics, and Materials Conference*, AIAA-2000-1630, AIAA, Reston, VA, 2000.
25. Zvonar, G.A., Luan, J., Lee, F.C., Lindner, D.K., Kelly, S., Sable, D., and Schelling, T., "High-frequency Switching Amplifiers for Electrostrictive Actuators," *Industrial and Commercial Applications of Smart Structures Technologies,* Vol. 2721, Society of PhotoOptical Instrumentation Engineers (SPIE), Bellingham, WA, 1996, pp. 465-475.

GOOD CHOICE OF HYBRID PIEZOELECTRIC DAMPING CONFIGURATION BASED ON CONTROL POWER REQUIREMENT—SERIES TYPE VERSUS SEPARATED TYPE

Kazuhiko Adachi,[1] Yoshifumi Awakua,[1] Takuzo Iwatsubo[1]

ABSTRACT

This paper aims at presenting the advantage of the separate type of the hybrid piezoelectric damping comparing with the previous hybrid piezoelectric damping from the viewpoint of active control power requirement under the severe vibration suppression performance condition, numerically and experimentally. The separate type of the hybrid piezoelectric damping has been proposed by the authors, in which active voltage source and passive tuned RL shunting circuit are separated from each other, and piezoelectric actuators to be used to active and passive dampings are placed different location on the host structure. Simple flexible cantilever beam with surface bonded piezoelectric ceramic tiles is used as a test structure.

INTRODUCTION

Recently, application of electric damping augmentation using piezoelectric material to vibration suppression for several types of the flexible structures: such as flexible robot arms [1, 2], sporting goods (e.g. skis [3], snowboards[3], waterskis [3], baseball bats [3], golf clubs [4]), buildings and so on, has been given enormous attention.

Because of the electro-mechanical coupling characteristic, piezoelectric material is used to not only active [5] but also passive [6, 7] vibration suppression devices which are bonded on (or embedded in) the host structure. Passive damping guarantees the stability of the whole system and low power requirement. On the other hand, active damping achieves high performance of the vibration suppression and necessarily requires external electric energy supply. Due to the advantages of both passive and active dampings, the vibration suppression system using passive/active hybrid type of piezoelectric devices recently studied [9, 8].

The configuration of hybrid piezoelectric damping for a simple flexible cantilever beam with surface bonded piezoelectric ceramic tiles can be classified into following three types. Type I is series type (integrated type): piezoelectric actuators bonded on (or embedded

[1]Department of Mechanical Engineering, Faculty of Engineering, Kobe University, Rokkodai-cho 1-1, Nada-ku, Kobe 657-8501, Japan.

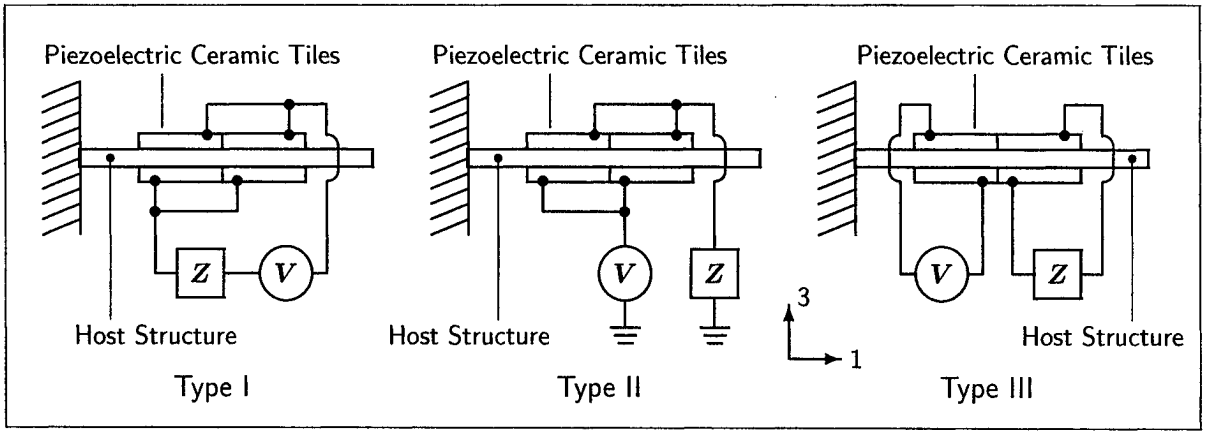


Figure 1 Hybrid piezoelectric damping: Tpye I $\sim$ III (for cantilever beam)

in) the host structure are driven by active voltage source with passive tuned RL shunting circuit in series. The configuration is shown in Figure 1. In the figure, $\boldsymbol{V}$ and $\boldsymbol{Z}$ indicate the active voltage source and the passive tuned RL shunting circuit, respectively. Type II is separated type in collocated condition shown in the figure: active voltage source and passive tuned RL shunting circuit are separated from each other, and both piezoelectric actuators to be used to active and passive dampings are collocated on the host structure. Type III is separated type in non-collocated condition shown in the figure: active voltage source and passive tuned RL shunting circuit are separated from each other, and piezoelectric actuators to be used to active and passive dampings are placed different location on the host structure, this type is proposed by the authors [11, 12]. Most of the previous studies, the configuration of the hybrid piezoelectric damping is restricted to Type I. There are few studies comparing with Type II, and it is pointed out that Type I is superior to Type II in vibration suppression performance [10].

This paper aims at presenting the advantage of Type III, that is the separated type in non-collocated condition, from the viewpoint of active control power requirement under the severe vibration suppression performance condition. In this study, vibration suppression performance is evaluated by using the gain of the accelerance transfer function of the closed loop system in modal space. The active control power requirement of Type III is numerically and experimentally compared with that of Type I and II by using the simple flexible cantilever beam with surface bonded piezoelectric ceramic tiles.

GOVERNING EQUATIONS OF HYBRID DAMPING

Governing equations of the flexible structures equipped with the hybrid piezoelectric damping are derived [11, 12].

$$\boldsymbol{M}\ddot{\boldsymbol{x}} + \boldsymbol{C}\dot{\boldsymbol{x}} + \boldsymbol{K}\boldsymbol{x} = \boldsymbol{f} + \boldsymbol{\Theta}\boldsymbol{q}\ , \quad \boldsymbol{L}\ddot{\boldsymbol{q}} + \boldsymbol{R}\dot{\boldsymbol{q}} + \boldsymbol{C}_p{}^{-1}\boldsymbol{q} = \boldsymbol{v} + \boldsymbol{\Theta}^{\mathsf{T}}\boldsymbol{x} \tag{1}$$

where $\boldsymbol{x}$ is the nodal displacement vector of the structure. $\boldsymbol{q}$ is the electric charge vector at the electrode of the piezoelectric ceramic tiles. Above governing equations are based on the following assumptions [10]: (a) the bending deflection of the structure is small

(compared with it length), (b) the piezoelectric ceramic tiles' displacement and strain are equal to the displacement and the strain at the surface of the structure. Thus, only uni-axial loading of the piezoelectric ceramic tiles in the 1-direction shown in Figure 1 is considered, (c) the poling direction of the surface bonded piezoelectric ceramic tiles is in the 3-direction shown in the figure, and (d) the applied voltage for the active damping is uniform.

Mass and stiffness matrices are given as following form,

$$\boldsymbol{M} = \rho_s \int_{V_s} {\boldsymbol{\Psi}_x}^{\mathsf{T}} \boldsymbol{\Psi}_x dV_s + \rho_p \int_{V_p} {\boldsymbol{\Psi}_x}^{\mathsf{T}} \boldsymbol{\Psi}_x dV_p, \ \boldsymbol{K} = \int_{V_s} \boldsymbol{N}_x^{\mathsf{T}} \boldsymbol{E}_s \boldsymbol{N}_x dV_s + \int_{V_p} \boldsymbol{N}_x^{\mathsf{T}} {\boldsymbol{E}_p}^D \boldsymbol{N}_x dV_p \tag{2}$$

where ρ_s and ρ_p are the material density of the structure and the piezo-elements. Lateral displacement of the structure can be derived from the nodal displacement $\boldsymbol{x}$ by using the interpolation function $\boldsymbol{\Psi}_x$. V_s and V_p indicate the volumes of the structure and the piezo-elements. Subscripts $(\cdot)_s$ and $(\cdot)_p$ indicate that the values are both the structural and the piezoelectric material's quantities, respectively. Mechanical strain $\boldsymbol{\varepsilon}_s$ of the structure can be derived from the nodal displacement by using the interpolation function $\boldsymbol{N}_x$. $\boldsymbol{E}_s$ and ${\boldsymbol{E}_p}^D$ are the elastic stiffness matrices of the structure and the piezo-elements. $\boldsymbol{C}$ is the damping matrix of the structure, in which proportional damping is assumed. Electro-mechanical coupling matrix is given as follows.

$$\boldsymbol{\Theta} = \int_{V_p} \boldsymbol{N}_x^{\mathsf{T}} \boldsymbol{h}^{\mathsf{T}} \boldsymbol{N}_q dV_p \tag{3}$$

where $\boldsymbol{h}$ is the matrix whose components are piezoelectric constants of the piezo-elements. $\boldsymbol{N}_q$ is the interpolation function which indicates the distribution of electric charge on the electrode of the piezo-elements. $\boldsymbol{f}$ is the external dynamic loading vector applied to the structure. $\boldsymbol{L}$ and $\boldsymbol{R}$ are diagonal matrices whose diagonal elements are inductances and resistances of the shunting electric circuits. $\boldsymbol{C}_p^{-1}$ is diagonal matrix given by,

$$\boldsymbol{C}_p^{-1} = \int_{V_p} \boldsymbol{N}_q^{\mathsf{T}} \boldsymbol{\beta}^{\varepsilon} \boldsymbol{N}_q dV_p \tag{4}$$

whose diagonal elements are capacitances of the piezo-elements. $\boldsymbol{v}$ is the external applied voltage for active damping.

The characteristic of the piezoelectric ceramic tiles is governed by the following constitutive equations of the material [13].

$$\boldsymbol{\sigma}_p = {\boldsymbol{E}_p}^D \boldsymbol{\varepsilon}_p - \boldsymbol{h}^{\mathsf{T}} \boldsymbol{D} \ , \quad \boldsymbol{E} = -\boldsymbol{h}\boldsymbol{\varepsilon}_p + \boldsymbol{\beta}^{\varepsilon} \boldsymbol{D} \tag{5}$$

where $\boldsymbol{\sigma}_p$, $\boldsymbol{\varepsilon}_p$, $\boldsymbol{D}$ and $\boldsymbol{E}$ are stress, strain, dielectric flux density and electric field vectors of the piezo-elements, respectively. $\boldsymbol{\beta}^{\varepsilon}$ is impermittivity matrix. Superscripts $(\cdot)^D$ and $(\cdot)^{\varepsilon}$ indicate that the values are obtained at constant dielectric flux density and constant strain.

EVALUATION OF HYBRID DAMPING

In this section, evaluations of the active control power requirement of the hybrid

damping are formulated. The coordinate transformation from physical space to modal space is applied to the governing equations (1). In the modal space, only diagonal components of the characteristic matrices are considered, and both passive and active dampings are tuned to the i-th structural vibration mode.

The governing equation of the hybrid damping Type I is,

$$\ddot{\eta}_i + 2\zeta_i\omega_i\dot{\eta}_i + {\omega_i}^2\eta_i = {\boldsymbol{\phi}_i}^{\mathsf{T}}\boldsymbol{f} + {\boldsymbol{\phi}_i}^{\mathsf{T}}\boldsymbol{\Theta}_I q \ , \quad L_I\ddot{q} + R_I\dot{q} + \frac{1}{C_{pI}}q = V_I + {\boldsymbol{\Theta}_I}^{\mathsf{T}}\boldsymbol{\phi}_i\eta_i \tag{6}$$

where η_i is i-th modal displacement, and $\boldsymbol{\phi}_i$ is corresponding to the i-th column of the modal matrix whose columns are the eigenvectors normalized with respect to the mass matrix. In this type, pairs of the piezoelectric ceramic tiles is connected to each other by the shunting electric circuit including the inductance L_I and the resistance R_I for the passive damping and the control voltage V_I for the active damping shown in Figure 1.

The governing equations of the hybrid damping Type II are,

$$\ddot{\eta}_i + 2\zeta_i\omega_i\dot{\eta}_i + {\omega_i}^2\eta_i = {\boldsymbol{\phi}_i}^{\mathsf{T}}\boldsymbol{f} + {\boldsymbol{\phi}_i}^{\mathsf{T}}\boldsymbol{\Theta}_{IIa}q_a + {\boldsymbol{\phi}_i}^{\mathsf{T}}\boldsymbol{\Theta}_{IIp}q_p \ ,$$

$$\frac{1}{C_{pIIa}}q_a = V_{II} + {\boldsymbol{\Theta}_{IIa}}^{\mathsf{T}}\boldsymbol{\phi}_i\eta_i \ , \quad L_{II}\ddot{q} + R_{II}\dot{q} + \frac{1}{C_{pIIp}}q = {\boldsymbol{\Theta}_{IIp}}^{\mathsf{T}}\boldsymbol{\phi}_i\eta_i \tag{7}$$

in which the control voltage V_{II} and the passive tuned RL shunting circuit (L_{II} and R_{II}) are separated from each other, and both piezoelectric actuators to be used to active and passive dampings are collocated on the structure shown in the figure.

The governing equations of the hybrid damping Type III are,

$$\ddot{\eta}_i + 2\zeta_i\omega_i\dot{\eta}_i + {\omega_i}^2\eta_i = {\boldsymbol{\phi}_i}^{\mathsf{T}}\boldsymbol{f} + {\boldsymbol{\phi}_i}^{\mathsf{T}}\boldsymbol{\Theta}_{IIIa}q_a + {\boldsymbol{\phi}_i}^{\mathsf{T}}\boldsymbol{\Theta}_{IIIp}q_p \ ,$$

$$\frac{1}{C_{pIIIa}}q_a = V_{III} + {\boldsymbol{\Theta}_{IIIa}}^{\mathsf{T}}\boldsymbol{\phi}_i\eta_i \ , \quad L_{III}\ddot{q} + R_{III}\dot{q} + \frac{1}{C_{pIIIp}}q = {\boldsymbol{\Theta}_{IIIp}}^{\mathsf{T}}\boldsymbol{\phi}_i\eta_i \tag{8}$$

where the control voltage V_{III} and the passive tuned RL shunting circuit (L_{III} and R_{III}) are also separated from each other, but piezoelectric actuators to be used to active and passive dampings are placed different location on the structure shown in the figure.

In this study, the design parameters of the hybrid dampings are decided by the followings. Control voltages for the active dampings are generated by using the state feedback control,

$$V = -\boldsymbol{G}\{\eta_i \ \dot{\eta}_i \ q \ \dot{q}\}^{\mathsf{T}} \tag{9}$$

where the static feedback gain $\boldsymbol{G}$ is obtained by solving a linear quadratic regulator problem whose performance index is defined by,

$$J = \int_0^\infty \left({\dot{\eta}_i}^2 + {\omega_i}^2{\eta_i}^2 + rV^2\right) dt \ . \tag{10}$$

r is weighting coefficient. On the other hand, the inductances and the resistances of the shunting electric circuits for the passive dampings Type II and III are obtained by the analogy with the single degree-of-freedom damped vibration absorber [6, 7], then these parameters are,

$$LC_p = \frac{1}{{\omega_i}^2} \ , \quad R = \frac{\sqrt{2}\mu}{1+\mu^2}\frac{1}{C_p\omega_i} \ . \tag{11}$$

In Type I, the value of the inductance of the shunting electric circuit can be designed by using Eq.(11), but there is no design expression for the resistance of the circuit. The value of the resistance is decided by using the value of the feedback gain corresponding to $\dot{q}$, in this study.

The evaluations of the active control power requirement of the hybrid dampings can be derived by using Eqs.(6) $\sim$ (8), (11). Following W_I, W_{II} and W_{III} are the evaluation for Type I, II and III, in which U is the specified control input achieving the same vibration suppression performance.

$$W_I = C_{pI} {V_I}^2 \tan\delta_I = \left\{ \left(U - \frac{\mu_I {\omega_i}^2}{\sqrt{2}} \eta_i \right)^2 \frac{1}{1+{\mu_I}^2} \frac{1}{{\omega_i}^2} \right\} \tan\delta_I \tag{12}$$

$$W_{II} = C_{pIIa} {V_{II}}^2 \tan\delta_{II} = \left\{ \left(U^2 - \frac{{\mu_{IIp}}^2 {\omega_i}^4}{2} {\eta_i}^2 \right) \frac{1+{\mu_{IIa}}^2}{{\mu_{IIa}}^2} \frac{1}{{\omega_i}^2} \right\} \tan\delta_{II} \tag{13}$$

$$W_{III} = C_{pIIIa} {V_{III}}^2 \tan\delta_{III} = \left\{ \left(U^2 - \frac{{\mu_{IIIp}}^2 {\omega_i}^4}{2} {\eta_i}^2 \right) \frac{1+{\mu_{IIIa}}^2}{{\mu_{IIIa}}^2} \frac{1}{{\omega_i}^2} \right\} \tan\delta_{III} \tag{14}$$

where $C_p V^2$ indicates the reactive power at the piezo-elements and $\tan\delta$ is the loss tangent of the piezo-elements. μ is the nondimensional resonant frequency ratio (that is the generalized electromechanical coupling coefficient in [6]) given by follows.

$$\begin{aligned} {\mu_I}^2 &= \frac{{\omega_i}^2 - \left(\omega_{Ii}^S\right)^2}{\left(\omega_{Ii}^S\right)^2}, \quad {\mu_{IIp}}^2 = \frac{{\omega_i}^2 - \left(\omega_{IIpi}^S\right)^2}{\left(\omega_{IIpi}^S\right)^2}, \quad {\mu_{IIa}}^2 = \frac{{\omega_i}^2 - \left(\omega_{IIai}^S\right)^2}{\left(\omega_{IIai}^S\right)^2}, \\ {\mu_{IIIp}}^2 &= \frac{{\omega_i}^2 - \left(\omega_{IIIpi}^S\right)^2}{\left(\omega_{IIIpi}^S\right)^2}, \quad {\mu_{IIIa}}^2 = \frac{{\omega_i}^2 - \left(\omega_{IIIai}^S\right)^2}{\left(\omega_{IIIai}^S\right)^2}. \end{aligned} \tag{15}$$

In these expressions, ω_{Ii}^S, ω_{IIpi}^S, ω_{IIai}^S, ω_{IIIpi}^S are ω_{IIIai}^S are corresponding to the i-th natural frequency of the structure whose surface bonded or embedded piezo-elements are in short circuit condition.

RESULTS AND DISCUSSIONS

The hybrid damping is experimentally tested by using a steel flexible cantilever beam with four pairs of piezoelectric ceramic tiles bonded on the surface of the beam. The hybrid damping is also numerically simulated by using the model with the same specification of the test structure. Experimental apparatus is shown in Figure 2. The beam is 0.3(m) long, 0.02(m) wide and 0.001(m) thick. Each piezoelectric ceramic tile is 0.03(m) long, 0.02(m) wide and 0.0003(m) thick (C-6 type, Fuji Ceramics Co., Japan). The poling direction of the piezoelectric ceramic tiles are shown in the figure. Other parameters are indicated in TABLE I. $v_{\max}$ is maximum allowable applied voltage of the piezoelectric ceramic tiles. Every piezoelectric ceramic tile pair is numbered from the clamped end, No.1 - 4, as shown in the figure. Only No.1 and 2 pairs are used in this study in order to suppress the first bending vibration mode. Feedback signal for the active damping is gen-

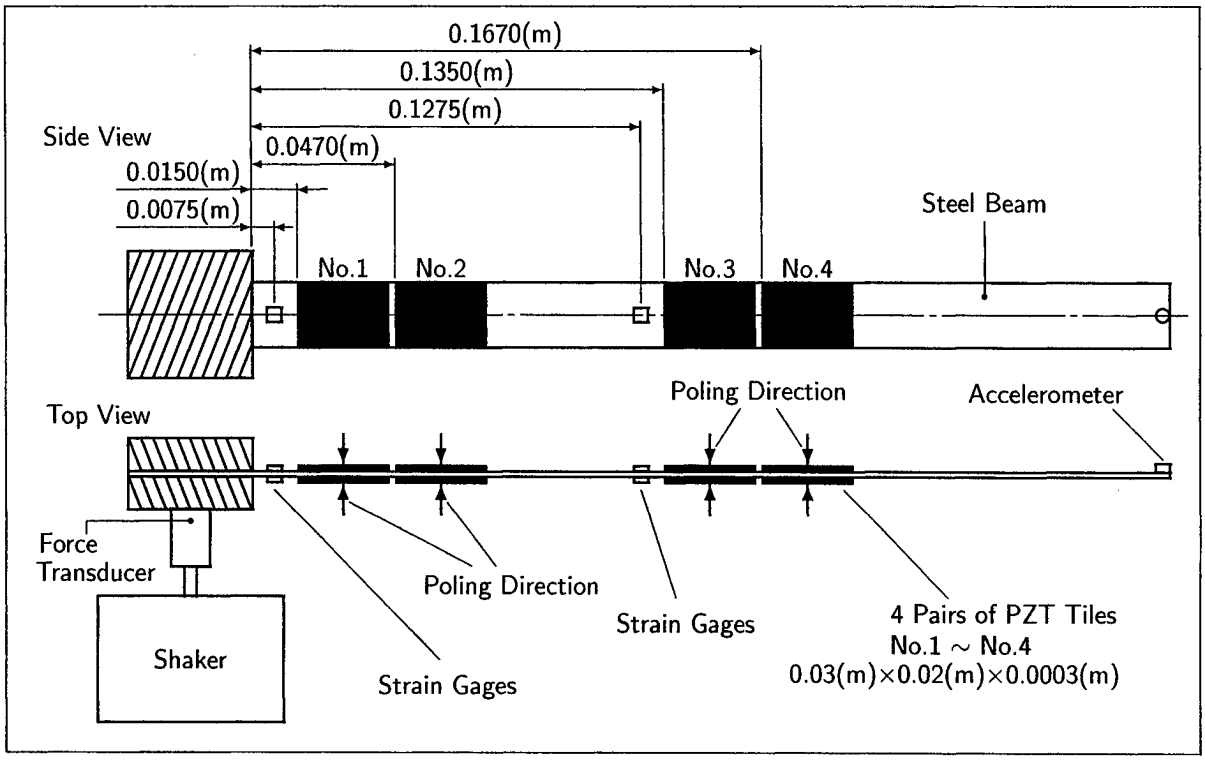


Figure 2 Flexible cantilever beam with surface bonded piezoelectric ceramic tiles

TABLE I. SPECIFICATION OF CANTILEVER BEAM AND PIEZO-ELEMENT

Cantilever Beam		Piezoelectric Ceramic Tile	
ρ_s	$7.86 \times 10^3(\mathrm{kg/m^3})$	ρ_p	$7.82 \times 10^3(\mathrm{kg/m^3})$
E_s	$2.06 \times 10^{11}(\mathrm{N/m^2})$	${E_{p11}}^D$	$1.39 \times 10^{11}(\mathrm{N/m^2})$
		h_{31}	$-1.20 \times 10^9(\mathrm{V/m})$
		${\beta_3}^\varepsilon$	$1.47 \times 10^8(\mathrm{m/F})$
		$v_{\max}$	$4.50 \times 10^2(\mathrm{V/mm})$

TABLE II. EIGENVALUES OF THE CANTILEVER BEAM

without piezo-element			with piezo-element		
	ω_i	ζ_i		ω_i	ζ_i
1st bending mode	8.170 (Hz)	0.01438	1st bending mode	9.278 (Hz)	0.01200
2nd bending mode	49.896 (Hz)	0.00553	2nd bending mode	51.947 (Hz)	0.01728

erated from the strain gages on the beam. Natural frequencies of the first and second bending vibration modes of the beam with and without the piezoelectric ceramic tiles under the open circuit condition are shown in TABLE II. The clamped end of the beam is excited by an elctrodynamic vibration generator. Accelerance transfer functions are computed by using a signal analyzer. Exciting force and tip acceleration are measured by using a force transducer (load cell) and an accelerometer. The transfer function from the exciting force to the control voltage for the active damping are also computed by the signal analyzer.

Experimental test results and numerical simulation results of the evaluation of active control power requirement of the hybrid dampings for first bending vibration mode of the

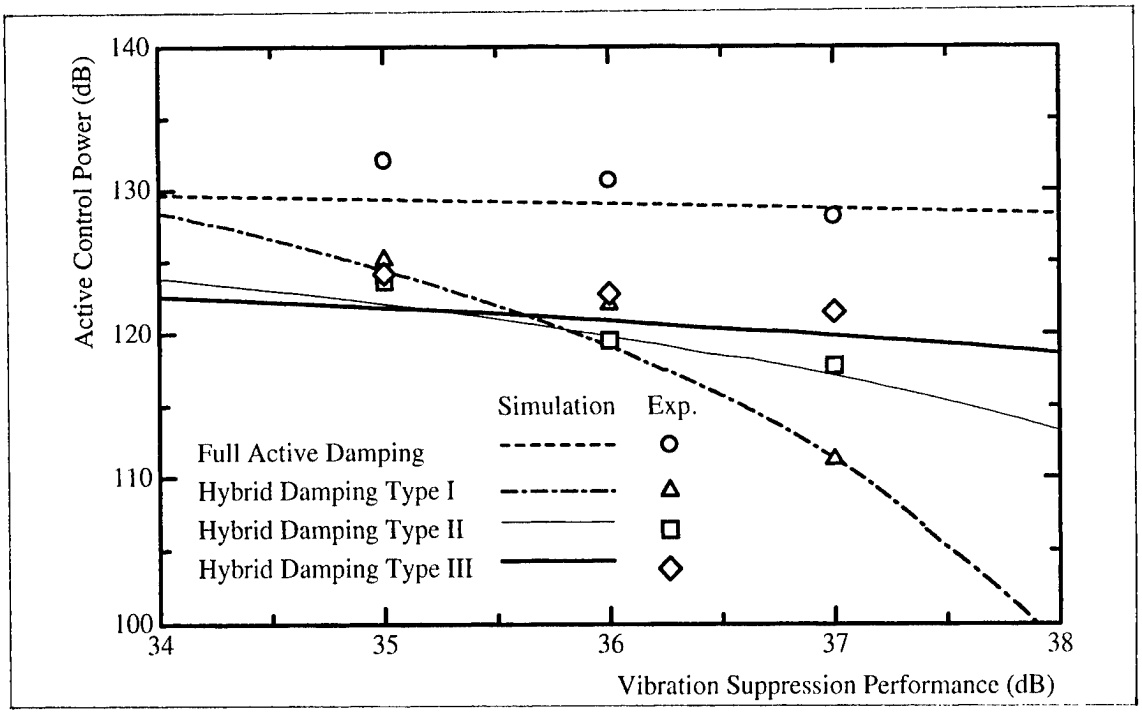


Figure 3 Evaluation of active control power requirement (1st bending vibration mode)

test structure are summarized by Figure 3. In this figure, the active control power requirement of the hybrid damping Type I, II, III and the full active damping are numerically and experimentally compared with each other. The active control power evaluated by Eqs.(12) $\sim$ (14) in vertical axis and the gain of the accelerance transfer function of the closed loop system at first resonant frequency in horizontal axis are plotted in the figure. The vibration suppression performance is not so severe (e.g. the gain of the accelerance transfer function is about 37(dB)), the hybrid damping Type I is superior to others, which had been already reported by other researchers [10]. On the contrary, the hybrid damping Type III is superior to the other types of the hybrid damping under the severe vibration suppression performance condition. According to the numerical simulation, the active control power requirement of Type III is successfully decreased compared with that of Type I under the severe condition (e.g. the gain of the accelerance transfer function is about 34(dB)). However, the difference among the hybrid dampings obtained by the experimental results is not clear.

CONCLUSIONS

Three different types of the hybrid piezoelectric damping are numerically and experimentally compared with each other by using the simple flexible cantilever beam with surface bonded piezo-elements from the viewpoint of active control power requirement under the severe vibration suppression performance condition. The results indicate that the hybrid damping whose configuration is Type III is superior to that with the other types of configurations (Type I and II) in active control power requirement. On the contrary, the vibration suppression performance is not so severe, the hybrid damping whose configuration is Type I is superior to others, which had been already reported.

ACKNOWLEDGMENTS

A part of this work was supported by Grants-in-Aid for Scientific Research for Young Investigator from the Ministry of Education, Science, Sports and Culture, Japan; Grant No.09750261 and No.11750185.

REFERENCES

1. Choi, S.B., Shin, H.C, Kim, H.K. and Kim, J.H. 1999. "Position Control of a Two-Link Flexible Manipulator using Piezoelectric Actuators," presented at the SPIE's 6th International Symposium on Smart Structures and Materials, Newport Beach, California, March 1-4, 1999, *Smart Structures and Materials 1999: Mathematics and Control in Smart Structures*, Vasundara V.Varadan, Ed. Proceedings of SPIE Vol.3667, pp.211-218.
2. Wilson, D.G., Parker, G.G., Starr, G.P. and Robinett, R.D. 1999. "Robust Adaptive Control of a Slewing Active Structure," presented at the SPIE's 6th International Symposium on Smart Structures and Materials, Newport Beach, California, March 1-4, 1999, *Smart Structures and Materials 1999: Smart Structures and Integrated Systems*, Norman M.Wereley, Ed. Proceedings of SPIE Vol.3668, pp.164-174.
3. http://www.acx.com/
4. Bianchini, E., Spangler, R. and Pandell, T. 1999. "The Use of Piezoelectric Dampers for Improving the Feel of Golf Clubs," presented at the SPIE's 6th International Symposium on Smart Structures and Materials, Newport Beach, California, March 1-4, 1999, *Smart Structures and Materials 1999: Smart Structures and Integrated Systems*, Norman M.Wereley, Editor, Proceeding of SPIE Vol.3668, pp.824-834.
5. Hagood, N.W., Chung, W.H. and von.Flotow, A. 1990. "Modelling of Piezoelectric Actuator Dynamics for Active Structural Control," *J. Intell. Mater. Syst. &Struct.*, 1, pp.327-354.
6. Hagood, N.W. and von.Flotow, A. 1991. "Damping of Structural Vibrations with Piezoelectric Materials and Passive Electrical Networks," *J. Sound Vib.*, 146(2), pp.243-268.
7. Hollkamp, J.J. 1994. "Multimodal Passive Vibration Suppression with Piezoelectric Materials and Resonant Shunts," *J. Intell. Mater. Syst. &Struct.*, 5, pp.49-57.
8. Agnes, G.S. 1995. "Development of a Modal Model for Simultaneous Active and Passive Piezoelectric Vibration Suppression," *J. Intell. Mater. Syst. &Struct.*, 6, pp.482-487.
9. Wang, K.W. and Kahn, S.P. 1995. "Structural Vibration Controls via Active-Passive Piezoelectrical Networks – A Hybrid Approach, " presented at International Conference on Structural Dynamics, Vibration, Noise and Control, Hong Kong, December 5-7, 1995, *Proc. of the Int. Conf. on Struct. Dyn., Vib., Noise and Control*, pp.1059-1064.
10. Tsai, M.S. and Wang, K.W. 1997. "Some insights on active-passive hybrid piezoelectric networks for structural controls," presented at the SPIE's 4th International Symposium on Smart Structures and Materials, San Diego, California, March 3-4, 1997, *Smart Structures and Materials 1997: Passive Damping and Isolation*, L.Porter Davis, Ed., Proceedings of SPIE Vol.3045, pp.82-93.
11. Adachi, K., Awakura, Y. and Iwatsubo, T. 2000. "Experimental investigation of hybrid damping for flexible structures by using surface bonded piezo-elements," presented at the SPIE's 7th International Symposium on Smart Structures and Materials, Newport Beach, California, March 5-9, 2000, *Smart Structures and Materials 2000: Damping and Isolation*, T.Tupper Hyde, Ed., Proceedings of SPIE Vol.3989, pp.312-321.
12. Adachi, K., Isobe, E. and Iwatsubo, T. 1997. "A Study of the Electromechanical Damping System to Vibration Suppression for Flexible Structures," presented at the 8th International Conference on Adaptive Structures and Technologies, Wakayama, Japan, October 29-31, 1997, *Eighth International Conference on Adaptive Structures and Technologies*, Y.Murotsu, C.A.Rogers, P.Santini, and H.Okubo, eds. Lancaster,PA: Technomic Publishing Co., Inc., pp.276-285.
13. *An American National Standard IEEE Standard on Piezoelectricity.* New York, NY: IEEE, ANSI/IEEE Std. 176-1987.

MECHANICAL PROPERTY OF METALLIC CLOSED CELLULAR MATERIALS CONTAINING POLYMER FOR SMART STRUCTURES

S. Kishimoto and N. Shinya

ABSTRACT

A new material for smart structures, which has a high energy-absorbing capacity and light weight, has been developed by cold isostatic pressing and sintering at high temperature. Powder particles of a polymer coated with a nickel-phosphorus alloy layer using electroless plating were pressed into pellets and sintered in vacuum at high temperature. A metallic closed cellular material containing polymer was then fabricated.

The physical, mechanical and ultrasonic properties of this material were measured. The density of this material is about 2.2-2.4g/cm^3 which is lower than that of an aluminum alloy. The compressive tests shows that one kind of these materials has a low Young's modulus and high-energy absorption. Ultrasonic measurement showed that the attenuation coefficient of this cellular material was very large. These results indicate that this metallic closed cellular material can be used for the materials in passive damping and energy absorbing systems.

INTRODUCTION

Many current research projects have been developing intelligent or smart structures. Particularly, materials for smart structures are becoming important in terms of vibration control and energy absorbing systems.

Recently, cellular materials are receiving renewed attention as structural and functional materials. Cellular materials have unique thermal, acoustic and energy absorbing properties that can be combined with their structural efficiency [1,2]. Therefore, many kinds of cellular materials have been tested as damping or energy absorbing materials [2-4]. However, most of the cellular materials fabricated up to now are open cellular polymers, open cellular metals, metal foams and woods. Though the closed cellular materials are thought to have many properties and applications for intelligent and smart structures, there is a lack of technique to produce the metallic closed cellular materials except for gas forming [4-8], the sintering of hollow powders [9] or two dimensional honeycomb structures [1].

Satoshi Kishimoto, National Research Institute for Metals, 1-2-1 Sengen,Tsukuba, Ibaraki 305-0047, Japan

Norio Shinya, National Research Institute for Metals, 1-2-1 Sengen,Tsukuba, Ibaraki 305-0047, Japan

In this study, a new material for smart structures, which has a high energy-absorbing capacity and light weight, has been developed by using electroless plating, cold isostatic pressing and sintering at high temperature. The physical, mechanical and ultrasonic properties of this material were measured. The utility of this metallic closed cellular material is also discussed.

CONCEPTUAL PROCESS

The metallic closed cellular material fabricating process is shown in Fig. 1. This process is as as follows: 1) Powdered polymer particles are coated with a metal layer using electroless plating. 2) The powder particles are pressed into pellets (green compacts) by cold isostatic pressing. 3) After sintering at high temperature in a vacuum, the closed cellular material is produced.

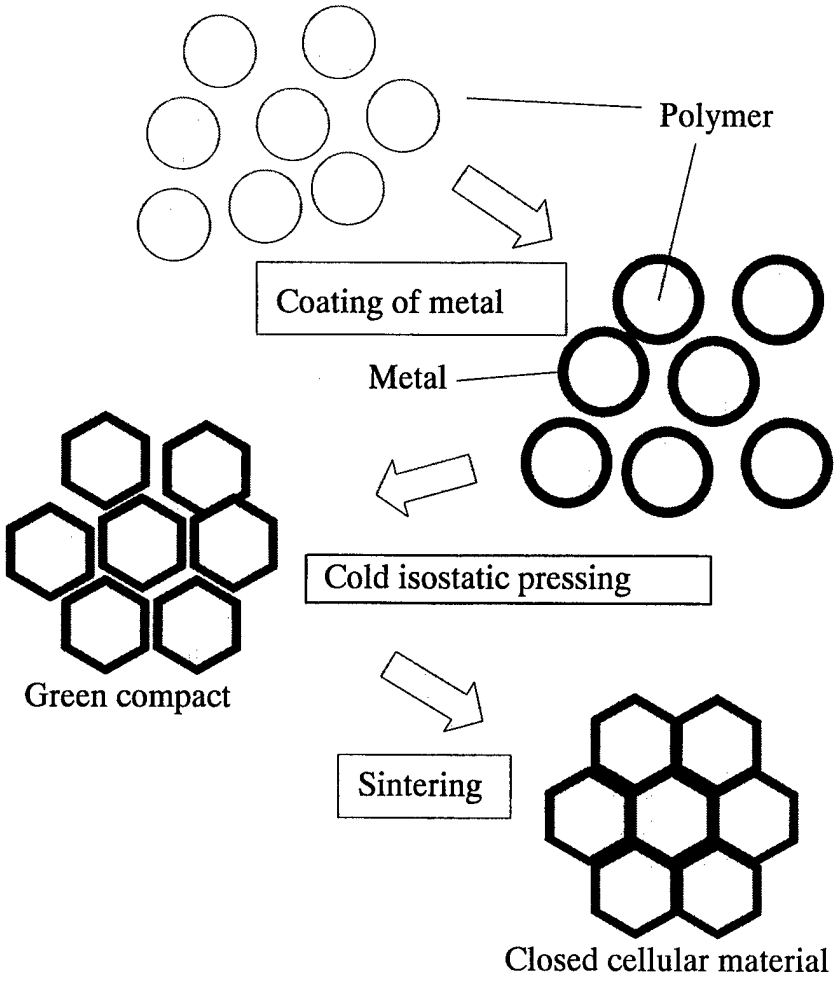


Figure 1.. Flow diagram of metallic closed cellular material fabricating process.

EXPERIMENTS

Preparing the metallic closed cellular material

Thermal plastic polymer particles of polystyrene with a 10 μm diameter were selected for this study. These polystyrene particles were coated with a 0.5 μm thick nickel-phosphorus alloy and 0.02 μm thick gold layer using electroless plating. Figure 2 shows the schematic diagram of a polystyrene particle coated with the Ni-P alloy and gold. These particles were pressed into two types of pellets (green compacts) with an 8mm and 16mm diameters and about 8 mm length by isostatic pressing at 200MPa and 90°C. After this, these green compacts were sintered for 1 h at 800°C and 850 °C in a vacuum.

Characterization

The microstructure of the green compacts before sintering, the cross-sections after sintering and fracture surface were observed using a scanning electron microscope (SEM). To observe the cross-section of this material, the specimen was cut and the cross-section surface was polished using emery paper (#600) and then 0.05μm Al_2O_3 powders.

To measure the mechanical properties, compressive tests were performed at room temperature. In addition, ultrasonic measurements were carried out to estimate the attenuation coefficient of this material. The measurement was carried out with a 6.4 mm diameter probe generating a longitudinal wave of 10MHz at room temperature.

RESULTS AND DISCUSSION

Microstructure

Figure 3 shows an SEM image of the green compact after cold isostatic pressing. An SEM image of the cross-section of this material after sintering at 800°C is shown in Fig. 4.

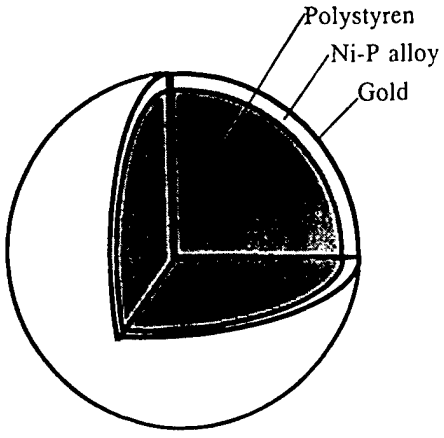


Figure 2. Schematic diagram of a polystyrene particle coated with the Ni-P alloy and gold.

As Fig. 3 shows, the polystyrene particles were deformed to polyhedra by the isostatic pressing. Also, Fig. 4 shows that cell walls of a nickel-phosphorus alloy are observed as bright parts and the material inside the cell walls is observed as darker parts. The amount of emitted secondary electrons per a primary electron of the polystyrene is smaller than that of the metals. During polishing, only 0.05μm Al_2O_3 powders were used. Therefore, the material inside the cell walls is thought to be polystyrene. This result indicates that the polystyrene remains inside the cell walls after heat treatment at 800℃ or 850℃ and this metallic closed cellular material containing the polymers can be produced using this technique.

Mechanical Properties

COMPRESSIVE TESTS

Compressive tests were carried out at room temperature. A typical example of the compressive test results is shown in Fig. 5. The sintering temperature and the density of each specimen is also indicated in Fig. 5. It is from about 2.2 g/cm^3 to 2.4g/cm^3 which is lower than that of an aluminum alloy. A specimen sintered at 850°C has a higher strength and density than specimens sintered at 800°C. The stress-strain curve shows a linear elastic region, a long plateau where the stress gradually increases and a wavy region where the stress repeatedly decreases and increases. Figure 5 shows the fracture surface of the compressive tested specimens sintered at 850°C. The cells on the fracture surface were crushed and broken. These fracture surfaces are almost parallel to the stress axis.

As shown in Fig. 5, the stress-strain curve has a linear elastic region, a long plateau region and a wavy region. After the linear elastic region, cracks occur in the direction parallel to the stress axis. It is postulated that the fracture initiates from a defect in this material. Therefore,

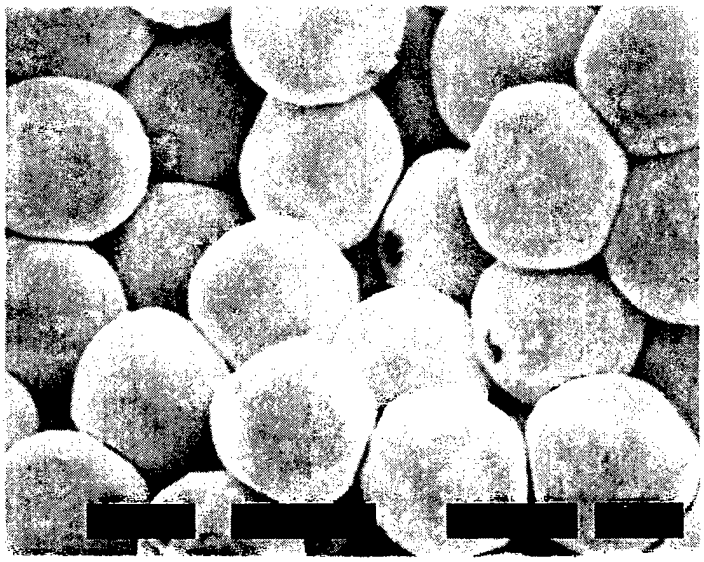


Figure 3. SEM image of green compact after isostatic pressing.

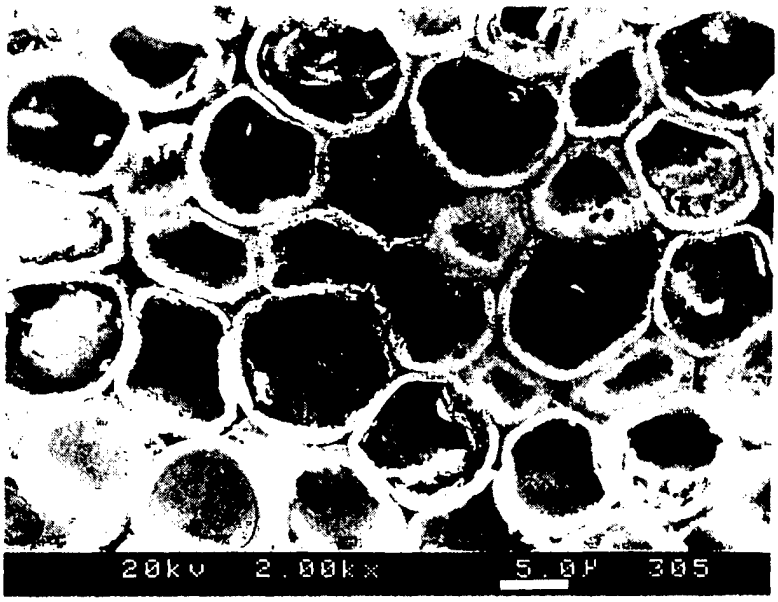


Figure 4. Cross-section of the metallic closed cellular material.

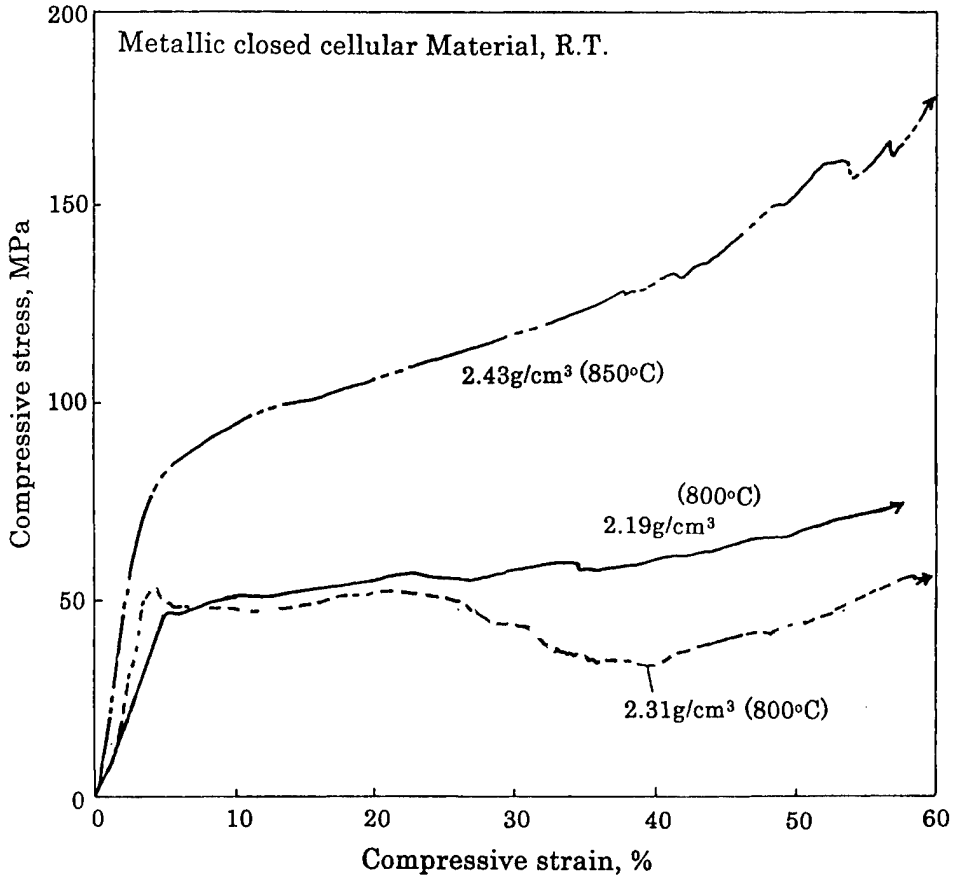


Figure 5 . Compressive stress-strain curve for metallic closed cellular material.

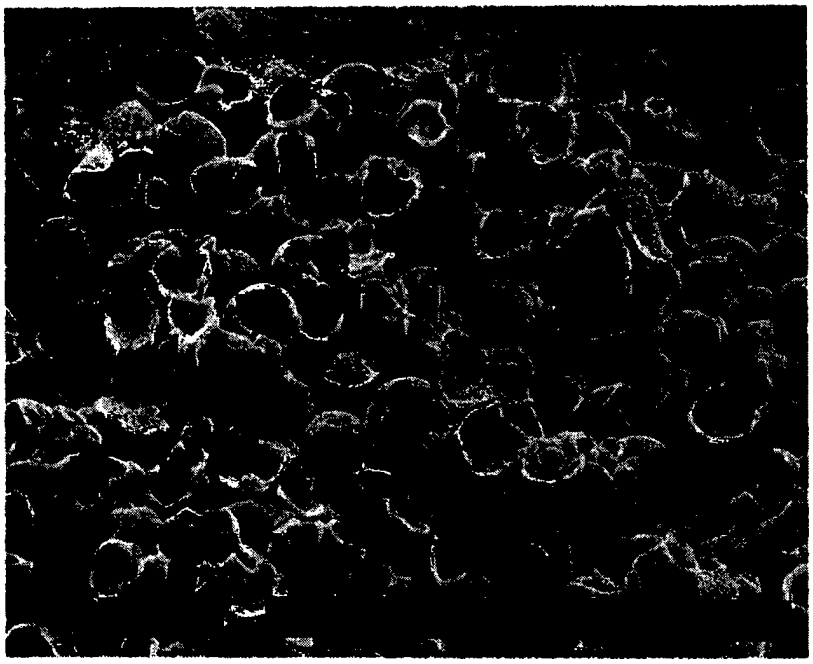


Figure 6. Fracture surface of metallic closed cellular material

if the metallic closed cellular material has only few defects, the plateau area of the stress-strain curve will continue longer during the compressive test. It should be considered that the specimen sintered at 850℃ has fewer defects than specimens sintered at 800℃. It seems that the presence of the plateau in the compressive stress-strain curve is responsible for the high energy-absorption. Therefore, this metallic closed cellular material seems to have a high energy-absorbing capacity. These results show that this material can be utilized as an energy absorbing material.

YOUNG'S MODULUS

Young's modulus was measured using the linear elastic region for each specimen, and the relationship between Young's modulus and density of this material is shown in Fig. 7. The change in Young's modulus depended on the density of the specimen. It should be considered that the density of this material can be controlled by pressure during the isostatic pressing and the sintering temperature. Therefore, it should be considered that Young's modulus of this material can be controlled by changing the pressure during the isostatic pressing and the sintering temperature.

Ultrasonic measurement

The ultrasonic attenuation of a 16mm diameter specimen sintered at 800°C was measured

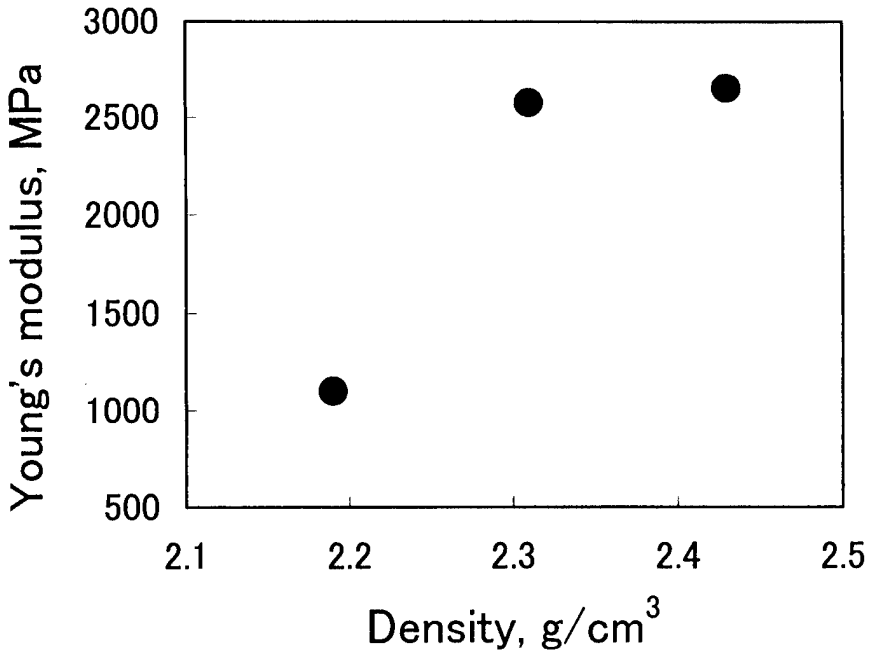


Figure 7 . Relationship between density and Young's Modulus of closed cellular materials.

at room temperature. The attenuation coefficient (about 3.8 – 5.9 dB/cm) is larger than that of metallic materials, but smaller than that of polystyrene (15.2dB/cm). In addition, as the temperature increases, the ultrasonic coefficient of this material gradually increases.

These results suggest that this material can be utilized as a passive damping material. In addition, as the temperature increases, the attenuation coefficient gradually increases. Therefore, it should be considered that the attenuation coefficient of this material can be controlled by changing the temperature.

CONCLUSION

A metallic closed cellular material containing a polymer has been developed. This metallic closed cellular material is very light and has a high energy absorption and a large ultrasonic attenuation coefficient. In addition, Young's modulus depended on the density of the specimen. These obtained results emphasize that this metallic closed cellular material can be utilized as an energy absorbing material and passive damping material.

REFERENCE

1. L.J. Gibson, M.F. Ashby, 1988, Cellular Solids - Structure and Properties, Pergamon Press, Oxford, pp. 42-68.
2. G.J. Davies, S. Zhen, 1983, "Metallic Foams: Their Production, Properties and Applications," J. of Materials Science, 18, pp.1897-1911.

3. T. Mukai, H. Kanahashi, T. Miyoshi, M . Mabuchi, T.G. Nieh and K. Higashi, 1999, "Experimental Study of Energy Absorption in a Closed-celled Aluminum Foam under Dynamic Loading, " Scripta Mater. 40, pp.921-927
4. S.K. Maiti, L.J. Gibson, M.F. Ashby, 1984, "Deformation and Energy Absorpton Diagrams for Cellular Solid," Acta Metall, 32, pp.1963-1975.
5. J.T. Beals, and M.S. Thompson, 1997, "Density Gradient Effect on Aluminum Foam Compression Behaviour," J. Mater. Sci. 32, pp. 3595-3600.
6. N. Chan and K.E. Evans, J. Mater., 1997, "Fabrication Methods for Auxetic Foams," Sci., 32, pp. 5945-5953.
7. Y. Sugiyana, J. Meyer, M.Y. He, H. Bert-Smith, J.Grenstedt, A.G. Evans, 1997, "On the Mechanical Performance of Closed Cell Al Alloy Foams," Acta Mater. 45, pp. 5245-5259.
8. J. Benhart, J. Baumeister. 1998, "Deformation Characteristics of Metal Foams," J. Material Sci., 33(18-998) 1431-1440.
9. D.J. David, A.P. Phillip and H.N.G. Wadly, June 1998, "Novel Hollow Powder Porous Structure," Porous and Cellular Materials for Structural Applications, Materials Research Society, Warrendate, pp.205-210.

Modeling

SHAPE CONTROL WITH KARHUNEN-LOÈVE-DECOMPOSITION

Weihua Zhang, Bernd Michaelis

ABSTRACT

The Finite Element Method is a powerful method that can be used to describe the dynamic behavior of mechanical systems. The most crucial problem to use this method is the large degree of freedom in FE-models. It is very difficult or even impossible to design controllers. Consequently, it is necessary to reduce the model. However, the model reduction deals only with the state variables, therefore the model reduction is not sufficient for the shape control, because a great number of reference and measured data are needed for the shape description and control.

In this paper, we introduce the Karhunen-Loève-Decomposition to perform the data reduction. In the Karhunen-Loève-Decomposition, we firstly transform the data from the real state space to the Karhunen-Loève state space. In this phase the maximal reduction of the state variables can be achieved. Then, we perform Modal-Decomposition to the reduced system. After these two phases we get a decoupled system and the number of the control loops which should be designed is also minimized.

1 INTRODUCTION

A powerful method, which can be used to describe the dynamic behavior of the mechanical systems, is the Finite Element Method (FEM). The description of mechanical systems with the FEM can be shown as:

$$\begin{aligned} \boldsymbol{M}\ddot{\boldsymbol{X}} + \boldsymbol{D}\dot{\boldsymbol{X}} + \boldsymbol{K}\boldsymbol{X} &= \boldsymbol{F}\boldsymbol{u} \\ \boldsymbol{Y} &= \boldsymbol{C}\boldsymbol{X} \end{aligned} \tag{1}$$

where $\boldsymbol{M}$, $\boldsymbol{D}$ and $\boldsymbol{K}$ are mass, damping and stiffness matrices (n×n) respectively. $\boldsymbol{C}$ is the measurement matrix (m×n), $\boldsymbol{F}$ the control matrix (n×p), $\boldsymbol{X}$ the (n×1) FEM displacement vector, $\boldsymbol{Y}$ the (m×1) measurement vector and $\boldsymbol{u}$ is the (p×1) control force vector. n is the number of degree of freedom (DOF), m is the number of sensors and p is the number of actuators.

Dipl. –Inf. Weihua Zhang and Prof. Dr. –Ing. habil. Bernd Michaelis, IESK Otto-von-Guericke-University Magdeburg, P.O. Box 4120, D-39016 Magdeburg

The most crucial problem to use this method is the large degree of freedom (DOF) in FE-models. It is very difficult or even impossible to design controllers. Consequently, it is necessary to reduce the model. There are many well known methods to reduce a large system [1][2][5]. However, the model reduction deals only with the state variables, therefore the model reduction is not sufficient for the shape control, because a great number of reference and measured data are needed for the shape description and control.

By using the data compression, the great number of reference and measured data are considerably reduced. One way to perform the data reduction is the Modal-Decomposition (MD)[7][8][9]. However, a relatively great number of modal components are still needed in order to achieve high accuracy.

In this paper, we introduce another way, the Karhunen-Loève-Decomposition (KLD), to perform the data reduction. In Section 2 the MD is briefly introduced. The principle of the KLD and how to use it in shape control is introduced in Section 3. The simulation result is given in Section 4.

2 MODAL-DECOMPOSITION

In the MD we define that $\boldsymbol{X}=\boldsymbol{\Phi}\boldsymbol{Q}$ with $\boldsymbol{Q}=[q_1\cdots q_n]^T$ and $\boldsymbol{\Phi}=[\boldsymbol{\varphi}_1\ldots\boldsymbol{\varphi}_n]$, where the superscript T means the matrix transpose, q_i $(i=1,\ldots,n)$ is the so called modal coordinate and $\boldsymbol{\varphi}_i$ $(i=1,\ldots,n)$ the i[th] mode shape calculated by $\boldsymbol{M}^{-1}\boldsymbol{K}\boldsymbol{\varphi}_i=\omega_i^2\boldsymbol{\varphi}_i$ and $\boldsymbol{\Phi}^T\boldsymbol{M}\boldsymbol{\Phi}=\boldsymbol{I}$, $\boldsymbol{\Phi}^T\boldsymbol{D}\boldsymbol{\Phi}=2\zeta_n\omega_n$, $\boldsymbol{\Phi}^T\boldsymbol{K}\boldsymbol{\Phi}=\omega_n^2$, with diagonal matrix $2\zeta_n\omega_n$ and ω_n^2. Then the system (1) can be rewritten as:

$$\begin{aligned}&\boldsymbol{\Phi}^T\boldsymbol{M}\boldsymbol{\Phi}\ddot{\boldsymbol{Q}}+\boldsymbol{\Phi}^T\boldsymbol{D}\boldsymbol{\Phi}\dot{\boldsymbol{Q}}+\boldsymbol{\Phi}^T\boldsymbol{K}\boldsymbol{\Phi}\boldsymbol{Q}=\boldsymbol{\Phi}^T\boldsymbol{F}\boldsymbol{u}\\&\boldsymbol{Y}=\boldsymbol{C}\boldsymbol{\Phi}\boldsymbol{Q}\end{aligned}\qquad(2)$$

This means that the system (1) will be decoupled by the MD. Now we can search a matrix $\boldsymbol{R}$ $(v\times m)$, so that the dominating modal coordinates $\boldsymbol{Q}_v$ with $v < m$ could be approximately calculated from $\boldsymbol{Y}$. There are many methods to determine $\boldsymbol{R}$, the possible ways are given in [7].

Analogically, we can obtain the matrix $\boldsymbol{T}$ for mapping back the modal forces from modal space to real space[8]. After using the MD and MC technique, the system input and the system output are reduced. All single loop controller design methods can be used here. But a relatively great number of modal components are still needed in order to achieve high accuracy.

3 KARHUNEN-LOÈVE-DECOMPOSITION

The Karhunen-Loève transformation was independently developed by Karhunen[3] and Loève[4] during the 1940s for the optimal series expansions of stochastic processes. In the shape control, the control process is not stochastic except of the measurement noise. Therefore, it is firstly necessary to extend the Karhunen-Loève transformation from the stochastic area to the deterministic area.

3.1 Karhunen-Loève-Decomposition for the deterministic processes

Consider any vector $\boldsymbol{p}\in\Re^n$ we can always find many different sets of n orthogonal basis vectors $w_\mu\in\Re^n\ \mu = 1,...,n$, such that

$$\boldsymbol{p}=\sum_{\mu=1}^{n} a_\mu \boldsymbol{w}_\mu = \boldsymbol{W}\boldsymbol{a} \quad \text{and} \quad \boldsymbol{a}=\boldsymbol{W}^T\boldsymbol{p} \tag{3}$$

The task of KLD is now to obtain an orthogonal basis matrix $\boldsymbol{W}$ so that the reconstruction error

$$\varepsilon=(\boldsymbol{p}-\hat{\boldsymbol{p}})^T(\boldsymbol{p}-\hat{\boldsymbol{p}})=\left(\sum_{\mu=1}^{n} a_\mu \boldsymbol{w}_\mu-\sum_{\mu=1}^{v} a_\mu \boldsymbol{w}_\mu\right)^2=\left(\sum_{\mu=1+v}^{n} a_\mu \boldsymbol{w}_\mu\right)^2 \tag{4}$$

and v are as small as possible. By forming a n×s observation matrix $\boldsymbol{P} = [\boldsymbol{p}^1,\boldsymbol{p}^2,...,\boldsymbol{p}^s]$ with s samples we can express Eq. (4) as

$$\varepsilon=\sum_{k=1}^{s}(\boldsymbol{p}^k-\hat{\boldsymbol{p}}^k)^T(\boldsymbol{p}^k-\hat{\boldsymbol{p}}^k)=\sum_{k=1}^{s}\sum_{\mu=1+v}^{n}\boldsymbol{w}_\mu^T a_\mu^k\sum_{\mu=1+v}^{n}a_\mu^k\boldsymbol{w}_\mu=\sum_{k=1}^{s}\sum_{\mu=1+v}^{n}(a_\mu^k)^2=\sum_{\mu=1+v}^{n}\boldsymbol{w}_\mu^T\boldsymbol{C}_p\boldsymbol{w}_\mu \tag{5}$$

Minimize the Eq. (5) using the eigenvalues solutions, we can get the orthogonal basis matrix

$$\boldsymbol{C}_p\boldsymbol{w}_\mu=\lambda_\mu\boldsymbol{w}_\mu \quad \textit{with} \quad \boldsymbol{W}=[\boldsymbol{w}_1\boldsymbol{w}_2...\boldsymbol{w}_n] \tag{6a}$$

and the reconstruction error

$$\varepsilon=\sum_{\mu=1+v}^{n}\lambda_\mu \tag{6b}$$

where $\boldsymbol{C}_p$ is the correlation matrix of data $\boldsymbol{P}$ with $\boldsymbol{C}_p=\boldsymbol{P}\boldsymbol{P}^T$ and $\boldsymbol{W}^T\boldsymbol{W}=\boldsymbol{I}$.

3.2 Karhunen-Loève-Decomposition in Input-Output Space

The simplest way of using the KLD for the shape control is directly to perform the KLD in the input-output space. We assume that we have a set of interesting measured data $\boldsymbol{Y}=[\boldsymbol{Y}_1,\boldsymbol{Y}_2,\cdots,\boldsymbol{Y}_s]$ (m×s). These data may be the reference data and/or the deformation due to the disturbance. These data can be a stationary value and/or a period of dynamical values. Using $\boldsymbol{Y}$ instead of $\boldsymbol{P}$ in Eq. (6), we can get the transformation matrix $\boldsymbol{W}_v=[\boldsymbol{w}_1\boldsymbol{w}_2...\boldsymbol{w}_v]$ with $v < m$ at a given reconstruction error. This way, we have only reduced the system output, but not the system input. It is obviously that we can't simply use the matrix $\boldsymbol{W}_v$ to map back from the forces $\boldsymbol{u}_{kl}$ in Karhunen-Loève space to the forces $\boldsymbol{u}$ in real space. Therefore we need a method to find this map $\boldsymbol{T}$ in order to close the control loop. Assuming that we have a controller of the form $\boldsymbol{G}_R(s)/s$ and the map T, we can get the relationship between the measurement and the reference in the Laplace transfer function form as follows:

$$\begin{aligned}\boldsymbol{Y}(s)&=\boldsymbol{G}(s)\boldsymbol{T}\left[s+\boldsymbol{G}_R(s)\boldsymbol{W}_v^T\boldsymbol{G}(s)\boldsymbol{T}\right]^{-1}\boldsymbol{G}_R(s)\boldsymbol{W}_v^T\boldsymbol{Y}_{ref}(s)\\ \boldsymbol{G}(s)&=\boldsymbol{C}\left[\boldsymbol{M}s^2+\boldsymbol{D}s+\boldsymbol{K}\right]^{-1}\boldsymbol{F}\end{aligned} \tag{7}$$

where the $\boldsymbol{G}(s)$ is the transfer function of the system (1). Now, our goal is to find the map $\boldsymbol{T}$ so that $\boldsymbol{Y}=\boldsymbol{W}_v\boldsymbol{W}_v^T\boldsymbol{Y}_{ref}$ in the stationary state. Using the final value therorem of the Lapace transform, we have

$$\boldsymbol{Y}(\infty)=\boldsymbol{G}(\infty)\boldsymbol{T}\left[\boldsymbol{W}_v^T\boldsymbol{G}(\infty)\boldsymbol{T}\right]^{-1}\boldsymbol{W}_v^T\boldsymbol{Y}_{ref}(\infty) \text{ with } \boldsymbol{G}(\infty)=\boldsymbol{C}\boldsymbol{K}^{-1}\boldsymbol{F} \tag{8}$$

Considering $\boldsymbol{W}^T\boldsymbol{W} = \boldsymbol{I}$, it is clear that $\boldsymbol{T} = \boldsymbol{G}(\infty)^+\boldsymbol{W}_v$,where the superscript + is in sense of the generalized inverse.

In this way, the system (1) can be rewritten as:

$$\begin{aligned} &\boldsymbol{M}\ddot{\boldsymbol{X}} + \boldsymbol{D}\dot{\boldsymbol{X}} + \boldsymbol{K}\boldsymbol{X} = \boldsymbol{F}\boldsymbol{T}\boldsymbol{u}_{kl} \\ &\boldsymbol{a} = \boldsymbol{W}_v^T\boldsymbol{C}\boldsymbol{X} \end{aligned} \tag{9}$$

where $\boldsymbol{u}_{kl}$ is the control force vector in Karhunen-Loève space. Now we have reduced the system input and the system output. But the system (9) is still coupled and the system DOF is not changed. The known model reduction methods[1][2][5], of course, can be used here to reduce the system DOF. However, if we perform the KLD not in input-output space, but in state space, we can reduce the system input/output and the system DOF simultaneously and decouple the system.

3.3 Karhunen-Loève-Decomposition in State Space

Now, we consider to perform the KLD in state space. We assume that we can measure all state variable $\boldsymbol{X}$ in system (1). In other words, the measurement matrix $\boldsymbol{C}$ in the system (1) becomes a $n \times n$ unit matrix. Analogous to section 3.2, we assume again that we have a set of s interesting state variables $\boldsymbol{X} = [\boldsymbol{X}_1, \boldsymbol{X}_2, \cdots, \boldsymbol{X}_s]$. This set of data could be the reference, deformation due to disturbance, stationary and/or a period of dynamical data in the state space. Again, using $\boldsymbol{X}$ instead of $\boldsymbol{P}$ in Eq. (6), we can get the transformation matrix $\boldsymbol{W}_v = [\boldsymbol{w}_1\boldsymbol{w}_2 \ldots \boldsymbol{w}_v]$ with $v < n$ at a given reconstruction error.

Theorem 1: The eigenvalue λ_μ of $\boldsymbol{C}_x$ in Eq. (6a) is zero for $\mu > s$ if Rank($\boldsymbol{X}$) = s and $s < n$.

Proof: we make the singular value decomposition of $\boldsymbol{X}$

$\boldsymbol{X} = \boldsymbol{U}\begin{bmatrix} \boldsymbol{\sigma}_s \\ \boldsymbol{0} \end{bmatrix}\boldsymbol{V}^T$ and rewrite Eq. (6a) as $\begin{bmatrix} \boldsymbol{\sigma}_s^2 & \boldsymbol{0} \\ \boldsymbol{0} & \boldsymbol{0} \end{bmatrix} = \boldsymbol{U}^T\boldsymbol{W}\boldsymbol{\Lambda}\boldsymbol{W}^T\boldsymbol{U}$

where $\boldsymbol{\Lambda} = diag([\lambda_1, \lambda_2, \ldots, \lambda_n])$. It is clear that the $\boldsymbol{\Lambda}$ includes only s no zero values. □

This means that, if we choose $v = s$ the reconstruction error ε will be also zero and

$$\boldsymbol{X} = \boldsymbol{W}_s\boldsymbol{a} \tag{10}$$

Substituting Eq. (10) into system (1) and pre-multiplying the matrix $\boldsymbol{W}_s^T$, the system (1) becomes:

$$\begin{aligned} &\boldsymbol{M}_{kl}\ddot{\boldsymbol{a}} + \boldsymbol{D}_{kl}\dot{\boldsymbol{a}} + \boldsymbol{K}_{kl}\boldsymbol{a} = \boldsymbol{F}_{kl}\boldsymbol{u} \\ &\boldsymbol{Y} = \boldsymbol{C}_{kl}\,\boldsymbol{a} \end{aligned} \tag{11}$$

with $\boldsymbol{M}_{kl} = \boldsymbol{W}_s^T\boldsymbol{M}\boldsymbol{W}_s$, $\boldsymbol{D}_{kl} = \boldsymbol{W}_s^T\boldsymbol{D}\boldsymbol{W}_s$, $\boldsymbol{K}_{kl} = \boldsymbol{W}_s^T\boldsymbol{K}\boldsymbol{W}_s$, $\boldsymbol{F}_{kl} = \boldsymbol{W}_s^T\boldsymbol{F}$, *and* $\boldsymbol{C}_{kl} = \boldsymbol{C}\boldsymbol{W}_s$. In the system (11) the DOF has been reduced from n to s. This reduction could be very large if we are only interested in a few states. In order to close the control loop we only need to find a map $\boldsymbol{R}_{kl}$ that maps the measurement space to the Karhunen-Loève space and a map $\boldsymbol{T}_{kl}$ that maps back from Karhunen-Loève space to the real control space. Considering again $\boldsymbol{W}^T\boldsymbol{W} = \boldsymbol{I}$ and in analogy to section 3.2 with our goal $\boldsymbol{X} = \boldsymbol{W}_s\boldsymbol{W}_s^T\boldsymbol{X}_{ref}$, we can obtain

$$\begin{aligned} &\boldsymbol{M}_{kl}\ddot{\boldsymbol{a}} + \boldsymbol{D}_{kl}\dot{\boldsymbol{a}} + \boldsymbol{K}_{kl}\boldsymbol{a} = \boldsymbol{F}_{kl}\boldsymbol{T}_{kl}\boldsymbol{u}_{kl} \\ &\boldsymbol{R}_{kl}\boldsymbol{C} = \boldsymbol{W}_s^T \quad \text{or} \quad \boldsymbol{R}_{kl} = \boldsymbol{W}_s^T\boldsymbol{C}^+ \\ &\boldsymbol{T}_{kl} = \boldsymbol{G}(\infty)^+\boldsymbol{W}_s \quad \text{with} \quad \boldsymbol{G}(\infty) = \boldsymbol{K}^{-1}\boldsymbol{F} \end{aligned} \tag{12}$$

Now, the system DOF, the system input and the system output n, p and m respectively have been reducded to s. But the system (12) is still coupled. This means that the controller design could be still difficult if s is relatively large. In analogy to the normal mechanical system (system (1)), however, we could make the MD on the system (12) if the conditions of system (12) and system (1) are the same.

Theorem 2: The matrix $\boldsymbol{M}_{kl}$, $\boldsymbol{D}_{kl}$ and $\boldsymbol{K}_{kl}$ are symmetric.

Proof: $\boldsymbol{K}_{kl}^T = (\boldsymbol{W}_s^T \boldsymbol{K} \boldsymbol{W}_s)^T = \boldsymbol{W}_s^T \boldsymbol{K}^T \boldsymbol{W}_s = \boldsymbol{W}_s^T \boldsymbol{K} \boldsymbol{W}_s = \boldsymbol{K}_{kl}$.

In analogy we can proof $\boldsymbol{M}_{kl}$ and $\boldsymbol{D}_{kl}$. □

Now, we can perform the MD to the system (11). We define that $\boldsymbol{a} = \tilde{\boldsymbol{P}} \boldsymbol{Q}_{kl}$ with $\boldsymbol{Q}_{kl} = [q_{kl_1}, q_{kl_2}, ..., q_{kl_s}]^T$ and $\tilde{\boldsymbol{P}} = [\tilde{p}_1 ... \tilde{p}_s]$. Then the system (11) can be rewritten as:

$$\begin{aligned} &\tilde{\boldsymbol{P}}^T \boldsymbol{M}_{kl} \tilde{\boldsymbol{P}} \ddot{\boldsymbol{Q}}_{kl} + \tilde{\boldsymbol{P}}^T \boldsymbol{D}_{kl} \tilde{\boldsymbol{P}} \dot{\boldsymbol{Q}}_{kl} + \tilde{\boldsymbol{P}}^T \boldsymbol{K}_{kl} \tilde{\boldsymbol{P}} \boldsymbol{Q}_{kl} = \tilde{\boldsymbol{P}}^T \boldsymbol{F}_{kl} \boldsymbol{u} \\ &\boldsymbol{Y} = \boldsymbol{C}_{kl} \tilde{\boldsymbol{P}} \boldsymbol{Q}_{kl} \end{aligned} \tag{13}$$

where q_{kl_i} ($i=1,...,s$) can be defined as the modal coordinates in the Karhunen-Loève space. The $\tilde{p}_i$ can be calculated by the solution of the eigenvalue problem of $\boldsymbol{K}_{kl} \tilde{\boldsymbol{p}}_i = \omega_{kl_i}^2 \boldsymbol{M}_{kl} \tilde{\boldsymbol{p}}_i$.

Theorem 3: The eigenvector $\tilde{p}_i$ is orthogonal with respect to the $\boldsymbol{M}_{kl}$ and $\boldsymbol{K}_{kl}$ matrices,

i.e. $\tilde{\boldsymbol{p}}_i^T \boldsymbol{M}_{kl} \tilde{\boldsymbol{p}}_i = m_i$, $\tilde{\boldsymbol{p}}_i^T \boldsymbol{K}_{kl} \tilde{\boldsymbol{p}}_i = k_i$, $\tilde{\boldsymbol{p}}_j^T \boldsymbol{M}_{kl} \tilde{\boldsymbol{p}}_i = 0$ and $\tilde{\boldsymbol{p}}_j^T \boldsymbol{K}_{kl} \tilde{\boldsymbol{p}}_i = 0$ with $i \neq j$.

Proof: Because of the symmetry of the matrices $\boldsymbol{M}_{kl}$ and $\boldsymbol{K}_{kl}$ and analogous to the proof of the orthogonality of eigenvectors for mechanical systems[6], we can prove it.□

Now, we can define the $\boldsymbol{M}_{kl}$ and $\boldsymbol{K}_{kl}$ as the mass and stiffness matrices, the $\tilde{p}_i$ and $\omega_{kl_i}^2 = k_i / m_i$ as eigenmode and eigenfrequency in the Karhunen-Loève space.

In order to obtain the decoupled modal coordinate $\boldsymbol{Q}_{kl}$ from the measured data $\boldsymbol{Y}$ and map back the modal forces to real space we only need to determine the $\boldsymbol{R}$ and $\boldsymbol{T}$ matrices. Comparing Eq. (11), (12) and (13), we can simply get

$$\begin{aligned} &\boldsymbol{u} = \boldsymbol{T} \boldsymbol{u}_{m\,kl} \text{ and } \boldsymbol{T} = \boldsymbol{T}_{kl} \tilde{\boldsymbol{P}} \\ &\boldsymbol{Q}_{kl} = \boldsymbol{R} \boldsymbol{Y} \text{ and } \boldsymbol{R} = \tilde{\boldsymbol{P}}^{-1} \boldsymbol{R}_{kl} \end{aligned} \tag{14a}$$

and Eq. (13) becomes

$$m_i \ddot{q}_{kl_i} + d_i \dot{q}_{kl_i} + k_i q_{kl_i} = k_i u_{mkl_i}, \quad i = 1,..., s \tag{14b}$$

where the $\boldsymbol{u}_{mkl}$ is the modal control forces in Karhunen-Loève space.

The system (14) gives us a reduced system in the DOF (n to s) as well as in the input (p to s) and output (m to s). How large the reduction can be done depends only on our interest. If we are only interested in a few states, this reduction could be quite large. The system (14) also gives us a decoupled system, all design methods for single loop controller can be used here.

3.4 Geometrical Interpretation of the KLD and MD

Considering each DOF as one dimension, the state of the system (1) at given input is a curve in the n-dimensional space. If the system input is equal to $\boldsymbol{F}^+ \boldsymbol{M} \boldsymbol{\varphi}_i \sin(\omega_i t)$, then the trace of the system state variables is the axis of the modal coordinates q_i. The basis matrix $\boldsymbol{W}$ in KLD represents the direction of the samples in the n-dimensional space. If the number of samples is one, the $\boldsymbol{w}_1$ is equal to the direction cosine of this sample. If the number of samples

is two and the second sample does not lie on the line constructed by first sample and the original, the w_1 and w_2 represent the plane constructed by the original point, the sample 1 and

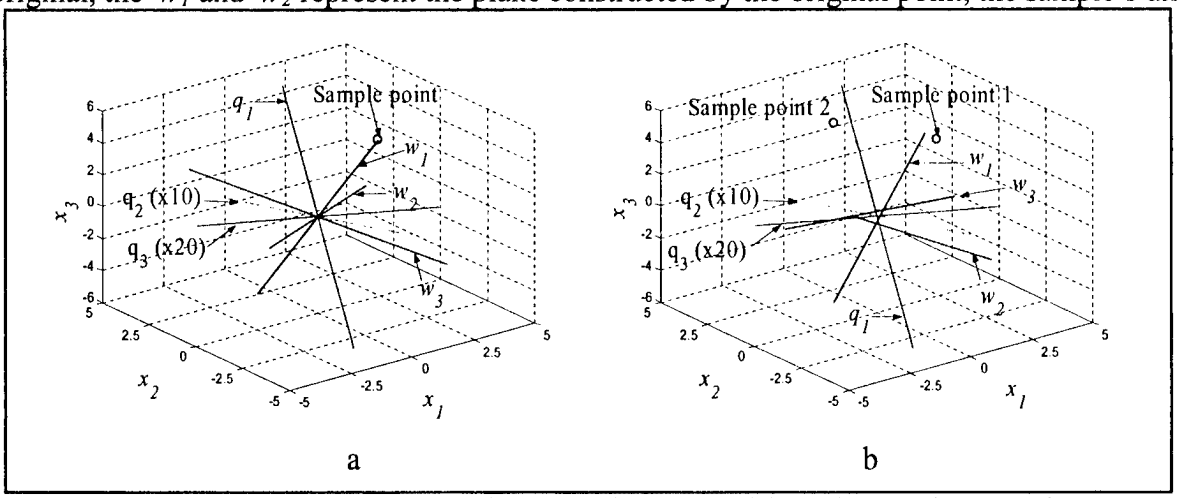


Figure 1: Geometrical interpretation of the KLD and MD. a) modal coordinate and one sample KLD basis matrix; b) modal coordinate and two samples KLD basis matrix

the sample 2 and the w_3 is the normal of this plane. In addition the projection of the samples on the w_1 is always larger than those on the w_2. The figure 1 shows the modal coordinate and KLD basis matrix W with one sample as well as two samples. This was calculated from following simple system[6]

$$\begin{bmatrix} 2 & & \\ & 1 & \\ & & 1 \end{bmatrix}\begin{bmatrix} \ddot{x}_1 \\ \ddot{x}_2 \\ \ddot{x}_3 \end{bmatrix}+\begin{bmatrix} 2.3 & -0.7 & \\ -0.7 & 1.5 & -0.7 \\ & -0.7 & 0.8 \end{bmatrix}\begin{bmatrix} \dot{x}_1 \\ \dot{x}_2 \\ \dot{x}_3 \end{bmatrix}+\begin{bmatrix} 3 & -1 & \\ -1 & 2 & -1 \\ & -1 & 1 \end{bmatrix}\begin{bmatrix} x_1 \\ x_2 \\ x_3 \end{bmatrix}=\begin{bmatrix} 2 & & \\ & 5 & \\ & & 3 \end{bmatrix}\begin{bmatrix} u_1 \\ u_2 \\ u_3 \end{bmatrix}$$

and the two samples are $[4,2,2]^T$ and $[0.94925,1.7471,2.3410]^T$. The choice of the system and samples is free.

It is shown that the modal coordinates are dependent only on the structure property of the system. If our control goal lies on or near on the q_1 axis, for example, we could use only the q_1 to describe the system. If it is not, we must use many q's to describe the system. The KLD basis matrix, however, is not dependent on the structure property of the system, but on our control goal. There are different basis matrix for the different sets of control goals (samples). The basis matrix is constructed in such way that the projection of the samples on w_{i+1} is always smaller than those on the w_i. This is why we can always use a small set of W to represent a complex system. It is also shown that every basis vector in KLD can be described by a linear combination of the modal coordinates.

4 SIMULATION RESULT

The simulation object is a (one dimensional) parabolic beam (360×25×2.2 mm) composed of carbon fiber composite material [Fig.2]. The beam is fixed on x = 0. In its basic form, the parabolic beam has a focal length (line) with 500 mm. The goal of the control is to change the focal length of the parabolic beam from 500 mm to 475 mm and/or to 525 mm. Each given focal length establishes a reference shape of control. Five 25×25×0.2 (l×w×t) mm piezoceramic patches are used as actuators and 5 strain gauges as sensors. The material constants of the carbon fiber composite material as well as the piezoceramic patches are listed in Table I.

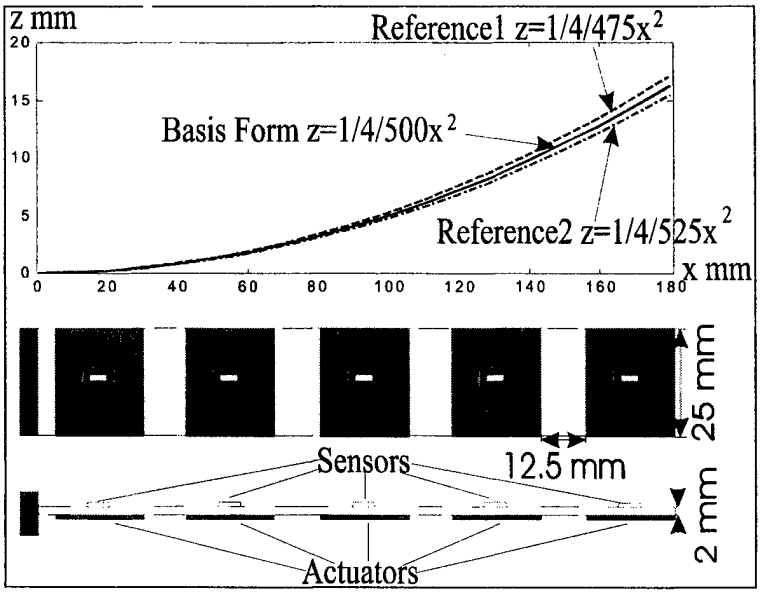


Figure 2: The set up of the simulation

TABLE I: MATERIAL CONSTANTS OF CARBON FIBER COMPOSITE AND PIEZOCERAMIC

Carbon fiber Composite:			
E-Mod.(N/m^2):			
E_{11}, E_{22}	4.76×10^{10}	E_{33}	1.11×10^{10}
G_{13},G_{23}	3.56×10^{9}	G_{12}	1.88×10^{10}
Poisson's ratioo:			
μ_{12}, μ_{23}	0.483	μ_{12}	0.241
Density ρ (g/cm^3): 1.542			
Piezoceramic:			
Elastic: (N/m^2)			
c_{11}	1.076×10^{11}	c_{33}	1.004×10^{11}
c_{12}	6.312×10^{10}	c_{44}	1.962×10^{10}
c_{13}	6.385×10^{10}	c_{66}	2.224×10^{10}
Piezoelectric:(N/Vm)			
e_{15}	12.0	e_{31}	-9.6
e_{33}	15.1		
Dielectric: (C/Vm)			
κ_{11}	1.98×10^{-9}	κ_{33}	2.10×10^{-9}
Density ρ (g/cm^3): 7.8			

Only a half of the system is considered in our simulation because of the symmetry and a FEM model with 396 DOFs, 5 system inputs and 5 system outputs is created.

According to the FEM model and given two reference shapes we can calculate the reference coordinates in the state space. These reference values are used as the samples. Using Eq. (6) and (10) we can get the system (11) as follows:

$$\begin{bmatrix} 1.2\times10^{-7} & 1.7\times10^{-9} \\ 1.7\times10^{-9} & 1.3\times10^{-7} \end{bmatrix}\begin{bmatrix} \ddot{a}_1 \\ \ddot{a}_2 \end{bmatrix} + \begin{bmatrix} 4.5\times10^{-5} & -2.6\times10^{-3} \\ -2.6\times10^{-3} & 5.6\times10^{-1} \end{bmatrix}\begin{bmatrix} \dot{a}_1 \\ \dot{a}_2 \end{bmatrix} + \begin{bmatrix} 0.11 & -6.5 \\ -6.5 & 1.4\times10^{3} \end{bmatrix}\begin{bmatrix} a_1 \\ a_2 \end{bmatrix} = \boldsymbol{F}_{kl}\boldsymbol{u}$$

$$\boldsymbol{Y} = \boldsymbol{C}_{kl}\begin{bmatrix} a_1 \\ a_2 \end{bmatrix}$$

After this step the system DOF is rapidly reduced from 396 to 2, because only two reference shapes are interesting. It is shown that the system is still coupled. Now we can use the theory 2 and 3 to decouple the system and obtain:

$$\begin{bmatrix} \ddot{q}_{kl1} \\ \ddot{q}_{kl2} \end{bmatrix} + \begin{bmatrix} 2.8\times10^{2} & \\ & 4.3\times10^{6} \end{bmatrix}\begin{bmatrix} \dot{q}_{kl1} \\ \dot{q}_{kl2} \end{bmatrix} + \begin{bmatrix} 6.9\times10^{5} & \\ & 1.1\times10^{10} \end{bmatrix}\begin{bmatrix} q_{kl1} \\ q_{kl2} \end{bmatrix} = \begin{bmatrix} 6.9\times10^{5} & \\ & 1.1\times10^{10} \end{bmatrix}\begin{bmatrix} u_{mkl1} \\ u_{mkl2} \end{bmatrix}$$

Up to now, the system input and output are also reduced to 2 and we have a decoupled 2×2 system. All design methods for single loop controller can be used to design controller according this system. Here, PID controller is used. Figure 3 shows the dynamic and static response of the system for reference 1. Table II gives the system accuracy with and without PID control. In the case of the no feedback control, expected control forces are given.

It is clear that the control case is better than the case without control. It is noted that the control algorithm can not increase the accuracy largely. If the higher accuracy is wanted, a) the sensor and actuator placement should be optimized and b) the number of actuators should be increased.

TABLE II: THE SYSTEM ACCURACY WITH AND WITHOUT PID CONTROL

	without	with
$\lvert f_r-f_m\rvert$ (mm)	0.86	0.76
$\sigma(f_r-f_m)$ (mm)	2.56	0.91

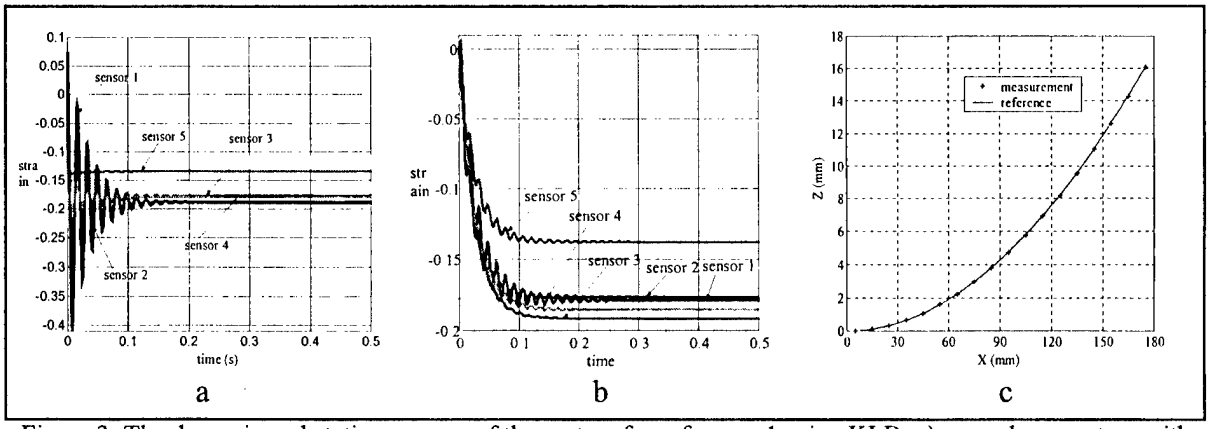


Figure 3: The dynamic and static response of the system for reference 1 using KLD. a): open loop system with expected control forces; b) closed loop system designed by KLD; c) the stationary values after KLD control

5 CONCLUSION

A new method using the KLD to realize the shape control is developed. Using the KLD the system DOF, system input and system output can be simultaneously reduced. This reduction is only dependent on the interest of the user and the reduction ratio may be very high. The reduced system is also decoupled, this simplifies the controller design. The simulation demonstrates the capability of this method.

ACKNOWLEDGMENTS

The work presented in this paper is supported by the project ADAMES of the Deutsche Forschungsgemeinschaft (DFG) and the Federal State of Sachsen-Anhalt.

REFERENCES

1. Gawronski,W. and Juang,J.N.: Model Reduction for Flexible Structures, in Control and Dynamic System, Vol.36, Ed. Leondes, C.T.,pp143-222.
2. Hu, A and Skelton, R: Model Reduction with Weighted Modal Cost Analysis, AIAA GNC Conference, Portland, Oregon, August 1990,pp295-303.
3. Karhunen, K.: Zur Spektraltheorie stochastischer Prozesse, Ann. Acad. Sci. Fenn., 34, 1946.
4. Loève, M.: Fonctions alèatoires du second ordre, In P. Lèvy, editor, Suppl. To Processus Stochastique et mouvement Brownien, Gauthier-Villars, Paris, 1948.
5. O'Callahan, Comparison of Reduced Model Concepts, Eighth International Modal Analysis Conference, Orlando, Florida, January 1990, pp422-430.
6. Thomson, William T: Theory of Vibration with Applications, 4th Edition, Chapman & Hall, London.
7. Zhang, W.; Lilienblum, T.; Michaelis, B.: Sensorfusion und Datenverdichtung für adaptive mechanische Systeme, 3th Magdebuger Maschinenbau-Tage, Sept. 11-13, 1997, Vol. 2, pp. 213-222.
8. Zhang, W.; Lilienblum, T.; Michaelis, B.: Data Compression for Control of Adaptive Mechanical Systems, Gabbert, U. (Hrsg.), VDI Fortschritt-Berichte, Reihe 11: Schwingungstechnik Nr. 268, Düsseldorf: VDI-Verlag 1998, pp. 323-332.
9. Zhang, W. and Michaelis, B.: Data Acquisition and Compression in Adaptive Mechanical Systems, IMTC/98 Instrument and Measurement Technology Conference, Minnesota, USA, May, 1998, pp. 1110-1115.

EXPERIMENTAL FLUTTER CONTROL OF A CANTILEVERED PLATE USING PIEZOELECTRIC ACTUATION AND MODERN CONTROL THEORY

Jae-Hung Han, Jong-Heung Park, Junji Tani, Jinhao Qiu, In Lee

ABSTRACT

This paper focuses on the experimental active flutter suppression of a cantilevered plate using piezoelectric actuation and modern control theory. Integration of a finite element method, a panel aerodynamic method, and the minimum state space realization yields the state space equation of motion for a fluttering plate. Distributed piezoelectric actuators are grouped into two equivalent actuators such that the controllability of the system is maximized. A series of controllers are designed based on modern control framework, and the flutter suppression performance is evaluated via the wind tunnel testing. Among the designed controllers, μ - synthesized controller shows the improved behavior over a wide flow speed range.

INTRODUCTION

Most aeroelastic phenomena have undesirable features: yielding stability margin reduction, performance degradation, and even sometimes, catastrophic structural failure. Therefore, there have been intensive efforts to understand aeroelastic behavior more accurately in order to avoid serious aeroelastic problems. As more lightweight materials are adopted in aerospace structures for energy efficiency, we have more chances to encounter various aeroelastic problems. In recent years, applications of active control to aeroelastic systems have been studied in order to favorably modify the behavior of aeroelastic systems.

One of the main objectives of the aeroelastic control is flutter suppression. Typically, control surfaces such as spoilers and flaps have been used to generate auxiliary aerodynamic lift and moment. The active flexible wing (AFW) program has demonstrated flutter suppression of a fighter-type scaled model in various maneuver modes by utilizing control surfaces and active control technology at NASA Langley research center [1]. The Benchmark Active Control Technology (BACT) model has been used as an active control test bed for evaluating new and innovative control methodologies [2]. Vipperman *et al.* [3] developed a wind tunnel model of a typical section airfoil with a trailing edge-flap and applied H_2– and μ–synthesized controls for

[1] Jae-Hung Han, Jong-Heung Park, Electronics and Telecommunications Research Institute, 161 Kajong-dong, Yusong-gu, Taejon, Korea.
[2] Junji Tani, Jinhao Qiu, Institute of Fluid Science, Tohoku University, Katahira 2-1-1, Sendai, Japan.
[3] In Lee, Dept. of Aerospace Engineering, Korea Advanced Institute of Science and Technology, Science Town, Taejon, Korea.

active flutter suppression. They reported that μ–synthesized control provided significantly better disturbance rejection than H_2 controller, particularly when the aeroelastic pole migration is dominant. Block and Strganac [4] constructed a unique test apparatus that makes experiments of plunge and pitch motion possible with prescribed stiffness characteristics. They investigated linear and nonlinear aeroelastic responses and controlled flutter phenomena using an optimal observer and full-state feedback.

Recent development of smart and/or intelligent structures gives us another alternative for active flutter suppression [5]. Among several functional materials, piezoelectric materials have drawn attention as possible actuation mechanisms for flutter prevention systems because of their simple structure and fast response time [6]. Lazarus *et al.* [7] successfully applied multi-input multi-output controls to suppress vibration and flutter of a plate-like lifting surface with surface-bonded piezoelectric actuators. Application of piezoelectric actuation to flutter control of a more realistic wing model was achieved under the piezoceramic aeroelastic response tailoring investigation (PARTI) program at NASA Langley research center [8]. Active flutter controls of wing-boxes and panels have also been investigated using piezoelectric strain actuators.

This paper investigates active flutter suppression of a swept-back cantilevered plate using piezoelectric actuation. The present work is based on the study by Lazarus *et al.* [7]; the main improvements lie in the actuator placement and the application of modern robust control theory. The aeroelastic model of the plate is determined in the state space equation form using a finite element method, a panel aerodynamic method, and a rational function approximation. The resulting state space aeroelastic equations enable us to efficiently analyze the system behavior and design controllers with a modern control framework. We also studied the problem of actuator placement. Only a few studies have been performed on the actuator location and selection for flutter suppression [9,10]. In this study, piezoelectric actuators, bonded symmetrically on the plate, are optimally grouped into two equivalent actuator sets using genetic algorithms to enhance controllability. H_2– and μ–synthesized control laws are designed and the effectiveness of the flutter suppression system is evaluated via wind tunnel testing. The preparation of the specimen and the experimental procedures are described. In the μ–synthesis design, a simple parametric uncertainty model is used to take into account the system changes with respect to airflow speed. Finally, the experimental results are provided and the performances of the two control methods are compared.

SYSTEM DESCRIPTION

The test article is a swept-back cantilevered plate with symmetrically surface-bonded piezoelectric actuators as shown in Figure 1. The base plate is made of A1080 aluminum (E = 68.6 Gpa, G = 25.5 Gpa, ρ = 2700 Kg/m^3) and the thickness of the plate is 0.45 mm. The swept-back configuration provides bending-torsion coupling of the structure so that the flutter speed can be lowered enough within wind tunnel operating speeds. Eighteen piezoceramics (Fuji Ceramics® C-91; E = 59 Gpa, G = 21.5Gpa, ρ = 7750 Kg/m^3, d = -330×10^{-12} m/V, thickness: 0.2 mm) are bonded on each surface of the base plate. The base plate is used as common electrical ground and very thin electric wires are connected to each actuator patch. Each electric line is also connected to a switch box in such a way that multiple actuators can be commanded by a single control signal. The wind tunnel testing was performed in the low-turbulence wind tunnel at the Institute of Fluid Science, Tohoku University in Japan. The wind tunnel is a closed-circuit tunnel with an effective velocity range of 5 to 70 m/sec. Both open and closed test sections are available, and in this study,

the open section was chosen to provoke aerodynamic disturbances. Two long-range laser displacement sensors (Keyence® LB-300) are used to measure the displacements of the plate. The sensing points are denoted in Figure 1. The effective range of sensors is 200 – 400 mm and they are located at 300 mm from the plate. The influence of the sensors on the airflow can be negligible. All control designs were implemented on a DSP board (dSPACE® DS1102). The DSP board has a Texas Instrument® TMS320C30 DSP chip as the main processor, and is equipped with 4 analog-to-digital and 4 digital-to-analog conversion channels. The sampling frequency used is 2 kHz, which is high enough compared with the dominant frequency band of the aeroelastic system. An FFT analyzer (Onosokki® CF-3400) was used to record and process sensor and control signals. Figure 2 shows the overall experimental setup.

NUMERICAL MODEL

Controller design for flutter suppression needs an accurate numerical model. Fortunately, numerical procedures for an aeroelastic model of a cantilevered plate in the subsonic flow are well established. In this paper, the aeroelastic model of the test article is determined in the state space equation form using a finite element method, a panel aerodynamic method, and a rational function approximation. By applying the finite element procedure by Han and Lee [11], the equation of motion for the swept-back cantilevered plate with distributed actuators can be obtained as follows:

$$[\underline{M}]\{\ddot{\eta}\}+[\underline{D}]\{\dot{\eta}\}+[\underline{K}]\{\eta\}=\sum_{L=1}^{M}\{\underline{F}_L\}V_L(t) \tag{1}$$

where $[\underline{M}]$, $[\underline{D}]$ and $[\underline{K}]$ are the generalized mass, damping, stiffness matrices, respectively; $\{\eta\}$ and $V_L(t)$ are the modal coordinate and the applied voltage to the Lth actuator. Actuation characteristics of piezoelectric actuators in modal domain are specified by $\{\underline{F}_L\}$ and modal sensing characteristics can be obtained from the sensitivity of the laser displacement sensors and mode shapes at the sensing points.

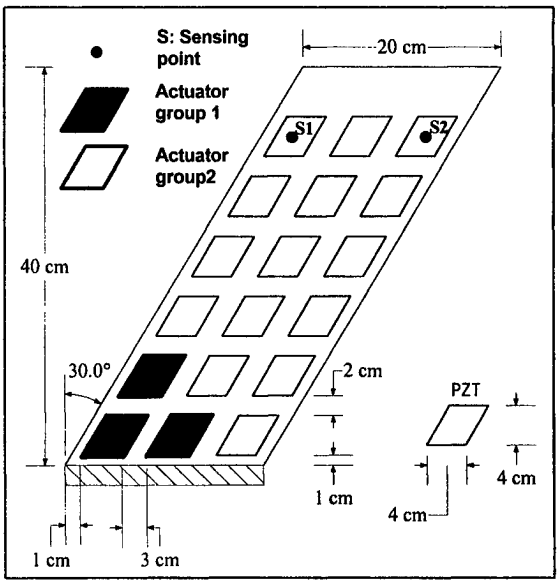


Figure 1. Configuration of the test model.

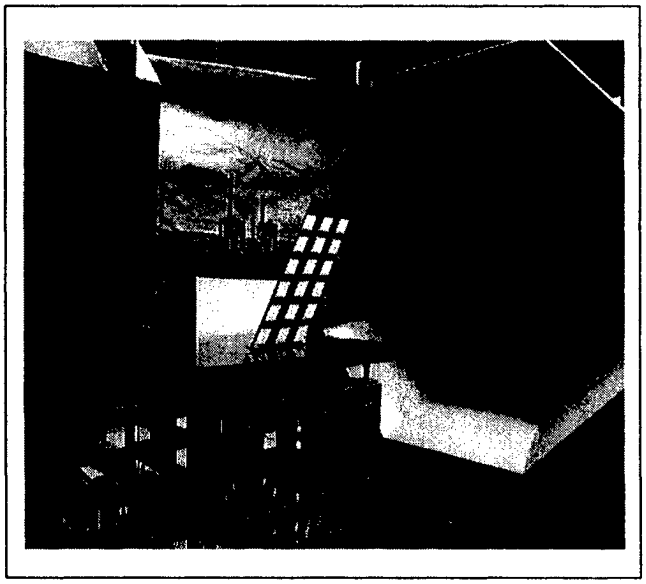


Figure 2. Wind tunnel test setup.

The linear relationship between the generalized aerodynamic force and the modal displacement is obtained from a doublet lattice method [12] as follows:

$$\{\underline{F}\} = q[\underline{Q}(k,M)]\{\eta\} \tag{2}$$

where q, k, and M are the dynamic pressure, the reduced frequency, and the Mach number, respectively. The aerodynamic influence coefficient $[\underline{Q}(k,M)]$ is a complex function of reduced frequency and flight condition. For a given Mach number and air density, $[\underline{Q}(k,M)]$ is calculated at several discrete reduced frequencies rather than as a continuous function of the circular frequency ω. Therefore, the aerodynamic influence coefficient matrices should be approximated as a rational function so that modern control theories are readily applicable to a resulting aeroelastic system. The minimum state method [13] approximates $[\underline{Q}(k,M)]$ by

$$[\underline{\tilde{Q}}(p)] = [A_0] + [A_1]p + [A_2]p^2 + [D]\left(p[I] - [R]\right)^{-1}[E]p \tag{3}$$

where p is the nondimensional Laplace variable given as $p = sb/V$. Here b and V are the reference length and the free stream velocity, respectively. $[R]$ is a diagonal matrix of which diagonal terms are distinct aerodynamic poles. The overall approximation procedure mainly consists of two parts: a root finding problem and a determination of other unknown matrices. The details are referred to [13]. Introducing the approximated aerodynamic force into Equation (1) yields a state space equation of the aeroelastic system.

$$\{\dot{x}\} = [A]\{x\} + [B]\{u\} \tag{4}$$

where the state vector $\{x\}$ consists of the modal displacement $\{\eta\}$, the modal velocity $\{\dot{\eta}\}$, and the augmented aerodynamic states $\{x_a\}$; the control input $\{u\}$ is the applied voltages to the piezoelectric actuators. Note that the number of the aerodynamic states equals to the number of aerodynamic poles. System matrix $[A]$ includes all aerodynamic effects such as apparent mass, aerodynamic damping and stiffness as well as structural mass, damping and stiffness.

ACTUATOR PLACEMENT AND CONTROLLER DESIGN

A series of numerical models have been obtained by using the procedures described above. We found that 10 structural states (5 modes) and 3 aerodynamic states were sufficient to represent the plant dynamics over the interesting flow range. The calculated flutter speed is 16.6 m/sec: whereas the experimental flutter speed is 17.1 m/sec. The flow speed that caused very large dynamic amplitude was chosen as the experimental flutter speed. Therefore, the nonlinear effects were dominant around the experimental flutter speed. The calculated and experimental flutter frequencies were 8.2 and 7.2 Hz, respectively. Using this numerical model, an optimal grouping of the piezoelectric actuators is sought by using genetic algorithms [14].

Flutter suppression problem can be viewed as a disturbance rejection problem as shown in Figure 3. We grouped 18 actuators into two equivalent actuator sets by common electrodes. The objective function for the actuator placement is based on the Hankel singular value (HSV) analysis

of P_{11} and P_{22}. Assuming the disturbance w as a white noise, we obtained the Hankel singular value $\bar{\gamma}_i$ and the corresponding principal direction $\bar{v}_i$ of the transfer matrix P_{11}. The transfer function matrix P_{22} is dependent upon the actuator patterns. For each candidate patterns, we calculated the Hankel singular value γ_i and the corresponding principal direction v_i of the transfer matrix P_{22}. The objective for the optimization was defined as

$$J = \sum_i \sum_j \bar{\gamma}_i^2 \bar{\gamma}_j^2 \left| \bar{v}_i^* v_j \right| \tag{5}$$

where * denotes the complex conjugate operator. By proper genetic operations, we found the optimal patterns as shown in Figure 1.

After obtaining the optimal actuator pattern, the controllers for the flutter suppression were designed using H_2 and μ-synthesis approaches. Since H_2 design follows standard LQG design methods, the explanation for the design procedures is omitted here. The block interconnection of the whole system for the μ-synthesis design is shown in Figure 4. The nominal open loop plant (Plant) is augmented by multiplicative uncertainty (ΔPlant), multiplicative weighting function (W_del), sensor noise weighting (W_noise), disturbance weighting (W_dist), control effort weighting (W_act), and performance weighting (W_perf). In addition, parametric uncertainty of the system is included to take into account the movement of the dominant pole. Since the damping value varies significantly without the frequency change near the flutter point, system matrix was transformed to bi-diagonal form and only the damping term was treated as parametric uncertainty. The nominal plant model is taken at the 16.5 m/sec, which is fairly close to the flutter point. By combining the uncertainty blocks, we can obtain augmented uncertainty structure.

The goal of μ-synthesis is to find the stable controller K that minimizes the peak μ value of the closed loop transfer function $F_L(P_{aug}, K)$:

$$\min_K \max_\omega \mu_\Delta (F_L(P_{aug}, K)) \tag{6}$$

The D-K iteration control design technique is generally used to solve the equation (6). The details can be referred to reference [15].

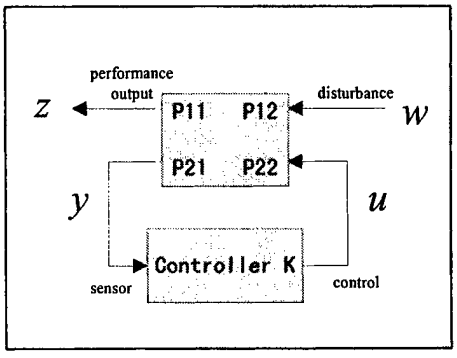


Figure 3. A disturbance rejection problem.

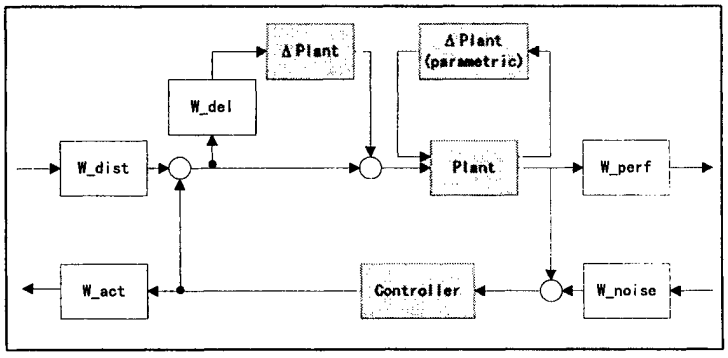


Figure 4. Interconnection of the system.

RESULTS AND DISCUSSION

Figure 5 shows representative flutter suppression results, where the power spectra of the sensor 1 signals are presented for both controlled and uncontrolled cases. At the flow velocity of 17 m/sec, which is slightly lower than the open loop flutter speed, both controllers successfully suppress fluttering vibrations. We can see couples of large peaks in the open loop response, which is two- or three- times harmonics of the flutter mode due to structural non-linearity. Suppression of flutter mode made these harmonics disappear. In contrast, two vibration modes are dominant at the flow velocity of 10 m/sec, which is quite below from the flutter speed. Application of H_2 controller induced another unstable mode. However, the μ-controller shows improved behavior at this speed. In addition, experimental flutter speed can be increased up to 18.8 m/sec using H_2 control, and up to 19.0 m/sec using μ-synthesized control. The μ-synthesized control not only shows better performance over a wide speed range, but also yields higher flutter speed.

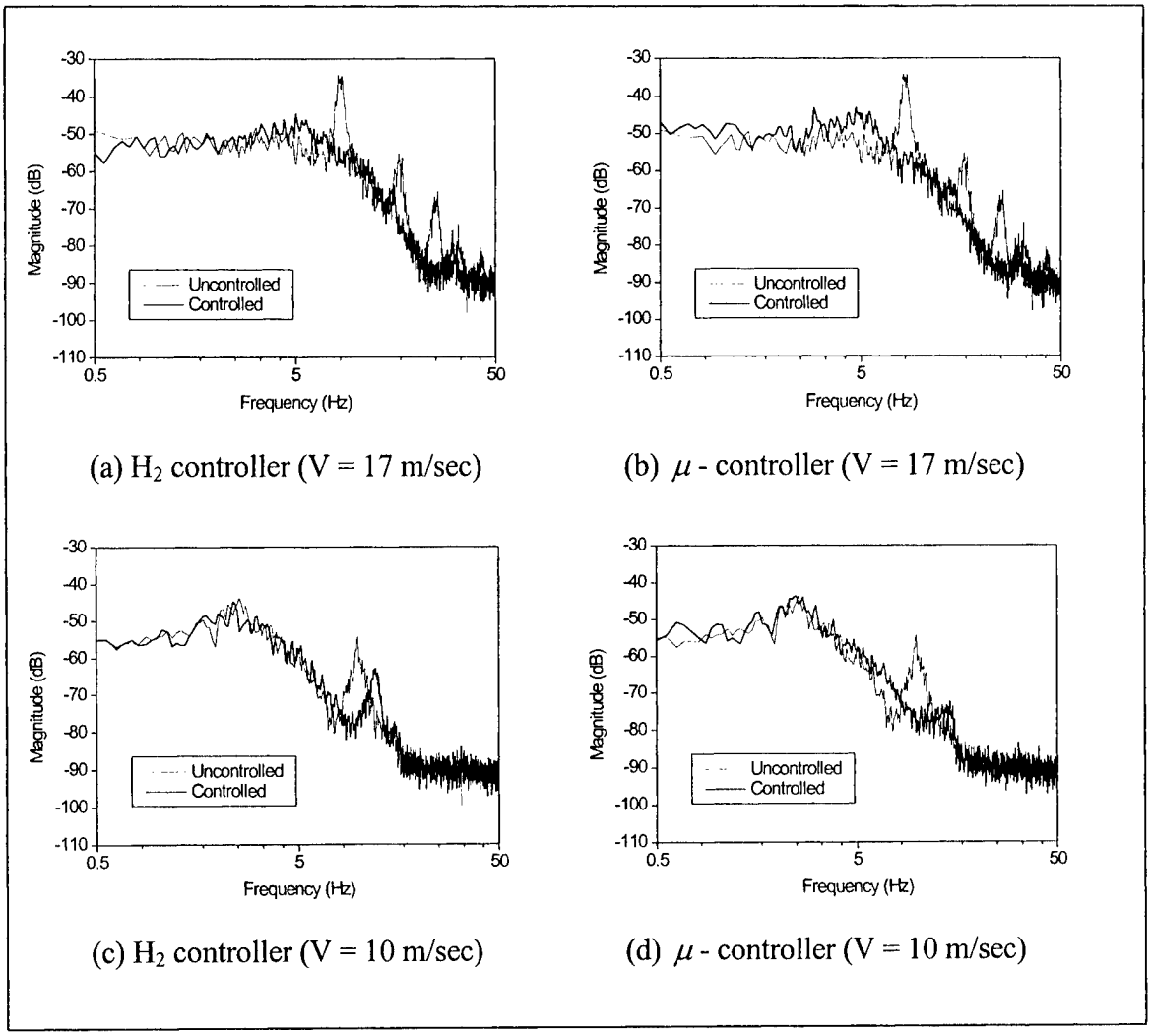


Figure 5. Experimental flutter suppression results.

CONCLUSIONS

This paper investigates active flutter suppression of a swept-back cantilevered plate using piezoelectric actuation and modern control theory. A finite element method, a panel aerodynamic method, and the minimum state space realization are utilized in the development of the equation of motion in state space form. The resulting state space equation is efficiently used for the analysis of the system and design of control laws with a modern control framework. Piezoelectric actuators, bonded symmetrically on the plate, are optimally grouped into two equivalent actuator sets using genetic algorithms to enhance controllability. H_2 and μ-synthesized control laws are designed and the flutter suppression performance is evaluated via the wind tunnel testing. In the μ synthesis design, a simple parametric uncertainty model is used to take into account the system changes with respect to varying airflow speed. The μ- synthesized controller shows improved behavior over a wide flow speed range. In order to further enhance the control performances, more effective torsional actuation mechanisms or actuators are requested.

REFERENCES

1. Waszak, M. R. and S. Srinathkumar. 1995. "Flutter Suppression for the Active Flexible Wing: A Classical Approach," *Journal of Aircraft*, 32 (1), pp. 61-67.
2. Waszak, M. R. June 1998. *Modeling the Benchmark Active Control Technology Wind-Tunnel Model for Active Control Design Applications.* NASA TP-1998-206270.
3. Vipperman, J. S., J. M. Barker, R. L. Clark, and G. J. Balas. 1999. "Comparison of μ- and H_2-Synthesis Controllers on Experimental Typical Section," *Journal of Guidance, Control, and Dynamics*, 22 (2), pp. 278-285.
4. Block, J. J. and T. W. Strganac. 1998. "Applied Active Control for a Nonlinear Aeroelastic Structure," *Journal of Guidance, Control, and Dynamics*, 21 (6), pp. 838-845.
5. Loewy, R. G. 1997. "Recent Developments in Smart Structures with Aeronautical Applications," *Smart Materials and Structures*, 6, pp. R11-R42.
6. Crawley, E. F. and J. de Luis. 1987. "Use of Piezoelectric Actuators as Elements of Intelligent Structures," *AIAA Journal*, 25 (10), pp. 1373-1385.
7. Lazarus, K. B., E. F. Crawley, and C. Y. Lin. 1997. "Multivariable Active Lifting Surface Control Using Strain Actuation: Analytical and Experimental Results," *Journal of Aircraft*, 34 (3), pp. 313-321.
8. Heeg, J. March 1993. *Analytical and Experimental Investigation on Flutter Suppression by Piezoelectric Actuation.* NASA TP-3241.
9. Nam, C., Y. Kim, and T. W. Weisshaar. 1996. "Optimal Sizing and Placement of Piezo-Actuators for Active Flutter Suppression," *Smart Materials and Structures*, 5, pp. 216-224.
10. Lim, K. B., R. C. Lake, and J. Heeg. 1998. "Effective Selection of Piezoceramic Actuators for an Experimental Flexible Wing," *Journal of Guidance, Control, and Dynamics*, 21 (5), pp. 704-709.
11. Han, J.-H. and I. Lee. 1998. "Analysis of Composite Plates with Piezoelectric Actuators for Vibration Control Using Layerwise Displacement Theory," *Composite Part B : Engineering*, 29 (5), pp. 621-632.
12. Albano, E. and W. P. Rodden. 1969. "A Doublet-Lattice Method for Calculating Lifting Disturbances in Subsonic Flow," *AIAA Journal*, 2 (2), pp. 279-285.
13. Karpel, M. and S. T. Hoadley. 1991. *Physically Weighted Approximations of Unsteady Aerodynamic Forces Using the Minimum-State Method.* NASA TP-3025.
14. Han J.-H. and I. Lee. 1999. "Optimal Placement of Piezoelectric Sensors and Actuators for Vibration Control of a Composite Plate Using Genetic Algorithms," *Smart Materials and Structures*, 8 (2), pp. 257-267.
15. Balas, G. J. *et al.* 1993. *μ Analysis and Synthesis Toolbox*, The Mathworks, Inc.

ROBUST FAULT DETECTION FOR SMART STRUCTURE CONTROL SYSTEMS

Hiroshi Okubo,[1] Yuki Tai,[2] Eiichi Muramatsu,[3] Hiroshi Tokutake[4]

ABSTRACT

The design models of highly flexible smart structures contain significant uncertainties due to model parameter errors and reduced-order modeling of the dynamics. Therefore, the design of model-based fault diagnosis should meet the requirements that the designed FDI(Failure Detection and Isolation) method has sufficient robustness with respect to such model uncertainties. This paper proposes a robust detection algorithm that is insensitive to the residual modes while it is highly sensitive to the component failure. It takes advantage of redundant sensors and suppresses errors due to residual modes by linear combinations of sensor outputs. The capability of the robust detection algorithm is demonstrated by a numerical simulation for a flexible smart beam.

INTRODUCTION

The use of lightweight, compact deployable system for the large space structure (LSS) leads to the difficulties that they are very flexible and structural vibration are easily excited due to disturbances in the space environment. Therefore, the concept of adaptive structures or active vibration control of LSS with sensors and actuators has received a great deal of attention in the last decades. Structures that have high degrees of freedom and a lot of imbedded sensors and actuators for e.g. vibration control are called smart structures. Since smart structures consists of many components, the possibility of failure is increased. Therefore, applications of model-based fault detection and isolation (FDI) techniques using analytical redundancies have been studied for such active control systems, where the failures are assumed to occur in the sensors and actuators. The design models of flexible space structures contain significant uncertainties due to model parame-

[1]H. Okubo, Osaka Prefecture University, 1-1 Gakuen-cho, Sakai, Osaka 599-8531, Japan
[2]Y. Tai, Graduate student, Osaka Prefecture University
[3]E. Muramatsu, Osaka Prefecture University
[4]H. Tokutake, Osaka Prefecture University

ter errors and reduced-order modeling of dynamics. Therefore, the design of model-based fault diagnosis should meet the requirements that the designed FDI method has sufficient robustness, where it is insensitive to disturbances while being highly sensitive to sensor and actuator faults. The robustness issues in model-based fault detection and fault isolation have received considerable attention in recent years. Since the outputs errors due to the reduced-order modeling and parameter uncertainty disturb the actual failure signals in sensors and actuators, it is difficult to detect the failure signals in the outputs errors if the magnitude of such disturbances is large. Such difficulties are likely to occur especially in highly flexible space structures having many vibration modes. Therefore it is needed to develop an effective FDI method that is robust to such system uncertainties.

MODEL OF UNCERTAIN SYSTEM AND FAULTS

When the plant dynamics are uncertain, the model used for estimation is imprecise and the residual signals for failure detection includes errors due to the uncertainty and are nonzero even for normal system operation without failure. The structure of an uncertain dynamic system including parameter variations, unmodeled higher order dynamics, disturbance input, observation errors, and possible failure in actuators or sensors can be expressed in liner state space form as :

$$\dot{\boldsymbol{x}}(t) = \begin{bmatrix} \dot{\boldsymbol{x}}_0(t) \\ \dot{\boldsymbol{x}}_r(t) \end{bmatrix} = \begin{bmatrix} \boldsymbol{A}_0 + \Delta\boldsymbol{A} & \boldsymbol{A}_{u1} \\ \boldsymbol{A}_{u2} & \boldsymbol{A}_r \end{bmatrix} \begin{bmatrix} \boldsymbol{x}_0(t) \\ \boldsymbol{x}_r(t) \end{bmatrix} + \begin{bmatrix} \boldsymbol{B}_0 + \Delta\boldsymbol{B} \\ \boldsymbol{B}_r \end{bmatrix} \boldsymbol{u}(t) + \begin{bmatrix} \boldsymbol{G}_0 \\ \boldsymbol{G}_r \end{bmatrix} \boldsymbol{w}(t) + \boldsymbol{f}_a(t) \tag{1}$$

$$\boldsymbol{y}(t) = \begin{bmatrix} \boldsymbol{C}_0 + \Delta\boldsymbol{C} & \boldsymbol{C}_r \end{bmatrix} \begin{bmatrix} \boldsymbol{x}_0(t) \\ \boldsymbol{x}_r(t) \end{bmatrix} + \boldsymbol{v}(t) + \boldsymbol{f}_s(t) \tag{2}$$

where $\boldsymbol{x}$ represents $N \times 1$ state vector, $\boldsymbol{x}_0$ is $n \times 1$ state vector (primary modes), $\boldsymbol{x}_r$ is $N-n \times 1$ state vector (secondary modes), $\boldsymbol{u}$ and $\boldsymbol{y}$ are $r \times 1$ input vector and $m \times 1$ output vector, respectively; and $\boldsymbol{w}$ and $\boldsymbol{v}$ are $p \times 1/m \times 1$ noise vector (Gaussian white noise) in input/output, respectively; and $\boldsymbol{f}_a$ and $\boldsymbol{f}_s$ are fault vector in actuators and sensors, respectively. N is the real order of the plant dynamics and n is the order of dominant part of the plant dynamics. $\boldsymbol{A}_0$,$\boldsymbol{B}_0$ and $\boldsymbol{C}_0$ are matrices of the linear nominal model to be used in the observer and controller, and $\Delta\boldsymbol{A}$,$\boldsymbol{A}_{u1}$,$\boldsymbol{A}_{u2}$,$\boldsymbol{A}_r$, $\Delta\boldsymbol{B}$,$\boldsymbol{B}_r$,$\Delta\boldsymbol{C}$ and $\boldsymbol{C}_r$ represent the parameter variations and plant uncertainty.

The state and output equations for the dominant part of the system ($\boldsymbol{A}_0$,$\boldsymbol{B}_0$,$\boldsymbol{C}_0$) can

be expressed as:

$$\dot{\boldsymbol{x}}_0(t) = \boldsymbol{A}_0 x_0(t) + \boldsymbol{B}_0 u(t) + \boldsymbol{G}_0 w(t) + \boldsymbol{E}\boldsymbol{d}(t) + \boldsymbol{f}_a(t) \tag{3}$$

$$\boldsymbol{y}(t) = \boldsymbol{C}_0 \boldsymbol{x}_0(t) + \boldsymbol{C}_r \boldsymbol{x}_r(t) + \Delta \boldsymbol{C} \boldsymbol{x}_0(t) + \boldsymbol{v}(t) + \boldsymbol{f}_s(t) \tag{4}$$

where

$$\boldsymbol{E} \equiv \left[\begin{array}{c|c|c} \Delta \boldsymbol{A} & \Delta \boldsymbol{B} & \boldsymbol{A}_{u1} \end{array} \right], \boldsymbol{d} \equiv \left[\begin{array}{c|c|c} \boldsymbol{x}_0(t) & \boldsymbol{u}(t) & \boldsymbol{x}_r(t) \end{array} \right]^T$$

Outputs and inputs of the system are processed by an appropriate algorithm to generate residual signals, which are quantities that represent the inconsistency between the actual outputs and the mathematical model outputs. The residuals are usually based on a (weighted) comparison between the actual outputs and estimated outputs generated from mathematical model. The residual generator uses an observer and to provide residual signals, which are dependent of uncertainties. The observer dynamics are described by the following equations:

$$\dot{\hat{\boldsymbol{x}}}_0(t) = (\boldsymbol{A}_0 - \boldsymbol{K}\boldsymbol{C}_0)\hat{\boldsymbol{x}}_0(t) + \boldsymbol{B}_0 \boldsymbol{u}(t) + \boldsymbol{K}\boldsymbol{y}(t) \tag{5}$$

$$\hat{\boldsymbol{y}}(t) = \boldsymbol{C}_0 \hat{\boldsymbol{x}}_0(t) \tag{6}$$

where $\hat{\boldsymbol{x}}$ is $n \times 1$ state estimation vector and $\hat{\boldsymbol{y}}$ $m \times 1$ output estimation vector. The dynamics of the state estimation error $[\boldsymbol{e}(t) = \boldsymbol{x}_0(t) - \hat{\boldsymbol{x}}_0(t)]$ are described as:

$$\begin{aligned} \dot{\boldsymbol{e}}(t) = (\boldsymbol{A}_0 - \boldsymbol{K}\boldsymbol{C}_0)\boldsymbol{e}(t) + \boldsymbol{G}_0 \boldsymbol{w}(t) + \boldsymbol{E}\boldsymbol{d}(t) \\ + \boldsymbol{f}_a(t) - \boldsymbol{K}(\boldsymbol{C}_r \boldsymbol{x}_r(t) + \boldsymbol{v}(t) + \boldsymbol{f}_s(t)) \end{aligned} \tag{7}$$

A residual vector is defined as:

$$\boldsymbol{r}(t) = \boldsymbol{W}\boldsymbol{e}_y(t) = \boldsymbol{W}[\boldsymbol{y}(t) - \hat{\boldsymbol{y}}(t)] \tag{8}$$

where $\boldsymbol{e}_y$ is measurement estimation errors, $\boldsymbol{W}$ is a suitable weighting matrix designed to give good isolability properties and insensitivity to uncertainty. The Laplace transform of the residual vector is described by the following equation:

$$\begin{aligned} \boldsymbol{r}(s) = &\boldsymbol{W}\boldsymbol{A}_{inv}\{\boldsymbol{f}_a(s) - \boldsymbol{K}\boldsymbol{f}_s(s)\} \\ &+ \boldsymbol{W}\boldsymbol{A}_{inv}\{\boldsymbol{E}\boldsymbol{d}(s) - \boldsymbol{K}\boldsymbol{C}_r\boldsymbol{x}_r(s)\} + \boldsymbol{W}\boldsymbol{A}_{inv}\{\boldsymbol{G}_0\boldsymbol{w}(s) - \boldsymbol{K}\boldsymbol{v}(s)\} \end{aligned} \tag{9}$$

where $\boldsymbol{A}_{inv} = (s\boldsymbol{I} - \boldsymbol{A}_0 + \boldsymbol{K}\boldsymbol{C}_0)^{-1}$. The first term of the right-hand-side of Eq.(9) represents the influence of failure. The second term represents the effect of the model uncertainty. The third term is disturbances due to input and output noises. Clearly the residual responds to both the failure and uncertainty. If the first term is much larger than other terms, it is easy to detect the failure from residual signals. That is, the residuals

must be isolated from the disturbances and uncertainty in order to minimize the false alarm rate resulting from the uncertainty.

DESIGN OF ROBUST RESIDUALS

Equation(9) shows that the residuals are not zero, even if no faults occur in the system. Therefore, it is impossible to distinguish the effects of faults from the effects of disturbances and uncertainty; i.e. parameter variations, disturbance input, the effects of modes truncated in the observer dynamics (residual modes), and so on. This paper proposes a robust detection algorithm that utilizes the multiple sensors distributed at different positions on the smart structure to reduce the effects of the residual modes. We assume for simplicity that no parameter variations exists and the system uncertainties are model truncation errors (the effects of residual modes), disturbances noises and the sensors and actuators failures, i.e., $\Delta \boldsymbol{A} = 0$, $\Delta \boldsymbol{B} = 0$, $\Delta \boldsymbol{C} = 0$. Furthermore, we assume the system matrix is block-diagonal; $\boldsymbol{A}_{u1} = 0$. This assumption usually holds for structural systems if modal coordinates and modal velocities are selected as the state variables and a proportional damping model is assumed. The discrete-time state equation of such uncertain reduced order dynamics system is given as

$$\boldsymbol{x}(k+1) = \boldsymbol{F}_0\boldsymbol{x}_0(k) + \boldsymbol{D}_0\boldsymbol{u}(k) + \boldsymbol{w}(k) + \boldsymbol{f}_a(k) \tag{10}$$

$$\boldsymbol{y}(k) = \boldsymbol{H}_0\boldsymbol{x}_0(k) + \boldsymbol{v}(k) + \boldsymbol{H}_r\boldsymbol{x}_r(k) + \boldsymbol{f}_s(k) \tag{11}$$

where $(\boldsymbol{F}_0,\boldsymbol{D}_0,\boldsymbol{H}_0)$ is the discrete-time system of $(\boldsymbol{A}_0,\boldsymbol{B}_0,\boldsymbol{C}_0)$, $\boldsymbol{x}_0(k) = \boldsymbol{x}_0(t_k)$, $\boldsymbol{u}(k) = \boldsymbol{u}(t_k)$, $\boldsymbol{w}(k) = \boldsymbol{w}(t_k)$, $\boldsymbol{v}(k) = \boldsymbol{v}(t_k)$, $\boldsymbol{x}_r(k) = \boldsymbol{x}_r(t_k)$, $\boldsymbol{f}_a(k) = \boldsymbol{f}_a(t_k)$, $\boldsymbol{f}_s(k) = \boldsymbol{f}_s(t_k)$ and $\boldsymbol{H}_r = \boldsymbol{C}_r$. The residual vector in the discrete-system is described as follows:

$$\begin{aligned}\boldsymbol{r}(z) =& \boldsymbol{W}(z\boldsymbol{I} - \boldsymbol{F}_0 + \boldsymbol{K}\boldsymbol{H}_0)^{-1}\{\boldsymbol{f}_a(z) - \boldsymbol{K}\boldsymbol{f}_s(z)\} \\ &- \boldsymbol{W}(z\boldsymbol{I} - \boldsymbol{F}_0 + \boldsymbol{K}\boldsymbol{H}_0)^{-1}\boldsymbol{K}\boldsymbol{H}_r\boldsymbol{x}_r(z) + \boldsymbol{W}(z\boldsymbol{I} - \boldsymbol{F}_0 + \boldsymbol{K}\boldsymbol{H}_0)^{-1}\{\boldsymbol{w}(z) - \boldsymbol{K}\boldsymbol{v}(z)\}\end{aligned} \tag{12}$$

where $\boldsymbol{K}$ is the n-order observer gain matrix and the second term represents the influence of residual modes. Clearly, the residual vector is not white due to spillover that decreases the performance of feedback control and failure detection. In the worst case, the system may become unstable.

This paper proposes here a method for generating robust residual signals that have good isolability of the failure signature and insensitivity to the influence of residual modes. It takes advantage of redundant sensors and eliminates the specified low-freqency residual modes by linear combinations of these outputs. Thereby, one can reduce the influence of the observation spillover by increasing the differences of the frequencies between the controlled modes and the higher-frequency residual modes.

The low-frequency residual modes and the high-frequency residual modes are defined as $\boldsymbol{x}_r^T(k) = [\boldsymbol{x}_{r1}^T(k) \mid \boldsymbol{x}_{r2}^T(k)]^T$. Let $\boldsymbol{L}$ be a matrix that represents the linear combinations

of outputs and satisfies $\boldsymbol{L}\boldsymbol{H}_{r1} = 0$, and the observation equation is rewritten with the new outputs $\boldsymbol{y}_m(k)$ as:

$$\begin{aligned}\boldsymbol{y}_m(k) =& \boldsymbol{L}\boldsymbol{y}(k) \\ =& \boldsymbol{L}\boldsymbol{H}_0\boldsymbol{x}_0(k) + \boldsymbol{L}\boldsymbol{H}_{r2}\boldsymbol{x}_{r2}(k) + \boldsymbol{L}\{\boldsymbol{v}(k) + \boldsymbol{f}_s(k)\}\end{aligned} \tag{13}$$

$$\begin{aligned}\boldsymbol{H}_{r1} =& [\boldsymbol{\Phi}_{n+1}, \cdots, \boldsymbol{\Phi}_{n+p}] : \text{the low-frequency residual modes} \\ \boldsymbol{H}_{r2} =& [\boldsymbol{\Phi}_{n+p+1}, \cdots, \boldsymbol{\Phi}_N] : \text{the high-frequency residual modes}\end{aligned}$$

where $\boldsymbol{\Phi}_i = [\boldsymbol{\phi}_{d,i}\ \boldsymbol{\phi}_{v,i}]$ is the output matrix corresponding to the ith vibration mode, $\boldsymbol{\phi}_{d,i}$ and $\boldsymbol{\phi}_{v,i}$ are the vectors that correspond to the displacement and velocity measurements of modal coordinates, respectively.

IDENTIFICATION OF THE FAILED SENSOR

This section proposes an algorithm to identify the failed sensor by using the redundancy of sensors. It is assumed that the sensors measure either displacement or velocity and the number of the low-frequency residual modes is p $(m - 2 \geq p)$ to utilize the redundancy. Therefore, $\boldsymbol{H}_{r1}$ is $m \times 2p$ output matrix corresponding to the low-frequency residual modes. The vector $\boldsymbol{\psi}_i^T$ that satisfies $\boldsymbol{\psi}_i^T \boldsymbol{H}_{r1} = 0$ is defined as:

$$\boldsymbol{\psi}_i^T = [\psi_{i,1}, \ldots, \underbrace{0}_{i\text{th}}, \ldots, \psi_{i,m}] \tag{14}$$

Now the linear combinations matrix $\boldsymbol{L}$ is defined as:

$$\boldsymbol{L} = \begin{bmatrix} \boldsymbol{\psi}_1^T \\ \boldsymbol{\psi}_2^T \\ \vdots \\ \vdots \\ \boldsymbol{\psi}_m^T \end{bmatrix} = \begin{bmatrix} 0 & \psi_{1,2} & \cdots & \cdots & \psi_{1,m} \\ \psi_{2,1} & 0 & & & \vdots \\ \vdots & & \ddots & & \vdots \\ \vdots & & & \ddots & \psi_{m-1,m} \\ \psi_{m,1} & \cdots & \cdots & \psi_{m,m-1} & 0 \end{bmatrix} \tag{15}$$

where $\boldsymbol{L}$ is $m \times m$ matrix and satisfies $\boldsymbol{L}\boldsymbol{H}_{r1} = 0$. Using this matrix $\boldsymbol{L}$, one can eliminate the influence of low-frequency residual modes and obtain new outputs for determining the failure sensor. The differences between each new outputs (e_{ij}) are described as:

$$e_{ij} = |y_{m,i} - y_{m,j}| \tag{16}$$

where $e_{ij} = e_{ji} (i \neq j)$, and $y_{m,i}$ are the ith element of $y_m(k)$. Let us introduce a $m \times 1$ vector $\boldsymbol{\eta}(k)$ where the element of $\boldsymbol{\eta}(k)$ is given as:

$$\eta_i(k) = \prod_{j=1}^{m} e_{ij} \quad (i \neq j) \tag{17}$$

If a failure occurrs at the qth sensor, the new outputs are written as:

$$\begin{cases} y_{m,q} = \delta \quad \delta \cong 0 \\ y_{m,i} = f_i \end{cases} \qquad (i \neq q) \tag{18}$$

where f_i is the magnitude of the influence of a sensor failure signal. e_{ij} is written as:

$$\begin{cases} e_{qi} = |\delta - f_i| \cong f_i & (i \neq q) \\ e_{ij} = |f_i - f_j| \cong \delta & (i \neq j) \end{cases} \tag{19}$$

therefore,

$$\begin{cases} \eta_q(k) = \prod_{i=1}^{m} e_{qi} \cong \prod_{i=1}^{m} f_i & (i \neq q) \\ \eta_i(k) = \prod_{j=1}^{m} e_{ij} \cong \delta^{m-1} & (i \neq j) \end{cases} \tag{20}$$

Although $\boldsymbol{\eta}(k)$ still includes the disturbances, such as noise errors and influences of high-frequency residual modes, this algorithm is useful for reducing influences of residual modes and it can specify the sensor where a failure has occurred. This algorithm is insensitive to disturbances inputted to all sensors while it is sensitive to the disturbance, i.e. failure applying to one sensor. Therefore one can identify the failed sensor by using this algorithm.

NUMERICAL SIMULATION

The capability of the robust failure detection algorithm is demonstrated by a numerical simulation for a smart beam equipped with piezoelectric actuators for active vibration control and damping enhancement. The proposed robust failure detection algorithm has been applied to sensor failure detection for smart structure control system. Figure 1 shows simple model of a flexible smart beam. Piezo-celamics (PZT'S) fixed on the both side of the beam are used as sensor and actuator pairs. The Kalman filter and optimal regulator are used for the observer and feedback controller, respectively. The dynamics of the smart beam is given by the Finite Element Method. It is assumed that the number of the vibration modes is 8 in the numerical simulation. The dynamics of the lowest 4

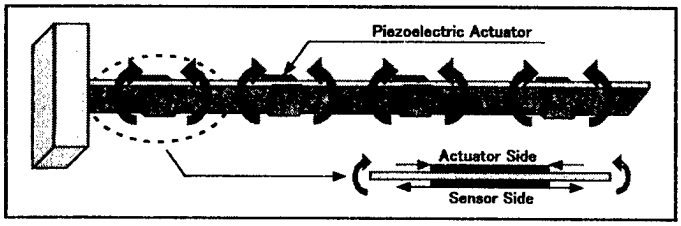


Figure.1: Model of a smart beam

vibration modes is used in the Kalman filter design and 5th, 6th/7th, 8th vibration modes are assumed as the low-frequency/high-frequency residual modes.

Feasibility of the proposed method of robust failure detection is tested for two types of sensor failures. Figure 2 compares the abilities of ordinary output errors (Kalman filter innovation process) and robust residuals for sensor failure detection. The simulated malfunctions are a small bias failure (Figure 2 (a) to 2 (c)), and a gain-type failure (Figure 2 (d) to 2 (f)), both in the second sensor at the time 0.5 sec. after initial impulse input. The norm of the robust residuals clearly indicates the small bias failure whereas that of the ordinal output error is disturbed by the high-frequency vibration modes truncated in the observer dynamics. Figure 2 (c) shows the alarm vector $\boldsymbol{\eta}(k)$ for detecting the failed sensor that clearly indicated the second sensor has failed. These figures demonstrate the discrepancy between the capabilities of the proposed robust residuals and that of ordinary output errors in indicating the failure signature. The result for a failure of a 10% gain reduction in the second sensor is shown in Figures 2(d) to 2(f). In case of the gain-type failure in sensor, the present robust residual is also useful in detecting failure and specifying the failed sensor.

CONCLUSION

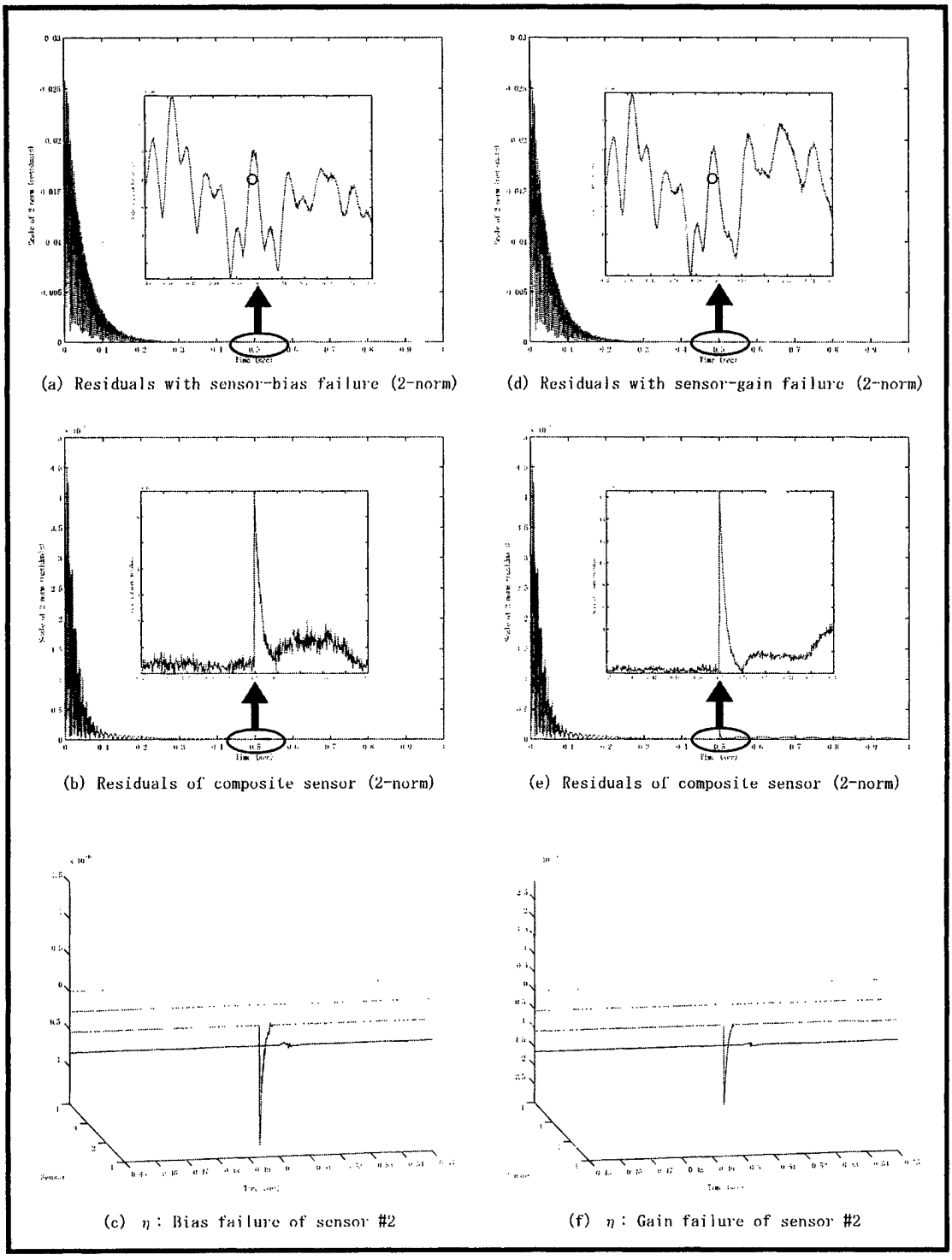
A method of robust fault detection has been proposed using residuals that have insensivity to uncertain plant dynamics by utilizing redundant sensors. The robust failure detection algorithm has been applied to a numerical example of a sensor failure for a flexible smart structure control system. Results of numerical simulations have shown that the proposed method remarkably reduces the disturbances to the residuals due to the truncated vibration modes and highly improves the performance of fault detection.

REFERENCES

Patton, R. J. and Chen, J. 1993. "Optimal Unknown Input Distribution Matrix Selection in Robust Fault Diagnosis," Automatica, pp. 837-841.

Okubo, H. 1991. "Failure Detection and Identification of Structural Control Systems," Proceedings of the IFAC/IMACS Symposium on Fault Detection, Supervision and Safety for Technical Processes, pp. 247-252.

Okubo, H. and Doyu, H. 1999. "Robust Fault Diagnosis for Reduced-Order Control of Flexible Space Structures," Proceedings of the 9th International Conference on Adaptive Structures and Technologies, pp. 429-437.



(a) Residuals with sensor-bias failure (2-norm)

(d) Residuals with sensor-gain failure (2-norm)

(b) Residuals of composite sensor (2-norm)

(e) Residuals of composite sensor (2-norm)

(c) η : Bias failure of sensor #2

(f) η : Gain failure of sensor #2

Figure.2: Results of numerical simulation

MODELING AND ANALYSIS OF ELLIPTICAL PIEZOELECTRIC LAMINATES WITH CLAMPED BOUNDARY

S.-W. Ricky Lee, H. L. Wong

ABSTRACT

This paper presents an effort of modeling and analysis for the sensing and actuation of elliptical piezoelectric laminates with clamped boundary conditions. The laminate contains a number of layers of structural and piezoelectric materials. The configuration of the laminate may be arbitrary. The functions of sensing and actuation are achieved through the in-plane strains in piezoelectric layers. An analytical model based on the classical lamination theory is developed. Closed form solutions are obtained for laminates with elliptical shape and clapmed boundary. The sensitivity of this piezoelectric structure is discussed in depth. Some unique phenomena are identified in the analysis. The results of the present study should be very useful for the design of laminated piezoelectric sensors and actuators.

INTRODUCTION

The study of intelligent materials and structures has attracted substantial attention from the community of engineering research in the past decade. In order to improve the performance of intelligent structures, sensors and actuators have to be integrated into structural materials to achieve the adaptability. Therefore, smart materials are a composite structure in nature. A typical example of such materials is a composite laminate with embedded piezoelectric layers. In the literature, Lee [1] explored the feasibility to use the composite of metal and piezopolymer for the actuation and sensing of torsion and bending. Crawley and Anderson [2] also introduced some analytical models for the actuation of composite laminates with piezoceramics. In addition, Lee and Sun [3] developed an integrated theory for the bending/twisting/shearing actuation and sensing of a laminated piezoelectric beam. Although there are a number of other papers in the same research area, most of them are for beam-type of structures.

The present study is conducted to analyze the clamped composite laminates with embedded piezoelectric materials. The function of sensing and actuation is achieved through the in-plane strains in piezoelectric layers. The configuration of the laminate may be symmetric or asymmetric to the midplane of the plate. An analytical model based on the classical lamination theory is developed in this study to investigate the response of this piezoelectric structure. Although PVDF film is considered in the present analysis, the developed model is valid for other kind of piezoelectric materials as well. Closed form

S. -W. Ricky Lee, Department of Mechanical Engineering, HKUST, Clear Water Bay, Hong Kong
H. L. Wong, Department of Mechanical Engineering, HKUST, Clear Water Bay, Hong Kong

solutions are obtained for laminates with elliptical shape and clamped boundary. Some unique characteristics are identified in the analysis. It is believed that the results of present study are very useful for the design of laminated piezoelectric sensors and actuators.

FORMULATION OF PIEZOELECTRIC LAMINATES

Consider a composite laminate composed of a number of linear elastic orthotropic layers. Each layer may be structural or piezoelectric materials. The configuration of stacking sequence and the orientation of principal axes are arbitrary. According to IEEE compact tensor notation, the linear elastic constitutive relations of piezoelectric materials can be expressed as

$$\varepsilon_p = S_{pq}^{\mathcal{E}}\sigma_q + d_{jp}\mathcal{E}_j \qquad i,j=1,2,3 \tag{1}$$

$$\mathcal{D}_i = d_{iq}\sigma_q + \mathcal{E}_{ij}^{\sigma}\mathcal{E}_j \qquad p,q=1,2,3,4,5,6 \tag{2}$$

where the vectors ε_p, σ_q, $\mathcal{D}_i$, and $\mathcal{E}_j$ represent total strains, mechanical stresses, electrical displacements, and electrical fields, respectively. In addition, the material properties in Eqs. (1) and (2) are the compliance matrix S_{pq}, the permittivity matrix $\mathcal{E}_{ij}$, and the piezoelectric strain/charge coupling matrix d_{iq}. For piezoelectric materials such as PVDF, the piezoelectric coupling in principal axes is of the form

$$\mathbf{d}_{iq} = \begin{bmatrix} 0 & 0 & 0 & 0 & d_{15} & 0 \\ 0 & 0 & 0 & d_{24} & 0 & 0 \\ d_{31} & d_{32} & d_{33} & 0 & 0 & 0 \end{bmatrix} \tag{3}$$

Note that the mechanical properties of PVDF are isotropic. Besides, all aforementioned electrical properties and vectors are ineffective in the layers of structural materials.

Since the structure under consideration in this study is a laminate and the electric field can be applied only in the thickness direction of piezoelectric layers, Eqs. (1) and (2) should be rearranged to accommodate the plane stress conditions. Therefore, the constitutive relations for each layer in the laminate become

$$\begin{Bmatrix} \sigma_x \\ \sigma_y \\ \tau_{xy} \end{Bmatrix} = \begin{bmatrix} \overline{Q}_{11} & \overline{Q}_{12} & \overline{Q}_{16} \\ \overline{Q}_{12} & \overline{Q}_{22} & \overline{Q}_{26} \\ \overline{Q}_{16} & \overline{Q}_{26} & \overline{Q}_{66} \end{bmatrix} \left(\begin{Bmatrix} \varepsilon_x \\ \varepsilon_y \\ \gamma_{xy} \end{Bmatrix} - \begin{Bmatrix} \overline{d}_{31} \\ \overline{d}_{32} \\ \overline{d}_{36} \end{Bmatrix} \mathcal{E}_3 \right) \tag{4}$$

$$\mathcal{D}_3 = \overline{d}_{31}\sigma_x + \overline{d}_{32}\sigma_y + \overline{d}_{36}\tau_{xy} + \mathcal{E}_{33}\mathcal{E}_3 \tag{5}$$

where $\overline{Q}_{ij}$ are the transformed reduced stiffness and $\overline{d}_{3j}$ are defined as

$$\begin{Bmatrix} \overline{d}_{31} \\ \overline{d}_{32} \\ \overline{d}_{36} \end{Bmatrix} = \begin{bmatrix} \cos^2\theta & \sin^2\theta \\ \sin^2\theta & \cos^2\theta \\ \sin 2\theta & -\sin 2\theta \end{bmatrix} \begin{Bmatrix} d_{31} \\ d_{32} \end{Bmatrix} \tag{6}$$

Note that the stresses and the strains in Eqs. (4) and (5) have been transformed to the global axes of the laminate and θ is the angle between the global x-axis and the major principal axis of each lamina. By introducing displacement-strain relations and integrating Eq. (4) through the whole laminate in the thickness direction, the constitutive equations of the laminate can be obtained as [4]

$$\begin{Bmatrix} N_x \\ N_y \\ N_{xy} \\ M_x \\ M_y \\ M_{xy} \end{Bmatrix} = \left[\begin{array}{ccc:ccc} A_{11} & A_{12} & A_{16} & B_{11} & B_{12} & B_{16} \\ A_{12} & A_{22} & A_{26} & B_{12} & B_{22} & B_{26} \\ A_{16} & A_{26} & A_{66} & B_{16} & B_{26} & B_{66} \\ \hdashline B_{11} & B_{12} & B_{16} & D_{11} & D_{12} & D_{16} \\ B_{12} & B_{22} & B_{26} & D_{12} & D_{22} & D_{26} \\ B_{16} & B_{26} & B_{66} & D_{16} & D_{26} & D_{66} \end{array}\right] \begin{Bmatrix} u^o_{,x} \\ v^o_{,y} \\ u^o_{,y} + v^o_{,x} \\ -w_{,xx} \\ -w_{,yy} \\ -2w_{,xy} \end{Bmatrix} - \begin{Bmatrix} N^p_x \\ N^p_y \\ N^p_{xy} \\ M^p_x \\ M^p_y \\ M^p_{xy} \end{Bmatrix} \tag{7}$$

where (u^o, v^o, w) are midplane displacements of the laminate in (x, y, z) directions, respectively, and all other symbols are defined as

$$(A_{ij}, B_{ij}, D_{ij}) = \int_{-h/2}^{h/2} \overline{Q}_{ij}(1, z, z^2)dz \tag{8}$$

$$[(N_x, N_y, N_{xy}), (M_x, M_y, M_{xy})] = \int_{-h/2}^{h/2} (\sigma_x, \sigma_y, \tau_{xy})[1, z]dz \tag{9}$$

$$[(N^p_x, N^p_y, N^p_{xy}), (M^p_x, M^p_y, M^p_{xy})] = \int_{-h/2}^{h/2} \begin{bmatrix} \overline{Q}_{11} & \overline{Q}_{12} & \overline{Q}_{16} \\ \overline{Q}_{12} & \overline{Q}_{22} & \overline{Q}_{26} \\ \overline{Q}_{16} & \overline{Q}_{26} & \overline{Q}_{66} \end{bmatrix} \begin{Bmatrix} \overline{d}_{31} \\ \overline{d}_{32} \\ \overline{d}_{36} \end{Bmatrix} \mathcal{E}_3[1, z]dz \tag{10}$$

Note that the superscript p implies piezoelectric effect and h is the total thickness of the laminate. The equilibrium equations for plates are

$$N_{x'x} + N_{xy'y} = 0 \tag{11}$$

$$N_{xy'x} + N_{y'y} = 0 \tag{12}$$

$$M_{x'xx} + 2M_{xy'xy} + M_{y'yy} + q = 0 \tag{13}$$

where q is the transverse distributed loading on the plate. Substituting Eq. (7) into the last three equations leads to the governing equations of the laminate in terms of displacements

$$\begin{aligned} &A_{11}u^o_{,xx} + 2A_{16}u^o_{,xy} + A_{66}u^o_{,yy} + A_{16}v^o_{,xx} + (A_{12} + A_{66})v^o_{,xy} + A_{26}v^o_{,yy} \\ &- B_{11}w_{,xxx} - 3B_{16}w_{,xxy} - (B_{12} + 2B_{66})w_{,xyy} - B_{26}w_{,yyy} = N^p_{x'x} + N^p_{xy'y} \end{aligned} \tag{14}$$

$$\begin{aligned} &A_{16}u^o_{,xx} + (A_{12} + A_{66})u^o_{,xy} + A_{26}u^o_{,yy} + A_{66}v^o_{,xx} + 2A_{16}v^o_{,xy} + A_{22}v^o_{,yy} \\ &- B_{16}w_{,xxx} - (B_{12} + 2B_{66})w_{,xxy} - 3B_{26}w_{,xyy} - B_{22}w_{,yyy} = N^p_{xy'x} + N^p_{y'y} \end{aligned} \tag{15}$$

$$\begin{aligned} &-B_{11}u^o_{,xxx} - 3B_{16}u^o_{,xxy} - (B_{12} + 2B_{66})u^o_{,xyy} - B_{26}u^o_{,yyy} - B_{16}v^o_{,xxx} - (B_{12} + 2B_{66})v^o_{,xxy} - 3B_{26}v^o_{,xyy} \\ &- B_{22}v^o_{,yyy} + D_{11}w_{,xxxx} + 4D_{16}w_{,xxxy} + 2(D_{12} + 2D_{66})w_{,xxyy} + 4D_{26}w_{,xyyy} + D_{22}w_{,yyyy} \\ &= q - M^p_{x'xx} - 2M^p_{xy'xy} - M^p_{y'yy} \end{aligned} \tag{16}$$

If the configuration of the laminate is symmetric with respect to the midplane, the in-plane deformation and the transverse deflection of the midplane are decoupled. Therefore, Eqs. (14)-(15) and Eq. (16) can be considered separately.

In the case of sensing, all piezoelectric loads in above equations vanish if there is no applied electric field and the self generated electric field is negligible. Subject to appropriate boundary conditions, Eqs. (14)-(16) should be solved for the displacement field of the laminate. Subsequently, from strain-displacement relation and Eq. (4), the stresses in each layer of the laminate can be obtained. The function of sensing for piezoelectric materials is achieved by measuring the accumulated electrical charge induced from the mechanical

loading. Therefore, from Eq. (5), the sensor equation for the *k*th layer of the laminate, if it is piezoelectric material, can be expressed as

$$\mathcal{G}_k = \int\int_S \mathcal{D}_3 \mathbf{dxdy} = \int\int_S (\bar{\mathbf{d}}_{31}\sigma_x + \bar{\mathbf{d}}_{32}\sigma_y + \bar{\mathbf{d}}_{36}\tau_{xy})_k \mathbf{dxdy} \tag{17}$$

where the domain S is the area covered by piezoelectric layers. The total electrical output of the whole sensor is simply the sum of Eq. (17) of all piezoelectric layers.

For actuation of the laminate, the mechanical loading q in Eq. (16) is assumed to be zero. The piezoelectric loads in Eq. (10) become the driving forces. The deformation of the laminate can be obtained by solving Eqs. (14)-(16) under specified boundary conditions.

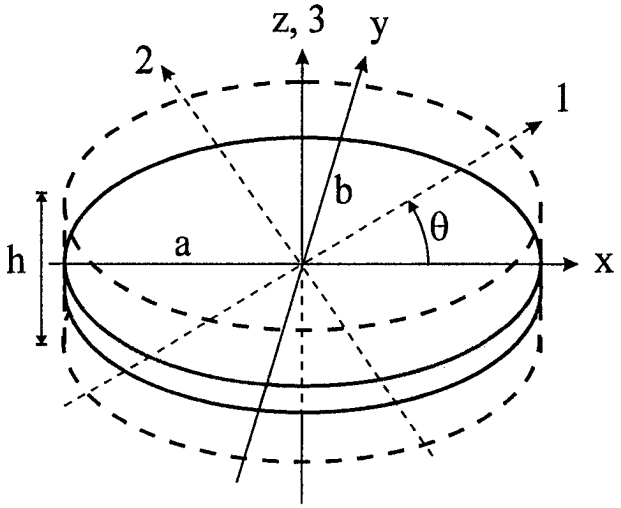


Figure 1. Configuration of elliptical laminate (1-2-3 are local axes; x-y-z are global axes)

SENSING OF CLAMPED ELLIPTICAL LAMINATES

Consider a clamped elliptical laminate with major axis length 2a and minor axis length 2b as shown in Figure 1, the boundary conditions are

$$\mathbf{u}^o = \mathbf{v}^o = \mathbf{w} = \frac{\partial \mathbf{w}}{\partial \mathbf{n}} = \mathbf{0}, \quad \mathbf{on}\ \frac{\mathbf{x}^2}{\mathbf{a}^2} + \frac{\mathbf{y}^2}{\mathbf{b}^2} = \mathbf{1} \tag{18}$$

where n denotes the normal direction on the boundary. With the absence of applied electrical field, the solutions for such a laminate under uniform transverse loading q are [5]

$$\mathbf{u}^o = \mathbf{q}(\mathbf{u}_1^o \frac{\mathbf{x}}{\mathbf{a}} + \mathbf{u}_2^o \frac{\mathbf{y}}{\mathbf{b}})(\mathbf{1} - \frac{\mathbf{x}^2}{\mathbf{a}^2} - \frac{\mathbf{y}^2}{\mathbf{b}^2}) \tag{19}$$

$$\mathbf{v}^o = \mathbf{q}(\mathbf{v}_1^o \frac{\mathbf{y}}{\mathbf{b}} + \mathbf{v}_2^o \frac{\mathbf{x}}{\mathbf{a}})(\mathbf{1} - \frac{\mathbf{x}^2}{\mathbf{a}^2} - \frac{\mathbf{y}^2}{\mathbf{b}^2}) \tag{20}$$

$$\mathbf{w} = \mathbf{q}\mathbf{w}_o(\mathbf{1} - \frac{\mathbf{x}^2}{\mathbf{a}^2} - \frac{\mathbf{y}^2}{\mathbf{b}^2})^2 \tag{21}$$

where $\mathbf{u}_1^o, \mathbf{u}_2^o, \mathbf{v}_1^o, \mathbf{v}_2^o,$ **and** $\mathbf{w}_o$ are undetermined constants. Substituting Eqs. (19)-(21) into (14)-(16) leads to a system of algebraic equations as follows.

$$[h_{ij}]\begin{Bmatrix} u_1^o \\ v_1^o \\ w_o \\ u_2^o \\ v_2^o \end{Bmatrix} = \begin{Bmatrix} 0 \\ 0 \\ 2 \\ 0 \\ 0 \end{Bmatrix} \tag{22}$$

where $[h_{ij}]$ is symmetric and the components are

$$\begin{cases} h_{11} = \dfrac{3A_{11}}{a^2} + \dfrac{A_{66}}{b^2}, \quad h_{12} = \dfrac{A_{12}+A_{66}}{ab}, \quad h_{13} = \dfrac{12B_{11}}{a^3} + \dfrac{4(B_{12}+2B_{66})}{ab^2} \\ h_{14} = \dfrac{2A_{16}}{ab}, \quad h_{15} = \dfrac{3A_{16}}{a^2} + \dfrac{A_{26}}{b^2}, \quad h_{22} = \dfrac{A_{66}}{a^2} + \dfrac{3A_{22}}{b^2} \\ h_{23} = \dfrac{12B_{22}}{b^3} + \dfrac{4(B_{12}+2B_{66})}{a^2b}, \quad h_{24} = \dfrac{A_{16}}{a^2} + \dfrac{3A_{26}}{b^2}, \quad h_{25} = \dfrac{2A_{26}}{ab} \\ h_{33} = \dfrac{48D_{11}}{a^4} + \dfrac{32(D_{12}+2D_{66})}{a^2b^2} + \dfrac{48D_{22}}{b^4} \\ h_{34} = \dfrac{12B_{16}}{a^2b} + \dfrac{12B_{26}}{b^3}, \quad h_{35} = \dfrac{12B_{16}}{a^3} + \dfrac{12B_{26}}{ab^2} \\ h_{44} = \dfrac{A_{11}}{a^2} + \dfrac{3A_{66}}{b^2}, \quad h_{45} = h_{12}, \quad h_{55} = \dfrac{3A_{66}}{a^2} + \dfrac{A_{22}}{b^2} \end{cases} \tag{23}$$

Therefore, $u_1^o, u_2^o, v_1^o, v_2^o,$ **and** w_o can be solved by inverting Eq. (22). The stresses in each piezoelectric layer can be calculated accordingly from strain-displacement relation and Eq. (4)

$$\begin{Bmatrix} \sigma_x \\ \sigma_y \\ \tau_{xy} \end{Bmatrix}_k = \begin{bmatrix} Q_{11}^p & Q_{12}^p & 0 \\ Q_{12}^p & Q_{11}^p & 0 \\ 0 & 0 & \dfrac{Q_{11}^p - Q_{12}^p}{2} \end{bmatrix}_k \left(\begin{Bmatrix} u_{,x}^o \\ v_{,y}^o \\ u_{,y}^o + v_{,x}^o \end{Bmatrix} - \bar{z}_k \begin{Bmatrix} w_{,xx} \\ w_{,yy} \\ 2w_{,xy} \end{Bmatrix} \right) \tag{24}$$

where $\bar{z}_k$ is the mid-ply z coordinate and Q_{11}^p, Q_{12}^p are the reduced stiffness of piezoelectric layers. Note that, since the stress in each ply varies linearly with respect to z, the stresses in Eq. (24) are evaluated at the midplane of each layer to represent the average effect. From Eqs. (17)-(24), the sensitivity of the *k*th layer can be evaluated as

$$\frac{\varphi_k}{q} = \begin{Bmatrix} \bar{d}_{31} \\ \bar{d}_{32} \\ \bar{d}_{36} \end{Bmatrix}_k^T \begin{bmatrix} Q_{11}^p & Q_{12}^p & 0 \\ Q_{12}^p & Q_{11}^p & 0 \\ 0 & 0 & \dfrac{Q_{11}^p - Q_{12}^p}{2} \end{bmatrix}_k \begin{Bmatrix} \Lambda_x \\ \Lambda_y \\ \Lambda_{xy} \end{Bmatrix}_k \tag{25}$$

where

$$(\Lambda_x)_k = \frac{1}{a}\left(u_1^o A - \frac{3u_1^o}{a^2} I_x - \frac{2u_2^o}{ab} I_{xy} - \frac{u_1^o}{b^2} I_y\right) + \frac{4w_o \bar{z}_k}{a^2}\left(A - \frac{3}{a^2} I_x - \frac{1}{b^2} I_y\right) \tag{26}$$

$$(\Lambda_y)_k = \frac{1}{b}\left(v_1^o A - \frac{v_1^o}{a^2} I_x - \frac{2v_2^o}{ab} I_{xy} - \frac{3v_1^o}{b^2} I_y\right) + \frac{4w_o \bar{z}_k}{a^2}\left(A - \frac{1}{a^2} I_x - \frac{3}{b^2} I_y\right) \tag{27}$$

$$(\Lambda_{xy})_k = \frac{1}{b}\left(u_2^o A - \frac{u_2^o}{a^2} I_x - \frac{2u_1^o}{ab} I_{xy} - \frac{3u_2^o}{b^2} I_y\right) + \frac{1}{a}\left(v_2^o A - \frac{3v_2^o}{a^2} I_x - \frac{2v_1^o}{ab} I_{xy} - \frac{v_2^o}{b^2} I_y\right) - \frac{16w_o \bar{z}_k}{a^2 b^2} I_{xy} \tag{28}$$

and

$$A = \iint_S dxdy, \quad I_x = \iint_S x^2 dxdy, \quad I_y = \iint_S y^2 dxdy, \quad I_{xy} = \iint_S xydxdy \tag{29}$$

If the domain S coincides with the area of the elliptical laminate, Eqs. (26)-(28) can be further simplified as

$$(\Lambda_x)_k = A\left(\frac{u_1^o}{a} + \frac{4w_o\bar{z}_k}{a^2}\right)\left(1 - \frac{3}{4c^2} - \frac{c^2}{4}\right) \tag{30}$$

$$(\Lambda_y)_k = A\left(\frac{v_1^o}{b} + \frac{4w_o\bar{z}_k}{b^2}\right)\left(1 - \frac{1}{4c^2} - \frac{3c^2}{4}\right) \tag{31}$$

$$(\Lambda_{xy})_k = A\frac{v_2^o}{a}\left(1 - \frac{3}{4c^2} - \frac{c^2}{4}\right) + A\frac{u_2^o}{b}\left(1 - \frac{1}{4c^2} - \frac{3c^2}{4}\right) \tag{32}$$

where $c = a/b$ and $A = ab\pi$ are the aspect ratio and the area of the elliptical plate, respectively. From Eqs. (30)-(32), it is interesting to observe that the sensitivity of a clamped circular ($c = a/b = 1$) piezoelectric laminate is zero. Furthermore, this feature holds for any stacking sequence and principal axis orientation. A detailed discussion on the sensitivity of circular piezoelectric laminates is given in the following section.

DISCUSSION ON THE SENSITIVITY OF CIRCULAR LAMINATES

In Eq. (25), there are a number of parameters which may affect the sensitivity. Among them are the pattern and the size of effective piezoelectric area (i.e., area covered with electrodes), the location of centroid, and the orientation of principal axes. These parameters may be manipulated to optimize a certain design. Assume that the centroid of domain S (effective piezoelectric area) coincides with the center of a circular piezoelectric laminate and either x or y is an axis of symmetry of S. Therefore, the product of area I_{xy} in Eqs. (26)-(28) vanishes. Further assume that $I_x = I_y$, then Eq. (25) becomes

$$\frac{\mathcal{P}_k}{q} = \begin{Bmatrix} \bar{d}_{31} \\ \bar{d}_{32} \\ \bar{d}_{36} \end{Bmatrix}_k^T \begin{bmatrix} Q_{11}^p & Q_{12}^p & 0 \\ Q_{12}^p & Q_{11}^p & 0 \\ 0 & 0 & \dfrac{Q_{11}^p - Q_{12}^p}{2} \end{bmatrix}_k \begin{Bmatrix} au_1^o + 4w_o\bar{z}_k \\ av_1^o + 4w_o\bar{z}_k \\ au_2^o + av_2^o \end{Bmatrix} \lambda \tag{33}$$

where the shape factor λ is defined as

$$\lambda = \frac{A}{a^2} - \frac{2J}{a^4} \tag{34}$$

and $J = I_x + I_y$ is the polar moment of area A. If S is a circular area with radius r, then

$$A = \pi r^2, \qquad J = \frac{\pi}{2} r^4 \tag{35}$$

From Eqs. (34) and (35), the shape factor may be expressed as

$$\lambda = \pi\xi^2(1 - \xi^2), \qquad 0 \le \xi = \frac{r}{a} \le 1 \tag{36}$$

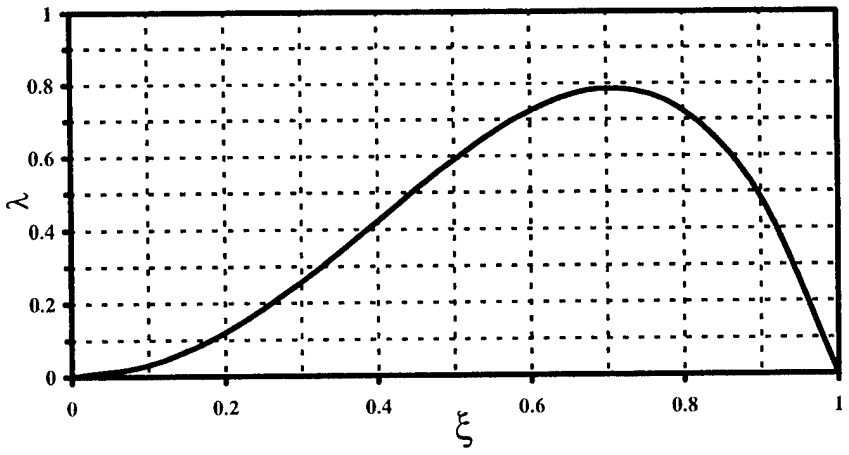


Figure 2. Effect of electrode size on the sensitivity of circular laminates

The symbol r may be considered as the radius of circular electrodes (effective piezoelectric area). It is interesting to note that the sensitivity is zero if the electrodes cover the whole circular laminate; i.e., r = a. Furthermore, this result is independent of the configuration of the laminate and the location of piezoelectric layers. The maximum sensitivity can be obtained with $\xi = 1/\sqrt{2}$. The normalized sensitivity of the aforementioned case is plotted in Figure 2.

ACTUATION OF CLAMPED ELLIPTICAL LAMINATES

In the case of actuation, the mechanical loading q in Eq. (16) is assumed to be zero. The piezoelectric resultants become the driving forces of deformation. However, if the electrodes of piezoelectric layers cover the whole area of the laminate, the piezoelectric loads are constant in both x and y directions. Therefore, all terms at the right hand side of Eqs. (14)-(16) are zero leading to trivial solution. As a result, uniform piezoelectric loads may induce internal stresses but cannot actuate deformation. The stresses can be calculated from Eq. (4).

A further study shows that the closed form solution can be obtained if the distribution of piezoelectric loads is quadratic in x or y direction; i.e., proportional to x^2, xy, y^2, or their linear combination. This distribution can be achieved by making a quadratic polarization profile of piezoelectric layers during manufacturing. Therefore, the piezoelectric strain/charge coupling coefficients in Eq. (6) are nonuniform in x or y direction and, from Eq. (10), so are the piezoelectric loads. The solutions of displacement field in this case are

$$\mathbf{u}^{o} = \mathcal{E}_3(\mathbf{u}_1^{o}\frac{\mathbf{x}}{\mathbf{a}} + \mathbf{u}_2^{o}\frac{\mathbf{y}}{\mathbf{b}})(1 - \frac{\mathbf{x}^2}{\mathbf{a}^2} - \frac{\mathbf{y}^2}{\mathbf{b}^2}) \tag{37}$$

$$\mathbf{v}^{o} = \mathcal{E}_3(\mathbf{v}_1^{o}\frac{\mathbf{y}}{\mathbf{b}} + \mathbf{v}_2^{o}\frac{\mathbf{x}}{\mathbf{a}})(1 - \frac{\mathbf{x}^2}{\mathbf{a}^2} - \frac{\mathbf{y}^2}{\mathbf{b}^2}) \tag{38}$$

$$\mathbf{w} = \mathcal{E}_3\mathbf{w}_0(1 - \frac{\mathbf{x}^2}{\mathbf{a}^2} - \frac{\mathbf{y}^2}{\mathbf{b}^2})^2 \tag{39}$$

If a quadratic polarization profile in x direction is assumed, then the piezoelectric loads can be expressed as

$$\begin{cases} (N_x^p, N_y^p, N_{xy}^p) = (\hat{N}_x^p, \hat{N}_y^p, \hat{N}_{xy}^p)\mathcal{E}_3 \dfrac{x^2}{a^2} \\ (M_x^p, M_y^p, M_{xy}^p) = (\hat{M}_x^p, \hat{M}_y^p, \hat{M}_{xy}^p)\mathcal{E}_3 \dfrac{x^2}{a^2} \end{cases} \tag{40}$$

where $\hat{N}_x^p, \hat{N}_y^p, \hat{N}_{xy}^p, \hat{M}_x^p, \hat{M}_y^p, \hat{M}_{xy}^p$ are constants depending on the configuration of the laminate. Substituting Eqs. (37)-(40) into (14)-(16) leads to

$$[h_{ij}]\begin{Bmatrix} u_1^o \\ v_1^o \\ w_o \\ u_2^o \\ v_2^o \end{Bmatrix} = \frac{2}{a^2}\begin{Bmatrix} \hat{N}_x^p \\ 0 \\ 2\hat{M}_x^p \\ 0 \\ \hat{N}_{xy}^p \end{Bmatrix} \tag{41}$$

where the components of $[h_{ij}]$ are given in Eq. (23). The unknown constants $u_1^o, u_2^o, v_1^o, v_2^o,$ **and** w_o can be calculated by inverting Eq. (41). From Eqs. (37)-(39), the deformation actuated by the electric field can be obtained accordingly.

CONCLUDING REMARKS

An analysis is presented in this paper for the sensing and actuation of clamped piezoelectric laminates. The laminate consists of layers of structural and piezoelectric materials with arbitrary configuration. An analytical model based on the classical lamination theory is developed. Closed form solutions are obtained for elliptical laminates with clamped boundary. The sensitivity of this piezoelectric structure is evaluated from the relation between the electrical output and the mechanical loading. The sensitivity becomes zero if the aspect ratio of the elliptical laminate is unity. The function of actuation is also studied. It is found that the electric field cannot actuate deformation of the laminate if the piezoelectric loads are uniform. However, if a quadratic polarization profile of piezoelectric layers is arranged, closed form solutions of displacement field can be obtained. The results of the present study are very useful for the design of laminated piezoelectric sensors and actuators.

REFERENCES

1. Lee, C. K. 1989. "Laminated Piezopolymer Plates for Torsion and Bending Sensors and Actuators," *Journal of Acoustical Society of Am*erica, Vol. 85, pp. 2432-2439.
2. Crawley, E. F. and E. H. Anderson. 1990. "Detailed Models of Piezoceramic Actuation of Beams," *Journal of Intelligent Material Systems and Structures*, Vol. 1, pp. 4-25.
3. Lee, S. -W. R. and C. T. Sun. 1995. "Bending/Twisting/Shearing Actuation and Sensing of Laminated Composite Beams with Piezopolymer Film," *Intelligent Materials and Systems*, P. Vincenzini, ed., Techna, Faenza, Italy, pp. 137-148.
4. Whitney, J. M. 1987. *Structural Analysis of Laminated Anisotropic Plates*, Technomic Publishing Co., Lancaster, PA, pp. 17-40.
5. Lee, S. -W. R. and C. T. Sun. 1995. "On the Apparent Bending Isotropy in Clamped Elliptic Laminated Plates," *Journal of Composite Materials*, Vol. 29, pp. 1601-1620.

STRUCTURAL VIBRATION SUPPRESSION IN LINEAR FEEDBACK CONTROL WITH ADAPTIVE GYROSCOPIC DAMPER SYSTEM

Atsuo Kobori, Satoru Ozawa, Hiroshi Furuya

ABSTRACT

Active control for the adaptive gyroscopic damper system which simulates a control law for the control moment gyro was proposed to suppress structural vibrations. The controller was designed to induce the control moment to the gimbal of the adaptive gyroscopic damper system by the linear feedback of the modal velocity of the structure, as is similar to the control moment gyro. The feedback gain of the controller was determined in terms of the gyro parameters so as to maximize the modal damping ratios. The results of the numerical simulations showed the improvement in performance and the limitation for suppressing structural vibrations with the adaptive gyroscopic damper system by the controller based on the control moment gyro.

INTRODUCTION

This paper investigates the possibility of the adaptive gyroscopic damper system by a linear feedback control law for improvement of performance to suppress structural vibrations actively.

The adaptive gyroscopic damper system (AGS) was proposed as the extension of the conventional gyroscopic damper under the concept of intelligent adaptive structure systems [1]. The conventional gyroscopic damper has passive characteristics similar to a tuned mass damper (TMD). Because the conventional gyroscopic damper has one natural frequency, several applications to the ground structures have been studied to suppress the fundamental vibration mode (e.g. [2]). On the other hand, as the AGS has a property of adjusting the natural frequency of the gimbal to that of the structural system by controlling the moment of inertia around its gimbal axis, the performance for suppressing the

Department of Built Environment, Tokyo Institute of Technology, 4259 Nagatsuta, Midori-ku, Yokohama, 226-8502, JAPAN.

vibration of one-DOF system was improved [3]. In addition, by extending this property, suppression of multiple modes vibration by quasi-static control for the AGS was demonstrated [4]. Moreover, the AGS has another property that the change of the moment of inertia indirectly generates the moment to the gimbal. With this property, the feasibility for active control with the AGS without the rotational damper was demonstrated [5].

The control moment gyro (CMG) has an actuator which can generate the control moment to the gimbal. It has been widely studied for active vibration suppression of structural systems because of its high performance for suppressing vibrations [6-8]. Thus, the AGS is expected to be able to improve the performance of active vibration suppression by simulating the CMG.

In this paper, active control for the adaptive gyroscopic damper system which simulates the control law for the control moment gyro is studied. The controller is derived from comparing the equation of motion of the AGS with that of the CMG using the modal velocity feedback of the structure at first. Then the feedback gain of the modal velocity is determined through maximizing modal damping ratios. Finally, the performance and the limitation for suppressing structural vibrations by the controller with the AGS are discussed through numerical simulations.

SYSTEM MODEL

The AGS can control the moment of inertia around its gimbal axis by changing the distance from the gimbal axis to appendage mass with actuators as shown in Fig. 1. The equation of motion for the AGS is derived by considering the time derivatives on the moment of inertia. The equilibrium equation for the derivative of the angular momentum becomes

$$\frac{d}{dt}(I_g\dot{\phi}) = -k_g\phi - c_g\dot{\phi} \tag{1}$$

where I_g, c_g, k_g, and ϕ are the moment of inertia, the damping coefficient, the spring constant, and the gimbal angle, respectively. From Eq.(1), the equation of motion for the AGS is derived as following.

$$I_g\ddot{\phi} + (c_g + \dot{I}_g)\dot{\phi} + k_g\phi = 0 \tag{2}$$

Because I_g is a time variable, Eq.(2) indicates that the vibration properties are determined by I_g and $\dot{I}_g$.

The flexible structure model with the AGS used in this paper is shown in Fig. 2. The cantilever beam equipped with the AGS at the tip is considered for the model. It is assumed that signals from the structure and the gimbal of the AGS are measured by sensors. The change of the moment of inertia, ΔI_g, is determined from these signals through the controller.

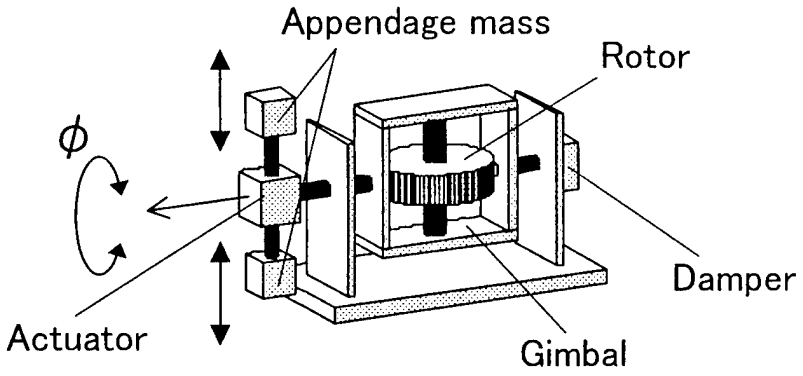


Fig.1 Concept of adaptive gyroscopic damper system

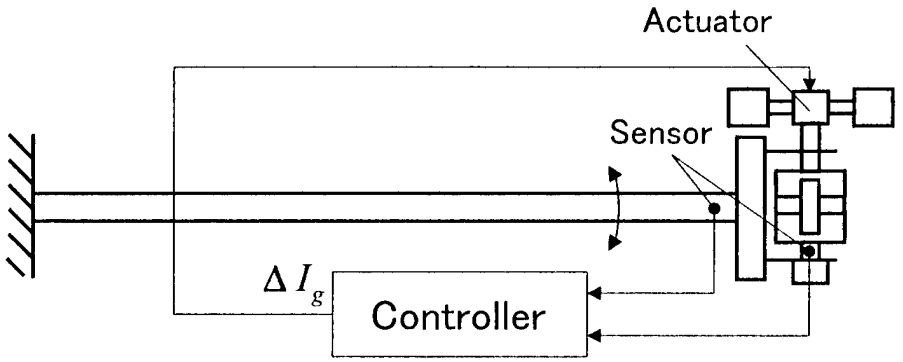


Fig. 2 Flexible structure model with AGS

CONTROL LAW

The control law for the moment of inertia is determined so that the control moment to the gimbal is induced by the linear feedback law for the CMG. The equations of motion for the first mode of the structure and the AGS are described as (see [4])

$$m_1\ddot{q}_1 + c_1\dot{\phi} + k_1 q_1 = 0 \tag{3}$$

$$(I_{g0} + \Delta I_g)\ddot{\phi} - c_1\dot{q}_1 + (c_g + \dot{\Delta I_g})\dot{\phi} + k_g\phi = 0 \tag{4}$$

where m_1, k_1, q_1, c_1, and I_{g0} are the modal mass, the modal stiffness, the modal displacement, the gyroscopic coefficient, and the initial value of the moment of inertia, respectively. The structural damping is considered as enough small to be neglected.

Alternatively, the equations of motion for the structure and the CMG controlled by the linear velocity feedback law are derived from $\Delta I_g = \dot{\Delta I_g} = 0$ and adding the feedback of the velocity of the structure, $-g\dot{q}$, in Eq.(4) as

$$m_1\ddot{q}_1 + c_1\dot{\phi} + k_1 q_1 = 0 \tag{5}$$

$$I_{g0}\ddot{\phi} - (c_1 + g)\dot{q}_1 + c_g\dot{\phi} + k_g\phi = 0 \tag{6}$$

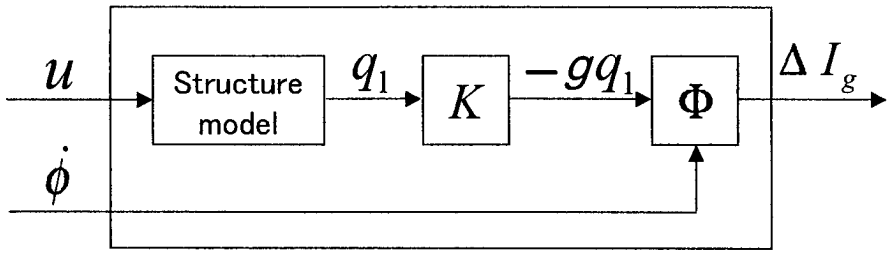


Fig. 3 Controller for moment of inertia

where g is the feedback gain.

The following relation is obtained from comparing Eq.(4) with Eq.(6).

$$\Delta I_g \ddot{\phi} + \Delta \dot{I}_g \dot{\phi} = -g\dot{q}_1 \tag{7}$$

Thus, the control law for the moment of inertia is derived as

$$\Delta I_g = \frac{1}{\dot{\phi}} \int_0^t -g\dot{q}_1 \, dt = -g\frac{q_1}{\dot{\phi}} \tag{8}$$

The controller for the moment of inertia is expressed as shown in Fig. 3. The displacement of the structure, u, and the angular velocity of the gimbal, $\dot{\phi}$, are measured by the sensors. The modal displacement, q_1, is obtained from u. Finally, ΔI_g is determined from Eq.(8) by using q_1 and $\dot{\phi}$.

DESIGN OF GYRO PARAMETERS

The damping coefficient and the natural frequency of the gimbal are designed for suppressing the structural vibration effectively. They are determined by maximizing the modal damping ratios. Thus, the feedback gain is expressed as a function with respect to the damping ratio which is a nondimensional parameter of the damping coefficient. Following analysis of the parameters is performed by the approach based on [8].

The characteristic equation of the system derived from Eqs.(5), (6) is

$$s^4 + 2\zeta_g\omega_g s^3 + \left({\omega_1}^2 + {\omega_g}^2 + \frac{c_1(c_1+g)}{m_1 I_{g0}}\right) s^2 + 2\zeta_g\omega_g{\omega_1}^2 s + {\omega_1}^2{\omega_g}^2 = 0 \tag{9}$$

where $\omega_1 = \sqrt{k_1/m_1}$, $\omega_g = \sqrt{k_g/I_{g0}}$, $\zeta_g = c_g/2I_{g0}\omega_g$.

Assuming that the solutions of Eq.(9) are expressed as

$$s_n = -\alpha_n \pm ip_n \ (n = 1, \ 2) \tag{10}$$

the modal damping ratios become

$$\zeta_n = \alpha_n / \sqrt{{\alpha_n}^2 + {p_n}^2} \tag{11}$$

The optimal solutions are derived by maximizing these modal damping ratios as

$$\gamma_T = 1 \tag{12}$$

$$(\zeta_g)_T = \sqrt{\frac{c_1(c_1+g)}{m_1 I_{g0}{\omega_g}^2}} = \sqrt{G + \frac{c_1 g}{m_1 I_{g0}{\omega_g}^2}} = \sqrt{G\left(1+\frac{g}{c_1}\right)} \tag{13}$$

where $\gamma_T = \omega_g/\omega_1$, and $G(= {c_1}^2/m_1 I_{g0}{\omega_g}^2)$ is a nondimensional parameter which dominates the effect of gyroscopic moment.

The maximum modal damping ratio is derived as a monotone increasing function (14) with respect to $(\zeta_g)_T$.

$$\zeta_1 = \zeta_2 = \sqrt{\frac{1}{8}\left(4 + {(\zeta_g)_T}^2 - \sqrt{\left(4+{(\zeta_g)_T}^2\right)^2 - 16{(\zeta_g)_T}^2}\right)} \tag{14}$$

Thus, the maximum $\zeta_1(=\zeta_2)$ can be increased by the increase of $(\zeta_g)_T$ and the corresponding value of g .

As a result of the analysis, the design of gyro parameters can be performed as the following procedures. At first, the spring constant, k_g, and the initial value of the moment of inertia, I_{g0} are determined so that the natural frequency of the gimbal is equal to that of the first mode of structure. Next, the damping ratio of the damper, $\zeta_g(=(\zeta_g)_T)$, is determined so that the modal damping ratio satisfies a required damping. After that, the feedback gain, g, is given by

$$g = \frac{c_1}{G}({(\zeta_g)_T}^2 - G) \tag{15}$$

Because ζ_g is in proportion to c_g, $(\zeta_g)_T$ has to be determined by taking into account c_g.

NUMERICAL EXAMPLES

Conditions for Parameters

The AGS can enlarge the modal damping ratios from that of the conventional gyroscopic damper by increasing $(\zeta_g)_T$ and corresponding g. When $(\zeta_g)_T$ is determined as A times that of the conventional gyroscopic damper, g is obtained from Eq.(15) as

$$g = c_1(A^2 - 1) \tag{16}$$

The moment of inertia is supposed to be controlled quickly enough to respond to the first mode vibration of the structure. However, the change of the moment of inertia has to be within a certain range. Assume the upper and lower limit of the moment of inertia are BI_0 and I_0/B, then the range of ΔI_g is set to be

$$-\left(1-\frac{1}{B}\right) I_{g0} \;\leq\; \Delta I_g \;\leq\; (B-1) I_{g0} \tag{17}$$

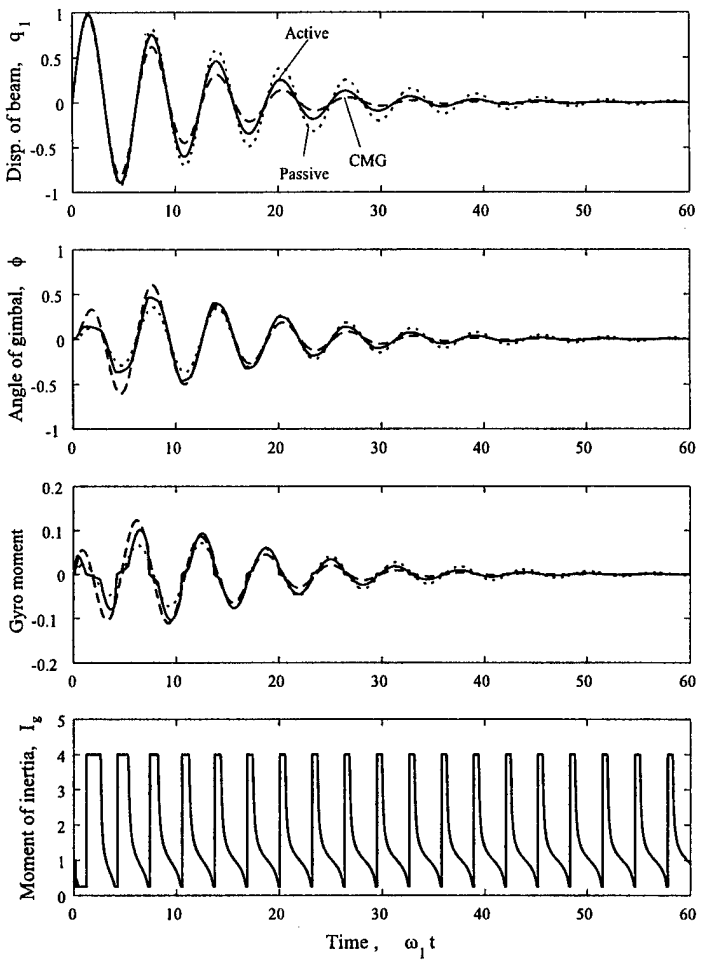


Fig.4 Time domain histories of vibrations with active AGS

Other structural properties are assumed as $m_1 = k_1 = I_{g0} = k_g = 1$, and $G = 0.04$ to simplify the simulations. Initial conditions are supposed that the gimbal angle, ϕ, is equal to zero and the non-zero velocity is given to the first mode vibration of the structure.

Results and Discussion

TIME DOMAIN HISTORIES OF VIBRATIONS

The time domain histories for $A = 1.7$ and $B = 4$ are indicated in Fig. 4. In this figure, the solid line (Active) indicates the time histories of the system where the moment of inertia is controlled by the control low. The broken line (CMG) indicates the time histories of the system where the AGS can induce the control moment equivalent to the CMG without the restriction of ΔI_g. The dotted line (Passive) indicates the time histories of the system where the AGS is equivalent to the conventional gyroscopic damper without control.

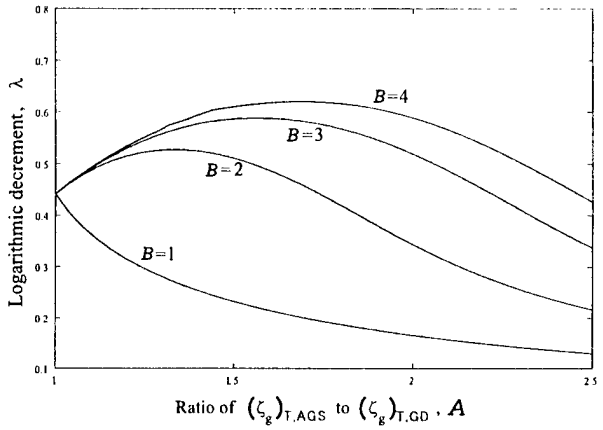


Fig.5 Logarithmic decrement due to change of A

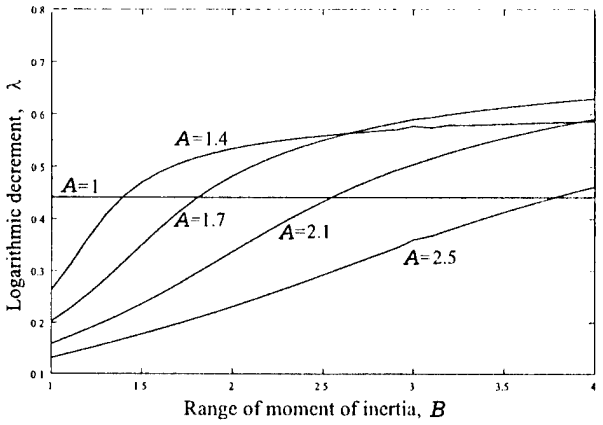


Fig.6 Logarithmic decrement due to change of B

The logarithmic decrement, λ, is employed to evaluate the effect on suppressing structural vibrations with the AGS. The averages of λ for 'Active', 'CMG', and 'Passive' through the time [0,60] are obtained as 0.630, 0.852, 0.441, respectively. Therefore, the performance of the AGS based on the CMG is improved as compared with the conventional passive gyroscopic damper.

EFFECTS OF PARAMETERS

The effects of A and B on λ are investigated to examine the performance of the AGS in Fig. 5 and 6. In Fig. 5, though λ descends as A increases for $B = 1$, the maximum values of λ exist and give the optimal values of A for B =2, 3, and 4. In Fig. 6, λ is constant for $A = 1$ because $g = 0$ from Eq.(16). For $A > 1$, λ monotonicaly ascends and gets closed to the CMG as B increases. Therefore, it is shown that the performance of damping improves as the range of the moment of inertia becomes larger.

CONCLUSIONS

The Active control for the adaptive gyroscopic damper system (AGS) based on the control moment gyro to suppress the vibrations of flexible structures was investigated. The control law for the moment of inertia was derived as the feedback of the modal displacement of the structure and the angular velocity of the gimbal. Through maximizing the modal damping ratios, the feedback gain of the controller was determined as the function of the damping ratio. The numerical simulations showed the improvement in the performance and the limitation depending on the range of the moment of inertia by the controller based on the control moment gyro.

REFERENCES

1. Furuya, H., Takahashi, T., and Ohmachi, T. 1998. "Concept of Adaptive Gyroscopic Damper and Vibration Suppression of Flexible Structures," *8th International Conference on Adaptive Structures and Technologies, Wakayama, Oct. 29-31, 1997*, eds. Y. Murotsu, C. A. Rogers, P. Santini, and H. Okubo, Technomic Publishing, pp. 247-254.
2. Nishihara, O. and Matsuhisa, H. 1996. "Design Optimization of Passive Gyroscopic Damper (Stability Degree Maximization)" Trans. Jpn. Soc. Mec. Eng., Vol. 62, No. 600, C, pp. 150-158.
3. Furuya, H., Takahashi, T., and Ohmachi, T. 1998. "Pseudo Feedback Control of Adaptive Gyroscopic Damper for Vibration Suppression," *39th AIAA/ASME/ASCE/AHS/ASC Structural Dynamics and Material Conference*, AIAA 98-1796, Long Beach, CA, April 20-23, pp. 830-834.
4. Kobori, A. and Furuya, H. 2000. "Vibration Suppression of Flexible Structures with Adaptive Gyroscopic System" Trans. Jpn. Soc. Mec. Eng., Vol. 66, No. 649, C, pp. 98-103.
5. Furuya, H. and Kobori, A. 1999. "Suppression of Multiple Modes Vibration of Flexible Structures with Adaptive Gyroscopic Damper System," *10th International Conference on Adaptive Structures and Technologies, Paris, Oct. 13-15, 1999*, eds. R. Ohayon, and M. Bernadou, Technomic Publishing, pp. 127-134,
6. Aubrun, J.N. and Margulies, G. 1979. "Gyrodampers for Large Space Structures," NASA CR159171.
7. Kazao, Y., Takahara, K., Yamada, M. and Sakamoto, S. 1992 "Active Vibration Control of a Structure Using Gyrostabilizers," *1st Int. Conf. on Motion and Vibration Control*, pp. 158-163.
8. Yang, Li-Farn, Mikulas, Jr., M.M., Park, K.C., and Su. R. 1995. "Slewing Maneuvers and Vibration Control of Space Structures by Feedforward/Feedback Moment-Gyro Controls," Trans. ASME, J. Dyn. Syst. Meas. Control, 117, pp.343-351.
9. Yu, Y., Matsunaga, T., and Ohkami, Y. 1997. "Displacement feedback Control of Proof-Mass Actuators for Vibration Suppression," Trans. Jpn. Soc. Mec. Eng., Vol. 63, No. 613, C, pp. 79-86.

A SIMPLE FINITE ELEMENT FOR SANDWICH SHELLS OF REVOLUTION WITH PIEZOELECTRIC TRANSVERSE SHEAR ACTUATOR

Ayech Benjeddou,[1] Valérie Gorge,[1] Roger Ohayon[1]

ABSTRACT

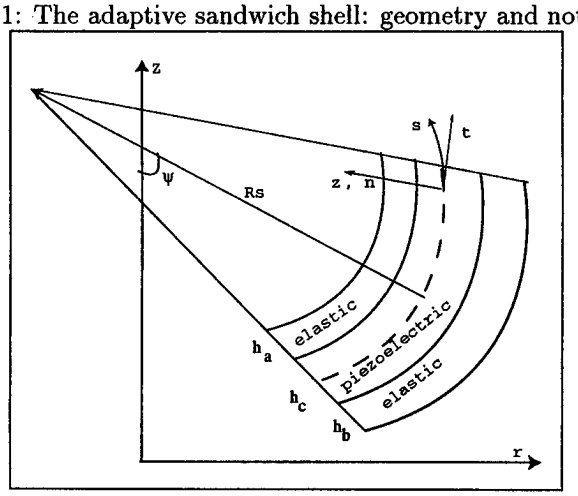
This work presents, for the first time, a finite element formulation for an adaptive sandwich shell of revolution that uses the shear actuation mechanism based on the transverse shear mode of piezoelectric materials. The theoretical model assumes the first-order shear deformation theory for each layer and enforces the displacement continuity conditions at the sandwich interfaces. The finite element discretization uses Fourier series decomposition through the shell circumference and linear Lagrange interpolation along its meridian for all variables. This results in a simple piezoelectric sandwich shell with nine mechanical and one electrical degrees of freedom per node. The element was validated through vibrations analysis of a short-circuited piezoceramic spherical shell.

INTRODUCTION

Application of a voltage difference on covering electrodes perpendicular to the initial poling direction of an embedded piezoelectric material induces transverse shear strains that bend the host structure. Conversely bending of the latter induces a difference of potentials on the same electrodes due to the transverse shear deformation of the embedded piezoelectric material. This is the so-called piezoelectric shear actuation/sensing mechanism. Recent bibliography [1], literature review [2] and survey [3] indicate that this mechanism was not investigated for shell structures. However, recently, theoretical formulations and analyses of arbitrary [4] and axisymmetric [5] piezoelectric adaptive shells with shear actuation have been presented. Corresponding numerical formulations and analyses are, thus, still to be made. Therefore, it is the aim of this work to present a finite element formulation of an adaptive sandwich shell of revolution that uses the transverse shear actuation/sensing mechanism. Hence, in the following, brief descriptions of theoretical and finite element models are presented. Then, the resulting piezoelectric sandwich shell element is validated through vibrations analysis of piezoceramic spherical shells.

[1]Structural Mechanics and Coupled Systems Laboratory, CNAM, 2 rue Conté, 75003 Paris, France

Figure 1: The adaptive sandwich shell: geometry and notations



PIEZOELECTRIC SANDWICH SHELL FORMULATION

The theoretical formulation of the piezoelectric sandwich shell, shown in figure 1, is based on the following main assumptions:

- The sandwich shell thickness is very small compared to the smallest radius of curvature.
- The deflection w of all layers is the same through the shell thickness.
- All layers are resisting membrane, bending and transverse shear stresses. However, the through thickness normal stress component is considered negligible.
- Perfect bonding occurs between all layers
- The facings are linearly elastic and can have different properties.
- The core is linearly piezoelectric and initially poled along the meridian, but fully electroded on its inner and outer skins. The electric potential is assumed linear through the core thickness.

Following above assumptions, the mechanical displacements in each layer are considered through thickness linear. They are then made continuous at the sandwich interfaces. Following [6], the mean and relative displacements and rotations of the face layers are retained as the mechanical independent variables. They follow the following notations,

$$\bar{x} = (x^a + x^b)/2 \quad , \quad \tilde{x} = x^a - x^b \tag{1}$$

where $x = u, v, \beta, \beta_\theta$, representing either of the in-plane displacements and bending rotations of the inner (a) and outer (b) faces. Taking into account (1), the displacements in the f-th face can be written as [5]

$$\begin{aligned} \underline{u}^f &= \left(\bar{u} \pm \tfrac{1}{2}\tilde{u}\right) + (z - z_f)\left(\bar{\beta} \pm \tfrac{1}{2}\tilde{\beta}\right) \\ \underline{v}^f &= \left(\bar{v} \pm \tfrac{1}{2}\tilde{v}\right) + (z - z_f)\left(\bar{\beta}_\theta \pm \tfrac{1}{2}\tilde{\beta}_\theta\right) \\ \underline{w}^f &= w \end{aligned} \tag{2}$$

where the '+' sign is for the inner face ($f = a$) and the '–' for the outer one ($f = b$).

The core displacements can also be written in terms of mean and relative variables,

$$\begin{aligned} \underline{u}^c &= \left(\bar{u} - \tfrac{\bar{h}}{4}\bar{\beta} - \tfrac{\tilde{h}}{4}\tilde{\beta}\right) + \tfrac{z}{h_c}\left(\tilde{u} - \bar{h}\bar{\beta} - \tfrac{\tilde{h}}{4}\tilde{\beta}\right) \\ \underline{v}^c &= \left(\bar{v} - \tfrac{\bar{h}}{4}\bar{\beta}_\theta - \tfrac{\tilde{h}}{4}\tilde{\beta}_\theta\right) + \tfrac{z}{h_c}\left(\tilde{v} - \bar{h}\bar{\beta}_\theta - \tfrac{\tilde{h}}{4}\tilde{\beta}_\theta\right) \\ \underline{w}^c &= w \end{aligned} \tag{3}$$

where $\bar{h}$ and $\tilde{h}$ are the mean and relative face thicknesses defined as in (1).

Applying the usual strain-displacement relations to equation (2), leads to the following f-th face in-plane and transverse shear strains, respectively,

$$\{\varepsilon^f\} = \left(\{\bar{e}\} \pm \tfrac{1}{2}\{\tilde{e}\}\right) + (z - z_f)\left(\{\bar{\chi}\} \pm \tfrac{1}{2}\{\tilde{\chi}\}\right) \quad , \quad \{\gamma^f\} = \{\bar{\gamma}\} \pm \tfrac{1}{2}\{\tilde{\gamma}\} \tag{4}$$

where mean and relative membrane, bending and shear strain vectors are given in [5].

Similarly, using equations (3) and (1) in the usual strain-displacement relations, leads to the following core in-plane and transverse shear strains, respectively,

$$\{\varepsilon^c\} = \left(\{\bar{e}\} - \tfrac{\tilde{h}}{4}\{\bar{\chi}\} - \tfrac{\bar{h}}{4}\{\tilde{\chi}\}\right) + z\left(\tfrac{1}{h_c}\{\tilde{e}\} - \tfrac{\bar{h}}{h_c}\{\bar{\chi}\} - \tfrac{\tilde{h}}{4h_c}\{\tilde{\chi}\}\right) \quad , \quad \{\gamma^c\} = \{\bar{\gamma}^c\} + \{\tilde{\gamma}^c\} \tag{5}$$

where the mean and relative transverse shear strains of the core can also be found in [5].

Following the last assumption, the electric potential in the core can be written as,

$$\varphi = \bar{\varphi} + z\tfrac{\tilde{\varphi}}{h_c} \tag{6}$$

where $\bar{\varphi}$ and $\tilde{\varphi}$ follow notations (1) for the prescribed or generated potentials φ^+ and φ^- on the inner and the outer skins of the core layer.

Introducing relations (6) in the usual electric field-potential one, leads to the following expressions for the in-plane and transverse electric field components in the piezoelectric core,

$$\{E_p\} = \{\bar{E}\} + z\{\tilde{E}\} \quad , \quad E_z = -\tfrac{\tilde{\varphi}}{h_c} \tag{7}$$

where $< E_p >=< E_s, E_\theta >$, $< \bar{E} >=< \bar{E}_s, \bar{E}_\theta >$, $< \tilde{E} >=< \tilde{E}_s, \tilde{E}_\theta >$ and $\bar{E}_s = -\bar{\varphi}_{,s}$; $\bar{E}_\theta = -\frac{1}{r}\bar{\varphi}_{,\theta}$; $\tilde{E}_s = -\frac{1}{h_c}\tilde{\varphi}_{,s}$; $\tilde{E}_\theta = -\frac{1}{h_c r}\tilde{\varphi}_{,\theta}$;

The zero normal stress reduced, converse in-plane and transverse piezoelectric constitutive equations of the core are, respectively,

$$\{\sigma^c\} = [Q^c]\{\varepsilon^c\} - [e_p]^T\{E_p\} \quad , \quad \{\tau^c\} = [Q_s^c]\{\gamma^c\} - \{e_s\}E_z \tag{8}$$

where in-plane and transverse elastic and piezoelectric matrices are given in [5].

Also the zero normal stress reduced, direct piezoelectric in-plane and transverse constitutive equations of the core are, respectively,

$$\{D_p\} = [e_p]\{\varepsilon^c\} + [\epsilon_p]\{E_p\} \quad , \quad D_z =< e_s > \{\gamma^c\} + \epsilon_{zz}E_z \tag{9}$$

The constitutive equations of the faces are deduced from those of the core (8) by substituting the superscript c with f and vanishing piezoelectric constants.

For admissible mechanical displacements $\delta\bar{u}$, $\delta\bar{v}$, δw, $\delta\bar{\beta}$, $\delta\bar{\beta}_\theta$, $\delta\tilde{u}$, $\delta\tilde{v}$, $\delta\tilde{\beta}$, $\delta\tilde{\beta}_\theta$ and electric voltage differences $\delta\bar{\varphi}$ and $\delta\tilde{\varphi}$, the extended d'Alembert principle can be written as,

$$\sum_{i=a}^{c}\left(\delta W_{\text{int}}^i - \delta W_{\text{in}}^i - \delta W_{\text{ext}}^i\right) = 0 \tag{10}$$

where δW^i_{int}, δW^i_{in}, δW^i_{ext} are the i-th layer internal, inertial and external virtual works.

Since the electromechanical coupling is present only via the internal work of the piezoelectric core and due to space limitation, only this quantity will be detailed here after. The other works follow closely the procedure presented in [6]. Hence, the internal virtual work of the piezoelectric core can be written as,

$$\delta W^c_{\text{int}} = \int_{\Omega^c} (<\delta\varepsilon^c> \{\sigma^c\} + <\delta\gamma^c> \{\tau^c\} - <\delta E_p> \{D_p\} - \delta E_z D_z)\ d\Omega^c \tag{11}$$

where Ω^c is the core volume. Substituting the constitutive equations (8, 9) in (11), δW^c_{int} can be decomposed into,

$$\delta W^c_{\text{int}} = \delta W^{cm} - \delta W^p - \delta W^e \tag{12}$$

where the superscripts m, p and e state for mechanical, piezoelectric and electric contributions to the virtual internal work of the core. The mechanical contribution can be added to those of the faces so that attention is now focused on the last two terms of (12). Hence, the piezoelectric virtual work is,

$$\delta W^p = \int_{\Omega^c} \left(<\delta\varepsilon^c> [e_p]^T \{E_p\} + <\delta\gamma^c> \{e_s\} E_z + <\delta E_p> [e_p] \{\varepsilon^c\} + \delta E_z <e_s> \{\gamma^c\}\right) d\Omega^c \tag{13}$$

It is worthy to notice, from (13), that the electromechanical coupling is between either the in-plane or transverse components. Hence, for the practical case of uniform potentials, equation (13) reduces to,

$$\delta W^p = \int_{\Omega^c} (\delta\gamma^c_{sz} e_{35} E_z + \delta E_z e_{35} \gamma^c_{sz})\ d\Omega^c \tag{14}$$

where e_{35} is the shear piezoelectric constant. The electromechanical coupling is now between the transverse component of the electric field and the transverse shear strain in $s - z$ plane only. For an actuation problem, the last term in (14) vanishes. Hence, substituting E_z and γ^c_{sz} with their expressions and integrating through thickness, equation (14) reduces to,

$$\delta W^p = \int_{A^c} \left(\frac{\delta\tilde{u}}{h_c} + \frac{\delta\bar{u}}{R_s} + \frac{\partial\delta w}{\partial s}\right) \bar{e}_{15} \tilde{\varphi}\ dA^c \tag{15}$$

where A^c is the core area. This expression was first presented in [5]. It indicates that the piezoelectric action, defined by this equation, depends on the piezoelectric shear constant, the applied voltage difference and the shell curvature. It proves also the importance of the transverse shear resulting from the sliding of the elastic face against the piezoelectric core, represented by the first term in (15). The presence of the shell meridian curvature shows that the pin-force model should be handled with great care if retained to represent the piezoelectric effect. Equation (15) also demonstrates the usefulness of using the mean and relative displacements as the model independent variables.

The virtual piezoelectric work of the core (13) can also be decomposed into mean and relative components using equations (5.2) and (7.1). Thus,

$$\delta W^p = (\delta\bar{W}_e + \delta\tilde{W}_e) + (\delta\bar{W}_\chi + \delta\tilde{W}_\chi + \delta\bar{\tilde{W}}_\chi + \delta\tilde{\bar{W}}_\chi) + (\delta\bar{W}_{\gamma z} + \delta\tilde{W}_{\gamma z}) \tag{16}$$

where e, χ and γ define the membrane, curvature and shear contributions. For shortness, their expressions will not be given here. However, it is worthy to recall that, for uniform potentials, expression (16) reduces to the shear contribution (14) only. Notice also that the coupling between mean and relative contributions is present only in the bending work, which reduces to these contributions for faces having the same thickness.

The electric contribution of the piezoelectric virtual work has the following expression,

$$\delta W^e = \int_{\Omega^c} (<\delta E_p> [\epsilon_p]\{E_p\} + \delta E_z \epsilon_{zz} E_z)\ d\Omega^c \tag{17}$$

where $[\epsilon_p]$ and ϵ_{zz} are the dielectric in-plane matrix and transverse constant. This contribution reduces to its last term for uniform potentials but vanishes completely for an actuation problem, i.e. for given potentials. The decomposition into mean and relative components of the first term in (17), using equation (7.1), leads to,

$$\delta W^e = (\delta \bar{W}^e + \delta \tilde{W}^e) + \delta W_z^e \tag{18}$$

Again, for uniform potentials, δW^e reduces to δW_z^e.

FINITE ELEMENT DISCRETIZATION

Mean and relative faces displacements and rotations, shell deflection and the core mean and relative electric voltage differences are first decomposed using Fourier series through the circumference, then interpolated using linear Lagrange polynomials along the meridian. Only symmetric Fourier series components are retained since it is well known [6] that, for free vibrations, symmetric and antisymmetric resulting problems have similar eigenvalues but opposite sign eigenvectors. Also for static analysis, a unique problem can be solved but with symmetric and antisymmetric load vectors.

Along the meridian, interpolation takes the following form,

$$X = N_1 X_1 + N_2 X_2 \tag{19}$$

where $N_1 = 1 - \frac{s}{L}$, $N_2 = 1 + \frac{s}{L}$. L is the element length and s its meridian coordinate. X is either of the model independent variables which are $\bar{u}$, $\bar{v}$, w, $\bar{\beta}$, $\bar{\beta}_\theta$, $\bar{\varphi}$, $\tilde{u}$, $\tilde{v}$, $\tilde{\beta}$, $\tilde{\beta}_\theta$, $\bar{\varphi}$, $\tilde{\varphi}$. X_1, X_2 are their corresponding nodal degrees of freedom (dof). Since all quantities are decomposed into mean and relative components, these are discretized separately using reduced dof vectors. The resulting matrices and vectors are then assembled to get the order of the whole dof vector,

$$<d> = <\bar{u}_1\ \bar{v}_1\ w_1\ \bar{\beta}_1\ \bar{\beta}_{\theta 1}\ \bar{\varphi}_1 \vdots \tilde{u}_1\ \tilde{v}_1\ \tilde{\beta}_1\ \tilde{\beta}_{\theta 1}\ \tilde{\varphi}_1 \mid \bar{u}_2\ \bar{v}_2\ w_2\ \bar{\beta}_2\ \bar{\beta}_{\theta 2}\ \bar{\varphi}_2 \vdots \tilde{u}_2\ \tilde{v}_2\ \tilde{\beta}_2\ \tilde{\beta}_{\theta 2}\ \tilde{\varphi}_2> \tag{20}$$

The order of this vector reduces from 22 to 20 for uniform potentials.

Geometric interpolation of the meridian follows also equation (19). That is, the elements are geometrically conic. It is known that this contributes to attenuate membrane locking for low order elements since the meridian curvature vanishes.

Discretization of equation (12), leads to the following element stiffness matrix

$$[k_e] = [k^{\mathrm{m}}] - [k^{\mathrm{p}}] - [k^{\mathrm{e}}] \tag{21}$$

The mechanical shell stiffness is the sum of the membrane, bending and shear ones,

$$[k^{\mathrm{m}}] = [k_e^{\mathrm{m}}] + [k_{\chi e}^{\mathrm{m}}] + [k_{\chi}^{\mathrm{m}}] + [k_{\gamma}^{\mathrm{m}}] \tag{22}$$

Similarly, discretization of the piezoelectric virtual work (16) leads to,

$$[k^{\mathrm{p}}] = [k_e^p] + [k_{\chi}^p] + [k_{\gamma}^p] \tag{23}$$

The electric shell stiffness matrix comes from the discretization of (18). Hence,

$$[k^{\mathrm{e}}] = [\bar{k}^{\mathrm{e}}] + [\tilde{k}^{\mathrm{e}}] + [k_z^{\mathrm{e}}] \tag{24}$$

Recall that for uniform potentials, this matrix reduces to its last contribution.

The mass matrix is the result of the discretization of the virtual inertial work and is the sum of the translation, rotation and their coupling,

$$[m_e] = [m_u] + [m_\beta] + [m_{u\beta}] \tag{25}$$

Discretization of the virtual work of external loads gives the element force vector, which could be the sum of mechanical and electrical loads,

$$\{f_e\} = \{f_e^m\} + \{f_e^e\} \tag{26}$$

All previous element rigidity and mass matrices and load vectors are written in the curvilinear coordinates. Hence, they should be transferred to the global cylindrical one. This is achieved through the transformation matrix $[P]$ as follows,

$$[K_e] = [P]^T[k_e][P] \quad , \quad [M_e] = [P^T[m_e][P] \quad , \quad \{F_e\} = [P]^T\{f_e\} \tag{27}$$

Assembling these element matrices and vector, according to (10), leads to,

$$[M]\{\ddot{D}\} + [K]\{D\} = \{F\} \tag{28}$$

where $\{D\}$ is the whole dof vector.

For validation purpose, only the following harmonic eigenvalue problem is to be solved,

$$\left(\begin{bmatrix} K_{uu} & K_{u\varphi} \\ K_{u\varphi}^T & K_{\varphi\varphi} \end{bmatrix} - \omega^2 \begin{bmatrix} M & 0 \\ 0 & 0 \end{bmatrix} \right) \begin{Bmatrix} q \\ \varphi \end{Bmatrix} = \begin{Bmatrix} 0 \\ 0 \end{Bmatrix} \tag{29}$$

Prior to its solution, the electric degrees of freedom are first condensed so that only the following reduced system is solved,

$$\left(\left[K_{uu} - K_{u\varphi} K_{\varphi\varphi}^{-1} K_{u\varphi}^T \right] - \omega^2 [M] \right) \{q\} = \{0\} \tag{30}$$

The condensed electric dof are then computed from

$$\{\varphi\} = -[K_{\varphi\varphi}]^{-1} [K_{u\varphi}]^T \{q\} \tag{31}$$

It is worthy to notice that mass matrices are all evaluated analytically, whereas the rigidity ones are evaluated numerically using Gauss rules. Therefore, to avoid shear locking, present in low order shear elements, only the shear contribution is under integrated.

TABLE I: EIGENFREQUENCIES (HZ) OF A PZT-4 SPHERICAL SHELL POLARIZED ALONG ITS MERIDIAN AND SHORT-CIRCUITED. VALUES BETWEEN PARENTHESES INDICATE ERRORS (%) WITH RESPECT TO AXISYMMETRIC EIGENVALUES.

circumferencial index / meridian index	0	1	2	3	4	5	6	7
1	3594	3597	3471	-	-	-	-	-
		(0.07)	*(-3.4)*	-	-	-	-	-
2	4327	4360	4241	4115	-	-	-	-
		(0.8)	*(-2)*	*(-4.9)*	-	-	-	-
3	4644	4700	4614	4502	4386	-	-	-
		(1.2)	*(-0.7)*	*(-3.1)*	*(-5.6)*	-	-	-
4	4843	4899	4849	4759	4654	4543	-	-
		(1.2)	*(0.1)*	*(-1.7)*	*(-3.9)*	*(-6.2)*	-	-
5	4999	5045	5025	4961	4876	4775	4662	-
		(0.9)	*(0.52)*	*(-0.8)*	*(-2.5)*	*(-4.5)*	*(-6.7)*	-
6	5133	5172	5180	5136	5077	4996	4891	4773
		(0.8)	*(0.9)*	*(0.05)*	*(-1.1)*	*(-2.7)*	*(-4.7)*	*(-7)*

NUMERICAL VALIDATION

The present piezoelectric sandwich finite element has been first validated through comparison of its results with those obtained with the elastic one [6]. However, since the shear piezoelectric actuation mechanism is explored for the first time here, numerical reference values were not found in the open literature. Therefore, vibrations of a short-circuited PZT-4 spherical shell is considered to check the validity of the present finite element formulation. The spherical symmetry involves well-known eigen frequencies multiplicities [7]. That is, multiplicity is equal to the number of node lines on the sphere. Using a cylindrical coordinate system, reference [8] has shown that we are expected to repeat those eigen frequencies for variable circumferencial index of the Fourier series decomposition, i.e. they are repeated from the circumferencial index zero to the number of frequency multiplicity.

Hence, a piezoceramic spherical shell, made of PZT-4, is considered. The PZT-4 properties are: density, $\rho = 7500$ kg.m^{-3}, elastic constants, $c_{11} = 115 \times 10^9$ N.m^{-2}, $c_{22} = c_{33} = 139 \times 10^9$ N.m^{-2}, $c_{12} = c_{13} = 74.3 \times 10^9$ N.m^{-2}, $c_{23} = 77.8 \times 10^9$ N.m^{-2}, $c_{44} = 30.6 \times 10^9$ N.m^{-2}, $c_{55} = c_{66} = 25.6 \times 10^9$ N.m^{-2}, piezoelectric constants, $e_{35} = e_{26} = 12.7$ C.m^{-2}, $e_{11} = 15.1$ C.m^{-2}, $e_{12} = e_{13} = -5.2$ C.m^{-2}, dielectric constants, $\epsilon_{11} = \epsilon_{22} = 1475\ \epsilon_0$, $\epsilon_{33} = 1300\ \epsilon_0$, where the vacuum permittivity is $\epsilon_0 = 8.854 \times 10^{-12}$ F.m^{-1}. The shell is 0.5 mm thick and has a radius of 5 cm.

The multiplicity repetitiveness of the eigenfrequencies is checked through the error evaluation with respect to the axisymmetric ones. Results are presented in table I for short-circuited ($\varphi = 0$) electric boundary conditions. It is clear, from these results, that the above mentioned spherical symmetry feature is well represented by the present simple conical piezoelectric sandwich finite element within a 7 % maximum error.

CONCLUSION

A piezoelectric sandwich shell of revolution finite element has been formulated and validated. It has the originality of using the shear mode of a piezoelectric core sandwiched between two elastic layers. The piezoelectric core is assumed poled along its meridian and fully covered with electrodes on its inner and outer skins. Hence, the electromechanical coupling is mainly between transverse shear strains and transverse component of the electric field.

Since the element has no deflection derivative dof, it is particularly suited for fluid-structure coupling analyses. Hence this formulation is being extended to axisymmetric shells filled with gas for structural-acoustics problems (interior noise reduction). Viscoelastic damping has also been considered for the core so that hybrid active-passive vibration control would be possible using the present finite element. This will be the subject of an up coming paper.

REFERENCES

1. Mackerle, J. 1998."Smart materials and structures - a finite element approach: a bibliography (1996-1997)," *Modelling Simul. Sci. Eng.*, 6, pp. 293–334.
2. Saravanos, D. A., and P. R. Heyliger. 1999. "Mechanics and computational models for laminated piezoelectric beams, plates and shells," *Appl. Mech. Rev.*, 52, pp. 305–320.
3. Benjeddou, A. 2000. "Advances in piezoelectric finite element modelling of adaptive structural elements: a survey," *Comput. Struct.*, 76, pp. 347–363.
4. Benjeddou, A. 2000. "Piezoelectric transverse shear actuation of shells," presented at the 4th Int. Colloq. on Computation of shell & spatial structures, June 4–7, 2000.
5. Benjeddou, A. 2000. "Piezoelectric transverse shear actuation of shells of revolution: theoretical formulation and analysis," presented at the Europ. Congress on Computational Methods in Appl. Sci. and Engng., September 11–14, 2000.
6. Benjeddou, A. and M. A. Hamdi. 1996. "A B-spline finite element for the dynamic analysis of sandwich shells of revolution," *Engineering Computations*, 13, 241–264.
7. Hamermesh, M. 1962. *Group theory and its application to physical problems.* Dover Publishing, chapter 9, pp. 325–337.
8. Ohayon, R., and B. Nicolas-Vullierme. 1981. "An efficient shell finite element for the computation of the vibrations of fluid-structure systems of revolution," tech. report # 76, ONERA, Chatillon, France.

Transducers

MINIATURE FREE FALL SENSORS

C. K. Lee, Y. H. Hsu

ABSTRACT

This paper describes an attempt to integrate the smart structure concept to the field of high-density data storage devices including magnetic disk drives, optical disk drives, CD (compact disks), and DVD (digital versatile disks), etc. With the rapid development of the data storage industry, methodologies that can be used to sense vibrations, free-fall, and impact have been actively pursued throughout the last two decades. As data storage devices are now moving into portable applications, early detection of impact or free-fall is increasingly becoming more important. Based on this major issue, the concept of measuring the motion of the required free-fall is re-examined. In this article, it is shown that a fundamental characteristic of a free-fall motion, which is the acceleration from zero to one gravity, will be introduced to provide the warning signal for the data storage device. The design concept and the experimental result of the miniature free-fall sensor will be detailed.

1.INTRODUCTION

Almost all of the vibration sensing attempts for portable storage devices have been concentrated on detecting the impact at the instant when the portable storage device hits the ground in order to feed the impact induced signal back to the system for its protective action [1]. One of the most important protection attempts is to take the read-write head to a safe position in order to prevent catastrophic impact to the media and the read-write head which may possibly occur when the impact-induced elastic wave arrives [2]. A simple analysis can show this attempt has almost no chance of becoming successful for the data storage devices adopted in today's notebook computers or digital still cameras. Taking hard disk drives as an example, the seek time that measures the time needed for the read-write head to move 3 cm is approximately 10 msec. An impact-induced elastic wave will have a propagation speed in the range of 3000 to 5000 m/sec. This indicates that the time between the impact and the impact-induced wave is in the range of 10 to 30 μ sec. The astounding three orders of time difference clearly states that a new line of thinking must be initiated. As optical disk drives, CD/DVD, etc., have a much slower seek time, this observation certainly is applicable as well. Accelerometers have always been considered as one of the most important vibration-sensing

* Institute of Applied Mechanics, National Taiwan University, Taipei 10764, Taiwan, R.O.C.

devices due to their size, sensitivity, and cost. However, the traditional design concepts of accelerometers fail to accomplish this goal as gravity induced acceleration will always be present throughout the free fall. To accomplish the above-mentioned task, an innovative free-fall sensor developed by using characteristics of flexible structures will be presented in this paper.

2. CONCEPTS OF FREE-FALL SENSORS

The time history of free-fall motion has previously never been examined in detail. The majority of the studies on impact detection has been concentrated on detecting the information generated by the impact wave induced when the object hits the ground. It is expected that the signal detected can be sent to the system controller to provide the actions needed for system to protect itself [1]. As all design goals of today's portable devices are based on being small and fast, the impact protection issues mentioned above is becoming more and more important. As previously mentioned, as impact waves take only 10 to 30 μsec to arrive at the delicate portion of the portable device which requires the impact protection, the signal obtained after the impact occurs, is too late to allow the system to protect itself. Compared to the tenth μsec shock arrival time, even for high speed devices such as hard disk drives that have a seek speed in the range of 3 cm per 10 msec is not fast enough to escape from the damage induced by the impact. The overall strategy related to the impact detection must thus be revisited.

Considering the case where a data storage device falls from a height of one meter, the time difference between the beginning of the device falling to impact is around 450 msec which is much longer than the 10 msec seek time mentioned above. This simple calculation indicates that a free-fall sensor will have a much better chance of accomplishing the protection tasks mentioned above. The key thought of the free falling sensing introduced herein lies on the fact that the acceleration changes from rest to a gravity constant g [3]. That is, the motion of the free-fall is a kind of forcing function. A ramp function from zero to one gravity can be used to approximate the forcing action. It is with this understanding that the rising of the acceleration can be detected and where the bold attempt described in this article as free-fall was thought to be not detectable. In the following sections, the concepts of the flexible structure control will be introduced to the point accelerometer design concept to facilitate the measurement of these kinds of motions.

2.1 Free-Fall Sensor Design

To measure the kind of low frequency signal as free-fall motion, the sensor structure itself must be very flexible or its first mode frequency must be low enough. The most familiar structure which comes to mind is the bending vibration of a beam or a plate [4]. But since its first mode frequency is low, the noise from the mode will always be present. This observation is a reflection that the performance of the point is determined by the sensor structure. This is also the reason why the usable bandwidth of typical point sensors are merely 5~10% of the first mode frequency. To have enough bandwidth, the first resonant mode of a typical point sensor is often as high as say 10 kHz to several hundred kHz. This effect can be clearly observed in Fig. 1, where Channel 1 is a photonic sensor, Channel 2 is an

accelerometer, and Channel 3 is an one-dimensional cantilever plate with it first resonant mode near 10 Hz. It is evident from Fig. 1 that the accelerometer signal was contaminated by the first resonant mode. It is not until the frequency is higher than 10 Hz that the sensor response becomes acceptable. On the other hand, the low frequency response of a flexible structure is extremely good. One thing that should be noted is that the 1 Hz vibration signal generated by the one-dimensional plate still suffers from the detrimental effect of the first resonant mode (Fig. 1a). This is the reason why the usable bandwidth of a point sensor is restricted by the characteristic of the sensor structure. There does exist some noise induced from the structure natural frequency which will alter the measured input signal waveform and phase.

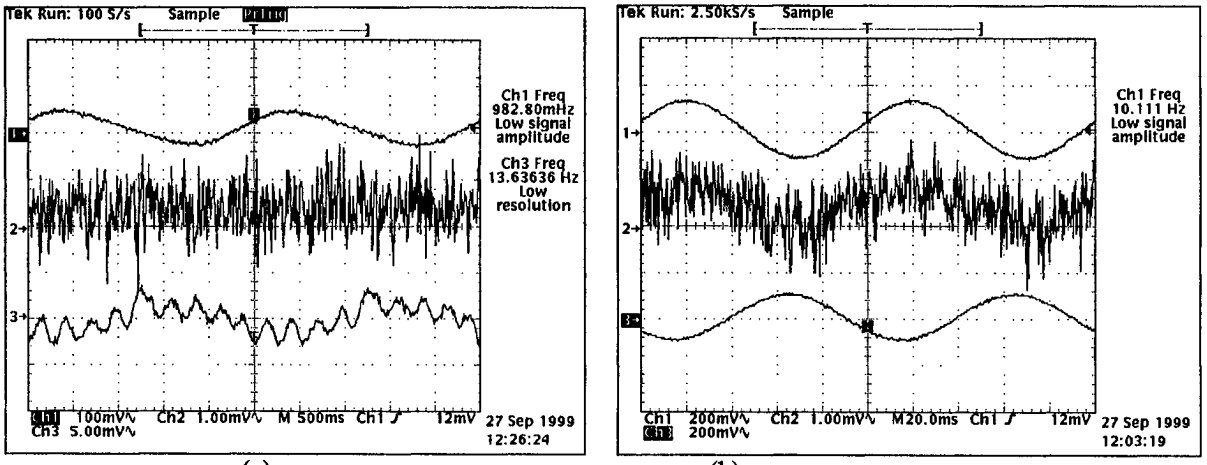


Figure 1 (a) Comparison of the time domain results from an one-dimensional cantilever plate (Ch3), a photonic sensor (Ch1), and an accelerometer (Ch2) at 10Hz (a) at 1Hz (b).

This property can easily be explained by a normal mode expansion of the structure. The following is the bending displacement of the structure [5]:

$$w(x,t)=\sum_{i=1}^{\infty} A_i(t)\Phi_i(x), \tag{1}$$

where $A_i(t)$ is the modal coordinates of the *i-th* mode, and $\Phi_i(x)$ represents the *i-th* mode shape. That is, the vibration of the structure is the combination of the mode shapes at all frequencies. The influence of the modes at different excitation frequencies can be examined by using the modal coordinates $A_i(t)$ mentioned above. As the vibrating frequency moves closer to the natural frequency, the structure vibration behaves similar to that mode. This characteristic holds true for a forced response [5] and this feature strongly influences the measurement data of free-fall motion. More specifically, once the externally applied force excites the sensor, the sensor structure characteristics will automatically kick in to influence or modify the signal generated. In other words, with the presence of the high frequency response of all of the natural modes, the signal induced by the free fall response and the system transient response will not be distinguishable. That is, the signal from the free-fall motion is distorted by the noise induced by the natural modes. The above discussions clearly states that the effect of the natural modes must be filtered out to provide a clear free fall signal free from the contamination of the modal response. It will also be shown later that the interface circuit of the free-fall sensor will influence the performance of the free-fall sensor.

2.2 Testing of Free-fall Sensors

To test the free-fall motion, the following experimental set-up (Fig. 2) was designed to measure the induced signal. A free fall sensor made by a one-dimensional plate was attached to a piece of a hard disk shaped iron block. An interface circuit was chosen for the free-fall sensor to tailor the free-fall signal generated. Letting the test specimen fall through a light switch made of a He-Ne laser and a photovaristor triggered the data taking. A resister R was chosen to form a voltage divider circuit to serve as the trigger signal for the oscilloscope. With this arrangement, the change in the photovaristor output voltage served as the reference to distinguish the signal induced from the free-fall motion signal from that of the impact signal.

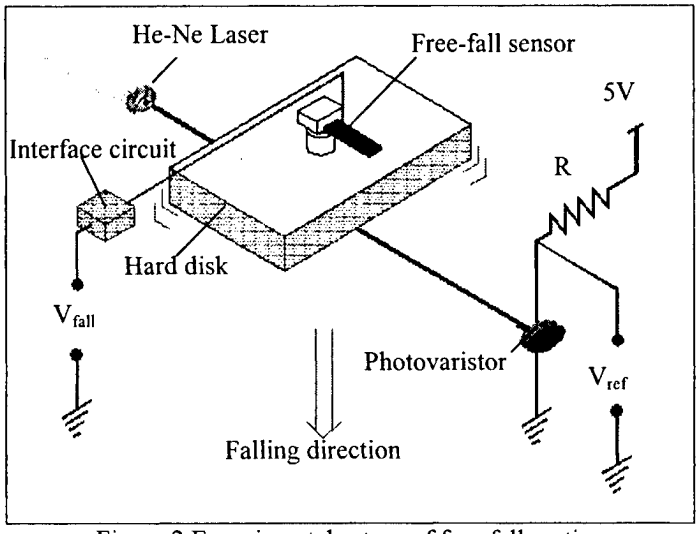


Figure 2 Experimental set-up of free-fall motion

A 50mm long, 5mm wide, and 0.01mm thick standard steel shim was set to form a one-dimensional cantilever plate, which served as the sensor structure. A uniform piezoelectric thin film was attached to this sensor structure to measure the forced response induced by the free-fall motion. The frequency of the first resonant mode of sensor was found to be around 30 Hz, which means that this sensor got excited easily by the external force. The experimental result is shown in Fig. 3, where Channel 1 was the trigger signal generated by the photovaristor with a 30% timing pre-trigger, and Channel 4 was the data measured by the PVDF sensor mounted onto the one-dimensional cantilever plate. It is obvious from Fig. 3(a) that the three force response events was detected, which in turn represents the responses induced by the beginning of the free-fall, the impact to the ground, and the bounce of the iron block. Also from Fig. 3(b), the time lag between the responses induced by the free-fall to the full transient response was about 20 ms, which corresponds to 50 to 100 Hz. As the first resonant mode was around 30 Hz, the 50 to 100 Hz external response measured will certainly be contaminated by the first mode response. This experimental data clearly demonstrates that the noise induced by the resonant mode of the sensor structure is a major hindrance for the development of the free-fall sensor as the response induced by the free fall and by the reaction of the resonant mode is not distinguishable. In other words, the signal generated was not the result of the free-fall, but from the external disturbance that will always be present such that the true free-fall response cannot be detected when it really occurs. This understanding leads to the conclusion that the

noise induced by the reaction of the structure mode must be eliminated or reduced in order to make the free-fall signal stand out.

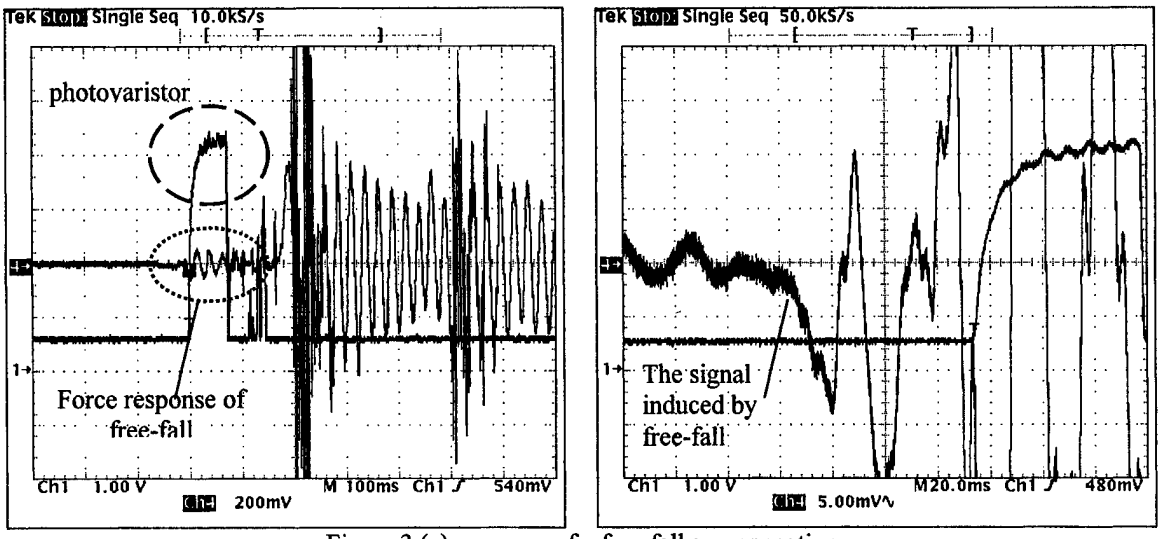
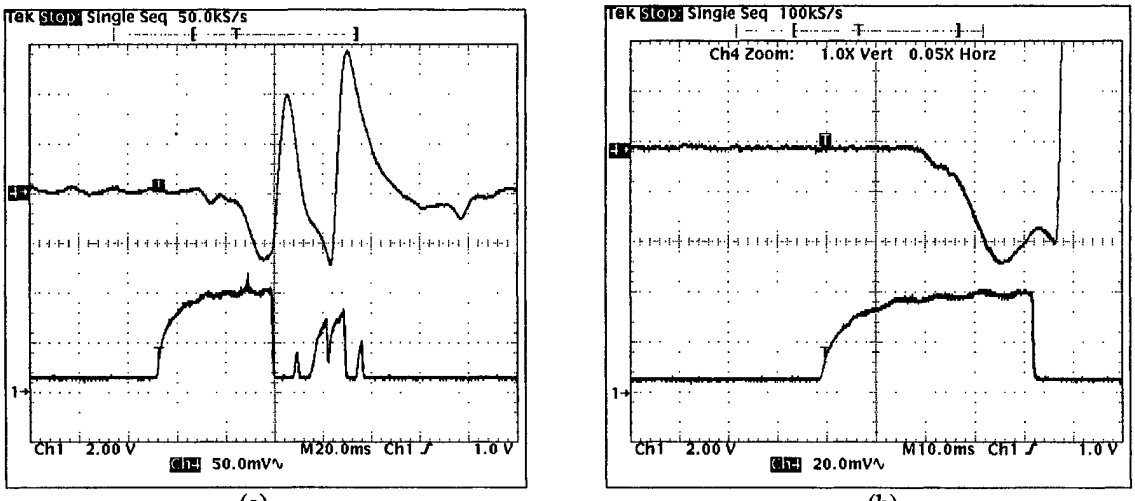


Figure 3 (a) response of a free-fall sensor motion
(b) magnified response of free-fall motion

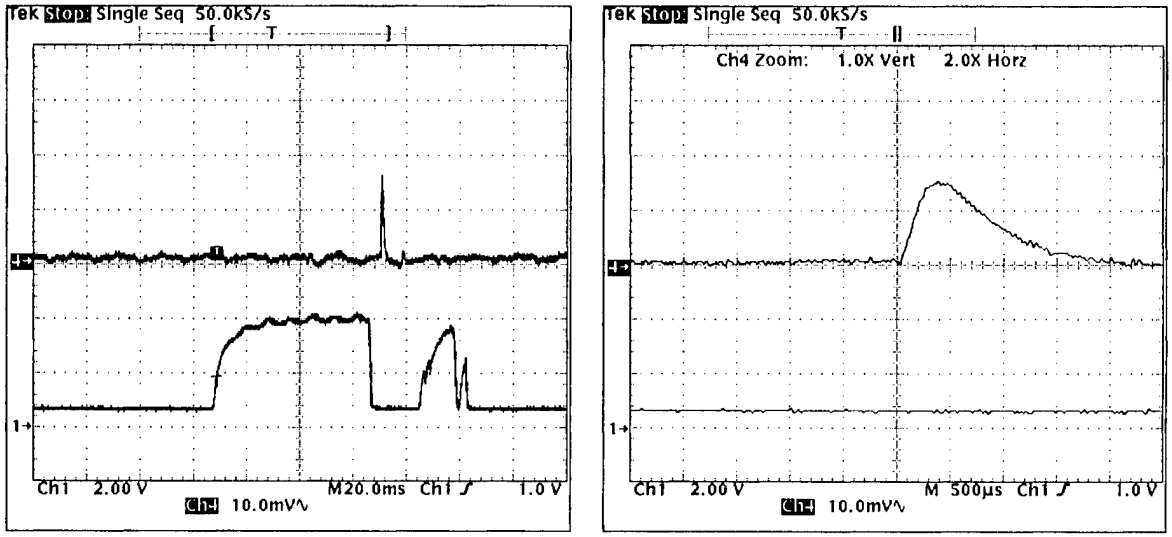
To minimize the influence of the natural mode, the simplest approach will be pushing the first mode frequency higher while at the same time introducing a low-pass filter to further reduce the natural mode effect. To accomplish this goal, a 20.1mm long, 6mm wide, and 1.8mm thick PZT was constructed in a one-dimensional cantilever plate configuration and chosen as the sensor structure where the first mode frequency was set at 1.41 kHz. The experimental results are shown in Fig. 4. A charge amplifier and a 2 pole low-pass filter were chosen as the interface circuit. Varying the corner frequency of the low-pass filter, it was discovered that the transient response could be filtered out when the corner frequency was set at 100 Hz. The experimental result are shown in Figs. 4(a) and 4(b), where almost all of the transient response is filtered out by the low-pass filter introduced. With the filter in place, the free-fall and the impact response were found to have an exponential decay behavior. It is also clear from the experimental data that the free-fall response is clearly discernable.



(a) (b)

Figure 4 (a) experimental result of the charge mode free-fall sensor with a –40 dB/decade low-pass filter

Figures 5(a) and (b) were experimental results obtained when the current amplifier was chosen as the interface circuit, which essentially converted the sensor into an acceleration rate sensor [3]. It should be noted that a low-pass filter was present and certainly had influence on the final sensor output. The rise time of the current amplifier was set at 0.1 ms, and the corner frequency of the low-pass filter was chosen at 1 kHz. It is clear that a pulse signal was generated by this current amplifier configuration. It should be noted that this pulse was generated due to the fact that the low-pass filter filtered out the low frequency response of our free-fall sensor. This pulse was induced at the time when the sensor structure began its transient response, which can be seen in the data shown in Figs. 4(a) and (b). Note also that the frequency of the pulse was about 500 Hz. More specifically, the experimental shown in Fig. 5 clearly demonstrates that when a current amplifier was used as the interface circuit, a pulse signal due to free fall can be generated. In other words, with the configuration disclosed here, it is possible to offer a single pulse signal to warn the beginning of a free fall.



(a) (b)

Figure 5 (a) experimental result of the charge mode free-fall sensor with a –40 dB/decade low-pass filter

3. DISCUSSIONS

The experimental results obtained clearly demonstrate the possibility of creating a free-fall sensor. It should be mentioned that the signal is the combined effect of the force response and the interface circuit used. Note also that the sensitivity is highly dependent upon the flexibility of the structure, which can be observed from difference between two free-fall sensors developed during the course of this research. The softer free-fall sensor can measure the falling motion earlier while suffering the influence of the transient modal responses. This result clearly demonstrates the importance of setting the first resonant mode frequency of the sensor structure. The higher the chosen first mode frequency, the more filtering effect can be introduced to distinguish the induced transient modal response. However, setting the first resonant mode frequency higher will certainly reduce the sensor response and may also introduce a mini-seconds time delay. On the other hand, the phase delay introduced by the interface circuit and the low-pass filter adopted also will introduce a time delay to the detected signal. Thus the higher the first mode frequency, the smaller will

be the influence on the phase delay induced by the low-pass filter, i.e., a lower influence to the true free-fall response.

The experimental data indicates that a pulse signal can be measured at about 80 ms after the beginning of the free fall, which translates to around a 370 ms lead time for the data storage device to provide an impact evasive reactive action. As 370 ms is much longer than the average 10 ms seek time of today's read write head to move out the disk, the suitability of the free-fall sensor developed is thus quite obvious. Taking the prosperous MEMS technology nowadays as an example, a micro accelerometer with about a kHz first resonant mode is common. Combining the above-mentioned perspectives indicates that taking a free-fall sensor to further improve the shock or impact resilience performance for data storage devices shall not be an impossible task anymore.

To enhance the performance of the free-fall sensor, the key thoughts include: (1) a good sensor structure flexibility, (2) a low first mode resonant frequency, (3) a proper low-pass filter to filter out the transient modal response, and (4) a negligible phase delay introduced by the interface circuit used. A good free-fall sensor definitely represents a good compromise to all these key thoughts. In the field of the flexible structure control, a series of a no phase delay low-pass filter were introduced in the spatial domain by integrating the distributed sensor concept to the development of point sensors, like accelerometers. This class of sensors, named *APROPOS* devices [6][7], was first reported at the 10th ICAST conference (Fig. 6). It was classified as a Point-Distributed sensor (*PoD sensor*). This kind of no-phase delay low-pass filter can filter out the transient modal response without introducing any phase delay. Combining the effect of the *APROPOS* device and the traditional RC filter, the first mode frequency of the sensor structure can be further reduced to a negligible level. Taking this approach, the free-fall sensor sensitivity can be further increased while nullifying the time delay introduced by the filter. It should be mentioned again that optimizing the force response of the sensor structure created the free-fall sensor in this article. To further improve the overall sensor response, the true motion of the free fall device during falling should be further investigated. A Michelson interferometer type interferometer like that of the Advanced Vibrometer/Interferometer Device (*AVID*) [8] will be introduced in the future to further unveil the influence of sensor structures to the detection of free-fall motion. In summary, measuring free-fall motion by using accelerometers or acceleration rate sensors has been successfully demonstrated and the influence of the interface circuit has also been verified experimentally.

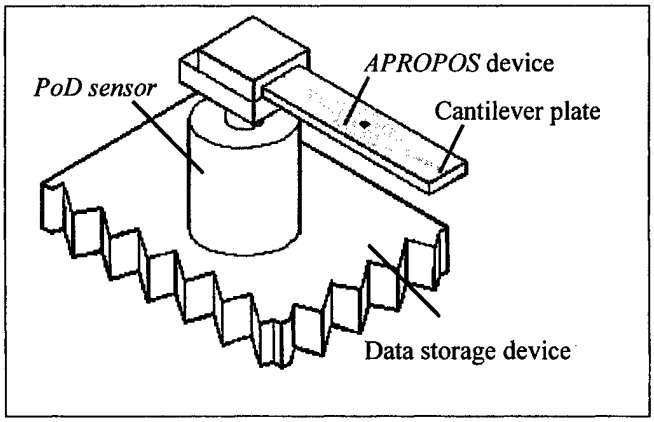


Figure 6. Schematic of a *PoD sensor*

4.REFERENCES

1. Ottesen, "Apparatus for Detecting and Correcting Extensive Vibration in a Disk File", IBM Technical Disclosure Bulletion.
2. Aric K. Menon, and B. K. Gupta, "Data Storage for the Millennium," *Datatech*, Spring 2000.
3. C. K. Lee, A. C. Munce, Jr., T. C. O'Sullivan "Disk drive with acceleration rate sensing," USA Patent No. 5,521,772, May 28, 1996.
4. K. F. Graff, *Wave Motion in Elastic Solids*, Dover Publications, Inc., New York, USA, 1975.
5. L. Meirovitch, *Element of Vibration*, McGraw-Hill Inc., Singapore, 1986.
6. C. K. Lee, Y. H. Hsu, C. T. Lin, W. H. Hsiao, H. C. Shih, S. H. Hsu, and H. S. Hsu, "Implementing *APROPOS* Device as Point Sensors," *Proc. 10th International Conference on Adaptive Structures and Technologies (ICAST'99)*, pp. 53-60, Technomic Publishing Co., Inc., Lancaster, Pennsylvania, USA (October 11-13, 1999).
7. Y. H. Hsu, C. K. Lee, W. H. Hsiao, C. T. Lin, H. C. Shih, S. H. Hsu, and H. S. Hsu, "*APROPOS* Device for Control-Structure Interactions," *Proc. 10th International Conference on Adaptive Structures and Technologies (ICAST'99)*, pp. 45-52, Technomic Publishing Co., Inc., Lancaster, Pennsylvania, USA (October 11-13, 1999).
8. "AVID, Advanced Vibrometer/Interferometer Device," AHEAD Optoelectronics, Inc., No. 13 Chin-ho Road, Chung-ho, Taipei hsien 235, Taiwan, R.O.C. (http://www.ahead.com.tw).

DESIGN AND TESTING METHODOLOGIES OF ROTATIONAL ACCELEROMETERS: A SMART STRUCTURE PERSPECTIVE

Y. H. Hsu,* C. K. Lee*

ABSTRACT

The concept of an *Autonomous Phase-gain ROtation/linear Piezoelectric Optimal Sensing (APROPOS)* device was adopted to the design of rotational accelerometers. It can be shown that the concept is applicable for mechanical systems such as shaft, which can be represented by using a second order partial differential equation. A no phase-delay low-pass filter was implemented by weighing the structure vibration strain spatially, which can be achieved by modifying the shape or the effective surface electrode of a thin layer piezoelectric film. With the introduction of the APROPOS concept, the usable bandwidth of the rotational accelerometer created can be shown to expand significantly. To verify the performance of the rotational accelerometer, which is difficult to test due to its wide bandwidth, the testing methodologies of a wideband rotational shaker developed is also detailed.

1. INTRODUCTION

The *APROPOS* (Autonomous Phase-gain ROtation/linear Piezoelectric Optimal Sensing) device concept was first reported at the 10th ICAST Conference in October 1999 [1,2], which clearly demonstrated that the design concept of the distributed sensor [3,4] can be successfully merged with that of point sensors to form Point-Distributed Sensors (*PoD Sensors*) [1]. One of the main advantages of this type of sensor is its ability to extend the useful bandwidth of the overall sensor beyond the limitation imposed by the sensor structure itself. The previously reported *APROPOS* devices were developed on flexible bending structures such as beams or one-dimensional plates, which have fourth-order characteristic polynomials. A total of four wave modes, two propagating and two evanescent waves, were presented in these sensor structures. It will be presented in this paper that rotational type *APROPOS* devices are possible as well. It should be noted that two propagating waves instead of four wave modes are presented in the sensor structures under torque. It will also be shown that this fundamental difference will have impact on the design of the rotational type *APROPOS* device. Both the design concept and the methodology of implementing the newly developed rotational *APROPOS* device will be detailed in this article. Due to the design innovations of adopting an *APROPOS* device to point rotational sensing devices, its operational bandwidth can be easily expanded to a kHz range. To verify the performance of this type of rotational

* Institute of Applied Mechanics, National Taiwan University, Taipei 10764, Taiwan, R.O.C.

APROPOS device, the bandwidth of the rotational shakers adopted must also be expanded as well. The methodologies adopted to expand the testing bandwidth of traditional rotational shakers are also presented. It will be shown in this paper that by using a matching filter, which has been well developed in high performance audio systems, a wide band rotational shaker can be implemented by placing a servomotor and a piezoelectric rotational shaker in tandem. In summary, the theory, the design of the experimental set-up, the experimental results, etc. will all be detailed in this article.

2. THE CONCEPT OF THE *APROPOS DEVICE*

. The fundamental thought of the *APROPOS* device can be developed by considering a methodology that controls the spatial weighting factors of structure wave modes with a shaped piezoelectric thin film mounted on top of an one-dimensional cantilever plate [1,2]. The *APROPOS* device can be implemented by the following two methods. The first method by the method of imaging [5]; which maps the wave modes on the finite domain to an infinite domain by considering the characteristics of the boundary such as that of fixed or free ends [2]. The second method involves adopting window functions to eliminate the effect of the waves outside the finite domain [6], i.e., making sure the weighting factors for the boundary is zero [1]. Both methods can expand the wave modes propagation between the boundaries of the finite structure into the infinite domain. That is, the combined effect of the *APROPOS* device and the wave modes in the structure is continuous in the infinite domain. Figure 1 further details this characteristic. The waves, which propagate to-and-from the fixed end, will have an 180^0 phase delay. However, the waves propagating to-and-from the free end will not induce any phase delay. More specifically, the waves will be continuous for the free end but will have a jump at the fixed end. By introducing the concept of the *APROPOS* device, the discontinuity can be eliminated by making sure the sensor has zero weighting at the fixed end as it is shown in Figure 1. In other words, the *APROPOS* device really specifies the spatial weighting factors for the wave modes, which can also be perceived by saying that the wave modes keep on seeing the effect of the *APROPOS* device as it propagates between the boundaries. With either of the two methods discussed above, the waves on the finite structure can be perceived as propagating continuously in the mapped infinite domain. That is, a domain from a minus infinite to infinity is constructed spatially with the two above-mentioned methods. Taking this perspective, it is then not surprising to realize that a no-phase delay filter can be implemented as the information of the past and future exit simultaneously at the same time, which are represented by the right and left propagating waves, while integrating the contribution of the signal within the *APROPOS* device.

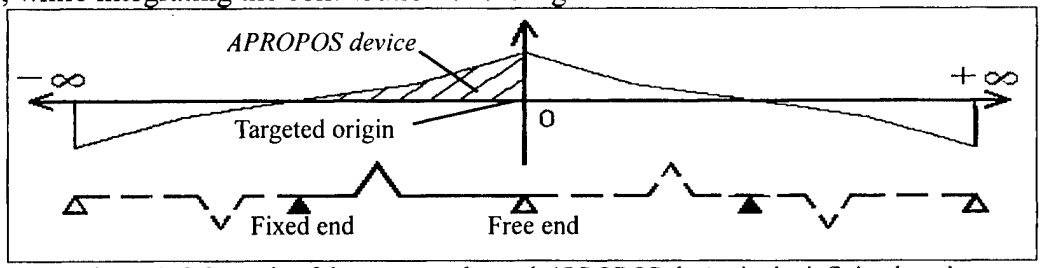


Figure 1. Schematic of the wave modes and *APROPOS device* in the infinite domain

2.1 Rotational *APROPOS* device Based Accelerometers

Compared to the governing equation of the bending of a one-dimensional plate, which is a fourth order partial differential equation (PDE), the torsional vibration of a shaft is a second

order PDE. More specifically, the governing equation of a torsional shaft can be written as [5]:

$$G\frac{\partial^2\theta(x,t)}{\partial x^2}-\rho\frac{\partial^2\theta(x,t)}{\partial t^2}=0 \tag{1}$$

where G constant is the shear modulus, ρ is the density, and θ is the twisting angle. Note that the damping effect is neglected in Eq. (1). Considering only the harmonic structure response, i.e., $\theta(x,t)=\theta(x)e^{i\omega t}$, leads to:

$$\frac{\partial^2\theta(x)}{\partial x^2}+k^2\theta(x)=0 \tag{2}$$

where

$$k^2=-\frac{\rho}{G}\omega^2 \tag{3}$$

is the dispersion relationship between the wave number k and frequency ω. Thus the general solution of the one-dimensional shaft with a solid circular cross section can be expressed as two propagating waves, *i.e.*, the right and the left propagating wave modes in Eq. (4):

$$\theta(x,t)=[w_{lp}e^{jkx}+w_{rp}e^{-jkx}]e^{jwt} \tag{4}$$

where w_{lp} and w_{rp} are wave mode amplitudes of the left and the right propagating waves. It should be noted that these wave modes really represent the fundamental characteristics of the structure. That is, the boundary condition determines the characteristic of the sensor structure and thus also the accelerometer overall performance. As the sensor characteristic is highly dependent to the characteristics of the sensor structure chosen, any methodology that can be used to reduce the overall sensor response dependency to that of the sensor structure itself will be highly valuable in tuning the overall sensor response. Thinking along this line, introducing the *APROPOS device* concept to create a no-phase delay low-pass filter so as to improve the sensor frequency response by extending the usable bandwidth will be invaluable. It should be noted that this series of spatial filter is fundamentally different from the traditional electric filter as a phase delay will be inevitably introduced into the sensor frequency whenever a traditional electric filter is introduced.

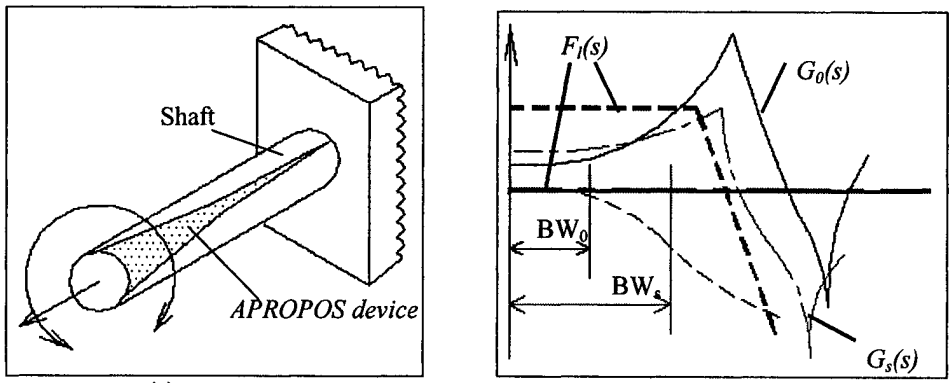


Figure 2. (a) Schematic of the rotational *APROPOS* device based accelerometer. (b) Schematic of the effect of the *APROPOS* device

The rotational *APROPOS* device based accelerometer and its effect is shown in Figure 2, where $G_0(s)$ is the original transfer function of the sensor structure, $G_s(s)$ is the sensor transfer function that has been tailored by the *APROPOS* device, $F_l(s)$ is the no-phase-delay low-pass

filter introduced by *APROPOS* device, BW_0 is the original bandwidth of the sensor structure, and BW_s is the enhanced bandwidth of the sensor once the *APROPOS* device is implemented.

2.2 Theory of Piezoelectric Laminates

Piezoelectric material has been extensively studied over the last twenty years. Coupling mechanical and electrical fields by using the piezoelectric effect can be expressed by the following governing equations: [7]

$$S_p = s_{pq}^E T_q - d_{ip} E_i, \quad D_i = d_{ip} T_q + \varepsilon_{ij}^T E_k, \tag{5}$$

where $i,k=1\sim3$, $p,q=1\sim6$, c_{pq} *are* the elastic stiffness constants, T_p, S_q are stress and strain; D_i and E_k represent electric displacement and electrical field, respectively. It is obvious from the governing equation that as an electric field is applied, a mechanical strain will occur [7]. On the other hand, when a force is applied on the material, a charge can be measured from the material surfaces. As piezoelectric materials of thin sheet form such as that of PVDF (polyvinylidene fluoride) film is used, a plane stress approximation was adopted to model the piezoelectric thin lamina. That is, Eq. (2) can be modified to $D_3 = \varepsilon_{33} + d_{31}T_1 + d_{32}T_2 + d_{36}T_6$ and the induced charge can only be detected from the thickness direction. Considering the effect of the skew angle [3,8,9], which refers to the angle between the principal axes of the piezoelectric material and that of the structures, this equation can be further modified to:

$$D_{3'} = \varepsilon_{3'3'} E_{3'} + d^0_{3'1'} P_{1'}(x',y') T_{1'} + d^0_{3'2'} P_{2'}(x',y') T_{2'} + d^0_{3'6'} P_{6'}(x',y') T_{6'}, \tag{6}$$

where the notation "'" represents the constants was referred to by the materials coordinate axes. Using Gauss' Law to find the signals detectable by surface electrode $S^{(12)}$, the charge signals generated by the *k-th* laminae becomes [3,8,9]:

$$q(t) = \iint_{S^{(12)}} F P_0 \left[e_{31} \frac{\partial u}{\partial x} + e_{32} \frac{\partial v}{\partial y} + e_{36} \left(\frac{\partial u}{\partial y} + \frac{\partial v}{\partial x} \right) \right] dxdy \cdot \tag{7}$$

If the vibration of the attached structure is purely shear strain, the piezoelectric thin film is attached to the surface of the one-dimensional circular shaft. Then the shear strain can be expressed as $\varepsilon_{\theta z} = rd\theta / dx$ only. Substituting Eq. (4) into Eq. (7), the sensor equation can be simplified as:

$$q_s(k) = jke_{36} r^2 \int_0^a R(x)[w_{lp} e^{jkx} - w_{rp} e^{-jkx}] dx \tag{8}$$

where

$$R(x) = \int_{-b/2}^{b/2} F(x,y) P_0(x,y) dy \tag{9}$$

is the effective surface electrode of the piezoelectric thin film. One of the fundamental drivers behind the design of the reported distributed sensors is the ability to choose a proper effective surface electric function *R(x)* [3,4]. In addition, the *APROPOS* device also uses the same perspective by weighing the wave modes in the infinite domain expanded by either using the method of imaging or the window functions. The key thought behind the *APROPOS* device lies on regarding each term of Eq. (8) as a two-sided Laplace transform [10]. With this observation, the Laplace transform table developed over the years can be used as a powerful mathematical tool to design *APROPOS* devices. One thing that should be mentioned here is that PVDF thin film does not have the d_{36} constant. The lack of this d_{36} constant can be compensated by choosing a proper polarization profile or by selecting the appropriate PVDF skew angle. It is known that the d_{31} and d_{32} constants of the PVDF at skew angles equal to $\pm \pi/4$ are the same, and is a minus between the d_{36} constant at $\pm \pi/4$, *i.e.*, $d_{31}(\pi/4) = d_{32}(\pi/4) = d_{31}(3\pi/4) = d_{32}(3\pi/4)$, $d_{36}(\pi/4) = -d_{36}(3\pi/4)$. With this observation,

it is clear that a pure shear sensor can be easily implemented by using the following configuration. Note that EMI (electromagnetic interference) shielding is automatically obtained by connecting the external electrode of the folded PVDF thin film to the ground.

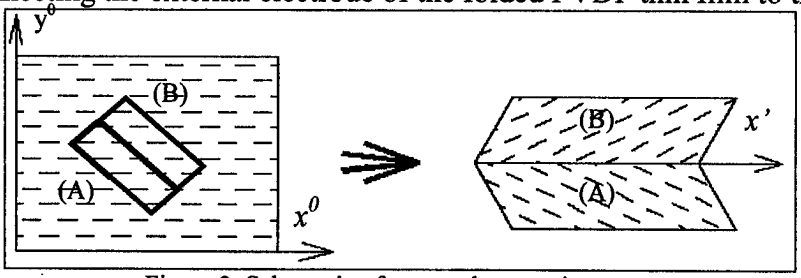


Figure 3. Schematic of a pure shear strain sensor

2.3 Implementation of Rotational *APROPOS Devices*

Considering the conceptual drawing shown in Fig. 1 again, it is clear that the *APROPOS* device is symmetric with respect to the targeted origin in the infinite domain, where the targeted origin is determined by the chosen origin. This characteristic determines the form of the wave mode amplitudes in Eq. (4) where the local characteristic of the targeted origin is embedded within. With this symmetry, the wave modes propagating to-and-from the targeted origin remains the same. The sensor equation can thus be reduced to:

$$q_s(k) = jke_{36}r^2(w_{lp} - w_{rp})\int_{-\infty}^{\infty} R(x)e^{-jkx}dx \qquad (10)$$

A no-phase delay filter can then be implemented by choosing an appropriate effective surface electrode *R(x)*. It should be emphasized that the characteristic of the rotational *APROPOS* device based accelerometer is the superposition of (1) all characteristics of the sensor structure, (2) its local performance, and (3) the filtering effect induced by using the *APROPOS* device concept. Considering the following Laplace table:

Table 1. (a) A right-sided Lapalce transformed pair where $F(s) = \int_0^{\infty} f(x)e^{-sx}dx$.

(b) A left-sided Laplace transformed pair where $F(s) = \int_{-\infty}^{0} f(x)e^{-sx}dx$.

(a)

f(x)	F(s)=£{f(x)}
$e^{-\alpha x}$	$\frac{1}{\alpha + s}$
$\sin(\gamma x)$	$\frac{\gamma}{s^2 + \gamma^2}$

(b)

f(x)	F(s)=£{f(x)}
$e^{\alpha x}$	$\frac{1}{\alpha - s}$
$\sin(\gamma x)$	$-\frac{\gamma}{s^2 + \gamma^2}$

It can be seen from this table that a –40dB/decade no-phase delay low-pass filter can be introduced by introducing $e^{-\alpha|x|}$ to the effective surface electrode. Another thing that should be noted is that sine function shaped effective surface electrode will produce a null output. In addition, the wave modes at the fixed end can be represented by odd functions and the wave modes at the free end can be represented by even functions as it was described above. Choosing the fixed end as the targeted origin and the corner wavenumber γ of the sine function set at $(2n+1)\pi/2$, a continuous sine function can then be imaged into the infinite domain. We can then choose an effective surface electrode as follows [3]:

$$R(x) = e^{-\alpha|x|} - e^{-\beta|x|} - c\sin[\gamma(x)]. \qquad (11)$$

The sine function is introduced to compensate for the effect where the exponential function

approaches zero only in the infinite domain, which means that the electrode shape must be reduced to zero at the boundary. By using the data shown in Table 1, it can be shown that the un-finished profile can be reduced to zero in the finite domain by using a sine function as the sine function integrates to zero in the two-sided Laplace transform. With Eq. (11), the characteristic of the rotational *APROPOS* device can be expressed as:

$$q(k) = jke_{36}r^2(w_{lp} - w_{rp})\left[\frac{(\beta^2 - \alpha^2)s}{(\alpha^2 - s^2)(\beta^2 - s^2)}\right], \tag{12}$$

which represents the creation of a –60dB/decade no-phase low-pass filter. It should be noted that Eq. (12) is also a filter that can be used to tailor sensor DC gain by merely choosing the proper corner wave number α and β. Note that the zero s in the numerator is induced by the odd function of the fixed end. With the implementation of this –60dB/decade no-phase low-pass filter, the usable bandwidth of the sensor can easily be expanded to 80~90% of the first mode frequency by the *APROPOS device*, which is significant as traditional sensors can only be used below 10% of the first mode frequency if 10% linearity is expected.

3. TESTING METHODOLOGY BY DEVELOPING A NEW SHAKER

With the size reduction of the testing structure, its operational bandwidth can be extended to kHz range. As traditional rotational shakers made by servomotors do not have enough bandwidth to verify the performance of the sensor, a new shaker was developed to facilitate the testing of the *APROPOS device* based sensor. More specifically, a servomotor can only introduce small loading at high frequency while creating a larger loading at low frequency. Generally speaking, the usable bandwidth of a servomotor is typically lower than a few hundred Hz range. To test the newly developed sensor up to a kHz range, a new shaker which was developed will be detailed herein.

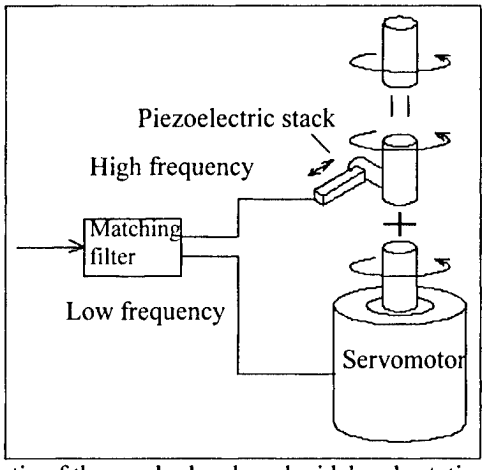


Figure 4. Schematic of the newly developed wideband rotational shaker to verify performance of rotational *APROPOS* devices.

The concept of the wideband rotational shaker is realized by embedding a piezoelectric stack to the servomotor to induce high frequency loading when the servomotor is out of range. That is, by making the servomotor and the piezoelectric stack responsible for low and high frequency ranges respectively, we created a new shaker. A matching filter was used to transmit the low frequency signal to the servomotor and the high frequency signal to the piezoelectric stack (Fig. 4). As a servomotor is proficient to induce low frequency rotations and a piezoelectric shaker is effective in the high frequency range, a wideband and flat

frequency response can be achieved at the newly developed tandem shaker by tuning the transfer function of the matching filter. It was found that the usable bandwidth of the rotational shaker created is expanded up to 10kHz or even higher depending on the performance of the piezoelectric stack.

4.EXPERIMENT SET-UP

To verify the effect of the rotational *APROPOS* device, a 50mm long, 10mm diameter wide silica gel one-dimensional shaft was chosen as the sensor structure. The experimental set-up is shown in Fig. 5(a). The characteristic of the shaft is measured by placing a uniform sensor to arrive at the frequency response curve shown in Fig. 5(b). It is obvious from the experimental results that the natural frequency of the shaft is located between several hundred to kHz, which indicates the necessity for a wideband rotational testing base. Considering Fig. 5(b), the damping effect of the first mode is large, which corresponds to a low quality factor.

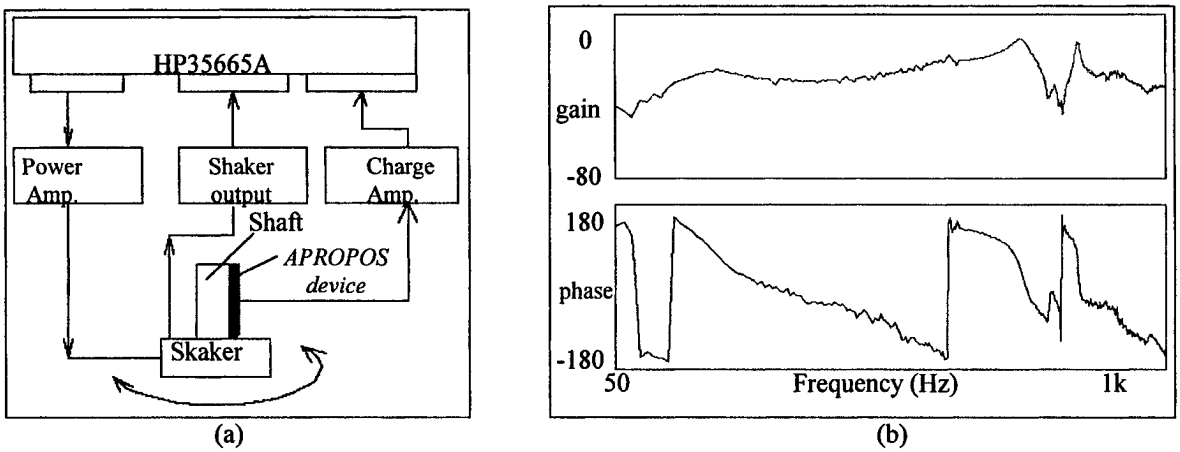


Figure 5. (a) The experiment set-up of an APROPOS device (b) The transfer function of the uniform sensor

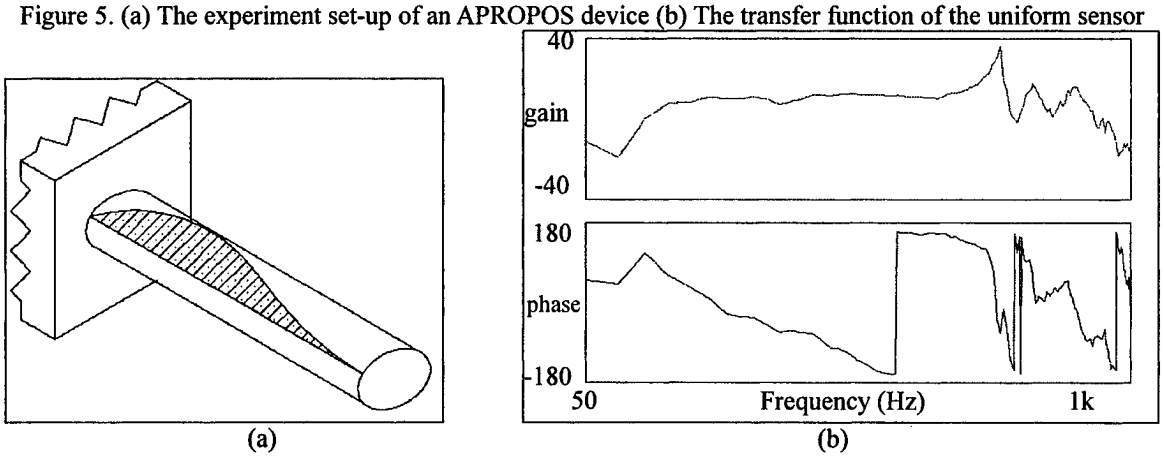


Figure 6. (a) Schematic of the rotational *APROPOS device* based accelerometer
(b) The transfer function of the *APROPOS device*

The corner frequency γ of the sine function was chosen to be 95Hz. Following the *APROPOS* device discussed above, the corner frequency α and β were chosen to be 200 and 250Hz respectively so as to reduce the second mode effect and thus enhance the bandwidth. The designed sensor profile and its sensor transfer function is shown in Fig. 6. It is obvious from Fig. 6(b) that the introduction of the –60 dB/decade low-pass filter from *APROPOS* device flattens the bandwidth of the rotational sensor. On the other hand, a DC gain is also introduced.

5.CONCLUSIONS

The concept of the *APROPOS* device for the second order partial differential equation system was successfully verified by using a one-dimensional shaft. It was shown that properly weighing all of the structure wave modes in infinite domain, which was mapped from the finite domain by using the method of imaging and window functions, a no-phase delay low-pass filter could be integrated into the sensor transfer function. It was verified that introducing the *APROPOS* device concept can enhance the usable bandwidth of rotational sensors. It should be mentioned again that the performance of a rotational *APROPOS* device based accelerometer is the superposition of the characteristic of the structure, the local performance of the targeted origin, and the extra no-phase-lag filtering induced by the *APROPOS* device. To verify the wide bandwidth performance of the rotational sensor, a methodology adopted to create a wideband rotational shaker was detailed. It was shown that taking a matching filter to have the low frequency driving signal being sent to the servomotor and high frequency driving signal to the piezoelectric stack could indeed create a wide bandwidth flat frequency response rotational shaker. In summary, the theory, the design of the experimental set-up for the rotational *APROPOS* device based accelerometer was successfully verified both theoretically and experimentally.

6. ACKNOWLEDGEMENTS

The authors would like to thank the continuous and generous financial support of this research from the National Science Council of Taiwan, R.O.C., and from AHEAD Optoelectronics, Inc. through Grants NSC 85-2622-E-002-017R, NSC 86-2622-E-002-023R, NSC 88-2218-E-002-005, and NSC 88-2622-E-002-001. The authors would like to express their appreciation to Measurement Specialties, Sensor Products Division (MSI) for continuously providing us with all the PVDF films used in fabricating the piezoelectric devices discussed in the research work. In addition, the close friendship with Dr. Kyung Park of MSI has made exploring this field enjoyable.

7.REFERENCES

1. Lee, C.K., Hsu, Y.H., Lin, C.T., Hsiao, W.H., Shih, H.C., Hsu, S.H., and Hu, H.S. "Implementing APROPOS Device as Point Sensors," *Proc. of International Conference on Adaptive Structure and Technologies (ICAST '99)*, Paris, France, 1999.
2. Hsu, Y.H., Lee, C.K., Hsiao, W.H., Lin, C.T., Shih, H.C., Hsu, S.H., and Hu, H.S., "APROPOS Device for Control-Structure Interactions" *Proc. of International Conference on Adaptive Structure and Technologies (ICAST '99)*, Paris, France, 1999
3. Lee, C. K., "Piezoelectric Laminates for Torsional and Bending Modal Control: Theory and Experiment," *Ph.D. Dissertation*, Cornell University, Ithaca, New York, USA, 1987.
4. Miller, D.W., Hall, S.R. and von Flotow, A.H., "Development of Spatially Convolving Sensors for Structural Control Applications," *Proceeding of the AIAA/ASME/ASCE/AHS Proceedings of the Structures, Structural Dynamics, and Materials Conference*, Long Beach, CA, USA, pp. 2283-2297, 1990.
5. Graff, K.F., *Wave Motion in Elastic Solids*, Dover Publications, Inc., New York, USA, 1975.
6. Harris, F.J., "On The Use of Windows for Harmonic Analysis with The Discrete Fourier Transform," *Proceedings of the IEEE*, Vol. 66, No. 1, January 1978.
7. Cady, W.G., *Piezoelectricity*, Vol. 1, McGraw-Hill, New York, New York, USA, pp. 1-8, 1946.
8. Lee, C.K., "Theory of Laminated Piezoelectric Plates for the Design of Distributed Sensors/Actuators: Part I . Governing Equations and Reciprocal Relationships," *J. Acoust. Soc. Am.*, Vol. 87, pp. 1144-1158, March 1990.
9. Lee, C.K., "Piezoelectric Laminates: Theory and Experiments for Distributed Sensors and Actuators", *Intelligent Structural Systems*, Kluwer Academic, Netherlands, pp. 75-167, 1992.
10. Alan V. Oppenheim and Ronald W. Schafer, *Signal and System*, Prentice-Hall, Inc., Upper Saddle River, New Jersey, USA, 1999.

DEVELOPMENT OF A SOFT TRIBO-SENSOR FOR MONITORING SKIN CONDITIONS

M. Tanaka, H. Ichinose, K. Numagami, Z. W. Jiang, S. Chonan

ABSTRACT

The present paper is concerned with the development of a haptic sensor system that monitors the condition of human skin. The base of the sensor is an aluminum shell, around which a rubber sponge layer, PVDF film, a protective layer of acetate film and gauze are applied in sequence. The sensor is attached to the tip of an elastic cantilevered beam and pressed against an area of skin. It is then moved by hand over the skin to allow the sensor to assess surface morphological features. Characteristics of the data are extracted by calculating the variance and distribution of power intensity over several segmented frequency ranges. Each set of data obtained is then used as a training set of data for a neural network that distinguishes skin with atopic dermatitis from normal healthy skin. The results showed that 100% recognition is achieved when using the constructed network system. Finally, the way in which morphological features changed in response to aging of the skin was examined in detail.

INTRODUCTION

Assessment of the pharmaceutical action of liniments on the skin of people with skin disease is a matter of clinical importance for the dermatologist, and one that has focused attention on the need to develop an objective technique for measuring the morphological

M. Tanaka , H. Ichinose and S. Chonan Department of Mechatronics and Precision Engineering, Tohoku University, Sendai 980-8579, Japan

K.Numagami Department of Dermatology, Tohoku University School of Medicine, Sendai 980-8574, Japan

Z.W.JiangDepartment of Mechanical Engineering, Yamaguchi University, Ube, 755-8611, Japan

features of skin[1].An evaluation of sustantation of the cosmetic efficacy of toiletries is another need requiring an objective measuring technique. Features that affect the health appraisal and/or physical beauty of skin include morphological features such as rashes, chaps and wrinkles.

The development of a technique for measuring skin morphology currently lags behind the development of other medical measuring techniques, likely due to the fact that dermal conditions can easily be assessed by visual inspection alone. However, the development of noninvasive technology in dermatology has advanced considerably over the last decade and several methods have been introduced that measure the mechanical properties of the dermis. These methods include the measurement of transepidermal water loss using an evaporimeter[2] and the image processing of a negative replica of dermis[3]. Such methods, however, can be categorized collectively as techniques that indirectly measure the dermis. The stylus which was originally developed to measure the roughness of a metallic surface, is a standard instrument used to measure the surface texture of skin[4]. A diamond stylus is allowed to traverse over the surface of the skin. This method is also not a direct method because of the movement generated on the skin surface while scanning the profile. To date, to the authors' knowledge, no reliable and reproducible measuring techniques have been reported that directly measure dermal surface conditions.

PVDF (polyvinylidene fluoride) piezofilm is flexible and very sensitive to sudden variations in stress or strain. Electrical currents generated by mechanical stress in piezoelectric materials decay as a result of dissipation of the charge. The voltage signal takes the form of a very brief potential wave at the onset of the applied force, and a similar brief wave at its termination. This signal increases with applied force but drops to zero when the force remains constant. There is no response during the stationary plateau of the applied stimulus, and the voltage drops to a negative peak as pressure is removed, and subsequently decays to zero[5]. The response is quite similar to the response of the Pacinian corpuscle in the human skin[6], one of the sensory receptors in the dermis.

The present paper reports our findings on the development of a haptic sensor for monitoring the surface conditions of human skin. PVDF polymer film is used as the receptor of a novel sensor that directly and non-invasively catalogues the morphological features of epidermis. The sensor is moved by hand over the skin, while attempting to maintain a constant speed and force. The voltage signal from the sensor is analyzed to assess the variation and distribution of power intensity over several segmented frequency ranges. In the present study, two experiments were carried out on this novel sensor system and signal processing. The first experiment analyzes the sensor's ability to discriminate between the conditions of normal healthy skin and that of skin with atopic dermatitis. The second experiment measures the effect of aging on the condition of normal healthy skin. In the first experiment, each set of data obtained was used as a training set of data for a neural network that identifies skin based on its specific morphological features. The results showed that the present sensor clearly distinguishes skin with atopic dermatitis from healthy skin. In the second experiment, the way in which morphological features

changed in response to aging of the skin was examined in detail. An attempt was made to determine whether the present sensor system and signal processing can be used to estimate the effect of aging on the skin.

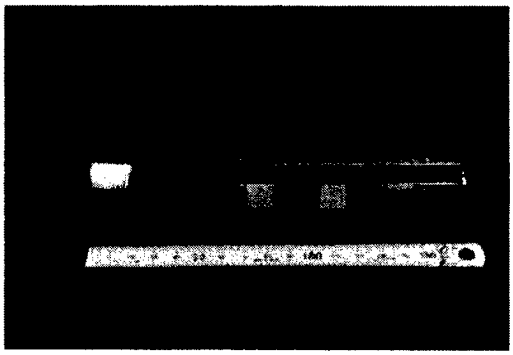


Figure1. Haptic-sensor.

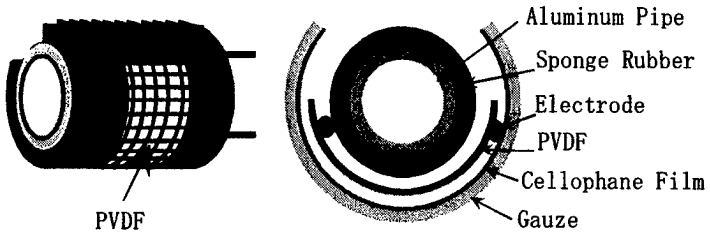


Figure 2. Schematic diagram of PVDF piezofilm Sensor

HAPTIC SENSOR SYSTEM

PVDF piezofilm sensor

The tactile sensor used for the measurement of skin surface conditions and a diagram of each part of the sensor are presented in Figs.1 and 2. The sensor is a layered medium, the construction of which is analogous to the human finger. It is composed of an aluminum shell, which can be regarded as the phalanx, a 3mm rubber sponge as the digital pulp, a PVDF piezopolymer film that is 28 μ m thick and 12mm across as the sensory receptor, an acetate film as the protective agent for the piezofilm, and a gauze on the surface acting as the fingerprint to enhance the tactile sensitivity of the sensor. The sensor is attached to the tip of an acrylic elastic beam and a strain gauge was mounted on the surface of the beam to monitor the force applied onto the skin by the sensor.

Measuring Apparatus

The sensor is moved by hand over the skin, while attempting to maintain a constant speed and force. The voltage signal from the PVDF sensory film is sent to a digital storage oscilloscope in the form of 8-bit quantitized digital signals of 4096 points and then transferred to a personal computer via a GPIB board for signal processing. The sampling frequency was held constant at 40kHz. During the process of measurement, it is important to minimize any potential difference between the surface of the skin and the sensor to reduce the overlap of noise with the sensor signal. To achieve this objective, the

subject was earthed as well as the sensor by fitting the grounding conductor around the wrist. Despite these precautions, some noise from the power source and due to aliasing were observed around 50Hz and 100MHz, respectively. Thus, a band-pass filter of cutoff frequencies 70Hz and 20kHz was inserted after the sensor to counter the noise effect.

PARAMETERS OF SKIN CONDITION

In the present study, signal processing was used in order to catalogue the data on skin morphology. First, variance was calculated as an index to extract the features on the collected data using the following equation;

$$V = \frac{1}{N}\sum_{j=1}^{N} (x(j) - \bar{x})^2 \tag{1}$$

Here, $x(j)$ is the j-th quantitized digital signal, x is the average of $x(j)$, and N is the total number of digital signals.

Next, FFT analysis was used to extract the features of the collected data. The obtained power spectrum was segmented into several segmented frequency ranges and the ratio of the power in a given individual frequency range to the power of the entire frequency range was calculated and used as the second index to describe the characteristics of the skin, as in the following;

$$\begin{aligned} (R_s)_i &= (S)_i / S, \\ (S)_i &= \int P(f)df, \qquad S = \sum_i (S)_i \end{aligned} \tag{2}$$

where $P(f)$ is the power spectrum density, S is the total power distributed over the frequency range considered, and $(S)i$ is the power at frequency level i.

RESULTS AND DISCUSSION

In this section, two experiments were carried out on the present sensor system and signal processing. The first experiment analyzes the sensor's ability to discriminate between the conditions of normal healthy skin and that of skin with atopic dermatitis, and the second measures the effect of aging on the condition of normal healthy skin.

Discrimination of Skin with Atopic Dermatitis

In this experiment, which assessed the sensor's ability to discriminate between healthy

skin and skin with atopic dermatitis, five (A-E) subjects enrolled. Skin from the neck of subject A, who was suffering from mossybackd atopic dermatitis was compared with the healthy skin of subjects B-E. The sensor was moved by hand over a prescribed region of skin, while attempting to maintain a constant speed and force. Each area of skin was measured 5 times to collect data for the calculation of variance and the power spectrum integration. The frequency range of the power spectrum integration is defined in Table 1.

One employs here the neural network-based training for the recognition of atopic and normal healthy skin. The neural network employed was a hierarchical network; the training method used was instructor-assisted training, in which the correct answers are provided as an aid to training; the training algorithm employed was back-propagation. Two networks were examined. One network used four power ratios $(Rs)i$, i= 1-4, as the cell input, while the other used the variance V in addition to the $(Rs)i$. Five sets of data were obtained for each area of skin. The neural network had an input sensory layer of 4 to 5 cells, an intermediate association layer with the same number of cells as the input layer, and an output response layer with a single cell. The correct output value was set to 1 for the atopic skin and 0 for the healthy skin. Training was repeated by using the gradient descent method until the error function became sufficiently small, up to 10^3 and 10^4 cycles. In this study, the networks were constructed three times separately for three sets of randomly selected initial values of synaptic weights. After completing the training of 12 individual networks, the recognition experiments were performed on the atopic skin and the healthy skin using the 5 newly obtained sets of data on each subject. The results obtained appear in Table 2. Here, the percentage denotes the rate of correct answers averaged across the three networks of randomly selected initial synaptic weights. Atopic dermatitis cannot be identified without the input of variance, and the recognition is perfect when the variance is introduced as the input.

TABLE I. SEGMENTED FREQUENCY RANGE FOR POWER SPECTRUM INTEGRATION.

Level	1	2	3	4
Frequency Range(Hz)	29-88	98-586	596-1191	1201-19990

TABLE II. RATE OF CORRECT ANSWERS ON THE DISCRIMINATION OF ATOPIC AND NORMAL SKIN.

Input Parameter	P inti		Pinti,V	
Cycle of Training	10^3	10^4	10^3	10^4
A	0%	0%	100%	100%
B	100%	100%	100%	100%
C	100%	100%	100%	100%
D	100%	100%	100%	100%
E	100%	87%	100%	100%

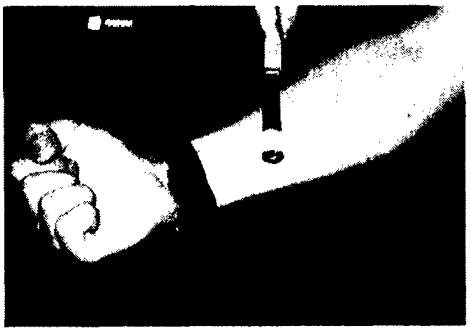


Figure 3. Placement on arm

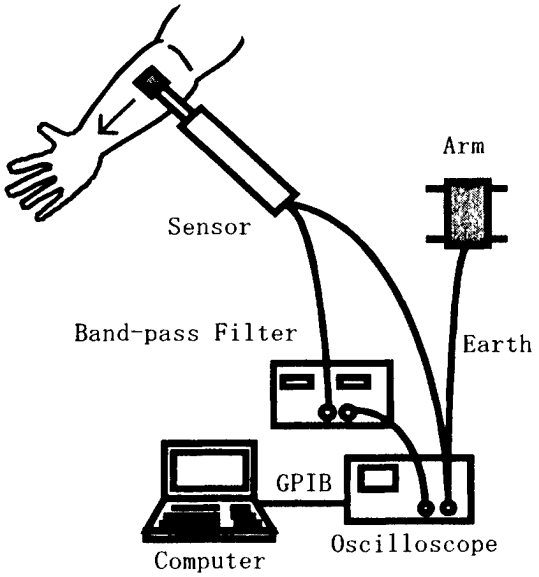


Figure 4. Setup of measuring instruments.

TABLE Ⅲ. NUMBER OF SUBJECTS.

	10s	20s	30s	40s	50s
Male	8	9	9	9	11
Female	9	9	9	9	10

TABLE Ⅳ. FREQUENCY RANGES ON POWER SPECTRUM INTEGRATION.

	Frequency range [Hz]		Frequency range [Hz]
Lv.1	70～146	Lv.5	1240～2490
Lv.2	156～302	Lv.6	2500～4990
Lv.3	312～615	Lv.7	5000～9990
Lv.4	625～1240	Lv.8	10000～19990

Measurement of Aging Effect

In this experiment, the effect of aging on the skin surface was measured using the present sensor system and signal processing. Subjects were 92 individuals ranging in age from those in their teens to those in their fifties, including roughly 10 males and 10 females for each decade age bracket. The breakdown of subjects per age bracket is given in Table 3. The skin condition of all subjects was determined by visual inspection to be normal and healthy prior to the experiment. The measurement position was the inside of

the right forearm. This area was selected due to its stable nature because it is always under clothing. Fig. 3 and Fig.4 show the system used in this experiment. Measurements were taken 5 times for each person and the experiment was carried out from early to mid February. The measurement environment was stable in terms of humidity and temperature.

First, the variance was calculated. Figures 5 shows the relationship between average variance and the different age brackets. In this figure, it can be seen that every value for male subjects is greater than that for females' and the largest value was observed for subjects in their fifties for both males and females. For females, the variance was very small. However, based on this result, by using the obtained variance it is difficult to estimate the age related to various skin conditions.

Next, the ratio of power spectrum integration Rsi was calculated and the relationship between average Rsi in each generation was determined. In this experiment, the frequency range was subdivided, as in table 4 in order to examine the effect of aging in detail. Figure 6 illustrates the relationship between the average Rs3 and Rs5 for each generation, in which the variance in frequency ranges among generations was the most remarkable. In the figure, the bars indicate the distribution from the maximum to minimum. From this figure, it can seen that the value of Rs3 for both males and females

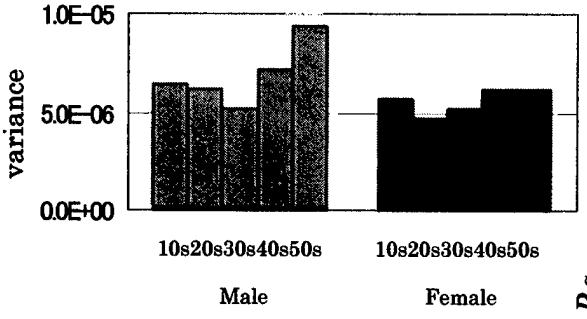


Figure 5 Variations of variance depending on ages.

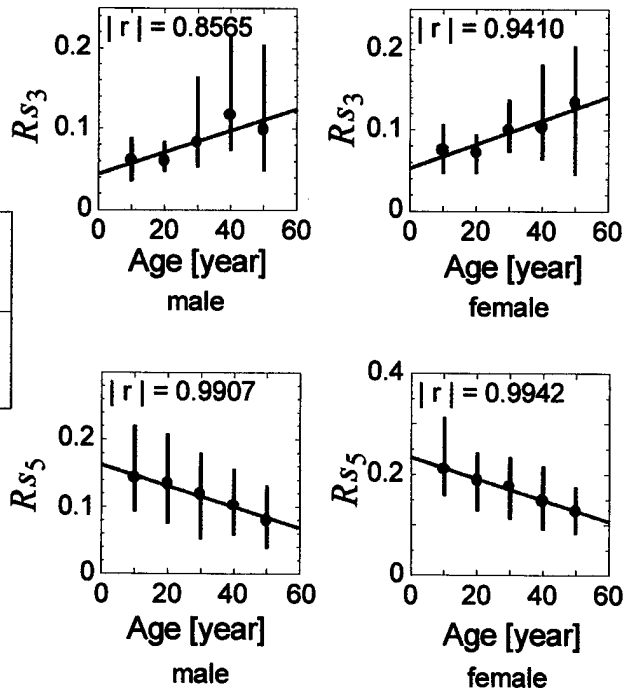


Fig.6 Variations of Rsi as functions of age.

increased with an increase in age, whereas the value of Rs5 decreased.

In this figure, the least-square regression line is plotted and the correlation coefficient of Rs with aging is noted. All obtained coefficients were very near to 1, and thus according to the regression line, one can estimate the age of skin conditions from the Rs.

CONCLUSIONS

A soft tribosensor with a PVDF piezopolymer film as a sensory receptor was designed and its effectiveness as a haptic sensor to monitor the condition of human skin was examined. Signals obtained by moving the sensor over the surface of skin were processed to obtain the variance and intensity of power at several segmented frequency ranges. In this section, two experiments were carried out on the present sensor system and signal processing. The first experiment analyzes the sensor's ability to discriminate between the conditions of normal healthy skin and that of skin with atopic dermatitis, and the second measures the effect of aging on the condition of normal healthy skin.

Both values were used as the input layer value of a neural network in attempt to identify the morphological condition of skin . Skin with atopic dermatitis was compared with healthy skin, and 100% recognition of the atopic skin was achieved by training the network using the variance and power intensity fraction. Furthermore, from the results on the effect of aging, the intensity of power at several segmented frequency ranges was found to have a clear correlation with the age of skin.

On going research is currently being directed towards the application of this sensor to the evaluation of sustantation of the cosmetic efficacy of toiletries on skin together with the accumulation of data on the recognition of dermatitis.

REFERENCES

1.H. Tagami, Perspective and prospective views of bioengineering of the skin, *Fragrance Journal* 10(1993), 11-15.

2.T. Yamamura, Measuring methods of skin surface water content, *Fragrance Journal* 10(1993), 35-41.

3.M. Takahashi, Recent methods to measure the skin aging, *Fragrance Journal* 10(1993), 16-26.

4.T.H. Cook, Profilometry of skin: a useful tool for the substantation of cosmetic efficacy, *Journal of the Society of Cosmetic Chemistry* 31(1980), 339-359.

5.G.Harsanyi, Sensing effects and sensitive polymers, in: Polymer Films in Sensor Applications, Technomic Publishing Company, Inc., Lancaster, Basel, 1995, p.97.

6.G.M. Shepherd, The somatic senses, in: Neurobiology, Third edition, Oxford University Press, New York, Oxford, 1994, p.27

ANGULAR PIEZOELECTRIC ACTUATORS FOR DYNAMIC APPLICATIONS

Marc E. Regelbrugge

ABSTRACT

This paper addresses design, construction and performance issues associated with actuators capable of producing angular oscillating motions at frequencies sufficient to enable their application to scanning optical systems. The actuators considered here employ piezoelectric stack-type driving elements coupled with integrally machined mechanical motion amplification mechanisms to produce angular motions up to several degrees at frequencies approaching the kilohertz range. The new motion amplification mechanism, called a "dual-flextensional" mechanism, produces angular output directly from extension of the embedded piezoelectric, induced-strain actuator. A parametric design study of this class of actuator mechanism is undertaken to quantify the effects of realistic design constraints on the efficiency of the mechanism. The study indicates that dual-flextensional mechanisms can successfully transmit in excess of two-thirds of the stack actuator's maximum output across a wide range of desired output motion and rate limits. Efficiency of the dual-flextensional actuators compares favorably with similarly sized, commercially available piezoelectric tilt-mirror actuators optimized for higher-frequency operation, yet the new actuators admit operation over much larger ranges of tilt motion for applications operating at frequencies in the sub-kilohertz range. Actuators with capabilities similar to those discussed in this paper are employed as fast scanning elements in optical systems.

INTRODUCTION

Numerous optical systems require small, articulated mirrors to provide optical-path adjustment or scanning capabilities. In many cases, such mirrors are required to operate at fairly high speeds to accommodate data-detector rates or jitter compensation. Mirrors employed for such applications are called Fast Steering Mirrors (FSMs). FSMs typically direct optical paths at points of relatively high optical gain to provide scanning profiles for downstream devices such as focusing lenses, photodetector arrays or other targets. FSM requirements include, in particular, three difficult aspects: 1) positioning must be highly accurate and repeatable, 2) the device must operate at relatively high frequency, and 3) the range of motion must be sufficient to direct the optical path over the entire objective. When combined, these three requirements indicate a strong potential for application of electrostrictive actuators as driving elements since they are very stiff and provide inherently repeatable motions with low hysteresis. The challenge for application of electrostrictive actuators to FSMs lies in amplifying the relatively low motion output of these actuators to a useful range of mirror rotation to

Marc E. Regelbrugge, Rhombus Consultants Group, Inc., 2565 Leghorn Street, Mountain View, California, USA 94043

provide sufficient steering amplitude for optical applications. Furthermore, this amplification must be done without unduly compromising the stiffness of the resulting assembly, as the FSMs are required to operate at relatively high frequencies.

Applications of piezoelectric and electrostrictive actuators to optical systems are not new. For example, a paper by Fanson [1] describes application of electrostrictive stack actuators to the articulating fold mirror of Hubble Space Telescope's wide field and planetary camera. The flextensional type of mechanism considered here has also seen considerable development and optimization. An excellent overview of a class of flextensional mechanisms can be found in the work of Claeyssen, et al. [2]. Finally, commercial, piezoelectrically driven tilt mirrors have existed in the marketplace for several years [3]. All of these efforts are targeted toward providing greater and/or more robust performance in sensitive optical systems, yet their operational characteristics vary widely over the frequency band from quasi-static (0 Hz) up to nearly 20 kHz. The present innovation and study attempt to broaden the range of applicability of induced-strain actuators to optical systems by validating the concept for a compact, yet highly capable device for mirror articulation and pointing control.

This paper presents and evaluates a concept for a new, single-axis angular actuator to activate tilt- and fast-steering mirrors over a larger range of motion than commonly addressed using induced strain driving elements. The actuator concept considered here is a specialization of flextensional-type actuators that utilizes a double stage, oblique lever arrangement to tilt a thin, flat mirror over a range of several degrees at frequencies of several hundred Hertz. After a short review of the mechanics of flextensional mechanisms, three-dimensional dynamic models are used to direct selection of appropriate design parameters and to assess operating performance characteristics of these new devices. Performance estimates obtained from these models are then reviewed to assess limits of practical applicability to FSM devices. Device efficiency is quantified relative to ideal motion amplification mechanisms that provide no opposing material or dynamic stiffness and no series compliance to degrade motion output. Efficiencies in the range of 70%, based on actuator capability, can be achieved. Output motions of 50 mrad, and operating frequencies up to 1 kHz have also been shown to be achievable with these new devices.

Elementary Mechanics of Hinge-Type Flextensional Mechanisms

The mechanism considered here is a specialization of flextensional-type mechanisms incorporating two, serial stages whose geometric arrangement amplifies the small displacements of an induced-strain actuator into significant angular motions of an actuated body — a flat steering mirror, in the present case. Each link of the mechanism consists of short, thin flexures on either end of a thicker length of structural material (e.g. steel or titanium). In the ideal case, these flexures act as hinges at either end of the link. Each stage, incorporating four such links, amplifies motions applied in one direction into much larger, orthogonally directed motions. This concept is illustrated in Figure 1, below.

A simple analytical model of one link, shown in Figure 2, is useful to understand basic operation of the mechanism as a whole, and the effects of certain geometric design parameters on that operation. Symmetry is invoked to simplify the model, so only one component of the linkage shown in Figure 1 is considered in the simple model.

Taking the geometric notation of Figure 2, we can develop kinematic expressions relating the linkage output (w) to the input motion (u):

$$\begin{aligned} w &= a - L\sin(\varphi - \theta) = a - L\left(\sin\varphi\cos\theta - \cos\varphi\sin\theta\right) \\ u &= L\cos(\varphi - \theta) - b = L\left(\cos\varphi\cos\theta + \sin\varphi\sin\theta\right) - b \end{aligned} \tag{1}$$

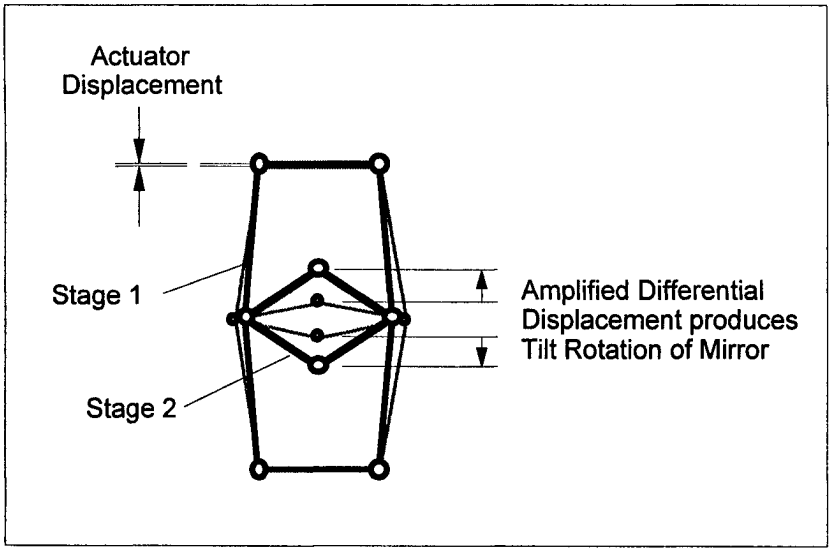


Figure 1. Dual-Flextensional Mechanism Concept for Tilt Mirror Application

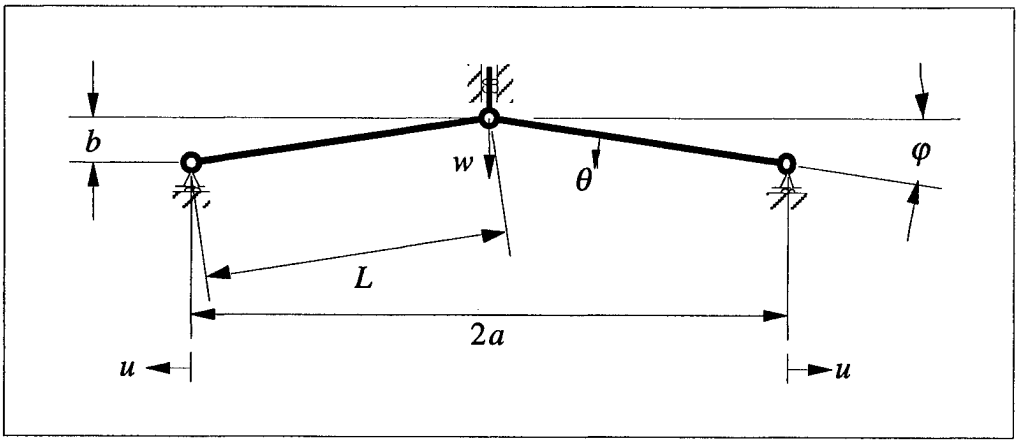


Figure 2. Basic Analytical Model of a Flextensional Link

Invoking the assumption of small deformation angles (θ), these relations simplify to

$$\begin{aligned} w &= a - L(\sin\varphi - \theta\cos\varphi) = L\theta\cos\varphi \\ u &= L(\cos\varphi + \theta\sin\varphi) - b = L\theta\sin\varphi \end{aligned} \tag{2}$$

The theoretical motion-amplification ratio of the mechanism is thus

$$\alpha = \frac{w}{u} = \cot\varphi \tag{3}$$

Assuming that each node of the linkage is associated with a rotational stiffness k_θ, the apparent, driven-point stiffnesses of the mechanism can be defined:

$$k_u = \frac{2k_\theta}{L^2 \sin^2 \varphi} \qquad k_w = \frac{2k_\theta}{L^2 \cos^2 \varphi}$$

These expressions uphold the necessary result that $k_w/k_u = \alpha^{-2}$.

Mechanical inefficiency arises in the mechanism by stretching and bending of the flexures. The effects of these influences will be examined here with the aid of three-dimensional, finite-element models of the entire mechanism.

Dual-Flextensional Mechanism

The mechanism shown in Figure 1 incorporates two flextensional motion-amplification stages in series. Theoretically, the motion amplification ratio of this assemblage should be the product:

$$\alpha_{mech} = \cot \varphi_1 \cot \varphi_2$$

Due to the finite stiffness of the mechanism's flexural hinges, the mechanism linkages present added parasitic stiffness that opposes actuator extension, and series compliance that reduces effective output stiffness and fundamental resonant frequency of the device. This latter quantity is of interest for dynamic applications because it limits the speed with which the mechanism can be controllably activated.

With a desire to evaluate mechanisms of this type under realistic assumptions, a parametric finite-element model of the two-stage mechanism was synthesized and employed to evaluate the ranges of output motion and supported-mirror resonant frequencies provided by mechanisms of the type shown in Figure 3. This mechanism incorporates a single, piezoelectric, stack-type actuator, and is shown supporting a small (25 mm x 12 mm) elliptical mirror element.

In the design analysis, the properties of the piezoelectric stack were chosen to match those of a commercially available, 8 mm-diameter, 20 mm-long, low voltage stack [4]. A generic, small mirror element was chosen to provide dynamic loading to the output of the mechanism. This mirror is a 25 mm-diameter, polished aluminum hexagonal element. Its mass was calculated to be roughly 5 grams, with tilt inertia of 220 gram-mm^2. The mirror element was held constant throughout the design study.

Mechanism design parameters considered were the link angles (φ_1 and φ_2), thicknesses and lengths of the solid flexures (parameters related to the joint stiffness k_θ), and relative widths of the two stages' links. A plot of the finite-element model is shown in Figure 4. The stack actuator is modeled as a bar oriented vertically in the central cavity of the first-stage linkage, and the mechanism is made of high-strength, stainless steel.

DESIGN STUDY RESULTS

The parametric finite-element model was exercised over the link-angle range $5° \le \varphi_1, \varphi_2 \le 15°$, with 0.1 mm-thick flexures between 1.0 and 1.25 mm long. The results of these simulations are plotted in Figure 5. This figure shows a group of relevant data points labelled "2-Stage Concept" that span the range of parameters examined in the present study for the dual-flextensional angular actuator design.

Also included in this figure are data points corresponding to three design cases of an "ideal" dual-linkage mechanism (i.e. using theoretical motion-amplification ratios), and two data points corresponding to commercially available piezoelectric tilt mirror actuators based on a simple lever mechanism. The lines labelled "$\omega\theta$ = const." refer to a constancy of the product of the maximum mirror tilt angle and the limiting, first resonant frequency of the mechanism. These lines reflects the capabilities of the chosen piezoelectric actuator when

stiffness is traded for output motion. The line passing through the "Ideal Model" data points reflects the actual capability of the example stack actuator. The dashed line below that reflects the derated capability of the actuator operating in the mechanism.

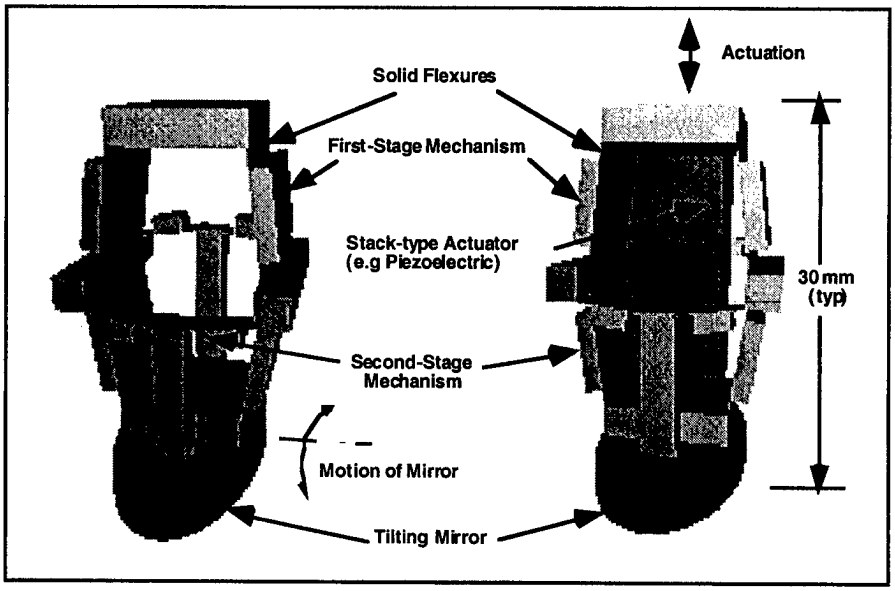


Figure 3. Views of Dual-Flextensional Mechanism supporting an Elliptical Tilt Mirror and with Actuator removed (left) and installed (right)

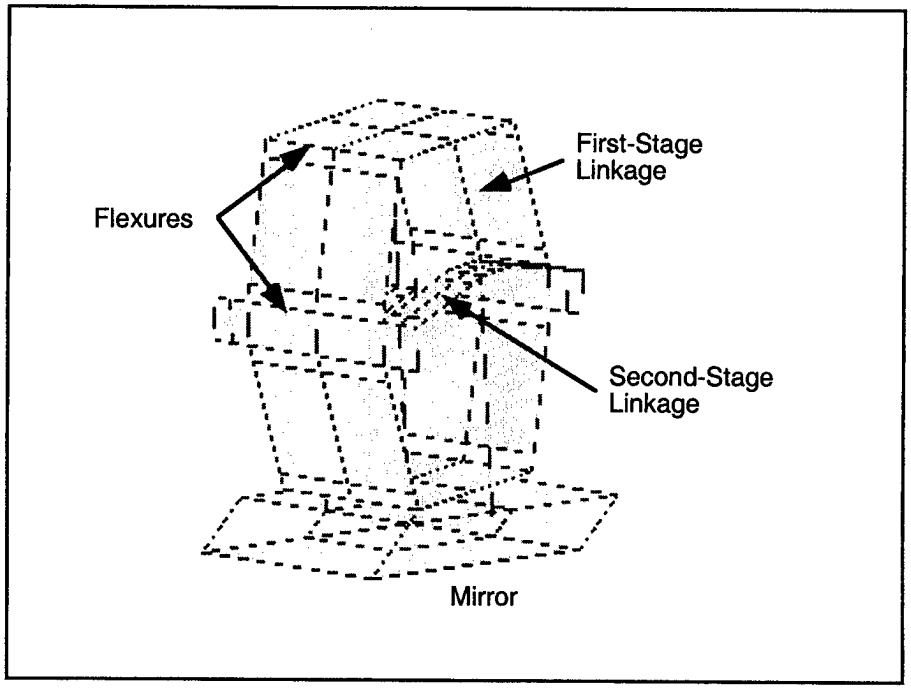


Figure 4. Dual-Flextensional Mechanism Parametric Finite Element Model

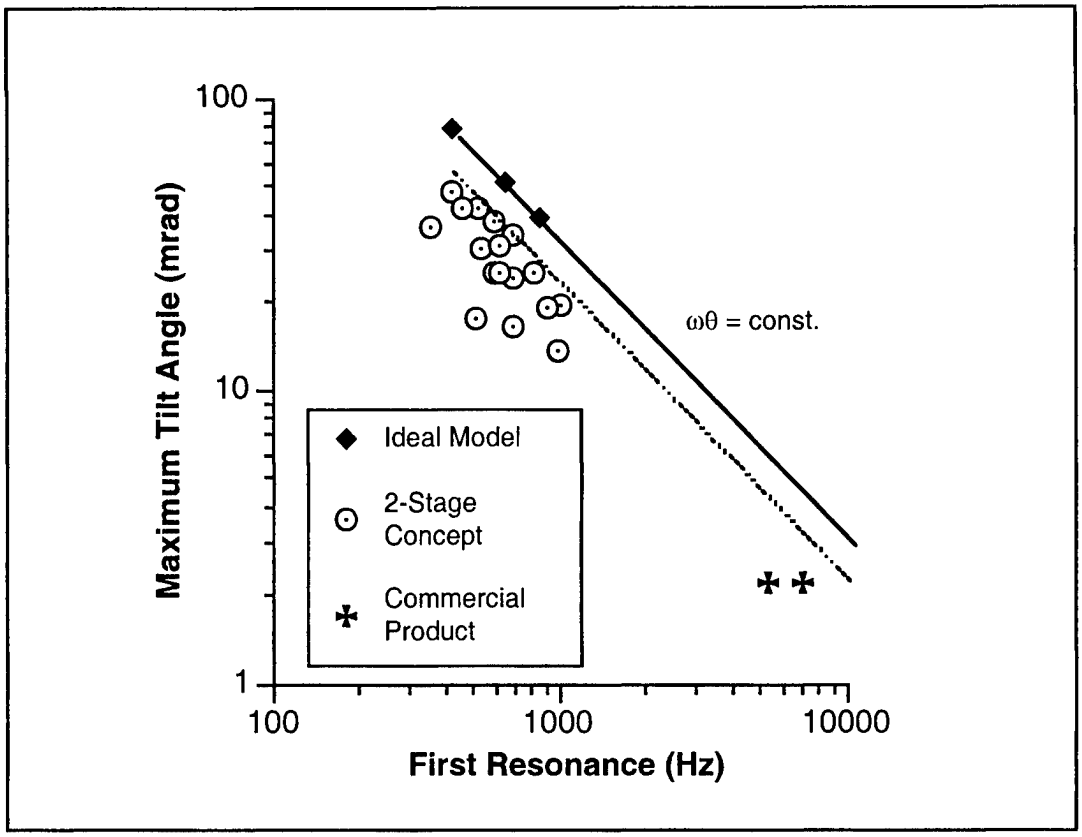


Figure 5. Design Study Results compared with Ideal and Commercial Mechanisms

The results shown in Figure 5 indicate that the dual-flextensional mechanism design is capable of producing roughly 50 mrad tilt at frequencies in the range of 400 Hz. This corresponds to a linear motion of ±0.3 mm at the mechanism output points, respectively, and an aggregate motion amplification factor of 20. Stiffening the mechanism to allow operation at higher frequency (1 kHz), provides only 10–15 mrad tilt motion at the supported mirror.

To quantify efficiency of the mechanism, we employ a metric of the product of frequency and motion ($\omega\theta$). This metric indicates how well the mechanism allows the actuator's capability to be applied to drive the objective, the tilt mirror in this case. For the cases analyzed, the maximum mechanism efficiency is 68%. This corresponds to an achievable frequency-motion product of 23 rad-Hz, compared with the theoretical actuator capability of 34 rad-Hz. Although this efficiency is in a moderate range, it nonetheless compares favorably with frequency-motion efficiencies calculated for commercially available devices, as examination of Figure 5 shows.

Finally, stresses due to bending deformations that are concentrated in the mechanism's thin flexures may be of concern. Stresses at maximum output (50 mrad) approach 900 MPa. As a result, material fatigue of the flexures should be an issue to be addressed further in mechanism design.

CONCLUSION

This paper has explored practical possibilities for design of a dual-flextensional mechanism to amplify the small motions typical of induced-strain actuators into significant angular motions of a supported component (e.g., a small mirror). Achievable angular output of the order of 3°, and maximum operating frequencies of the order of 1 kHz have been validated by realistic

design models. Additionally, the efficiency of the mechanism was determined to be of the order of 60–70%; comparable to the efficiencies of simpler, commercially available tilt mirrors.

While the full range of possible design solutions for this type of actuator have not been explored here, the present study does quantify the mechanical limitations of this type of mechanism with sufficient fidelity to enable appropriate estimates of performance for such mechanisms employing larger actuators to provide greater motion. Evidence of this assertion comes from the relatively wide range of output characteristics achievable at mechanism efficiencies in the range 60–68%, as shown in Figure 5. Thus, similar mechanisms which may be assumed to be realizable based on the present study, will be able to deliver at least 60% of their theoretical output if properly designed. For example, mechanisms capable of 100 mrad tilt angles should be feasible using 40 mm-long variants of the piezoelectric actuator considered in this short study.

Finally, the present study has shown that solid-state actuation can be extended into larger motions ranges for optical systems that do not require very high frequency adjustments for operation. The dual-flextensional concept described here offers a compact and efficient device for this class of applications.

REFERENCES

1. Fanson, J., "Articulating Fold Mirror for the Wide Field and Planetary Camera," *Proc. Fourth Int'l Conf. and Adaptive Structures*, E. J. Breitbach, B. K. Wada and M. C. Natori, eds., Technomic, Lancaster, PA, 1994.
2. Claeyssen, F., et al., "High Stroke/Precise Positioning Piezo Actuators and Motors," *Proc. Tenth Int'l. Conf. on Adaptive Structures and Technologies*, R. Ohayon, M. Bernadou, eds., Technomic, Lancaster, PA, 2000.
3. Model S-224 Technical Datasheets, Physik Instrumente GmbH, Waldbronn, Germany.
4. Model P-830.10 Low Voltage Actuator Datasheet, Physik Instrumente GmbH, Waldbronn, Germany.

A SELF-SENSING ACTUATOR USING PIEZOELECTRIC FILMS WITH DIFFERENT THICKNESS FOR VIBRATION CONTROL OF CURVED STRUCTURES (PROPOSITION OF PRINCIPAL CONCEPTS AND APPLICATIONS TO CANTILEVER AND CIRCULAR RING)

Tsutomu Nishigaki, Mitsuru Endo

ABSTRACT

A self-sensing actuator using piezoelectric two films with different thickness and area, which are closely installed on one surface of general curved structures and are treated as two capacitors in the active RC bridge circuit, is proposed from the view-point of symplification of hardware aspects of devices toward the realization of smart structures. In the first half of this paper, it is implied that this device is effective in the following points; 1) compensation of ME noises, 2) ability of obtaining high feedback gain and enough control power and 3) compensation of temprature for pyroelectric effect. Vibration control effects are estimated by theoretical analyses of free vibration response of a cantilever which is an example of fundamental flexible structures, and the guideline for constructing control circuit is shown. Then, the validity of proposed self-sensing actuator scheme is verified by conducting the experiment of free vibration response of a cantilever. In the second half of this paper, application of the proposed method to the vibration control of curved structures is investigated. A flexible circular ring is treated as an example of curved structures and fundamental equations of the circular ring with the proposed self-sensing actuator are derived and vibration control effects are estimated by numerical analysis. Then, the vibration control experiment is performed using an aluminum circular ring, and it is shown that the lowest vibration mode is efficiently controlled.

INTRODUCTION

Piezoelectric films are flexible, light weight, thin sheet-like elements and can be easily bonded on general curved structures as distributed sensors/actuators for vibration control application. Therefore, with these elements combined with control circuits, smart curved structures are expected to be realized. However, as shown in figure 1(a), in the vibration of curved structure, in-plane motion (IP) and bending motion (BD) are coupled, and in general strain distribution along the thickness direction is not symmetric. For that reason, in general, the system tends to be unstable when sensor and actuator are bonded on the opposite surfaces of the curved structure as in figure 1(b). Actually, even in the case of straight beam, it has been observed in the authors' bending vibration control experiment of a flexible beam using rectangular-shaped piezoelectric film sensor/actuator pairs, that the system became unstable due to the effect of in-plane strain, which was not considered in the theoretical model[1,2]. In such case, if a self-sensing actuator[3] bonded on one surface is used, as shown in figure 1(c), the system may become stable

Department of Mechanical Sciences and Engineering, Tokyo Institute of Technology, 2-12-1, O-okayama, Meguro-ku, Tokyo, 152-8552 Japan.

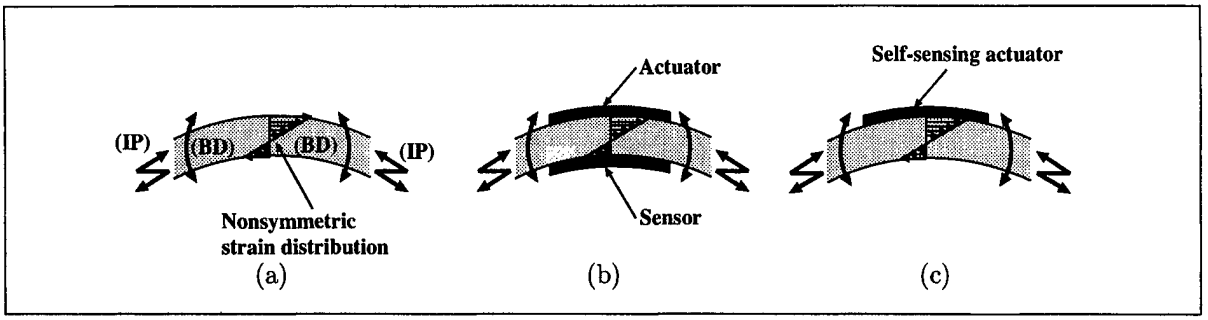


Figure 1. Sensing and actuation of a curved structure using distributed sensor/actuator. (a) In-plane motion(IP) and bending motion(BD); (b) Sensor and actuator bonded on both surfaces of the structure; (c) Self-sensing actuator bonded on one surface of the structure.

in principle. In this method, the bridge circuit is constructed usually by using refernce capacitor and the piezoelectric element is used as the actuator and as the sensor simultaneously. However, the difficulty in using a self-sensing actuator is that the stability of the system strongly depends on the balancing of the bridge circuit. To date, a lot of studies exist concerning the self-sensing actuator(e.g. [4,5,6,7,8,9,10]). In these studies, piezoceramic bimorph actuators were mainly treated, and in order to overcome the above-mentioned difficulty, one of the application of the dummy element[4,5], improvement of software aspects of devices introducing robust control theory[6] or the concept of virtual bridge circuit[7] was studied. However, since bimorph actuator and piezoceramics were treated, effective methods for curved structure have not been developed. When we turn our focus on the application of piezoelectric films, compensations of 1) ME noises, 2) interference between the sensor and the actuator and 3) temperature variation are essentially important for balancing bridge circuit and obtain effective control power.One way to overcome these problems is to introduce control theory and solve them from the software aspects by using computer powers. However, from the viewpoint of realization of smart structure, it is further

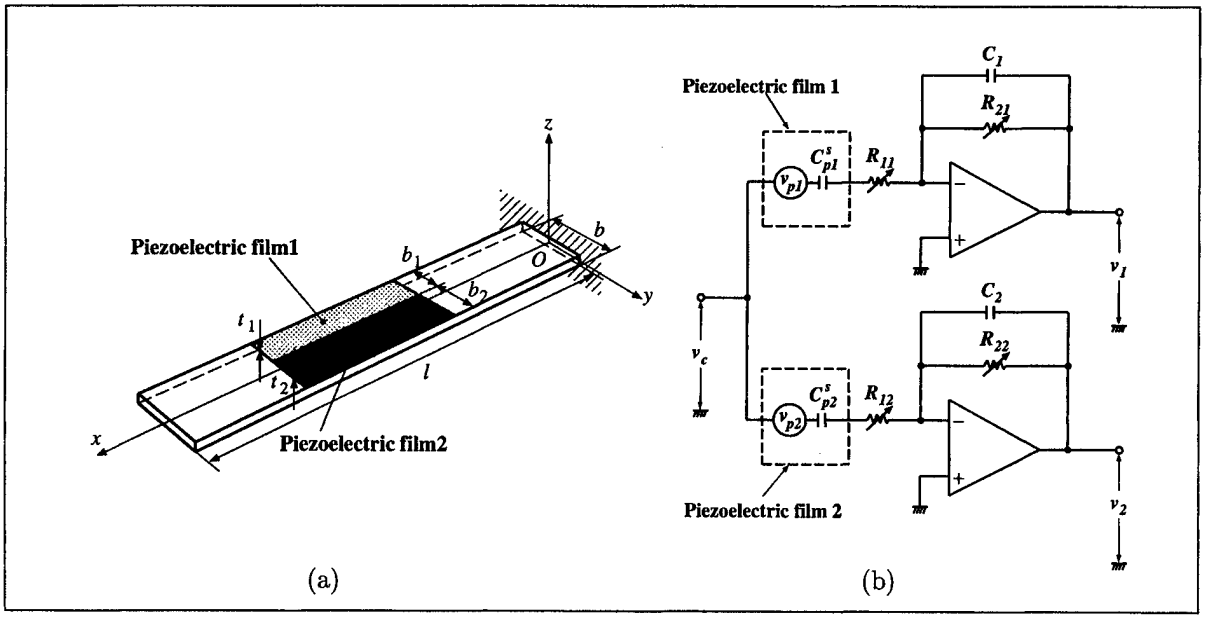


Figure 2. Proposed self-sensing actuator. (a) Piezoelectric films with different thickness and area applied to a cantilever beam; (b) Active RC bridge circuit using two operational amplifiers.

important that symplification of hardware aspects of devices and to compose structural element, sensor, actuator and controller in well balance such that the entire system can be simpler and smarter. From this standpoint, a self-sensing actuator using piezoelectric films which can be directly applied to curved strucuture is developed in this study.

PRINCIPAL CONCEPTS

Now, we propose a self-sensing actuator using piezoelectric films with different thickness and area, which are closely installed on one surface of structures and treated as two capacitors in the active RC bridge circuits. In the present method, thickness and shape of each piezofilm are adjusted such that capacitance of two films become equivalent each other, and thus balancing of the bridge circuit is easy to maintain. From the view-point of developing smart structure, this method is expected to be effective in the following view-points:

1. As piezoelectric films are used, shaping of two films is easy to implement and thus spatial filtering effect can be used in the design of this device.
2. This device is easily fitted to general curved structures.
3. Magneto-electrical noises are cancelled by common mode rejection effects of the bridge circuit and differential amplifier.
4. Pyroelectric effects are cancelled by the same reason as 3.
5. This device is far smarter than those methods in which the reference capacitor is placed out of the structure, and besides the power of the reference element can be utilized effectively.
6. Magneto-electrical interference between the sensor and the actuator in this device may be much less than using two films separately as sensor and as actuator.

In the next sections, fundamental caracteristics of the proposed self-sensing actuator are studied with by applying to vibraiton control of a cantilever, and the application to a circuiar ring is discussed.

CANTILEVER CASE

Modelling of Self-Sensing Actuator and Characteristics of the Bridge Circuit

As shown in figure 2(a), suppose two rectangular-shaped piezofilms with different thickness are closely bonded on one surface of cantilever beam. Let t_{cn} and $S_n(n{=}1,2)$ be thickness and area of piezofilm 1 and 2, and consider the two films shaped under the following condition:

$$\frac{S_1}{t_{c1}} = \frac{S_2}{t_{c2}} \tag{1}$$

Under the condition (1), capacitances of two films may become equivalent. Is should be noted here that the condition (1) is not restricted by the shapes of two films. Considering velocity feedback in order to add damping, active RC bridge circuit is constructed with these two films as in figure 2(b). C^s_{pn} and v_{pn} are equivalent capacitances and output voltages of film and R_{ij} and C_i are resistances and capacitances, respectively. v_c is feedback voltage. Sensor output voltage v_s is defined as:

$$v_s = v_1 - v_2 \tag{2}$$

In order to implement equation (2) to obtain sensor output, a differential amplifier is connected in series with the bridge circuit. If the frequency is low enough, v_s is described as:

$$v_s = -T^* \left(K_{p1} - K_{p2}\right) \frac{\partial}{\partial t} \left(\left.\frac{\partial u}{\partial x}\right|_{x_2} - \left.\frac{\partial u}{\partial x}\right|_{x_1} \right) \tag{3}$$

where $T^* \equiv C_{p1}^s R_{21} = C_{p2}^s R_{22}$, and K_{pn} are constants which are decided from the parameters of the film. From equation (3), v_s is not affected by v_c, and therefore, a self-sensing actuator is constructed.

Theoretical analysis

Equations of motion of the cantilever beam with piezofilms in modal coordinates are derived as follows[1,2,11]:

$$\{\ddot{q}_j\} + 2[\zeta][\Omega]\{\dot{q}_j\} + [\Omega^2]\{q_j\} = \{f_j\} + \{f_j^{\text{inp}}\} \tag{4}$$

where q, ζ, Ω and f_j^{inp} are generalized coordinate, modal damping ratio, natural frequency and generalized input force, respectively. f_j is generalized force of piezofilm actuator and described as follows:

$$f_j = k \sum_{n=1}^{2} b_n v_{an} \Phi_j \tag{5}$$

where v_{an} are voltages applied to each films, b_n is width of films, k is a constant. Φ_j is as follows:

$$\Phi_j = \frac{\partial \phi_j(x_2)}{\partial x} - \frac{\partial \phi_j(x_1)}{\partial x} \tag{6}$$

where ϕ_j are normalized mode shape functions of Bernoulli-Euler beam. Output voltages of piezofilms are derived as follows:

$$v_{pn} = \sum_{j=1}^{J} K_{pn} \Phi_j q_j \tag{7}$$

Consider direct feedback control as the vibration control law and it is defined as follows:

$$v_c = g v_s \tag{8}$$

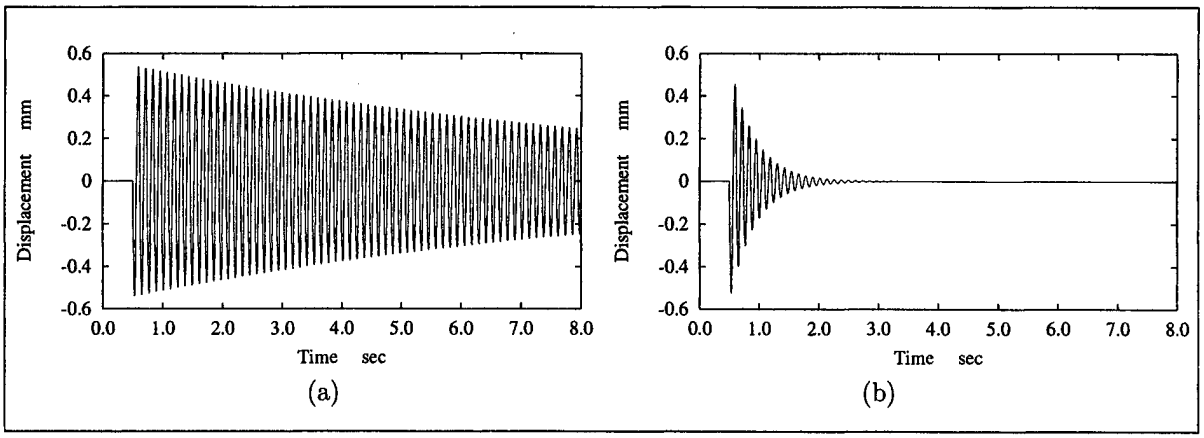


Figure 3. Displacement response of the cantilever beam (Theoretical results). (a) Without control; (b) With control.

Solving equations (4),(7) and (8) together with bridge circuit dymamics, time response of the system is caluculated. An aluminum beam of length 225mm, width 32mm, thickness 0.5mm is considered, and two piezofilms of thickness 30μm and 100μm and width 6mm and 20mm, are bonded on one surface. Feedback gain g is set to 430. Length of films are 100mm and they are bonded from x_1=30mm to x_2=130mm. Figure 3 shows the displacement response of the beam under the condition that an impact force is appled to the tip of the beam. From figure 3, it can be said that the lowest vibration mode is efficiently controlled. Effect of parameter mismatch of the bridge circuit was also considered in this analysis by perturbing time constants T^* from $\pm 0.1\%$ to $\pm 1\%$, and it was concluded that the mismatch of time constants in the bridge circuit is desirable within $\pm 0.1\%$ to obtain the vibration control effects.

Experiment

An experimental apparatus shown in figure 4 was manufactured. Parameters of this experi-

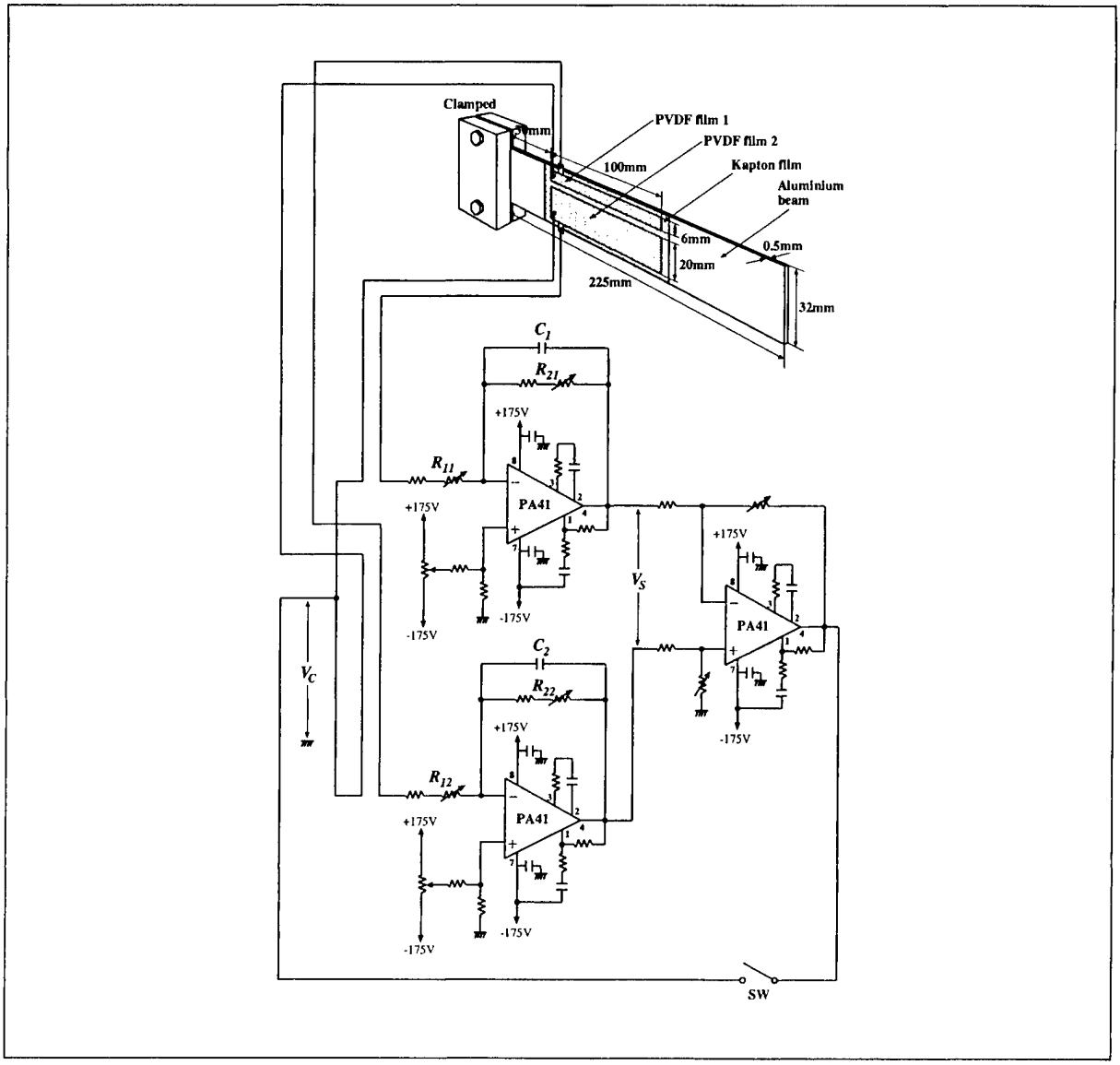


Figure 4. Experimental apparatus

ment are the same as those used in the theoretical analysis. A Capton film of thickness 12.5μm is bonded between the beam and the piezofilm(PVDF) for electrical insulation. Three power operational amplifiers(PA41) are used to construct active RC bridge circuit and differential amplifier. Displacement responses of the beam with and without control are shown in figure 5, and it was verified that effettive control effect is obtained.

APPLICATION TO CIRCULAR RING

Application of the proposed method to the curved structure is described in this section, and a flexible circular ring is treated as an example of curved structures. Figure 6 shows the circular ring with piezofilms of different thickness bonded on outer surface of it. Using coordinate systems shown in figure 6, fundamental equations are derived based on the Hamilton's principle and equations of motions in modal coordinates are derived as follows:

$$\ddot{\boldsymbol{x}}_{kj} + 2\boldsymbol{C}\boldsymbol{\Omega}\dot{\boldsymbol{x}}_{kj} + \boldsymbol{\Omega}^2\boldsymbol{x}_{kj} = \boldsymbol{T}^{\mathrm{t}}_{kj}(\boldsymbol{F}_{kj} + \boldsymbol{F}^{\mathrm{inp}}_{kj}) \tag{9}$$

where

$$\boldsymbol{x}_{kj} = \boldsymbol{T}^{\mathrm{t}}_{kj}\boldsymbol{u}_{kj} \tag{10}$$

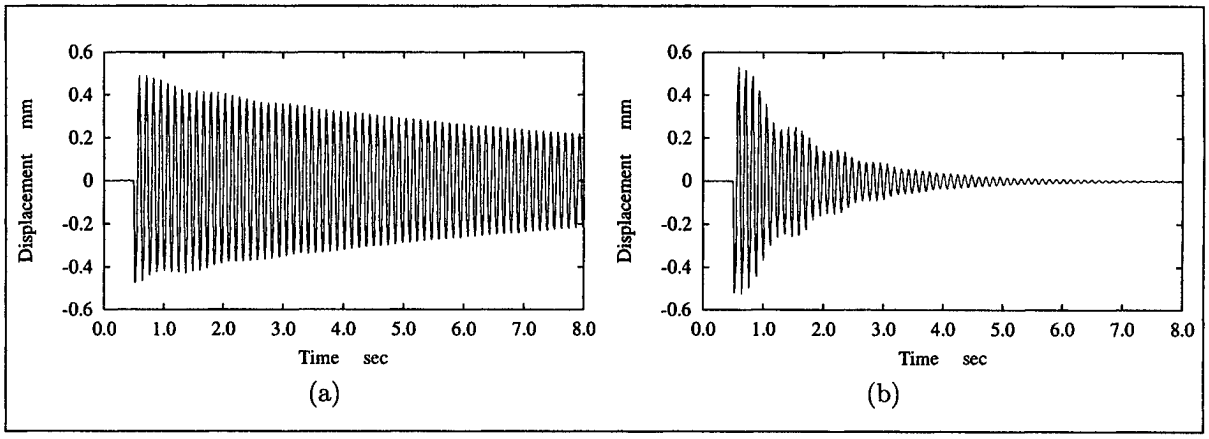


Figure 5. Displacement response of the cantilever beam (Exprimetal results). (a) Without control; (b) With control.

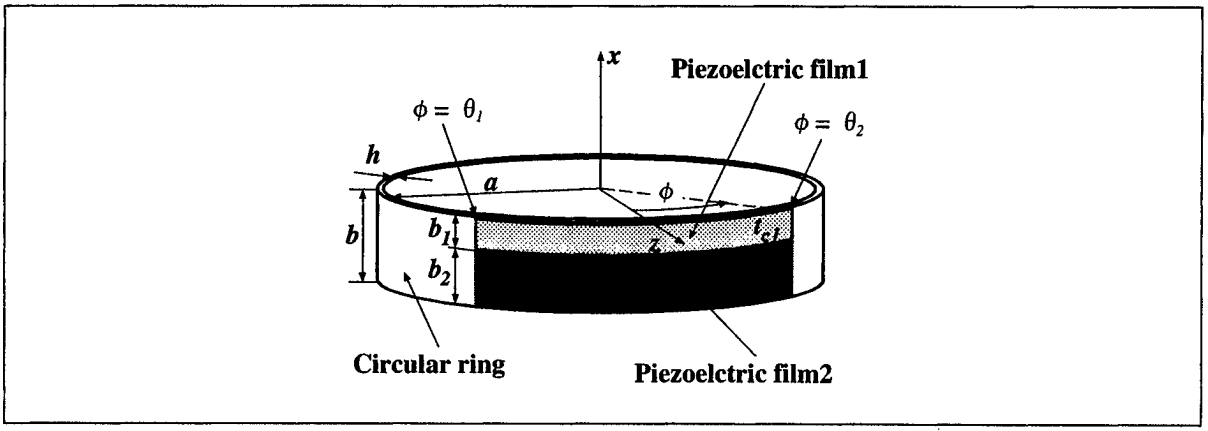


Figure 6. Application to circular ring

$$\boldsymbol{C} = \begin{bmatrix} \zeta_{1j} & 0 \\ 0 & \zeta_{2j} \end{bmatrix}, \quad \boldsymbol{\Omega} = \begin{bmatrix} \omega_{1j} & 0 \\ 0 & \omega_{2j} \end{bmatrix} \tag{11}$$

where $\boldsymbol{x}_{kj}$ is a vector of generalized coordinate and $\boldsymbol{T}_{kj}$ is a matrix consisting of normalized eigenvectors of the system matrix $\boldsymbol{A}_{kj}$. ω_{1j}, ω_{2j} and ζ_{1j}, ζ_{2j} are natural frequencies and modal damping ratios of transverse component mode and circumferential component mode, respectively. $\boldsymbol{F}_{kj}$ and $\boldsymbol{F}_{kj}^{\mathrm{inp}}$ are the vectors of generalized force of piezofilm actuator and generalized input force, respectively. Superscript t describes matrix transpose. Solving equation (9) combined with direct feedback control law and bridge circuit dynamics which are the same as cantilever case, time history of the system is caluculated. An aluminum circular ring of radius 100mm, width 40mm, thickness 0.5mm and two piezofilms of thickness 40μm and 100μm bonded on outer suafaces of it is considered. These films are bonded from ϕ_1=-π/4 rad to ϕ_1=π/4 rad. Feedback gain g is set to 400. An experimental apparatus was also manufactured which has the same parameters as mentioned above, and has the same electrical circuit as shown in figure 4, and free vibration responses of the circular ring with and without control under the condition that an impact force is applied to the position ϕ=0 are caluculated and measured in theoretical analysis and experiment. Figure 7 shows the displacement responses of the lowest vibration mode (circumferential wave number j is 2) of the circular ring with and without control. In these figures, figures (a) and (b) show the theoretical results and figures (c) and (d) show the experimental results. From these figures, it is observed that efficient control effect is obtained and the results of theory and experiment are in excellent agreement.

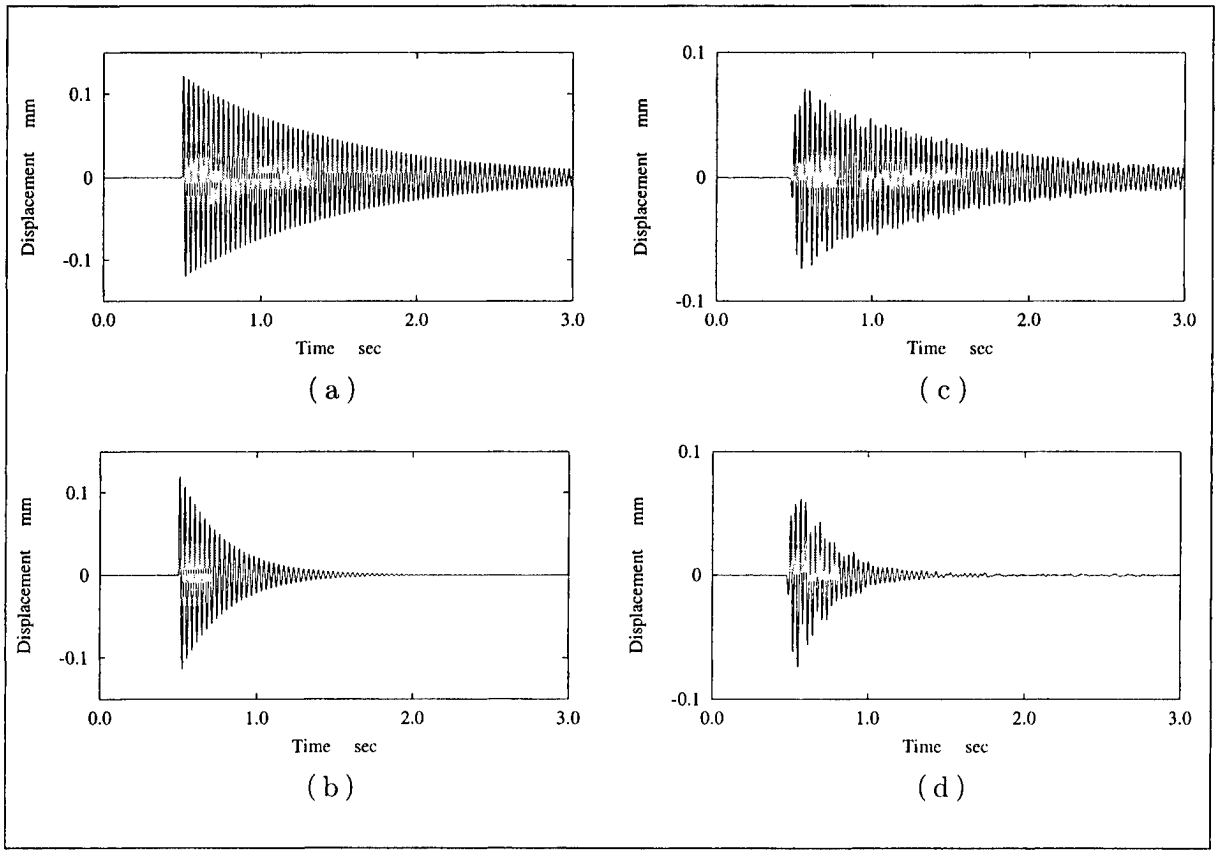


Figure 7. Displacement response of the lowest mode of circular ring. (a) Without control(theory); (b) With control(theory); (c) Without control(experiment); (d) With control(experiment).

CONCLUSIONS

In this report, a self-sensing actuator using piezoelectric films with different thickness and area, which are closely installed on one surface of structures and are treated as two capacitors in the active RC bridge circuit was proposed. Fundamental equations were derived for the case in which the proposed method was applied to a cantilever beam, which was an example of fundamental flexible structures. Based on these equations, vibration control effects were estimated by theoretical analysis. It was also shown that the mismatch of time constants in the bridge circuit was desirable within ±0.1%. Free vibration control experiments were performed using a cantilever beam and it was shown that the lowest vibration mode was efficiently controlled. In the second half of this paper, application to curved structures was studied and a flexible circular ring was treated. Fundamental equations were derived using the Hamilton's principle and free vibraion responses were caluculated and compared with those of experiments. It was shown that the lowest vibration mode was efficiently controlled, and thus the proposed method is effective in the vibration control of curved structures. The proposed technique will be extended to the multi-mode vibration control case, in which shaping of two films will have large effects on the control effects of each vibration mode.

ACKNOWLEDGEMENT

The authors would like to thank Mr. Atsushi Kawano; graduate student of Tokyo Institute of Technology, for his assistance in deriving fundamental equations and carrying out theoretical analyses.

REFERENCES

1. Nishigaki, T., Odawara, Y., and Endo, M. 1995. "Multimodal Vibration Control of a Cantilever Beam with Collocated Bonded Piezoelectric Film Sensors and Actuators," *Proc. MIMR*, pp. 399-402.
2. Nishigaki, T., Odawara, Y., and Endo, M. 1997. "Vibration Seinsing and Control of a Flexible Beam Using Piezoelectric Films," *Trans. JSME ser.C*, 63(615), pp. 3728-3734.(in Japanese)
3. Dosch, J. J., Inman, D. J. and Garcia, E. 1992. "A Self-Sensing Actuator for Collocated Control," *J. Intell. Mater. Syst. and Struct.*, 3, pp. 166-185.
4. Splanger, R. L. and Hall, S. R. 1994. "Broadband Active Structural Damping using Positive Real Compensation and Piezoelectric Simultaneous Sensing and Actuation," *Smart. Mater. Struct.*, 3, pp. 448–458.
5. Jones, L., Garcia, E. and Waites, H. 1994. "Self-Sensing Contol as Applied to a PZT Stack Actuator Used as a Micropositioner," *Smart. Mater. Struct.*, 3, pp. 147–156.
6. Oshima, K., Takigami, T. and Hayakawa, Y. 1996. "Robust Vibration Control of a Cantilever Beam Using Self-Sensing Actuator," *Trans. JSME ser.C*, 62(604), pp. 4499-4506.(in Japanese)
7. Takigami, T., Oshima, K. and Hayakawa, Y. 1998. "Tracking Control of a Cantilever Beam Using Self-Sensing Actuator Based on Virtual Bridge Circuit," *Trans. JSME ser.C*, 64(624), pp. 2931-2938.(in Japanese)
8. Guo, C. C. and Tani, J. 1994. "Sensorless Vibration Control of A Cantilever Beam," *Proc. 74th JSME Spring Annual Meeting*, 940(10), pp. 669-671.(in Japanese)
9. Tzou,H.S. and Hollkamp,J.J., 1994. "Collocated Independent Modal Control with Self-Sensing Orthogonal Piezoelectric Actuators (Theory and Experiment)," *Smart Mater. Struct.*, 3. pp. 277-284.
10. Ogasawara, A., Sasaki, M. and Oishi, A., 1998. "Positioning Control of a Self-Sensing Micro PVDF Actuator," *Trans. JSME ser.C*, 64(620), pp. 1320-1326.(in Japanese)
11. Nishigaki, T., Inoue, H., and Endo, M. 1999. "Vibration Control of a Beam with Piezoelectric Film Sensors/Actuators," *Trans. JSME ser.C*, 65(633), pp. 1937-1945.(in Japanese)
12. Nishigaki, T., Kawasaki, Y., and Endo, M. 1999. "Vibration Control Experiments of a Simply Supported Beam with Triangular-Shaped Piezoelectric Film Sensor/Actuator," *Trans. JSME ser.C*, 65(637), pp. 3493-3498.(in Japanese)

VARIABLE FREQUENCY FLEXURAL PIEZOELECTRIC TRANSDUCERS FOR HIGH POWER LINEAR CHIRP TRANSMISSION

Julien E. Bernard, George A. Lesieutre

ABSTRACT

To overcome low radiation resistance, low frequency underwater transducers must be operated in the vicinity of resonance. To provide maximum velocity at resonance, they are often designed as high Q narrowband devices. Various approaches have been used to increase the bandwidth of these transducers, including impedance matching layers and velocity feedback, among others. However, these approaches often result in reduced peak sensitivity (response level at the resonance frequency). In contrast, low frequency transducers with a variable and controllable resonance frequency, offer the double advantage of increased effective bandwidth and maximum sensitivity at almost all frequencies within the bandwidth.

The responses of fixed frequency and variable frequency piezoelectric ceramic tonpilz transducers to a linear chirp were calculated and compared. The resonance frequency of the fixed frequency tonpilz was set to the center frequency of the linear chirp, while that of the variable frequency tonpilz was matched to the dominant frequency of the chirp at all times. The results show that the variable frequency transducer can efficiently transmit linear chirps of much larger bandwidth.

A method of varying the first resonance frequency of some widely used underwater transducers, trilaminar flexural piezoceramic bars and disks, is also presented. Positive bias electric fields are added to the driving AC field to generate either a tensile in-plane load. This load modifies the effective flexural rigidity of the transducer, which in turn affects its resonance frequencies.

INTRODUCTION: THE LINEAR FREQUENCY MODULATED CHIRP

Linear frequency modulated (LFM) chirps are signals of the form:

$$s(t) = w_\tau(t)\sin(\omega_c(t)t) \tag{1}$$

Julien Bernard, Penn State University, 229 Hammond, University Park, PA 16802.
George A. Lesieutre, Penn State University, 229 Hammond, University Park, PA 16802.

where:

$$\omega_c(t) = \omega_0 + \beta t/2 \tag{2}$$

$$\beta = 2\frac{\Delta\omega}{\tau} \tag{3}$$

$w_\tau(t)$ is a windowing function of duration τ, $\sin(\omega_c(t)t)$ is the signal "phase," $\omega_c(t)$ is the carrying frequency, ω_0 is the initial carrying frequency, $\Delta\omega$ is the frequency sweep, and β is the (instantaneous) frequency sweep rate. The carrying frequency at the center of the pulse:

$$\omega_{\tau/2} = \omega_0 + \beta\tau/4 = \omega_0 + \Delta\omega/2 \tag{4}$$

is referred to as the center carrying frequency. Another frequency of interest is the terminal carrying frequency, which is the carrying frequency at the end of the pulse:

$$\omega_\tau = \omega_0 + \beta\tau/2 = \omega_0 + \Delta\omega \tag{5}$$

Figure 1 shows a linear frequency modulated (LFM) chirp windowed by a rectangular function. LFM chirps are used in active SONAR as they provide good resolution in both range and velocity [1]. With constant frequency (CW) pulses, the range is proportional to τ, whereas the doppler shift resolution is inversely proportional to τ. Hence, a trade-off between range and velocity resolutions must be made when choosing the duration of the CW pulse. With LFM chirps, the range resolution is proportional to τ, and the doppler shift resolution is proportional to β. Thus high range and velocity resolutions can be achieved simultaneously by using a short, high sweep rate LFM chirp.

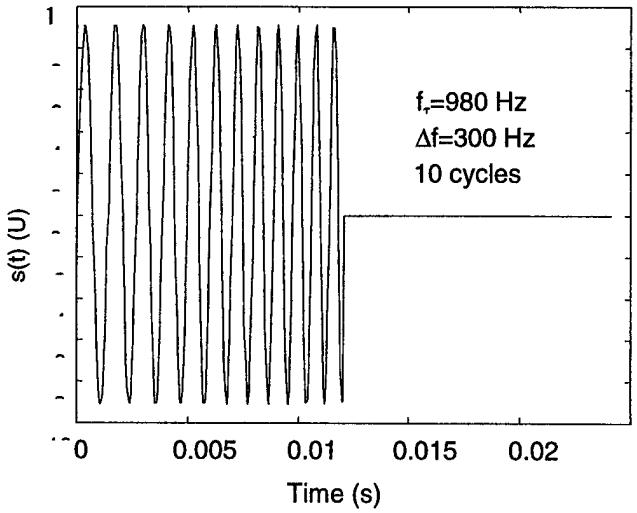


FIGURE 1. A LINEAR FREQUENCY MODULATED CHIRP

The instantaneous frequency of a complex signal is given by the derivative of the phase. The instantaneous bandwidth is governed only by the amplitude. In the case of a LFM chirp *s(t)*, defined by Eq. (1), the instantaneous frequency is:

$$\langle \omega \rangle_t = \omega_0 + \beta t \tag{6}$$

THE TRANSMISSION OF A LFM CHIRP BY A NARROW BAND, FIXED FREQUENCY TRANSDUCER

The response of a hypothetical low frequency piezoceramic transducer to various LFM chirps is now addressed. The transducer under consideration is a tonpilz transducer. The driving element is a stack of piezoceramic rings operating in the k_{33} mode. The head mass is assumed to be in an infinite baffle. For simplicity, the tail mass is assumed to be sufficiently heavy so that it can be approximated by a fixed boundary condition. The dimensions are reported on Figure 2, while the material properties are summarized in Table 1.

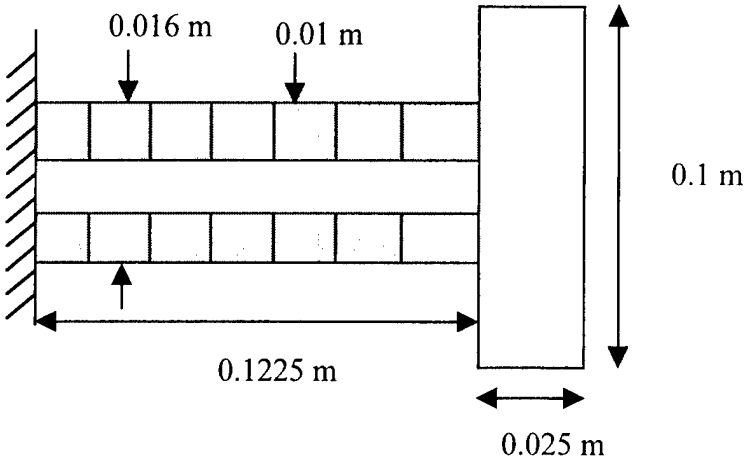


FIGURE 2. A TONPILZ TRANSDUCER

TABLE 1: MATERIAL PROPERTIES

		ρ (kg/m^3)	s_{33}^E(m^2/N)	e_{31}(C/m^2)	$\varepsilon_{33}^T/\varepsilon_0$
Head mass	Stainless Steel 316 MIL-S-18262-3	8020	-	-	-
Piezoceramic rings	PZT 5A	7750	18.8 10^{-12}	15.8	1700

The transducer was modeled as a bar vibrating in the longitudinal direction with one end fixed and the other end connected to the head mass. A one-term modal expansion was used to derive the lumped parameter elements of an equivalent circuit model, shown in Figure 3, about the first resonance frequency. For this, the mode shape corresponding to the first resonance frequency in presence of the head mass was selected. Finally, because the size of the transducer is much smaller than the acoustic wavelength at the resonance frequency, the

radiation mechanical resistance was obtained by using the analytical expression for the low frequency radiation resistance of a baffled circular piston [2]. This expression was then evaluated at the transducer resonance frequency. For more details about equivalent circuits, see [3]. Table 2 summarizes the values of the elements of the equivalent circuit of Figure 3. It also lists the transducer undamped resonance frequency, its mechanical quality factor, and its –3 dB bandwidth. The transducer was also modeled using an axisymmetrical finite element model in ANSYS, and the values of the undamped resonance frequency and quality factor were found to match almost exactly the analytical values. Also, no other mode than the first longitudinal mode was observed in the vicinity of the first longitudinal mode resonance frequency.

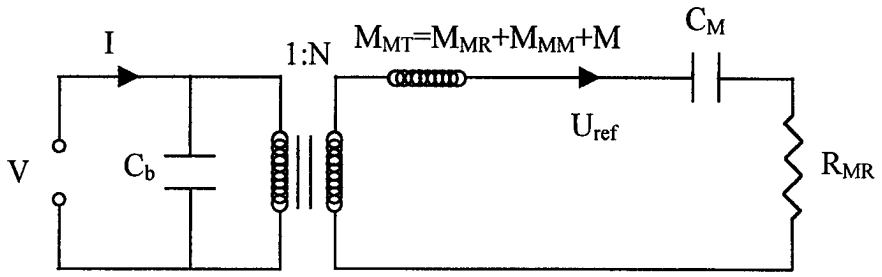


FIGURE 3. EQUIVALENT CIRCUIT MODEL OF TONPILZ TRANSDUCER

TABLE 2: EQUIVALENT CIRCUIT PARAMETERS

M (kg)	M_M (kg)	M_{MR} (kg)	C_M (m/N)	R_{MR} (Ns/m)	N (N/V)	f_0 (Hz)	Q_M	B_{-3dB} (Hz)
1.575	0.0575	0.342	$1.3355\ 10^{-8}$	256.34	0.44798	980	47.43	20.66

The value of the quality factor of the transducer is typical of low frequency transducers. Due to size limitations, low frequency underwater transducers are usually much smaller than the acoustic wavelength. This results in low radiation resistance and high radiation reactance, or mass loading. The two combined yield a high quality factor for the transducers. The quality factor being the inverse of the –3 dB fractional bandwidth, low frequency transducers are typically narrow band.

Figure 4 shows the Wigner time-frequency distribution (WD) [4-9] of the transducer velocity in response to an LFM chirp input. As expected, the acoustic energy density is quite different from that of the input signal. At any instant, the acoustic energy density is mostly concentrated around the transducer resonance frequency, instead of following the chirp instantaneous frequency (solid line).

Any low ripple, wide band signal whose bandwidth is in excess of the transducer –3 dB bandwidth appears to the transducer as an impulse. This fact seriously limits the use of low frequency transducers for active SONAR, which requires the use of short, high sweep and hence, wide band, LFM chirps. Though it is possible to design optimal input signals which result in an output signal closer to the desired LFM chirp, this can only be done by reducing the acoustic energy density in the vicinity of the transducer resonance frequency. Of greater interest is to find a technique such that the output acoustic energy density is maximum at all frequencies within the bandwidth of the LFM chirp.

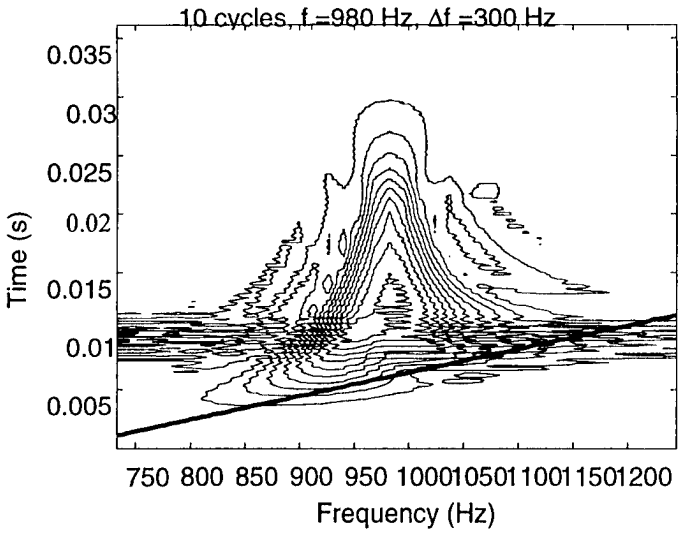


FIGURE 4: CONTOUR PLOT OF THE WD OF THE VELOCITY RESPONSE OF THE FIXED FREQUENCY TONPILZ TRANSDUCER TO A 10 CYCLE, HIGH FREQUENCY SWEEP LFM CHIRP

THE TRANSMISSION OF A LFM CHIRP BY A NARROW BAND, VARIABLE FREQUENCY TRANSDUCER

Numerous techniques have been developed to transform existing fixed frequency transducers into actively-tuned transducers [10-13]. Most of them consist of varying the stiffness of the transducer actively. Though the use of wide band, tunable, high frequency transducers for LFM chirp transmission has been investigated [10], that of narrow band, tunable low frequency transducers remains to be explored. In this section, the hypothetical tonpilz transducer is assumed to be tunable in frequency.

At this point, it not obvious how to obtain the optimal transducer resonance frequency as function of time. For the transmission of a LFM chirp, the most intuitive choice is the instantaneous frequency of the desired chirp. Hence the resonance frequency of the transducer is assumed to be of the form:

$$\omega_r(t) = \omega_0 + \beta t = \omega_\tau + \beta(t - \frac{\tau}{2}) \tag{7}$$

where ω_τ is the center instantaneous frequency. If the transducer is excited by a wide band signal, the output will have a linearly varying instantaneous frequency equal to the transducer resonance frequency, only slightly delayed in time. Figure 5 shows the WD of the tunable transducer velocity in response to a LFM chirp of instantaneous frequency $<\omega>_i = \omega_r(t)$. As expected, the acoustic energy density is quite similar to that of the input signal. At any instant, the acoustic energy density is mostly concentrated around the transducer resonance frequency, which follows the chirp instantaneous frequency (solid line). The transducer rings for a while at the maximum resonance frequency, increasing the acoustic energy density at this frequency with respect to others.

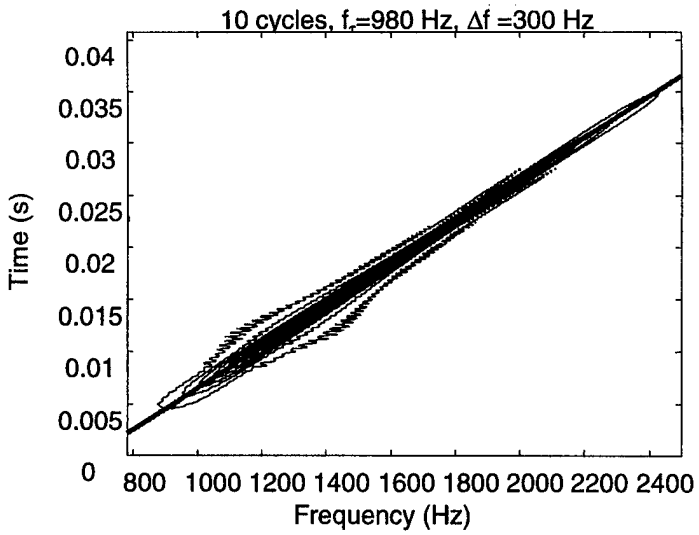


FIGURE 5. CONTOUR PLOT OF THE WD OF THE VELOCITY RESPONSE OF THE VARIABLE RESONANCE FREQUENCY TONPILZ TRANSDUCER TO A 10 CYCLE, HIGH FREQUENCY SWEEP LFM CHIRP

TUNABLE RESONANCE FREQUENCY FLEXURAL TRANSDUCERS

Medium power underwater transducers, used for long range active SONAR and long range oceanographic applications, generally operate in the frequency range from 10 to 5000 Hz. Typically, they are of bi- or tri-laminar flexural beam or disk construction, and are operated near resonance. The top and bottom layers are made of an active piezoelectric material, such as PZT.

The approach to making this type of transducer tunable involves the use of in-plane, membrane loads to change the effective lateral stiffness of the device. If the membrane load is compressive, the resonance frequencies decrease towards zero as the buckling load is approached; if the membrane load is tensile, the resonance frequencies increase, as in a drumhead. For this type of transducer, membrane loads may be applied by imposing a bias electrical field across the piezoelectric elements while simultaneously preventing in-plane motion of the edges of the flexural element. Figure 6 illlustrates this concept.

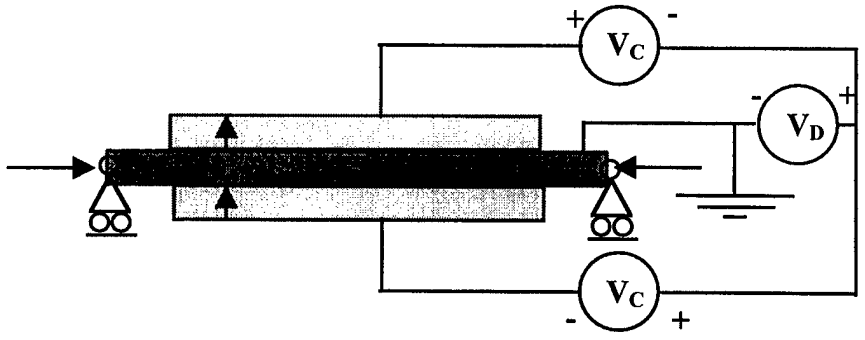


FIGURE 6. ACTIVE MEMBRANE LOADS CHANGE THE EFFECTIVE LATERAL STIFFNESS

A mathematical model of a trilaminar flexural beam transducer was developed for design analysis studies. The goal of the design was to define transducer dimensions, material properties, and mechanical supports that would yield simultaneous high membrane load (relative to the buckling load) and high electromechanical coupling coefficient. A high ratio of membrane load to buckling load implies a high tunable frequency range, while a high coupling coefficient implies high transducer efficiency. This design goal was pursued while respecting limits on the applied electrical field and the mechanical stresses in the device.

The resulting nominal design had a base length-to-thickness ratio of 116, a piezoelectric-to-base thickness ratio of 1.0, about 90% piezoelectric coverage, and elastic end supports to approximate a simply-supported boundary. An important aspect of the design was the detail of the elastic support. PZT-5H was adopted as the piezoelectric material, while the base layer was stainless steel. This transducer design had a tuning sensitivity of 15%/kV of applied bias field, and a coupling coefficient of about 0.3.

A prototype of this nominal design was fabricated and evaluated in the laboratory. The frequency shift per bias field and the coupling coefficient were then measured experimentally. In a typical test, the bias field was adjusted to a new value, then the electrical impedance of the device was measured over a range of frequencies that included the resonance frequency. The short-circuit resonance frequency was found at the zero (minimum) of the impedance frequency response function, while the open-circuit resonance frequency was found at the pole (peak) of the same function [14].

Figure 7 shows the open-circuit resonance frequencies as a function of the bias field. As the field exceeds the coercive field of the piezoelectric material, polarization reversal is clearly observed. Nevertheless, the tuning sensitivity for this design can be established as about 5%/kV. In addition, a typical value for the coupling coefficient was 0.2.

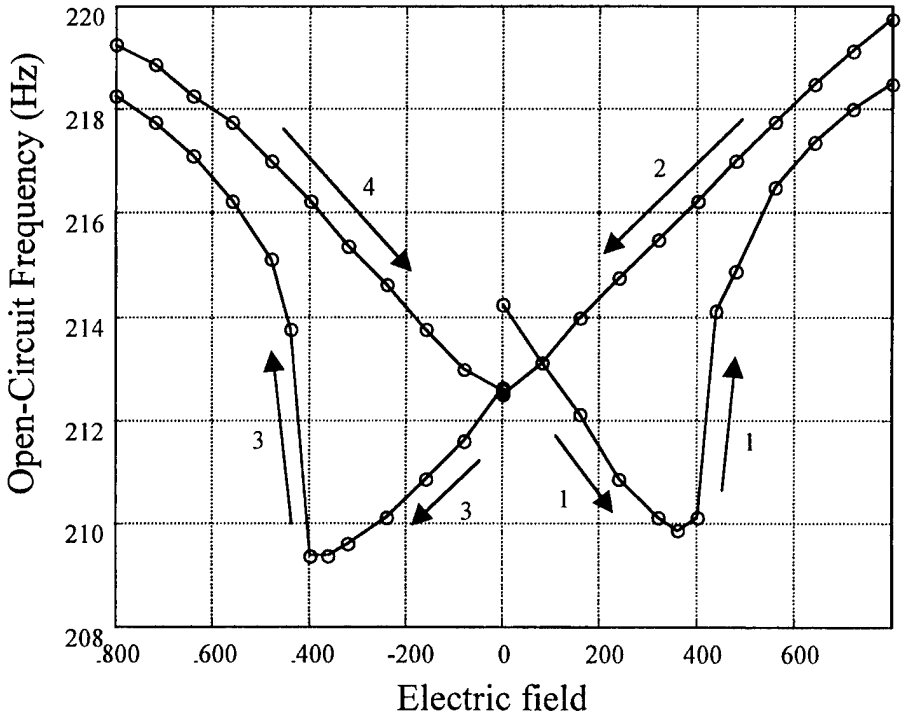


FIGURE 7. OPEN-CIRCUIT RESONANCE FREQUENCIES OF THE TRANSDUCER

Both the tuning sensitivity and the coupling coefficient were somewhat lower than expected. This is likely due to a combination of inadequate axial constraint, polarization switching due to combined stress-field effects, and stiffening due to an insulating coating.

SUMMARY

High range and velocity resolutions can be achieved simultaneously in underwater transducers by projecting a short, high sweep rate LFM chirp. A transducer with a tunable resonance frequency can effectively transmit linear chirps of a much larger bandwidth than can a fixed-frequency transducer. Furthermore, a tunable transducer also has considerably higher sensitivity than those that use damping as a means of increasing bandwidth.

A method of varying the first resonance frequency of some widely-used underwater transducers, trilaminar flexural piezoceramic bars and disks, was also described. Positive bias electric fields are added to the driving AC field to generate a tensile or compressive membrane load. This load modifies the effective flexural rigidity of the transducer, which in turn affects its resonance frequencies. Experiments verified the concept, but tunability was somewhat lower than predicted; performance is expected to improve in continuing research.

REFERENCES

1. Nielsen, R., O., "SONAR Signal Processing", Artech House, Inc, 1991.
2. Kinsler, L. E., et al, "Fundamentals of Acoustics", Wiley, 1982.
3. Wilson, O., B., "An Introduction to the Theory and Design of SONAR Transducers", Naval Postgraduate School, 1985.
4. Pei, S.-C., "The Wigner Distribution of Linear Time-Variant Systems", IEEE Transactions on Acoustics, Speech, and Signal Processing, October 1998, Vol. 36, No. 10, pp. 1681-1684.
5. Boudreaux-Bartels, G., F., "Time Varying Filtering and Signal Estimation Using Wigner Distribution Synthesis Techniques", IEEE Transactions on Acoustics, Speech, and Signal Processing, June 1986, Vol. ASSP-34, No. 3, pp. 442-451.
6. Claasen, T., "The Aliasing Problem in Discrete-Time Wigner Distributions", IEEE Transactions on Acoustics, Speech, and Signal Processing, October 1983, Vol. ASSP-31, No. 5, pp. 1067-1072.
7. Saleh, B., E., "Time-Variant Filtering of Signals in the Mixed Time-Frequency Domain", IEEE Transactions on Acoustics, Speech, and Signal Processing, December 1985, Vol. ASSP-33, No. 6, pp. 1479-1485.
8. Yen, N., "Time and Frequency Representation of Acoustic Signals by Means of the Wigner Distribution Function: Implementation and Interpretation", Journal of Acoustical Society of America, June 1987, Vol. 81, No. 6, pp. 1841-1850.
9. Cohen, "Time-Frequency Analysis", Prentice Hall, 1995.
10. Alwi, H., A., "Chirp Response of an Active-Controlled Thickness Drive Tunable Transducer", Journal of Acoustical Society of America, March 2000, Vol. 107, No. 3, pp. 1363-1373.
11. Larson, G. D., "State Switched Transducers: A new Approach to High-Power, Low-Frequency Underwater Projectors," Journal of Acoustical Society of America, March 1998, Vol. 103, No. 3, pp. 1428-1441.
12. Newnham, R. E., "Tunable Transducers as Smart Materials," Proceedings of Transducers'91 1991 International Conference on Solid-State Sensors and Actuators, June 24-28 1991.
13. Bernard, J., Lesieutre, G., A., "Design and Realization of Variable Frequency Flexural Piezoceramic Transducers, Proceedings of the SPIE Smart Structures and Materials Conference: Smart Structures and Integrated Systems, Newport Beach, CA, March 1-5, 2000, Vol. 3985, pp. 689-704.
14. Lesieutre, George A., and Davis, Christopher L., "Can A Coupling Coefficient Of A Piezoelectric Device Be Higher Than Those Of Its Active Material?" Journal of Intelligent Material Systems and Structures, Vol. 8, No. 10, October, 1997, pp. 859-867.

Adaptive Space Structures

SOFT DOCKING OF VARIABLE GEOMETRY TRUSS WITH REDUNDANT DOF BY IMPEDANCE CONTROL CONSIDERING JOINT FRICTIONS

Kei Senda, Shinsuke Nishimoto, Yoshisada Murotsu

ABSTRACT

This paper proposes an impedance control of redundant systems considering joint frictions. It is applied to an autonomous docking system composed of a variable geometry truss (VGT) with redundant degree of freedom to realize soft dockings with non-cooperative target satellites. The proposed impedance control achieves the desired impedance with the redundancy utilized by introducing a feedforward compensation of the joint frictions estimated by a disturbance observer in joint space. Numerical simulations and experiments for the redundant docking system examine the effectiveness of the proposed method. A docking experiment using the proposed control method is also successfully performed and the shock of collision is suitably reduced for soft dockings.

INTRODUCTION

Future space development will perform frequent orbital rendezvous dockings of the international space station and space vehicles. Autonomous docking systems and force controls, e.g., an impedance control [1], will be necessary to realize autonomous soft dockings with non-cooperative satellites approaching with relative velocities and miss-alignments. For the docking mechanism, a variable geometry truss (VGT) with redundant degree-of-freedom (DOF) is expected to realize high stiffness, accuracy, and a large workspace. Therefore, this study proposes an impedance control for redundant systems with joint frictions and applies it to a docking mechanism composed of VGT.

An accurate dynamics model is necessary for an impedance control because the feedback gains determined by the desired mechanical impedance of the end-effector are relatively small. An impedance control for redundant systems has been proposed and its effectiveness has been examined by numerical simulations [2, 3]. But the control does not consider joint frictions that are difficult of accurate modeling and may not achieve the desired impedance when the controlled plant has large uncertainties. To avoid this problem, a method based on position control has been proposed [4], where a desired trajectory of end-effector satisfying the desired impedance is first resolved, then a high gain feedback

[1]Kei Senda, Associate Professor, Osaka Prefecture Univ., 1-1 Gakuen-cho, Sakai, Osaka 599-8531, Japan
[2]Shinsuke Nishimoto, Graduate Student, Osaka Prefecture University
[3]Yoshisada Murotsu, President of Osaka Prefectural College of Technology

control moves the system to truck the trajectory, and finally the desired impedance of end-effector is apparently realized. This control is no more a force control. There is a method that models joint frictions as a disturbance in the manipulation space causing the error from the desired impedance and the disturbance is eliminated by a feedforward compensator using a disturbance observer [5]. With this method, the joint frictions affect joint response and the system redundancy cannot be utilized well even if the desired manipulation variables are realized. Another similar method uses a disturbance observer in the joint space and compensates the joint frictions by a feedforward control using the estimation [6]. The disturbance observer in the joint space has been applied to only linear systems.

Based on references[2, 3], this study proposes an impedance control utilizing redundancy. The method estimates the joint frictions by a disturbance observer and eliminates the frictions by a feedforward compensator. Experimental verification is also an objective of this study.

The rest of this paper is organized as follows. In the next section, introduced are an experimental docking mechanism composed of the VGT with redundancy and its mathematical model. The impedance control utilizing the redundancy is proposed considering the joint frictions. The other controllers are also introduced for comparison. Finally, numerical simulations and experiments of the docking mechanism examine the effectiveness of the proposed method.

MODEL OF DOCKING SYSTEM COMPOSED OF PLANAR VGT

The model examined in this paper is an experimental docking system composed of a planar VGT illustrated in Figure 1 or its mathematical model. The planar VGT is a parallel manipulator that has a series of pantograph. The VGT changes its configuration varying θ_i by expansion and contraction of variable length members. An end-effector for dockings is connected to the tip of truss mechanism by a revolution joint. The base of VGT model is fixed to the inertial coordinate frame. The docking mechanism is supported on a planar flat table by air-pads and can move without friction from the table.

Each variable length member has a prismatic joint with a ball bearing driven by an AC servomotor. Accurate modeling is almost impossible because of uncertainty of frictions in variable length members. A spring-dashpot system called PD-member is attached between the end-effector and the revolution joint. Other links are fixed length members. All components are rigid. It has a sensor to measure applied force/torque at the end-effector. A vision sensor system with two CCD cameras measures position and attitude of a target satellite at video rate.

Its specifications are listed in TABLE I where the variable length member 1 is a part of the variable length member with the AC servomotor and the variable length member 2 is the other. Averages of friction parameters in variable length members are 1.13 N in the maximum static friction, 0.72 N in Coulomb friction, and 14.4 Ns/m of viscous friction coefficient. The same parameters of the revolution joint are 3.1 Nm, 2.7 Nm, and 0.078 Nms, respectively. See also reference [7] for details of the experimental system.

The equation of motion of the system is

$$\boldsymbol{M}(\boldsymbol{\theta})\ddot{\boldsymbol{\theta}} = \boldsymbol{F} - \boldsymbol{\tau}_f \tag{1}$$

$$\boldsymbol{F} = \boldsymbol{\tau} + \boldsymbol{J}^T(\boldsymbol{\theta})\boldsymbol{f} - \boldsymbol{h}(\dot{\boldsymbol{\theta}}, \boldsymbol{\theta}) \tag{2}$$

TABLE I: SPECIFICATIONS OF VGT

	Length [m]	Mass [kg]	Inertia [kg · m^2]
Fixed-length member	0.376	0.09	1.07×10^{-3}
Variable length member 1	0.226	6.73	9.19×10^{-2}
Variable length member 2	0.298	1.65	1.10×10^{-2}
End effector	0.263	1.30	4.97×10^{-3}

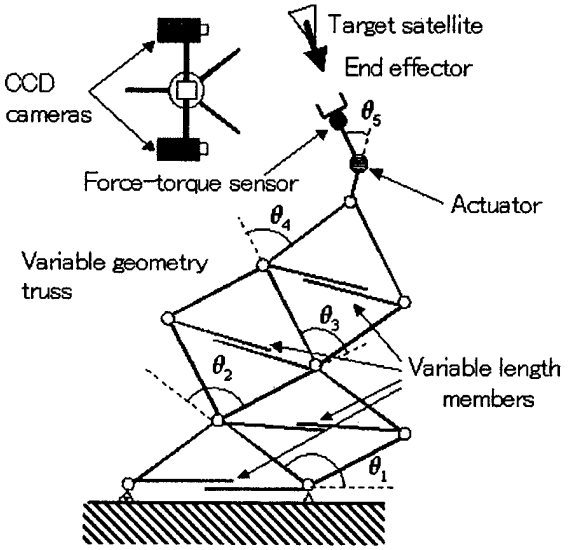


Figure 1: Docking system model

where $\boldsymbol{\theta} = [\theta_1, \ldots, \theta_n]^T$ is the joint variable vector, $\boldsymbol{M} \in \boldsymbol{R}^{n \times n}$ the mass matrix, $\boldsymbol{h} \in \boldsymbol{R}^{n \times 1}$ the centrifugal force and Coriolis force, $\boldsymbol{\tau} = [\tau_1, \ldots, \tau_n]^T$ the control torque, $\boldsymbol{\tau}_f = [\tau_{f1}, \ldots, \tau_{fn}]^T$ the joint friction torque, and $\boldsymbol{f} \in \boldsymbol{R}^{m \times 1}$ the external force applied to the end-effector. The Jacobian matrix $\boldsymbol{J} \in \boldsymbol{R}^{m \times n}$ relates $\boldsymbol{\theta} \in \boldsymbol{R}^{n \times 1}$ to the manipulation variable vector $\boldsymbol{y} \in \boldsymbol{R}^{m \times 1}$ where $m < n$ for redundant systems. In examples shown later, the manipulation variables are position and orientation of end-effecter, $m = 3$, and the system has 4 variable length members and a revolution joint, i.e., $n = 5$.

IMPEDANCE CONTROL OF REDUNDANT SYSTEMS CONSIDERING JOINT FRICTIONS

Impedance Control without Considering Joint Frictions

Dynamics of the plant is Eq. (1) and its kinematics is given by

$$\dot{\boldsymbol{y}} = \boldsymbol{J}\dot{\boldsymbol{\theta}} \tag{3}$$

where $\boldsymbol{y}$ is position and orientation of the end-effecter. Friction $\boldsymbol{\tau}_f = 0$ is assumed in this control method. The joint velocity is given by a generalized solution of Eq. (3) as

$$\dot{\boldsymbol{\theta}} = \boldsymbol{J}^{\sharp}\dot{\boldsymbol{y}} + (\boldsymbol{I} - \boldsymbol{J}^{\sharp}\boldsymbol{J})\boldsymbol{\xi} \tag{4}$$

where $\boldsymbol{J}^{\#} \triangleq \boldsymbol{J}^T(\boldsymbol{J}\boldsymbol{J}^T)^{-1}$ is the right pseudo inverse of $\boldsymbol{J}$. Differentiating this with respect to time yields

$$\ddot{\boldsymbol{\theta}} = \boldsymbol{J}^{\sharp}(\ddot{\boldsymbol{y}} - \dot{\boldsymbol{J}}\dot{\boldsymbol{\theta}}) + (\boldsymbol{I} - \boldsymbol{J}^{\sharp}\boldsymbol{J})\{\dot{\boldsymbol{J}}^T(\boldsymbol{J}^{\sharp})^T(\dot{\boldsymbol{\theta}} - \boldsymbol{\xi}) + \dot{\boldsymbol{\xi}}\} \tag{5}$$

where $\boldsymbol{\xi}$ is an arbitrary vector.

The desired impedance of the manipulation variable is given as

$$\boldsymbol{M}_d\ddot{\boldsymbol{y}} + \boldsymbol{D}_d\dot{\boldsymbol{y}}_e + \boldsymbol{K}_d\boldsymbol{y}_e = \boldsymbol{f} \tag{6}$$

where $\boldsymbol{y}_e = \boldsymbol{y} - \boldsymbol{y}_d$ and $\boldsymbol{y}_d$ is desired $\boldsymbol{y}$. The impedance control utilizing redundancy is

$$\boldsymbol{\tau}_{IC} = \boldsymbol{M}\ddot{\boldsymbol{\theta}}_{IC} + \boldsymbol{h} - \boldsymbol{J}^T\boldsymbol{f} \tag{7}$$

$$\ddot{\boldsymbol{\theta}}_{IC} = \boldsymbol{J}^{\sharp}(\ddot{\boldsymbol{y}}_{IC} - \dot{\boldsymbol{J}}\dot{\boldsymbol{\theta}}) + (\boldsymbol{I} - \boldsymbol{J}^{\sharp}\boldsymbol{J})\{\dot{\boldsymbol{J}}^T(\boldsymbol{J}^{\sharp})^T(\dot{\boldsymbol{\theta}} - \boldsymbol{\xi}) + \dot{\boldsymbol{\xi}}\} \tag{8}$$

$$\ddot{\boldsymbol{y}}_{IC} = \boldsymbol{M}_d{}^{-1}(-\boldsymbol{D}_d\dot{\boldsymbol{y}}_e - \boldsymbol{K}_d\boldsymbol{y}_e + \boldsymbol{f}) \tag{9}$$

where $g(\boldsymbol{q})$ is a scalar objective function to be minimized by the utilization of redundancy and $\boldsymbol{\xi}$ is given by

$$\boldsymbol{\xi} = -k\nabla g(\boldsymbol{\theta}) \tag{10}$$

The control realizes the desired impedance and decrease $g(\boldsymbol{\theta})$ gradually if there is no uncertainty in friction and the control model exactly matches to the plant.

Method Based on Position Control

The manipulation variable vector of one sampling ahead is computed by Eq. (6) satisfying the desired impedance from measured $\boldsymbol{y}_e$, $\dot{\boldsymbol{y}}_e$, and $\boldsymbol{f}$. A resolved acceleration control utilizing redundancy seemingly achieves the desired impedance by positioning control to truck the computed manipulation variable vector. Its control law is almost the same as Eqs. (7)–(9) whereas following $\ddot{\boldsymbol{y}}_{RAC}$ is used instead of $\ddot{\boldsymbol{y}}_{IC}$:

$$\ddot{\boldsymbol{y}}_{RAC} = \ddot{\boldsymbol{y}}_d - \boldsymbol{K}_D\dot{\boldsymbol{y}}_e - \boldsymbol{K}_P\boldsymbol{y}_e \tag{11}$$

Manipulation variable error may be small for sufficiently large feedback gains $\boldsymbol{K}_D$ and $\boldsymbol{K}_P$ even if joint frictions affect the control. In later examples, this control method is used whereas another method based on position control is realized by computing a desired joint trajectory and large servo gains of joint control.

Disturbance Observer in Manipulation Space

The impedance control to Eq. (1) is represented as follows when joint friction $\boldsymbol{\tau}_f \neq 0$:

$$\boldsymbol{f} = \boldsymbol{M}_d\ddot{\boldsymbol{y}} + \boldsymbol{D}_d\dot{\boldsymbol{y}}_e + \boldsymbol{K}_d\boldsymbol{y}_e + \boldsymbol{M}_d\boldsymbol{J}\boldsymbol{M}^{-1}\boldsymbol{\tau}_f \tag{12}$$

This is not equivalent to Eq. (6). Define the fourth term in the right-hand of Eq. (12) as controlled impedance error $\boldsymbol{\delta}_I$ as

$$\boldsymbol{\delta}_I = \boldsymbol{f} - \boldsymbol{M}_d\ddot{\boldsymbol{y}} - \boldsymbol{D}_d\dot{\boldsymbol{y}}_e - \boldsymbol{K}_d\boldsymbol{y}_e \tag{13}$$

Because $\ddot{\boldsymbol{y}}$ is derived from $\dot{\boldsymbol{y}}$, a low-pass filter is equipped to reduce high frequency noises:

$$\tilde{\boldsymbol{\Delta}}_I = \frac{a_1}{s+a_1}\boldsymbol{\Delta}_I \tag{14}$$

where $\boldsymbol{\Delta}_I$ and $\tilde{\boldsymbol{\Delta}}_I$ are Laplace transforms of $\boldsymbol{\delta}_I$ and its estimation $\tilde{\boldsymbol{\delta}}_I$, and a_1 denotes the cut-off frequency of the low-pass filter. Eq. (14) can be considered as an observer because its time-domain representation is

$$\dot{\tilde{\boldsymbol{\delta}}}_I = -a_1(\tilde{\boldsymbol{\delta}}_I - \boldsymbol{\delta}_I) \tag{15}$$

The $\tilde{\boldsymbol{\delta}}_I$ asymptotically converges to $\boldsymbol{\delta}_I$ under the assumption of $\dot{\boldsymbol{\delta}}_I = 0$ because $a_1 > 0$. Estimation delay can be small enough for practical use because the asymptotic convergence becomes more quickly as cut-off frequency makes higher. Feedforward compensation using the estimation yields a control being the same as Eqs. (7)–(9) but Eq. (8) is replaced by

$$\ddot{\boldsymbol{\theta}}_{IC} = \boldsymbol{J}^{\sharp}(\ddot{\boldsymbol{y}}_{IC} + \boldsymbol{M}_d{}^{-1}\tilde{\boldsymbol{\delta}}_I - \dot{\boldsymbol{J}}\dot{\boldsymbol{\theta}}) + (\boldsymbol{I} - \boldsymbol{J}^{\sharp}\boldsymbol{J})\{\dot{\boldsymbol{J}}^T(\boldsymbol{J}^{\sharp})^T(\dot{\boldsymbol{\theta}} - \boldsymbol{\xi}) + \dot{\boldsymbol{\xi}}\} \tag{16}$$

The end-effector response is

$$\boldsymbol{f} = \boldsymbol{M}_d\ddot{\boldsymbol{y}} + \boldsymbol{D}_d\dot{\boldsymbol{y}}_e + \boldsymbol{K}_d\boldsymbol{y}_e + \boldsymbol{\delta}_I - \tilde{\boldsymbol{\delta}}_I \tag{17}$$

and the desired impedance is exactly satisfied when $\tilde{\boldsymbol{\delta}}_I = \boldsymbol{\delta}_I$. The estimation $\tilde{\boldsymbol{\delta}}_I$ of Eq. (15) is rearranged as

$$\dot{\tilde{\boldsymbol{\delta}}}_I = -a_1\boldsymbol{M}_d(\ddot{\boldsymbol{y}} - \ddot{\boldsymbol{y}}_{IC}) \tag{18}$$

Disturbance Observer in Joint Space

This method estimates and compensates $\boldsymbol{\tau}_f$. From Eq. (1), $\boldsymbol{\tau}_f$ is calculated as

$$\boldsymbol{\tau}_f = \boldsymbol{\tau} + \boldsymbol{J}^T\boldsymbol{f} - \boldsymbol{M}\ddot{\boldsymbol{\theta}} - \boldsymbol{h} \tag{19}$$

Because $\ddot{\boldsymbol{\theta}}$ in this equation is derived from $\dot{\boldsymbol{\theta}}$, it is estimated by the following low-pass filter similar to Eq. (14):

$$\tilde{\boldsymbol{T}}_f = \frac{a_2}{s+a_2}\boldsymbol{T}_f \tag{20}$$

where $\boldsymbol{T}_f$ and $\tilde{\boldsymbol{T}}_f$ are Laplace transforms of the joint friction $\boldsymbol{\tau}_f$ and its estimation $\tilde{\boldsymbol{\tau}}_f$, and a_2 denotes the cut-off frequency of the low-pass filter. A time-domain representation of Eq. (20) is

$$\dot{\tilde{\boldsymbol{\tau}}}_f = -a_2(\tilde{\boldsymbol{\tau}}_f - \boldsymbol{\tau}_f) \tag{21}$$

The $\tilde{\boldsymbol{\tau}}_f$ asymptotically converges to $\boldsymbol{\tau}_f$ under the assumption of $\dot{\boldsymbol{\tau}}_f = 0$ because $a_2 > 0$. The obtained control law is equivalent to Eqs. (7)–(9) but Eq. (7) is replaced by

$$\boldsymbol{\tau}_{IC} = \boldsymbol{M}\ddot{\boldsymbol{\theta}}_{IC} + \boldsymbol{h} - \boldsymbol{J}^T\boldsymbol{f} + \tilde{\boldsymbol{\tau}}_f \tag{22}$$

Because the affects of joint friction can be eliminated when $\tilde{\boldsymbol{\tau}}_f = \boldsymbol{\tau}_f$, the desired impedance is exactly realized and the redundancy can be effectively utilized. Eqs. (19), (22), and (21) yield a rearrangement of estimation $\tilde{\boldsymbol{\tau}}_f$ as

$$\dot{\tilde{\boldsymbol{\tau}}}_f = -a_2\boldsymbol{M}(\ddot{\boldsymbol{\theta}} - \ddot{\boldsymbol{\theta}}_{IC}) \tag{23}$$

where $\boldsymbol{M}$ is obtained with relatively small amount of computation by the inverse dynamics [10]. Hence the computation for this estimation would not disturb the real time control.

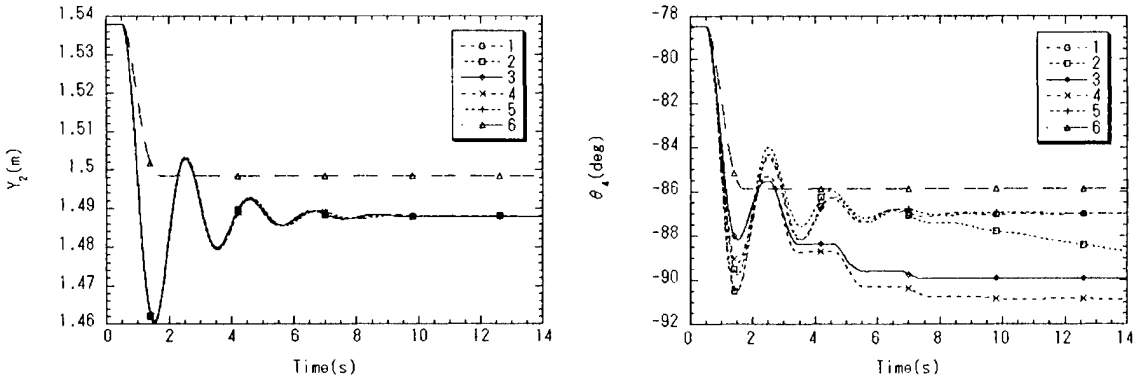


Figure 2: Responses of the end-effector and joint 4 (simulations)

NUMERICAL SIMULATIONS

Shown here are numerical simulations for the docking mechanism. Desired impedance of the end-effector is given by

$$\begin{aligned} \boldsymbol{M}_d &= \text{diag}(10.0 \text{ kg } 10.0 \text{ kg } 10.0 \text{ kgm}^2) \\ \boldsymbol{D}_d &= \text{diag}(12.0 \text{ kg/s } 12.0 \text{ kg/s } 12.0 \text{ kgm}^2/\text{s}) \\ \boldsymbol{K}_d &= \text{diag}(100 \text{ kg/s}^2 \text{ } 100 \text{ kg/s}^2 \text{ } 100 \text{ kgm}^2/\text{s}^2) \end{aligned}$$

A step external force $\boldsymbol{f} = (0.0 \text{ N} \quad -5.0 \text{ N } 0.0 \text{ Nm})^T$ for $t \geq 0.5$ s is applied to the end-effector. For redundancy utilization, the objective function is

$$g = \sum_{i=1}^{N} \left(\frac{1}{\theta_{i,max} - \theta_i} + \frac{1}{\theta_i - \theta_{i,min}} \right) \tag{24}$$

that tries to keep each variable length member in its center of length. The cut-off frequencies of the filters are $a_1 = a_2 = 275$ rad/s.

Figure 2 shows time histories of the second element y_2 in $\boldsymbol{y}$ and the fourth element θ_4 in $\boldsymbol{\theta}$. In the figure, cases 1 and 6 are results of the impedance control without considering joint frictions, case 2 does not utilize the redundancy as $\boldsymbol{\xi} = \dot{\boldsymbol{\xi}} = \boldsymbol{0}$, case 3 the method based on position control, case 4 the disturbance observer in manipulation space, and case 5 the proposed method using the disturbance observer in joint space. In cases 1 and 2, the plant is Eq. (1) without friction. But the original plant of Eq. (1) is used in cases 3 through 6. Case 1 is regarded as the ideal response and performances of other controls can be evaluated by the error from case 1. All controls designed for the continuous system are directly realized as digital controllers with 5 ms sampling time. Because of the present realization, control performance of case 2 becomes worse and θ_4 is unstable. Because this inconvenience never happens in other controls, discussed below are only the controls utilizing redundancy. The left figure shows that cases 3, 4, and 5 achieve the desired impedance even though the joint frictions are exist, but case 6 is far from the desired because the control law does not compensate the friction. Right figure illustrates that cases 3, 4, and 6 are affected by the frictions. Only case 5 achieves the same good performance as that of the ideal case 1. As a result, the proposed control method using the disturbance observer in joint space is the most effective among them.

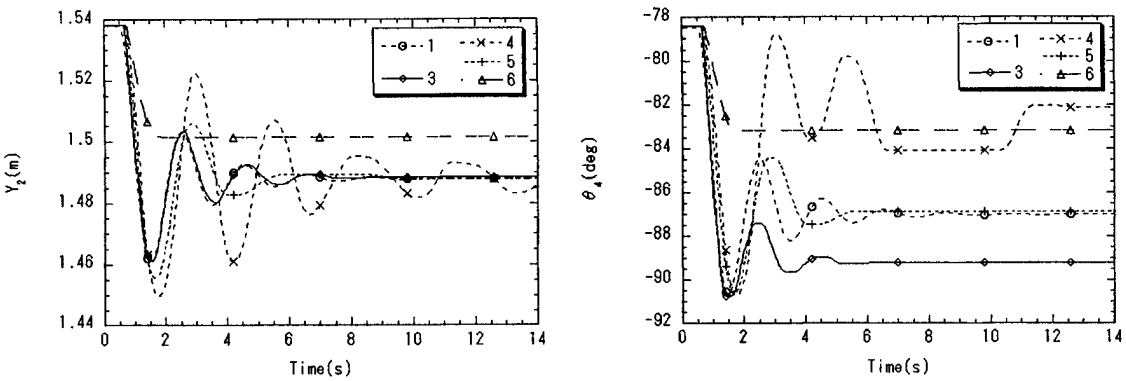


Figure 3: Responses of the end-effector and joint 4 (experiments)

EXPERIMENTS

Figure 3 shows experimental results under almost the same conditions as those of the previous section. Only the filter cut-off frequencies $a_1 = a_2 = 10$ rad/s here are unavoidably lower than the previous numerical simulations because of noises and unmodelled dynamics. Control methods are the same as the previous section of the same number. Cases 3 through 6 are experimental results whereas case 1 is the numerical simulation of the ideal response. The end-effector response of case 3 is the closest to case 1 but its θ_4 response is far different from the ideal one. Performance of case 4 becomes worse because of the low cut-off frequencies. Because of the same reason, case 5 is also affected little in y_2 response but the θ_4 response is the closest to the ideal response. Case 6 is far from the ideal case leaving offsets in both y_2 and θ_4 from the desired. Case 5 of the proposed method is totally the most effective among them. As a result, the proposed control method performs the best in the experiments as well as the numerical simulations.

A docking experiment is examined by using the proposed control method where an approaching target satellite is docked to the system. The force/torque sensor at the end-effector measures shocks of collision. By the magnitude of shocks, the control effect is compared to a case without control whose control input is zero. The mass of the target satellite is 5.9 kg and the approaching velocity of the target satellite is approximately 0.2 m/s. Both controlled and non-controlled cases are illustrated in Figure 4. In the controlled case, the maximum force of the shock is reduced as 1/10 of the non-controlled case. The results examine that the proposed control method reduces the shock and enables to realize soft dockings.

CONCLUDING REMARKS

This paper has proposed an impedance control of redundant systems considering joint frictions. It has been applied to an autonomous docking system composed of the planar VGT with redundant degree of freedom to realize soft dockings with non-cooperative target satellites. The proposed impedance control has achieved the desired impedance with the redundancy utilized by introducing the feedforward compensation of the joint friction estimated by the disturbance observer in joint space. The numerical simulations and the experiments for the redundant docking mechanism have examined the effectiveness of the proposed method. The docking experiment using the proposed control method has been successfully carried out. The shock of collision has been suitably reduced for soft dockings.

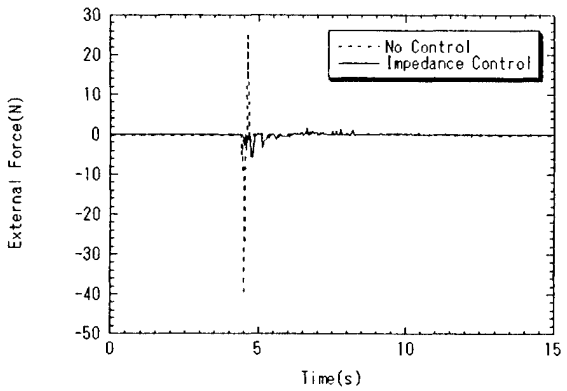


Figure 4: Shocks of docking (experiments)

A part of this work was financially supported by a Grant-in-Aid for Scientific Research from Ministry of Education, Science, Culture, and Sports of Japan; Casio Science Promotion Foundation; Special Research Promotion Foundation for Graduate School of Osaka Prefecture University.

REFERENCES

[1] Hogan, H. 1985. "Impedance Control; An Approach to Manipulation, Part I~III," *ASME Journal of Dynamic System, Measurement and Control*, 107(1), pp. 1–24.

[2] Senda, K. et al. 1998. "Some Control Methods for Redundant Manipulators and Application to Planer Variable Geometry Truss," *Eighth International Conference on Adaptive Structures and Technologies*, Y. Murotsu et al. (eds.), Technomic Publishing, pp. 353–362.

[3] Senda, K. 1999. "Quasioptimal Control of Space Redundant Manipulators," *AIAA Guidance, Navigation, and Control Conf.*, Portland, OR, pp. 1877–1885.

[4] Hatagi, M. et al. 1995. "Impedance Control of Manipulators Based on a Robust Position Control," *Proc. of JSME Annual Conf. on Robotics and Mechatronics*, A, pp. 371–374. (in Japanese)

[5] Harada, T. et al. 1994. "Robust Impedance Control of a Manipulator Using Disturbance Observer," *Trans. Japan Society of Mechanical Engineers*, Ser. C, 60(569), pp. 225–230. (in Japanese)

[6] Ohnishi, K. 1993. "Review: Robust Motion Control by Disturbance Observer", *J. of Robotics Society of Japan*, 11(4), pp. 486–493. (in Japanese)

[7] Murotu, Y. et al. 1997. "Control Experiments of a Docking Mechanism Composed of a Planar Variable Geometry Truss," *J. Intel. Mat. Syst. and Struc.*, 8(9), pp. 784–791.

[8] Canudas de Wit, et al. 1991. "Adaptive Friction Compensation in Robot Manipulators: Low Velocities," *Int'l J. Robotics Research*, 10(3), pp. 189–199.

[9] Tsutsumi, M. et al. 1995. "Mathematical Model of Feed Drive Mechanical System and Friction for CNC Machine Tools," *J. of Japan Society for Precision Engineering*, 61(10), pp. 1458–1462. (in Japanese)

[10] Senda, K., H. Kawano, A. Ando, and Y. Murotsu. 1999. "Efficient Formulation of Inverse Dynamics and Control Application to a Planar Variable Geometry Truss," *Smart Materials and Structures*, 8(6), pp. 839–846.

DESIGN OF STATICALLY INDETERMINATE GEOMETRY ADAPTIVE TRUSS WITH WIRE MEMBER ACTUATORS

Kazuyuki Hanahara, Yukio Tada

ABSTRACT

We deal with geometry adaptive truss with length-adjustable actuated wire members in this study. One of the important points of this type of mechanical system is its statically indeterminate topology. A combinatorial design approach based on a number of possible truss units is proposed and formulated. Interference among the truss members augmented by the statical indeterminacy is another topic. The geometrical relationship is formulated and a motion planning approach taking account of the interference is introduced. Examples of topology design and geometry adaptation motion are also conducted; the practicability of the adaptive truss with wire members is demonstrated.

INTRODUCTION

A geometry adaptive truss is a mechanical system which has a configuration of a truss structure and a number of length-adjustable actuated members[1]. Studies concerned with this kind of mechanical system have been reported so far; most of them have dealt with the geometry adaptive truss consisting of rigid length-adjustable members accommodated with telescopic actuators[2][3]. Apart from these conventional adaptive trusses consisting of rigid members, the authors have reported another type of adaptive truss that consists of non-actuated rigid members and a number of wire members as its actuators[4][5]. This type of adaptive truss must have a statically indeterminate topology in order to keep stability under various mechanical conditions, because of the lack of rigidity of wire members. In this study, we deal with a kinematical design of mechanical system of this type.

One of the important points of design of an adaptive truss with wire members is its topology. That is, it has a statically indeterminate topology in order to keep stability as a structure; at the same time, however, it must have the ability to perform a kinematic motion in accordance with the lengths change of actuated wire members as a mechanism. A combinatorial design approach based on a number of truss units having different topologies is adopted and discussed for this problem. Another important topic is the interference among the truss members augmented by the statically indeterminate topology. We formulate the kinematical relationship taking account of such interference and develop an

Kazuyuki Hanahara and Yukio Tada, Department of Computer and Systems Engineering, Faculty of Engineering, Kobe University, Rokkodai, Nada, Kobe 657-8501, Japan

approach of adjusting some of the geometrical parameters to this issue.

Feasibility of the adaptive truss with wire member actuators as well as the proposed design approach is discussed through design examples. Computer simulation of kinematic motion is also conducted and the influence of the wire member characteristics and the interference among truss members is considered.

GEOMETRY ADAPTIVE TRUSS WITH WIRE MEMBERS

Adopting Wire Members as Actuators

The following advantages are expected for a geometry adaptive truss by adopting wire member actuators:

Light weight Wire members are much lighter than rigid telescopic actuators in general and beneficial to reduce the total weight.

Large stroke Stroke of a wire member actuator is expected to be very large, because its length can be easily adjusted by winding on and off.

Simple and flexible actuation mechanism No linear guide or ball-screw mechanism are required. More flexible design of actuation mechanism is available by using such as pulleys to arrange placement of wire members.

However, the following important characteristic of a wire member must be taken into account:

Lack of rigidity under compression A wire member can not hold any compressive force; that is, it does not work as a truss member in such a case.

Therefore, the geometry adaptive truss with wire members must have a statically indeterminate topology in order to keep structural stability under various mechanical conditions.

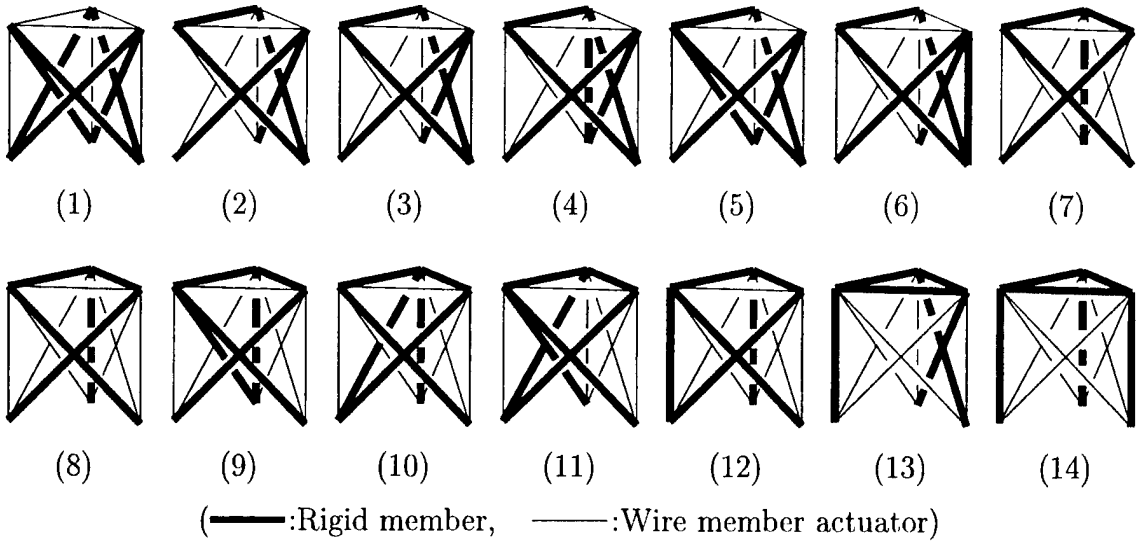


Figure 1 Possible topologies of a truss unit[5]

Topologies of Possible Truss Unit

We deal with an adaptive truss of column-type triangular shape which consists of a number of truss units[3]. Possible placement of wire member actuators of a truss unit has been studied[5]; the obtained possible topologies are shown in Figure 1. These truss units are designed under the following conditions:

- stable under various nodal forces
- having more than six wire members

An adaptive truss is obtained as an assemblage of these truss units.

KINEMATICS AND MOTION PLANNING

Formulation Based on Nodal Positions Vector

Conventionally, the kinematical relationship of a geometry adaptive truss is formulated between the actuated member lengths vector and the workspace vector which is used to describe the task to be attained[3]. This type of formulation is, however, not appropriate for an adaptive truss with wire members because its statical indeterminate topology prevents independent change of the wire member lengths.

From this point of view, the nodal positions vector $\boldsymbol{X} = [\boldsymbol{x}_1^T, \cdots, \boldsymbol{x}_{N_x}^T]^T$ is adopted to describe the kinematical relationship. The geometrical relationship between the total member lengths vector $\boldsymbol{L} = [l_1, \cdots, l_{N_l}]^T$ and the nodal positions vector $\boldsymbol{X}$ can be expressed in the following form:

$$\boldsymbol{L} = \boldsymbol{L}(\boldsymbol{X}). \tag{1}$$

The workspace vector $\boldsymbol{W}$ is expressed in terms of the nodal positions vector $\boldsymbol{X}$ in general; the relationship can be formulated as

$$\boldsymbol{W} = \boldsymbol{W}(\boldsymbol{X}). \tag{2}$$

The inverse kinematic problem of an adaptive truss with wire members can be formulated as

$$\text{Find } \boldsymbol{X} \text{ such that } \begin{cases} \boldsymbol{B}^R \boldsymbol{L}(\boldsymbol{X}) = \underline{\boldsymbol{L}^R} \\ \boldsymbol{W}(\boldsymbol{X}) = \underline{\boldsymbol{W}} \end{cases} \tag{3}$$

where $\underline{\boldsymbol{L}^R}$ is the constant lengths of rigid members and $\underline{\boldsymbol{W}}$ is the target workspace vector to be attained. The boolean matrix $\boldsymbol{B}^R$ is adopted to extract the rigid member lengths $\boldsymbol{L}^R$ from $\boldsymbol{L}$. The wire member lengths vector $\boldsymbol{L}^W$ to be achieved by actuation is then obtained as

$$\boldsymbol{L}^W = \boldsymbol{B}^W \boldsymbol{L}(\boldsymbol{X}) \tag{4}$$

where $\boldsymbol{B}^W$ is a boolean matrix adopted to extract the wire member lengths $\boldsymbol{L}^W$ from $\boldsymbol{L}$.

Incremental Motion Planning

Referring to the inverse kinematic problem (3), the motion planning problem in an incremental form is formulated as follows:

$$\text{Minimize } g = g(d\boldsymbol{X}) \text{ with respect to } d\boldsymbol{X} \text{ subject to } \begin{cases} \dfrac{\partial \boldsymbol{W}}{\partial \boldsymbol{X}} d\boldsymbol{X} = \underline{d\boldsymbol{W}} \\ \boldsymbol{B}^R \dfrac{\partial \boldsymbol{L}}{\partial \boldsymbol{X}} d\boldsymbol{X} = 0 \end{cases} \tag{5}$$

where g is the objective function which evaluates the incremental motion. The kinematic wire member increment $d\boldsymbol{L}^W$ to be achieved is obtained from the solution of the problem (5) as follows:

$$d\boldsymbol{L}^W = \boldsymbol{B}^W \frac{\partial \boldsymbol{L}}{\partial \boldsymbol{X}} d\boldsymbol{X}. \tag{6}$$

In case of the objective function g in a quadratic form, the solution of problem (5) can be obtained as

$$d\boldsymbol{X} = \begin{bmatrix} \dfrac{\partial \boldsymbol{W}}{\partial \boldsymbol{X}} \\ \boldsymbol{B}^R \dfrac{\partial \boldsymbol{L}}{\partial \boldsymbol{X}} \end{bmatrix}^+ \begin{bmatrix} \underline{d\boldsymbol{W}} \\ 0 \end{bmatrix}, \tag{7}$$

where $[\cdot]^+$ indicates an appropriate generalized inverse[6].

TAKING ACCOUNT OF MEMBER INTERFERENCE

Interference among members must be taken into account for the motion planning of a geometry adaptive truss. It is more significant in the case of the adaptive truss with wire members because of its statically indeterminate topology.

Geometrical Relation between Two Members

We take account of distances among truss members. The common normal vector to members i and j is expressed as

$$\boldsymbol{n}_{ij} = (\boldsymbol{x}_{\beta_i} - \boldsymbol{x}_{\alpha_i}) \times (\boldsymbol{x}_{\beta_j} - \boldsymbol{x}_{\alpha_j}), \tag{8}$$

where $\boldsymbol{x}_{\alpha_i}, \boldsymbol{x}_{\beta_i}$ and $\boldsymbol{x}_{\alpha_j}, \boldsymbol{x}_{\beta_j}$ are the end nodal positions of members i and j, respectively. It is normalized to be unit length as

$$\boldsymbol{e}_{ij} = \boldsymbol{n}_{ij} / \sqrt{\boldsymbol{n}_{ij}^T \boldsymbol{n}_{ij}}. \tag{9}$$

The geometrical relation about the intersection of members i and j in the direction of $\boldsymbol{e}_{ij}$ is expressed as

$$\boldsymbol{x}_{\alpha_i} + p_{i(j)}(\boldsymbol{x}_{\beta_i} - \boldsymbol{x}_{\alpha_i}) + q_{ij}\boldsymbol{e}_{ij} = \boldsymbol{x}_{\alpha_j} + p_{j(i)}(\boldsymbol{x}_{\beta_j} - \boldsymbol{x}_{\alpha_j}), \tag{10}$$

where $p_{i(j)}$ and $p_{j(i)}$ indicate the positions of the intersection on members i and j respectively and q_{ij} is the distance. Introducing matrix $\boldsymbol{A}_{ij}$ and vector $\boldsymbol{p}_{ij}$ expressed as

$$\boldsymbol{A}_{ij} = \left[(\boldsymbol{x}_{\beta_i} - \boldsymbol{x}_{\alpha_i}), -(\boldsymbol{x}_{\beta_j} - \boldsymbol{x}_{\alpha_j}), \boldsymbol{e}_{ij}\right], \qquad \boldsymbol{p}_{ij} = \begin{bmatrix} p_{i(j)} \\ p_{j(i)} \\ q_{ij} \end{bmatrix},$$

Eq.(10) is rewritten as follows:

$$\boldsymbol{A}_{ij}\boldsymbol{p}_{ij} = \boldsymbol{x}_{\alpha_j} - \boldsymbol{x}_{\alpha_i}. \tag{11}$$

The distance and intersection positions on the members, $\boldsymbol{p}_{ij}$, is then calculated as

$$\boldsymbol{p}_{ij} = \boldsymbol{A}_{ij}^{-1}(\boldsymbol{x}_{\alpha_j} - \boldsymbol{x}_{\alpha_i}).$$

Motion Planning Taking Account of Interference

We develop the following procedure for the motion planning problem (5) in order to take account of the member interference.

1. Solve the incremental motion planning problem.

2. For members i and j which possibly interfere with each other and satisfy the following condition:

$$0 \leq p_{i(j)} \leq 1 \quad \text{and} \quad 0 \leq p_{j(i)} \leq 1,$$

calculate the distance q_{ij}. In the case that $|q_{ij}| \leq \underline{d}_{ij}$ where $\underline{d}_{ij}$ is the constraint value determined by the diameters of both members, another equality constraint

$$\frac{\partial q_{ij}}{\partial \boldsymbol{X}} d\boldsymbol{X} = \underline{d}_{ij} - q_{ij} \qquad (q_{ij} > 0) \tag{12}$$

or

$$\frac{\partial q_{ij}}{\partial \boldsymbol{X}} d\boldsymbol{X} = -\underline{d}_{ij} - q_{ij} \qquad (q_{ij} > 0) \tag{13}$$

is added to the current motion planning problem.

3. In the case of no other constraints coming from member interference detected, the procedure finishes with the last solution $d\boldsymbol{X}$.

4. In the case that the number of constraints is larger than the dimension of the nodal positions vector, the procedure terminates with no solution.

5. Repeat iteratively from **1.** with the updated motion planning problem including the added constraints.

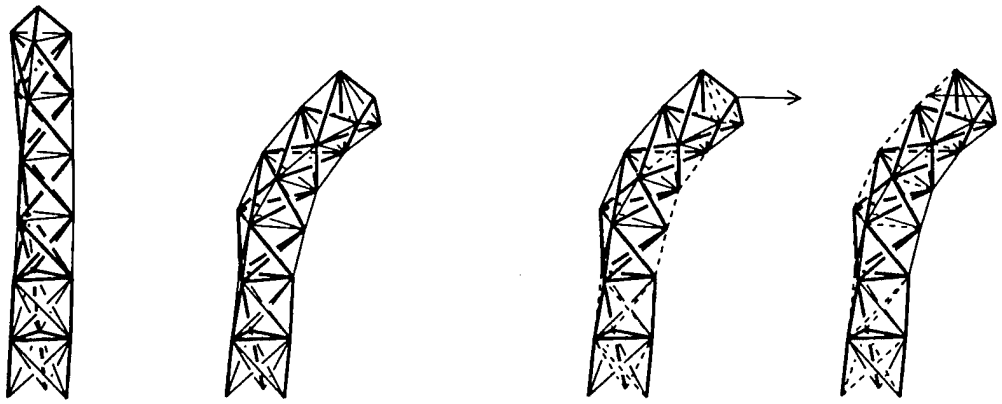
DESIGN APPROACH BASED ON COMBINATION OF UNITS

We introduce the following design variable which expresses a combination of unit types shown in Figure 1: $\boldsymbol{U} = [u_1, \cdots, u_{N_u}]$, where u_n denotes the type of nth unit and N_u is the number of units of the adaptive truss to be designed. The design problem can be formulated as

$$\text{Minimize } h = h(\boldsymbol{U}) \text{ with respect to } \boldsymbol{U} \tag{14}$$

where h is the criterion function which evaluates design candidates.

An adaptive truss with wire members obtained as an assemblage of truss units as they shown in Figure 1 can not resolve the interference among members. In order to cope with



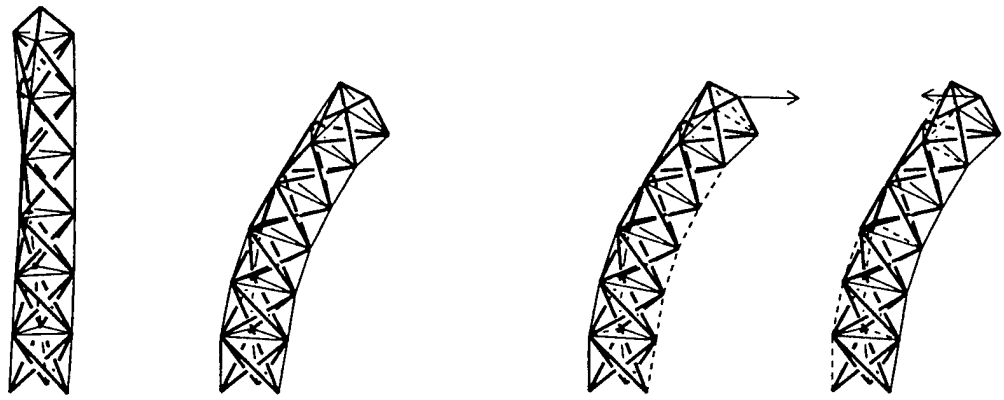
(a) Initial position (b) Attain target (c) Right-ward (d) Left-ward

$\boldsymbol{W}$(m) [0, 0, 6.5] [2, 0, 5] $\Delta\boldsymbol{W}$(mm) [10, 16, −7] [−9, 7, 6]

Geometry adaptation Behavior under tip-end load

(▬▬:Rigid member, ——:Wire under tension, - - - - -:Wire under compression)

Figure 2 Motion and mechanical behavior of obtained design A



(a) Initial position (b) Attain target (c) Right-ward (d) Left-ward

$\boldsymbol{W}$(m) [0, 0, 6.5] [2, 0, 5] $\Delta\boldsymbol{W}$(mm) [27, −5, −15] [−23, −16, 11]

Geometry adaptation Behavior under tip-end load

(▬▬:Rigid member, ——:Wire under tension, - - - - -:Wire under compression)

Figure 3 Motion and mechanical behavior of obtained design B

this interference problem, we adopt a modification of the initial geometry of assembled truss; that is, the triangular column is twisted so that the member interference is cleared at the initial position.

DESIGN AND MOTION EXAMPLES

We demonstrate a simplified example of the proposed combinatorial design approach in the previous section. Only the unit types 1 and 14 in Figure 1 are taken into consideration from the viewpoint of their symmetrical geometry. Design of an adaptive truss of 6 units is

conducted. The twist angle used for the resolution of member interference, 10(deg)/unit, is determined a priori. A tip-end node is added at the peripheral end; its nodal position is used as the workspace vector.

We introduce rectangular workspace area to be attained: $\boldsymbol{W}_L \leq \boldsymbol{W} \leq \boldsymbol{W}_U$, where $\boldsymbol{W}_L$ and $\boldsymbol{W}_U$ denote the lower and upper limits of the area. The adopted criterion is the norm of displacements under the loads in 26 directions at the 27 grid points in the workspace area. Two different designs A and B are conducted; the limits of the rectangular workspace area are $\boldsymbol{W}_L = [-2, -2, 5]^T(\mathrm{m})$ and $\boldsymbol{W}_U = [2, 2, 7]^T(\mathrm{m})$ for design A and $\boldsymbol{W}_L = [-2.5, -2.5, 4]^T(\mathrm{m})$ and $\boldsymbol{W}_U = [2.5, 2.5, 7]^T(\mathrm{m})$ for design B. All combinations of truss units of types 1 and 14 are examined to find the optimal designs in this study.

Figures 2 and 3 show the obtained optimal designs. As shown in the figures, Design A consists of lower two type-14 units and upper four type-1 units, while Design B consists of type-1 units only. Figures 2(b) and 3(b) show the motions of geometry adaptation based on the obtained designs, attaining the target workspace $\underline{\boldsymbol{W}} = [2, 0, 5]^T(\mathrm{m})$. These motions take account of the member interference constraint; the results demonstrate the kinematical feasibility of the adaptive truss with wire member actuators.

Figures 2(c), (d) and 3(c), (d) show the mechanical behaviors of the adaptive trusses after the motion, under horizontal tip-end loads of 100N. Design B, which is obtained based on larger workspace area to be attained, has lower stiffness than Design A. This indicates the difference of kinematical and mechanical characteristics of unit types 1 and 14; the type-1 unit is superior in kinematical motion and the type-14 unit is superior in mechanical stiffness. These results also demonstrate the significance of topology design of the adaptive truss with wire members.

Another remarkable point is the nonlinear stiffness coming from the particular wire member characteristics: the lack of stiffness under compression. It is confirmed by comparing the results in Figures 2(c) and (d) or 3(c) and (d); that is, the magnitude of nodal displacement is significantly affected by the orientation of the load.

CONCLUDING REMARKS

Wire is light and stable under tensile force and has the flexibility fitting to a small storage space; it is expected to be a promising structural member in various future space applications. We apply wire to length-adjustable actuated members of a geometry adaptive truss. Such a structural system must have statically indeterminate topology in order to keep stability under various mechanical conditions. The following two topics concerning the statical indeterminacy are discussed in this study.

Topology design of geometry adaptive truss with wire members is discussed from a combinatorial point of view. Design problem based on the possible types of truss units is formulated. We conduct design examples of adaptive truss of triangular column-type; obtained designs indicate the feasibility and the importance of topology design.

We also study about kinematical interference among truss members augmented by the statical indeterminacy. Geometrical relationship is formulated and an incremental motion planning approach taking account of the interference is proposed. Geometry adaptation motion taking account of the interference is conducted with the designed adaptive truss and the practicability of this kind of mechanical system is confirmed.

We are now considering making use of the nonlinear stiffness particular to the adaptive

truss with wire members. Some interesting applications may be reported in the future conference.

REFERENCES

1. Miura, K., Furuya, H. and Suzuki, K., 1985, "Variable Geometry Truss and Its Application to Deployable Truss and Space Crane Arm", *Acta Astronautica*, 12(7/8), 599-607.
2. Hughes, P. C., Sincarsin, W. G. and Carroll, K. A., 1991, "Trussarm – A Variable-Geometry-Truss Manipulator", *Journal of Intelligent Material Systems and Structures*, 2(2), 148-160.
3. Tanaka, M., Seguchi, Y. and Hanahara, K., 1991, "Kinematics of Adaptive Truss Permitting Nodal Offset (Configuration and Workspace Reach)", *Journal of Intelligent Material Systems and Structures*, 2(3), 301-327.
4. Hanahara, K., Sugiyama, Y. and Anshita, H., 1996, "Statically Indeterminate Geometry Adaptive Truss with Wire Members", *Seventh International Conference on Adaptive Structures*, Santini, P., Rogers, C. A. and Murotsu, Y. eds., Technomic Publishing, 163-170.
5. Hanahara, K. and Tada, Y., 1998, "Kinematics and Motion Planning of Geometry Adaptive Truss with Wire Member Actuators", *Proceedings of the Fourth International Conference on Intelligent Materials*, 152-153.
6. Rao, C. R. and Mitra, S. K., 1971, *Generalized Inverse of Matrices and its Applications*, John Wiley & Sons.

OPTIMUM POSTURE DETERMINATION OF ADAPTIVE STRUCTURE BY IMMUNE ALGORITHM

Yukio Tada, Yasumasa Oda

ABSTRACT

In this paper, an adaptive truss structure is a target of design. As in the optimum posture determination problem of an adaptive truss structure there are many elements to be treated simultaneously, it is thought to be difficult to obtain the global optimum solution due to the existence of many local optimum solutions. Then, for solving the optimum posture determination problem, we propose to use Immune Algorithm (IA) which is superior in the global convergence. And we examine that the learning ability of IA can reduce time for search.

INTRODUCTION

In this paper, we treat a posture determination problem of an adaptive structure used as a soft docking mechanism of a spaceship and a robot arm capturing a floating flight unit[1]. Lots of studies about posture determination of adaptive structure have been reported[2][3]. Because in an optimum posture determination of a truss when the position of the load is constrained in addition to the direction of the load there are many elements to be treated at the same time, it is difficult to solve it with a mathematical programming method. So in this study, we consider the problem that determines an optimum posture of an adaptive truss structure by using Immune Algorithm (IA)[4] which has an ability of adaptation and learning ability, that is one of information systems based on a living being's information processing.

IMMUNE ALGORITHM

A general procedure of IA is as follows [4];

1. Initialization
   By reading data from database or using random numbers, generate individuals and set population of the initial generation.

Department of Computer and Systems Engineering, Faculty of Engineering, Kobe University,
1-1 Rokkodai, Nada, Kobe 657-8501, Japan

2. Memorization of effective solution
   Calculate the affinity of each individual and memorize effective individuals that have high possibility to be used in future into database.
3. Examination of end condition
   When the end condition is satisfied, the best indidual is regarded as the optimum solution.
4. Reproduction
   Delete some individuals of low exception, and generate the same numbers of indivisuals by using random numbers.
5. Cross over
   GA-like crossover
6. Mutation
   GA-like mutation
   At this point, a population of a new generation is created.
7. Return to step2

PROBLEM FORMULATION

We consider the truss shown in Fig.1(b), which is made by truss modules shown in Fig.1(a). This model has an actuator on each stage and can change its posture by expanding and contracting diagonal members by actuators (double marks). In addition, in order to receive load we especially establish two members by triangle shape to the top

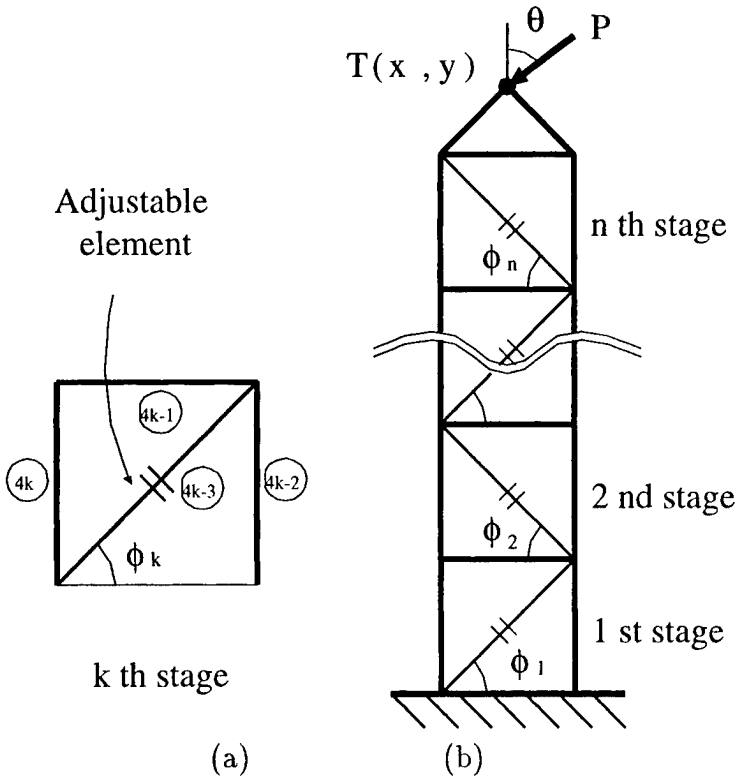


Fig.1 Model of adaptive truss structure

of the truss. This study considers the problem that determines optimum posture that can support a load as large as possible within its strength for loading from various directions at various positions.

We formulate this problem as an optimization problem with stress constraint. It is assumed that a n-stages adaptive truss structure consists of $4n$ members including n variable-length members. We adopt diagonal member's angles ϕ_k $(k{:}1\cdots n)$ as design variables.

Regarding the highest utilization of all members as a utilization of the whole structure, the problem is formulated as

$$\textit{Find} \qquad \phi_k \ (k = 1, \cdots, n) \tag{1}$$

$$\textit{such that} \qquad F = P / Max_{j=1,\cdots,4n}\left(\frac{S_j(x)}{\sigma_j A_j}\right) \rightarrow Max \tag{2}$$

$$\textit{subject to} \qquad |S_j(x)| \leqq \sigma_j A_j \ (j = 1, \cdots, 4n) \tag{3}$$

$$0 < \phi_k < 90 \ (k = 1, \cdots, n) \tag{4}$$

where S_j is the internal force of the j-th member, σ_j is the allowable stress of the j-th member and A_j is the cross sectional area of the j-th member. Therefore, $\sigma_j A_j$ is the permissible force of the j-th member.

The objective function in Eq.(2) is the supportable load of the whole truss and we search for its maximum value by changing design variables ϕ_k. Optimum posture is obtained when we can't increase utilization of all members any more. In the following calculation, as the maximum utilization of members automatically becomes 1 for a temporary load P by the denominator of Eq.(2), it is not necessary to treat explicitly the stress constraint, Eq.(3).

APPLICATION OF IA

In this study, we use IA in the optimum posture determination problem formulated by Eqs.(1)-(4). As the objective function in IA we use the following f_v instead of F in Eq.(2),

$$f_v = \left(1 - \frac{1}{1+F}\right) \tag{5}$$

where f_v is introduced for standardizing F between 0 and 1.

As the tip of the truss must satisfy the position constraint in the case that both the direction and the position of the load are specified, a new constraint is added to the problem, Eqs.(1)-(4). Then, if the distance from the position of the load to that of the tip of the truss is over a threshold, a penalty is added. So, we modify the objective function as follows,

$$f_v = \begin{cases} \left(1 - \frac{1}{1+F}\right) & d_v \leq D \\ \left(1 - \frac{1}{1+F}\right) - \left(\frac{d_v}{1+d_v}\right) & d_v > D \end{cases} \tag{6}$$

where d_v is the distance from the position of the load to that of the tip of the truss and D is a threshold of the position constraint. In this study, we set $D = 1.0$, where the length of the fixed member is 1.0. By setting the objective function as this, we can obtain

the maximum supportable load when the position of the tip of the truss is constrained as a loading position. We regard the objective function as affinity. Control variables are angles from the diagonal members to the horizontal plane and its range is from 0[*deg.*] to 90[*deg.*]. To solve this optimization problem by IA, we need to code antibodies. We code 'the angle of diagonal member on each stage' multiplied by 10 to the gene of antibody and allow each variable to vary from 0[*deg.*] to 90[*deg.*] by 0.1[*deg.*]. For example, when variables on respective stages are 42.1, 71.4, 28.5, 79.1, 80.6, 21.1, 27.7, 54.5, 33.6 and 45.9[*deg.*], the gene is corded as shown in Fig.2.

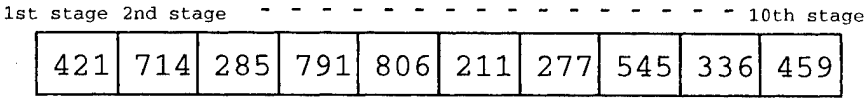


Fig.2 Cording

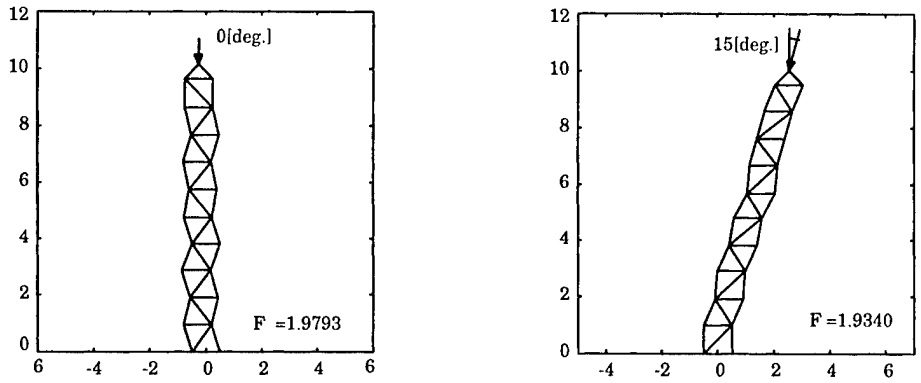
In this problem, in the case that the position of the tip of the truss is constrained, variables that can satisfy the position constraint are limited. So, we spend lots of time for obtaining the solution with maximum supportable load satisfying the position constraint with initial population generated by random numbers. Then, we memorize variables that satisfy the position constraint once obtained into database and we set them to initial population for solving problem with the same position constraint. Thereby, we can reduce time for search. In this way, we utilize the learning ability of IA.

RESULT

As numerical examples, we discuss the problem in the case that only the direction of the load is specified and that when not only the direction but also the position of the load is constrained as (2,8). An object of design is the 10-stages adaptive truss structure, and the number of antibodies is 200. As the end condition, we terminate the generation change when 500 generation is over.

In The Case That Only The Direction Of Load Is Given

In this case, we use IA before learning because the search is not so complicated. We show the optimum postures obtained when the direction of the load $\theta = 0$ [*deg.*] and



(a) $\theta = 0$[*deg.*] (b) $\theta = 15$[*deg.*]

Fig.3 Optimum postures when only the loading direction is given

15[*deg.*] in Figs.4(a) and (b). In both figures, the maximum supportable load is written in respective figures. It is found from Figs.3(a) and (b) that the truss changes its posture to be parallel to the direction of the load. In the case of other loading directions, similar results are obtained.

In The Case That Both The Direction And The Position Of Load Are Constrained

OPTIMIZATION BY IA BEFORE LEARNING

We discuss the problem in the case that not only the direction but also the position of the load are constrained. In the first instance, we use IA before learning. IA before learning has no data in database in which effective antibodies are stored, and we generate initial population by using random numbers. The position of the load is (2,8). Fig.4 shows optimum postures for the load between $\theta = -75[deg.]$ and $\theta = 75[deg.]$ when IA before learning is used. In this case, as the tip of the truss must satisfy the position constraint the truss can't be parallel with the direction of the load. But, when the position of the load is (2,8), the truss can take its posture most nearly to be parallel to the direciton of the load at $\theta = 15[deg.]$. We show some data obtained by the optimization in Table 1. F is the maximum supportable load, d_v is the distance from the position of the load to the tip of the truss and a is the affinity of the antibody. It is found from Table 1 that in most cases, the member of maximum utilization is the fixed member at root of truss. Then, if we strengthen those members, the truss can support a further larger load. The maximum supportable load is the highest at $\theta = 15[deg.]$. This is because of the reason mentioned before.

Table 1 Variation of maximum supportable load, most loaded member's number, distance and affinity when $T(x, y) = (2, 8)$ before learning

loading direction : θ	maximum supportable load : F	most loaded member	distance between load and tip : d_v	affinity : a
-75	0.1179	2	0.0750	0.1055
-60	0.1131	2	0.0583	0.1016
-45	0.1286	8	0.0505	0.1140
-30	0.1536	18	0.0999	0.1331
-15	0.2063	2	0.0715	0.1710
0	0.3936	2	0.0963	0.2824
15	1.2217	25*	0.0916	0.5499
30	0.5111	4	0.0974	0.3382
45	0.2536	8	0.0975	0.2023
60	0.1728	2	0.0706	0.1473
75	0.1361	2	0.0880	0.1198

(* : adaptive member)

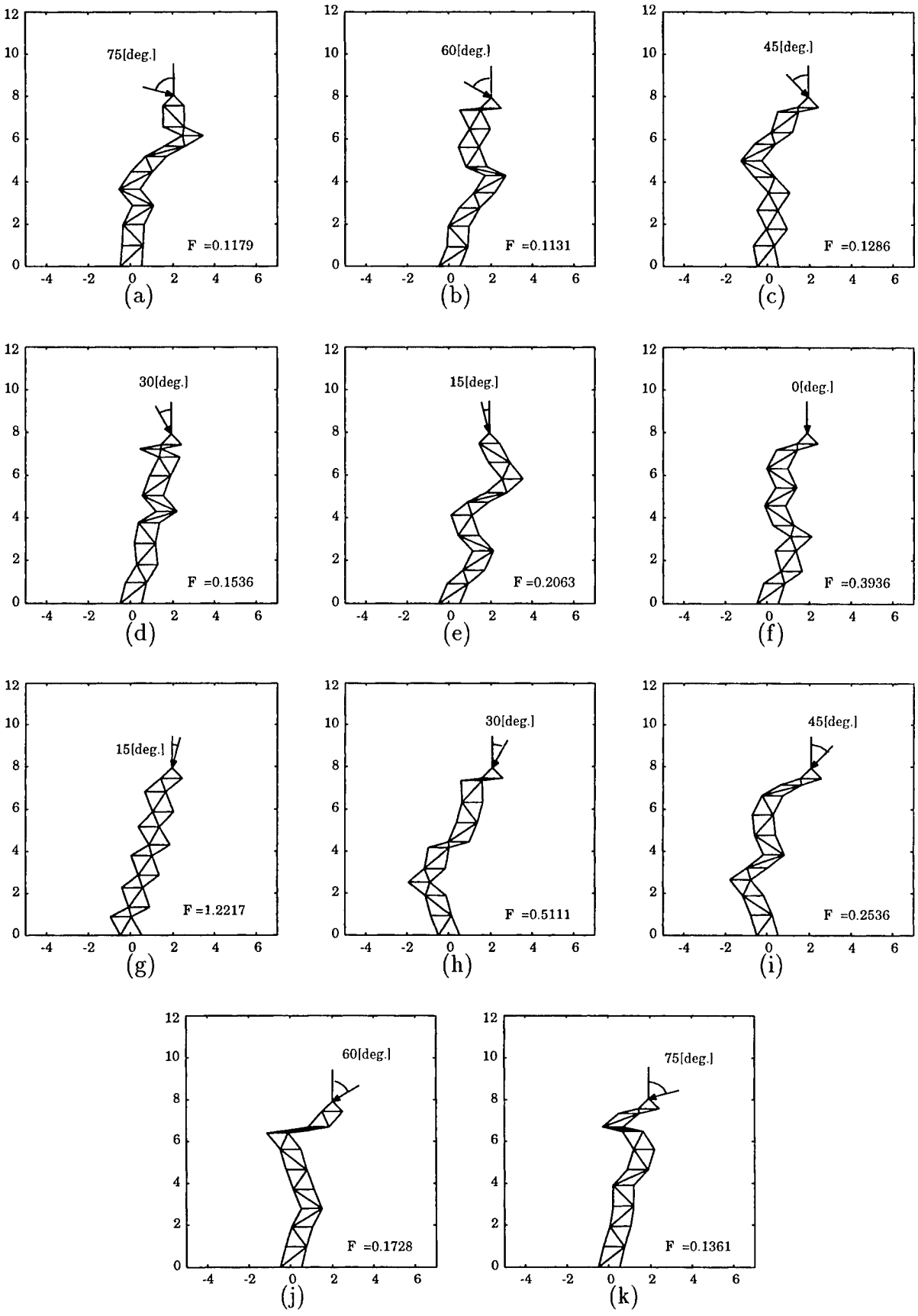
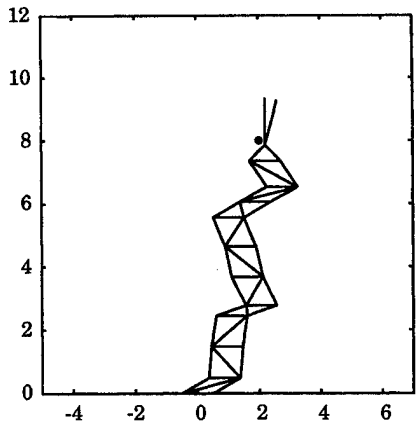
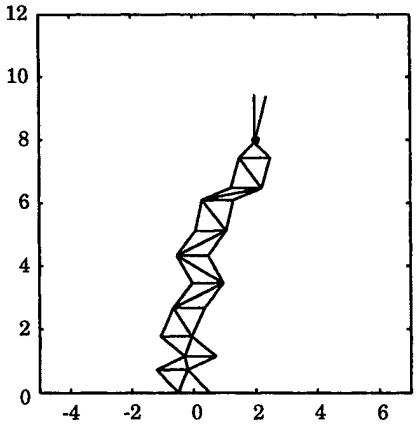


Fig.4 Optimum postures for the load between $\theta = -75[deg.]$ and $\theta = 75[deg.]$ when $T(x, y) = (2, 8)$ before learning

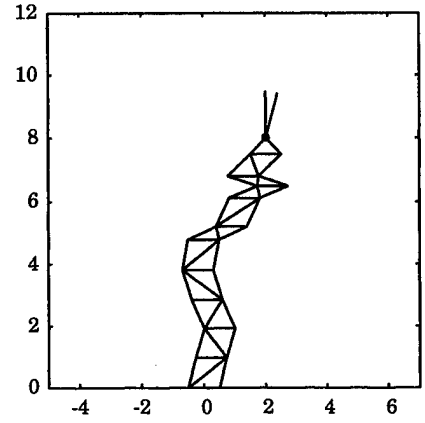


(a)3rd generation

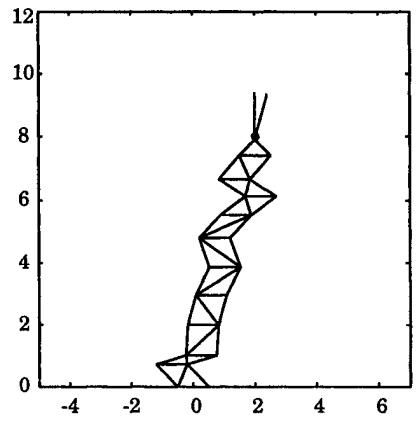


(b)10th generation

Fig.5 Best postures in some generations by IA before learning for the load $\theta = 15[deg.]$ when $T(x, y) = (2, 8)$

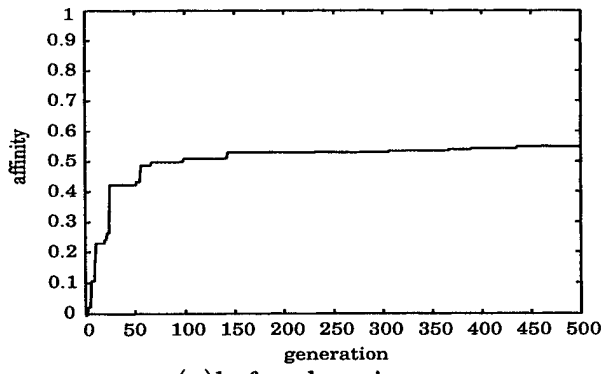


(a)1st generation

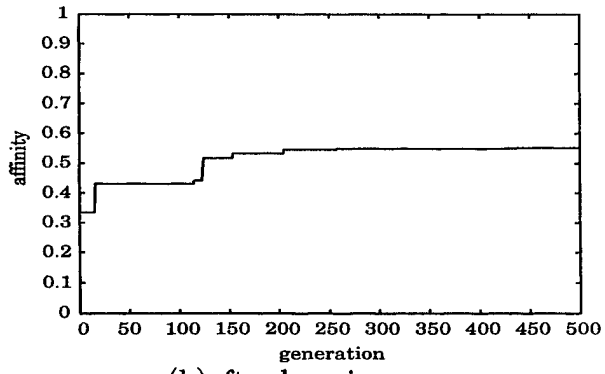


(b)20th generation

Fig.6 Best postures in some generations by IA after learning for the load $\theta = 15[deg.]$ when $T(x, y) = (2, 8)$



(a)before learning



(b)after learning

Fig.7 Variation of affinity ($\theta = 15[deg.]$, $T(x, y) = (2, 8)$)

OPTIMIZATION BY IA AFTER LEARNIG

To examine the effect on the search by using learning ability of IA, we use IA after solving 5 problems of the same position constraint and different loading directions. By learning, effective antibodies to the position constraint (2,8) are memorized in database. In other words, optimum solutions obtained in the case of directions $\theta = 60[deg.], -45[deg.], 75[deg.], 30[deg.] and -75[deg.]$ are memorized. We set these data to initial population. And we solve the problem in the case of direction $\theta = 15[deg.]$. Fig.5 shows the best posture in some generations by IA before learning and Fig.6 shows the best posture in some generations by IA after learning. In figures, the mark · represents the given loading position. In the case of IA before learning, during early generations the truss tries to satisfy the position constraint. On the other hand, in the case of IA after learning, from the first the truss already satisfies the position constraint. This is because in the case of IA after learning initial antibodies consist of those that satisfy the position constraint in database. Fig.7(a) shows the variation of the affinity obtained by IA before learning and Fig.7(b) shows the variation of the affinity obtained by IA after learning. In the case of IA after learning, a solution candidate with higher affinity is obtained in early generation than those by IA before learning. For example, in 20 th generation, the affinity is 0.243 in the case of IA before learning and 0.430 in the case of IA after learning. So, we can realize reduction of time for search by learning ability of IA. Thus, we examined that IA after learning is effective in optimum posture determination problem in the case that the position of the load is constrained.

CONCLUSION

In this paper, we obtained the various postures with the similar affinity for various initial populations by IA and showed the effectiveness of the proposed method. In the case that both the direction and the position of the load are constrained, we examined the effect of learning ability of IA on a searching ability.

REFERENCES

(1)Das, S. K., Utku, S. and Wada, B. K. 1990. "Inverse Dynamics of Adaptive Structures Used as Space Cranes" , *Journal of Intelligent Material Systems and Structures*, 1, pp.50-75.

(2)Tanaka, M. and Hanahara, K. 1992. "Stochastic Approach to Static Control of Adaptive Truss under Imperfection of Adjustable Member Lengths", *Journal of Intelligent Material Systems and Structures*, 3, pp.617-629.

(3)Utku, S. and Wada, B. K. 1993."Adaptive Structures in Japan", *Journal of Intelligent Material Systems and Structures*, pp.437-451.

(4)Ishida, Y., Hirayama, H., Fujita, H., Ishiguro, A. and Mori, K. 1998. " Immunity-Based Systems and Its Applications " (in Japanese), Corona Publishing Co., LTD., pp133-161.

DECENTRALIZED STATIC SHAPE CONTROL OF LARGE-SCALED GEOMETRY ADAPTIVE TRUSS BY TWO-PERSON GAME APPROACH

Masao Tanaka,[1] Noriyo Ichinose[2]

ABSTRACT

The geometry adaptive truss (GAT) is a structural system with hyper-redundant kinematic degrees of freedom (DOFs) in general and the redundancy is an important feature in the geometry adaptation to its structural mission and/or environment. The static control of geometrical shape becomes a key problem for the geometry adaptation. The increase of the number of kinematic DOFs is beneficial for the flexibility and dexterity of the geometry adaptation, but it makes the size of shape control problem larger at the same time. The decentralization is a promising approach to overcome such a difficulty due to the large problem size. In this study, the shape control problem of large-scaled GAT is reduced to a collection of two-person games defined for the individual of truss modules, and formulated as multi-objective min-max problems in a decentralized manner. Numerical studies are conducted for a backyard structure application and the effectiveness of the proposed approach is demonstrated.

INTRODUCTION

The GAT[1][2] is a statically determinate truss of variable length members, and is a mechanism with hyper-redundant kinematic DOFs in general. The hyper-redundancy is an important feature for the geometry adaptation of the GAT to its structural mission and/or environment. The static control of geometrical shape, thus, becomes a key problem for the geometry adaptation, and efforts have been devoted to this problem from viewpoints of the shape adaptation[3, 4], the configuration control[5, 6, 7] and so on [8, 9, 10, 11]. When the number of kinematic DOFs of GAT increases, the geometry adaptation capability becomes more flexible and dexterous, and the problem size of the shape control becomes larger as well. The decentralized shape control is considered as a promising concept to overcome the difficulty caused by the increase of the problem size. The authors have reported the decentralized motion-planning for the mast-type GAT as a space manipulator by means of two-parson game approach and examined for tip-end positioning with obstacle avoidance [12].

In this study, the concept of the decentralized shape control is extended to the plane-type

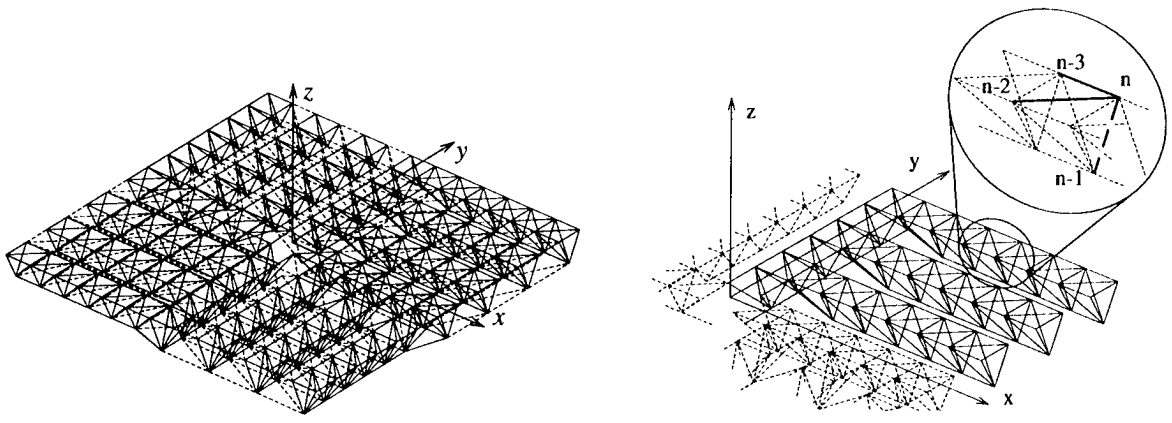
[1]Professor, [2]Graduate student, Division of Mechanical Science, Department of Systems and Human Science, Graduate School of Engineering Science, Osaka University, 1-3 Machikaneyama, Toyonaka, Osaka 560-8531, Japan

GAT as the backyard structure for realizing a free-form surface. That is, the frontal side of the plane-type GAT works as the surface realizing the target configuration, and the other side plays the complementary role for structural function such as to maintain the maneuverability as a mechanism or the sufficient stiffness as a structure. Thus, the objective function of the geometry adaptation problems has multiple objectives of the primal mission for the working surface and complementary missions for the others. The multi-objective problem of the shape control is formulated as a minimization problem, and is decomposed into a collection of two-person games. Each two-person game becomes the min-max problem in which a real player works as a minimizer under the existence of the corresponding virtual player as a maximizer. The effectiveness of the proposed formulation is examined through numerical studies.

STATIC SHAPE CONTROL PROBLEM

GAT for Backyard Structure

The shape control of GAT for a backyard structure is responsible to realize and maintain the target surface. The GAT considered in this study is of a rectangle truss structure of plane-type and has active and passive variable length members as shown in Fig.1. The basic constitution is made of four primal columns along x and y axes stemming from the supporting bases at the origin of coordinate system. Secondary columns branch out of the primal column in clockwise direction at each two bays of the primal column (Fig.1(b)). It is just like a blade of traditional windmill. All the truss members of primal and secondary columns are of active. Passive members are provided to fill the gaps among the primal and secondary columns as shown in Fig.1(a). The whole structure is connected to the base structure by eight base nodes at the center of structure, and the surface in the positive direction of z-axis is the working surface. Each column is made



(a) Planer backyard structure (solid line: active members, broken line: passive members)

(b) Arrangement of active variable length members and active truss module

Figure 1. Geometry adaptive truss of plane-type

of tetrahedral truss modules. In this structure, each column has the topology of helical mast and the rate-type kinematic equation [13] is represented by

$$\frac{d\boldsymbol{X}_n}{dt} = \frac{\partial \boldsymbol{X}_n}{\partial \boldsymbol{L}_n}\boldsymbol{V}_n + \frac{\partial \boldsymbol{X}_n}{\partial \boldsymbol{X}_{n-1}}\frac{d\boldsymbol{X}_{n-1}}{dt} + \frac{\partial \boldsymbol{X}_n}{\partial \boldsymbol{X}_{n-2}}\frac{d\boldsymbol{X}_{n-2}}{dt} + \frac{\partial \boldsymbol{X}_n}{\partial \boldsymbol{X}_{n-3}}\frac{d\boldsymbol{X}_{n-3}}{dt} \tag{1}$$

for the module n of each column, where $\boldsymbol{L}_n = [l_{n1}, l_{n2}, l_{n3}]^T$ and $\boldsymbol{V}_n = d\boldsymbol{L}_n/dt$ denote the member length and its rate of the module n, and $\boldsymbol{X}_n$ stands for the position of node n.

Conventional Formulation

As the backyard structure of the free-form surface prescribed, the primal objective of the static shape control of the GAT is to make the working surface realize the target shape. In order to describe a free-form surface in a parametric manner, the bicubic B-spline surface representation is employed:

$$\boldsymbol{f}(u,v) = \sum_{i=0}^{m-1}\sum_{j=0}^{n-1} N_i(u)N_j(v)\boldsymbol{X}_{ij}^c \tag{2}$$

where $N_i()$ denotes cubic B-spline basis function with coordinate parameter u and v, and $\boldsymbol{X}_{ij}^c (0 \leq i < m, 0 \leq j < n)$ stands for the position of control points. The shape error of GAT is, then, written as the distance between the truss node k on the working surface and the target surface function:

$$e(\boldsymbol{X}_k(t)) = \min_{u,v} |\boldsymbol{X}_k(t) - \boldsymbol{f}(u,v)| \tag{3}$$

By using this shape error, the instantaneous shape difference is defined as

$$h(t) = \sum_{k \text{ on working surface}} \frac{\boldsymbol{e}(\boldsymbol{X}_k(t))^T \boldsymbol{e}(\boldsymbol{X}_k(t))}{\boldsymbol{e}(\boldsymbol{X}_k^*)^T \boldsymbol{e}(\boldsymbol{X}_k^*)} \tag{4}$$

in a normalized form for the static shape control, where $\boldsymbol{X}_k^*$ is the reference home position of node k.

The secondary objective of the shape control problem is defined for the complementary role as structural function to utilize the redundant kinematic DOFs of the GAT. Among many candidates for such objectives, the joint range availability (JRA) [8] is employed toward the flexible maneuverability as a mechanism in this study. That is, the JRA measure is defined as

$$g_n(t) = \sum_{i=1}^{3} \left\{ \frac{l_{ni}(t) - l_{ni}^*}{l_{ni}^*} \right\}^2 \tag{5}$$

for individual truss module n, where l_{ni}^* is the neutral median of the length variation of member ni, and is summed up over all active truss modules resulting the second objective function of JRA index $g(t)$. The static shape control problem of the plane-type GAT is, thus, formulated as a set of minimization problems in an incremental manner:

$$
\begin{aligned}
\text{minimize} \quad & \int_{t_i}^{t_{i+1}} \{\alpha_1 h(t) + \alpha_2 g(t)\}\, dt \\
\text{with respect to} \quad & \boldsymbol{V}_1(t), \boldsymbol{V}_2(t), \ldots, \boldsymbol{V}_M(t) \\
\text{subject to} \quad & \boldsymbol{L}_n^l \le \boldsymbol{L}_n(t_i) + \int_{t_i}^{t_{i+1}} \boldsymbol{V}_n d\tau \le \boldsymbol{L}_n^u \\
& \boldsymbol{V}_n^l \le \boldsymbol{V}_n(t) \le \boldsymbol{V}_n^u \qquad (t_i \le t \le t_{i+1}) \\
& \det\left(\frac{\partial \boldsymbol{L}_n}{\partial \boldsymbol{X}_n}\bigg|_{t=0}\right) \cdot \det\left(\frac{\partial \boldsymbol{L}_n}{\partial \boldsymbol{X}_n}(t)\right) > 0 \quad (t_i \le t \le t_{i+1}) \\
& \qquad\qquad (i = 1, 2 \ldots)
\end{aligned} \tag{6}
$$

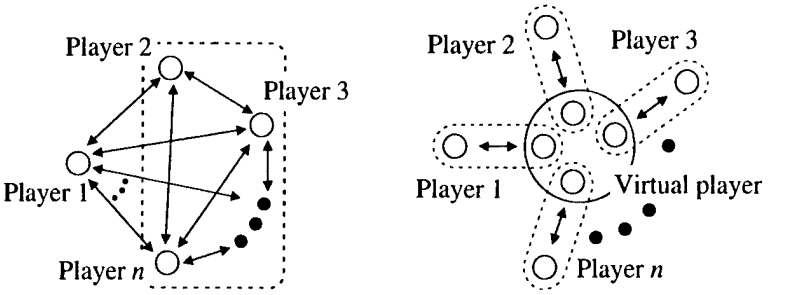
DECENTRALIZED FORMULATION

Two-person Game Approach

In the game theory, the two-person game is the most fundamental one played by two players only. That is, each player decides its own strategy only by paying attention to strategy by the opponent player. In the case of the shape control of GAT, it is natural to assign a player to individual truss module consisting of active truss members, since it is the basic constitutive unit for the geometry adaptation as the whole GAT. In this context, the problem can be considered as a game played by the number of players that is identical to the number of active truss modules. This is, a n-person game [14]. The n-person game formulation is, of course, a kind of decentralized formulation, but the difficulty due to problem size is not resolved. It, however, is also possible to recognize the problem as a two-person game, when all the players except one behaves as a single player opponent to the player excepted (Fig.2(a)). This excepted player might be similar to an individual investor gaming with the market reflecting the strategies of all other investors. Hence, the shape control problem of the GAT as the whole is considered as a collection of two-person games played by the player for an individual truss module and the virtual player that behave differently depending on the opponent player (Fig.2(b)).

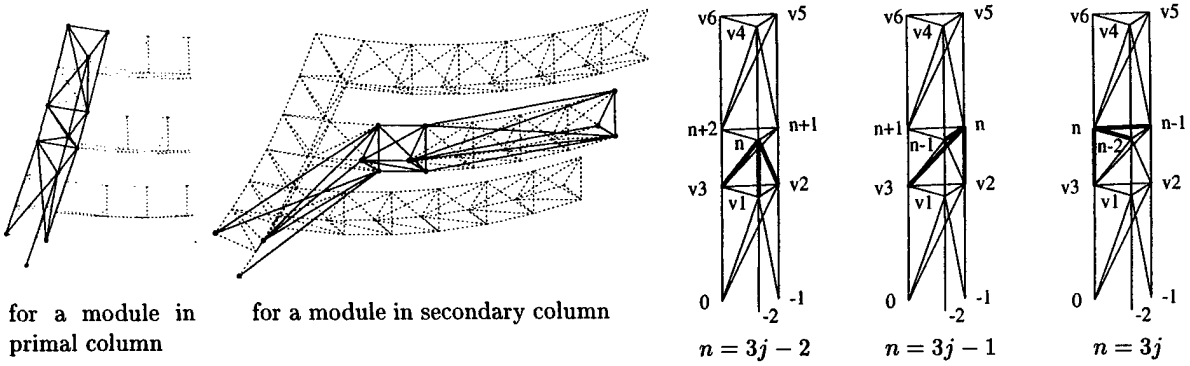
Definition of Problem for Individual Truss Module

It is assumed that each player for a truss module n has the current positions of six nodes of truss bay with the module n, of three nodes at the supporting base of primal column, and of three end nodes of secondary or primary column in which the module is. It also knows the target



(a) n-persion game (b) Collection of two-person games

Figure 2. Decentralized approach by two-person game.



(a) Examples of virtual modules (b) Nodal number of virtual modules

Figure 3. Virtual modules

shape on which its nodes on working surface should be placed. Based on these informations, the player n for the truss module n constructs a kinematic model for the shape control by means of virtual modules as illustrated in Fig.3(a). Figure 3(b) shows the numbering of node in virtual modules. Three of which are defined between the truss bay and three end nodes of the column, and three of which are between the truss bay and three base nodes. The virtual player n opponent to the player n has the freedom to adjust the member lengths of virtual modules $v1, v2, v3, v4, v5$ and $v6$, and seeks a strategy to obstruct the behavior of the player n as much as possible. Under the presence of such a virtual player n, the player n chooses such a rate of member lengths $\boldsymbol{V}_n$ that gives strategy characterized by the min-max problem:

$$
\begin{aligned}
\text{minimize} \quad & \left[\begin{array}{rc} \text{maximum} & \displaystyle\int_{t_i}^{t_{i+1}} \{\alpha_1 h(t) + \alpha_2 g_n(t)\}\, dt \\ \text{with respect to} & \boldsymbol{W}_u(t) \\ \text{subject to} & \boldsymbol{W}_u^l \le \boldsymbol{W}_u(t) \le \boldsymbol{W}_u^u \\ & u \in [v1, v2, v3, v4, v5, v6, 3j-2, 3j-1, 3j],\ u \ne n \end{array} \right] \\
\text{with respect to} \quad & \boldsymbol{V}_n(t) \\
\text{subject to} \quad & \boldsymbol{L}_n^l \le \boldsymbol{L}_n(t_i) + \int_{t_i}^{t_{i+1}} \boldsymbol{V}_n d\tau \le \boldsymbol{L}_n^u \\
& \boldsymbol{V}_n^{l)} \le \boldsymbol{V}_n(t) \le \boldsymbol{V}_n^u \\
& \det\left(\frac{\partial \boldsymbol{L}_n}{\partial \boldsymbol{X}_n}\bigg|_{t=0} \right) \cdot \det\left(\frac{\partial \boldsymbol{L}_n}{\partial \boldsymbol{X}_n}(t) \right) > 0 \\
& \qquad\qquad (0 \le t_i < t < t_{i+1} \le T_e)
\end{aligned} \tag{7}
$$

where $\boldsymbol{W}_u(t)$ denotes the rate of member lengths of the virtual module u, and T_e dose the termination time on the shape adaptation. Thus, the player n is able to decide the strategy, the rate of member lengths $\boldsymbol{V}_n$, based on this problem not depending on the strategy of other players k, $k \ne n$.

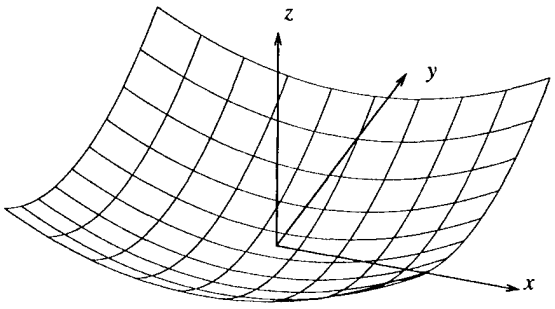
NUMERICAL STUDIES

Consider a GAT of 288 active modules with 864 kinematic DOFs. It has 336 triangle patches making the working surface, and the total number of members is 1224 including passive members.

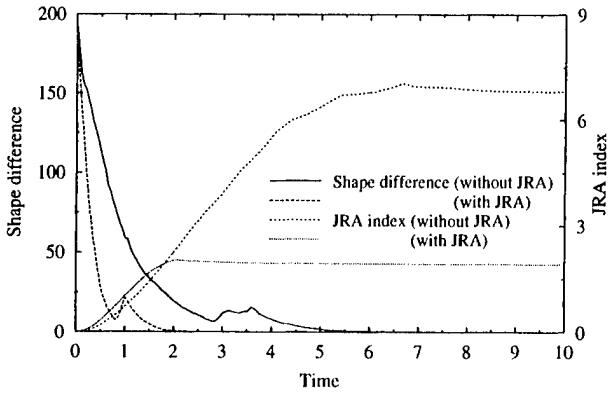
The neutral length is $\sqrt{2.5}$ for members connecting primal and secondary columns, $\sqrt{2}$ for diagonal members and 1.0 for others. These neutral positions result the shape of flat surface shown in Fig.1, and is used as the initial shape in the following cases. The purpose of the static shape control is to realize the target shape on working surface maintaining the dexterity of the GAT as the mechanism. The JRA index $g(t)$ is zero, that is the minimum, at the initial shape.

Parabolic Surface

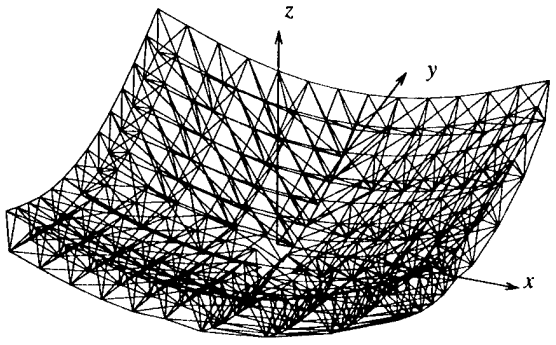
The target shape is given by a parabolic function of $0.04(x^2+y^2)$ (Fig.4(a)). Figure 4(b) shows the time history of the instantaneous shape difference $h(t)$ and the JRA index $g(t)$, and Fig.4(c) and (d) illustrate the shapes adapted to the prescribed surface. In accordance with the shape adaptation, the shape difference decreased and converged after 2000 rounds of gaming. The resulted shape difference is reduced from $h(0) = 192.0$ to $h(T_e) = 8.176 \times 10^{-3}$ and 7.664×10^{-3} with/without consideration of JRA measure showing the satisfactory geometry adaptation. By taking the JRA index $g(t)$ into account, the JRA index is reduced from $g(T_e) = 6.803$ to 1.920. The convergence in shape difference is faster when the JRA index is considered and it will be caused by the complex configuration of objective functions. The temporary increase of the shape difference was not observed in the cases of GAT with smaller number of DOFs. This also suggests the difficulty of the shape control problem of large size. In spite of these minor difficulties, the proposed approach resulted the shape adaptation satisfactory.



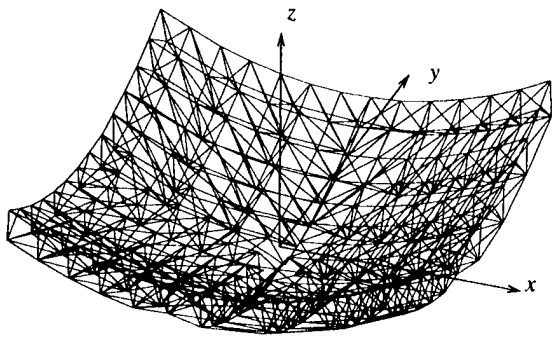
(a) Target shape of working surface



(b) Shape difference $h(t)$ and JRA index $g(t)$

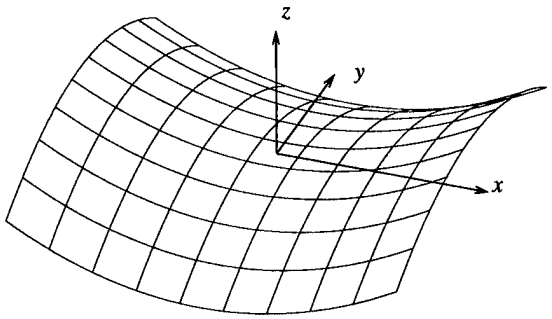


(c) Adapted shape without consideration of JRA
$h(T_e) = 7.664 \times 10^{-3}, g(T_e) = 6.803$

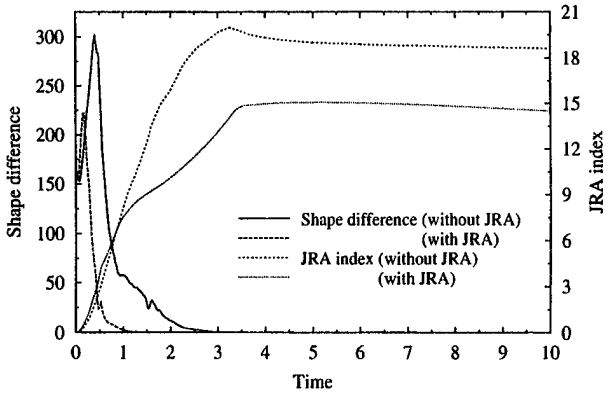


(d) Adapted shape with consideration of JRA
$h(T_e) = 8.176 \times 10^{-3}, g(T_e) = 1.920$

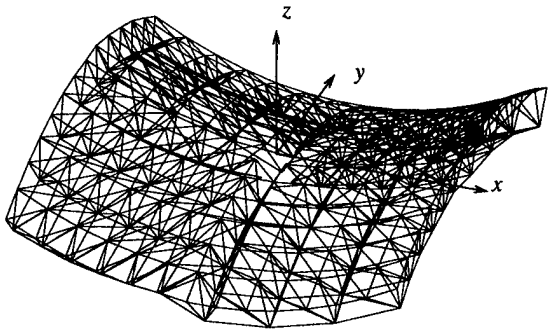
Figure 4. Parabolic surface case



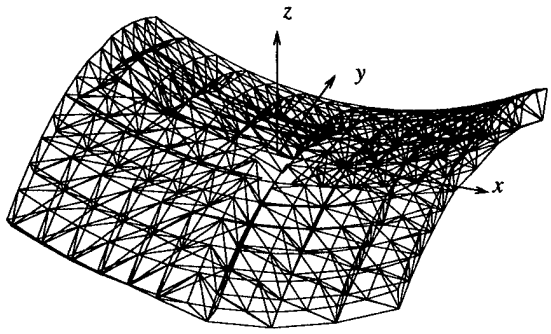
(a) Target shape of working surface



(b) Shape difference $h(t)$ and JRA index $g(t)$



(c) Adapted shape without consideration JRA
$h(T_e) = 8.581 \times 10^{-2}, g(T_e) = 18.62$



(d) Adapted shape with consideration JRA
$h(T_e) = 8.442 \times 10^{-2}, g(T_e) = 14.53$

Figure 5. Saddle surface case

Saddle Surface

The second target shape is the saddle surface function of $0.04(x^2 - y^2)$ (Fig.5(a)). Figure 5(b) shows the time history of indices $h(t)$ and $g(t)$. The shapes adapted are illustrated in Fig.5(c) and (d). The resulted shape difference is $h(T_e) = 8.581 \times 10^{-2}$ and 8.442×10^{-2} with/without consideration of JRA measure, and the JRA index is reduced from $g(T_e) = 18.62$ to 14.53 by taking the JRA index into account. Although the temporary increase of the shape difference is again observed in this case, the proposed approach resulted the shape adaptation satisfactory.

CONCLUSIONS

The static shape control problem of the plane-type GAT of hyper-redundant kinematic system is formulated in terms of the two-person game. The subproblem for individual active truss module is considered as a game played by a player for the truss module and a virtual player representing all the other truss modules. This enables us to deal with the whole problem as a collection of two-person games, which treated in decentralized manner. Through the numerical studies, the effectiveness of the proposed approach is demonstrated for the backyard structure application for quadratic shape of working surface.

REFERENCES

[1] Miura, K. and Furuya, H., "Adaptive Structure Concept for Future Space Applications", *AIAA Journal*, Vol. 26 , No. 8 (1988), pp. 995–1002.

[2] Wada, B. K. and Fanson, J. L., "Adaptive Structures", *Journal of Intelligent Material Systems and Structures*, Vol. 1 , No. 2 (1990), pp. 157–174.

[3] Murotsu, Y., Senda, K., Mitsuya, A., Kawano, H. and Ando, A., "Control Experiments of a Docking Mechanism Composed of a Planar Variable Geometry Truss", *Journal of Intelligent Material Systems and Structures*, Vol. 8 , No. 9 (1997), pp. 784–791.

[4] Matsuzaki, Y., Ichiyanagi, A. and Yoshida, T., "Motion Control of Adaptive Space Structures based on Artificial Potential Method", *Journal of Spacecraft and Rockets*, Vol. 35 , No. 4 (1998), pp. 496–501.

[5] Tanaka, M., Hanahara, K. and Seguchi, Y., "Configuration Control of the Truss-type Parallel Manipulator by the modular Neural Network Model", *JSME International Journal Series III*, Vol. 35 , No. 1 (1992), pp. 89–95.

[6] Boutin, B. A., Misra, A. K. and Modi, V. J., "Dynamics and Control of Variable-Geometry Truss Structures", *Acta Astronautica*, Vol. 45 , No. 12 (1999), pp. 717–728.

[7] Avilé, R., Ajuria, G., Amezua, E. and Gómez-Garay, V., "A finite element approach to the position problems in open-loop variable geometry trusses", *Finite Elements in Analysis and Design*, Vol. 34 (2000), pp. 233–255.

[8] Klein, C. A. and Blaho, B. E., "Dexterity Measures for Design and Control of Kinematically Redundant Manipulators", *The International Journal of Robotics Research*, Vol. 6 , No. 2 (1987), pp. 72–83.

[9] Kimura, S., Takahashi, M., Okuyama, T., Tsuchiya, S. and Suzuki, Y., "A Fault-Tolerant Control Algorithm Having a Decentralized Autonomous Architecture for Space Hyper-Redundant Manipulators", *IEEE Transactions on Systems, Man, and Cybernetics - Part A*, Vol. 28 , No. 4 (1998), pp. 521–527.

[10] Chen, C.-L. and Lin, C.-J., "Motion Planning of Redundant Robots", *Journal of Robotic Systems*, Vol. 14 , No. 12 (1997), pp. 839–850.

[11] Uphoff, I. E. and Chirikjian, G. S., "Discretely Actuated Manipulator Workspace Generation by Closed Form Convolution", *Transactions of the ASME, Journal of Mechanical Design*, Vol. 120 , No. 2 (1998), pp. 245–251.

[12] Tanaka, M. and Ichinose, N., "Decentralized Motion Planning of Geometry Adaptive Truss by Two-person Game Approach", *"Tenth Int. Conf. Adaptive Struct. Tech."*, Technomic, (1999), pp. 346–353.

[13] Seguchi, Y., Tanaka, M., Yamaguchi, T., Sasabe, Y. and Tsuji, H., "Dynamic Analysis of Truss-Type Flexible Arm", *JSME International Journal Series III*, Vol. 33 , No. 2 (1990), pp. 183–190.

[14] Tanaka, M. and Hiraishi, Y., "Note on Game Theory Approach to Decentralized Motion Planning of Adaptive Truss", *"Eighth Int. Conf. Adaptive Struct. Tech."*, Technomic, (1997), pp. 373–382.

CONCEPTS OF REDUNDANT SPACE STRUCTURES USING MULTI-CELLULAR INFLATABLE ELEMENTS

Hiraku Sakamoto,[1,2] Kosei Ishimura,[1,2] M. C. Natori,[1] Ken Higuchi[1]

ABSTRACT

Concepts of redundant space structures using multi-cellular inflatable elements are proposed in this paper. Although inflatable elements are essentially vulnerable against punctures, adopting modular elements can localize the damages. The results of analytical studies on cantilever inflatable tubes show that small internal pressures are still needed to prevent the deformation of the cross-section, which causes a stiffness drop, even when the membrane is successfully rigidized. The adoption of multi-cellular rigidized inflatable elements with sublimating make-up gas system will realize stiff structures over a long mission life. The modularized structures also have advantages regarding easy ground testing and manufacturing.

INTRODUCTION

For the near future space exploration missions, we need to develop easy construction technologies of highly precise and very large space structures, such as large parabolic antennas, solar reflectors or solar sails, on the earth/moon orbits or in deep space. Such structures are fundamentally required to have high packaging efficiency, low weight and high reliability for minimizing the launching cost. Resent development of inflatable rigidizable membrane, shape memory materials and other new materials enables us to create innovative concepts of deployable space structures, instead of conventional mainly mechanical deployable structures, which keep their structural stiffness by using latch mechanisms.

Some large space structures (LSS) consist of some kinds of repeated elements, which result in modularized structures. The space structures with multi-modules including the new elements would show some possibilities of new adaptive and redundant space structures. For example, a reflector structure using modularized inflatable elements with back-up trusses has

[1] Institute of Space and Astronautical Science, Space Structures Laboratory, 3-1-1 Yoshinodai, Sagamihara, Kanagawa 229-8510, Japan.
[2] Graduate Student, Department of Aeronautics and Astronautics, the University of Tokyo, Japan.

been proposed by one of the authors [1, 2], but whole structures could consist of only new elements such as inflatable elements. Bearing this in mind, we propose in this paper the concepts of redundant space structures using multi-cellular inflatable elements. In the following, we first summarize the characteristics of inflatable elements and relevant efforts on them, and after that, we introduce and discuss the new structure concepts. Finally we report the analytical studies on cantilever inflatable tubes that support the advantages for the structures using multi-cellular inflatable elements.

CHARACTERISTICS AND CATEGORIES OF INFLATABLE ELEMENTS

Concepts of inflatable deployable space structures have been under development since the early 1960s when the ECHO balloon satellites were successfully sent into orbit [3], and some primal analyses for the structure design were made [4]. Since the middle of 1990s, as requirements for larger space structures increases, inflatable elements have come to the great attention of many researchers as promising space structure elements in the new century. Major advantages of using inflatable elements in space are their high packaging efficiency, extremely light weight and high deployment reliability.

However, inflatable elements essentially have three major problems in the following. 1) Environmental threats such as space debris or meteorites, atomic oxygen, ultraviolet and radiation damage eventually result in leakage of the system. 2) As consisting of thin membrane, inflatable elements are poor regarding their structural accuracy. In particular, development of large inflatable reflector structures with high surface precision is quite challenging. 3) Because of the high flexibility, free inflation deployment of inflatable elements could be very volatile. This problem was clearly evidenced by the in-orbit deployment of the Inflatable Antenna Experiment (IAE) flown in May 1996 [5]. Therefore deployment control is significantly required for stability.

In order to ameliorate the first problem regarding leakage, many researches have been done with respect to rigidization of membrane after the deployment in space so that the elements can keep their shapes and stiffness even when they lose the internal pressure. As possible rigidization technologies, thermal/solar radiation cure, UV cure, metal yielding, foam inflation and other methods have been discussed [6]-[10]; however, there are still some difficulties to establish practical technologies yet.

Inflatable elements discussed so far fall into three primary categories [11]: Constantly inflated (CI) elements which need to maintain internal gas pressure over the life of the mission, rigidized inflatable (RI) elements which require inflation gas only during initial deployment, and single inflation (SI) elements such as the Mars Pathfinder landing bags. (A word "continuously" is used in Ref. [11] instead of "constantly.") Since SI systems have only limited applications, we do not treat them in this paper.

SPACE STRUCTURES USING MULTI-CELLULAR INFLATABLE ELEMENTS

Multi-Cellular Inflatable Elements

We propose the concepts of redundant space structures using multi-cellular inflatable elements. As shown in Fig. 1, we introduce some concepts of beam structures, plate structures and reflector structures consisting of modular inflatable elements. These structures can easily have structural redundancy, i.e. even if some cells are punctured in space and lose the internal pressures, the damage remains local and does not harm the whole system; in addition, multi-cellular inflatable elements can keep redundancy not only after deployment but also during the deployment in space. Furthermore, ground testing and manufacturing of large inflatable structures can be easier by adopting multi-cellular elements, just as present deployable modularized structures such as modular mesh antenna [12]. Multi-cellular inflatable elements could also enable us to design stiffer structures with less gas, applying relatively high internal pressures where stress is concentrated, and less pressures where is not.

Both of non-rigidized constantly inflated (CI) elements and rigidized inflatable (RI) elements could be used as the multi-cellular inflatable elements. In the following, we discuss each of these two in detail.

Constantly Inflated (CI) Elements as Multi-Cellular Elements

One possibility of redundant structures is to use non-rigidized constantly inflated (CI) elements as the multi-cellular. Since the non-rigidized membrane cannot sustain compressive

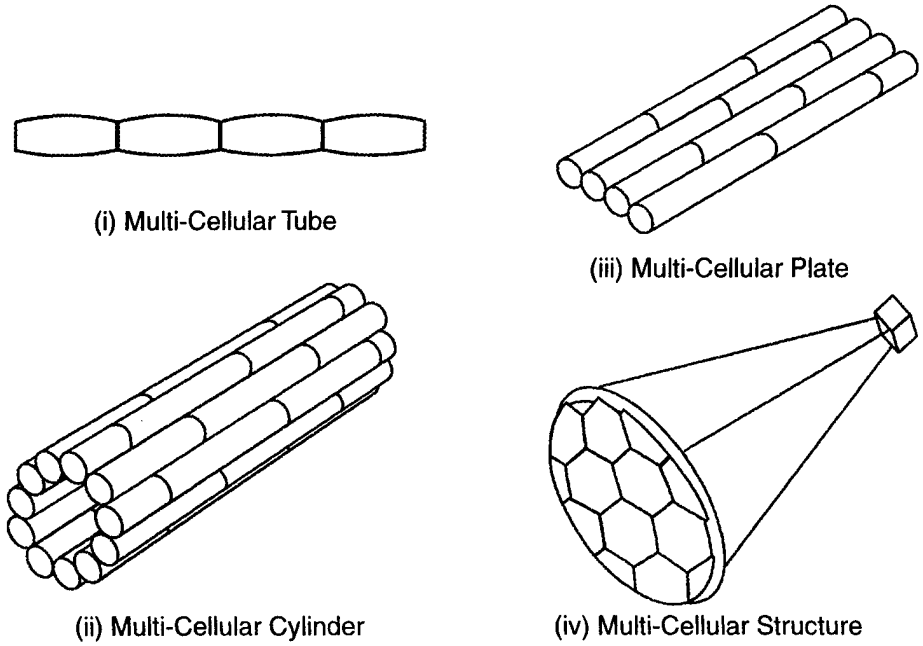


Figure 1. Examples of Multi-Cellular Inflatable Elements

stress by itself, CI elements need considerably high internal pressure to provide tension on the membrane, and it is known that wrinkling on membrane causes a sudden drop of their stiffness. Therefore CI elements are not appropriate to the members that need stiffness. However, CI elements could make shape control easier. Reflector structures, for instance, require high structural accuracy. Multi-cellular CI elements could be used for such applications combined with mechanisms to control the internal pressures in each cell. For practical uses of non-rigidized CI elements, concepts of modularization should be adopted in the near future; otherwise only one puncture to the membrane causes the critical failure of the total structure system.

Rigidized Constantly Inflated (RCI) Elements as Multi-Cellular Elements

Even when the membrane is rigidized in space, keeping internal pressure in inflatable elements over the life of the mission can be very effective for stiffness. We call in the following the rigidized inflatable elements with make-up gas, as rigidized constantly inflated (RCI) elements. By adopting the multi-cellular concept with RCI elements, the elements can also have redundancy against damage.

Regarding inflation method for multi-cellular RCI elements, sublimating systems are the most appropriate, because RCI elements need only much smaller internal pressure than CI elements. According the Ref. [8], sublimating inflation systems have been used since the ECHO balloon satellites in 1960s. The operating principle for sublimating powders is to release the powder within the interior of the inflatable elements after orbit insertion. In space conditions the powders will sublime into a gas that provides vapor pressures in the range of 10^{-1} to 10^{0} Pa. These powders provide self pressure regulation if excess powder is carried and allowed to sublimate as make-up gas. Nitrogen tanked gas system could be combined with sublimating systems, in order to supply the gas for initial deployment.

FUNDAMENTAL ANALYSES OF CANTILEVER INFLATABLE TUBES

Cantilever Inflatable Tubes

In order to know physical characteristics of inflatable elements and obtain fundamental knowledge for structural designing, simplest models of inflatable elements, i.e. cantilever inflatable tubes are numerically investigated. The authors carried out the two kinds of analyses: the analysis of CI tubes and of RI tubes.

Analysis of Cantilever Constantly Inflated (CI) Tubes

First, we reviewed the analysis of simple cantilever inflatable tubes with non-rigidized thin membrane modeled by Comer and Levy [13]. Their analytical model is similar to conventional Euler-Bernoulli beam theory but the influence of wrinkles on membrane is well introduced. Figure 2 shows the model whose radius of the cross-section is r, length of the

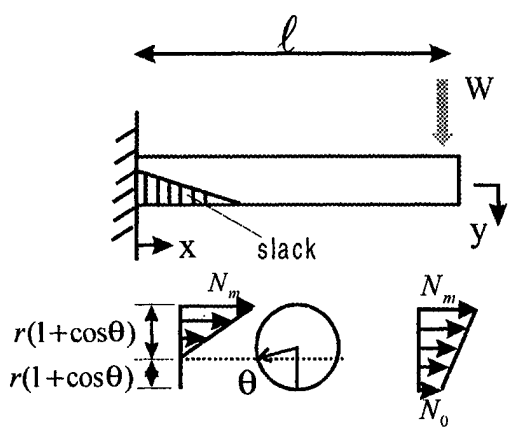


Figure 2. Model of cantilever constantly inflated (CI) tube

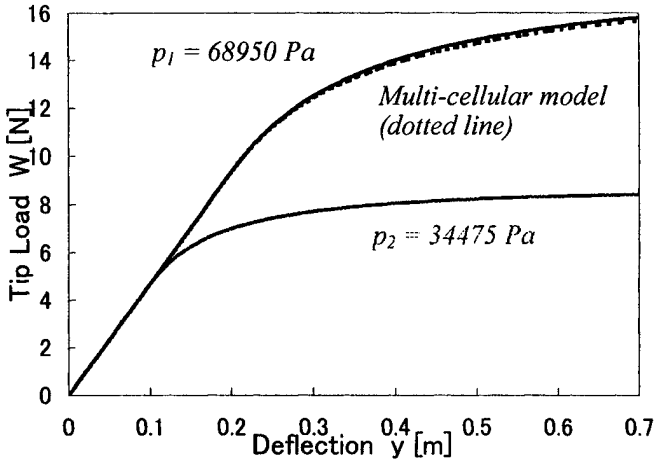


Figure 3. Load-deflection curves for CI tubes

tube ℓ, and internal pressure p. As the concentrated tip load W increases, the bending stress equilibrates the axial tension in thin membrane on the concave side of the tube, and wrinkling begins in that region. The membrane wrinkles because non-rigidized membrane is incapable of resisting compressive stresses. The model is also based on the assumption that the internal pressure maintains the circular shape of the cross-section, and plane sections remain plane (Kirchhoff-Love's hypothesis). The angle θ in the slack region is given by

$$\frac{M(x)}{pr^3} = \frac{\pi(2\pi - 2\theta + \sin 2\theta)}{4[(\pi-\theta)\cos\theta + \sin\theta]} \quad (0 < \theta < \pi) \tag{1}$$

The second moment of area is given by

$$\begin{cases} I = r^3 t\left[\pi - \theta + \left(\dfrac{\sin 2\theta}{2}\right)\right] \; ; \; \dfrac{\pi pr^3}{2} < M < \pi pr^3 \\ I = \pi r^3 t \; ; \; M < \dfrac{\pi pr^3}{2} \end{cases} \tag{2}$$

Using Eqs. (1) and (2), deformation of the tube is obtained by solving the differential equation of the beam theory:

$$\frac{d^2y}{dx^2} = -\frac{M(x)}{EI} \tag{3}$$

Main et al. [14] pointed out that the results of numerical analysis by this model well correspond to their experimental results, if an effective modulus of membrane is used in the calculations instead of cataloged Young's modulus. The solid lines in Fig. 3 show the results of numerical calculations, when $r = 4$ *cm*, $\ell = 80$ *cm* and the effective modulus $Et = 39{,}800$ *N/m*. These results show wrinkles on membrane have dominant effect on the stiffness of CI tubes, and high internal pressure is needed to avoid wrinkling.

Figure 4 shows a cantilever inflatable tube with two cells, and the cell near the root has higher internal pressure (p_1). The result of numerical calculation for this model is shown by

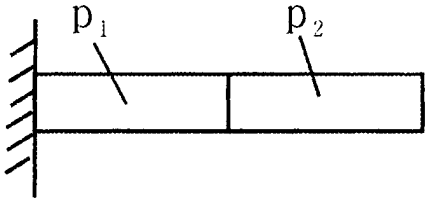


Figure 4. Multi-cellular inflatable tube

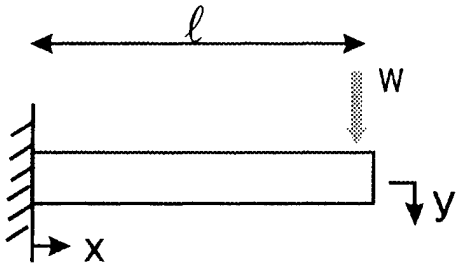


Figure 5. Model of Cantilever rigidized inflatable (RI) tube

the dotted line in Fig. 3, which describes the multi-cellular inflatable tube is approximately as stiff as a previous single-cellular model whose whole internal pressure is p_I. It seems that multi-cellular tubes enable us to design stiff structures using less gas. The results in Fig. 3 also indicate that avoiding wrinkling by rigidizing membrane is very effective for stiffness: Inflatable tubes with successfully rigidized membrane do not need high internal pressure for their stiffness, compared with non-rigidized CI tubes.

Analysis of Cantilever Rigidized Inflatable (RI) Tubes

Thus we secondly made numerical analysis on cantilever inflatable tubes with rigidized membrane as shown in Fig. 5. This time it is assumed that membrane is isotropically rigidized and can resist compressive stresses. The previous model is assumed the circular cross-section of tubes never changes; on the other hand in this RI model, flattening of the cross-section is taken into consideration, since we applied much less internal pressures than before. For example, when a drinking-straw is bent between the fingers into a curved arc of steadily increasing curvature, it is found that the cross-section of the entire tube becomes progressively more oval as the curvature increases. The flatter the cross-section becomes, the smaller second moment of area the tube has. This ovalisation of circular cross-section of tubes is called Brazier effect and experimental results are well predicted by Brazier's theory [15] as follows:

$$M = \frac{2}{\sqrt{3}}\pi Erth(c - 2c^3) \quad \text{where} \quad c = \frac{\sqrt{3}}{2}\frac{r^2}{h}C, \quad h = \frac{t}{\sqrt{1-\nu^2}} \tag{4}$$

$$\zeta = \frac{4}{3}c^2\left(1 + \frac{p}{p^*}\right)^{-1} \quad \text{where} \quad p^* = \frac{Eth^2}{4r^3} \tag{5}$$

$$I = \pi r^3 t\left(1 - \frac{3}{2}\zeta + \frac{5}{8}\zeta^2\right) \tag{6}$$

In Eqs. (4)-(6), M is the moment applied to a unit length of the tube, E is Young's modulus of the membrane, r is the initial radius of the cross-section, t is the thickness of membrane, C is the curvature of the center-line of the tube, ν is the Poisson's ratio of membrane, ζ is a



Figure 6. ζ as a dimensionless measure of the flattening of the cross-section

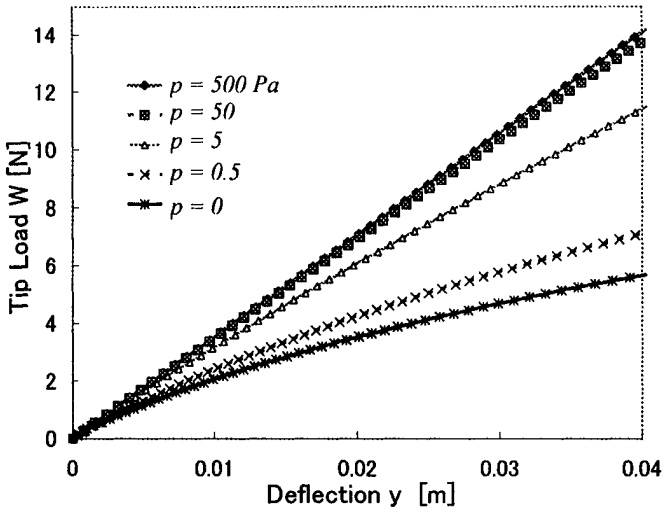


Figure 7. Load-deflection curves for rigidized inflatable (RI) tubes

dimensionless measure of the flattening of the cross-section as shown in Fig. 6, p is the internal pressure and I is the second moment of area. The load-deflection curves for RI tubes with various internal pressures are given by numerically solving the differential equation (3) using Eqs. (4)-(6).

Figure 7 shows the result of numerical calculations for various internal pressure when $E = 10\ GPa$, $r = 4\ cm$, $t = 30\ \mu m$, $\nu = 0.3$ and $\ell = 80\ cm$. These results indicate that RI tubes cannot support the relatively high loading level due to the ovalisation of the cross-section when they lose internal pressure. With small internal pressures (10^{-1} to $10^{2}\ Pa$), however, RI tubes can maintain their stiffness. Therefore we can conclude that even when the membrane of inflatable elements is rigidized, keeping small internal pressure in the elements over the life of the mission can be considerably effective for keeping stiffness of the elements.

These results show that the concept of rigidized constantly inflated (RCI) elements, which is rigidized inflatable elements with make-up gas to keep their internal pressures, is effective. RCI elements can be stiffer than any other inflatable elements; since rigidization of membrane avoids wrinkling, which causes a drop of the stiffness, and internal pressure avoid deformation of the cross-section, which also cause a drop of the stiffness. Much less make-up gas is necessary for RCI elements than CI elements, as RCI elements need only small internal pressure.

CONCLUSION

Concept of modularized space structures using multi-cellular inflatable elements is one of the innovative and feasible structure concepts using new materials. Although inflatable elements are essentially vulnerable against damages, structures can have redundancy by consisting of modularized elements, i.e. even if some cells are punctured and lose their

internal pressures, the damages remains local and do not harm the total system. Modularization of large structures also makes ground testing and manufacturing easier. The analytical studies on cantilever inflatable tubes show that rigidization of membrane is quite effective for stiffness because it avoids wrinkling of membrane which causes a stiffness drop; however, small internal pressures are still needed even for rigidized inflatable elements to prevent the deformation of the cross-section which also causes a stiffness drop. Therefore redundant system is effective both for rigidized and non-rigidized inflatable elements.

REFERENCES

1. Natori, M., H. Furuya, S. Kato, Y. Takesita and Y. Sakai. 1988. "A Reflector Concept Using Inflatable Elements," presented at 16th International Symposium on Space Technology and Science, Sapporo, Japan, May 1998, pp. 459-467.
2. Kato, S., Y. Takeshita, Y. Sakai, O. Muragishi, Y. Shibayama and M. Natori. 1989. "Concept of Inflatable Elements Supported by Truss Structure for Reflector Application," Acta Astronautica, Vol. 19, No. 6/7, pp. 539-553.
3. Wilson, A. 1981. "A History of Balloon Satellites," Journal of British Interplanetary Society, Vol. 34, pp. 10-22.
4. Leonard, R. W., G. W. Brooks and H. G. McComb Jr. 1960. "Structural Considerations of Inflatable Reentry Vehicles," NASA TN D-457.
5. Freeland, R. E. and G.R. Veal. 1998. "Significance of the Inflatable Antenna Experiment Technology," AIAA Paper 98-2104.
6. Higuchi, K., M.C. Natori, H. Hatta, and R. Yokota. 1996. "Inflatable Space Rigidized Structure: Adaptivity and Fundamental Experiment," presented at 20th International Symposium on Space Technology and Science, Gifu, Japan, May 19-25, 1996.
7. Grahne, M. S., D. Cadogan, C. R. Sandy, and K. Moriyama. 1998. "Inflatable Space Structures: A New Paradigm for Space Structure Design," presented at 21st International Symposium on space Technology and Science, Omiya, Japan, May 24-31, 1998.
8. Freeland, R. E., G. D. Bilyeu, G. R. Veal and M. M. Mikulas. 1998. "Inflatable Deployable Space Structures Technology Summary," IAF Paper 98-1.5.01.
9. Derbes, B. 1999. "Case Studies in Inflatable Rigidizable Structural Concepts for Space Power," AIAA Paper 99-1089.
10. Allred, R., L. Harrah, A. Hoyt, R. McElroy, R. Wise and M. Lou. 2000. "Inflatable Spacecraft using Rigidization-on-Command Concept," AIAA Paper 2000-1637.
11. Roe, L. A. 2000. "Inflation Systems for Near-Term Space Missions," AIAA Paper 2000-1570.
12. Mitsugi, J. and T. Yasaka. 1990. "Deployable Modular Mesh Antenna - Concept and Feasibility -", presented at 17th International Symposium on Space Technology and Science, Tokyo, Japan, May 1990, pp. 599-604.
13. Comer, R. L. and S. Levy. 1963. "Deflections of an Inflated Circular-Cylindrical Cantilever Beam," AIAA Journal, Vol.1, No.7, pp. 1652-1655.
14. Main, J. A., S. W. Peterson and A. M. Strauss. 1994. "Load Deflection Behavior of Space-Based Inflatable Fabric Beams," Journal of Aerospace Engineering, Vol.7, No.2, pp. 225-238.
15. Calladine, C. R. 1983. Theory of Shell Structures, Cambridge University Press, Chapter 16.

Health Monitoring

IMPROVED SURFACE TREATMENT OF SMA FOILS AND DAMAGE SUPPRESSION OF SMA-FOIL EMBEDDED CFRP LAMINATES

Toshimichi Ogisu, Norio Andou, Junji Takaki, Tomonaga Okabe, Nobuo Takeda

ABSTRACT

The authors have been conducting research and development studies on some applications of embedded SMA foil sensors and actuators in CFRP laminates for weight reduction and improvement of reliability for next generation aircraft. The goal of this research is to develop a method for the suppression of damage growth in CFRP laminates. It is certified that one of key technologies is bonding properties between SMA foils and CFRP laminates.

In this paper, improvement of bonding properties between SMA foils and CFRP and confirmation of suppression effects of damage growth are described. Some surface treatments (sol-gel method, anodic-oxidation method and spattering method) were performed on SMA foils. Then, peel resistance and single lap shear strength tests were performed using surface treated SMA foils. It was found that treatment by 10%NaOH is most effective treatment for improvement of bonding properties. The treated surface was found porous and rough, which is supposed to provide anchoring effects of SMA/CFRP interfaces.

Then, quasi-static load-unload tests were performed using the optimum treatment as mentioned above to investigate the damage behavior of quasi-isotropic CFRP laminates with embedded SMA foils. Micro-mechanisms of fracture behavior and the correlation between the crack density and the residual strain were discussed. The recovery stress of the SMA foil generated at over Af temperature showed capability of suppression for onset of transverse cracks in quasi-isotropic CFRP laminates with embedded SMA foils.

Toshimichi Ogisu, Norio Ando and Junji Takaki, Fuji Heavy Industries Ltd. Utsunomiya Plant, Aerospace Division, 1-1-11 Yonan, Utsunomiya-city, Tochigi prefecture 320-8564, JAPAN.
Tomonaga Okabe and Nobuo Takeda, Graduate School of Frontier Sciences, The University of Tokyo, c/o Komaba Open Laboratory (KOL),The University of Tokyo, 4-6-1 Komaba, Meguro-ku, Tokyo 153-8904, JAPAN

INTRODUCTION

An application of the smart material and structural systems is highly demanded in aerospace fields, especially. The recent studies suggest possible applications of SMA for these smart systems for suppression of damage growth. Shimamoto et al [1] have demonstrated the reduction in the stress intensity factor for SMA wire embedded epoxy resin using a photoelasticity technique. Taya and Furuya [2] calculated the stress intensity factor as a function of the crack growth rate for SMA wire embedded aluminum composites. Then, they confirmed that pre-strained SMA provided delay effects of the crack growth rate in fatigue test cycles.

Such stress reduction effects will provide a drastic weight reduction and higher performance in aircrafts by shifting the design concept from no crack growth design to damage growth control design for CFRP structures. Furthermore, Kobayashi, Ogihara and Takeda [3] have confirmed that pre-strained SMA provides delay effect of damage onset and the strength increase using GFRP cross-ply laminates with embedded SMA wires. The authors have been conducting research and development studies on applications of embedded SMA foil sensors and actuators in CFRP laminates [4]. The goal of the present research is the suppression of damage growth in CFRP laminates. So, in this paper, the following subjects are discussed.

1) Improvement of bonding properties between SMA foils and CFRP
2) Damage behavior of quasi-isotropic CFRP laminates with embedded SMA foils treated by the improved surface treatment

A CONCEPT OF CRACK GROWTH SUPPRESSION USING SMA FOILS

System Concept

SMA has a shape recovery effect caused only by heating when pre-strain was given to the material. This function is generated by phase transformation from the martensite phase induced by deformation (M' phase) to the austenite phase (A phase). At the same time, SMA is a metallic material. Therefore, electrical resistance of SMA is changed by change of cross section due to strain. In smart material and structural systems, these functional properties of SMA are important features for realizing a smart system as a sensor and actuating element in composite laminates.

On the other hand, CFRP laminates have some characteristic damages in the weakest layer (specifically transverse cracks) at the rather low strain level of approximately 0.3% due to the residual tensile strain generated while the laminate was cured at high temperatures. If the damage can be detected and the initiation and the growth of the damage can be suppressed, the design concept of CFRP structures can be changed. In the present design concept, no crack growth concept is applied in aircraft design due to poor damage detection. The damage tolerance design concept using a smart structure system can be established once the damage detection and suppression scheme is provided in CFRP laminates.

So, the authors proposed a concept of damage (especially transverse crack) growth suppression induced by heating pre-strained SMA foils embedded in CFRP laminates. Figure 1 shows the concept of the recovery stress distribution to suppress damages.

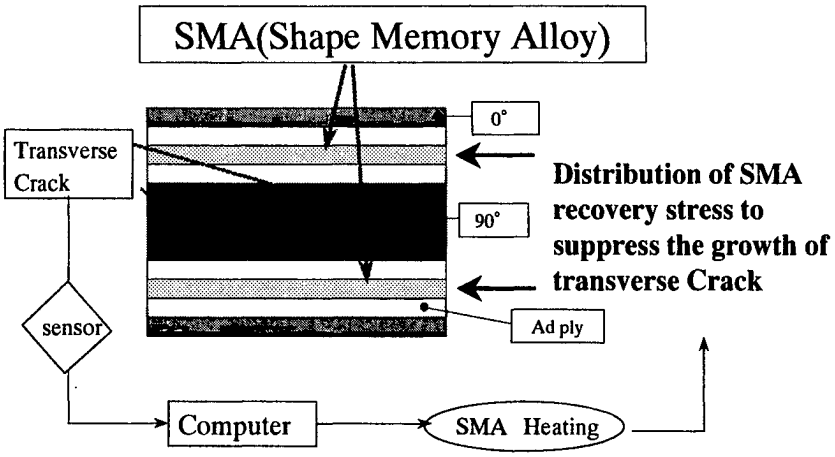


Figure.1 Distribution of Recovery Stress in SMA foils to suppress the damage growth

Recovery Stress of SMA Foil

It is supposed that the recovery stress of SMA is generated in the following process when CFRP laminates were manufactured with embedded pre-strained SMA foils.

1) Place test specimens to a tensile test machine at R.T., and load up to the pre-determined strain level.
2) After unloading, measure the residual strain.
3) Place and clamp pre-strained SMA with keeping the pre-strain level. Then, lay up into laminates.
4) Heat up to 180°C which is the cure temperature of CFRP. Then, maintaining the temperature for 90 minutes.
5) Cool down to R.T.

Figure 2 shows the schematic diagram of recovery stress in order to introduce the compressive residual stress in 90-degree plies after the fabrication. The recovery stress is zero at the first state. The stress-strain curve of SMA in tensile tests at R.T. is shown as OA (route ①). Some portion of the SMA foils is transformed into the M' phase. When the applied stress is removed, the SMA reaches the strain of ε_B due to relaxation of the elastic deformation. In this case, Young's modulus in the unloading route ② is the same with that in the loading stage. During the CFRP laminate fabrication at 180°C(route ③), the strain remains at ε_B. Since the SMA is exposed over the Af temperature (about 65°C), the entire strain consist of plastic and elastic strains. Therefore, the strain returns from C to D. However, the recovery stress does not return to zero at R.T. and the strain reaches D through BC (route ③), CC' (route ④) and C'D. Therefore, CFRP laminates with embedded SMA foils generate the recovery stress of D-D' even at R.T. So, the pre-strained SMA with plastic deformation of ε_B is considered to generate the recovery stress of D-E (route ⑤) for temperature change between 80°C and R.T.

As the results of these tests, it was confirmed that pre-strain levels from 1% to 4% did not cause any difference in the shrinking stress.

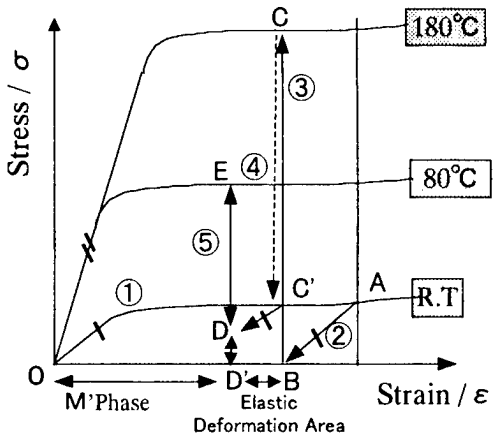


Figure 2. Schematic Concept of Recovery Stress

IMPROVEMENT OF SURFACE TREATMENT OF SMA FOILS

Experimental Procedure for Improvement of Surface Treatment of SMA Foils

As mentioned above, it is necessary to improve the bonding properties of the interface between SMA foils and CFRP laminates for achievement of a smart material and structural system. Generally speaking, surface treatments of metal are conducted to generate anchor effects with roughness of the metal surface, to produce a porous oxide layer, and to improve the wetting properties.

SMA foils contain strong oxide surface layers as received after the fabrication. Such oxide layers reduce the bonding property. Therefore, the authors developed an acid solution cleaning method. The cleaning of SMA foils were conducted by soaking them into 3% fluoride acid–15% nitric acid solution for three minutes, which had been found optimum in our preliminary studies. After that, pre-treatment was performed on SMA foils. Treated SMA foils were used for both peel resistance and single lap shear strength tests. TABLE I shows several methods for pre-treatment of SMA foils conducted in the present stady.

TABLE I. PRE-TREATMENT CONDITIONS OF SMA FOILS

No.	Material	acid solution cleaning	Pre-treatment	Peel Test	Shear Test
1	SMA/Ti-Ni	fluoride acid - nitric acid	Previous Treatment	Tested	--
2		3% fluoride acid - 15% nitric acid	Spattering	Tested	Tested
3			Sol Sel	Tested	Tested
4			Ion Plating (Ti coating)	Tested	Tested
5			Ion Plating (Cr coating)	Tested	Tested
6			Anodic Oxide (10% sodium hydroxide)	Tested	Tested
7			Anodic Oxide (10% phosphoric acid)	Tested	--

Results of Peel Resistance and Single Lap Shear Strength Tests

Specimens were manufactured by bonding Al sheets and SMA foils using AF126 (epoxy like as Metlbond 1515-3) adhesive. These tests were performed in accordance with ASTM D3167 for peel resistance tests and ASTM D 3165 for single lap shear tests.

Figures 3 and 4 show the results of peel resistance strength and single lap shear strength, respectively. The peel resistance strength of SMA using pre-treatment No.4 (Ion plating, Ti coating) was the highest at 1.17

N/mm. and showed three times as high as that in the previous report [4]. However, this process tends to provide a large scatter in the strength. Furthermore, the single lap shear strength showed data of 25~30MPa in all pre-treatments except the spattering method. This shear strength is equivalent to the strength of bonding between metals (approximately 30MPa) which is at good level for actual application. The authors further researched for the optimum pre-treatment conditions for practical applications in accordance with the results of these tests. As a result, we concluded the for practical applications pre-treatment of SMA foils by anodic oxide treatment using 10% NaOH solution were most appropriate at present.

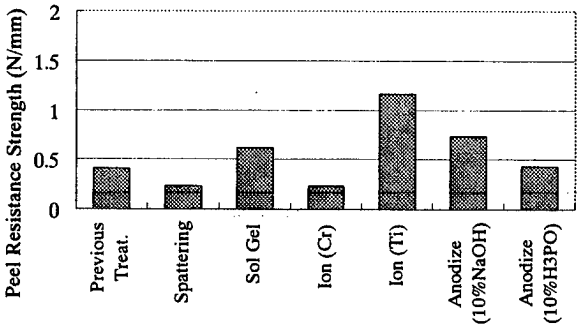


Figure 3. Dependence of peel resistance strength for several surface treatments of SMA foils

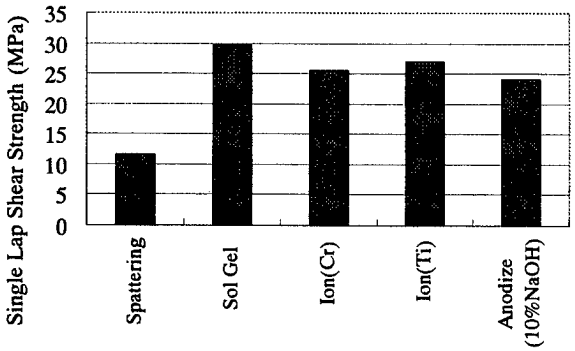


Figure 4. Dependence of single lap shear strength for several surface treatments of SMA foils

Surface Observation after Surface Treatment of SMA Foils

In general, improvements of the bonding property between metal and resin made in the following ways.

1) anchor effects by roughness of metal surface
2) chemical bonding between metal and resin(mainly hydrogen bonding)
3) improvements of wetting property between metal and resin.

It is expected that the factor 1) is most effective in improvement of bonding property between SMA and CFRP. So, the authors focussed on the surface roughness and contents of the surface oxide film after surface treatment in this paper. Then, four different test specimens (no treatment, only acid cleaning, anodic oxide treatment by 10%NaOH and 10%H_3PO_4) were characterized through surface investigation by measurement of roughness, X-ray diffraction patterns of thin films, SIMS (Secondly Ion Mass Spectroscopy) analysis and FE-SEM (Field Emission-Scanning Electron Microscopy) observation. Figure 5 shows an FE-SEM image of the SMA foil treated with anodic oxide by 10%NaOH solution. The surface of SMA foil after the anodize treatment has a very rough surface which is easy to generate anchor effects. Other test results also certified good bonding properties of the surface treatment using anodic oxide by 10%NaOH solution.

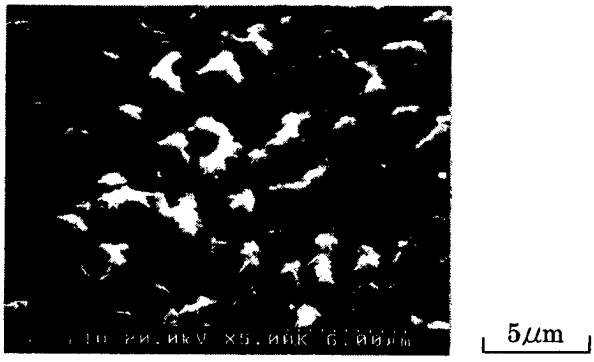


Figure 5. FE-SEM Image of SMA Foils Treated with Anodic Oxide by 10%NaOH Solution

DAMAGE BEHAVIOR OF QUASI-ISOTROPIC CFRP LAMIINATES WITH EMBEDDED SMA FOILS

Test Specimen of CFRP Quasi-isotropic Laminates with Embedded SMA Foils

TABLE II shows the stacking sequence and the test condition of quasi-isotropic CFRP laminates with embedded SMA foils. Ad is the adhesion layer between SMA and CFRP. Dimensions of the test specimen are 250mm in length, 35mm in width and 1.9mm in nominal thickness. The gage length is 50mm. In this study, The used CFRP prepreg system is T300/F593 (HEXCEL, prepreg thickness: 0.2mm). Epoxy adhesive films (Metlbond 1515-3, Cytec Industries, thickness: 0.127mm) were used to increase the adhesion between CFRP and SMA. Ti-Ni SMA foils (Furukawa Electric Co., Ltd.) were used in chemical composition of Ti-50.2%Ni. For manufacture of test specimens, SMA foils was cleaned and roughened by 3% fluoride acid-15% nitric acid to remove the oxide film created when the material was mechanically rolled. Furthermore, the SMA foils were anodic oxide treated with 10% NaOH solution. SMA foils stretched to the pre-strain were used to be embedded in CFRP laminates. The SMA foils were fixed on the fixture jig to keep the length during the curing at 180°C.

TABLE II. STACKING SEQUENCE AND TEST CONDITION OF QUASI-ISOTROPIC LAMINATES SPECIME

No.	Stacking Sequence	Test Condition	Num.of Test Piece
1	[45/0/-45/90]s	RT,DRY	3
2	[45/0/-45/90]s	80°C, DRY	3
3	[45/0/-45/90/Ad/SMA/Ad/90/-45/0/45]s	RT,DRY	3
4	[45/0/-45/90/Ad/SMA/Ad/90/-45/0/45]s	80°C, DRY	3

Ad : Adhesive Layer (thickness=0.127mm)

Test Procedure of Load-Unload Tests

The test was performed at a constant cross-head speed (1m/min) at both R.T. and 80°C using test specimens as shown in TABLE II. The specimens were loaded until predetermined strain levels as shown in TABLEIII. After that, the specimens were unloaded until zero loads at same test speed. Then, the residual strain was measured in every unloaded step. Such loaded–unloaded cycles were conducted up to failure of test specimens. The strain was measured with strain gages (Tokyo Sokki Ltd., FCU-6-5-1L) adhered on both sides at center of test specimens through a dynamic strain measurement device (Tokyo Sokki Ltd. DRA-101A) in real time. Residual strain, Young's modulus and transverse crack densities were acquired from these test data. Transverse crack density was detected by irradiation of black light after immersing a penetrant solution in free edge of test specimens after each cycle. The transverse crack density was defined as the number of cracks divided by the gage length (5cm).

TABLEIII. TEST CONDITION OF LOAD-UNLOAD TEST

Test Name	Applied Strain(%)	Test Speed	Condition	Num. of Test piec
Load-Unload	0.20 0.40 0.50 0.60 0.70 0.80 0.90 1.00 1.20 Failure	1mm/min	R.T. DRY 80°C, DRY	3

Test Results

Typical test results of the load-unload tests were shown in Figure 7. The transverse cracks were generated at 0.6% strain at both temperatures R.T. ans 80°C in CFRP laminates and the number of cracks increased as the applied strain increased. On the other hand, in CFRP laminates with SMA foils, the transverse cracks did not occur until 0.8% strain at 80°C. It was supposed that the onset of transverse cracks was suppresses by embedded SMA caused to phase transformation from M' phase to A phase on SMA. Figure 8 shows the edge photos of specimens with embedded SMA tested at 80°C.

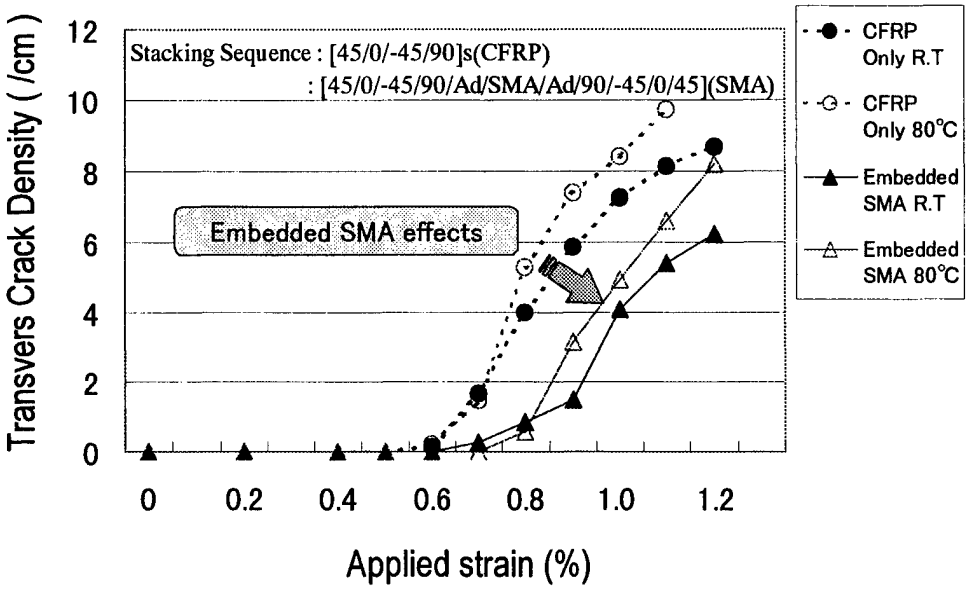


Figure 7. Transverse Crack Density as a Function of Applied Strain for CFRP Laminates with and without embedded SMA

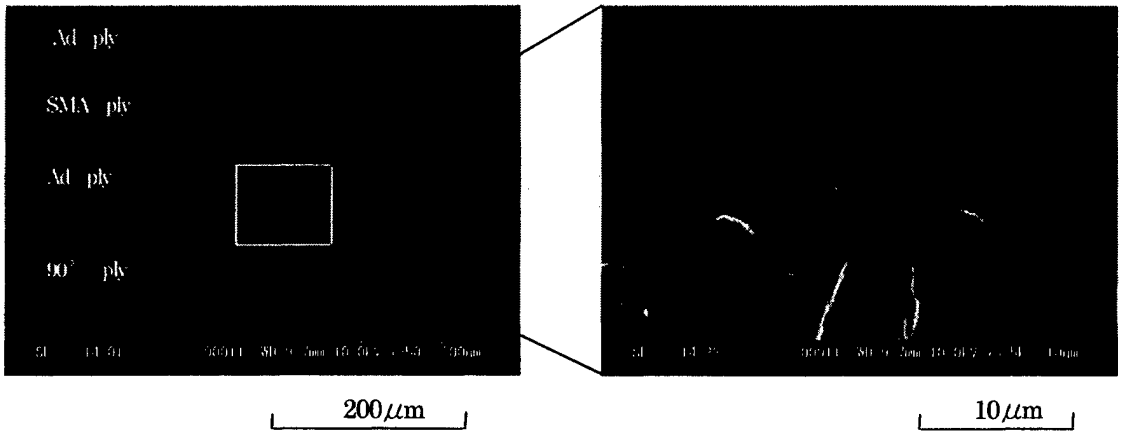


Figure 8. A tip of first transverse crack generated at 0.8% strain of [45/0/-45/90/Ad/SMA/Ad/90/-45/0/45] CFRP laminates tested at 80°C

CONCLUSION

In this paper, for development of a damage suppression system in CFRP laminates with embedded SMA foils, the following results were obtained.

1) It was confirmed by the results of surface observation and analysis that the surface after anodic oxide treatment by 10% NaOH solution was most appropriate for practical applications to generate anchor effects.
2) From the results of load–unload tests for CFRP quasi-isotropic laminates with embedded pre-strained SMA foils, it was supposed the pre-strained SMA foils could suppress the onset of transverse cracks.

ACKNOWLEDGEMENTS

This research was conducted as a part of the "R&D for smart Material and Structure System" project within the Academic Institutions Centered Program supported by NEDO (New Energy and Industrial Technology Development Organization), Japan.

REFERENCE

[1] A.Shimamoto, M.Taya, Y.Furuya, "*Enhancement of Strength and Crack-closure by Utilizing Shape Memory Effects of TiNi Fibers Reinforced Composite*", Proc. of JSME, Material and Mechanics Division Meeting (Vol.B), 1995, pp.67-68

[2] M.Taya, Y.Furuya, "*Enhancement of Mechanical Strength and Fatigue Resistance of TiNi Fiber/ Al Composites by Shape Memory Effect*", Smart Structural System Symposium, (1996.Mar) pp101-111

[3] A.Kobayashi, S.Ogihara, H.Yoshinari and N.Takeda, "*Damage Development in Composite Laminates with Embedded SMA Wires*", Proc. Japan SAMPE Symposium , 1999, pp.65-68

[4] T.Ogisu, M.Nomura,H.Kikukawa and N.Takeda, "*Development of Health Monitoring System Using Embedded SMA Foils in CFRP Laminates*", Proc.2nd International Workshop on Structural Health Monitoring, 1999, pp.317-326

DEVELOPMENT OF STRUCTURAL HEALTH MONITORING SYSTEMS FOR SMART COMPOSITE STRUCTURE SYSTEMS

Nobuo Takeda

ABSTRACT

The present R&D status of our structural health-monitoring group (SHMG) is summarized. Activities of the SHMG are conducted as a university-industry collaboration program at the University of Tokyo along with 10 research organizations. The research themes include: (1) development of high-performance sensor system technology with newly-developed sensors, (2) development of a damage detection and self-diagnosis system for structural integrity based on micro-mechanical damage identification, and (3) development of application technology for model structures. The sensor technology includes: (1) development of small diameter optical fiber sensor, (2) damage suppression in composite laminate systems with embedded shape-memory alloy films, and (3) development of maximum strain memory sensors with electrically conductive composite systems. The sensor output is correlated with the underlying damage evolution in structures such as aircrafts, satellites, high-speed trains and large-scale civil infrastructures.

INRODUCTION

Light-weight composite material systems have been progressively used as structural members in various applications. However, more use has been proposed as primary structural members under severe operating conditions. In such applications, durability evaluation and health monitoring systems are two key technologies to be investigated.

Nobuo Takeda, Department of Advanced Energy, Graduate School of Frontier Sciences, and Department of Aeronautics and Astronautics, School of Engineering, The University of Tokyo, 7-3-1 Hongo, Bunkyo-ku, Tokyo 113-8656, Japan, E-mail: takeda@compmat.rcast.u-tokyo.ac.jp

The author has been proposing a so-called "experimental micro-mechanics of composites" to bridge the gap between material fabrication and macroscopic mechanical properties. Based on in-situ observation using optical, scanning electron, and/or scanning acoustic microscopes with loading devices, microscopic deformation and damage has been quantified. Moreover, theoretical models have been established for damage evolution. These efforts can provide the methodology for the durability evaluation or the damage tolerance design of composites [1-4]. In real structural applications, however, since the strains applied to the composite structures are random and uncertain, the real-time strain monitoring is necessary to predict the present damage status in composites based on the above durability evaluation method. Moreover, if the damage can be detected by using sensors, more reliable estimation of the damage status or the residual life can be made.

In Japan, a new "R&D for Smart Material/Structure System (SMSS)" project started in October 1998 as one of the Academic Institutions Centered Program supported by NEDO (New Energy and Industrial Technology Development Organization), Japan. This SMSS project includes four sub-themes: (1) structural health monitoring, (2) smart manufacturing, (3) active/adaptive structures, and (4) actuator materials development. The author acts as a group leader in the structural health monitoring group, which consists of 10 research organizations. Our structural health monitoring group (SHMG) is currently developing a health monitoring system, which conducts a real-time damage detection and self-diagnosis as well as damage control in light-weight composite structural systems.

The research themes include:

(a) development of high-performance sensor system technology with newly-developed sensors,

(b) development of a damage detection and self-diagnosis system for structural integrity based on micro-mechanical damage identification, and

(c) development of application technology for model structures.

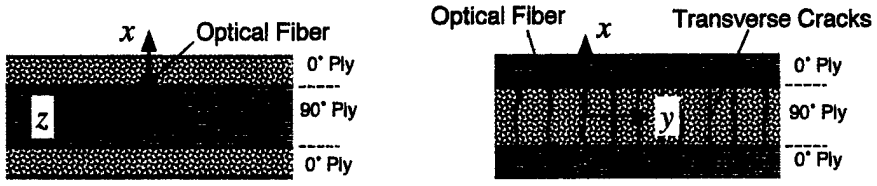
The sensor output is correlated with the underlying damage evolution in structures such as aircrafts, satellites, high-speed trains and large-scale civil infrastructures. The latest results in SHMG research efforts are reported for each research theme.

SUMMARY OF RECENT ACCOMPLISHMENTS OF SHMG

Detection of Transverse Cracks in CFRP Laminates with FBG Sensors – Univ. Tokyo

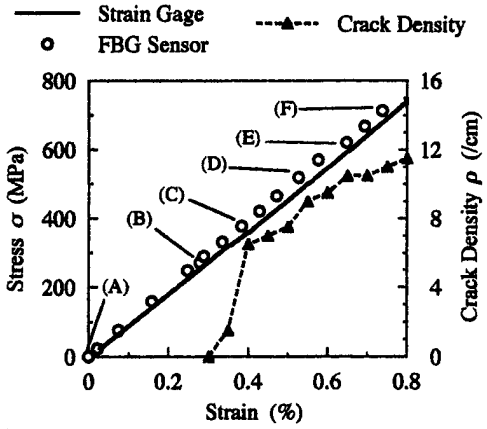
Fiber Bragg Garting (FBG) optical fiber sensors have been developed to measure strain, temperature and so on, through the shift of the wavelength peak in the reflected light. A uniform strain within the gage section (typically 10 mm) is normally assumed. When an FBG sensor is embedded in 0-degree ply to detect transverse cracks in a 90-degree ply, a

non-uniform strain distribution due to the initiation and evolution of transverse cracks causes the wavelength distribution in the reflected light (Fig. 1) [5]. Figure 2(a) shows the stress and crack density as a function of strain measured by a strain gage and a FBG sensor. A careful examination of the wavelength distribution can be used to detect the evolution of transverse cracks in composite laminates (Fig. 2(b)). With increasing transverse crack density, the shape of the reflection spectrum was distorted; the intensity of the highest peak became small, some peaks appeared around it, and the spectrum became broad. As the crack density was close to saturation, the spectrum became narrow again and the highest peak recovered its height. These experimental observations can be well explained by the theoretical prediction (Fig. 2(c))[5].

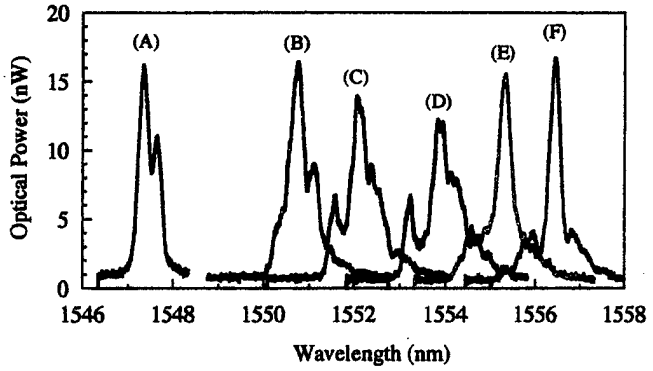


(a) normal (b) parallel to loading

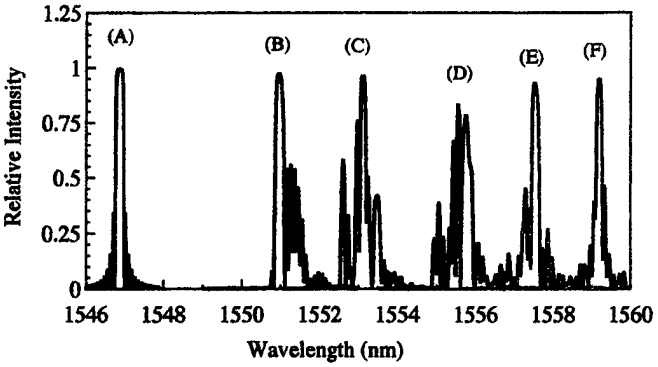
Fig. 1 Cross-sections of CFRP cross-ply laminate with an embedded FBG sensor



(a) Stress and crack density versus strain



(b) Measured reflection spectra

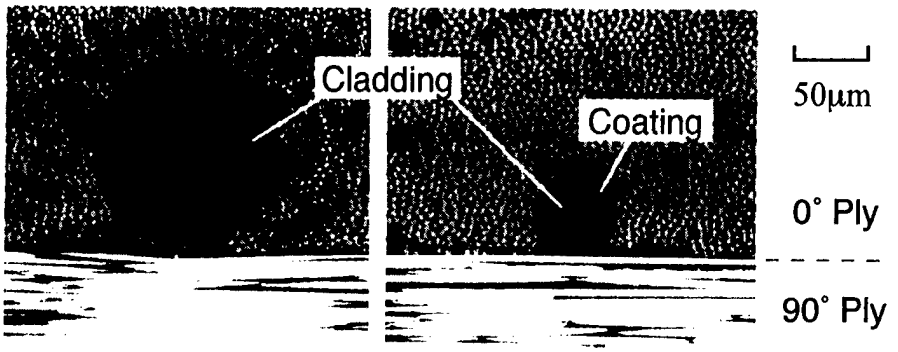


(c) Calculted reflection spectra

Fig. 2 Reflection spectra at various tensile strains. Points (A) to (F) in (a) correspond to those in (b) and (c)

Development of Small-Diameter Optical Fiber Sensors – Hitachi Cable

The first notable accomplishment in our university-industry collaboration is the development of small-diameter optical fibers and the application to the FBG sensors. The developed optical fiber is with 40 μm in cladding diameter and 52 μm in polyimide coating diameter, which is easily embedded within one CFRP ply of 125 μm in thickness. Such optical fibers have mechanical properties similar to those of conventional optical fibers with 125 μm in cladding diameter and do not cause any reduction in strength of composites when embedded parallel to reinforcing fibers in laminas (Fig. 3)[6]. The developed FBG sensors also have optical sensitivities similar to those of conventional 125 μm-cladding diameter FBG sensors. The polyimide coating is highly compatible with epoxy or other high-temperature polymer matrix of CFRP composites under high-temperature exposure during fabrication and also in high-temperature use.



(a) Conventional optical fiber without coating (b) Newly-developed Small-diameter optical fiber

Fig. 3 Optical fibers embedded within lamina

Identification of Impact Damage Parameters in Composites Using Embedded Optical Fiber Sensors – Kawasaki Heavy Industries

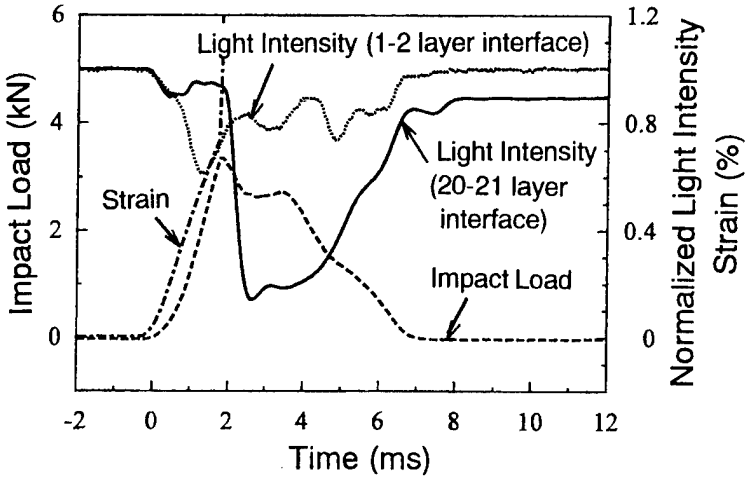


Fig. 4 Normalized optical intensity, load and surface strains in impacted $[0_2/90_2]_S$ cross-ply laminates

Real-time detection of impact load on composite laminates was successfully made with embedded small-diameter optical fibers [7]. Figure 3(b) shows a small-diameter optical fiber embedded parallel to reinforcing carbon fibers in $[0_2/90_2]_S$ cross-ply laminates. Instrumented Charpy impact tests were made, and the optical loss during impact was recorded as a function of time simultaneously with the impact load and the surface strains measured by strain gages (Fig. 4). The bending loss can be observed only during impact loading. The magnitude of optical loss is found to be proportional to the magnitude of the impact load.

Strain and Damage Monitoring of CFRP Space Satellite Structures Using Optical Fiber Sensors – Mitsubishi Electric

Honeycomb sandwich panels with thin CFRP face sheets are used as space satellite structures, and are subjected to severe thermal and mechanical environmental conditions. Low-cost fabrication is highly required for future satellites and a structural health monitoring system is essential during fabrication as well as in practical use [8]. Figure 5 shows a specimen for simple compression test of a honeycomb sandwich panel where a small-diameter optical fiber is embedded within CFRP face sheets. The change in optical intensity can be an excellent indicator of compression failure in such structures as shown in Fig. 6.

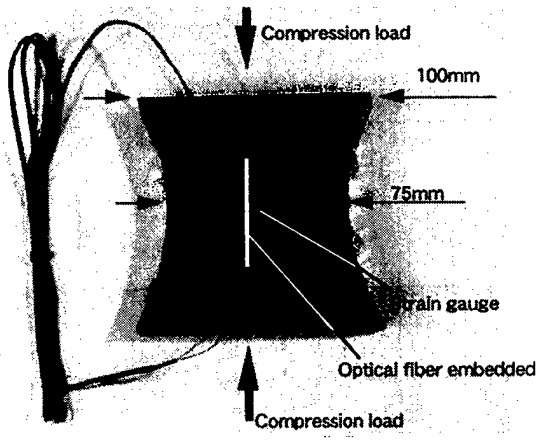


Fig. 5 Compression test of sandwich panel

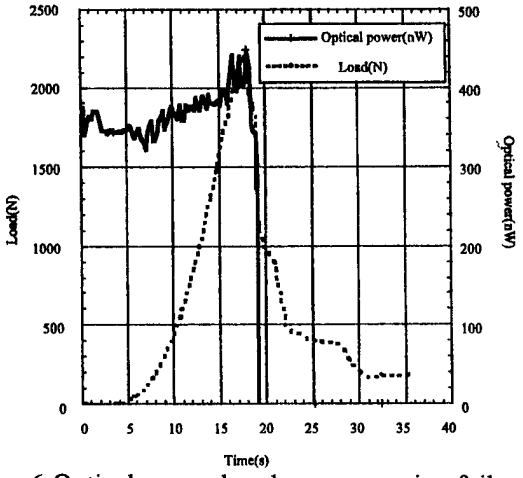


Fig. 6 Optical power loss by compression failure

Damage Suppression and Control in CFRP Laminates with Embedded SMA Films – Fuji Heavy Industries

Shape memory alloy (SMA) films are embedded and used to suppress and control microscopic damages in CFRP laminates such as transverse cracks and delamination [9]. Improvement of interlaminar shear strength (ILSS) between SMA films and CFRP laminas was made using spattering, sol-gel, ion-plating and anodic-oxidation. A high ILSS was

obtained similar to that of CFRP laminates alone. SMA films were stretched into the phase transformation region. Then, they were embedded in CFRP laminates with the deformation kept by the fixture jig during the fabrication in order to introduce the shrinking stress in 90-degree plies. Such shrinking stresses were found to suppress the evolution of transverse cracks in cross-ply laminates (Fig.7).

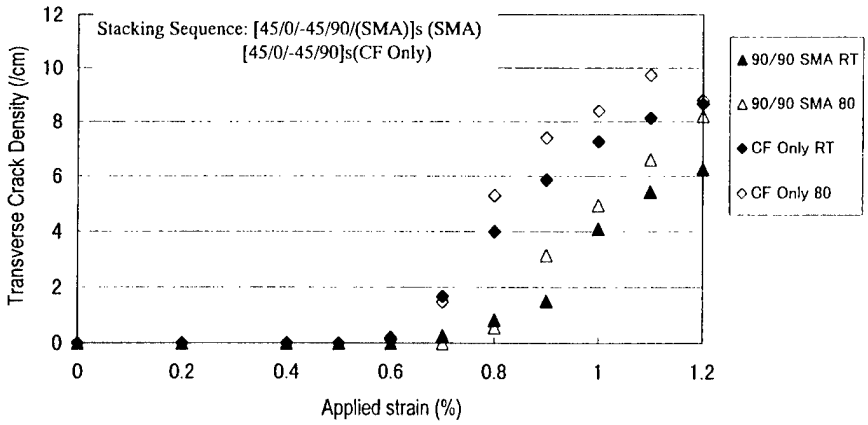


Fig. 7 Transverse crack density vs. strain for CFRP quasi-isotropic laminates with and without embedded 2% pre-strained SMA films

Quantitative Evaluation of Electric Properties of CFGFRP Hybrid Composites as a Maximum Strain Memory Sensors – Toray

Failure of low-elongation carbon fibers in CFGFRP hybrid composites under tensile loading causes the increase in electrical resistance and can be used to detect the maximum strain applied to composites after unloading. A systematic study was conducted to evaluate the relation between fiber failures and electrical resistance quantitatively [10].



Fig. 8 Fiber failure in CFGFRP

Figure 8 shows fiber failures observed in CFGFRP hybrid composites in tension. Based on such quantitative observations, a Monte Carlo simulation was successfully conducted to predict the change in electrical resistance due to tensile strain and fiber failures.

Self-Diagnosis Function of Electrically-Conductive FRP Containing Carbon Particles – JFCC

Carbon particles or flakes were dispersed into the epoxy matrix to introduce the high electrical conductivity in glass fiber unidirectional or textile composites [11].

Compared with CFGFRP hybrid composites, higher sensitivity could be obtained. Moreover, a linear resistance change due to tensile strain was achieved in a wider strain range, as shown in Fig. 9. The residual resistance after unloading increased with increasing applied maximum strain (Fig.10). This composite has an appropriate self-diagnosis function as a low-cost sensor to be embedded in concrete infrastructures.

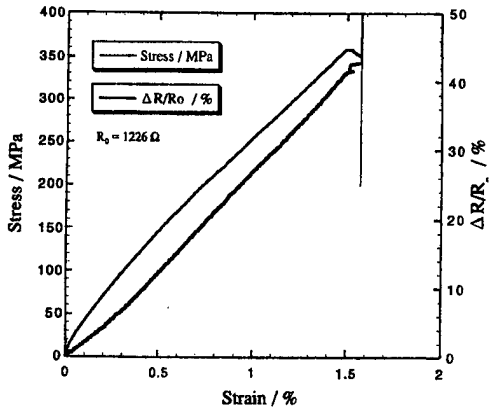


Fig. 9 Electrical resistance and stress vs. strain

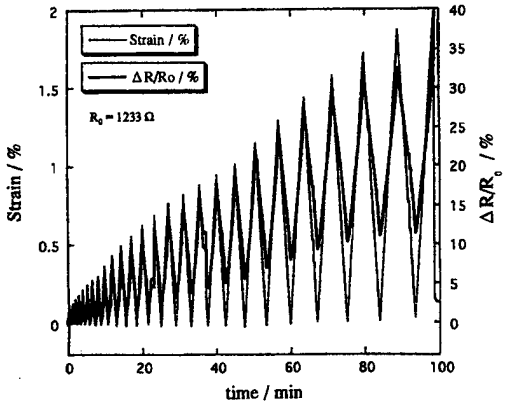


Fig. 10 Maximum and residual resistance

Due to lack of space, only titles are cited for four other research themes :

(1) **Impact Damage Monitoring of Composite Structures Using Integrated Acoustic Emission (AE) Sensor Network – Aerospatiale-Matra** : An integrated AE network system is being developed for practical industrial use in aircraft structures [12]. A Learning by Experience approach was developed to assess the AE behavior of a composite structure, combined with the use of a portable and reliable AE event generator.

(2) **Integrated Global and Local Strain Measurement Using Distributed BOTDR (Brillouin Optical Time Domain Reflectmetry) and FBG Sensors – Mitsubishi Heavy Industries** : Improvement of spatial resolution, temper-ature compensation and dynamic strain measurement are conducted. Integrated BOTDR and FBG strain measurement systems are being made for aerospace structures [13].

(3) **Damage Detection of Transparent Composites Using Light Transmission and Reflection Measurement for High-Speed (Magrev) Train – Hitachi** : Microscopic damages in semi-transparent alumina fiber reinforced epoxy composites are detected using light transmission and reflection technique under severe electro-magnetic and low-temperature conditions for load-supporting structures in Magrev trains [14].

(4) **Development of FBG Sensor Elements and Real-Time Monitoring Systems for Large-Scale Infrastructures – Shimizu** : A multiplex FBG sensor element network system is established for structural health monitoring of infrastructures. In particular, a real-time monitoring system is installed to record strains and deformations in hysterisis dampers for urban earthquake mitigation [15].

CONCLUSIONS

The latest results were summarized in the structural health monitoring project for smart composite structure systems in Japan. This research was conducted as a part of the "R&D for Smart Material/Structure System" Project within the Academic Institutions Centered Program supported by NEDO (New Energy and Industrial Technology Development Organization), Japan.

REFERENCES

1. N.Takeda and S.Ogihara, 1994. "In-situ Observation and Probabilistic Prediction of Microscopic Failure Process in CFRP Cross-ply Laminates", *Comp. Sci. Tech.*, 52(2): 183-196.
2. N.Takeda, S.Ogihara and A.Kobayashi, 1995. "Microscopic Fatigue Damage Progress in CFRP Cross-Ply Laminate Composites", Composites, 26(12): 859-868.
3. N.Takeda, H.Niizuma, S.Ogihara and A.Kobayashi, 1997. "Application of Micro-Line/ Grid Methods to Temperature-Dependent Microscopic Deformation and Damage in CFRP Laminates", *Exp. Mech.*, 37(2): 182-187.
4. N.Takeda and S.Ogihara, 1998. "Micromechanical Characterization of Local Deformation in Interlaminar-Toughened CFRP Laminates", *Composites: Part A*, 29A: 1545-1522.
5. Y.Okabe, S.Yashiro, T.Kosaka and N.Takeda, 2000. "Detection of Transverse Cracks in Composites by Using Embedded FBG Sensors", Proc. SPIE, Vol. 3893, in press.
6. K.Satori, Y.Ikeda, Y.Kurosawa, A.Hongo and N.Takeda, 2000. "Development of Small-Diameter Optical Fiber Sensors for Damage Detection in Composite Laminates", Proc. SPIE, Vol. 3893, in press.
7. H.Tsutsui, T.Sanda, Y.Okabe and N.Takeda, 2000. "Real-Time Detection of Impact Load on Composite Laminates with Embedded Small-Diameter Optical Fiber", Proc. SPIE, Vol. 3893, in press.
8. S.Kabashima, T.Ozaki and N.Takeda, 2000. "Damage Detection of Satellite Structures by Optical Fiber with Small Diameter", Proc. SPIE, Vol. 3893, in press.
9. T.Ogisu, M.Nomura, N.Andou, J.Takaki, D.-Y.Song and N.Takeda, 2000. "Development of Damage Suppression System Using Embedded SMA Foil Sensor and Actuator", Proc. SPIE, Vol. 3893, in press.
10. D.-Y.Song, N.Takeda, A.Kitano and K.Yoshioka, 2000. "Quantitative Evaluation of CFRP and CFGFRP Hybrid Composites as a Maximum Strain Memory Sensor", Proc. SPIE, Vol. 3893, in press.
11. Y.Okuhara, S.-G.Shin, H.Matsubara, H.Yanagida and N.Takeda, 2000. "Self-Diagnosis Function of FRP Containing Electrically Conductive Phase", Proc. SPIE, Vol. 3893, in press.
12. J.Saniger and L.Reithler, 1999. "Impact Assessment and Monitoring in Composite Struc-tures with Acoustic Emission Sensors: A Learning by Experience Approach", Proc. 1st Symp. Smart Mater., 119-122.
13. T.Yamaura, Y.Inoue, H.Kino and K.Nagai, 1999. "Development of Structural Health Monitoring System Using Brillouin Optical Time Domain Reflectmeter", Proc. 2nd Int. Workshop on Structural Health Monitoring,
14. H.Aoyama, K.Tanaka, H.Watanabe and N.Takeda, 1999. "Health Monitoring Technology for Alumina-Fiber-Reinforced Plastics", Proc. 6th Japan Int. SAMPE Symp.,
15. A.Mita, 1999. "Emerging Needs in Japan for Health Monitoring Technologies in Civil and Building Structures", Proc. 2nd Int. Workshop on Structural Health Monitoring, 56-67.

A WIRELESS TRANSMISSION SYSTEM FOR MONITORING CABLE TENSION OF CABLE-STAYED BRIDGES USING PVDF PIEZOELECTRIC FILMS

W. H. Liao, D. H. Wang

ABSTRACT

In this paper, polyvinylidene fluoride (PVDF) piezoelectric films are used as the sensors to acquire the dynamic responses of stayed-cables of a cable-stayed bridge, from which the tension of the stayed-cables can be determined. Signal retrieval from the PVDF film sensors via wireless transmission technology is developed, which could be used for the wireless *in-situ* monitoring of the cables tension. The principle, feasibility, and configuration of the wireless system for monitoring the stayed-cables tension of a cable-stayed bridge are investigated. Also the validating experiment is performed on a small-scale stayed-cable model in the laboratory. Results show that the proposed wireless monitoring system is suitable for *in-situ* monitoring of the stayed-cables tension.

INTRODUCTION

Compared to continuous bridges, cable-stayed bridges are supported by cables instead of piers in the internal supports. By monitoring the dynamic responses of the stayed-cables, the cables tension can be determined. Moreover, the overall operational condition of the bridge and whether the further maintenance and replacement of cables are needed can be determined [1]. Therefore, the *in-situ* tension monitoring of the stayed-cables is important and necessary.

In recent years, several researchers have studied the monitoring methods for stayed-cables of cable-stayed bridges [2-5]. However, wires are needed to transmit the sensors data to the data logger with the methods proposed in the above cited papers. The wires of the *in-situ* monitoring system are easy to be damaged during the construction and the service, so the wireless transmission of the monitored signal is desired. More recently, Pines and Lovell studied a remote wireless damage detection method for monitoring the health of large civil structures [6]. However, the wireless data transmission is confined to two computers. Therefore the sensing signals could not be wirelessly transmitted to the host computer for data acquisition and the main advantage of wireless monitoring is not exploited. Bennett et al. studied a wireless monitoring system for highways using strain gauge sensors [7]. In his system, the data is wirelessly transmitted via the TX2/RX2 modules to the data logger

Smart Materials and Structures Lab, Department of Automation and Computer-Aided Engineering, The Chinese University of Hong Kong, N. T., Hong Kong.

positioned by the side of the road. But the module TX2/RX2 only can work with one channel and the transmission performance on the lower frequency is poor [8].

In this paper, a novel wireless monitoring system for stayed-cables tension is proposed and developed. The principle, feasibility, and configuration of the wireless monitoring system for the stayed-cables are illustrated and the validating experimental results are presented.

THEORETICAL FUNDAMENTAL

For a stayed-cable with small sag and the inclination θ shown in Figure 1, when both ends are fixed, the stayed-cable tension can be determined by the following equation [4]

$$T = \frac{A\rho\pi^4 n^4 \left(\sigma^{(s)}\right)^3}{\pi^4 n^4 \left(\sigma^{(s)}\right)^3 + 2E\left\{\rho g L\cos\theta\left[1+(-1)^{(n+1)}\right]\right\}^2}\left(\frac{2Lf_{zn}}{n}\right)^2 \tag{1}$$

where $n=1, 2, 3, \ldots$; ρ is the mass per unit volume; A is the cross-sectional area; L is the length of the stayed-cable; f_{zn} is the resonance frequencies of mode n; E is the elasticity modulus of the stayed-cable; $\sigma^{(s)}$ is the static axial stress. Equation (1) is the formula for obtaining the stayed-cable tension, from which we can see that the key problem of the tension measurement is to precisely measure the mode frequencies of the stayed-cable.

For the stayed-cable shown in Figure 1, only the in-plane transverse vibration with finite motion is considered. Ignoring the quadratic term and using the separation-of-variables method, the non-linear strain-displacement relation can be expressed as

$$\varepsilon_w(x,t) = \frac{1}{2}\frac{\rho g\cos\theta(L-2x)}{\sigma^{(s)}}\sum_{n=1}^{\infty}\frac{\partial\psi_n(x)}{\partial x}z_n(t) \tag{2}$$

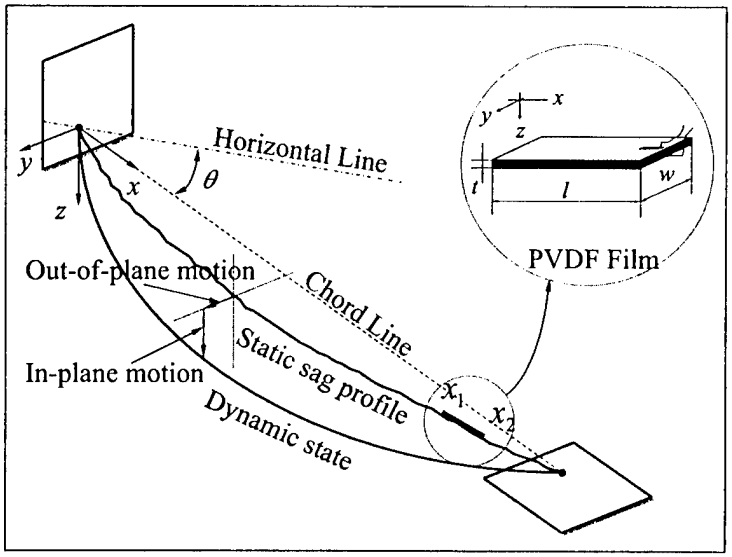


Figure 1. Analytical model of the stayed-cable with PVDF film sensor

where $\psi_n \approx \sin(n\pi x/L)$ are the mode shapes of in-plane vibration modes. Only the lower Nth modes are considered and let $[z(t)]=[z_1(t) \quad z_2(t) \quad \cdots \quad z_N(t)]^T$, Equation (2) can be written as

$$[z(t)]=[A]^{-}\frac{2\sigma^{(s)}\varepsilon_w(x,t)}{\rho g\cos\theta(L-2x)}+([I]-[A]^{-}[A])[Y_1] \tag{3}$$

where $[A]=\left[\frac{\pi}{L}\cos\frac{\pi x}{L} \quad \frac{2\pi}{L}\cos\frac{2\pi x}{L} \quad \cdots \quad \frac{N\pi}{L}\cos\frac{N\pi x}{L}\right]$; $[\ ]^{-}$ represents the pseudo-inverse of matrix; $[Y_1]$ is a constant vector ($[Y_1]\in C^N$); $[I]$ is an identity matrix with appropriate dimensions. Equation (3) represents the relationship between the modal displacement and the strain on arbitrary position along the cable axle. When a slice of finite length of PVDF film is glued on the surface of the steel cable between x_1 and x_2 in the x-y plane as shown in Figure 1, the strain of the PVDF film can be expressed as

$$\varepsilon(t)=\int_{x1}^{x2}\varepsilon_w(x,t)dx \tag{4}$$

where $|x_2-x_1|=l$. Substituting Equation (2) into Equation (4), then

$$\varepsilon(t)=\left[\int_{x1}^{x2}G_1\cos\frac{\pi x}{L}dx \quad \cdots \quad \int_{x1}^{x2}G_i\cos\frac{i\pi x}{L}dx \quad \cdots \quad \int_{x1}^{x2}G_N\cos\frac{N\pi x}{L}dx\right][z(t)] \tag{5}$$

where $G_i=i\pi\rho g\cos\theta/2\sigma^{(s)}\left[1-2\left(x/L\right)\right]$ and $i=1\sim N$. From Equation (5), we can obtain

$$[z(t)]=[B]^{-}\varepsilon(t)+([I]-[B]^{-}[B])[Y_2] \tag{6}$$

where $B=\left[\int_{x1}^{x2}G_1\cos\frac{\pi x}{L}dx \quad \cdots \quad \int_{x1}^{x2}G_i\cos\frac{i\pi x}{L}dx \quad \cdots \quad \int_{x1}^{x2}G_N\cos\frac{N\pi x}{L}dx\right]$; $[Y_2]$ represents a constant vector ($[Y_2]\in C^N$).

When considering that the slice of PVDF piezoelectric film (with dimensions $l\times w\times t$, as shown in Figure 1) is subject to an even pull force only in the x direction, the free charge accumulated on the surface is

$$Q(t)=Q(t_0)+E_P d_{31}\varepsilon(t)lw \tag{7}$$

where $\varepsilon(t)$ is the strain along x direction; E_P is the elasticity modulus of PVDF piezoelectric material; d_{31} is the piezoelectric constant. From Equation (7), we can infer that the charge output of the PVDF piezoelectric film is in direct proportion to the strain $\varepsilon(t)$, so as to form strain transducer. The charges that accumulate on the surface of PVDF film are easy being discharged even though the loop is locked. So a high input impedance amplifier is desired in

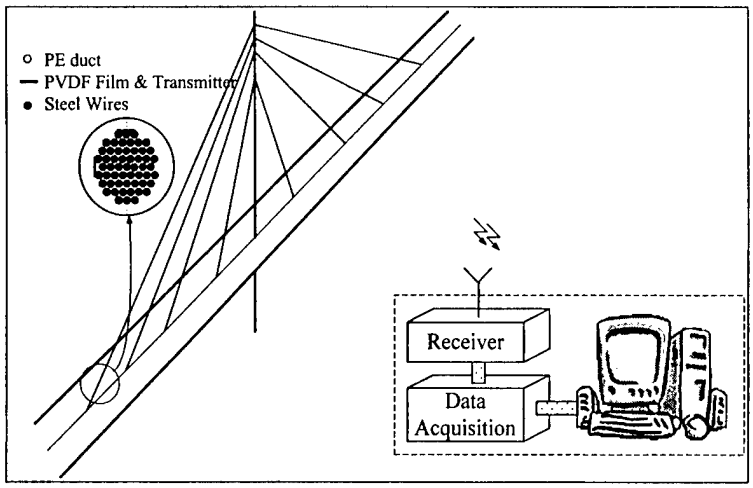


Figure 2. Overview of the wireless monitoring system for a cable-stayed bridge

order to assure the accuracy of measurement. The circuit of the charge amplifier adopted in this paper is shown in Figure 3. From Equations (2)~(3), the equation can be derived

$$[z(t)] = [B]^{-} \frac{K[Q(t) - Q(t_0)]}{E_P d_{31} lw} + ([I] - [B]^{-}[B])[Y_2] \tag{8}$$

where K is the gain of the charge amplifier. From Equation (8), we can infer that the mode coordinates can be obtained by measuring charges accumulated on the surface of PVDF piezoelectric films, which is the fundamental for in-situ monitoring the cables tension through PVDF piezoelectric films.

CONFIGURATION OF THE WIRELESS MONITORING SYSTEM

The overview of the wireless monitoring system used for cable-stayed bridge is illustrated in Figure 2. The strain variation of the stayed-cables induced by the cables vibration is monitored by using PVDF piezoelectric films through implanting the PVDF film sensors between the polyethylene (PE) duct and the steel wires of the cables. This signal is then wirelessly transmitted to the receiver at the monitoring center located at one end of the bridge or in the mobile measuring vehicle. At last, the data would be collected by the host computer and the tension of the cables can be calculated. The components of the frequency-based wireless system developed in this paper include the wireless transmitter subsystem, the wireless receiver subsystem, and the data acquisition subsystem.

The circuit diagram of the transmitter subsystem is shown in Figure 3. A high input impedance amplifier around LF353 is used to realize charge to voltage alternation and amplification of the PVDF sensor. A voltage to frequency (V/F) converter ADVFC32 is adopted to convert the PVDF output voltage into frequency signal. There are two advantages here: one is the ability of avoiding signal distortion because the transmitted signal is in the frequency response range of the transmitter; the other is the immunity from the noises. The

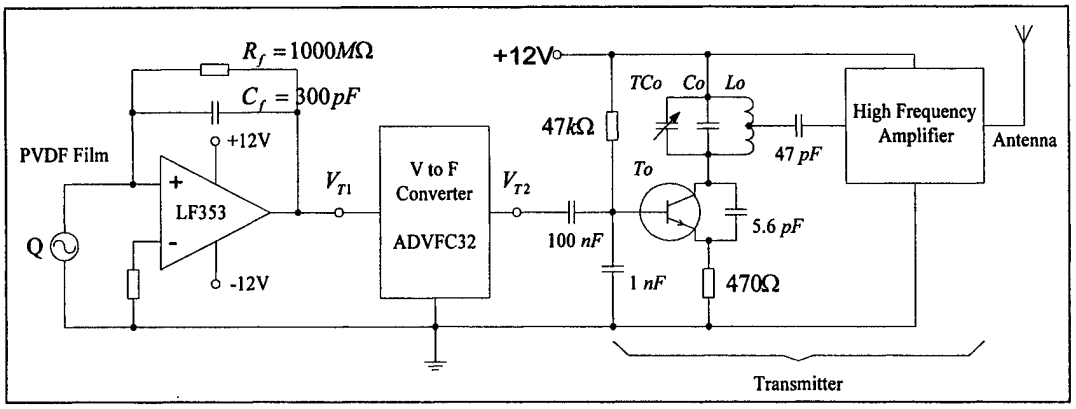


Figure 3. Circuit diagram of the transmitter subsystem

frequency output V_{T2} of the ADVFC32 is then fed to a transmitter. The transmitter circuit adopted here is basically a RF oscillator that operates around 100 *MHz*. The oscillator circuit, which is connected as a Hartley oscillator, consists of the tank circuit (made up of coil *Lo* and the trim capacitor *TCo* as shown in Figure 3), the transistor *To* and the feedback capacitor *Co*. In the case of the Hartley oscillator, the frequency of oscillation is given by [9]

$$f_o = \frac{1}{2\pi\sqrt{L_o(TC_o + C_o)}} \tag{9}$$

where *Co*=10 *pF*, *TCo*=5~20 *pF*, and *Lo*=84.5 *nH*. Through changing the trim capacitor *TCo*, the RF can be tuned to different resonant frequency. If each stayed-cable is attached with one transmitter, then different cables can be monitored simultaneously through tuning the transmitters to different resonant frequencies.

The second stage of the transmitter amplifies the output RF signal. Output power from this stage will be maximum when it is tuned to oscillate at the same frequency as the previous stage. This signal is fed to the aerial and radiated as radio waves. In the cable tension monitoring, the cable steel wire may be the most suitable antenna.

The block diagram of the receiver subsystem is shown in Figure 4. A commercially available receiver TECSUN PL757 is used to receive the RF signal, and the received signal is obtained through the earphone socket and fed to the signal processing circuit as shown in

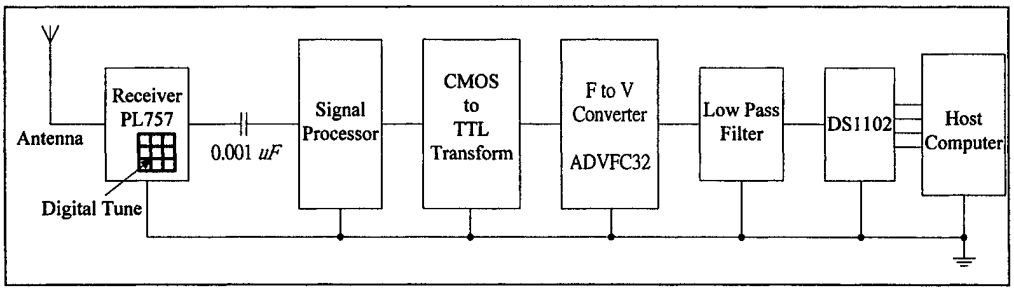


Figure 4. Block diagram of the receiver subsystem

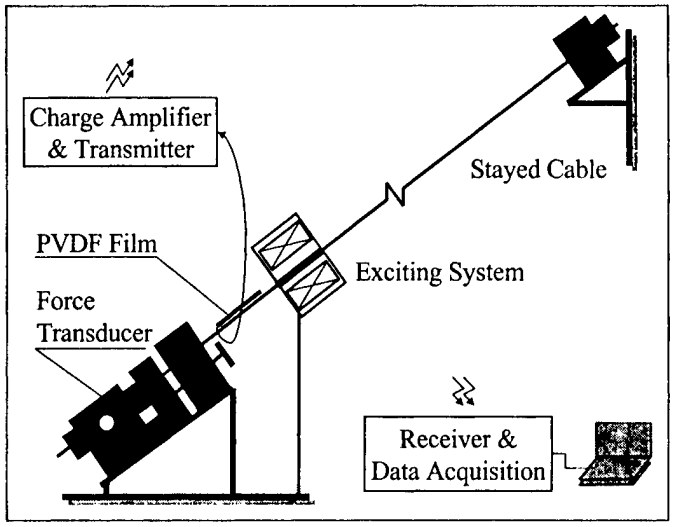


Figure 5. Schematic of experimental setup

Figure 4. The function of the signal processor is to realize the amplification of the output signal of PL757. The output signal of the signal processor is transformed into TTL level signal through the CMOS to TTL transform unit. The TTL level signal is the modulated vibration signal of the corresponding cable through V/F converter. In order to obtain the vibration signal of the cable, the demodulated technology need to be used to recover the vibration signal. Here, the F/V converter using the ADVFC32 chip is utilized to achieve V/F conversion. Since the reconstructed signal of ADVFC32 has a considerable amount of carrier feed through, it is desirable to filter any frequency in the carrier range of 50 *kHz* to 500 *kHz*. In this paper, a low pass filter with cutoff frequency 1 *kHz* is used.

The Floating-Point Controller Board (DS1102, dSPACE) is used as the A/D converter to collect data for the host computer positioned at the monitoring center as shown in Figure 4. The DS1102 board is built around Texas Instruments TMS320C31 floating-point Digital Signal Processor (DSP). In the experiment, only the AD subsystem of DS1102 board is used to collect the data from the receiver in time-sharing mode.

EXPERIMENTAL VALIDATION

In order to validate the performance of the wireless system for monitoring the stayed-cables tension, an experiment is carried out on a small-scale stayed-cable model. The parameters of the cable model are shown in Table I.

TABLE I. PROPERTIES OF CABLE MODEL

Parameters	Values
Length (L)	2.606 m
Inclination (θ)	25.23 °
Cross-sectional area (A)	5.024×10^{-5} mm^2
Modulus of elasticity (E)	196 GNm^{-2}
Static tension ($T^{(s)}$)	140 N
Mass/unit length (ρA)	0.264 kgm^{-1}

The schematic diagram of the wireless monitoring experimental setup, which is composed by the stayed-cable model, the upper and lower anchor joints, the non-contact exciting system, the signal acquiring and transmitting subsystem, the signal receiver subsystem and the force transducer, is shown in Figure 5.

To emulate the external disturbance, the non-contacting exciting system, which is based on the electromagnetic force produced by electromagnetic coils, is used to induce the in-plane vibration of the stayed-cable model. The PVDF piezoelectric film (Jinzhou Electronic Material) with the dimension of $l \times w \times t = 70mm \times 8mm \times 0.2mm$ is glued on the surface of the steel cable and positioned 10 *mm* above the lower anchoring joint, in the *x-y* plane, as shown in Figure 1. The force transducer (Type *BLR-1*, Chengdu Scientific Instrument) and strain meter (Type *6M72*, SAN-EI Instrument) are used to measure the cable tension directly.

The first four mode frequencies and amplitudes of the monitored signals transmitted to and received from the wire and wireless systems are shown in Table II, also the tension of the stayed-cable calculated from corresponding frequencies is shown. In Table II, T is the tension measured by the force transducer directly; f_{wn} and $f_{w\ln}$ are the frequencies measured with the wire and the wireless systems, where n is the mode number, $\Delta f_{wln} = f_{wln} - f_{wn}$; p_{wn} and p_{wln} are the power spectrum densities of mode n, $Mp_{wln} = p_{wln}/p_{wn}$; T_{wn} and T_{wln} are the tension of the cable determined from f_{wn} and f_{wln}, $\Delta T_{wn} = T_{wn} - T$, $\Delta T_{w\ln} = T_{wln} - T$, and $\Delta T_{wl/wn} = T_{wln} - T_{wn}$. It is clear that the frequencies of all vibration modes transmitted through the wireless system are not changed and the PSD amplitudes of all vibration modes are amplified with the same gain ($Mp_{w\ln} = 51.02$ as shown in Table II) for all modes as compared to the transmitted signals. The tension monitored by the wireless system and the wire system is identical, so the wireless system for monitoring the tension of the stayed-cable is feasible and valuable.

TABLE II. FREQUENCIES, AMPLITUDES, AND TENSION AND ITS RELATIVE ERROR THROUGH WIRE AND WIRELESS SYSTEMS FOR THE FIRST FOUR MODES.

Mode		1	2	3	4
T (*N*)			140.00		
Wire System	f_{wn} (*Hz*)	5.078125	8.984375	13.281250	17.578125
	p_{wn} ($\times 10^{-3}$ V^2)	3.2584186	2.7725375	3.7381710	0.8183200
	T_{wn} (*N*)	140.51	144.72	140.01	138.49
	$\Delta T_{wn}/T$ (%)	0.36	3.37	0.01	-1.08
Wireless System	f_{wln} (*Hz*)	5.078125	8.984375	13.281250	17.578125
	p_{wln} (V^2)	0.166245850	0.141455990	0.190723010	0.041750968
	T_{wln} (*N*)	140.51	144.72	140.01	138.49
	$\Delta T_{wln}/T$ (%)	0.36	3.37	0.01	-1.08
Δf_{wln} (*Hz*)		0	0	0	0
Mp_{wln}		51.02	51.02	51.02	51.02
$\Delta T_{wl/wn}/T$ (%)		0	0	0	0

CONCLUSIONS

In this paper, the wireless transmission method with frequency analysis for in-situ monitoring cables' tension using PVDF piezoelectric films as sensors is put forward and both its theoretical analyses and experimental results are presented. The wireless transmission system utilizing a RF transmitter built around transistors, a V/F and F/V converter, a commercially available radio receiver PL757 is developed and the cable tension monitoring experiment is performed and validated on a small scale stayed-cable model. Not only the multi-cables' tension can be wirelessly monitored simultaneously using the system presented in this paper, but also the far reach range to 1 *km* can be realized. The experimental results show that the wireless monitoring system proposed and developed in this paper is suitable for the *in-situ* monitoring the stayed-cable tension of a cable-stayed bridge wirelessly.

ACKNOWLEDGEMENTS

This research is partially supported by the CUHK Research Committee Funding # 2050232.

REFERENCES

1. Wang, W. T. 1997. *Replacement Project of Stayed-Cables for Cable-Stayed Bridges*, Civil Transportation Publishing House, Beijing, China.
2. Weischedel, H. R. and H. W. Hohle. 1995. "Quantitative Nondestructive in-service Evaluation of Stay Cables of Cable-Stayed Bridges: Methods and Practical Experience," *Proceedings of SPIE, Nondestructive Evaluation of Aging Bridges and Highways*, Vol. 2456, pp. 226-236.
3. Bronnimann, R., P. M. Nellen, and U. Sennhauser. 1998. "Application and Reliability of a Fiber Optical Surveillance System for a Stay Cable Bridge," *Smart Materials and Structures*, 7(2), pp. 14-19.
4. Wang, D. H., J. S. Liu, D. G. Zhou, and S. L. Huang. 1999. "Using PVDF Piezoelectric Film Sensors for in-situ Measuring the Stayed-Cables' Tension of Cable-Stayed Bridges," *Smart Materials and Structures,* 8(3), pp. 554-559.
5. Ko, J. M., Y. Q. Ni, and T. H. T. Chan. 1999. "Dynamic Monitoring of Structural Health in Cable-Supported Bridges," *Proceedings of SPIE, Smart Structures and Materials 1999: Smart Systems for Bridges, Structures, and Highways*, Vol. 3671, pp. 161-172.
6. Pines, D. J. and P. A. Lovell. 1998. "Conceptual Framework of a Remote Wireless Health Monitoring System for Large Civil Structures," *Smart Materials and Structures*, 7(3), pp. 627-636.
7. Bennett, R., B. Hayes-Gill, J. Crowe, R. Armitage, D. Rodgers, and H. Adrian. 1999. "Wireless Monitoring of Highways," *Proceedings of SPIE, Smart Structures and Materials 1999: Smart Systems for Bridges, Structures, and Highways*, Vol. 3671, pp. 173-182.
8. Wang, D. H., W. Sun, W. H. Liao, W. J. Li, and S. L. Huang. 2000. "Wireless *in-situ* Monitoring of Stayed-Cable Tension of Cable-Stayed Bridges Using PVDF Sensors," Proceedings of the International Forum cum Conference on Information Technology and Communication at the Dawn of the New Millennium, pp. 457-466.
9. Jaeger, R. C. 1997. *Microelectronic Circuit Design*, The McGraw-Hill Companies, Inc., pp 983-1041.

IMPEDANCE-BASED MONITORING OF STRESS IN THIN STRUCTURAL MEMBERS

Masato Abe, Gyuhae Park, Daniel J. Inman

ABSTRACT

This paper presents application of the impedance-based health monitoring technique on identification of stress in thin structural elements, such as strings, bars, or plates. The basic principle behind this technique is to utilize high frequency structural excitations through a surface-bonded piezoelectric sensor/actuator to detect stress in structural point impedance. Flexural wave propagation properties in thin structural members change with applied tensile stress, which can be measured by impedance measurement. Test results demonstrate the capability and the effectiveness of this technology to monitor the condition of stress in structural members.

INTRODUCTION

Development of an on-line structural health monitoring is the key to manage and maintain the large stock of aging civil infrastructure with minimum cost and human resources. The goal of this technique is to allow systems and structures to monitor their own integrity while in operation and throughout their lives, minimizing maintenance processes and inspection cycles. On-line health monitoring technology can also be applied to diagnose safety and performance of structures during/after the severe extreme events, accidents, or natural disasters such as earthquakes and hurricanes.

Extensive analysis and investigations have been focused on integrating smart material technology into health monitoring systems [1]. This is due to the fact that smart materials possess very important characteristics for fault detection and diagnostics. In particular, they can serve as sensors, as well as actuators for those systems that do not contain natural exciting forces. Furthermore, they come in variety of sizes and abilities, allowing them to be placed everywhere, even in remote and inaccessible locations to actively monitor the conditions of various types of structures.

Masato Abe, Department of Civil Engineering, The University of Tokyo, Tokyo 113-8656, Japan.
Gyuhae Park, Daniel J. Inman, Center for Intelligent Material Systems and Structures, Virginia Polytechnic Institute and State University, Blacksburg, VA 24061-0261, USA.

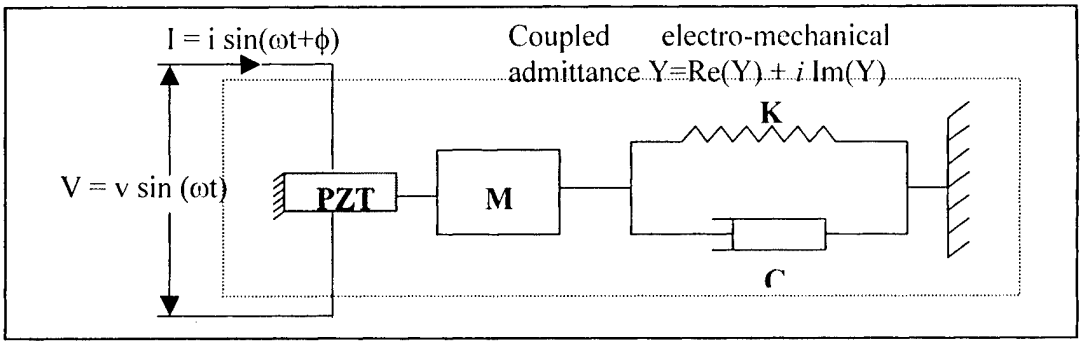


Figure 1. 1-D model used to represent a PZT-driven dynamic structural system

The impedance-based structural health monitoring techniques [2] have been extended to for the application of pre-stress monitoring in structural members in this paper. Pre-stressed structural members are commonly found in civil engineering practice, such as pre-stressed concrete/masonry/earth structures, stay-cables in cable supported bridges and roofs, steel girders in composite bridges, membrane roofs, tensegrity and inflatable structures, and so on. Pre-stress introduced into these members play essential role in resistance mechanism as is typically seen in the case of pre-stressed concrete. Hence, several works are found to develop handy impact-echo based method, by which first or second natural frequencies are measured to correlate with the stress in cables. However, low order natural frequencies are strongly influenced by the effect of boundary conditions, whose reliable identification is extremely difficult. In addition, monitoring of global modes generally gives global properties of the structure and lacks the resolution to identify the conditions local structural members, whereas evaluation of stress in local members such as pre-stressing bars or strings is required here.

In this paper, stress monitoring method is proposed which uses higher frequencies obtained by impedance based method and applying wave propagation analysis. In the frequency range of proposed method, local wave propagation effect, which is insensitive to boundary conditions, is dominant, and stress can be identified reliably. Formulations and experimental verifications are presented for one-dimensional bar-like structural members and two-dimensional plate-like members.

PRINCIPLE OF IMPEDANCE-BASED HEALTH MONITORING TECHNIQUE

Piezoceramic transducers (PZT) acting in the 'direct' manner produce an electrical charge when stressed mechanically. Conversely, a mechanical strain is produced when an electrical field is applied. The process to be used with the impedance-based monitoring method utilizes both the direct and converse versions of the piezoelectric effect to obtain an impedance signature for the structure. When a PZT wafer attached to a structure is driven by a fixed alternating electric field, a small deformation is produced in the PZT wafer and the attached structure. The induced mechanical vibration is transferred back to the PZT wafer in the form of an electrical response. When a damage or stress change causes the mechanical dynamic response to change, it is manifested in the electrical response of the PZT wafer.

The electromechanical modeling which quantitatively describes the process is presented in Figure 1. The surface-bonded PZT is considered to be a thin bar in axial vibration due to an applied alternating voltage. One end of the bar is considered fixed, whereas the other end is connected to the external structure. This assumption regarding the interaction at two discrete points is consistent with the mechanism of force transfer from the bonded PZT transducer to the structure. The solution of the wave equation for the PZT bar connected to the structure leads to the following equation for a frequency-dependent electrical admittance [3]:

$$Y(\omega) = i\omega a\left(\bar{\varepsilon}_{33}^{T}(1-i\delta) - \frac{Z_s(\omega)}{Z_s(\omega)+Z_a(\omega)} d_{3x}{}^2 \hat{Y}_{xx}^{E}\right) \tag{1}$$

In equation (1), Y is the electrical admittance (inverse of impedance), Z_a and Z_s are the PZT material's and the structure's mechanical impedances, respectively, Y_{xx}^{E} is the complex Young's modulus of the PZT with zero electric field, d_{3x} is the piezoelectric coupling constant in the arbitrary x direction at zero stress, ε_{33}^{T} is the dielectric constant at zero stress, δ is the dielectric loss tangent of the PZT, and a is a geometric constant of the PZT. This equation indicates that the electrical impedance of the PZT bonded onto the structure is directly related to the mechanical impedance of a host structure. Experimental implementation of the impedance-based structural health monitoring technique has been successfully conducted on several complex structures; a four bay space truss [2], an aircraft structure [4], a massive steel bridge joint [5], complex precision parts [6].

WAVE PROPAGATION IN THIN STRUCTURAL MEMBERS

The effect of stress to wave propagation in thin structural members are analytically studied here. Effect of applied stress on wave numbers and wave frequencies is derived analytically. Because wave frequencies are directly related to the electrical admittance by equation (1) as shown in [7], the equations derived here can be used to inversely solve the stress value from impedance measurement.

One-dimensional thin structural element

One-dimensional thin structural elements are commonly used as tensile bars/strings for pre-stressed concrete/masonry/earth structures, or structural strings and cables. These members are thin and flexible, and subject to relatively large tension force. By PZT attached on surface, surface tension/compression is applied and flexural wave is to be excited in the member. Equation of motion for wave propagation which includes these dominant effects is given by:

$$EI\frac{\partial^4 w}{\partial x^4} + \rho A\frac{\partial^2 w}{\partial t^2} - T\frac{\partial^2 w}{\partial x^2} = q, \tag{2}$$

where, E: Young's modulus of the structural member, I: second moment of inertia of the cross section, ρ: mass density, A: cross sectional area, T: tension force, w: flexural deflection, q: external distributed force. Note that tension force is appearing directly in the equation of motion. Assuming the wave traveling in the x direction, the solution to equation (2) is given by:

$$w = We^{i\omega t}e^{ikx}. \tag{3}$$

Substituting equation (3) to equation (1), one obtains wave number k in terms of T and ω:

$$k = \frac{\pm\sqrt{-T \pm \sqrt{T^2 + 4EI\rho A\omega^2}}}{\sqrt{2EI}}. \tag{4}$$

It can be seen from this equation that frequency of wave of the same wave number will change by the application of tension or compression.

For the wave of the same wave number, the original frequency without tension ω_0 will be changed to ω_1 by application of tensile force T as:

$$\omega_1 = \sqrt{\frac{\omega_0(T + \alpha\omega_0)}{\alpha}}, \tag{5}$$

where $\alpha = \sqrt{EI\rho A}$. The corresponding tension value is inversely obtained from equation (5) as,

$$T = \frac{\alpha(\omega_1^2 - \omega_0^2)}{\omega_0}, \tag{6}$$

If the tension value is changed to $T+\Delta T$, the new frequency ω_2 can be expressed in terms of ω_1 as,

$$\omega_2 = \frac{\sqrt{4\alpha^2\omega_1^2 + 2\Delta T\sqrt{T^2 + 4\alpha^2\omega_1^2} - 2\Delta TT}}{2\alpha}, \tag{7}$$

which inversely gives,

$$\Delta T = \frac{2\alpha^2(\omega_2^2 - \omega_1^2)}{-T + \sqrt{T^2 + 4\alpha^2\omega_1^2}} \tag{8}$$

By equations (6) and (8), variation of stress is directly related to the variation of wave frequency. Therefore, impedance-based method can be applied to stress detection through measurement of the variation of wave frequency for the wave of the same wave number.

Two-dimensional thin structural elements

Pre-stressed two-dimensional thin structural elements, such as plates, shells, and membranes are used to introduce pre-stress into steel girders in composite bridges, to control shape of membrane roof/inflatable structures, and so on. These structures have relatively low stiffness with high in-plane tension/compression force. For structures with relatively small curvatures, the equations of motion can be approximated by that of flat plate at the close vicinity of the PZT. The equation of motion with in-plane tension/compression force is given by:

$$D\left(\frac{\partial^4 w}{\partial x^4} + 2\frac{\partial^4 w}{\partial x^2\partial x^2} + \frac{\partial^4 w}{\partial y^4}\right) + \rho h\frac{\partial^2 w}{\partial t^2} - N_x\frac{\partial^2 w}{\partial x^2} - N_{xy}\frac{\partial^2 w}{\partial x\partial y} - N_y\frac{\partial^2 w}{\partial y^2} = q, \tag{9}$$

where, N_x, N_y, N_{xy}: force per unit area, i.e., $N_x=\sigma_x h$, $N_y=\sigma_y h$, and $N_{xy}=\sigma_{xy} h$, D: bending stiffness of the plate $= Eh^3/[12(1-\nu^2)]$, h: thickness of the plate, ρ: mass density, w: flexural deflection, q: distributed external force.

A two-dimensional wave solution for equation (9) is given by:

$$w = We^{i\omega t}e^{ik(x\cos\theta + y\sin\theta)}, \tag{10}$$

where θ is the direction of wave propagation. Then, the wave number k is derived as:

$$k = \frac{\pm\sqrt{-N \pm \sqrt{N^2 + 4D\rho h\omega^2}}}{\sqrt{2D}} \tag{11}$$

where

$$N = N_x \cos^2\theta + N_y \sin^2\theta + 2N_{xy}\cos\theta\sin\theta \tag{12}.$$

For the same wave number k and direction θ, the original frequency ω_0 will be changed to ω_1 by the introduction of pre-stress N.

$$\omega_1 = \sqrt{\frac{\omega_0(N + \beta\omega_0)}{\beta}}, \tag{13}$$

where $\beta = \sqrt{D\rho h}$. It can easily be observed that the same formulas derived for one-dimensional case, i.e., equations (5) to (8), can be applied to this case by just replacing T by N and α by β. From equation (12), the value of N is maximized for the wave traveling in the direction of maximum principle stress and minimized for the direction of minimum principle stress. Therefore, the maximum/minimum change in stress can be identified by measuring maximum/minimum change in ω.

EXPERIMENTAL VERIFICATION

The fundamental concept and theory developed in the previous section is applied to simple structural element examples in this section.

One-dimensional thin structural element

Figure 2 shows the experimental configuration for uni-directional tensile bar. Aluminum bar with cross section 0.787mm x 18.54mm and length 500mm is used for the host structure, and Lead Zirconate Titanate with cross section 0.267mm x 12mm x 18mm is used for the PZT. Figure 3 shows the difference of impedance signature with and without tensile loading. The difference is clearly observed in medium frequency range, while this difference appears to diminish for higher frequency range. This phenomenon is also expected from equations (5) or (7), where contribution of tension becomes relatively smaller as frequency ω increases. Therefore, appropriate frequency range of measurement is to be selected for each application based on equation (5) for one-dimensional case and (13) for two-dimensional case.

From the measurement result of Figure 3, the difference shift in frequency $\Delta\omega$ is identified as 140Hz. Using equation (6), the introduced stress is evaluated as 5.8MPa. On the other hand, by the measurement of strain gauge adjacent to the PZT, the stress value is measured to be 8.7MPa. This difference is likely to be due to the stress transfer at the interface of piezoelectric material and aluminum, and stress redistribution to the piezoelectric material. Assuming that the interface of piezoelectric material and aluminum is rigidly connected and cross sections of both materials are fully active, the stress value consistent to the strain gauge measurement is calculated as 7.2MPa.

From this experiment, impedance measurement is shown to have the capability to detect change in stress. However, further study on the interface stress transmission and modeling will be necessary to achieve accurate identification of stress.

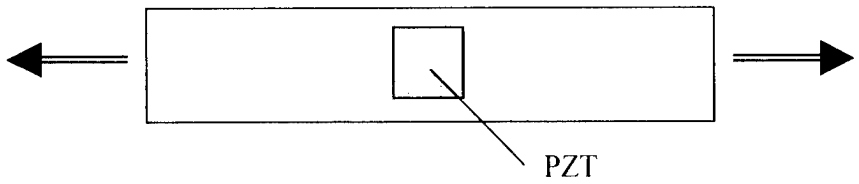
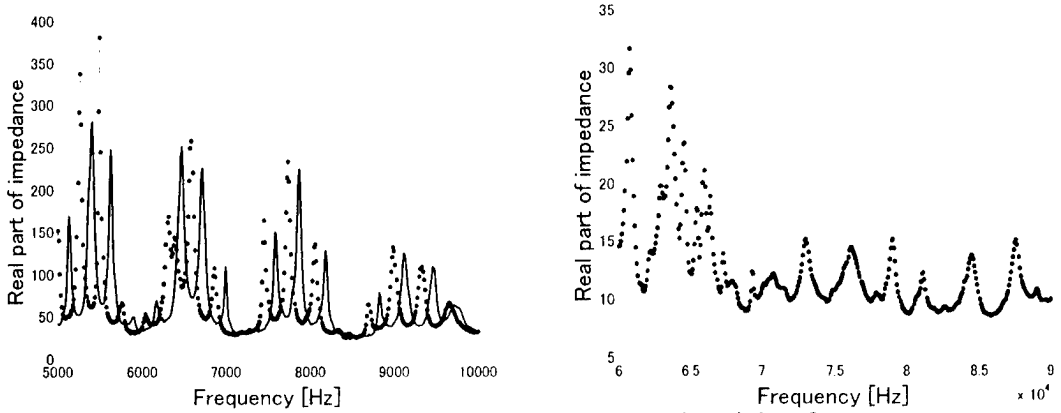


Figure 2. Experimental configuration for the bar



(a) Medium frequency range (b) Higher frequency range

Figure 3. Measured impedance for the bar with and without tension
Dotted line = without tension, solid line = with tension

Two-dimensional thin structural element

A plate specimen with PZT shown in Figure 4 is employed to demonstrate applicability of the proposed method to two-dimensional application. The same materials of the previous test are used for the experiment.

The dimension of the aluminum plate is 0.457mm x 300mm x 300mm and a PZT with dimension of 0.267mm x 20mm x 20mm is placed at the center of the host structure. The impedance measurement with and without loading is shown in Figure 5. From the measurement, maximum shift of frequency is observed to be 90Hz and minimum to be 0Hz, which gives 2.4MPa and 0MPa. Here, the identification of corresponding peaks of impedance with and without tension is made intuitively based on the apparent similarity in shapes of impedance. Strain gauge measurement provides two principle stresses as 8.4MPa and 0MPa. Again, identified value by impedance measurement is much lower as is similar to the previous case. Including the effect of PZT on stress distribution, consistent stress with strain gauge measurement is 5.4MPa, which is still higher than the impedance measurement. This difference is more pronounced than the one-dimensional case because the host plate is thinner in this case.

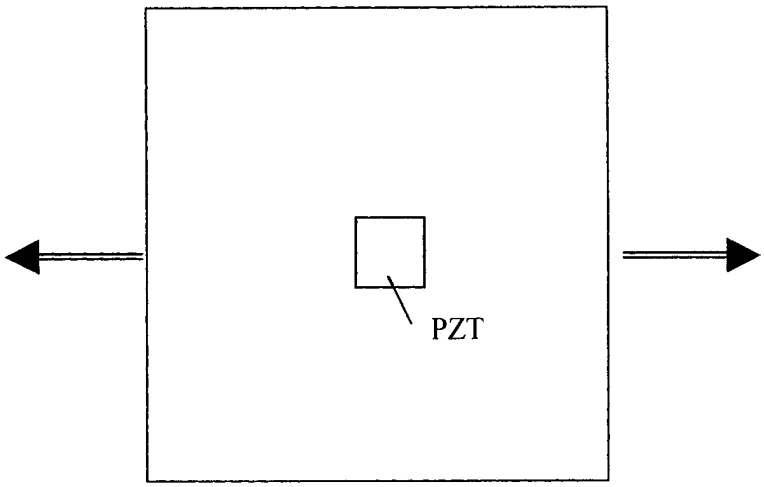


Figure 4. Experimental configuration for the plate

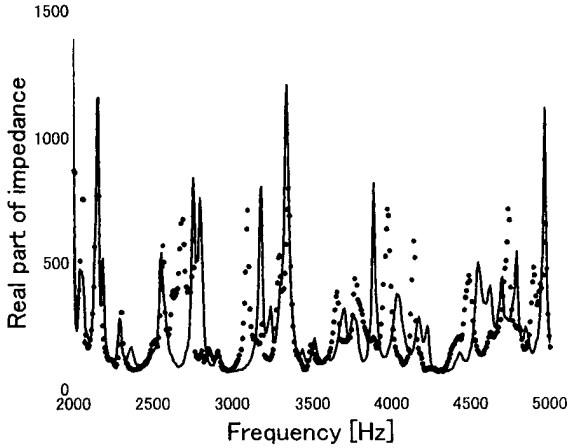


Figure 5. Measured impedance for the plate with and without tension
Dotted line = without tension, solid line = with tension

CONCLUSIONS

A health monitoring method based on impedance measurements has been modified and experimentally implemented for application to stress measurement in thin structural members.

Based on the equation of wave propagation of thin structural members, relationship among difference of stress, wave numbers and frequencies is established for both one-dimensional and two-dimensional structural members. The variation of stress can be identified by measuring

wave frequencies corresponding to the same wave number before and after the occurrence of variation, which can be obtained by impedance measurement.

Experimental study using simple structural elements, i.e., a bar as an example of one-dimensional structural member, and a plate as an example for two-dimensional one, shows that the proposed method can detect change in stress in these members. However, the measured value does not match with that of the strain gauge measurement. Further studies in modeling of interface stress transmission between the host structure and piezoelectric sheet will be necessary to establish accurate measurement technique. Also, identification of corresponding peaks in impedance measurement needs to be improved by possibly including neural networks or other method in the data processing.

In this study, one piezoelectric patch is used for each measurement. By using multiple, spatially distributed embedded piezoelectric materials, simultaneous measurement of wave number k and direction of propagation θ will be made possible, which improves the accuracy and provides more detailed information on the state of structures.

ACKNOWLEDGEMENTS

This work is supported by the National Science Foundation, grant No. CMS-9701471, through the Multidisciplinary Center for Earthquake Engineering Research (MCEER). The research work is conducted during the first author's stay at the Center for Intelligent Material Systems and Structures (CIMSS) of Virginia Polytechnic Institute and State University, which is supported by the Ministry of Education of Japan and Visiting Scholar Program of CIMSS. The authors gratefully acknowledge this support.

REFERENCES

1. Inman,D.J. (1998). "Smart Structures Solutions to Vibration Problems." *Proceedings, International Conference on Noise and Vibation Engineering*, Leuven, Belgium, 1-12.
2. Sun, F., Chaudhry, Z., Liang, C., and Rogers, C.A. (1995). "Truss Structure Integrity Identification Using PZT Sensor-Actuator," *Journal of Intelligent Material Systems and Structure*, V.6, 134-139.
3. Liang, C., Sun, F., and Rogers, C.A. (1994) "Coupled Electromechanical Analysis of Adaptive Material System -- Determination of Actuator Power Consumption and System Energy Transfer," *Journal of Intelligent Material Systems and Structures*. V.5, 21-20.
4. Chaudhry, Z., Joseph, T., Sun F., and Rogers, C.A. (1995). "Local-Area Health Monitoring of Aircraft via Piezoelectric Actuator/Sensor Patches," *Proceedings, SPIE 1995 North American Conference on Smart Structures and Materials*, San Diego, CA, Vol. 2443, 266-276.
5. Ayres, J., Lalande, F., Chaudhry, Z., and Rogers, C.A. (1996). "Qualitative Health Monitoring of a Steel Bridge Structure via Piezoelectric Actuator/Sensor Patches," *Proceedings, SPIE Nondestructive Evaluation Techniques for Aging Infrastructure & Manufacturing*, Scottsdale, AZ, Vol. 2946, 211-218.
6. Lalande, F., Childs, B., Chaudhry, Z., and Rogers, C.A. (1996) "High-Frequency Impedance Analysis for NDE of Complex Precision Parts," *Proceedings, SPIE Conference on Smart Structures and Materials*, San Diego, CA, SPIE Publishing, Vol. 2717, 237-245
7. Park, G., Cudney, H., and Inman, D.J. (1999) "Developing a model based health monitoring technique using structural impedance sensors", *Proceedings, 2nd International Conference on Identification in Engineering Systems*, Swansea, UK, 506-515.

SIMULTANEOUS MEASUREMENT OF STRAIN AND TEMPERATURE OF STRUCTURES USING FIBER OPTIC SENSOR

Hyun-Kyu Kang,[1] Chi-Young Ryu,[1] Chang-Sun Hong,[1] Chun-Gon Kim[1]

ABSTRACT

This paper presents the simultaneous measurement of strain and temperature using fiber Bragg grating/extrinsic Fabry-Perot interferometric(FBG/EFPI) sensor. This hybrid sensor consists of a fiber Bragg grating element encapsulated in EFPI sensor. Temperature can be measured from FBG part and strain from EFPI. We have analytically derived the relationship of the sensor outputs to measurands(strain and temperature) and yielded the characteristic matrix of sensor. Therefore, it is not necessary to perform sensor calibration for each sensor. By the derived relationship, we could measure directly and simultaneously the strain and temperature using a single sensing element. The fiber optic sensor was surface-mounted on an aluminum alloy beam together with an electrical resistance strain gage and a thermocouple. The wavelength-swept fiber laser (WSFL) was used as a light source to supply high signal power. The simultaneous measurement of thermal strain and temperature was performed in a thermal chamber. Experimental results of fiber optic sensor show good agreements with those of conventional gages such as strain gage and thermocouple.

INTRODUCTION

The measurement for strain and temperature is quite attractive to structural monitoring with sensors. Fiber optic sensor (FOS) offers various advantages over conventional gages. Several techniques have been reported for the simultaneous measurement of strain and temperature using FOSs in recent years. For the simultaneous measurement of strain and temperature, we need two sensing elements that can supply two equations with respect to two parameters. Many of the approaches have concentrated on using various type sensors[1-5]. In most approaches, sensor calibrations were performed to obtain the characteristics matrixes, which represent the relationship of the sensor outputs to measurands. These are time-consuming and may lead to the lack of accurate measurements.

In this paper, we present a useful method that can be used to simultaneously measure the strain and the temperature without sensor calibrations. The relationship of the sensor outputs

[1] Division of Aerospace Engineering, Korea Advanced Institute of Science and Technology, 373-1, Kusong-dong, Yusong-gu, Taejon, 305-338, Korea

to the strain and the temperature change is analytically derived for the fiber Bragg grating/extrinsic Fabry-Perot interferometric (FBG/EFPI) hybrid sensor. We have conducted the experiment of simultaneous measurement of the thermal strain and the temperature. The thermal strain and the temperature of specimen were measured directly using the characteristic matrix of the sensor derived through the analytic formulation. Also, we compared the results of FOS with those of the electrical strain gage and the thermocouple.

ANALYTIC RELATIONSHIP

In general, the relationship of the sensor outputs ϕ_1 and ϕ_2 to any combination of strain ε and temperature change ΔT can be given by

$$\begin{Bmatrix} \phi_1 \\ \phi_2 \end{Bmatrix} = \begin{bmatrix} K_{1\varepsilon} & K_{1T} \\ K_{2\varepsilon} & K_{2T} \end{bmatrix} \begin{Bmatrix} \varepsilon \\ \Delta T \end{Bmatrix} = \mathbf{K} \begin{Bmatrix} \varepsilon \\ \Delta T \end{Bmatrix} \tag{1}$$

where the coefficients of the matrix **K** are the strain and temperature sensitivities of the sensors. In order to obtain these coefficients of the characteristics matrix of the sensor, in almost researches calibration experiments have been performed before the application of sensors. This equation is then inverted to yield the strain and the temperature from ϕ_1 and ϕ_2 as following

$$\begin{Bmatrix} \varepsilon \\ \Delta T \end{Bmatrix} = \begin{bmatrix} P_{1\varepsilon} & P_{2\varepsilon} \\ P_{1T} & P_{2T} \end{bmatrix} \begin{Bmatrix} \phi_1 \\ \phi_2 \end{Bmatrix} = \mathbf{P} \begin{Bmatrix} \phi_1 \\ \phi_2 \end{Bmatrix} \tag{2}$$

where the matrix **P** is the inverse matrix of **K** in (1). However, if specifications of sensors such as gage length vary, calibration experiments must be performed again to obtain coefficients of matrix **K** for each sensor that has different specifications. The great limitation of method requiring matrix inversion is that the inversion is often poorly conditioned because of a small determinant and consequently gives large errors and low accuracy sometimes.

Figure 1 is a schematic diagram of the FBG/EFPI sensor. FBG was encapsulated in a silica capillary tube to be isolated from the external strain. The EFPI cavity was formed between two cleaved fiber ends inserted into the capillary tube. The FBG is in strain-free condition and is only affected by the temperature change within the capillary tube, while the

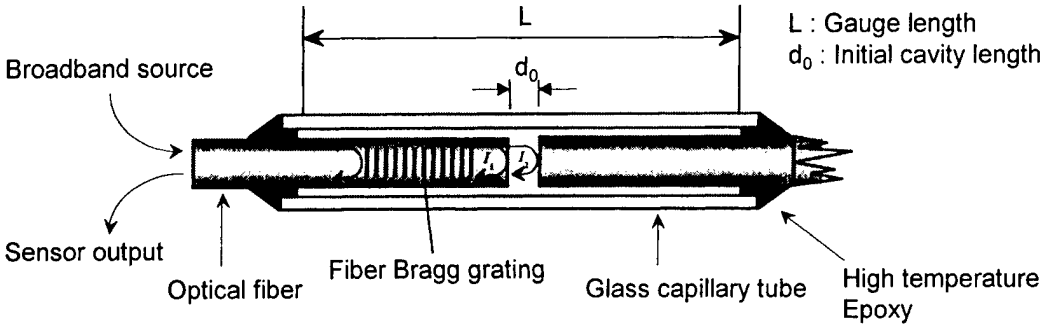


Figure 1. Configuration of FBG/EFPI sensor.

interferometric signal of EFPI is affected by both thermal and mechanical strains. When a broadband light illuminated with this sensing element, reflected spectrum of the Bragg grating element had a narrow bandwidth with high reflectivity whereas the sinusoidal wave with a fraction of the total optical power was reflected through the EFPI sensor, a low finesse interferometer.

For an FBG, Bragg condition is given by $\lambda_B=2n_e\Lambda$, where λ_B is the Bragg wavelength of FBG, n_e is the effective index of the fiber core, and Λ is the grating period. The shift of Bragg wavelength due to the strain and temperature can be expressed as

$$\Delta\lambda_B = \lambda_B\left[\left(\alpha_f + \xi_f\right)\Delta T + \left(1 - p_e\right)\varepsilon\right]. \tag{3}$$

where α_f is the coefficient of thermal expansion (CTE), ξ_f is the thermo-optic coefficient, and p_e is the strain-optic tensor of optical fiber, respectively. For the FBG/EFPI sensor, because the FBG in a glass capillary tube is in strain-free condition, $\varepsilon = 0$, (3) can be simplified in terms of only the temperature change as

$$\Delta\lambda_B = \lambda_b\left(\alpha_f + \xi_f\right)\Delta T\,. \tag{4}$$

Therefore, the temperature change can be expressed as

$$\Delta T = \frac{1}{\alpha_f + \xi_f}\cdot\frac{\Delta\lambda_B}{\lambda_B}. \tag{5}$$

The response of absolute EFPI(AEFPI) sensor comes from thermal strain as well as applied strain of a structure. When perfectly bonded to structure, the thermal deformation of FOS bonded to or embedded in a material exhibits that of the structure itself. The cavity length, d_i, at any measuring instant can be measured from peaks of reflected spectrum as

$$d_i = \frac{m\lambda_1\lambda_2}{2(\lambda_2 - \lambda_1)} \qquad i = 0, 1, 2... \tag{6}$$

where λ_1 and λ_2 are two wavelengths that are $2m\pi$ out of phase and m is an integer. The i is the number of measuring instant, and in case of initial state, $i=0$. If the EFPI sensor has a gage length of L, the applied strain can be expressed as

$$\varepsilon = \frac{d_n - d_0}{L} = \frac{\Delta d}{L}. \tag{7}$$

where Δd is the change of cavity length, and d_n, d_0 are the final and initial cavity lengths.

When the temperature change and strain are applied to structures with embedded or attached an FBG/EFPI sensor, the lengths of internal optical fibers in capillary tube are changed with their CTE only by temperature change while external capillary tube subjects to both thermal and mechanical strains of structures. Therefore, the strain measured from the

EFPI interferometric signal can be described by

$$\varepsilon_{EFPI} = \varepsilon_{tot} - \varepsilon_{f,T} = \frac{\Delta d}{L} \tag{8}$$

where ε_{tot} is the sum of mechanical and thermal strain, $\varepsilon_{f,T}$ is the thermal strain of internal optical fibers, respectively. We want to obain the total strain of structure, that is, the strain of the capillary tube. From (8) we can get the equation for total strain as

$$\varepsilon_{tot} = \frac{\Delta d}{L} + \varepsilon_{f,T} = \frac{\Delta d}{L} + \frac{L - d_0}{L} \cdot \alpha_f \cdot \Delta T . \tag{9}$$

Substituting (5) into (9) leads to

$$\varepsilon_{tot} = \frac{\Delta d}{L} + \frac{L - d_0}{L} \cdot \frac{\alpha_f}{\alpha_f + \xi_f} \cdot \frac{\Delta \lambda_B}{\lambda_B} . \tag{10}$$

By combining (5) and (10), we can yield the relationships of the sensor outputs to measurands as

$$\begin{Bmatrix} \varepsilon \\ \Delta T \end{Bmatrix} = \begin{bmatrix} \frac{1}{L} & \frac{L - d_0}{L} \cdot \frac{\alpha_f}{\alpha_f + \xi_f} \cdot \frac{1}{\lambda_B} \\ 0 & \frac{1}{\alpha_f + \xi_f} \cdot \frac{1}{\lambda_B} \end{bmatrix} \begin{Bmatrix} \Delta d \\ \Delta \lambda_B \end{Bmatrix} . \tag{11}$$

From (11), it is readily apparent that the characteristic matrix of a sensor is changed according to sensor specifications such as gage length, Bragg wavelength, the CTE and thermal-optic coefficient of optical fibers. In the conventional method, all sensors with different specifications must be calibrated to obtain the characteristic matrix before the field use. However, we can generate simply the matrix with known parameters of sensors using (11) and measure directly and simultaneously the strain and the temperature of structures.

EXPERIMENTS AND DISCUSSION

A 10 *mm* long FBG was encapsulated in a silica capillary tube(140/300 μm) to be isolated from the external strain. The EFPI cavity was formed between the fiber end face of the FBG element and gold-coated fiber end surface in the capillary tube. The optical fiber of the FOS has the CTE of 0.5 *ppm/℃* and the thermo-optic coefficient of *6.2 ppm/℃*. The FOS had the gage length of 27.15 *mm*, the initial cavity length of 541 μm, and the Bragg wavelength of 1536.96 *nm* as shown in TABLE I.

TABLE I. SPECIFICATIONS OF FBG/EFPI SENSOR

Spec.	Symbol	Value
Gage length	L	27.15 *mm*
Coefficient of thermal expansion	α_f	0.5 *ppm/℃*
Thermo-optic coefficient	ξ_{sf}	6.2 *ppm/℃*
Bragg wavelength	λ_B	1536.96 *nm*
Initial cavity length	D_0	541 *μm*

The thin deposition of metal such as gold or aluminum on the end of the fiber enclosing the cavity increases the interface reflectivity and enhances the finesse of the cavity and sensitivity of the sensor. The finesse, F, is the parameter used to characterize Fabry-Perot cavities[6]. In this work, we deposited the gold on the second reflecting fiber end to increase the finesse of the sensor. The Fig. 2 shows reflected spectrums of the sensor without gold deposition and the sensor with gold deposition on the reflecting fiber end, respectively. As can be seen from the Fig. 2, the gold deposition increases the finesse of EFPI sensor and the intensity of the signal.

A wavelength-swept fiber laser (WSFL)[7] was used to interrogate the sensor as Figure 3. The WSFL was in a unidirectional ring configuration with isolators, a 3-*dB* output coupler, and an Er^{3+}-doped fiber pumped by a laser diode at 980 *nm*. An Fabry-Perot (F-P) tunable filter was used as the intracavity scanning filter and had a 3-dB bandwidth of 0.27 *nm* and a free spectral range of 58 *nm*. We modulate the F-P filter with a triangular waveform to produce a wavelength sweep over 40 *nm* from 1525 to 1565 *nm* at 200 *Hz* repetition rate. The output power of the WSFL was over 1000 times as large as that of amplified spontaneous emission (ASE) of an LD-pumped Er^{3+}-doped fiber (EDF)[8].

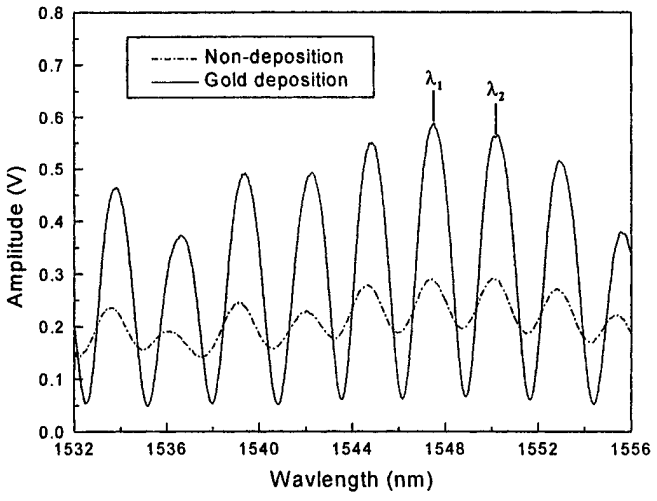


Figure 2. Comparison of reflected spectrum of sensors with gold deposition.

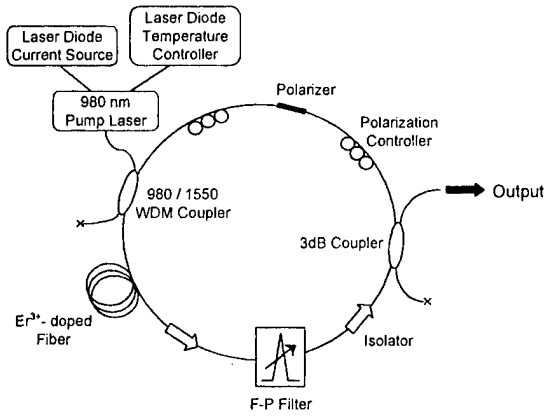


Figure 3. Configuration of wavelength-swept fiber laser (WSFL) system.

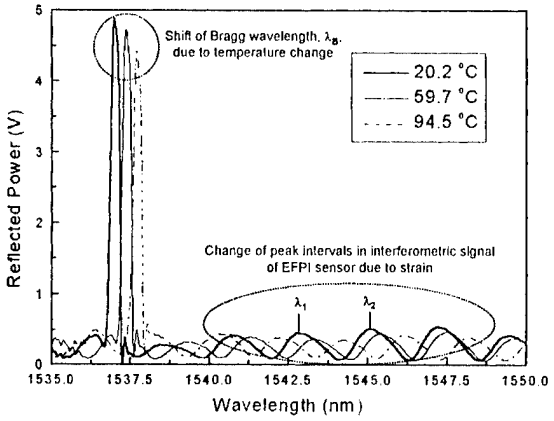


Figure 4. Reflected spectrum of the FBG and EFPI sensors along the temperature elevation

A FOS, a strain gage, and a thermocouple were attached on the both side of a alluminum alloy beam. The strain gage and K-type thermocouple were used to serve as a reference source for the strain and the temperature. The beam was clamped and placed in a thermal chamber. The reflected signals of the FOS were acquired through DAQ board, and processed and saved by a signal processing program. The response of the FOS attached on the cantilever beam was tested in a thermal chamber with the temperature range from 20 to 100 ℃.

Substituting specifications of the sensor in TABLE I into (11), we can obtain the relatitionship of sensor output to measurands as following :

$$\begin{Bmatrix} \varepsilon \\ \Delta T \end{Bmatrix} = \begin{bmatrix} 36.82 & (\mu\varepsilon/\mu m) & 47.40 & (\mu\varepsilon/nm) \\ 0 & (^{o}C/\mu m) & 97.17 & (^{o}C/nm) \end{bmatrix} \begin{Bmatrix} \Delta d & (\mu m) \\ \Delta\lambda_B & (nm) \end{Bmatrix} \tag{12}$$

Figure 4 shows the reflected spectrum of the FBG/EFPI sensor attached on the cantilever beam subject to thermal loading in a thermal chamber. From this specturm, we can measure the temperature change by detecting the wavelength shift of the FBG, $\Delta\lambda_B$, and measure the strain by determining the change of cavity length from the interferometric signal of the EFPI, Δd.

The comparison of strain from the FOS with electirical strain gage (ESG) was represented in Figure 5 and the comparison of temperature from the FOS with thermocouple was plotted in Figure 6. As can be seen from the Figure 5 and 6, it is apparent that simultaneous measurement of the strain and temperature change with the FBG/EFPI sensor can be sucessively performed by using the analytic formulation without the sensor calibrations. The correlation between strains measured by FOS and strain gage was 99.8 % and the temperature measurement had a correlation of 99.9 %. We could find a little deviation in experimental results that the standard deviations of the strain and the temperature measurement were about 35.9 $\mu\varepsilon$ and 1.1 ℃, respectively.

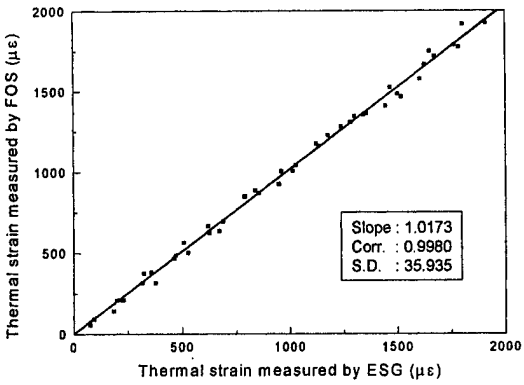


Figure 5. Thermal strains measured by FOS and ESG.

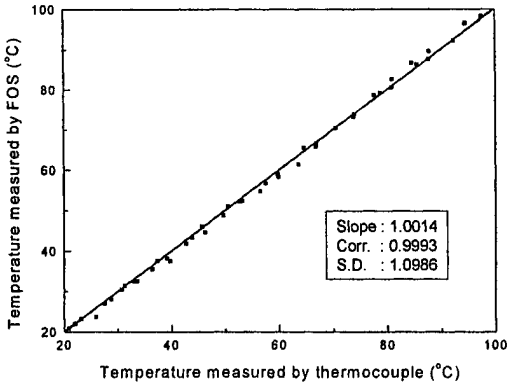


Figure 6. Temperatures measured by FOS and thermocouple.

Since a number of calibration experiments and the statistical process of calibration data must be necessary to obtain the coefficients of a characteristic matrix, sensor calibration experiments are time consuming and non-economical work. Hence the method using the analytic formulation is more efficient for the real use of fiber optic sensors.

CONCLUSIONS

For the simultaneous measurement of the strain and temperature using the FBG/EFPI sensor, we have derived analytically the relationship of the sensor outputs to measurands and yielded the characteristics matrix of sensor without sensor calibrations. Using this relationship, the simultaneous measurement of the thermal strain and temperature change of an aluminum alloy beam was performed in a thermal chamber. The strain and temperature measured by the FOS were compared with those measured by strain gage and thermocouple, respectively. Good correlations were obtained between FOS and conventional gages such as strain gage and thermocouple. From experimental results, this proposed method showed to be simple and useful for the simultaneous measurement of two parameters using fiber optic sensors.

ACKNOWLEDGEMENTS

The authors would like to thank the Ministry of Science and Technology, Korea, for the financial support by a grant from the Critical Technology 21 project.

REFERENCES

1. Xu, M. G., J.-L. Archambault, L. Reekie and J. P. Dakin. 1994. "Discrimination between strain and temperature effects using dual-wavelength fibre grating sensors", *Electronics Letters*, Vol.30, No.13, pp.1085-1087.
2. Patrick, H. J., G. M. Williams, A. D. Kersey, J. R. Pedrazzani, and A. M. Vengsarkar. 1996. "Hybrid fiber

Bragg grating / long period fiber grating sensor for strain / temperature discrimination," *IEEE Photonics Technology Letters*, Vol. 8, No. 9, pp. 1223-1225.

3. Bhatia, V., D. Campbell, R. O. Claus, and A. M. Vengsarkar. 1997. "Simultaneous strain and temperature measurement with long-period gratings", *Optics Letters*, Vol.22, No. 9, pp.648-650.
4. Liu, T., G. F. Fernando, L. Zhang, I. Bennion, Y. J. Rao and D. A. Jackson. 1997. "Simultaneous strain and temperature measurement using a combined fibre Bragg grating/extrinsic Fabry-Perot sensor," in *12th International Conference on Optical Fiber Sensors: (OFS-12)*, G. W. Day and A. D. Kersey, Editors, Proc. SPIE 3746, VA, USA, pp.40-43.
5. Jin, X. D. and J. S. Sirkis, J. K. Chung, and V. S. Venkat. 1998. "Embedded in-line fiber etalon/Bragg grating hybrid sensor to measure strain and temperature in a composite beam," *J. of Intelligent Material Systems and Structures*, Vol. 9, No. 3, pp.171-181.
6. Tran, T. A., J. A. Greene, and K. A. Murphy, V. Bhatia, M. B. Sen, and R. O. Claus. 1995. "EFPI manufacturing improvements for enhanced performance and reliability," *in Smart Structures and Materials 1995: Industrial and Commercial Applications of Smart Structures Technologies*, C. Robert Crowe, Editor, Proc. SPIE 2447, San Diego, California, pp.312-323.
7. Yun, S. H., D. J. Richardson and B. Y. Kim. 1998. "Interrogation of fiber grating sensor arrays with a wavelength-swept fiber laser," *Optics Letters*, Vol. 23, No. 11, pp.843-845
8. Hong, C. S., C. Y. Ryu, B. Y. Koo, C. G. Kim, S. H. Yun. 2000. "Strain monitoring of smart bridge using fiber Bragg grating sensor system with wavelength-swept fiber laser," in *Smart Structures and Materials 2000: Smart Systems for Bridges, Structures, and Highways*, S. C. Liu, Editor, Proc. SPIE Vol. 3988, pp.371-379.

IMPACT DAMAGE MONITORING OF COMPOSITE PANELS BY EMBEDDED SMALL-DIAMETER OPTICAL FIBERS

Hiroaki Tsutsui, Akio Kawamata, Tomio Sanda, Nobuo Takeda

ABSTRACT

It is well known that barely visible damage is often induced in composite structures subjected to out-of plane impact, and the mechanical properties of the composites decrease markedly. So far, for the significance of the damage monitoring, the impact tests of the CFRP laminate plates with embedded optical fibers with 125 μm in cladding diameter were conducted. And it was found possible to detect impact load and impact damage in real-time by measuring optical intensity responses and strain responses. The goal of this study is that small-diameter optical fiber sensors, which will have no serious effect on mechanical properties of the composites, are applied in composite panels, and the possibility of the detection of impact damage in the composites by the sensors are demonstrated.

First of all, the impact tests and the compressive strength tests after impact were conducted in order to investigate the impact characteristics of the composite. Next, as a sensor for detecting the impact load and the impact damage in the composite panels, the optical fibers with 40 μm in cladding diameter were used. And the impact test of the composite panels with embedded optical fibers, which have the wide range characteristics of bending loss, was conducted. The optical intensity in the optical fibers in impact testing and after the test was measured, and the relationship among impact energy, the minimum optical intensity and the residual optical intensity after impact was investigated.

INTRODUCTION

CFRP composites have been used extensively for aerospace structures taking advantage of its high specific strength and stiffness. But the application to primary structures is limited because of its low CAI strength. When composite laminates are subjected to out-of-plane impact, serious damages, such as delamination and matrix cracks, are often induced in composites, and in-plane properties decrease. Then compressive load causes local buckling easily and the progress of the damage leads to final fracture of the composites. Thus CAI strength is regarded as an important design criterion, and many studies have been made on the

Hiroaki Tsutsui, Akio Kawamata, Tomio Sanda, Kawasaki Heavy Industries LTD, 1 Kawasaki-cho Kakamigahara City, Gifu-Pref., 504-8710, Japan.
Nobuo Takeda, The University of Tokyo, 4-6-1 Komaba, Meguro-ku, Tokyo, 153-8904, Japan.

problem including the fracture mechanism [1], [2].

The objective of the present study is to develop a health monitoring system for detecting the occurrence, position and size of the damage induced in the composite structures subjected to transverse impact load. As mentioned above, the delamination induced in composites by impact loading has the damage area which depends on an impact energy. And the compressive strength of composites decreases in proportion to the area. If the sensors embedded in composite structures can detect the impact loading when the composites are subjected to out-of-plane impact, it may be able to detect the occurrence of impact damage and estimate the effect of damage.

So far, for the significance of the damage monitoring, the impact tests of the composite panels with embedded optical fibers with 125 μm in cladding diameter were conducted [3] And it was found possible to detect impact load and impact damage in real-time by measuring the optical intensity and strain responses. However, the insertion of foreign objects into the composites causes the decrease in the strength of the structures. In this paper, as the sensors for detecting the impact damage in the composites, polyimide coated optical fibers with 40 μm in cladding diameter are used, and such optical fibers embedded inside laminas cause no serious effect on the mechanical properties of composites [4]. The relationship between the impact loading, the optical loss of the optical fiber and impact damage are studied by impact tests of the composite panels with embedded optical fiber sensors.

IMPACT CHARACTERISTICS OF CFRP COMPOSITE PANELS

Specimens and Test Method

The impact tests and the compression tests after impact in accordance with the SACMA method [5] is conducted in order to investigate the relationship among impact energy, delamination area and residual compressive strength as the impact characteristics of the composite panels.

As shown in Fig.1, quasi-isotropic CFRP composite panels were prepared using T300/3601 laminates; $[+45/0/-45/90]_{4S}$ with 152.4mm in length and 101.6mm in width. In impact test, a drop-weight impact machine and the frame support specified in SACMA method were used (Fig.2). The impactor with a hemi-spherical tap whose diameter is 15.75mm and mass is 5.44kg was dropped in the center of the panels. Specimens were subjected to various impact loads by changing the dropping height of the taps. After the impact test, delamination size in each panel was measured by ultrasonic C scan. Then the CAI strength of the panels was measured by compressive tests. Cross sections of the specimens subjected to impact load were observed in order to investigate the damage state.

Result of Impact Test and Compressive Strength Test

Figure 3 shows the relationship between impact energy per unit thickness and the delamination area induced in the composites. It is confirmed that the delamination area induced in the composites increases linearly as the impact energy per unit thickness increases The relationship between impact energy per unit thickness and CAI strength is shown in Fig. 4. It is found that the CAI strength decreases rapidly as the impact energy increases. In reference [6], there is a criterion that a visible impact damage defines the damage with 0.05 inch or

deeper dent for thin laminates. The impact energy that a tap results in the dept in the composites is shown as thick lines in both Figs.3 and 4. The delamination area, which is barely visible, and the residual strength of the composites can be estimated by detecting the impact energy using sensor responses in the composites.

The CAI strength of the composite panels with 3 embedded optical fibers with 125 μm in cladding diameter is shown as triangle marks in Fig.4. Here, the direction of the optical fibers are parallel to 0° reinforced fibers were embedded in composites. The embedded optical fibers in composites had no serious effect on the CAI strength.

Next, the damage state of the composite panels subjected to impact load with different impact energy levels was observed. Figure 5 (a) shows the photograph of the cross section A-A' of the specimens in Fig.1 by an optical microscope. Also Fig.5 (b) shows the schematic of damage state inside the square frame in Fig.5 (a). It is found that impact damage consists of delamination and matrix cracks, and the damage is generated in a conical shape from the impact point to the rear surface of impact. The delamination density per unit width length and the crack density per unit area are shown in Fig.6. It is found that crack density increases from the center of the thickness to the rear surface of impact.

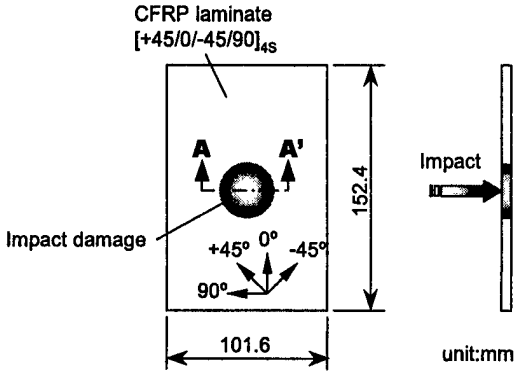


Figure 1. Specimen of impact test

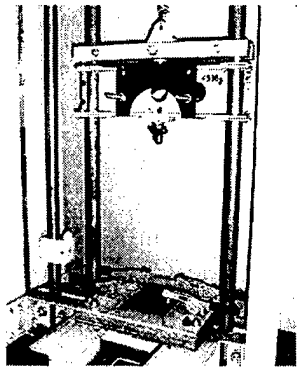


Figure 2. Impact testing machine

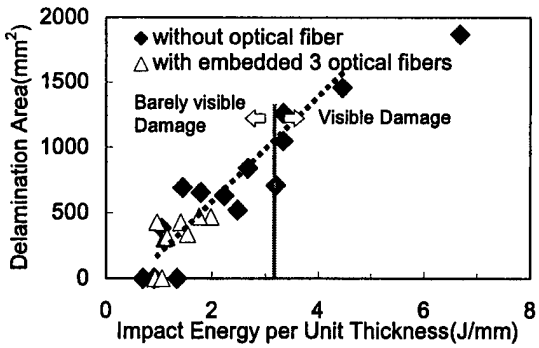


Figure 3. Relationship between impact energy and delamination area

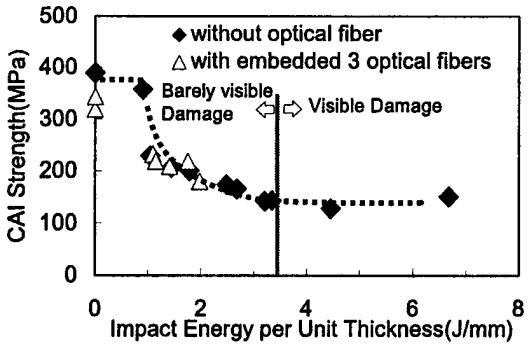
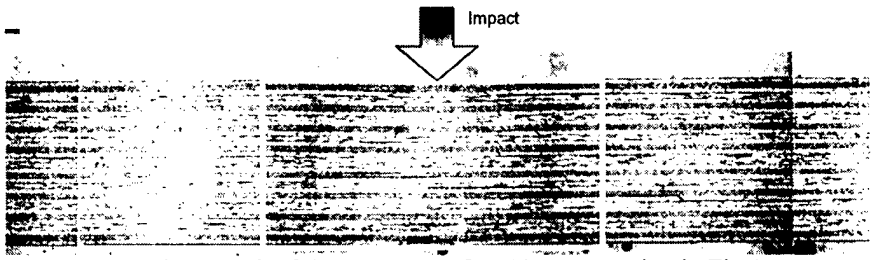
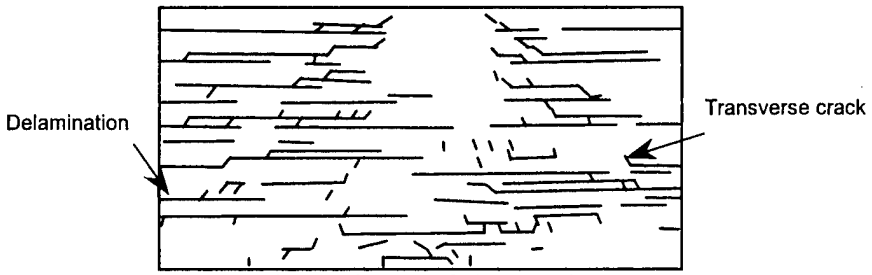


Figure 4. Relationship between impact energy and CAI strength



(a) Photograph of damage state of A-A' cross section in Fig.1



(b) Sketch of a part of photograph (a)

Figure 5. Observation of the cross section of CFRP specimen at impact energy = 0.955J/mm

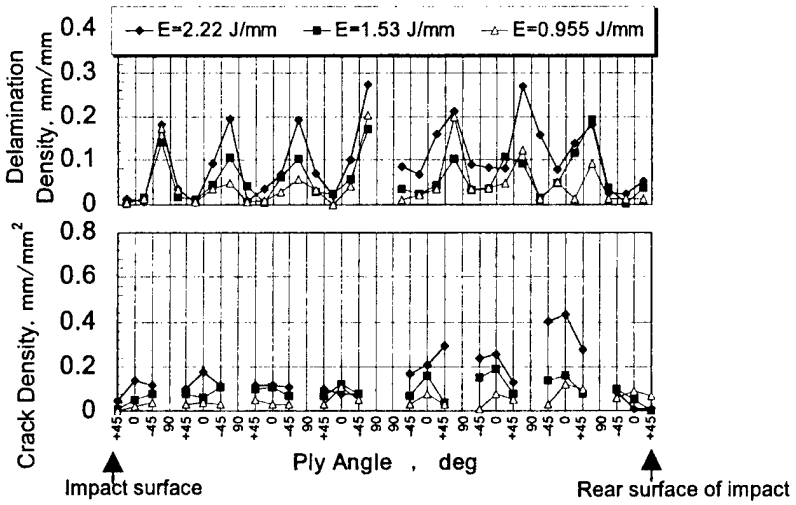


Figure 6. Distribution of delamination density and crack density in thickness direction

TABLE I. Classification of optical fibers

Optical fiber	Mode	Core diameter μm	Cladding diameter μm	Coating diameter μm
SM(125)	single	9.5	125	250(UV)
SM(40)	single	8.5	40	52(polyimide)
MM(40)	multi	20	40	52(polyimide)

THE METHOD OF DETECTING IMPACT DAMAGE IN COMPOSITES

Optical Fiber Sensor

Optical fiber sensors which are light and small in diameter can measure several physical quantities, such as strain, temperature and deformation. Therefore the optical fiber can be embedded in CFRP composites easily. In this study, using this attractive optical fiber sensor, the possibility of detecting impact damage in composites is discussed.

In order to detect impact damage, we use the relationship between impact load responses and the responses measured by optical fiber sensors. The measured optical responses are the optical loss induced by the bending deformation of optical fibers and the strain measured by fiber bragg grating (FBG) sensors. In this paper, the fundamental study on the detection of impact damage in composite panels using optical loss of optical fibers is mainly explained.

Characteristics of Bending Loss of Optical Fibers

The embedded conventional optical fibers with 125 μm in cladding diameter have the possibility of some serious effect on the mechanical properties. Therefore the utilization of small-diameter optical fibers [7] with 40 μm in cladding diameter as embedded optical fibers in the composites are discussed.

In order to investigate the optical loss by bending deformation of the optical fibers, bending tests of optical fibers were conducted. Figure 7 shows the characteristic of bending loss for three types of optical fibers that are (1) single-mode fibers with 125 μm in cladding diameter, (2) single-mode fibers with 40 μm in cladding diameter and (3) multi-mode fiber with 40 μm in cladding diameter (Table I). In this test, the optical fibers were wound N times (N=1) around a metal cylinder with smooth surface, and the optical intensity of each fiber was measured. As shown in Fig.7, the experimental values of an optical fiber with 125μm in cladding diameter agree with the theoretical values [8] which tend to change rapidly when the radius changes from 5 mm to 20 mm. For small-diameter optical fibers, it is confirmed that the bending loss of a single-mode fiber is similar to that of a 125μm diameter fiber. But the bending loss of a multi-mode fiber has a different characteristic: the change of optical intensity covers a wide range of the radius of the optical fiber. Thus, a multi-mode optical fiber was selected as an embedded small-diameter fiber in composites.

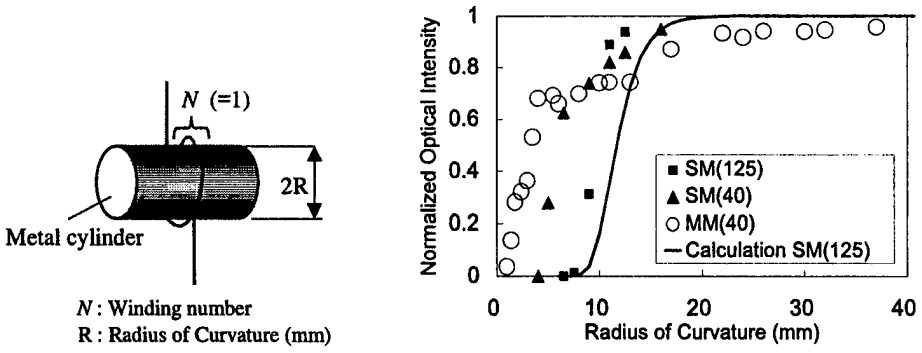


Figure 7. Characteristics of the bending loss of optical fibers

DETECTION OF IMPACT DAMAGE BY USING OPTICAL LOSS

Specimens and Test Method

To discuss the relationship between optical loss and impact loading, quasi-isotropic composite panels $[+45/0/-45/90]_{4S}$ with embedded optical fibers were prepared as specimens for impact tests. The specimens were 152.4mm in length and 101.6mm in width. CFRP T300/3601 were used as composite materials and molded at 180°C by using an autoclave. The optical fibers were polyimide coated multi-mode fibers with 40 μm in cladding diameter. The embedded positions of the optical fibers were the interlaminar resin between 1 and 2 plies near the impact surface, and also between 20 and 21 plies near the rear surface of impact where the density of impact damage is expected to be high. The direction of the embedded optical fibers was parallel to 0° reinforcing fibers.

The impact tests were conducted in the same way as CFRP specimens without embedded optical fibers. Semi-conductor strain gauge was attached on the surface of the tap, and the dynamic load had been calibrated beforehand by compressive loading test. Figure 9 indicates the schematic of the impact test system. The light with 1550nm wavelength from the optical source went through a single-mode fiber with 125 μm in cladding diameter and an optical connector between 125μm and 40μm fibers, and was introduced into one end of an optical fiber embedded in composite specimens. The other end of the optical fiber was connected to an optical detector and the optical intensity was measured real-time during the impact loading. The outputs of semi-conductor gauges, foil strain gauges and the optical intensity were stored in a computer as digital data through an A/D converter.

Result of Impact Test

Figure 10 shows a typical example of the impact response. This figure indicates the time history of the impact load, normalized optical intensity and the strain. Here, normalized intensity I_i/I_0 means the optical intensity I_i(W) divided by the initial optical intensity (before impact test) I_0 (W). I_i means the minimum optical intensity in impact testing (i=M) and residual optical intensity after impact (i=R). The response of the specimen tensile strain as

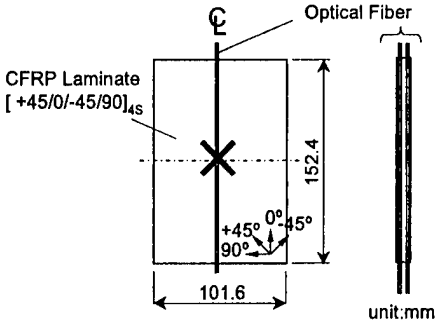


Figure 8 CFRP specimen with embedded optical fibers

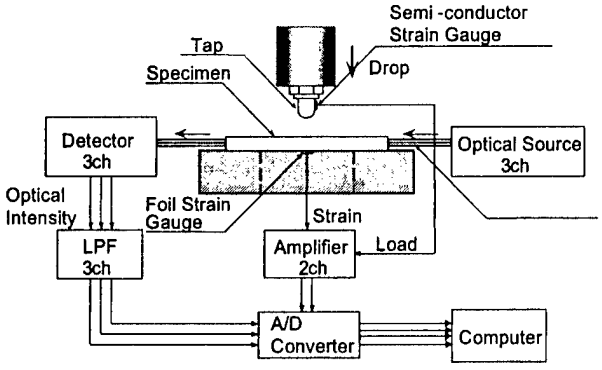


Figure 9. Schematic of impact test system

well as the impact load is well correlated with the dynamic normalized intensity behavior And it is found that the normalized intensity response becomes discontinuous at the same time as the impact load response changes rapidly approximately at 2msec. It is supposed that the impact damage just occurred at that time.

The minimum normalized intensity in impact testing versus impact energy was plotted in Fig.11 (a). The black squares indicate normalized optical intensity in optical fibers embedded near the impact surface, and the intensity decreases as the impact energy increases. It is supposed that the local deformation of optical fiber embedded near the impact surface in impact loading caused the decrease in the intensity since the intensity recovered after impact. It is concluded that it is possible to detect the impact load by using the variation of the optical intensity and the relationship between impact energy and optical intensity in the optical fiber embedded in composites. Moreover, it is possible to predict the damage area and residual strength by using the impact characteristics of composites.

The circles in Fig.11 (a) indicate the normalized optical intensity embedded near the rear surface of impact. The intensity decreased remarkably and became zero after impact energy went over about 1 J/mm. It is supposed that the bending deformation of embedded optical fibers by impact damage in composites caused optical loss. And all optical fibers that the intensity became zero have not been cut since the intensity recovered as shown in Fig.10.

Figure 11 (b) shows the residual normalized intensity after impact test. The normalized intensity of optical fibers embedded near the rear surface of impact did not almost change at the impact energy that did not result in damage in composites. However the intensity decreased as impact energy increased more than 1 J/mm, where the energy caused impact damage in composites. So the detecting the occurrence of the impact damage in composites and impact energy loaded on the composites is possible by monitoring the decrease in the residual normalized intensity. This means the possibility to detect impact damage in composites by using more simple measurement system than that for real-time measurement.

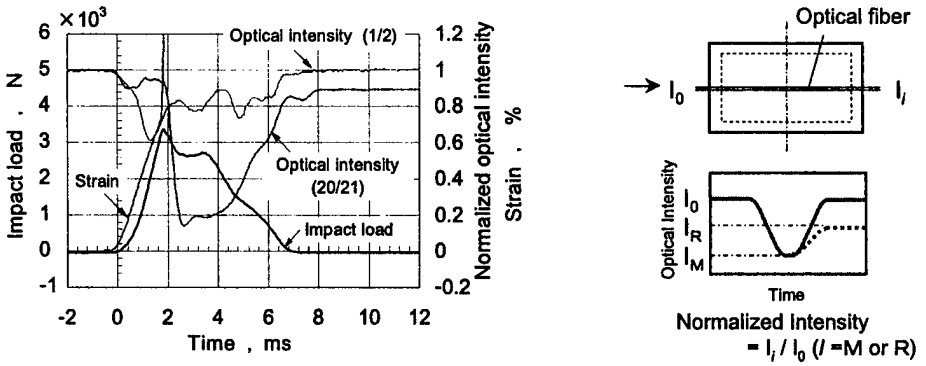
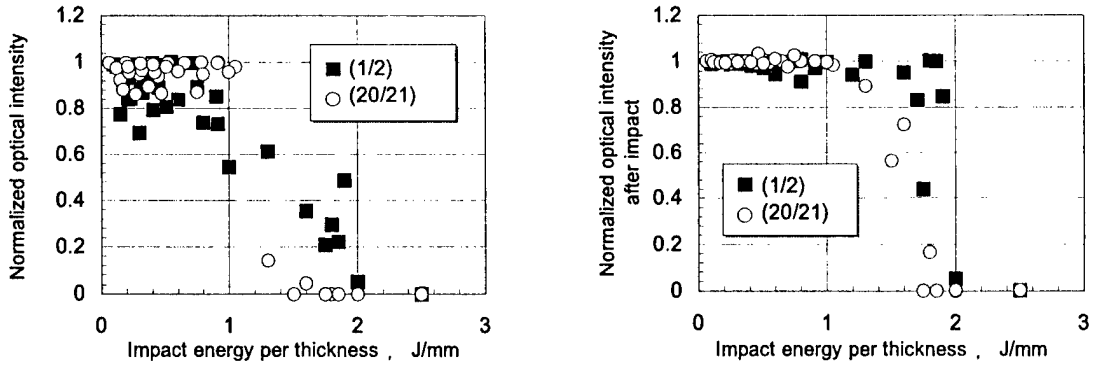


Figure 10 Typical response of optical intensity, impact load and strain in impact testing (bandwidth=1kHz)



(a) Minimum optical intensity in impcat testing (b) Residual optical intensity after impcat

Figure 11 Relationship between impact enrgy and normalized optical intensity

CONCLUSIONS

In this study, small-diameter optical fibers, which had no serious effect on the mechanical properties of composites, were used as embedded sensors in near the impact surface and the rear surface of impact in composites. It was found possible to detect impact load in real-time by measuring the optical loss induced by bending deformation of optical fibers in impact loading. And it was confirmed that the discontinuous optical intensity responses and the intensity after impact events could indicate the occurrence of damage in composites. In near future, the impact test of skin-stringer panels with embedded small diameter optical fibers for measuring optical intensity and FBG sensors for measuring strain responses, is conducted in order to investigate the method of detection of impact damage in the structural element level using optical fiber sensors.

ACKNOWLEDGMENT

This study was conducted as a part of the "R&D for Smart Material/Structure System" project within the Academic Institutions Centered Program supported by NEDO (New Energy and Industrial Technology Development Organization), Japan.

REFERENCES

1. Hitchen, S. A. and R. M. J. Kemp, "The effect of stacking sequence on impact damage in a carbon fiber/ epoxy composite", Composites, 26(3), pp. 207-214, 1995.
2. Soutis, C. and P. T. Curtis, "Prediction of the post-impact compressive strength of CFRP laminates composites", Composites Science and Technology, Vol.56, pp. 677-684, 1996.
3. Tsutsui, H., N. Takeda, K. Bansaku and T. Sanda, "Damage monitoring of CFRP subjected to impact load using optical fiber sensor", Proc. 6th Japan International SAMPE Symposium, Vol.2, pp. 991-994. 1999.
4. Carman, G. P., C. Paul and G. P. Sendeckyj, "Transverse strength of composites containing optical fibers", SPIE 1917, pp. 307-316, 1993.
5. SACMA recommended test method for compression after impact properties of oriented fiber-resin composites, SACMA, SRM 2R-94
6. Advanced certification methodology for composite structures, NAWCADPAX-96-262-TR, 1997
7. Satori, K., Y. Ikeda, Y. Kurosawa, A. Hongo and N. Takeda, "Development of small-diameter optical fiber sensors for damage detection in composite laminates", SPIE 3986, pp. 104-111, 2000.
8. Snyder, A. W. and J. D. Love, Optical waveguide theory, CHAPMAN & HALL, 474-486, 1983.

SIMULTANEOUS HEALTH MONITORING AND CONTROL OF PANELS

Daniel J. Inman,[1] Thomas Hegewald[1]

ABSTRACT

Vibration of aircraft panels is a major source of fatigue and requires the addition of damping material to increase fatigue life and reduce noise transmitted to the interior. In addition, monitoring the health of panels represents an addition need of modern aircraft. The usual treatment of added damping brings a substantial weight penalty. In addition passive damping treatments are limited in frequency range and subject to variation with temperature. This paper examines the possibility of using active vibration suppression implemented through smart materials to perform damping in structural plates subject to both structural and acoustic loading. In addition we examine the use of the hardware used for active control to implement simultaneous health monitoring. Experimental results are presented indicating a high level of damping available through a single piezoceramic patch serving as an actuator and a fiber optic sensor. Analytical and experimental results indicate that simultaneous health monitoring and vibration suppression using piezoceramic actuation, fiber optic sensing and reasonable electronics is completely feasible and can do so over a range of temperatures against both acoustic and mechanical excitation.

INTRODUCTION

The problem of simultaneously monitoring the health of a structure and active vibration suppression on the same structure represent opposing goals. The goal of active vibration suppression is to reduce the structure's response as quickly as possible. On the other hand, diagnostic, or health monitoring, generally requires that the response be examined as long as possible. Furthermore, if the same hardware is to be used for both vibration suppression and health monitoring the possibility of signals' interfering with each other presents itself. To solve these problems the impedance method of health monitoring it used. The impedance

[1] Center for Intelligent Material Systems and Structures, Department of Mechanical Engineering, MC 0261, Virginia Tech, Blacksburg, VA 24051

method uses a high frequency, low voltage, self-sensing signal to determine small changes in stiffness, damping and mass of a structure [1].

The control law chosen needs to not interfere with the diagnostic measurements and at the same time provide robustness to analysis. In particular the control must not depend on an analytical model and must continue to provide vibration suppression as the panel heats up. In the case of the aircraft panel demonstrated here, the control hardware and diagnostic hardware were required to be the same in order to minimize the amount of hardware in an aircraft. A piezoceramic patch was chosen for the actuator and sensor, building on the concept of a self-sensing actuator [2]. The control law was chosen to be Positive Position Feedback (PPF) [3-5] because it can be applied to an experimental model and because its closed loop stability depends only on knowing the systems natural frequencies. Thus, the PPF control law may be applied with hope of success as long as experimentally determined frequencies are available.

A previous paper [6] focuses on the diagnostics aspects. This paper focuses on the control aspects and how vibration suppression is maintained in the presence of thermal disturbance.

THE IMPEDANCE METHOD

The impedance method of structural health monitoring has been well documented in the literature and the reader is referred to references [1] and [6] for more detailed descriptions. Here the method is review briefly. The main point of using the impedance method here is that the method works off of a very low voltage (~1volt) excitation in the kilohertz range so that it does not interfere with the control law for active vibrations suppression. Furthermore, it is shown that this method detects damage while the control law is turned on so that vibration suppression is occurring simultaneously. This works because the high frequency impedance signal is not part of the control bandwidth.

The basic concept of this impedance-based structural health monitoring technique is to monitor the variations in the structural mechanical impedance caused by the presence of damage. Since structural mechanical impedance measurements are difficult to obtain, this non-destructive evaluation technique utilizes the electromechanical coupling property of piezoelectric materials. This method uses one piezoceramic (PZT) patch for both sensing and actuating. The interaction of a PZT patch with its host structure can be described by a simple impedance model as described in [1]. The PZT is considered as a thin bar undergoing axial vibrations in response to the applied sinusoidal voltage.

Damage in the structure is reflected in changes of the parameters such as mass, stiffness, or damping. Assuming that the piezoceramics' parameters remain constant any changes in the mechanical impedance (Z_s) change the overall admittance of the combined structure and PZT system. Previous experiments have shown that the real part of the overall impedance contains sufficient information about the structure and is more reactive to damage than the magnitude of the imaginary part. Therefore, the impedance analyses is confined to the real part of the complex impedance. The actual health monitoring is performed by saving a healthy impedance signature of the structure, and comparing the signatures taken over the structure's service life. The impedance measurements are taken with a HP 4194A Impedance Analyzer, however a simple measurement across a resistor would do. A frequency range from 45 kHz to 55 kHz proved to be an optimum for this structure.

ACTIVE CONTROL

This research uses a special vibration test rig for evaluating the performance of different vibration suppression systems on a representative aircraft panel. A 400 by 500-mm test panel is clamped rigidly in a frame and can be excited in various frequencies with an electromagnetic shaker or driven acoustically. To simulate temperature fluctuations the temperature on the panel can be increased up to 65°C (150°F). The active controller utilizes three positive position feedback filters implemented through a digital signal processor board. First, a PPF controller with up to five filters was used to perform vibration suppression across a wide band of frequencies while the temperature remains constant. Next the PPF control philosophy was adapted to handle temperature changes in the panel by using a "quasi" adaptive control approach. Two different adaptation methods to perform vibration suppression in the presence of thermally induced frequency changes of the representative panel were developed. To adjust the PPF filter parameters an open-loop adaptation method and an auto-tuning method were investigated. The open-loop adaptation method uses a measurement of the plate temperature and a look-up table with pre-determined parameters to update the filters accordingly. The auto-tuning methods identify the frequencies of the poles and zeros in the structure's collocated transfer function. From the knowledge of the pole and zero locations the optimal PPF parameters are calculated online.

The results show that both adaptation methods are capable of reducing the vibration levels of the test specimen over the temperature range of interest. Three PPF filters with parameter adaptation through temperature measurement achieve magnitude reductions of the resonance peaks as high as 13.6 decibel. Using the auto-tuning method resonance peak reductions up to 17.4 decibel are possible. The pole/zero identification routine proves to detect the frequencies correctly. The average identification error remained at around one percent even in the presence of external disturbances.

The PPF control method is described briefly here while detailed descriptions can be found in Ref. [3]. This control law uses a generalized displacement measurement from the test article to accomplish the feedback and uses a displacement measurement to accomplish control. Positive position feedback control is a stable and relatively simple control method for vibration suppression. The control law for a positive position feedback controller consists of two equations, one describing the structure and one describing the compensator:

$$\text{Structure: } \ddot{\xi}(t) + 2\gamma\omega\dot{\xi}(t) + \omega^2\xi(t) = g\omega^2\eta(t) \qquad (1)$$

$$\text{Compensator: } \ddot{\eta}(t) + 2\gamma_f\omega\dot{\eta}(t) + \omega_f^2\eta(t) = g\omega_f^2\xi(t) \qquad (2)$$

where g a positive scalar gain, ξ is the modal coordinate, η is the filter coordinate, ω and ω_f are the structural and filter frequencies, respectively, and γ and γ_f are the structural and filter damping ratios, respectively. The positive position terminology in the name positive position feedback comes from the fact that the position coordinate of the structure equation is positively fed to the filter, and the position coordinate of the compensator equation is positively fed back to the structure. In effect, a positive position feedback controller behaves much like an electronic vibration absorber.

The system's parameters and the overall control system's performance were measured using a two-channel HP Dynamic Signal Analyzer. This signal analyzer was used to get the frequency response function between the plate and the clamping frame using two accelerometers, one on the bottom center of the plate and one on the clamping frame. This

yields equation (1) for each mode. Then, the filter defined by equation (2) is designed to provide the required damping.

Several adaptive schemes have been developed since research on adaptive systems began in the 1950s. Those schemes include model reference adaptive control (MRAC), self-tuning regulators (STR), and gain scheduling. Model reference control utilizes an "ideal" model of the plant. The adjustment mechanism varies the controller parameters until the behavior of the plant/controller system matches the behavior of the reference model. The second, very important adaptive control scheme is the self-tuning regulator. Similar to the model reference approach, self-tuning regulators contain an inner and an outer feedback loop. In contrast to MRAC where the system behavior is matched to a reference, STR attempts to identify the plant. The plant parameters are estimated using the input and the output of the plant. Using those plant parameters, an on-line design procedure calculates the controller parameters.

Neither of the two adaptive schemes was actually used in this research. MRAC did not seem well suited for the problem. Having a reference model for the test plate with highly damped vibration modes could lead to decent performance of the active control system. However, the significant shifts of the test plate's mode frequencies due to temperature variations would require either a new reference model for each temperature or a vast control effort (actuator voltage) to drive the mode frequencies back to the original frequency values. The STR could not be implemented in its original form due to the lack of a suitable on-line estimation method for the multi-order plant.

Instead of using those closed-loop adaptation schemes, an open-loop scheme called gain scheduling was investigated first. Gain scheduling measures the external operating conditions that lead to the variations in the plant parameters. This measurement is used to update the controller parameters from the schedule. The schedule has to be determined beforehand, experimentally, or analytically. Unfortunately gain scheduling is an open-loop adaptation method, meaning there exists no feedback path from the output of the plant to the controller parameter computation. With regard to some definitions of adaptive control, gain scheduling is not always considered an adaptive technique. The operating condition measured was the temperature of the test structure.

Because there is no feedback to the controller parameter computation, the gain scheduling method presents the possibility of note providing the correct gains. To overcome this disadvantage of the open-loop process, another adaptive scheme called auto-tuning was investigated. Auto-tuning represents a modified STR system where the plant identification and the controller design are initiated by an operator. After the controller parameters are calculated, the system switches in the "control mode" and no further parameter adjustments are done. Figure 1 shows the elements of a system with auto-tuning. Note that the system contains a block labeled "Probe Signal." The probe signal is used to excite the plant in a defined way, hence simplifying the estimation process. Although many different excitation signals such as random excitation, fixed sine excitation, or impact excitation are possible as probe signals this research utilized a sine sweep signal as probe the signal. Due to the lack of continuous parameter adjustments, auto-tuning is not considered as an adaptive control technique by many definitions of adaptive control.

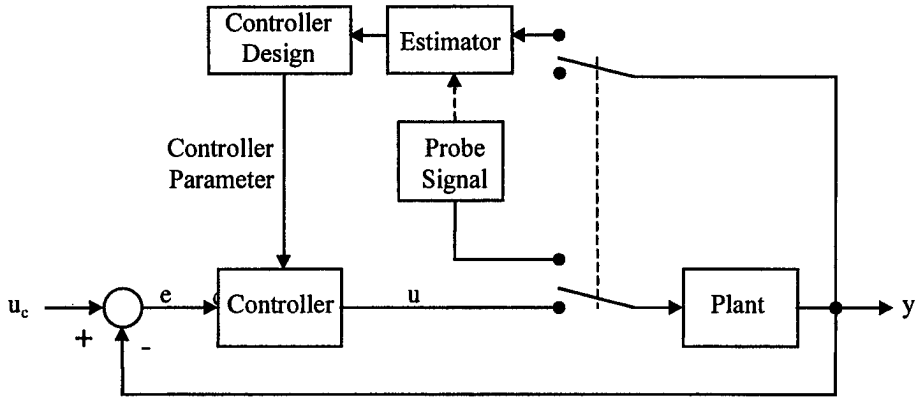


Figure 1. Block Diagram of a System with Auto-Tuning.

RESULTS

To simulate damage on the plate one or two bolts of the clamping frame were loosened from 25 ft-lb. to 10 ft-lb. Note that at this level of torque the bolt is still very tight with no slip occurring at all. Since the task consisted of simultaneous health monitoring and active control with the same actuators for both the control and the health monitoring system needed to be de-coupled. The impedance method is very sensitive to disturbing voltages in the measuring circuit. The controller however creates exactly those disturbances by generating the control signal. A simple capacitor of 390 nF in series with the impedance analyzer blocked efficiently the control signal from the impedance analyzer. All health monitoring data was taken while the shaker was exiting the plate with a periodic chirp signal from 0 to 200 Hz. The active controller was also switched on and increased the damping of the first few modes of the plate significantly. For comparing impedance signatures, a qualitative damage assessment has been developed. The assessment is made by computing a scalar damage metric, defined as the sum of the squared differences of the real impedance at every frequency step. Equation (3) gives the damage metric M in a mathematical form. The used variables include: $Y_{i,1}$ the healthy impedance at the frequency step i, $Y_{i,2}$ the impedance of the structure after the structure has been altered, and n the number of frequency steps

$$M = \sum_{i=1}^{n} \left[\mathrm{Re}(Y_{i,1}) - \mathrm{Re}(Y_{i,2}) \right]^2 \tag{3}$$

The damage metric simplifies the interpretation of the impedance variations and summarizes the information obtained by the impedance curves. Different damage metric values of the plate are presented in Figure 2. Note the difference in the metric between one bolt loosened and two bolts loosened. Keep in mind, that this damage assessment is going on while the active control scheme is continuing to add damping to the system while the structure is being excited with a shaker.

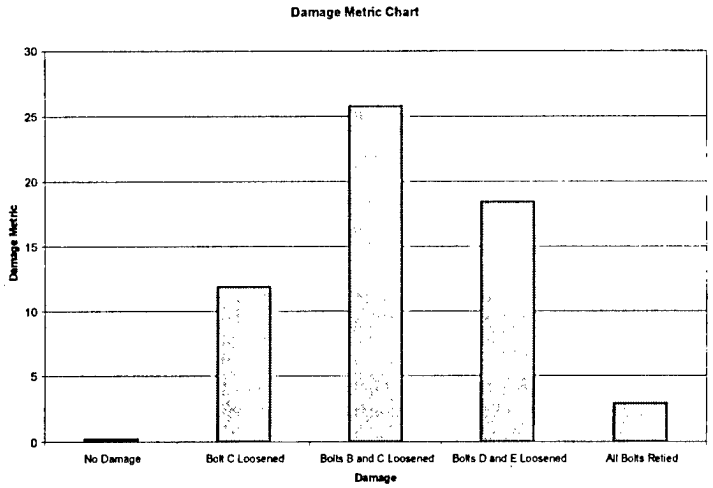


Figure 2. Damage Metric Chart of Different Impacts to the Plate.

The control results are straightforward. First an experimental result is given for the case of constant temperature. Figure 3 illustrates the open loop transfer function along with the closed loop control provided by five PPF controllers. The controller is able to suppress the all the modes in the bandwidth from 0 to 400 Hz. Thus, a broadband controller is simultaneously controlling the structural vibration response while the impedance method is monitoring the health of the structure.

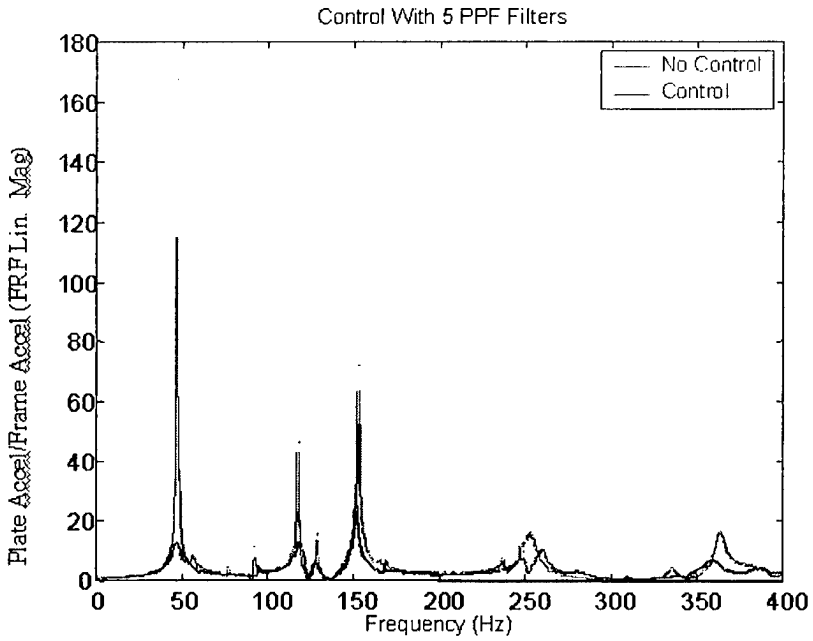


Figure 3. Broadband Vibration Suppression Using Five PPF Controllers

Next consider controlling the vibrations as the temperature is increased. Since the plate is clamped all the way around, the temperature increases the stiffness. Figure 4 illustrates that the quasi adaptive control law suggested above is able to maintain the vibration suppression even though the applied thermal load drastically changes the systems natural frequencies.

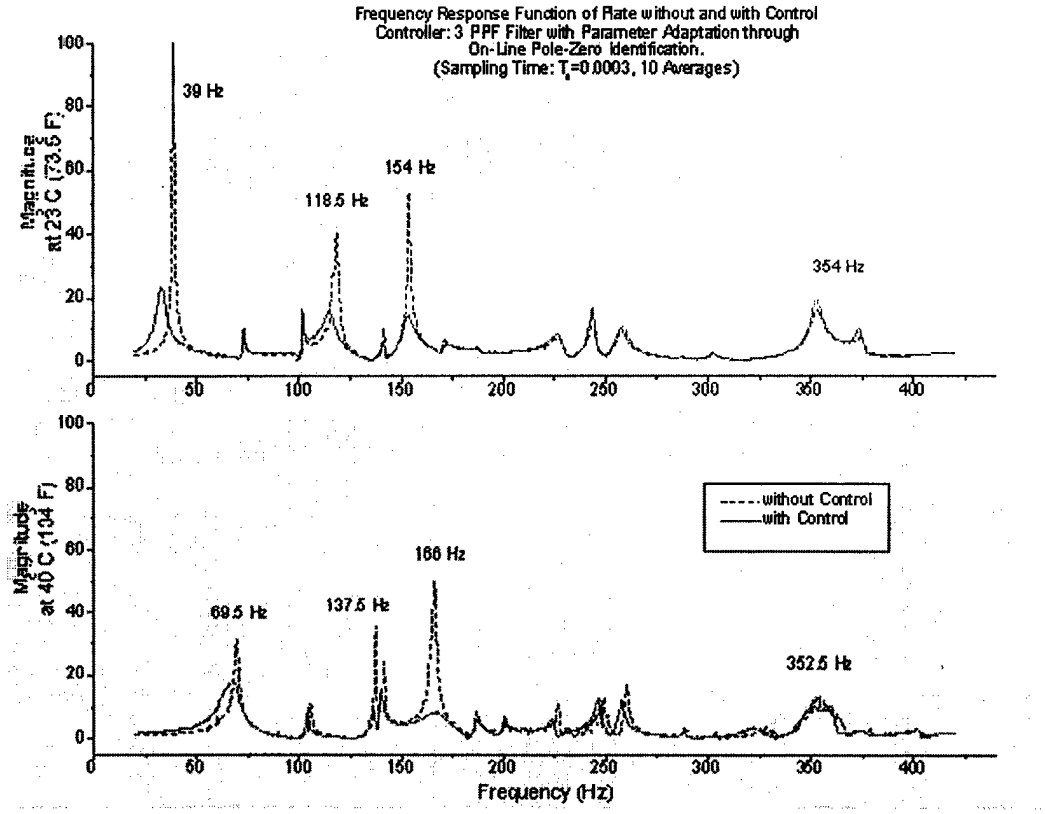


Figure 4 Vibration Suppression in the Presence of Temperature Changes.

SUMMARY

The ability to perform simultaneous health monitoring and active vibration suppression has been illustrated and experimentally verified. Furthermore, the active control of panel vibrations in the presence of temperature changes has been illustrated. These experimental results do not depend on any model of the system and hence are applicable to complex structures. The control method and the health monitoring method were performed with the same hardware at the same time. These results indicate that it may be possible to perform simultaneous health monitoring and control on real structures outside of the laboratory setting.

Applications of smart materials to problems of interest to the private sector are now fairly routine to solve. In addition the use of smart materials has been shown to be extremely beneficial in numerous cases. The only thing that holds back the wide spread use of smart material in industry is the lack of good, design-based models that are easily accessible by industrial designers.

ACKNOWLEDGEMENTS

The author would like to thank the Flight Sciences Department, Raytheon Systems Company for both suggesting and funding this work and for the excellent technical monitoring of Richard A. Ely. In addition, thanks is due the National Science Foundation (CMS-9713453-001) and the Airforce of Office of Scientific Research (F49620-99-1-0231) for funding work in control, smart structures and health monitoring used in this effort. Dr. Guyhae Park provided the expertise in health monitoring using the impedance-based method.

REFERENCES

[1] Park, G., Kabeya, K., Cudney, H. H. and Inman, D. J., 1999. "Impedance-Based Structural Health Monitoring for Temperature Varying Applications," *JSME International Journal*, Series A, Vol. 42, No. 2, pp. 249-258.

[2] Dosch, J. J., Inman, D. J., Garcia, E., 1992, "A Self-Sensing Piezoelectric Actuator for Collocated Control," *Journal of Intelligent Material Systems and Structures*, Vol. 3, pp. 166-185.

[3] Fanson, J. L., Cauhey, T. K., 1990, "Positive Position Feedback Control for Large Space Structures," *AIAA Journal*, Vol. 28, No. 4, pp. 717-724.

[4] Poh, S., Baz, A., 1990, "Active Control of a Flexible Structure Using a Modal Positive Position Feedback Controller," *Journal of Intelligent Material Systems and Structures,* Vol. 1, pp. 273-288.

[5] Friswell, M. I., Inman, D. J., 1999, "The relationship between Positive Position Feedback and Output Feedback Controllers," *Journal of Smart Materials and Structures*, Vol. 8, pp. 285-291.

[6] Inman, D. J., Ahmadian, M. and Claus, R.O., 2000, "Simultaneous Active Damping and Health Monitoring of Aircraft Panels", IUTAM Symposium on Smart Structures and Structronics, to appear.

Shape Memory Materials

PASSIVE DAMPING AUGMENTATION OF A VIBRATING BEAM USING PSEUDOELASTIC SHAPE MEMORY ALLOY WIRES

Farhan Gandhi,* Gautier Chapuis**

ABSTRACT

This paper examines the effectiveness of pseudoelastic Shape Memory Alloy (SMA) wires for passive damping of flexural vibrations of a clamped-free beam with a tip mass. A finite element model of the system is developed and validated with experimental results. The SMA behavior is modeled using amplitude-dependent complex modulus. Numerical simulations indicate that the damping introduced by the SMA wires will increase for higher excitation force amplitudes that produce higher strain levels in the SMA wires. Increasing the wire cross-section area provides more damping at low force excitation amplitudes, but reduced damping at higher amplitudes. The angle between the beam and the SMA wires is an influential parameter, and a value in the 10-20 deg. range was found to introduce maximum damping. The underlying physical mechanisms are examined in detail. System damping depends only mildly on the SMA wire length, and is unaffected by the tip mass.

1. INTRODUCTION

Nickel-Titanium (Ni-Ti) Shape Memory Alloys (SMAs) are known to exhibit stress/strain pseudoelastic hysteresis associated with *stress-induced* austenite-martensite phase transformations, when subjected to cyclic stress/strain loadings above a critical temperature (the austenite finish temperature). Distinct from the more commonly used Shape Memory effect (whereby *temperature-induced* phase transformations are exploited for use in low frequency actuators), pseudoelastic hysteresis of SMAs can potentially be exploited for *passive* damping augmentation in various mechanical, civil, and aerospace applications. A damper can be designed with SMA wires pre-stressed (or pre-strained) to a level somewhere in the middle of the pseudoelastic range [1]. Cyclic variations in stress and strain around the baseline, as the system undergoes vibration, will then result in energy dissipation due to hysteresis in the SMA.

If SMAs are integrated into structures, they would have several potential advantages over traditional damping materials such as elastomers. For example, the energy dissipated per unit volume (a measure of damping capacity) is much higher than that provided by commonly used elastomeric materials [2]. Additionally, available damping from elastomers can reduce significantly at low temperatures, compromising damper performance in critical systems. Since SMA damper temperature can be controlled by electrical heating, degradation in performance due to temperature variation can be avoided. Clearly, high damping capacity and controllability of SMA-based damping systems make them attractive candidates for structural damping augmentation. In recent years there have already been some studies reported demonstrating the use of pseudoelastic SMAs for passive structural damping augmentation (see for example Refs. 3-8). However, many of these studies have assumed an overly simplified SMA hysteresis behavior (often due to lack of suitable models), and do not focus on

*Assistant Professor, Department of Aerospace Engineering, The Pennsylvania State University, 233 Hammond Building, University Park, PA 16802, USA, e-mail: *fgandhi@psu.edu*
**Graduate Assistant.

several fundamental issues such as the impact of the SMA damper configuration or excitation amplitude on system damping.

In recent years there have also been continued efforts in SMA material characterization and development of constitutive models suitable for structural dynamics applications. In particular, there has been emphasis on experimentally determining the SMA pseudoelastic hysteresis behavior over a range of excitation frequencies. With hysteresis data previously reported only at very low strain rates (quasi-static conditions), unsuitable for vibration damping applications, the first author and co-workers experimentally characterized the SMA hysteresis behavior up to frequencies of 10 Hz [2, 9]. There has also been an emphasis on development of simple yet accurate SMA constitutive models that can be easily integrated into structural finite element analyses. From this standpoint, thermodynamic-based SMA constitutive models [10-13] that require calculation of martensite-austenite phase fractions and transformations as a function of stress and temperature, have limited appeal. A better approach is to characterize SMAs using *complex modulus*. The complex modulus approach, frequently used in structural dynamics for characterizing damping materials [14-16], comprises of a storage modulus (representative of stiffness) and a loss modulus (representative of damping), both of which are frequency- and temperature-dependent. In addition, for nonlinear materials the complex modulus also varies with excitation amplitude [17-19]. A complex modulus representation of SMA behavior, as presented in Ref. 20, can be easily integrated into structural analyses, and influence of the SMA on structural response or modal damping can then be readily calculated.

The detailed characterization of SMA hysteresis behavior and availability of complex modulus representations thereof, provides a tremendous opportunity to develop finite element analyses and conduct parametric studies to provide detailed physical insight, as well as optimization studies to evaluate the most effective SMA design configurations for structural damping augmentation.

2. OBJECTIVES AND APPROACH OVERVIEW

In the present study a clamped-free vibrating beam with a tip mass and symmetrically mounted pseudoelastic SMA wires (schematic sketch shown in Figure 1) is considered to obtain a fundamental understanding of the influence of SMA damper configuration and system parameters, as well as operational parameters such as excitation force amplitude; on the performance of the SMA-based structural damping treatment.

The beam is subjected to a harmonic excitation force near the tip, and the bending response of the beam to this input excitation is calculated. An amplitude-dependent complex-modulus characterization of SMA hysteresis behavior is used, based on experimental data from Refs. 9 and 21. On account of the nonlinear behavior of the SMA wires, the beam periodic response is calculated iteratively, and damping in the fundamental mode of vibration is examined. After verifying the accuracy of the finite element analysis through experimental validation, the excitation force amplitude, SMA wire cross-section area, wire length, angle between the wires and the beam, and the tip mass are varied; and the influence of these variations on system damping is evaluated and physically explained.

3. ANALYTICAL MODEL AND SOLUTION SCHEME

To examine the effectiveness of the symmetrically mounted pseudoelastic SMA wires in introducing passive damping in the clamped-free beam with tip mass, a finite element discretization of the system is carried out (Fig. 1). The beam is assumed to undergo pure bending deformations with no extension or transverse shear (Euler-Bernoulli beam theory). The SMA wires are subjected to a pretension load, T. The angle between the wires and the undeformed beam is θ. The SMA behavior is described using complex modulus. With the beam oscillating in the horizontal plane, the gravitational force on the tip mass is not considered. Section 3.1 describes the development of the finite element equations of motion. This is followed by a description of the procedure used to calculate the system

response under a tip harmonic excitation, $P = P_o e^{j\omega t}$, in Section 3.2, and a description of the method used to calculate the damping in Section 3.3.

3.1 Finite Element Equations of Motion

In the finite-element analysis, the Euler-Bernoulli beam is spatially discretized into several elements, each having 4 degrees of freedom: w_1 and w_2 representing the transverse displacements at the left and right nodes, and w_1' and w_2' representing the slope at the two nodes. The transverse displacement within any element is then assumed to vary as a cubic function of the nondimensional local coordinate, ξ ($0 \le \xi \le 1$), and is related to the elemental degrees of freedom as:

$$w = (1-3\xi^2+2\xi^3)w_1 + (\xi - 2\xi^2 + \xi^3)w_1' + (3\xi^2 - 2\xi^3)w_2 + (-\xi^2+\xi^3)w_2' \tag{1}$$

where l is the length of the element. Using the above assumed displacement function, the element stiffness and mass matrices can be obtained from expressions of the element strain energy and kinetic energy, respectively. The finite element stiffness and mass matrices are given in Sections 3.1.1 and 3.1.2, respectively, the effect of the SMA wires is mathematically described in detail in Section 3.1.3, and the modified global equations of motion are presented in Section 3.1.4.

3.1.1 BEAM ELEMENT STIFFNESS MATRIX

The element bending stiffness matrix under the influence of a constant tensile force, F, is derived from the element strain energy, U:

$$U = \frac{1}{2}\int_{\substack{element\\length}} EI(w'')^2 dx + \frac{1}{2}\int_{\substack{element\\length}} F(w')^2 dx = \frac{1}{2}q^T K_1 q + \frac{1}{2}q^T K_2 q \tag{2}$$

where:

$$K_1 = \frac{EI}{l}\begin{bmatrix} 12 & 6l & -12 & 6l \\ 6l & 4l^2 & -6l & 2l^2 \\ -12 & -6l & 12 & -6l \\ 6l & 2l^2 & -6l & 4l^2 \end{bmatrix} \text{ and } K_2 = \frac{F}{l}\begin{bmatrix} 6/5 & l/10 & -6/5 & l/10 \\ l/10 & 2l^2/15 & -l/10 & -l^2/30 \\ -6/5 & -l/10 & 6/5 & -l/10 \\ l/10 & -l^2/30 & -l/10 & 2l^2/15 \end{bmatrix} \tag{3}$$

$$\text{and } q = \begin{bmatrix} w_1 & w_1' & w_2 & w_2' \end{bmatrix} \tag{4}$$

In Eq. 3, the flexural stiffness, EI, would assume different values for the portions of the beam with and without the tip mass. The longitudinal force, F, is due to the pre-tension, T, in the SMA wires and can be shown to be $F = -2T\cos\theta$ (for portions of the beam inboard of the point of attachment of the wires. Then, the total element stiffness matrix is $K = K_1 + K_2$ for the portion of the beam under pre-compression, and $K = K_1$ for the portion of the beam outboard of the point of attachment of the wires.

3.1.2 BEAM ELEMENT MASS MATRIX

The element mass matrix, M, is obtained from the element kinetic energy T:

$$T = \frac{1}{2}\int_{\substack{element\\length}} m(\dot{w})^2 dx + \frac{1}{2}\int_{\substack{element\\volume}} \rho b(\dot{u})^2 dV \tag{5}$$

In Eq. 5 m is the mass per unit length, ς is the mass density and b is the beam width. The first term represents the element translational kinetic energy due to transverse motion, and the second term represents the element rotational kinetic energy due to longitudinal motion. The element mass matrix due to translational kinetic energy, M_1, and the rotational kinetic energy, M_2, are given by:

$$M_1 = \frac{ml}{420}\begin{bmatrix} 156 & 22l & 54 & -13l \\ 22l & 4l^2 & 13l & -3l^2 \\ 54 & 13l & 156 & -22l \\ -13l & -3l^2 & -22l & 4l^2 \end{bmatrix} \quad \text{and} \quad M_2 = \frac{\alpha}{30}\begin{bmatrix} 36/l & -3 & -36/l & -3 \\ -3 & 4l & 3 & -l \\ -36/l & 3 & 36/l & 3 \\ -3 & -l & 3 & 4l \end{bmatrix} \tag{6}$$

It should be noted that the mass per unit length, m, and the rotational inertia, α, assume different values for the portion of the beam without the tip mass. The total element mass matrix is $M = M_1 + M_2$.

3.1.3 INFLUENCE OF SMA WIRES

In Section 3.1.1, the pretension in the SMA wires was shown to influence the stiffness matrix by subjecting the beam to a steady compressive force. In addition, the SMA wires undergo cyclic variations in strain due to the oscillations of the beam. The corresponding changes in the SMA wire force directly act on the beam at the point of attachment. This section develops the equations to represent this effect.

Figure 2 shows one of the SMA wires (wire 1) in a deformed configuration due to the beam transverse deflection and rotation at the point of attachment. From the figure, the deformed length is:

$$(L + \Delta L)^2 = (h - w_k)^2 + (X - w_k' t_b/2)^2 \tag{7a}$$

Further, the undeformed wire length can be expressed as

$$L^2 = h^2 + X^2 \tag{7b}$$

Subtracting Eq. 7b from 7a and neglecting the terms in ΔL^2, w_k^2, and $w_k'^2$ (which are of higher order),

$$2L\Delta L = -2hw_k - 2Xw_k' t_b/2 \tag{8a}$$

Eq. 8a can be re-written to obtain the net change in length:

$$\Delta L = -\frac{h}{L} w_k - \frac{X}{L}\frac{t_b}{2} w_k' = -sin\theta\, w_k - cos\theta \frac{t_b}{2} w_k' \tag{8b}$$

Thus, the extensional strain in wire 1 associated with the beam deflections is:

$$\varepsilon_1 = -\frac{sin\theta}{L} w_k - \frac{cos\theta}{L}\frac{t_b}{2} w_k' \tag{9}$$

Similarly, it can be shown that the extensional strain in wire 2 is $\varepsilon_2 = -\varepsilon_1$. Using the complex modulus representation of SMA material behavior, the corresponding stresses in wires 1 and 2 are $\sigma_1 = (G' + jG'')\varepsilon_1$ and $\sigma_2 = (G' + jG'')\varepsilon_2 = -\sigma_1$. The forces in wire 1 can then be expressed as

$$F_1 = A(G' + jG'')\varepsilon_1 = -\frac{A(G' + jG'')}{L}(sin\theta\, w_k + cos\theta \frac{t_b}{2} w_k') \tag{10}$$

and the force in wire 2 is $F_2 = -F_1$. From the forces in individual wires, the net transverse force and moment exerted by both SMA wires on the beam is obtained. From Fig. 3, the net transverse force is:

$$F_Z = F_1 \sin\theta - F_2 \sin\theta = 2F_1 \sin\theta \tag{11}$$

Introducing Eq. 10 into Eq. 11 yields:

$$F_Z = -\frac{2A(G' + jG'')}{L}(\sin^2\theta\, w_k + \sin\theta\cos\theta\frac{t_b}{2} w_k') \tag{12}$$

From Fig. 3, the net bending moment, M, is:

$$M = F_1 \cos\theta(t_b/2) - F_2 \cos\theta(t_b/2) = 2F_1 \cos\theta(t_b/2) \tag{13}$$

Introducing Eq. 10 into Eq. 13 yields:

$$M = -\frac{2A(G' + jG'')}{L}\left(\sin\theta\cos\theta(t_b/2)\, w_k + \cos^2\theta(t_b/2)^2\, w_k'\right) \tag{14}$$

3.1.4 GLOBAL EQUATIONS OF MOTION

The element stiffness and mass matrices are assembled to obtain the global stiffness and mass matrices. After application of geometric boundary conditions the global finite element equations of motion are expressed as

$$M^G \ddot{q}^G + K^G q^G = F^{SMA} + F^{ext} \tag{15}$$

where K^G is the global stiffness matrix, M^G is the global mass matrix, q^G is the vector of global degrees of freedom, F^{SMA} represents the loads exerted on the beam by the SMA wires, and F^{ext} represents the external excitation on the system. In the present study, the external excitation comprises only of a concentrated force acting near the beam tip (as seen in Fig. 1). The only non-zero elements in F^{SMA}, are the force F_Z (Eq. 12) and moment M (Eq. 14) at the node point where the SMA wires are attached to the beam.

Equations 12 and 14 can be represented in the following form,

$$\begin{Bmatrix} F_Z \\ M \end{Bmatrix} = -\frac{2A(G' + jG'')}{L}\begin{bmatrix} \sin^2\theta & \sin\theta\cos\theta(t_b/2) \\ \sin\theta\cos\theta(t_b/2) & \cos^2\theta(t_b/2)^2 \end{bmatrix}\begin{Bmatrix} w_k \\ w_k' \end{Bmatrix} \tag{16}$$

Since the loads exerted by the SMA wires on the beam are motion-dependent, they will have an influence on the global stiffness matrix. It should be noted that in the 2×2 matrix above, only the (1,2) term retains significance (while the (1,2), (2,1) and (2,2) terms become negligible) for very slender beams (except for values of $\theta \to 0$). The global finite element equations of motion are then written as:

$$M^G \ddot{q}^G + (K' + jK'')q^G = F^{ext} \tag{17}$$

The augmented global stiffness matrix is now complex due to the complex modulus of the SMA wires.

3.2 Solution of Equations of Motion using Harmonic Balance

Since the complex modulus approach is used for characterization of the SMA behavior the system is analyzed in the frequency domain. The response to the transverse excitation force, $P = P_o e^{j\omega t}$,

acting close to the beam tip, is calculated using the Harmonic Balance method. The applied force and the resulting response in Eq. 17 can be expressed as:

$$F^{ext} = F_0 e^{j\omega t} \quad \text{and} \quad q^G = (q_r - jq_i)e^{j\omega t} \tag{18}$$

Using Eq. 18 in Eq. 17, it can be shown that

$$\begin{bmatrix} K' - \omega^2 M^G & K'' \\ K'' & -(K' - \omega^2 M^G) \end{bmatrix} \begin{Bmatrix} q_r \\ q_i \end{Bmatrix} = \begin{Bmatrix} F_0 \\ 0 \end{Bmatrix} \quad \text{or} \quad \begin{Bmatrix} q_r \\ q_i \end{Bmatrix} = \begin{bmatrix} K' - \omega^2 M^G & K'' \\ K'' & -(K' - \omega^2 M^G) \end{bmatrix}^{-1} \begin{Bmatrix} F_0 \\ 0 \end{Bmatrix} \tag{19}$$

After calculating the system response (q_r and q_i) at any excitation frequency, ω, the amplitude, q_o, of the response at some desired nodal degree-of-freedom, k, near the beam tip can then be obtained as

$$q_o = \sqrt{q_r(k)^2 + q_i(k)^2} \tag{20}$$

It should be emphasized that since G' and G'' of the SMA wires are dependent on strain amplitude (which implies that K' and K'' in Eqs. 17 and 19 depend on response amplitude), q_r and q_i have to be evaluated iteratively at any frequency. A guess value of G' and G'' is used to first calculate q_r and q_i. With the beam displacement and slope then available at the point of attachment of SMA wires, the strain amplitude in the SMA wires can be calculated using Eq. 9. Based on this strain amplitude, an updated value of G' and G'' is now introduced and the process is repeated until convergence. A flowchart of this iterative solution procedure is shown in Fig. 4. The compliance response function of the system, $H(\omega) = q_o(\omega)/F_o$, can then be obtained by calculating the response q_o over a range of excitation frequencies.

3.3 Evaluation of System Damping

After calculating the system response (as described in Section 3.2), the modal damping can be evaluated. One measure of damping is the modal damping ratio calculated by applying the half-power bandwidth method to the Compliance Response function, H(ω). However, the half-power bandwidth method and the modal damping ratio are rigorously applicable only for linear systems. Alternatively, the modal loss factor, η, which represents a ratio of dissipated energy dissipated, D, to the maximum energy stored in a cycle, U_{max}, can be calculated. For a linear system, the modal loss factor *at resonance* condition is simply twice the modal damping ratio. In the present study the modal loss factor at resonance is used as a quantitative measure of damping. It can be shown that the maximum stored energy in a cycle is given by [21]

$$U_{max} = \tfrac{1}{2}\left(q_r^T K' q_r + q_i^T K' q_i\right) \tag{21}$$

and the energy dissipated in a cycle, D, is given by [21]

$$D = \pi\left(q_r^T K'' q_r + q_i^T K'' q_i\right) \tag{22}$$

Alternatively, since energy is only dissipated in the SMA wires, the dissipated energy can be obtained by calculating the area inside the hysteresis loop:

$$D = \left(\int \sigma d\varepsilon\right) V = \pi G'' \varepsilon_o^2 V \tag{23}$$

where V is the wire volume and ε_o is the SMA strain amplitude. The loss factor is then obtained as:

$$\eta = \frac{1}{2\pi} \frac{D}{U_{max}}\bigg|_{\omega=\omega_r} \tag{24}$$

In Eq. 24, U_{max} is the sum of the energy stored in the SMA wires (U_{SMA}) and in the beam. Noting that $U_{SMA} = \frac{1}{2} G' \varepsilon_0^2 V$, and using the definition for SMA material loss factor, $\eta_{SMA} = G''/G'$, it can be shown that the modal loss factor of the system can be expressed in the following form:

$$\eta = (U_{SMA}/U_{max})\big|_{\omega=\omega_r} \eta_{SMA} \tag{25}$$

4. SMA AMPLITUDE-DEPENDENT COMPLEX MODULUS

In Section 3 the complex modulus approach is used to represent the SMA behavior in the finite element formulation. The complex modulus, which is strongly amplitude-dependent for SMAs, is calculated from hysteresis data obtained through cycling pre-strained SMA wires in an MTS machine. These tests, over a range of strain amplitudes and frequencies, are described in Refs. 9 and 21. Figure 5 shows the variation of the storage modulus, G', and the loss modulus, G'', versus strain amplitude for several excitation frequencies. It is seen that storage modulus decreases for higher strain amplitudes, while the loss modulus displays a maximum at moderate strain-amplitudes. Further, both storage and loss moduli show relatively small variations with changes in frequency (between 0.5-10 Hz). Therefore, for simplicity, the complex modulus is assumed to be invariant with the excitation frequency in this study. A "master-curve" (Fig. 6a) is then generated using a least square polynomial approximation (Ref. 21) of the data in Fig. 5. The variation of the SMA loss factor, $\eta_{SMA} = G''/G'$, versus strain amplitude, is shown on Fig. 6b.

5. RESULTS AND DISCUSSION

The finite element analysis and the response and damping calculation methods outlined in Section 3, are first validated against experimental measurements (Section 5.1). Thereafter, variation in damping with excitation amplitude, as well as parameters such as SMA wire area, wire length, wire angle relative to the beam, and tip mass, are numerically examined. The pretension force in the SMA wires is selected to allow the wires to be strained inside the hysteresis loop, while ensuring that the beam does not buckle.

5.1 Description of Experiment and Validation with Test Data

The experimental setup used to validate the finite element formulation is depicted schematically in Fig. 7. The base of the setup is a 1" thick aluminum plate, fixed on a sturdy table. A net of holes is drilled on the surface of the plate to fix clamps and mountings. An additional plate is welded on the side to fix a shaker. As seen in the figure, two wire clamps, one beam clamp, and a system of pulleys are installed on the plate. The beam clamp holds an aluminum beam that has a mass attached at its end. The tip mass comprises of steel slabs screwed on the beam. The SMA wires are clamped between the beam and the pieces of steel constituting the tip mass. The wires pass through the wire clamps installed on the base plate. These clamps can be tightened, holding the wires in place. After passing through the system of pulleys, the ends of the wires are attached to adjustable tip masses used to introduce pretension in the wires.

The shaker is connected to the beam tip by a "stinger" of low flexural stiffness and high axial compressive stiffness to decouple the structure from the rotary inertia of the shaker. A load cell is installed between the stinger and the structure to monitor the force input to the system. An accelerometer is placed on the other side of the beam, at the same axial location to monitor the

acceleration near the tip of the beam in the transverse direction. The accelerometer and load cell signals are monitored using a digital signal analyzer and recorded for processing.

The system properties are given below: The aluminum beam has a length of 41 cm, a width of 48.4 mm, and a thickness of 5.05 mm. The SMA wires are 12.8 cm in length, 0.51 mm in diameter, are mounted at an angle of 19.1 deg. relative to the beam, and have a pretension of 87N. The tip mass is 1.22 Kg and extends along the beam length from 35 cm to 38 cm. The shaker, load cell and accelerometer are connected 1 cm from the beam tip. The SMA wires were pre-cycled to approximately 400 stress/strain cycles (as suggested in Ref. 9) at strain amplitudes corresponding to the maximum tip displacement available with the shaker, to stabilize the hysteresis behavior before collecting data.

Random noise tests as well as sine dwell tests were carried out. The amplitude of the compliance frequency response function is shown in Fig. 8. The correlation between the finite element predictions and experimental results is very good. Due to limitations of the shaker, large excitation input could not be achieved so results in Fig. 8 do not display nonlinear behavior associated with the amplitude-dependent modulus of the SMA wires.

For the correlation results in Fig. 8, the values of SMA storage and loss modulus used in the finite element analysis were $G' = 4.15x10^6$ psi and $G'' = 0.15x10^6$ psi (instead of $G' = 3.85x10^6$ psi and $G'' = 0.11x10^6$ psi, as seen in Fig. 6a). The higher value for G' was used because of the lower ambient temperature during the beam vibration test (Ref. 9 suggests that G' at 70F is higher than that at 90F). The larger value of G'' used is meant to account for factors such as friction at the wire clamps, etc., in an approximate sense.

5.2 Variation in Excitation Force Amplitude

Figure 9a shows compliance response functions corresponding to different excitation force amplitudes. For the simulations in this section and in Section 5.3, the following system properties are used: The beam length is 50 cm, width is 80 mm, and thickness is 3.5 mm. The SMA wires are 12.8 cm in length, have a cross-sectional area of 0.203 mm^2, are mounted at an angle of 20 deg. relative to the beam, and have a pretension of 87N. The tip mass is 14 Kg and extends along the beam length from 40 cm to 47 cm. From Fig. 9a it is seen that for larger excitation forces, the compliance response function clearly displays the characteristics of a nonlinear softening system (since the SMA storage modulus decreases, Fig. 6a, implying that the wires "soften" at higher strain amplitudes), and the peak response is observed at lower frequencies. Figure 9b shows the variation in modal damping versus force amplitude. Damping is seen to increase up to a force amplitude of 4.6N. Over this force amplitude range (0-4.6N) the peak-to-peak strains in the SMA increase up to a level of 2.7% (see Fig. 9c). Recall from Fig. 6b that the SMA wire loss factor increases significantly up to a peak-to-peak strain level of 2.7%, and decreases thereafter. Thus, when the force amplitude exceeds 4.6N and peak-to-peak strains in the SMA wires exceed 2.7% the system damping reduces due to the decrease in the SMA wire loss factor. The increase in damping seen in Fig. 9b (up to 4.6N) causes reductions in the peaks of the compliance response function in Fig. 9a. The decrease in damping beyond 4.6N causes the response peaks in Fig. 9a to increase again.

5.3 Influence of Parameter Variations on Modal Damping

5.3.1 INFLUENCE OF SMA WIRE CROSS-SECTION AREA

Figures 10a and 11a show compliance response functions, at low and high excitation force amplitudes respectively, for varying values of SMA wire cross-sectional area. In both figures the system natural frequency is seen to increase as the wire area increases. This is reasonable as the system stiffness increases linearly as the wire area increases (see Eq. 16).

Figure 10b shows the variation in modal damping versus SMA wire area (normalized by the baseline wire area) for low excitation force amplitude, and Fig. 10c shows the corresponding variation in SMA peak-to-peak strain. Similar results for high excitation force amplitude are shown in Figs. 11b and 11c. It should be recalled that the modal loss factor depends on the product of the SMA wire loss factor, η_{SMA}, and the strain energy ratio, U_{SMA}/U_{max} (Eq. 25). At low force amplitudes, the SMA peak-to-peak strain shows little absolute variation with increasing wire area (Fig. 10c). Thus, the SMA wire loss factor, η_{SMA}, is relatively unchanged, and it can be deduced that the increase in modal loss factor in Fig. 10b is due to a corresponding increase in strain energy ratio. At a higher force amplitude, the SMA peak-to-peak strains sharply decrease between 3% and 0.75%, with increasing wire area (Fig. 11c). A decrease in strain over this range corresponds to a sharp decrease in SMA wire loss factor, η_{SMA} (see Fig. 6b). Then, the overall variation in modal damping seen with increasing wire area (Fig. 11b) is a combination of an increase due to increasing strain energy fraction and a decrease due to a reduction in SMA wire loss factor.

5.3.2 INFLUENCE OF SMA WIRE LENGTH

Figures 12a and 13a show compliance response functions, at low and high excitation force amplitudes respectively, for varying values of SMA wire length. In both figures the system natural frequency is seen to decrease as the wire length increases. This is consistent with Eq. 16, which indicates that influence of SMA wires on system stiffness is inversely proportional to the wire length.

Figures 12b and 13b show that for both low as well as high excitation force amplitudes the system damping has relatively low sensitivity to SMA wire length. The peak-to-peak strains in the SMA wire (Figs. 12c and 13c) do not show much sensitivity to wire length either. Consequently, the SMA wire loss factor, η_{SMA} (which depends on the wire strain), does not vary significantly with wire length. Since the strain energy ratio, U_{SMA}/U_{max}, also has low sensitivity to wire length, it can be deduced from Eq. 25 that the overall system damping would not be highly sensitive to the SMA wire length.

5.3.3 INFLUENCE OF ANGLE, θ, BETWEEN SMA WIRES AND BEAM

Figures 14a and 15a show compliance response functions, at low and high excitation force amplitudes respectively, for varying values of the angle, θ, between the beam and the wires. From Eq. 16 it is seen that the influence of the wires on the system stiffness is dominated by the $sin^2\theta$ term (the other terms are smaller since the beam is slender). Thus, as θ increases, the system stiffness increases, resulting in the increase in natural frequency seen in Figs. 14a and 15a.

Figures 14b and 15b show the variation in system damping versus θ, for low and high excitation force amplitudes, respectively. The corresponding peak-to-peak strain amplitudes in the SMA wire are shown in Figs. 14c and 15c. The strain levels in the wire are seen to decrease asymptotically with increasing θ, and show little change for values of θ greater than 30 or 40 degrees. Thus the wire loss factor, η_{SMA}, is unchanged over this range, and it can be deduced that the decrease in system damping seen in Figs. 14b and 15b must be associated with a reduction in the strain energy ratio, U_{SMA}/U_{max} (Eq. 25). Figure 16 shows the mode shapes of the beam for wire angles of 15°, 30°, and 90°, respectively. Clearly, as θ increases in the range of 30°-90°, the significant change in the mode shape (more curvature along the beam length for the same displacement at the point of attachment of the SMA wire) would result in a larger fraction of the strain energy being stored in the beam, and a smaller fraction in the SMA wires. At very low values of θ, the system damping could again decrease because the strain in the SMA wires *per unit tip displacement of the beam* is small (Eq. 9). This is clearly seen at low force amplitudes (Fig. 14b). At higher force amplitudes (Fig. 15b), however, this effect appears to be compensated by the increase in SMA wire loss factor, η_{SMA}, due to increased

strain amplitude levels. An angle of around $\theta = 15$ deg. between the wire and the beam appears to be optimal.

5.3.4 INFLUENCE OF TIP MASS

Figures 17 and 18 show compliance response functions, at low and high excitation force amplitudes respectively, for increasing values of tip mass. In each of these figures the system natural frequency is seen to decrease as the tip mass increases, but the peak (resonant) response amplitude is independent of the tip mass. Thus, the tip mass has no influence on the operating peak-to-peak strain levels in the SMA wires or the operating wire loss factor, η_{SMA} (for a given force excitation amplitude). Consequently, the system damping is also independent of the tip mass. For the two force excitation amplitudes considered, the resonant peak-to-peak strains in the SMA wire are 0.026% and 2.15%, respectively, and the corresponding system loss factor values were 2.6% and 31.5%, respectively, *irrespective of the tip mass.*

6. SUMMARY AND CONCLUDING REMARKS

A finite element analysis is developed of a clamped-free vibrating beam with a tip mass, and symmetrically mounted pseudoelastic SMA wires to introduce passive damping. The finite element results showed excellent correlation with experimental results. The SMA behavior is represented using an amplitude-dependent complex modulus (based on previously reported experimental data). The beam is subjected to a harmonic excitation force near the tip, and its bending response is calculated using the Harmonic Balance method. The response calculation is iterative on account of the nonlinear behavior of the SMA wires. Damping in the fundamental mode of vibration is examined by considering the system loss factor at resonance. The effects of excitation force amplitude, SMA wire cross-section area, wire length, the angle between the SMA wire and the beam, and the tip mass, on available damping, were examined in detail. The following observations were drawn:

1. The *SMA wire loss factor* increases with strain amplitude up to about 2.7% peak-to-peak strain. Thus, in general, larger amount of damping is available at higher excitation force amplitudes that produce operational strain amplitudes in the SMA wire around this range. In the present study it was seen that modal loss factors varied from around 2.5% at low excitation force amplitudes, to over 30% for high excitation levels.
2. In addition to the operational SMA wire loss factor (which depends on the strain amplitude in the wire), system damping depends on the fraction of the strain energy in the SMA wire (relative to the total strain energy in the system). Higher values of this *strain energy ratio* result in better damping performance.
3. *Dependence on SMA wire cross-section area* - At low excitation levels, more damping is available for larger cross-section wire cross-section area. However, at higher excitation levels, the damping may decrease with increasing cross-section area. This is because even though the strain energy ratio increases, there is a significant reduction in the SMA wire loss factor at the lower strain amplitudes obtained in the thicker (stiffer) wires.
4. *Dependence on SMA wire length* - The damping level is only mildly sensitive to this parameter.
5. *Dependence on the angle between the SMA wire and the beam* – The available damping is strongly dependent on this parameter, with the optimal value being in the range of 15-20 deg. For larger angles, the strain energy ratio reduces due to a significant change in the mode shape of the beam.
6. The damping introduced in the system by the SMA wires is *independent of the tip mass.*

REFERENCES

1. Hodgson, D. E., "Using Shape Memory Alloys," Shape Memory Applications, Inc., 1988.
2. Wolons, D., Gandhi, F., and Malovrh, B., "Experimental Investigation of the Pseudoelastic Hysteresis Damping Characteristics of Shape Memory Alloy Wires," *Journal of Intelligent Material Systems and Structures*, Vol. 9, No. 2, Feb. 1999, pp. 116-126.
3. Inaudi, J. A., Kelly, J. M., Taniwangsa, W., and Krumme, R. C, "Analytical and Experimental Study of a Mass Damper using Shape Memory Alloys," *Proceedings of Damping '93*, San Francisco, California, Feb. 1993, pp. HAA-1 – HAA-20.
4. Witting, P. R., and Cozzarelli, F. A., "Design and Seismic Testing of Shape Memory Structural Dampers," *Proceedings of Damping '93*, San Francisco, California, Feb. 1993, Paper No. ECC.
5. Rivin, E., Xu, L., "Damping of NiTi Shape Memory Alloys and its Application for Cutting Tools," NCA-Vol. 18/DE-Vol. 80, Materials for Noise & Vibration Control, ASME 1994, pp. 35-41.
6. Thompson, P., Balas, G. J. and Leo, P. H., "The Use of Shape Memory Alloys for Passive Structural Damping," *Smart Materials and Structures*, Vol. 4, 1995, pp. 36-41.
7. Yiu, Y. C., and Regelbrugge, M. E., "Shape Memory Alloy Isolators for Vibration Suppression in Space Applications," *American Institute of Aeronautics & Astronautics*, AIAA-95-1120-CP, 1995.
8. Clark, P. W., Aiken, I. D., Kelly, J. M., Higashino, M., and Krumme, R. C., "Experimental and Analytical Studies of Shape Memory Alloy Dampers for Structural Control," SPIE Vol. 2445, pp. 241-251.
9. Wolons, D., "An Experimental Investigation of the Pseudoelastic Damping Characteristics of NiTi Shape Memory Alloy Wire," *M.S. Thesis,* The Pennsylvania State University, Department of Aerospace Engineering, Dec. 1997.
10. Tanaka, K., "A Phenomenological Description on Thermomechanical Behavior of Shape Memory Alloys," *J. Pressure Vessel Tech.*, Vol. 112, pp. 158-163, 1990.
11. Liang, C., and Rogers, C., "One-Dimensional Thermomechanical Constitutive Relations for Shape Memory Alloys," *American Institute of Aeronautics and Astronautics*, AIAA-90-1027-CP, 1990.
12. Brinson, L. C., "One-Dimensional Constitutive Behavior of Shape Memory Alloys: Thermomechanical Derivation with Non-Constant Material Functions and Redefined Martensite Internal Variable," *Journal of Intelligent Material Systems and Structures*, Vol. 4, April 1993.
13. Boyd, J. G., and Lagoudas, D. C., "A Constitutive Model for Simultaneous Transformation and Reorientation in Shape Memory Materials," *Mechanics of Phase Transformations and Shape Memory Alloys*, ASME, AMD-Vol. 189/PVP-Vol. 292, 1994.
14. Lazan, Benjamin, J., *Damping of Materials and Members in Structural Mechanics*, Pergamon Press, Oxford, First Edition, 1969.
15. Nashif, A. D., Jones, D. I. G. and Henderson, J. P., *Vibration Damping*, J. Wiley & Sons, New York, 1985.
16. Flugge, W., *Viscoelasticity*, Blaisdell, 1967.
17. Gandhi, F., and Chopra, I., "An Analytical Model for a Nonlinear Elastomeric Lag Damper and Its Effect on Aeromechanical Stability in Hover," *Journal of the American Helicopter Society*, Vol. 39, No. 4, Oct. 1994.
18. Gandhi, F., and Chopra, I., "Analysis of Bearingless Main Rotor Aeroelasticity Using an Improved Time-Domain Nonlinear Elastomeric Damper Model," *Journal of the American Helicopter Society*, Vol. 41, No. 3, pp. 267-277, July 1996.
19. Gandhi, F., and Chopra, I., "A Time-Domain Non-Linear Viscoelastic Damper Model," *Smart Materials and Structures*, Vol. 5, pp. 517-528, 1996.
20. Gandhi, F., and Wolons, D., "Characterization of the Pseudoelastic Damping Behavior of Shape Memory Alloy Wires using Complex Modulus," *Smart Materials and Structures*, Vol. 8, pp. 49-56, 1999.
21. Chapuis, G., "Use of Pseudoelastic Shape Memory Alloy Wires for Passive Damping Augmentation of a Vibrating Beam," *M.S. Thesis,* The Pennsylvania State University, Department of Aerospace Engineering, Dec. 1999.

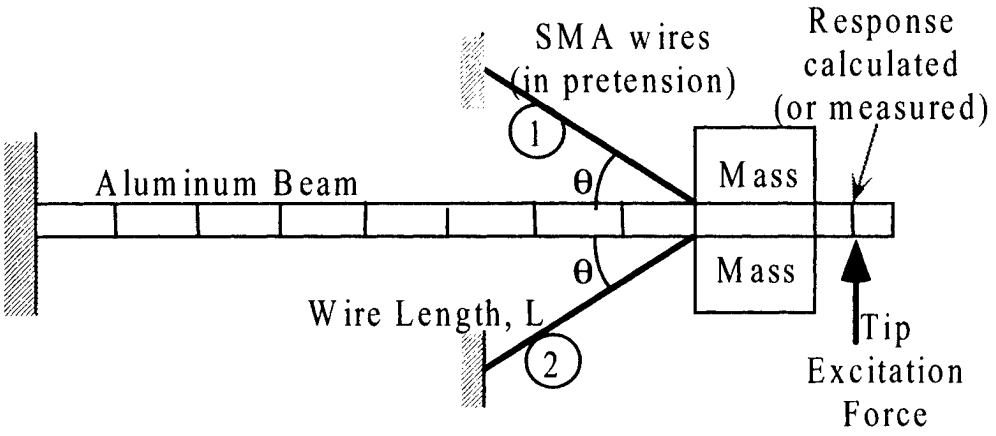


Fig. 1: Schematic sketch of clamped-free beam with tip mass and symmetrically mounted pseudoelastic SMA wires to introduce damping of flexural vibrations

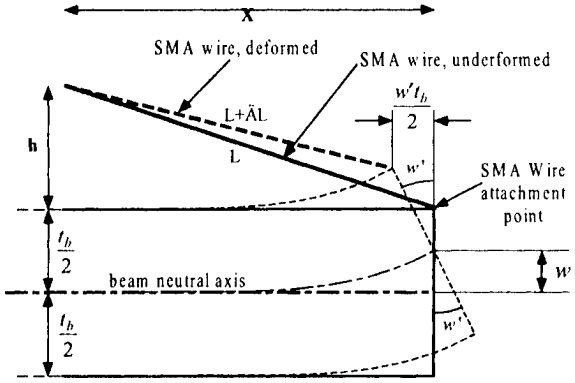


Fig. 2: Schematic of SMA wire in deformed configuration

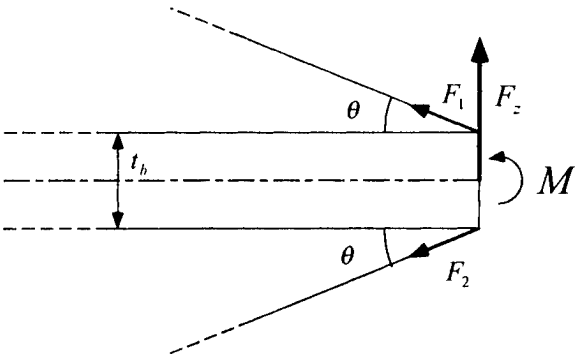


Fig. 3: Force and moment exerted on the beam by the SMA wires at the point of attachment

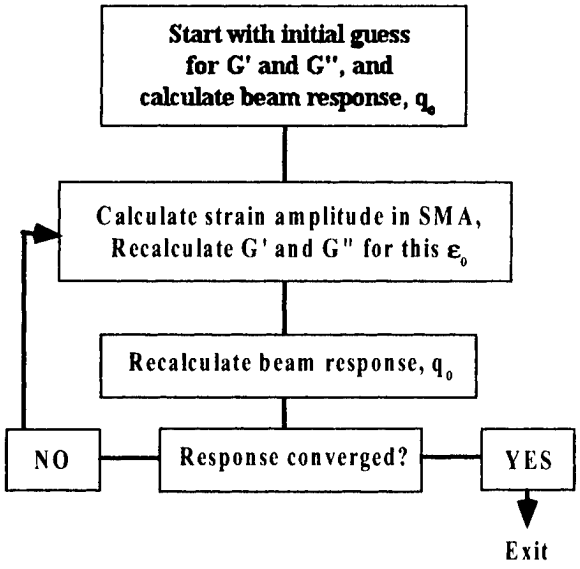


Fig. 4: Flowchart depicting the iterative scheme used to calculate the system response

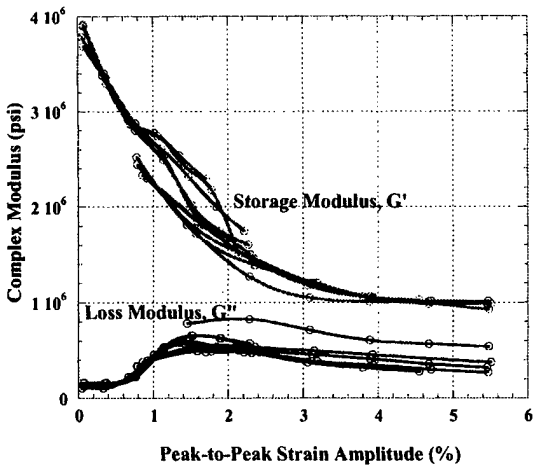


Fig. 5: Compilation of data showing SMA complex modulus variation v/s strain amplitude

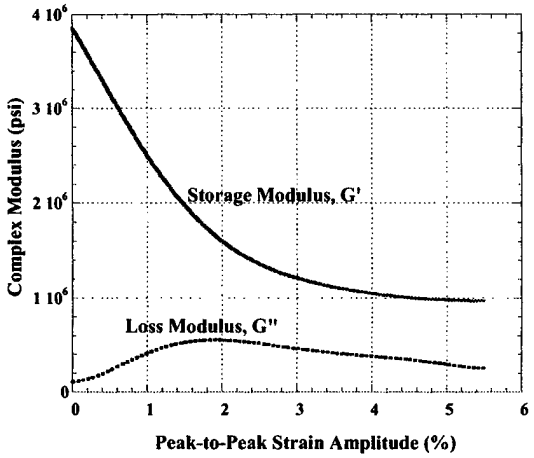


Fig. 6a: Approximation of SMA complex modulus variation versus strain amplitude

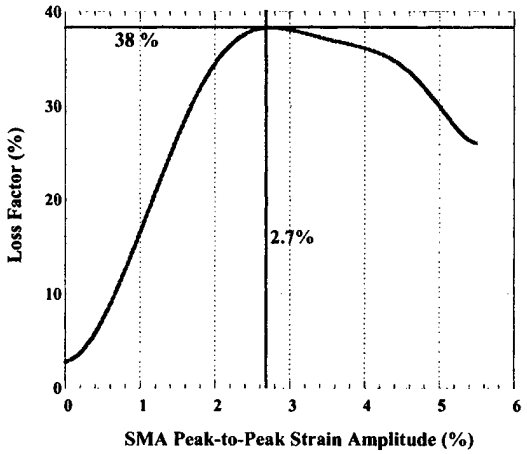


Fig. 6b: SMA wire (material) loss factor versus strain amplitude

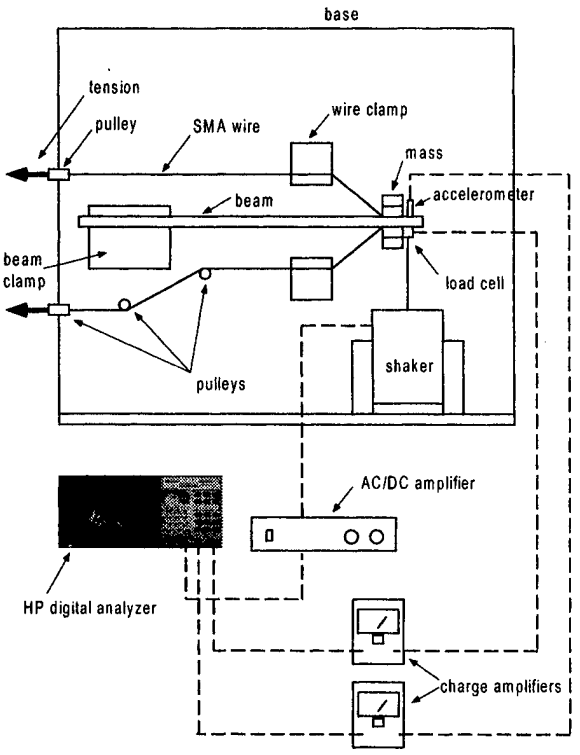


Fig. 7: Schematic of Experimental Setup

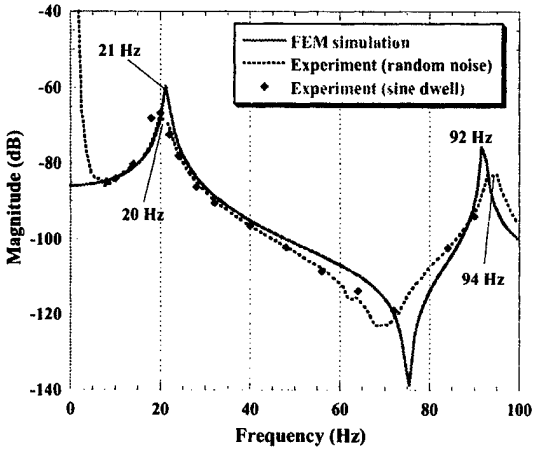


Fig. 8: Frequency Response Function, validation of FEM simulation with experimental data

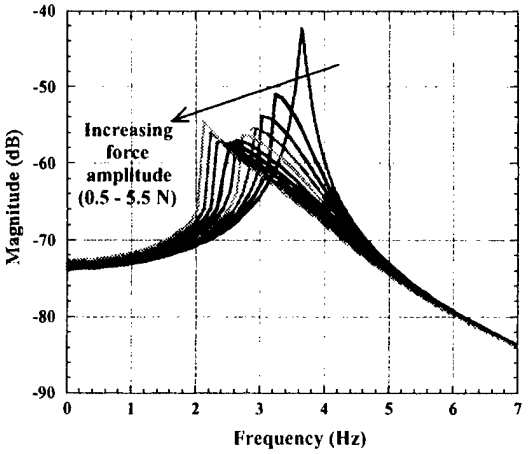


Fig. 9a: Compliance Response Functions for increasing values of excitation amplitude, P_o

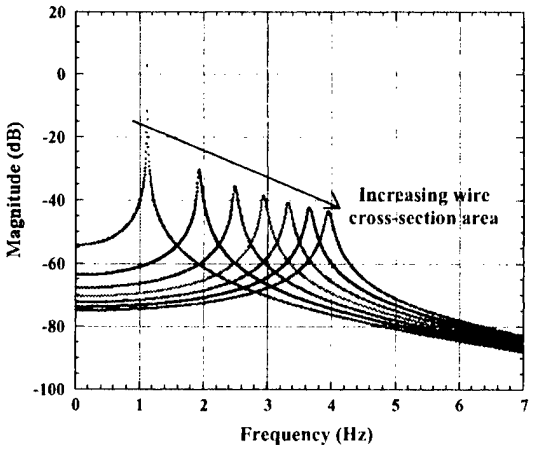


Fig. 10a: Compliance Response Function for increasing SMA cross-section area, $P_o = 0.01N$

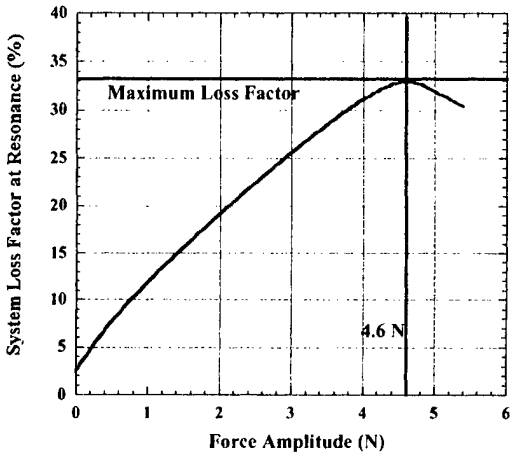


Fig. 9b: Variation of modal damping versus excitation force amplitude, P_o

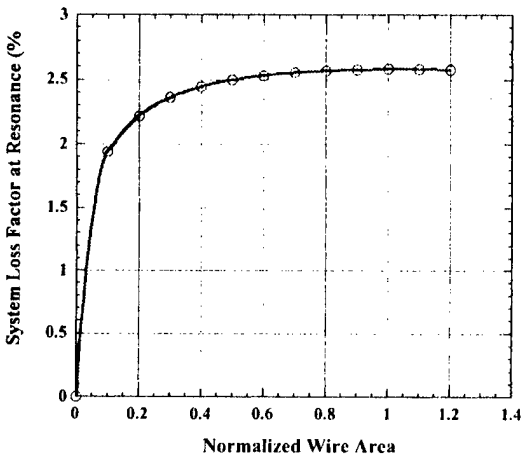


Fig. 10b: Variation of modal damping versus SMA wire cross-section area, $P_o = 0.01N$

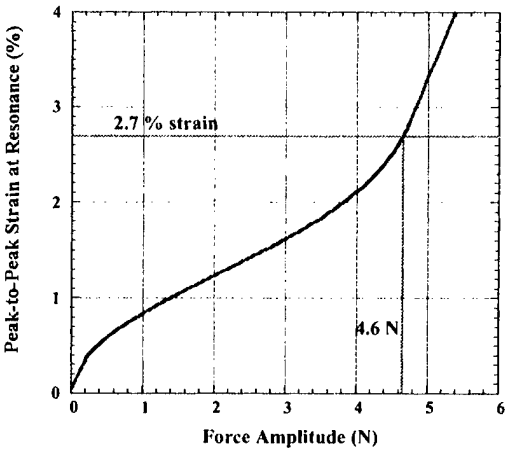


Fig. 9c: Variation of SMA wire strain level at resonance versus excitation amplitude, P_o

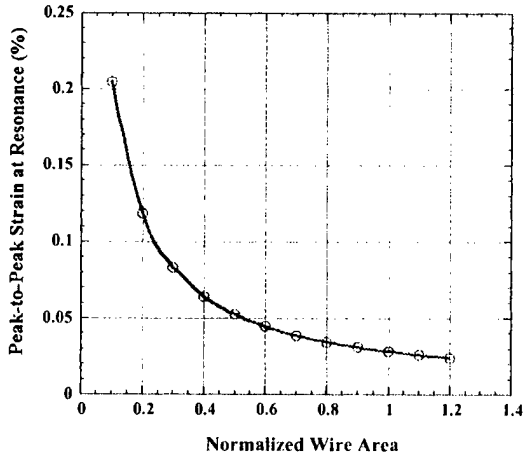


Fig. 10c: Variation of SMA wire strain level versus SMA wire cross-section area, $P_o = 0.01N$

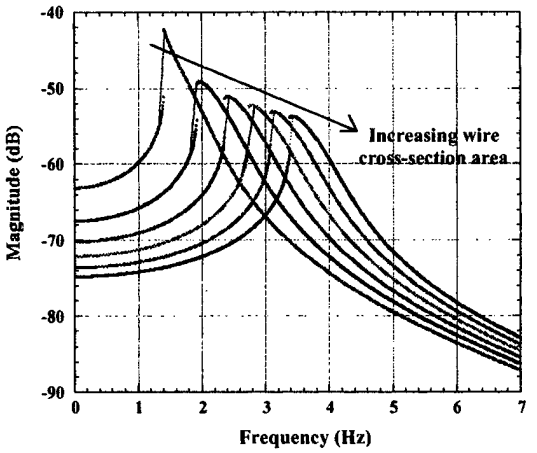


Fig. 11a: Compliance Response Function for increasing SMA cross-section area, $P_o = 1.0N$

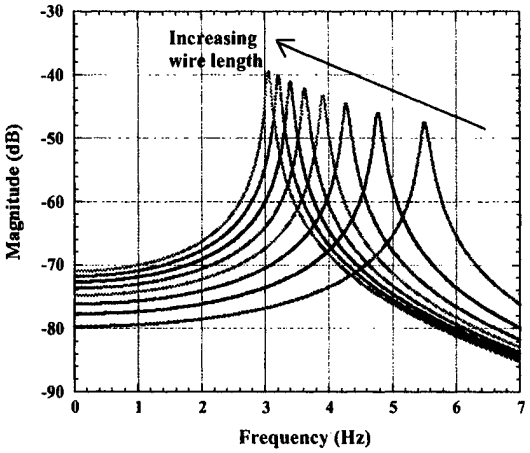


Fig. 12a: Compliance Response Function for increasing SMA wire length, $P_o = 0.01N$

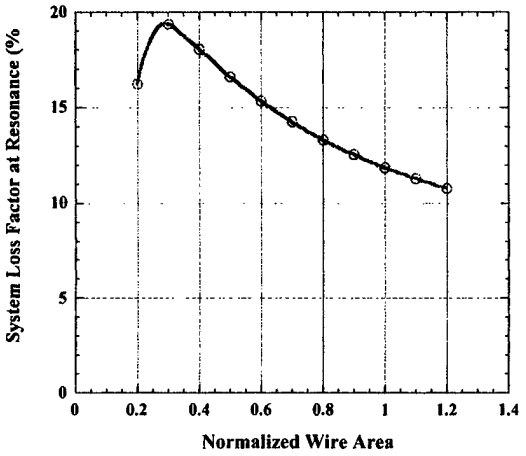


Fig. 11b: Variation of modal damping versus SMA wire cross-section area, $P_o = 1.0N$

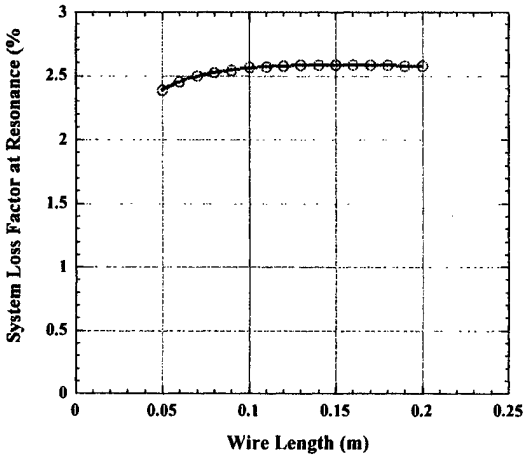


Fig. 12b: Variation of modal damping versus SMA wire length, $P_o = 0.01N$

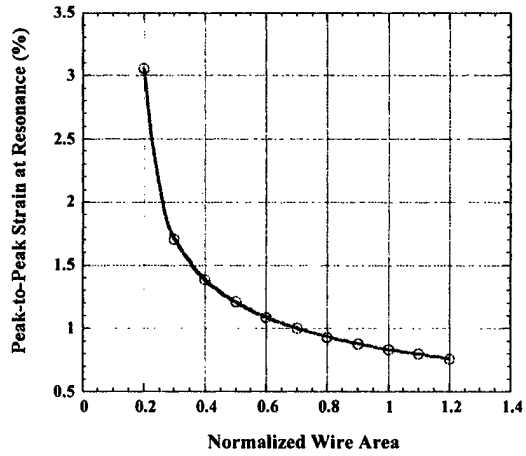


Fig. 11c: Variation of SMA wire strain level versus SMA wire cross-section area, $P_o = 1.0N$

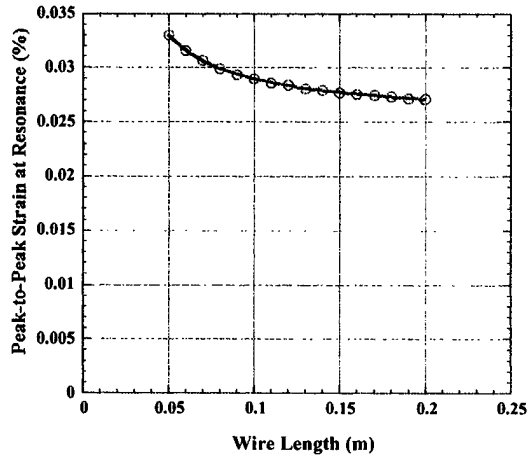


Fig. 12c: Variation of SMA wire strain level versus SMA wire length, $P_o = 0.01N$

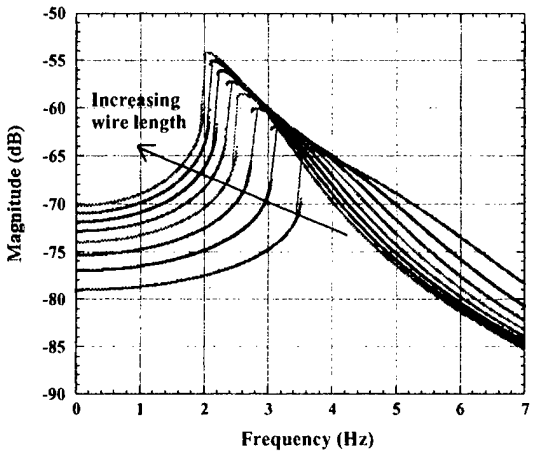


Fig. 13a: Compliance Response Function for increasing SMA wire length, $P_o = 4.0N$

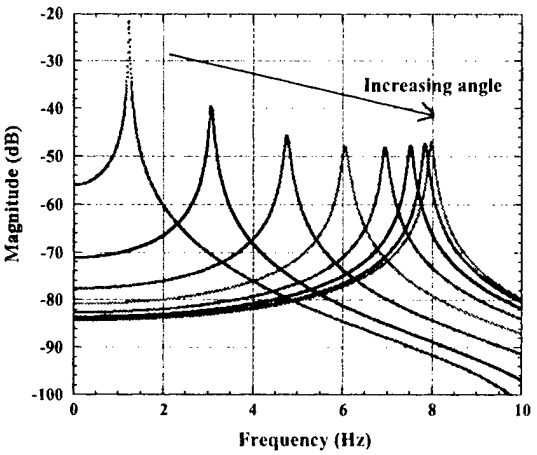


Fig. 14a: Compliance Response Function for increasing angle, θ, $P_o = 0.01N$

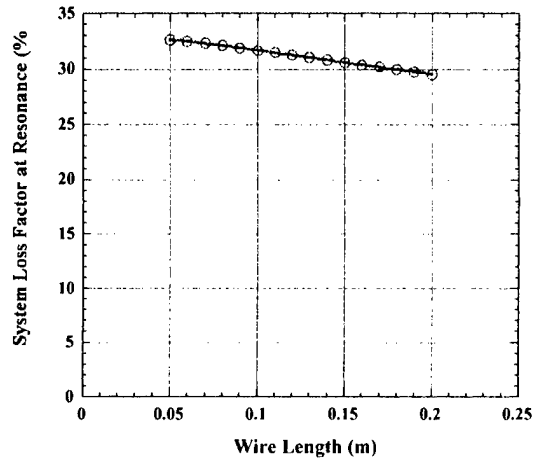


Fig. 13b: Variation of modal damping versus SMA wire length, $P_o = 4.0N$

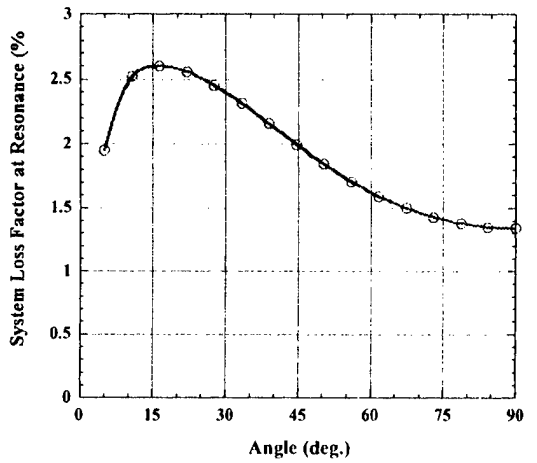


Fig. 14b: Variation of modal damping versus angle, θ, between wire and beam, $P_o = 0.01N$

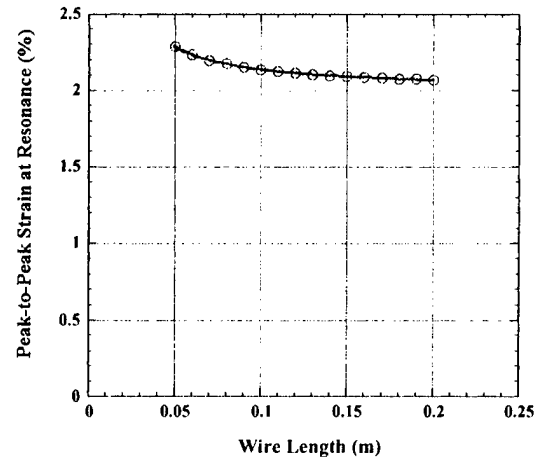


Fig. 13c: Variation of SMA wire strain level versus SMA wire length, $P_o = 4.0N$

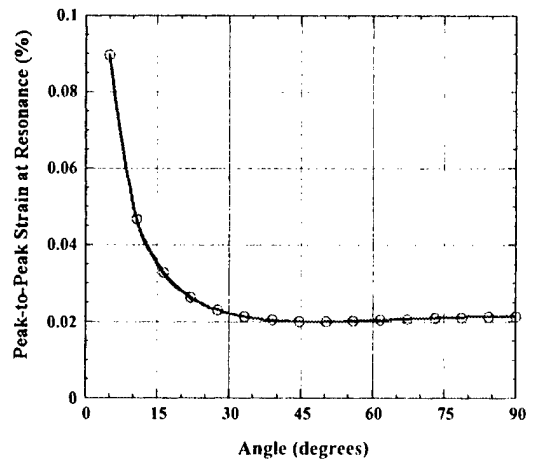


Fig. 14c: Variation of SMA wire strain level versus angle θ, $P_o = 0.01N$

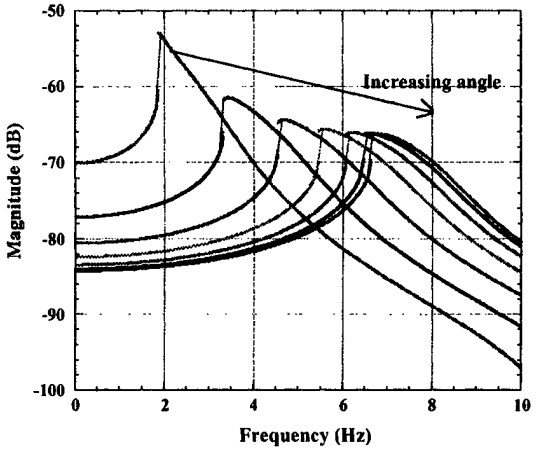


Fig. 15a: Compliance Response Function for increasing angle, θ, $P_o = 4.0N$

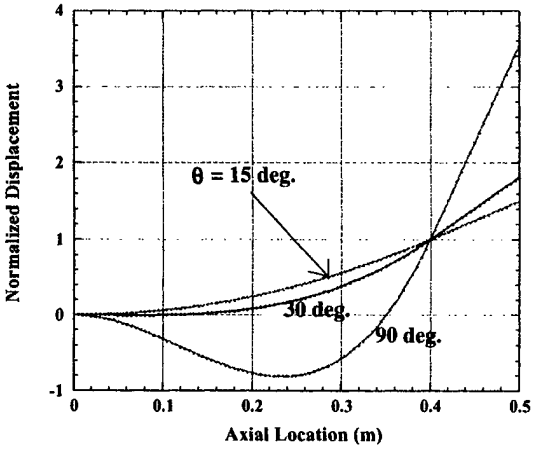


Fig. 16: Mode shapes of the beam for different values of the angle, θ, between beam and wire

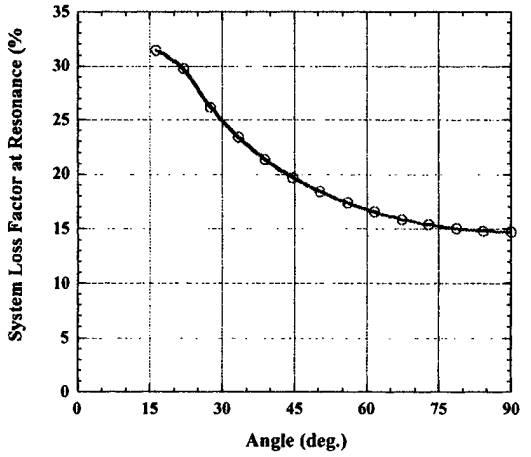


Fig. 15b: Variation of modal damping versus angle, θ, between wire and beam, $P_o = 4.0N$

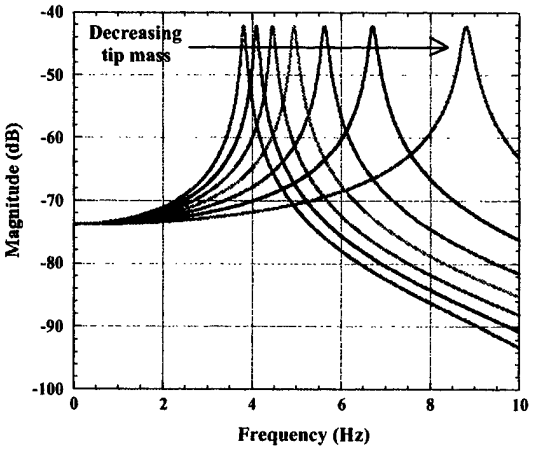


Fig. 17: Compliance Response Function for increasing values of tip mass, $P_o = 0.01N$

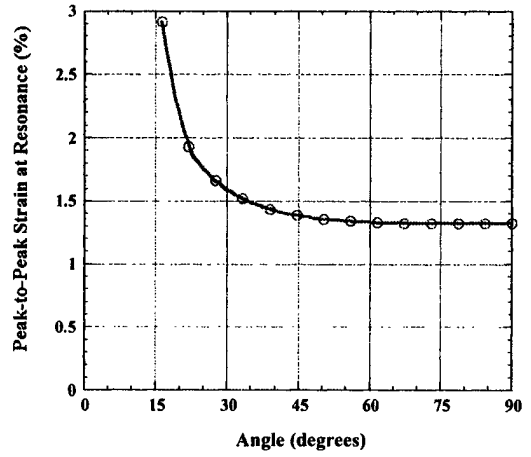


Fig. 15c: Variation of SMA wire strain level versus angle θ, $P_o = 4.0N$

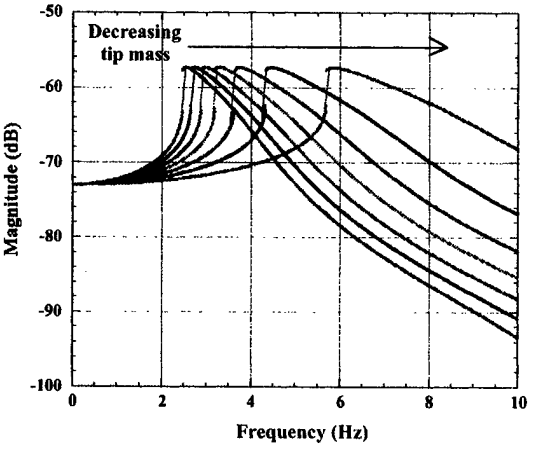


Fig. 18: Compliance Response Function for increasing values of tip mass, $P_o = 4.0N$

DAMPING WITH SHAPE MEMORY ALLOYS FOR STRUCTURAL SYSTEMS

Christian Boller, Peter Konstanzer, Yuji Matsuzaki, Tadashige Ikeda

ABSTRACT

To examine damping characteristics of a structure coupled with Shape Memory Alloys (SMAs), a series of numerical simulations were carried out. The structural model we considered consisted of a cantilever steel beam supported with SMA wires at the tip. The pseudoelastic transformation model that the third author and his coworkers proposed was applied to estimate the stress-strain relationship of the SMA wires. For estimating the temperature of the wires an energy and heat flow equation was introduced. The results showed that the damping performance could be made significantly better by using the SMA wires as a damping material. Moreover, it was found that there was an optimal heat transfer condition. Finally, the temperature change of the SMA wire was more than 30 K during one period in a quasi-adiabatic case. Since the transformation stress depends on the temperature, the effect of temperature change should be taken into account for analyses of vibration behaviors of a structure coupled with SMAs.

INTRODUCTION

Shape Memory Alloys (SMAs) show the pseudoelastic behavior in some temperature range. Because their stress-strain relationships show a large hysteresis loop then, they are expected as a damping material, a shock absorber, and so on. However, since their behaviors are non-linear and complicated due to the phase transformation, before applying SMAs to an actual structural system, one must collect fundamental data and present a theoretical model to understand the mechanism of these behaviors and to perform trade-off studies toward an optimal design of the system.

Although in most experiments on SMA wires measurements have been performed under quasi-static and isothermal conditions [for example, 1, 2], in some experiments they have been performed at various strain rates. McCormik et al. [3] measured the temperature of a SMA wire

---

Christian Boller, EADS Military Aircraft, P.O.Box 80 11 60, 81663 Munich, Germany.
Peter Konstanzer, DaimlerChrysler AG, Research and Technology, P.O.Box 80 04 65, 81663 Munich, Germany.
Yuji Matsuzaki and Tadashige Ikeda, Department of Aerospace Engineering, Nagoya University, Chikusa, Nagoya 464-8603, Japan.

during the pseudoelastic transformation at strain rates from 6.7×10^{-5} to 6.7×10^{-2} (s^{-1}) and observed that the temperature change strongly depended on the strain rate. Wolons et al. [4] measured pseudoelastic loops up to 10 (Hz) and showed that the loops were significantly modified depending on the frequency of cyclic loading. It can be seen from these two experiments that the assumption of the isothermal condition may not be used for an analysis of behaviors of SMAs alone or structures coupled with SMAs vibrating at a relatively high strain rate or frequency, for instance, at a strain rate higher than approximately 10^{-4} (s^{-1}) in a still air.

With respect to theoretical models, the third author and his coworkers proposed a one-dimensional isothermal pseudoelastic constitutive model based on a thermaodynamical energy introducing a concept of a phase interaction energy, which is the energy dissipated during phase transformation [5-7]. Using a simple model of mass-spring connected to a SMA wire they examined a passive damping effect of the SMA in an isothermal condition [8]. Moreover, coupling an energy and heat flow equation with this constitutive model to consider the temperature change of SMAs, they performed a numerical analysis on the phase transformations of a SMA wire at some strain rates and showed theoretically that the strain rate and the temperature were very influential to the SMA behaviors [9, 10].

In this paper using this theoretical model including the effect of temperature change, damping performance of a structure coupled with SMAs is investigated. Especially, we examine the effect of volume fraction of the SMA and heat transfer to surrounding environment on the damping behaviors.

ANALYTICAL MODEL

Cantilever Beam Model

Figure 1 shows a schematic diagram of a beam structure coupled with SMA wires. The structure consists of a cantilever steel beam supported by SMA wires at the tip. SMA wires are completely in the austenite phase in the stress free state at the room temperature and are pre-strained so that the stress-strain relationship during vibration lies around the center of the bounding pseudoelastic hysteresis loop. The load acting on the beam can be calculated using

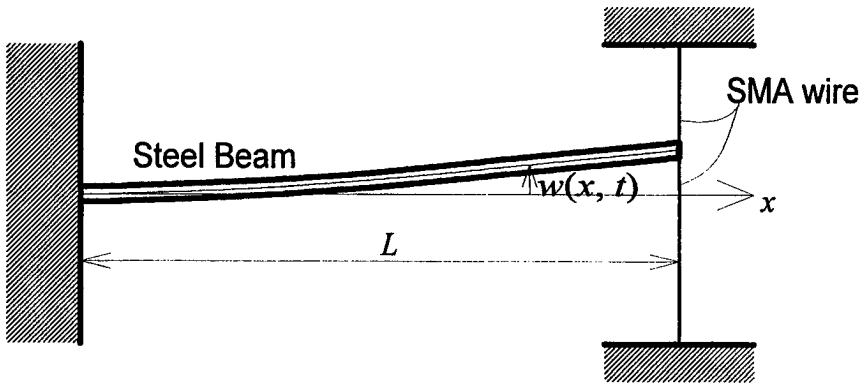


Figure 1. Schematic diagram of a model of cantilever beam supported with SMA wires at the tip.

the stress-strain-temperature relationship of a SMA wire presented by Kamita et al. [5-7] and the energy and heat flow equation presented by Matsuzaki et al. [9, 10]. To estimate the motion of the steel beam Euler-Bernoulli beam theory is used.

Stress-Strain Relationship of the SMA wire

According to Kamita et al.'s model [5-7], the stress and strain during the martensitic and reverse transformation are given by the following formula:

$$\sigma(z,T,\phi_a)=\frac{-kE\varepsilon_0+\sqrt{F(z,T,\phi_a)}}{k-1}, \tag{1.1}$$

$$\varepsilon(\sigma,z,T)=\frac{\sigma}{E_I}+\alpha(T-T_0)+z\varepsilon_0, \tag{1.2}$$

where

$$F(z,T,\phi_a)=k^2E^2\varepsilon_0^2+kE^2\alpha^2(k-1)^2(T-T_0)^2+2k(k-1)E\left(\psi+\frac{\partial\phi_a}{\partial z}\right),$$
$$E_I=\frac{kE}{1+(k-1)z},\ k=E_1/E_2,\ E=E_2,\ \psi=(S_{01}-S_{02})T-(U_{01}-U_{02}). \tag{1.3}$$

z, T, ε_0, α, E_i, T_0, S_{0i}, and U_{0i} denote the martensite volume fraction, the temperature of the wire, the strain associated with the lattice structure of the martensite, the thermal expansion coefficient, the Young's modulus, and the temperature, the entropy, and the internal energy in the initial state, respectively. The quantities with the subscripts 1 and 2 represent those for austenitic and martensitic phase, respectively. ϕ_a is the phase interaction energy function and given as follows:

$$\phi_a=\begin{cases}\phi_{aM}(z,T) & \text{for martensitic transformation}\\ \phi_{aA}(z,T) & \text{for reverse (austenitic) transformation,}\end{cases} \tag{1.4}$$

When no phase transformation occurs, the stress-strain relationship is given by Eq. (1.2) with a fixed value of z.

Energy and Heat Flow Equation

The temperature of the wire is changed by the latent heat due to the phase transformation, the heat transfer to the surrounding environment, and the energy dissipation during the phase transformation process. According to Matsuzaki et al.'s model [9, 10] the temperature is estimated by the following energy and heat flow equation:

$$\rho CdT=\rho H_L dz+\dot{Q}dt+dE_D, \tag{2.1}$$

where

$$\dot{Q} = \frac{4h}{d}[T_S - T(t)], \tag{2.2}$$

$$dE_D = \frac{\{\sigma - \sigma_{\phi_a=0}\}\{d\varepsilon + d\varepsilon_{\phi_a=0}\}}{2}. \tag{2.3}$$

ρ, C, H_L, $\dot{Q}$, t, dE_D, d, h, and T_S denote, respectively, the density, the specific heat capacity, the latent heat, the energy exchange between the wire and the surround environment per unit time and unit volume, the time, the energy dissipated during the phase transformation process per unit volume, the diameter of the wire, the convection coefficient between the wire and the surrounding environment, and the temperature of the surrounding environment. $\sigma_{\phi_a=0}$ and $\varepsilon_{\phi_a=0}$ are, respectively, the stress and strain in the hypothetical case where no phase interaction energy is assumed to be needed during the phase transformation process.

Equation of Motion of the Beam

Using Euler-Bernoulli beam theory, the equation of motion of a cantilever beam is given as follows:

$$D\frac{\partial^4 w(x,t)}{\partial x^4} + \mu\frac{\partial^2 w(x,t)}{\partial t^2} = f(x,t), \tag{3.1}$$

where x, w, D, and μ denote the coordinate in the longitudinal direction, the deflection, the flexural rigidity, and the mass per unit length of the beam. f is the distributed transverse loading. Since a concentrated force due to the SMA wire acts on the beam at its end in this case, f is given by the following formula:

$$f(x,t) = F(t)\delta(x - L)\ , \tag{3.2}$$

where

$$F(t) = \{\sigma_u(t) - \sigma_l(t)\}\frac{\pi d^2}{4}. \tag{3.3}$$

F, σ_u, σ_l, δ, and L are, respectively, the force due to the SMA wires, the stress of the upper and lower wire, the Dirac delta function, and the length of the beam.

According to modal analysis, we assume the deflection of the beam can be approximated by

$$w(x,t) = \sum_{n=1}^{\infty} q_n(t) W_n(x), \tag{4}$$

where $W_n(x)$ and $q_n(t)$ are the natural modes of the cantilever beam and the generalized coordinates, respectively.

Then the equation of motion is written in terms of q_n and shown as follows:

$$\omega_n{}^2 q_n(t) + 2\varsigma_n \omega_n \frac{dq_n(t)}{dt} + \frac{d^2 q_n(t)}{dt^2} = \frac{f_n(t)}{\mu}, \tag{5.1}$$

where we introduce a viscous damping force of the steel cantilever beam system. The generalized load due to the SMA wire, $f_n(t)$, is given by

$$f_n(t) = F(t) W_n(L). \tag{5.2}$$

NUMERICAL ANALYSIS

Parameters

A series of numerical simulations are performed using MATLAB, where the first three modes are considered. The property of the SMA wire used here is based on the experimental data of Ref. [1]. First we estimate the phase interaction energy function from the stress-strain data at temperatures of 333K and 373K:

$$\begin{aligned} \frac{\partial \phi_{aM}}{\partial z} &= \left(2.18\times10^{-5} T + 4.57\times10^{-4}\right) + z\left(1.63\times10^{-6} T + 4.89\times10^{-4}\right), \\ -\frac{\partial \phi_{aA}}{\partial z} &= \left(2.22\times10^{-5} T - 0.880\times10^{-4}\right) + (1-z)\left(4.90\times10^{-6} T - 7.27\times10^{-4}\right). \end{aligned} \tag{6}$$

Other material constants of the SMA wire are as follows:

E_1 = 8.27×10 (GPa), E_2 = 2.76×10 (GPa), α = 1.04×10^{-7} (K^{-1}), C = 4.70×10^2 (J/kg K), ε_0 = 4.80×10^{-2}, ρ = 6.49×10^3 (kg/m^3), H_L = 1.82×10^4 (J/kg), S_{01} - S_{02} = 3.97×10^5 (J/K m^3), U_{01} - U_{02} = 1.16×10^8 (J/m^3).

The material constants of the steel beam, the dimensions of the system, and the initial condition are as follows:

D = 1.09×10^2 (N/m^2), μ = 1.95 (kg/m), ζ_i = 1.30×10^{-3} (i = 1, 2, and 3), L = 1.00 (m), the pre-strain of the SMA wire = 3.50×10^{-2}, the initial length of the SMA wire = 1.00 (m), T_S = 3.53×10^2 (K), $w(0, L)$ = 3.50×10^{-2} (m), $T(0) = T_S$.

Results

Figure 2 shows the effect of wire diameter, that is, volume fraction of the SMAs, on the oscillatory behavior of the beam for $h = 2\times10^5$ (W/m^2 K). The thin, thick, and dashed curves represent the tip displacement for $d = 0$, 5×10^{-5}, and 1×10^{-4} (m), respectively, where $d = 0$ (m) means the steel beam alone. It is seen that even the SMA wire with a diameter of 5×10^{-5} (m) shows a good performance as a damping material, and the thicker the wire diameter, the better the damping performance. The amplitude of vibration decreases almost linearly until it becomes approximately 3×10^{-3} (m) and then the small amplitude vibration continues both for $d = 5\times10^{-5}$ and 1×10^{-4} (m). The stress-strain relationship of the upper SMA wire is shown in Fig. 3. The area of the stress-strain hysteresis loop, which is actually spiral shape, decreases with increase of number of cycles and finally the loop becomes a line, where no energy dissipation occurs. The strain range of this line is approximately 0.006, which corresponds to a tip displacement of 3×10^{-3} (m). The temperature is almost constant in this case (see dashed curve in Fig. 6) because the heat generated during the phase transformation process transfers to the surrounding environment immediately due to the high convection coefficient.

Next we examine the effect of heat transfer to the surrounding environment on the oscillatory behavior of the structure. Figure 4, 5, and 6 show the tip displacements, and stress-strain and temperature-strain curves of the upper SMA wire for $d = 5\times10^{-5}$ m, respectively. The thin, thick, and dashed curves represent those relationships for $h = 2\times10$, 2×10^3, and 2×10^5 (W/m^2 K), which correspond to a quasi-adiabatic case, an intermediate case, and a quasi-isothermal case, respectively. It can be seen from Fig. 4 that the damping performance for $h = 2\times10^3$ (W/m^2 K) is the best of the three. When $h = 2\times10^3$ (W/m^2 K), since the speed of heat transfer to the surrounding environment is slower than the speed of self-heating and cooling of the SMA due to the latent heat and the energy dissipation, the temperature of the SMA wire is different from the room temperature. In this case the temperature during the loading process is higher and the temperature during the unloading process is lower than for $h = 2\times10^5$ (W/m^2 K) in a wide strain range. Since the transformation stress increases with rise of the temperature, the difference between the martensitic and the reverse transformation stress becomes larger than that for $h = 2\times10^5$ (W/m^2 K) and the dissipated energy also becomes larger. As for the behavior for $h = 2\times10$ (W/m^2 K), the temperature increases approximately linearly during the loading and decreases approximately linearly during the unloading for the first several cycles, where the maximum temperature change is more than 30K. Moreover, the temperature during the loading is lower than the temperature during the unloading. This is because the heat generated inside the SMA can hardly transfer to the surrounding environment. Since the difference between the phase transformation stresses becomes smaller in this case, the amplitude of vibration decreases most slowly of the three. After the stress-strain relationship becomes a line, the temperature decreases monotonically because no self-heating and cooling due to the phase transformation occurs.

CONCLUSION

To examine damping performance of a structure coupled with SMAs, numerical simulations were performed using a model of cantilever steel beam supported with SMA wires at the tip. The results showed that the damping performance could be made significantly better by using SMA wires. Moreover, it was found that there was an optimal heat transfer condition. Finally, the temperature change during one period was more than 30 K in a quasi-adiabatic case. Since the transformation stress depends on the temperature, the effect of temperature change should be taken into account when one analyzes the vibration behaviors of a structure coupled with SMAs.

REFERENCES

1. Lin, P.H., Tobushi, H., Tanaka, K., Hattori, T., and Makita, M. 1994. "Pseudoelastic Behavior of TiNi Shape Memory Alloy Subjected to Strain Variations," *J. of Intelligent Material Systems and Structures*, **5**, pp. 694-701.

2. Miyazaki, S., Otsuka, K., and Suzuki, Y. 1981. "Transformation Pseudoelasticity and Deformation Behavior in a Ti-50.6at%Ni Alloy, *Scripta Metallurgica*, **15**, pp. 287-292.

3. McCormick, P.G., Liu, Y., and Miyazaki, S. 1993. "Intrinsic Thermal-Mechanical Behaviour Associated with the Stress-Induced Martensitic Transformation in NiTi," *Materials Science and Engineering*, **A167**, pp. 51-56.

4. Wolons, D., Gandhi, F., and Malovrh, B. 1998. "Experimental Investigation of the Pseudoelastic Hysteresis Damping Characteristics of Shape Memory Alloys Wires," *J. of Intelligent Material Systems and Structures*, **9**, pp. 116-126.

5. Kamita, T. and Matsuzaki, Y. 1996. "Pseudoelastic Theory of Shape Memory Alloys," *Proceed. of SPIE's 1996 Symposium on Smart Structures and Materials*, **2717**, pp. 509-516.

6. Kamita, T. and Matsuzaki, Y. 1998. "One-Dimensional Pseudoelastic Theory of Shape Memory Alloys," *Smart Materials and Structures*, **7**, pp. 489-495.

7. Matsuzaki, Y., Kamita, T., and Ishida, A. 1997. "Stress-Strain-Temperature Relationship of Shape Memory Alloys," *Proceed. of SPIE's 1997 Symposium on Smart Structures and Materials*, **3241**, pp. 230-236.

8. Matsuzaki, Y., Kamita, T., and Yamamoto, T. 1998. "Vibration Characteristics of Shape Memory Alloys," *Proceed. of SPIE's 1998 Symposium on Smart Structures and Materials*, **3329**, pp. 562-569.

9. Matsuzaki, Y., Naito, H., and Yamamoto, T. 1998. "Pseudoelastic Behavior of Shape Memory Alloys with Temperature Change," *Proceed. of 40th Structures and Strength Conference*, Japanese Society for Aeronautics and Space Science, pp. 209-212.

10. Matsuzaki, Y., Naito, H., and Ikeda, T. 1999. "Pseudoelastic Thermal Behavior of Shape Memory Alloys," *Proceed. of 10th International Conference on Adaptive Structures and Technologies*, pp. 208-214.

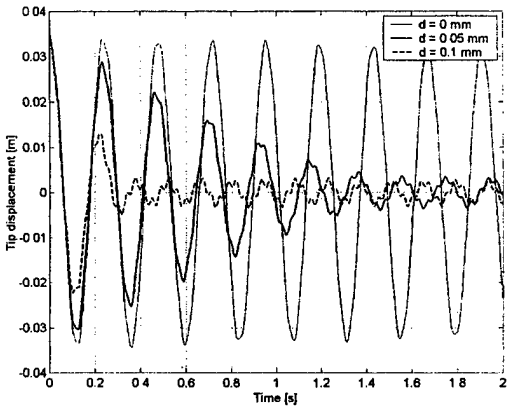


Figure 2. Effect of wire diameter on the oscillatory behavior.

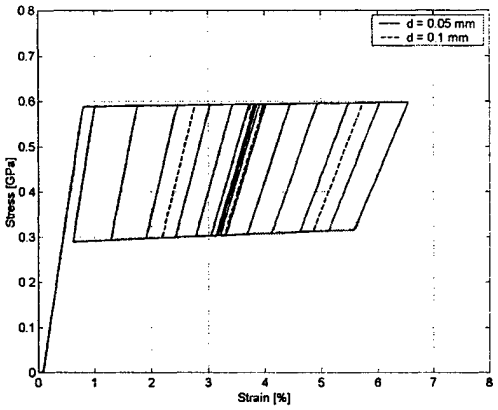


Figure 3. Effect of wire diameter on the stress-strain relationship.

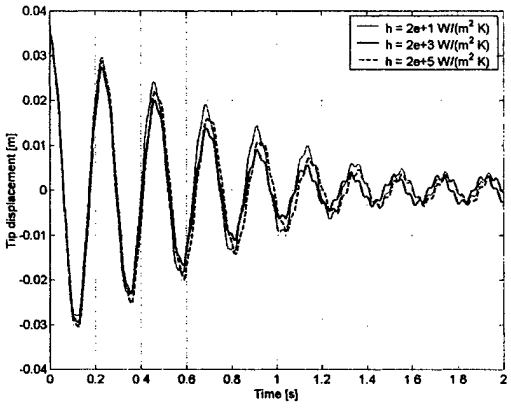


Figure 4. Effect of convection coefficient on the oscillatory behavior.

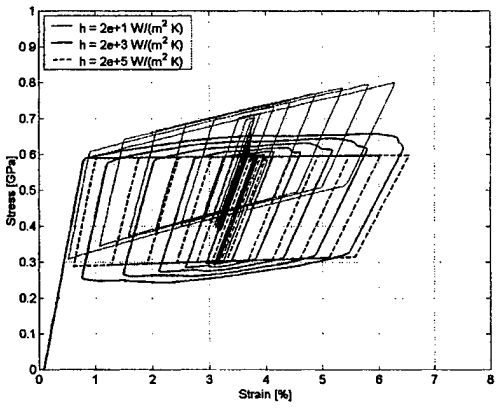


Figure 5. Effect of convection coefficient on the stress-strain relationship.

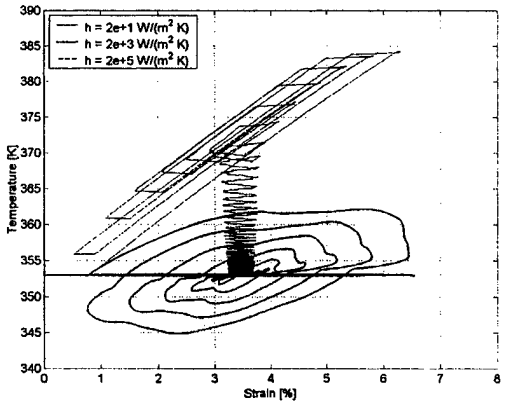


Figure 6. Effect of convection coefficient on the temperature-strain relationship.

STRESS-STRAIN RELATIONSHIP OF PSEUDOELASTIC TRANSFORMATION OF SHAPE MEMORY ALLOYS DURING LOADING CYCLES

Hisashi Naito,[1] Ken Funami,[1] Junpei Sato,[1] Yuji Matsuzaki,[1] Tadashige Ikeda[1]

ABSTRACT

This study examines analytically the effect of loading cycles on stress-strain hysteresis loops of pseudoelasticity of shape memory alloys. To account for the decrease in phase transformation stresses, etc., the effect of residual martensite is taken into account in a thermomechanical model which is based on the phase interaction energy function proposed in our previous studies. A functional form of volume fraction of the residual martensite which monotonically increases with increasing loading cycles has been determined using experimental stress-strain loops measured at a very low strain rate. It is shown that a simple function of the volume fraction of the residual martensite may model complicated behavior of the transformations during the loading cycles.

INTRODUCTION

Shape memory alloys (SMAs) have attracted great attention of many investigators engaged in structures and structural dynamics research because of their potential applicability to smart structural systems. SMAs reveal very interesting but complicated thermomechanical behaviors, such as shape memory effect and pseudoelasticity due to crystal phase transformations among the austenite characterized by body-centered tetragonal and the twinned and the detwinned martensite by face-centered cubic.

In order to use such SMAs effectively as active or passive component materials of a smart structure, it is very important to fully understand the thermomechanical characteristics of their complex behavior. At the same time it is necessary to develop a thermomechanical model of SMAs representing complexity of constitutive relationships observed in experiments, so that we may analyze and design smart structural systems using such a thermomechanical model. Hence, several investigators presented analytical theories founded on thermomechanical and energy bases [for instance, 1-7]. Among them, introducing a general function of the dissipation potential for the transformations called the phase interaction energy function (PIEF), Kamita and Matsuzaki [7] proposed a one-dimensional pseudoelastic model,

[1]Department of Aerospace Engineering, Nagoya Univesity, Chikusa,Nagoya 464-8603, Japan.

which may model Tanaka's transformation kinetics [2] theoretically and represent available experimental results on pseudoelastic hysteresis quantitatively. They have also pointed out that the stress-induced phase transformations take place along stable equilibrium paths, so that the transformations are not of a jump-type phenomenon as predicted previously using a specific form of the dissipation potential [1, 3, 4]. Taking into account the effect of temperature in the PIEF, Matsuzaki, Kamita and Ishida [8] studied the pseudoelastic hysteresis at different temperatures and compared to available measured data [9]. Damped oscillations of a simple mass-spring system connected with a SMA [10] wire were also studied to show the effectiveness of SMA's pseudoelasticity for passive damping. The effect of loading rate on the pseudoelastic behavior was analytically studied to show that the loading rate had a strong influence on the temperature change of the SMA materials [11]. The thermomechanical model based on the PIEF was also proved to be effective in treating the shape memory effect [12].

One of remarkable features of SMAs is large hysteresis observable during pseudoelastic austenite-martensite phase transformations in a loading and unloading process above the austenite finish temperature. It is seen that the stress-strain hysteresis observed in experiments considerably changes especially in an early stage of cyclic loading. For instance, martensitic and reverse transformation stresses decrease with increasing number of the cycles while the residual strain at zero applied stress increases. The change in physical, mechanical and functional properties is considered due to training effect of stress, strain, or thermal cycling. In the early phase of cycling, adjustment or annihilation of local irregularity may clearly take place on grain boundaries and interfaces between the austenite and the martensite but also in the interior of crystals. At the same time, there occurs formulation of defects, such as dislocations and cracks, and may these defects are combined to produce arrays of the defects during the cycles. These arrays may act as local obstacles against the transformations and lead to the formation of intrusions.

In an intruded domain surrounded by the boundaries and interfaces containing the defects, especially the strained martensite may remain without transforming back to the austenite during the unloading process. Such martensitic domain keeps internal stresses and strains as residual. The residual stress is nothing but a pre-stress in the phase of loading. When an external stress is applied, the apparent martensitic transformation start stress becomes smaller. As the number of cycles increases, these training effects will diminish gradually. The training effect was analytically studied by Tobushi and his coworkers [13], taking into account directly the loading cycles in the expressions of residual strain at zero applied stress and the martensite and the reverse transformation start temperature.

In the present analysis, to represent the complex constitutive behaviors during the loading cycles, we will take into account the effect of the residual martensite in the thermomechanical model based on the phase interaction energy function (PIEF). The present model is, therefore, based on more fundamental approach than the analysis proposed in Ref. 13.

ANALYSIS OF PSEUDOELASTIC TRANSFORMATIONS

Introduction of residual martensite

In a one-dimensional model of a simple conventional pseudoelastic transformation, we

usually consider two volume fractions, one for the austenite denoted by z_1 and the other for the martensite by z_2 where $z_1 + z_2 = 1$. During the loading process, the alloy changes from the initial state defined by $z_2 = 0$ to the final state by $z_2 = 1$ and it is opposite for the unloading.

To treat the effect of the residual martensite on the constitutive relationship during the transformations, we will consider the martensite and the residual martensite separately, even though their thermomechanical properties are the same. In addition to the volume fractions z_1 and z_2, therefore, we introduce one more volume fraction for the residual martensite denoted by z_{2R}. At the initial virgin state of the alloy we assume that the crystal phase is fully austenitic, that is, $z_1 = 1$, $z_2 = z_{2R} = 0$. In the course of the martensitic transformation during the first loading process, z_2 increases from 0. The change in the volume fractions will be described using a variable z for z_2. For the first loading, therefore, $z_2 = z$, $z_1 = 1 - z$ and $z_{2R} = 0$ while z changes from 0 to 1. We assume that z_2 becomes unity at the end of the martensitic transformation for any number of cycle, N, that is, $z_2 = 1$, $z_1 = z_{2R} = 0$. The unloading process, therefore, always starts from the state which is fully martensitic. It is assumed, however, that only some portion of the martensite may transform into the austenite, while the rest remains as the residual martensite. Then, the fraction of the residual martensite in the unloading process of the (N-1)st cycle is denoted by $f(N)$. The volume fraction of the martensite which may transform into the austenite is $1 - f(N)$, and in the course of unloading of the (N-1)st cycle, the fractions are described as $z_2 = z$, $z_1 = (1 - f(N))(1 - z)$ and $z_{2R} = f(N)(1 - z)$ for which z changes from 1 to 0. At the end of the (N-1)st unloading, we have $z_2 = 0$, $z_1 = 1 - f(N)$ and $z_{2R} = f(N)$. The loading process of the Nth cycle starts with this set of the fractions. The volume fraction of the residual martensite increases with increasing number of loading cycles because of the accumulation of defects. $f(N)$ is, therefore, always greater than $f(N-1)$.

In this model we have distinguished the martensite and the residual martensite and considered the process from the martensite to the residual martensite for the unloading and the opposite process at an instantaneous moment of the change from the loading to the unloading. As their thermomechanical properties are exactly the same, these processes are non-transformational, so that neither latent heat is generated nor energy is dissipated.

Residual stresses and strains

First, we evaluate the amount of residual stresses and strains of the austenite and the martensite of a mixed state of the alloy without external stress at the end of the (N-1)st unloading process. As mentioned above, the volume fractions of the austenite and the residual martensite are $1 - f(N)$ and $f(N)$, respectively. It is assumed that they have the same amount of strain at the zero applied stress. Therefore, the austenite is positively strained by ε_{10} from a natural state of zero strain to induce a tensile stress σ_{10} (positive) while the residual martensite is negatively strained by ε_{2R0} to produce a compressive stress σ_{2R0} (negative).

Taking into account the volume fractions of the austenite and the residual martensite, we have the equation of stress balance at zero applied stress as

$$(1-f(N))\sigma_{10}+f(N)\sigma_{2R0}=0, \tag{1}$$

where

$$\sigma_{10}=E_1\{\varepsilon_{10}-\alpha_1(T-T_0)\},\ \sigma_{2R0}=E_2\{\varepsilon_{2R0}-\alpha_2(T-T_0)\}. \tag{2}$$

Like in our previous studies [7, 8, 10-12], the thermomechanical relationship for the transformations will be analyzed using the Helmholtz free energies of the austenite and the martensite, and the phase interaction energy. The specific energy of the alloy material in the mixed state of the austenite, the detwinned martensite and its residual martensite is assumed as

$$\phi=(1-f(N))(1-z)\phi_1+z\phi_2+f(N)(1-z)\phi_{2R}+(1-f(N))\phi_a, \tag{3a}$$

$$\phi=(1-f(N+1))(1-z)\phi_1+z\phi_2+f(N+1)(1-z)\phi_{2R}+(1-f(N+1))\phi_a, \tag{3b}$$

for the loading and the unloading of the Nth cycle, respectively. The Helmholtz free energy densities ϕ_i are defined by

$$\phi_i=\frac{1}{2}E_i(\varepsilon_i-\varepsilon_{i0})^2-\alpha_iE_i(\varepsilon_i-\varepsilon_{i0})(T-T_0)-C_i\left(T-T_0-T\log\frac{T}{T_0}\right)$$
$$+U_{i0}-TS_{i0},$$
$$\text{for } i=1,\ 2 \text{ and } 2R \tag{4}$$

where $\varepsilon_{10}=0$, and ε_{20} is the macroscopic strain associated with the lattice structure at a fully detwinned martensite. We assume $\varepsilon_{2R0}=\varepsilon_0/2$. Parameters C_i, E_i, α_i, U_i and S_i are specific heats, Young's modulus, thermal expansion rates, specific internal energies, and specific entropies of the austenite and the martensite, respectively. T is the temperature of the alloy. A suffix 0 attached to ε_i, U_i, S_i and T denotes a reference state. The temperature is assumed to keep uniform in the material. The densities of the austenite and the martensite are assumed to be the same, that is, $\rho=\rho_1=\rho_2=\rho_{2R}$. ϕ_a is the phase interaction energy function, which is rewritten as

$$\phi_a(z,T)=\begin{cases}\phi_{MT} & \text{for martensitic transformation (MT),}\\ \phi_{RT} & \text{for reverse transformation (RT).}\end{cases} \tag{5}$$

Stress-strain-temperature relationship

The extended potential energy π is defined as $\pi=\phi-\bar{\sigma}\varepsilon$, where $\bar{\sigma}$ is an externally applied stress. Applying the potential energy minimum theorem and manipulating mathematical operations along the same line with our previous analysis, we obtain the stress-strain equilibrium state defined by

$$\sigma(z,T,N) = -\left[I(N,T) + \sqrt{I(N,T)^2 - 4H(N)\{J(N,T) + (1 - f(N))\partial\phi_a/\partial z\}} \right] \Big/ 2H(N), \tag{6}$$

where I, J and H are functions of N and T. Their mathematical expressions are given in Ref. 14. The forms of both functions $\phi_a(z,T)$ and $f(N)$ are to be determined using stress-strain curves measured in an experiment.

NUMERICAL EXAMPLE

We performed a numerical simulation analysis of stress-strain during loading cycles using an experimental result on a TiNi shape memory alloy wire (Lot No. Ef3256) of 0.2mm in diameter and 273K in Af, produced by Kanto Tokushu Steel Company. In Fig. 1 curves for the cycle of N=1, 10, 100 and 1000 are plotted. The curves were measured at a strain rate of 1.0×10^{-3} sec^{-1} and room temperature Tr of 293K in our laboratory. The loading strain was so slow that the thermal equilibrium was kept between the material and the surrounding environment, that is, T=Tr=293K. Numerical values used in the calculation are:

$E_1 = 4.25\times10$ (GPa), $E_2 = 1.87\times10$ (GPa), $k = E_1/E_2 = 2.27$, $T = 293$ (K),
$\alpha = 1.04\times10^7$ (K^{-1}), $C = 4.70\times10^2$ (J/kg K), $\varepsilon_{20} = 2.8\times10^{-2}$, $\varepsilon_{2R0} = 1.4\times10^{-2}$,
$\psi_1 = (S_{01} - S_{02})T - (U_{01} - U_{02}) = 1.76\times10^7$ (J/m^3),
$\psi_2 = (S_{01} - S_{02R})T - (U_{01} - U_{02R}) = 1.35\times10^7$ (J/m^3).

Using the stress-strain curve of the first cycle, we fixed numerically the phase interaction energy function, actually its first derivative form, as given by

$$\frac{\partial\phi_{aM}}{\partial z} = 4.183\times10^6 + 2.74\times10^5 z, \tag{7a}$$

$$-\frac{\partial\phi_{aA}}{\partial z} = 4.057\times10^6 + 7.14\times10^5(1 - z). \tag{7b}$$

To determine a functional form for the fraction of the residual martensite $f(N)$, we assume it in a simple form of

$$f(N) = \beta(1 - 1/N^{\gamma}), \tag{8}$$

where numerical values of parameters β and γ are selected using available experimental results, so that the stresses and strains at the martensite transformation start and finish as well as those at the reverse transformation be well predicted analytically. Numerical selection was made through application of a least-square error method regarding the start and finish stresses. The procedure of selection of β and γ is detailed in Ref. 14. One set of the well-fitted values is $\beta = 0.974$ and $\gamma = 0.0998$. In Fig. 2, numerical results corresponding

to the curves shown in Fig. 1 are illustrated. Agreement between the experimental and the numerical stress-strain curves is very good.

CONCLUSION

We have analyzed the influence of loading cycles on the stress-strain relationship of pseudoelasticity of shape memory alloys. To account for the change in thermomechanical behaviors, the effect of residual martensite is taken into account in the thermomechanical model based on the phase interaction energy function. The functional form of volume fraction of the residual martensite has been determined using experimental stress-strain loops measured at a very low strain rate at our laboratory. The volume fraction of the residual martensite in a very simple form has well modeled complicated behaviors of the phase transformations during the loading cycles.

REFERENCES

1. Falk, F. 1983. "One-Dimensional Model of Shape Memory Alloys," *Archieves of Mechanics*, 35-1, pp. 63-84.
2. Tanaka, K. 1986. "A Thermomechanical Sketch of Shape Memory Effects: One-Dimensional Tensile Behavior," *Res. Mechanica*, 18, pp. 251-263.
3. Mueller, I., and Xu, H. 1991. "On the Pseudo-Elastic Hysteresis," *Acta Metallic Materials*, 39, pp. 263-271.
4. Raniecki, B., Lexcellent, C., and Tanaka, K. 1992. "Thermodynamic Model of Pseudoelastic Behaviour of Shape Memory Alloys," *Archieves of Mechanics*, 44-3, pp. 261-284.
5. Brinson, L.C. 1993. "One-Dimensional Constitutive Behavior of Shape Memory Alloys: Thermomechanical Derivation with Non-Constant Material Functions and Redefined Martensite Internal Variable," *J. of Intelligent Material Systems and Structures*, 4, pp. 229-242.
6. Boyd, J.G., and Lagoudas, D.C. 1994. "Thermomechanical Response of Shape Memory Composites," *J. of Intelligent Material Systems and Structures*, 5, pp. 333-346.
7. Kamita, T., and Matsuzaki, Y. 1998. "One-Dimensional Pseudoelastic Theory of Shape Memory Alloys," *Smart Materials and Structures*, 7, pp. 489-495.
8. Matsuzaki, Y., Kamita, T., and Ishida, A. 1997. "Stress-Strain-Temperature Relationship of Shape Memory Alloys," *Proceed. of SPIE's 1997 Symposium on Smart Structures and Materials*, 3241, pp. 230-236.
9. Lin, P.H., Tobushi, H., Tanaka, K., Hattori, T., and Makita, M. 1994. "Pseudoelastic Behavior of TiNi Shape Memory Alloy Subjected to Strain Variations," *J. of Intelligent Material Systems and Structures*, 5, pp. 694-701.
10. Matsuzaki, Y., Kamita, T., and Yamamoto, T. 1998. "Vibration Characteristics of Shape Memory Alloys," *Proceed. of SPIE's 1998 Symposium on Smart Structures and Materials*, 3329, pp. 562-569.
11. Matsuzaki, Y., Naito, H., and Ikeda, T. 2000. "Pseudoelastic Thermal Behavior of Shape Memory Alloys," *Proceed. of 10th Int. Conf. Adaptive Structures and Technologies*, Technomic Pub., Lancaster, pp. 208-214.
12. Naito, H, Matsuzaki, Y., Ikeda, T. 2000. "Deformation Behavior of Shape Memory Alloys in Various Temperature Ranges," *Proceed. of SPIE's 2000 Symposium on Smart Structures and Materials*, 3992, pp. 463-473
13. Tobushi, H., Iwanaga, H., Tanaka, K., Hori, T., and Sawada, T. 1991. "Stress-Strain-Tempreture Relations of TiNi Shape Memory Alloy Suitable for Thermomechanical Cycling," *Trans. Jpn. Soc. Mech. Eng.*, Ser. A, 57-543, pp. 2747-2752.
14. Sato, J. 2000. "Pseudoelastic Behavior of Shape Memory Alloys," Bachelor's thesis, Dept. of Aerospace Engineering, Nagoya University

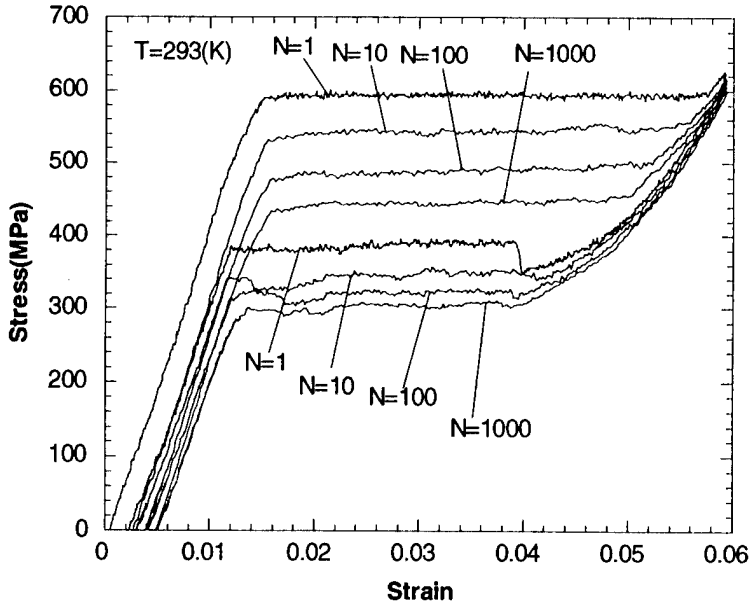


Fig. 1 Experimental Result

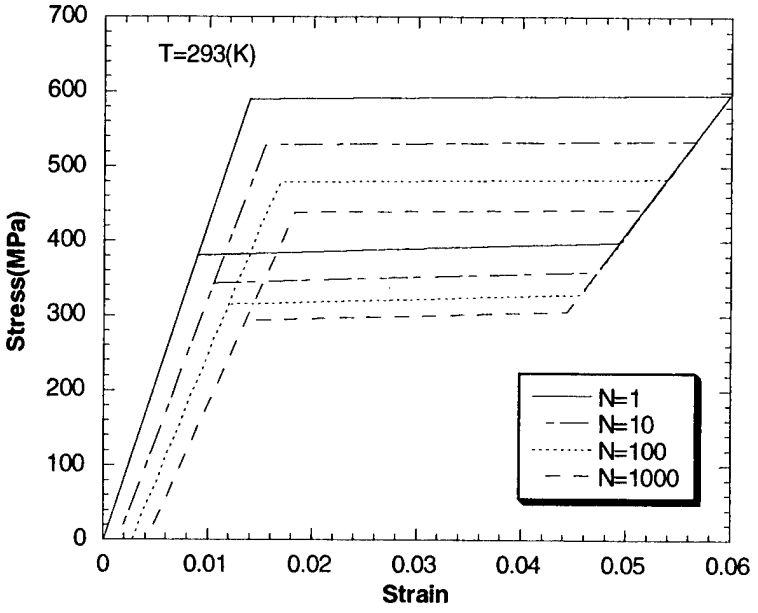


Fig. 2 Numerical Result

BEHAVIORS OF THE SUPERELASTIC SMA COLUMNS UNDER COMPRESSIVE LOADING-UNLOADING CYCLES

Muhammad Ashiqur Rahman, Jinhao Qiu, Junji Tani

ABSTRACT

Some buckling and postbuckling behaviors of the superelastic SMA columns are observed from the axial load versus end shortening curves for a wide range of slenderness ratio (L/k) and compared with those of the SUS304 and Al columns. The experimental procedure comprises of compressive loading on the columns far beyond the point of instability followed by unloading allowing the buckled columns to recover the shapes. It is found that the slender SMA columns buckle elastically while they are in the austenite phase and at lower loads in comparison with the slender Al columns. However, for decreasing L/k, the buckling resistance of the superelastic SMA materials increases most significantly among the three materials used in the investigation and for low L/k, it is comparable to that of SUS304 column. It is also observed that, particularly the slender SMA columns can sustain the buckling load with least change in magnitude for the postbuckling compression. Moreover, for some of the SMA columns, the recovery force increases notably during unloading; contrary to the generally observed trend that load falls off monotonically during unloading of a buckled column. Furthermore, if the slenderness ratio is not too low, they remarkably recover the initial shapes with negligible residual strains when completely unloaded. The above mentioned unique phenomena can be attributed to the special nature of SMA's stress-strain curve and the superelasticity itself. On the other hand, for the whole range of slenderness ratio considered in this study, Al and SUS304 columns are permanently bent after a complete cycle.

INTRODUCTION

Columns made of traditional engineering materials become practically useless once they buckle, due to the fact that usually too large deformation takes place immediately after buckling. Functional material like the superelastic Shape Memory Alloys (SMA) have the unique capability to fully regain the original shape from a deformed state when the mechanical load, which causes the deformation, is withdrawn. The recoverable strains can be on the order of 10% [1,2]. Thus columns made of the superelastic SMA materials may be used under repeated

Institute of Fluid Science, Tohoku University, Katahira 2-1-1, Aoba-ku, Sendai-shi 980-8577, Japan

loading-unloading cycles. Though an enriched literature is readily available mostly on the theoretical constitutive modeling for the superelastic SMA materials, the study on the buckling and postbuckling behavior of columns made of the same materials is rare. Thus the present study is devoted to determine the buckling loads and also to observe the postbuckling behavior of the superelastic SMA columns (some times termed only as the SMA columns in this paper) through a loading-unloading cycle. Similar data are also obtained for SUS304 and Al columns under the same testing conditions for valid comparison. Results are obtained for a wide range of slenderness ratio (48-368) which is supposed to cover all practically useful lengths of columns during applications.

It is a well-known fact that the theoretical buckling loads of structures are higher than those are during applications. The reasons behind this discrepancy between the theoretical and practical buckling loads are mainly attributed to the unavoidable (and often undetected as well) imperfections (physical and/or geometrical) which can not be fully taken into account during theoretical calculations. Predictions of buckling loads for structures based on eigen value solutions usually result in ideal and therefore much higher buckling loads than their real values during applications. Alternately, predictions of buckling loads for structures based on large deformation theory may yield more realistic solutions than the corresponding eigen value solutions under certain conditions as delineated below.

According to Thompson and Hunt [3], the buckling characteristics of any structure, whatever the type of buckling is, may be best comprehended if the equilibrium path of the deformed structure under load is determined for both the prebuckling and postbuckling zones. The first instability of the equilibrium equations on the equilibrium configuration path would correspond to the critical load for any type of buckling. Thus, to accurately determine the buckling loads and observe the postbuckling behaviors, both prebuckling and postbuckling zones of the deformed columns have been comprehensively traced for a complete loading-unloading cycle through the axial load versus end shortening curve, or, mathematically through the equilibrium path.

TEST CONDITIONS AND EXPERIMENTAL PROCEDURE

The experimental method to observe the behaviors of the columns under the compressive loading-unloading cycles is demonstrated in the Figures 1(a), (b). At first, the columns were inserted into the fixtures. During loading, the moving fixture moved towards the fixed one until its predetermined final position (Δ_{set}) was reached. In the mean time, the column buckled. Immediately after the final point of displacement was reached, the moving fixture was moved away from the fixed one. Thus, the profusely deformed column was allowed to gradually recover its shape before the loading. The unloading process was stopped and the cycle ended when the load became approximately zero. The value of Δ after the complete cycle corresponds to the residual axial strain (ε) of the columns.

The materials, configurations and conditions used in this study are as follows. Materials: SMA (Ti49.3 at% Ni50.2at% V0.5at%), Stainless steel (SUS304) and Aluminum. Diameter of the columns (D) = 2 mm, unsupported length, L (mm) =24, 34,44,54, 64,74, 84, 109, 134, 159, 184. Austenite finish temperature of SMA =-3^{0}C. Room temperature range =23^{0}C- 30^{0}C. Machine used= Instron, speed of the cross head during loading-unloading cycle = 2 mm/min. Δ_{set} = 3% for all the columns. Manufacturer of SMA: TOKIN Corporation (Japan).

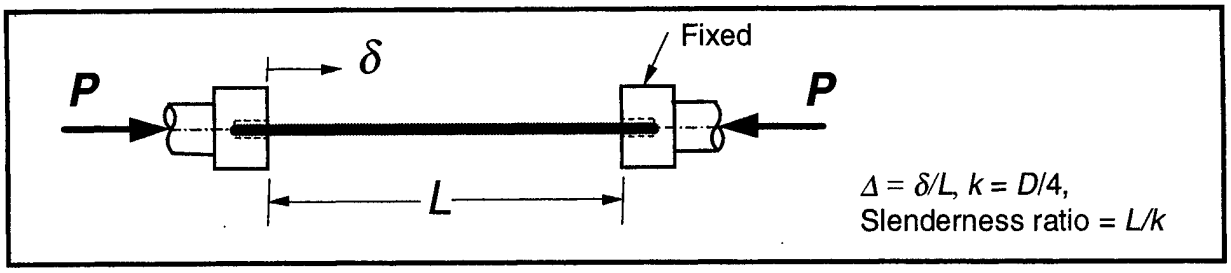


Figure 1 (a). Column inserted into the fixtures.

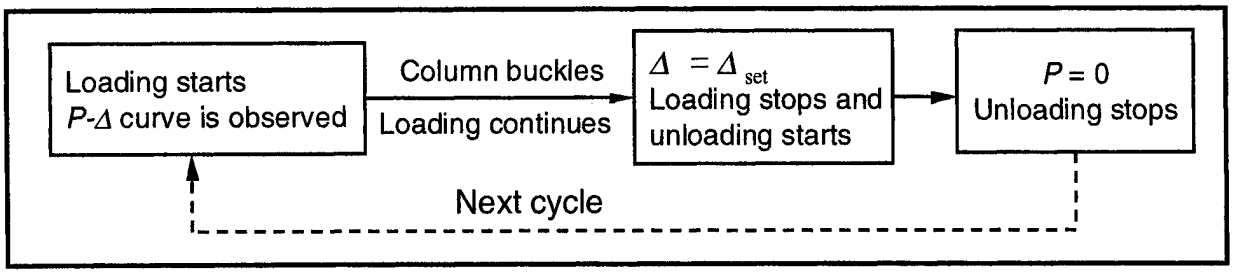


Figure 1(b). Experimental procedure.

RESULTS AND DISCUSSION

The load-end shortening (P-Δ) curves of the deformed columns during the cycle help to determine the buckling loads and also to observe different postbuckling behaviors of the columns. The peak points of those curves are taken as the buckling loads. To precisely discuss and interpret those P-Δ curves, the material properties of the columns, that is, the stress-strain curves and the stress induced martensitic (SIM) phase transformation for the SMA, are briefly discussed below.

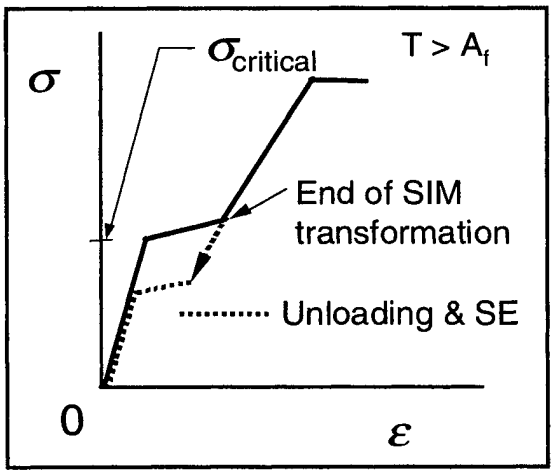


Figure 2(a). Idealized stress-strain diagram for the superelastic SMA.

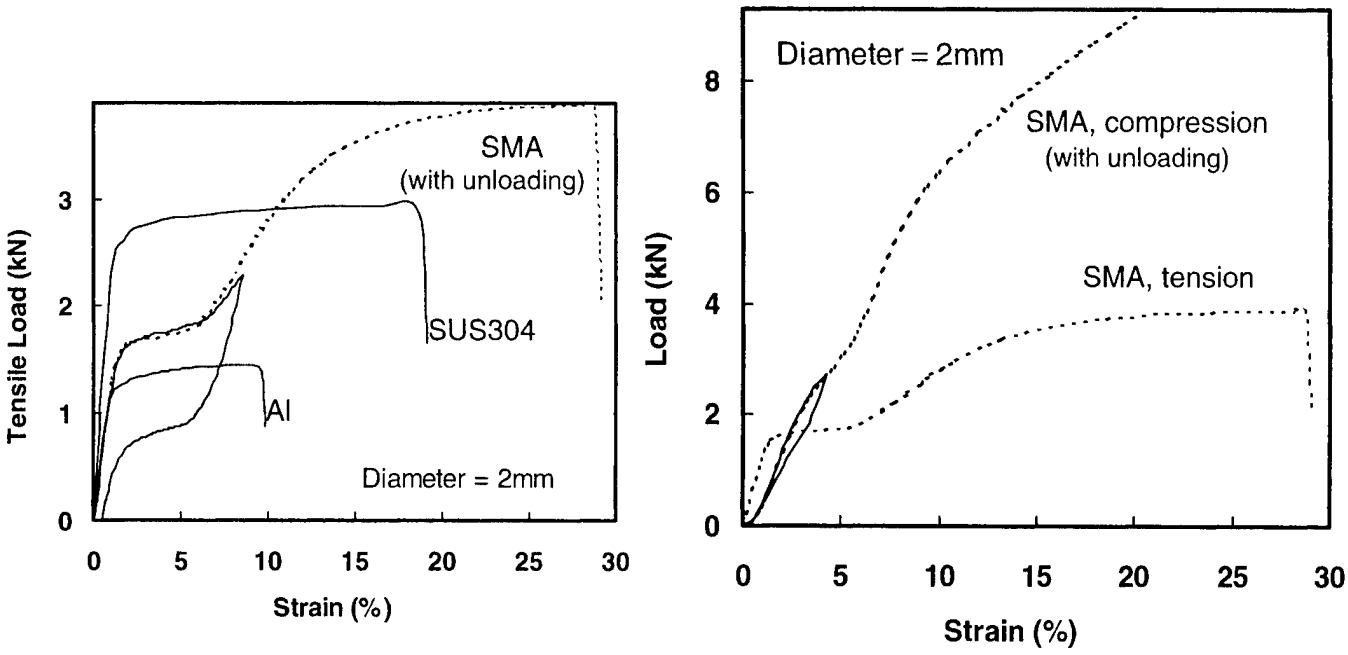
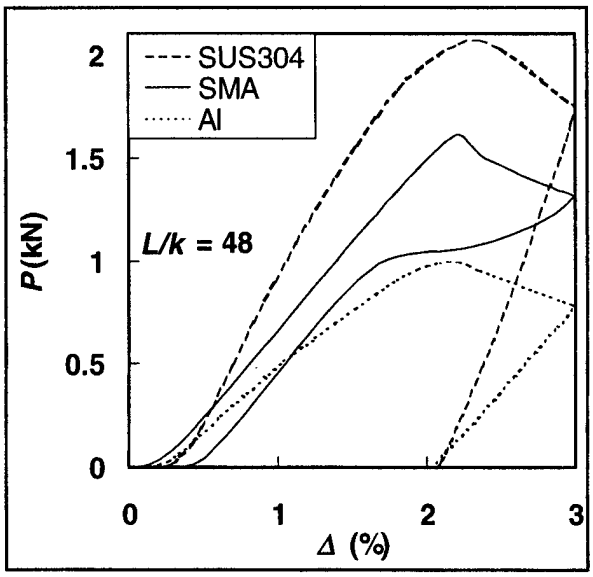


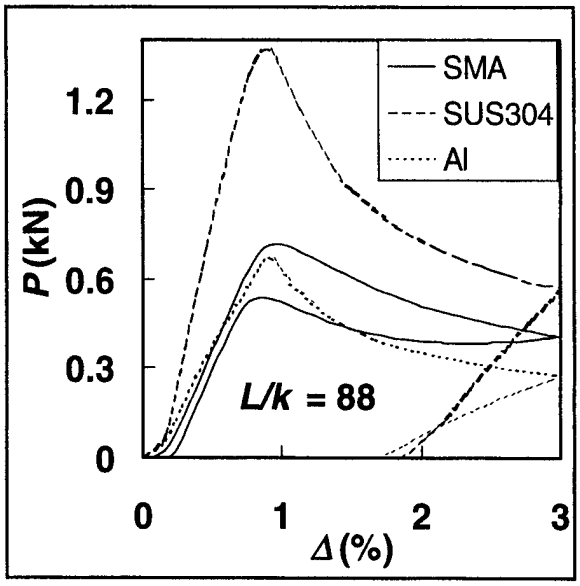
Figure 2(b). Experimental load-displacement curves for the SMA, SUS304 and Al rods.

The idealized stress-strain diagram (Figure 2(a)) for the superelastic SMA has three distinct portions. The first linear portion represents the parent austenite phase. If the stress exceeds the critical value, transformation of the stress induced martensite (SIM) phase starts. When unloaded from any point of this transformation process, the SMA returns to its parent austenite phase and can recover the strains through a hysteresis, which is known as the pseudoelasticity or superelasticity (SE). During experiment, separate SMA specimens were used to check the SE. It can be verified from the experimental tensile load-deformation curve (Figure 2(b)) that after the complete phase transformation for the SMA, plastic slip occurs although material stiffness increases. It is also noteworthy that for large strains the same material has significantly higher strength in compression than in tension (unlike the Al and SUS304 materials). It should be noted here that the deformation of the specimen during experiment was measured directly from the displacement of the loading fixture. For the compression test (Figure 2(b)), to avoid any bending effect of the specimen, L/k was kept less than 12 [4].

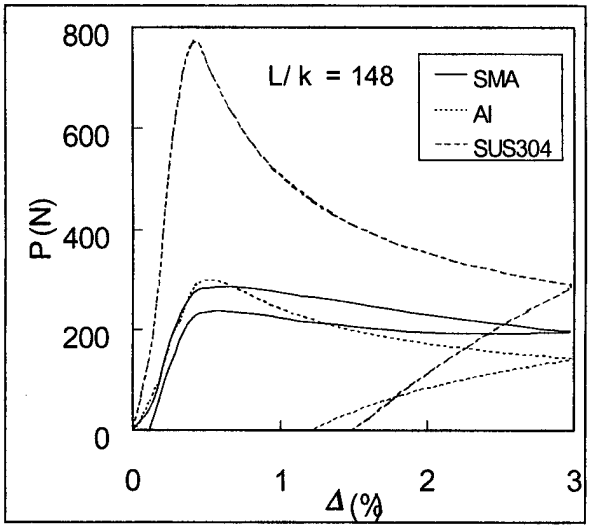
Comparative buckling and postbuckling behaviors of the columns with different L/k are demonstrated by the P-Δ curves as shown in Figures 3(a)-(d). It can be observed that the nature of the P-Δ curves for the SMA columns changes notably with L/k. Naturally, shorter is the column, higher is its buckling load and larger is the corresponding prebuckling deformation (Figures 3(a), (b)). For a certain value of the axial load, the most critical section of the column becomes fully plastic and initiates its failure. As verified by experiments, Al has the lowest yield strength among the three materials. Thus Table 1 shows that the short Al columns (L/k=48-108), have the lowest buckling loads. Moreover, once started plastic deformation continues without appreciable change in the load's magnitude for the case of Al and SUS304 rods (Figure 2(b)). That is why, the buckling loads change by small magnitude with L/k for the short SUS304 and Al columns as shown by Figure 4 and Table 1.



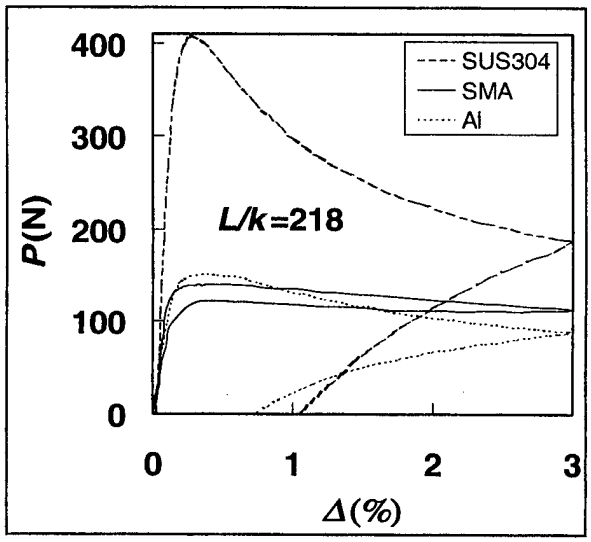
(a)



(b)



(c)



(d)

Figures 3(a)-(c). Axial load-end shortening curves for the columns.

On the other hand, among the three materials, SMA column's buckling load increases most significantly with the decreasing *L/k* (Figure 4). As mentioned, the superelastic SMA material has significantly higher strength in compression than in tension particularly for large strains. It helps short SMA columns to show high buckling resistance. Moreover, it appears that, for too short columns SIM phase transformation is triggered on during continuous compression. After the complete SIM transformation the stiffness of the SMA increases significantly. This increase of the material stiffness may enable too short SMA column to easily sustain much higher buckling load than that of a short SUS304 column [5].

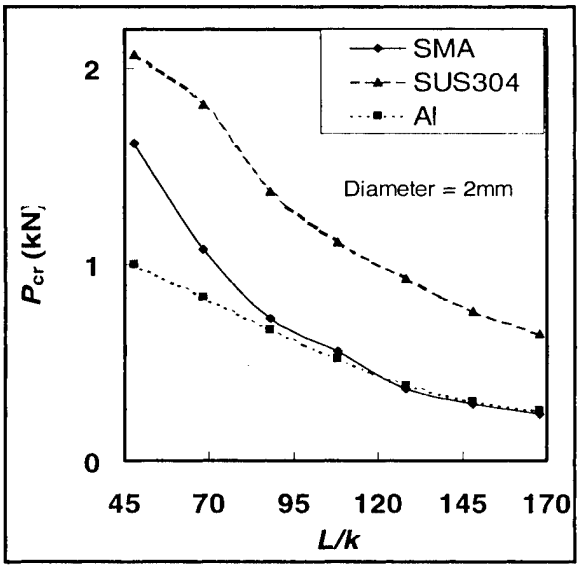


Figure 4. Buckling load versus slenderness ratio.

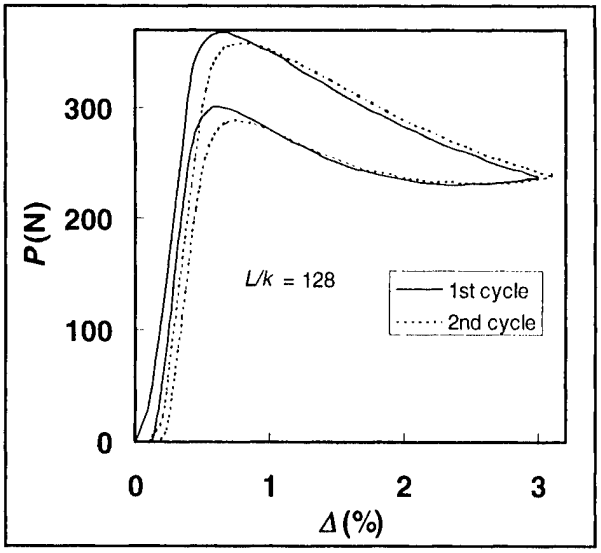


Figure 5. Consecutive cycles for the SMA columns.

However, unlike the short SMA columns, the slender ones can not sustain much axial compression and buckle elastically while they are in the austenite phase (Figures 3(c), (d)). Thus, having the lowest Young's modulus among the three materials, too slender SMA columns have the lowest buckling loads. Table 1 shows that for L/k =128-368, the buckling loads of Al columns are higher than those of SMA columns by 5%-15%. Usually this difference increases with the increasing slenderness ratios. In the same manner, for the above range of the slenderness ratio the buckling loads for SUS304 columns are much higher (about 2.5-3.3 times) than those for SMA columns.

The accuracy of the experimental buckling loads of the present study (Table 1) can be checked by the famous Euler formula ($4\pi^2EI/L^2$, symbols having their usual meanings) for both ends-clamped slender columns. Considering Young's modulus of SUS304 to be 200GPa, for L/k = 218, 268, 318 and 368 the experimental buckling loads are 82%-91% of their theoretical values according to the above formula. Higher is the slenderness ratio, better is the prediction by theory. Thus it can be concluded that the results obtained for columns of other materials and of different slenderness ratios using the same method are also accurate.

One noteworthy postbuckling characteristic of the slender superelastic SMA column is its unique shape recovery due to superelasticy. The measured value of ε after the complete loading-unloading cycle (Table 1) gives a rough estimation of the shape recovery capability of the buckled columns. As seen, after the first cycle the axial residual strain is within 0.04% for L/k =218–368 and around 0.2% for L/k =88-168. Higher is the L/k, better is the shape recovery and it can be concluded that for the present condition of loading those SMA columns (L/k =218–368) will show almost the same buckling and post buckling behaviors for a few repeated cycles. For shorter columns the buckling loads fall gradually after the first cycle (Figure 5). But it is noteworthy that the cumulative residual strains even after two consecutive cycles are too small for the SMA columns (Figure 5 and Table 1).

TABLE 1[1]. BUCKLING LOADS AND RESIDUAL AXIAL STRAINS OF THE COLUMNS

L/k	Material	P_{cr} (N)	ε (%)	*L/k*	Material	P_{cr} (N)	ε (%)
48	SUS304	2041, 2060, 2070	2.1	168	SUS304	638, 648, 648	1.4
	SMA	1481, 1501, 1614	0.35		SMA	226, 232, 234	0.15
	Al	981, 991, 991	2.1		Al	240, 245, 254	1.0
68	SUS304	1638, 1717, 1815	2.0	218	SUS304	426, 427, 427	1.1
	SMA	1020, 1060, 1079	0.3		SMA	137, 139, 143	0.04
	Al	814, 824, 834	1.9		Al	153, 154, 155	0.75
88	SUS304	1364, 1373, 1373	1.9	268	SUS304	294, 295, 307	0.9
	SMA	697, 716, 726	0.2		SMA	90, 91, 91	0.04
	Al	638, 667, 667	1.7		Al	103, 105, 105	0.5
108	SUS304	1118, 1158, 1177	1.8	318	SUS304	217, 217, 218	0.65
	SMA	520, 540, 559	0.2		SMA	65, 66, 66	0.02
	Al	500, 520, 520	1.5		Al	71, 74, 76	0.35
128	SUS304	893, 922, 932	1.6	368	SUS304	165, 167, 167	0.55
	SMA	358, 363, 367	0.2		SMA	52, 53, 53	0.02
	Al	378, 383, 387	1.3		Al	53, 56, 59	0.22
148	SUS304	765, 769, 769	1.5				
	SMA	280, 285, 286	0.15				
	Al	299, 301, 301	1.2				

[1]For each type of material at least 3 tests were performed for a particular *L/k*. Three highest values of P_{cr} and the corresponding maximum ε are shown.

Table 2 compares the load sustaining capability of the columns in the postbuckling region. It can be noted that load falls drastically for the short columns of Al and SUS304 if the compression is continued up to Δ=3%. On the other hand, the superelastic SMA columns (if not too short) can easily sustain the load with least change in magnitude. For instance, for SMA columns with *L/k* = 368, the load falls from its peak value (that is, from the buckling load) only by 4% in magnitude up to the last point of loading. For the same slenderness ratio, the fall in load's magnitude is 5 times more for Al columns and almost 10 times more for SUS304 columns (see also Figures 3 (c) and (d)).

The shape recovery process of the buckled columns actually starts with the unloading and ends when the load becomes approximately zero. It is found that for *L/k* = 68-148, recovery force of the buckled SMA columns increases quite significantly as if they push the loading fixtures

TABLE 2. LOAD'S VARIATION BETWEEN THE CRITICAL POINT AND AT Δ = 3%.

	Percent fall between the load at the point of instability and load at Δ=3%						
L/k	368	318	268	218	168	128	88
SMA	4	5	12	20	27	36	43
Al	20	26	31	44	51	57	58
SUS304	38	45	49	55	63	63	58

during unloading (Figures 3 (b) and 5). The above phenomenon is contrary to the notion that load falls off monotonically during unloading of a buckled column. It is due to the fact that at one stage of the unloading process reverse phase transformation occurs and as soon as the material returns to the parent austenite phase its stiffness increases. Due to superelasticity the buckled SMA column tends to recover its undeformed shape and the increasing stiffness make them to push the loading fixture. However, having low bending stiffness, too slender SMA columns do not show this phenomenon.

CONCLUSIONS

Some buckling and postbuckling characteristics of the superelastic SMA columns have been observed using the load-deformation curves. It is found that below the slenderness ratio of 100, buckling resistance of the superelastic SMA columns increases most significantly among the three materials used in the investigation. Short SMA columns can sustain high critical loads comparable to those of SUS304 columns. It is also observed that the SMA columns if not too short can sustain the buckling load with least change in magnitude if the compression is continued far beyond the point of instability. Though the slender SMA columns buckle at slightly lower loads compared to slender Al columns, they particularly exhibit this interesting characteristic. Moreover, for L/k = 68-148, the recovery force of SMA columns increases significantly during unloading from the postbuckled state. Furthermore, if the slenderness ratio is not too low, the initial shape before the cycle is recovered when they are unloaded from the post buckled state. This useful feature indicates that in the practical applications, the SMA columns can be used for repeated compressive loading-unloading cycles. On the other hand, for the whole range of slenderness ratio considered in this study, Al and SUS304 columns are permanently bent after the first cycle. Thus, below the slenderness ratio of 100, not only SMA column's buckling load is significantly higher than that of a Al column, but its shape is also recovered when the load is withdrawn even from a huge postbucking deformation. The unique stress-strain curves along with the property of superelasticity enable them to exhibit such exceptional behaviors.

REFERENCES

1. Otsuka, K. and Wayman, C. M. 1998. "*Shape memory materials*". Cambridge University Press.
2. Brinson, L. C. 1993. "One-dimensional constitutive behavior of shape memory alloys: Thermomechanical derivation with non-constant material functions and redefined martensite internal variable". *J. Intell. Matls. Sys. & Struct.*, 4, pp.229-242.
3. Thompson, J. M. T. and Hunt, G.W. 1973. "*A general theory of elastic stability*". John Wiley and Sons.
4. Johnson, W. 1972. "Impact strength of materials", Edward Arnold.
5. Rahman, M. A., Qiu, J. and Tani, J. 2000. "Behavior of the short superelastic SMA columns under compressive loading-unloading cycles". Proceedings of the JSME Tohoku Branch Conference (in Japanese), pp.67-68.

SUPERELASTIC PROPERTIES OF TiNi SHAPE MEMORY ALLOY UNDER VARIOUS LOADING CONDITIONS

Jian-ming Gong, Hisaaki Tobushi, Kazuyuki Takata, Kayo Okumura

ABSTRACT

Superelasticity is one of the important mechanical properties of shape memory alloy (SMA). In the present paper, the superelastic behavior of TiNi SMA under various loading conditions with different experimental temperatures and strain rates was investigated. The characteristics of transformation stress during full and partial cyclic deformation were analyzed. After mechanical training with cyclic deformation, two-way deformation appears during the heating and cooling process under no load. The modulus of elasticity during the internal loop is expressed by the mixed rule with the function of transformation strain.

1 INTRODUCTION

TiNi shape memory alloy (SMA) is a promising candidate for practical applications of intelligent materials, since its characteristic performance is presently superior to other existing SMAs[1]. In TiNi SMA, superelasticity (SE) is one of the most important mechanical properties and appears at temperature above A_f due to the stress-induced martensitic transformation.

Because the martensitic transformation (MT) is induced not only by temperature but also by stress, effect of various loading conditions with different temperature and strain rate on superelasticity of TiNi SMA is important. In the past decades, stress-strain relationship and simple cyclic deformation with respect to SE of TiNi SMA were studied[2~6]. However, it is necessary to understand further superelastic behavior of TiNi SMA subjected to various loading conditions in order to design perfect SMA elements.

In the present study, the superelastic behaviors of TiNi SMA under the conditions of cyclic full and partial loading and unloading with different experimental temperatures and strain rates were investigated. The characteristics of martensitic transformation stress during cyclic deformation were analyzed. After cyclic deformation, two-way deformation was studied by heating and cooling under no load. The mixed rule with the function of transformation strain was proposed to express the modulus of elasticity during the internal loop.

2 EXPERIMENTAL METHOD

2.1 Material and specimen

Materials were Ti-55.4 Wt% Ni SMA wires, 0.75 mm in diameter. A Straight line was shape-memorized through shape-memory processing by keeping at 673 K for 1 h followed by cooling in a furnace. The A_f point of specimens determined by tensile tests was about 323K.

Jian-ming Gong, Department of Mechanical Engineering, Nanjing University of Chemical Technology, Nanjing 21009, China.

Hisaaki Tobushi, Kazuyuki Takata and Kayo Okumura, Department of Mechanical Engineering, Aichi Institute of Technology, 1247 Yachigusa, Yagusa-cho, Toyota 470-0392, Japan.

2.2 Experimental apparatus

The experimental apparatus was a SMA property testing machine composed of a tensile machine and a heating-cooling device [7]. The specimens were heated by hot air or cooled by liquefied carbon dioxide. Displacement was measured with an extensometer of 20mm gauge length. Temperature was measured with a thermocouple, 0.1 mm in diameter, on the surface in the central part of the specimens.

2.3 Experimental procedure

Tensile tests to a prescribed maximum strain ε_0 were carried out at a constant temperature T above A_f. In each test, strain rate was kept constant during the loading and unloading processes. The following experiments were performed.

1. Full loading and unloading tests with N cycles were carried out at different temperatures and strain rates.
2. After mechanical training with cyclic deformation, heating and cooling under no load were carried out.
3. Cyclic partial loading and unloading were carried out by gradually decreasing strain amplitude in the following methods:
   (1) decreasing the maximum strain with constant minimum strain
   (2) increasing the minimum strain with constant maximum strain
   (3) decreasing the maximum strain and increasing the minimum strain

3 EXPERIMENTAL RESULTS AND DISCUSSION

3.1 Superelastic behavior under cyclic full loading and unloading

The stress–strain curves with 100 cycles and strain rate of 1%/min at the different experimental temperatures are shown in Fig.1. The stress-strain curve with 100 cycles and strain rate of 50%/ min at experimental temperature of 353K is shown in Fig.2.

As seen from Fig.1, the overshoot at the start points of MT diminishes with an increase in N. The MT stress decreases markedly in the early cycles but approaches a certain saturated value afterward. In the case of low experimental temperature at strain rate of 1%/min shown in Fig.1(a), MT stage is expressed by the clear plateau. However, in the case of high temperature at strain rate of 1%/min shown in Fig.1(b) and 1(c), the clear plateau does not appear but the stress-strain curve is expressed by a gentle curve with an increase in cycles. In the stress-strain curve with high strain rate of 50%/min shown in Fig.2, the MT stress has little undulation, and the transformation region is not expressed by a horizontal yield plateau but has a certain slope.

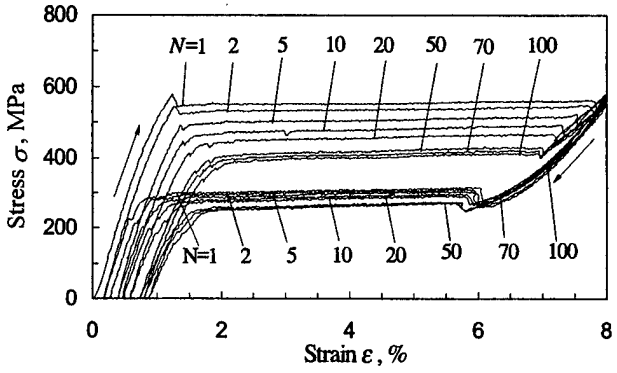
The relationship between decrease in the MT stress $\Delta\sigma_M$ and the number of cycles N and that between residual strain ε_r and N are shown in Fig.3. As seen in Fig.3, during cyclic deformation, $\Delta\sigma_M$ and ε_r remaining after each unloading increase with increasing number of cycles, but all these values exhibit a decreasing rate. The relationship between $\Delta\sigma_M$ and ε_r is shown in Fig.4. Fig.4 shows the fact that the amount of decrease in MT stress is almost proportional to residual strain. The reason for the appearance of these cyclic deformation behaviors may be considered as follows. During cyclic loading and unloading, dislocations accumulate around the microscopic defects in the material due to cyclic movement of the interface between the parent phase and the M-phase. Based on the increase in the dislocation density, the residual strain appears and internal stress increases [8]. Internal stress may assist the formation of the stress-induced martensite, and increasing in the internal stress causes decreasing in MT stress. Therefore $\Delta\sigma_M$ and ε_r increase at the same decreasing rate.

3.2 Two-way deformation behavior after cyclic deformation

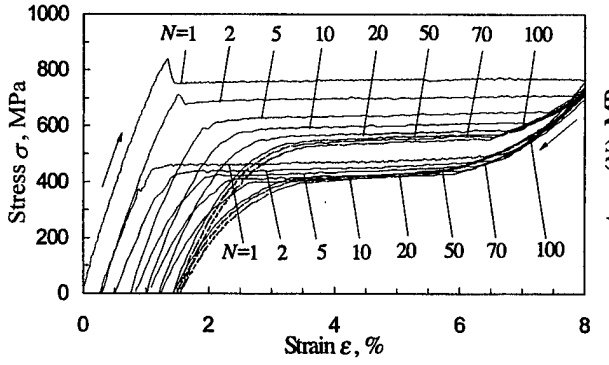
The variation in strain with temperature under no load after mechanical training with 20 cycles is shown in Fig.5. Fig.5a and 5b show relationship between strain and temperature after mechanical training at T_0=333K and at T_0=353K, respectively. In the case of T_0=333K shown in Fig.5(a), strain decreases when heating from 333K to 343K (1) and keeps constant during heating (2) and cooling (3) above 343K. Strain increases during cooling below 343K (4) and

decreases during heating from 303K (5). In the case of T_0=353K shown in Fig.5(b), strain keeps constant during heating (1) and cooling (2) above 353K, increases during cooling below 340K (3)and decreases during heating from 303K (4). Thus, it can be seen that the TiNi SMA exhibits two-way deformation behavior after mechanical training.

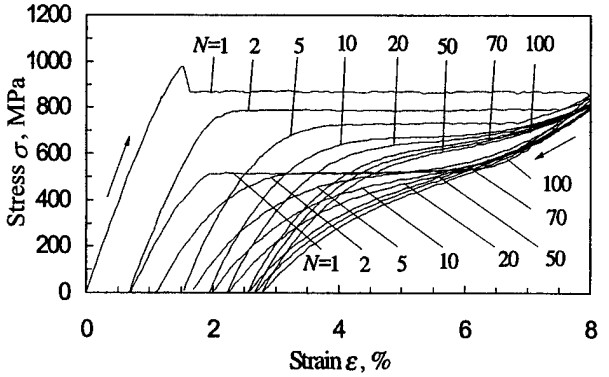
The reason for appearance of two-way behavior of strain may be considered as follows. Internal stress remains in the material after cyclic deformation with 20 cycles. Internal stress is about 150MPa when T_0=353K (see $\Delta\sigma_M$ at N=20 in Fig.3(a)). 325K and 315K are the starting temperatures of the R-phase and its reverse transformation determined by DSC, respectively, and 309K and 343K are the finishing temperatures of the R-phase and its reverse transformation, respectively. Austenite transforms only to the R-phase under the action of the internal stress when cooling from 343K to 303K, and strain increases. When heating from 303K to 343K, the R-phase transforms back to austenite, and strain decreases. Heating and



(a) T=353K



(b) T=373K



(c) T=393K

Figure 1. Stress-strain curves under cyclic full loading and unloading at strain rate of 1%/min

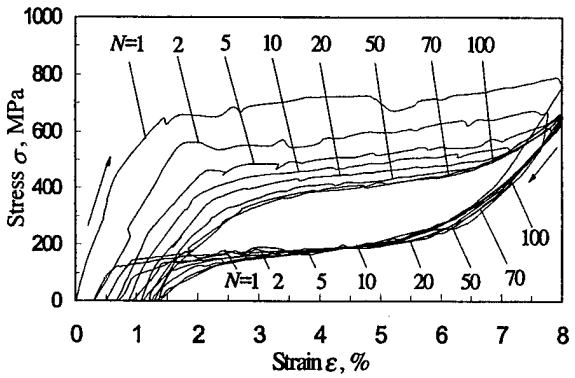
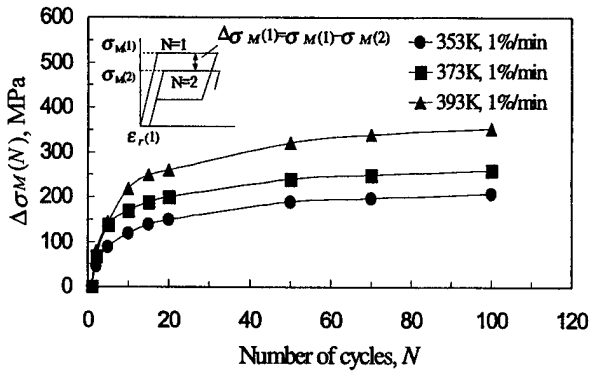
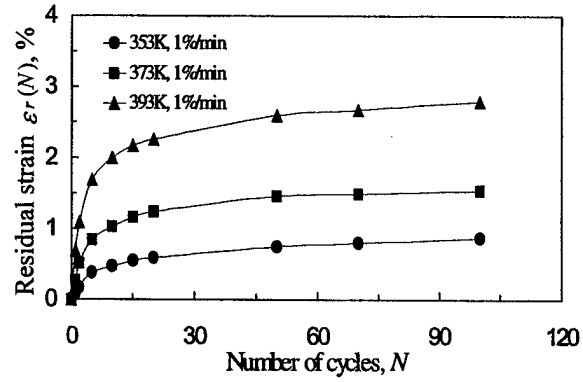


Figure 2 Stress-strain curves under cyclic full loading and unloading at strain rate of 50%/min



(a) Amount of decrease in the MT stress $\Delta\sigma_M$



(b) Residual strain ε_r

Figure 3. Dependence of decrease in the MT stress and residual strain on the number of cycles

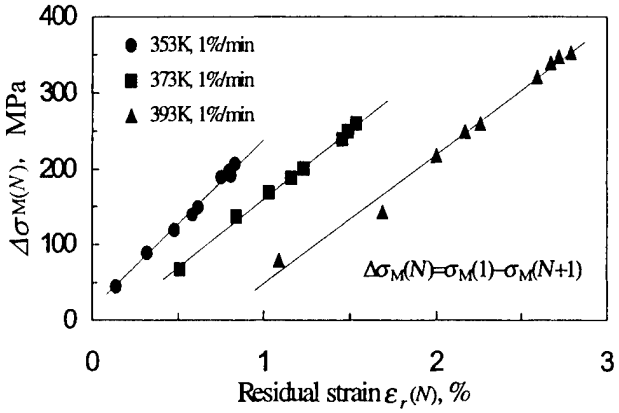
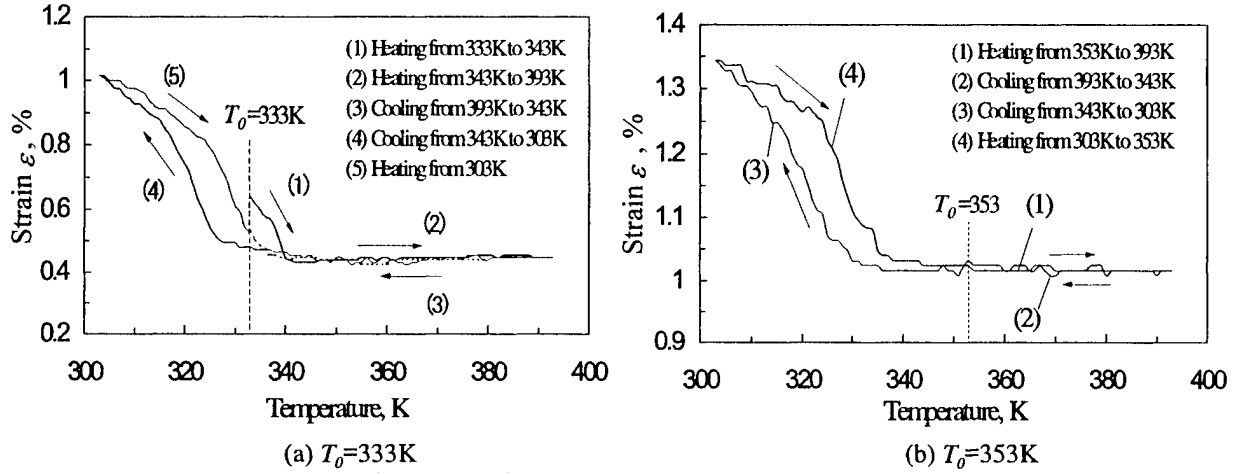


Figure 4. Relationship between decrease in the MT stress and residual strain



(a) T_0=333K (b) T_0=353K

Figure 5. Strain-temperature curves under no load

cooling between 343K and 393K do not result in any phase transformation, and therefor strain keeps constant. In the case of T_0=333K shown in Fig.5(a), the reason for decrease in strain during heating from 333K to 343K (1) is that the R-phase remaining in the material after mechanical training transforms back to austenite. Therefore, two-way deformation behavior of the TiNi SMA is related to the R-phase transformation.

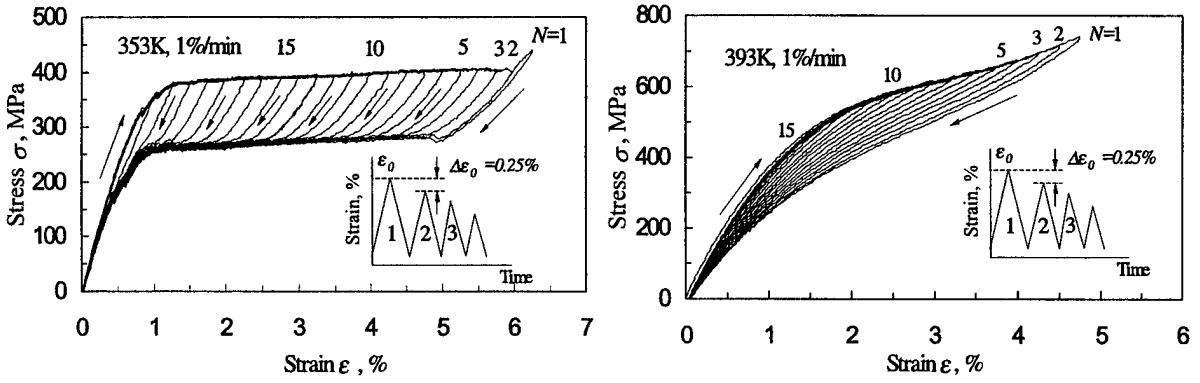
3.3 Superelastic behavior under cyclic partial loading and unloading

3.3.1 Cyclic properties under gradually decreasing strain amplitude with constant minimum strain

After mechanical training with cyclic deformation of 100 cycles at temperature T_0, the maximum strain ε_0 decreased at intervals $\Delta\varepsilon_0$ of 0.25% till down to ε_0 of 1%. During cyclic loading and unloading, the minimum strain was kept constant by perfect unloading. The stress-strain curves at temperature T_0 of 353K and 393K are shown in Fig.6(a) and 6(b), respectively. As seen in Fig.6(a), the MT stress and the reverse transformation stress almost keep constant under cyclic partial loading and unloading. The starting and completing conditions of the transformation are prescribed by a certain constant stress at low-temperature. As seen in Fig.6(b), at higher temperature, the starting and completing conditions of the transformation become unclear. Both transformations do not appear under constant stresses but appear under arbitrary stresses. Therefor stress plateau does not appear and the stress-strain curves are expressed by the gentle curves.

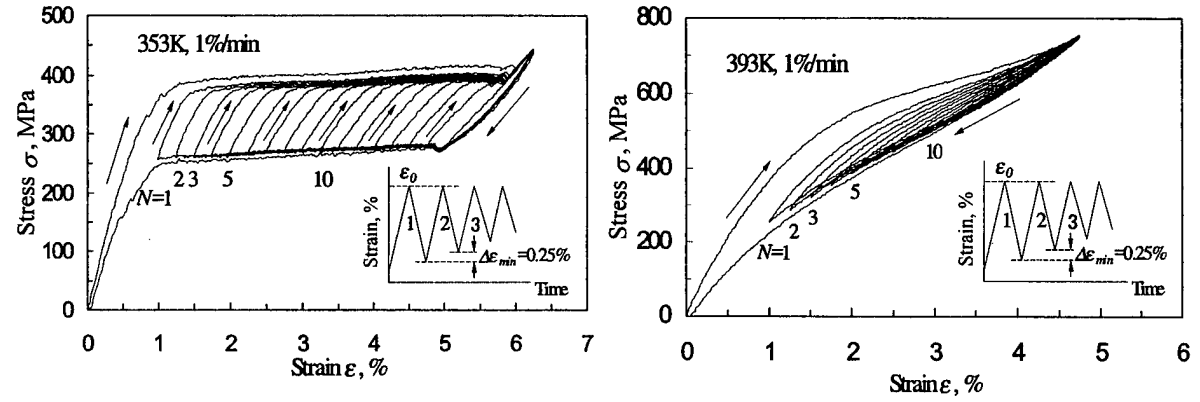
3.3.2 Cyclic properties under gradually decreasing strain amplitude with constant maximum strain

For specimens by mechanical training with cyclic deformation of 100 cycles at temperature T_0, the minimum strain ε_{min} increased at intervals $\Delta\varepsilon_{min}$ of 0.25% from 1% by keeping maximum strain ε_0 constant during cyclic partial loading and unloading. Fig.7(a) and 7(b) show the stress-strain curves at the test temperature T_0 of 353K and 393K, respectively. As seen in Fig.7(a) at T_0=353K, the MT stress and the reverse transformation stress basically keep constant. The starting and completing conditions of the transformation have the same property as that mentioned in section 3.3.1. The MT stress in N=1 is 400MPa which is the same value as



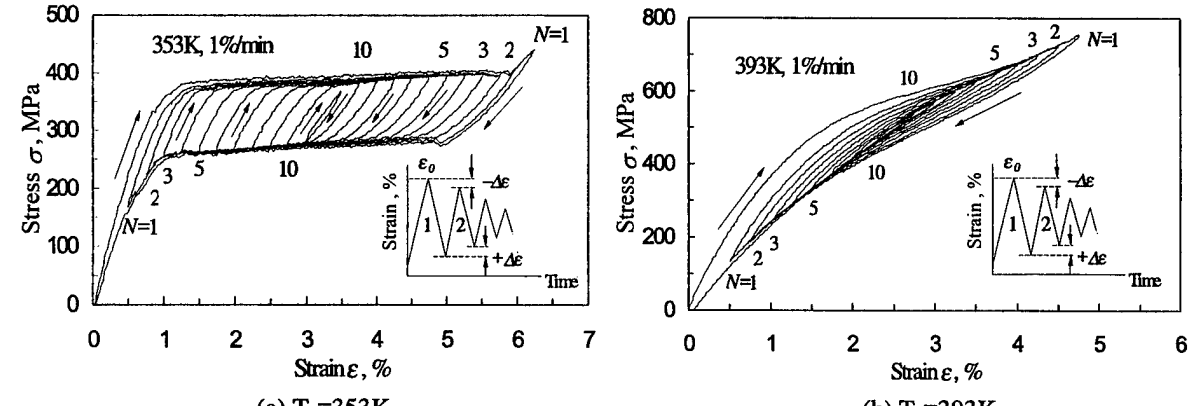
(a) T_0=353K (b) T_0=393K

Figure 6. Stress-strain curves under a constant minimum strain and gradually decreasing strain amplitude



(a) T_0=353K (b) T_0=393K

Figure 7. Stress-strain curves under a constant maximum strain and gradually decreasing strain amplitude



(a) T_0=353K (b) T_0=393K

Figure 8. Stress-strain curves under gradually decreasing strain amplitude

observed in Fig.6(a). The MT stress after N=2 is 370 MPa which is lower than that in N=1 and does not depend on the minimum strain. The reason why the MT stress after N=2 is lower than that in N=1 may be explained as follows. During the partial unloading process, the reverse transformation appears in the region of stress plateau. Although most reverse transformation appears in the stress plateau of 250MPa down to strain of 1%, some part of reverse transformation does not complete at the point of strain, 1%. In the case of following reloading, the M-phase remains in the material and therefor it is not necessary for the MT to nucleate the M-phase, resulting in low MT stress. On the contrary, in the case of perfect unloading, it is necessary for the MT to nucleate the M-phase and therefor the MT stress is high.

As seen in Fig.7(b) at T_0=393K, the starting and completing conditions of the MT and the reverse transformation are unclear which are the same inclination observed in Fig.6(b).

3.3.3 Cyclic properties under gradually decreasing strain amplitude

For specimens by mechanical training with cyclic deformation of 100 cycles at temperature T_0, the maximum strain decreased and the minimum strain increased at internals $\Delta\varepsilon$ of 0.25% during loading and unloading, respectively. The stress-strain curves obtained by the test are shown in Fig.8(a) and 8(b). The starting and completing conditions of the transformation also have the same trend as that observed in the sections 3.3.1 and 3.3.2. In the case of T_0=353K, both transformation stresses are almost constant without depending on strain. In the case of T_0=393K, the MT stress decreases and the reverse transformation stress increases, respectively, with decreasing strain amplitude.

4 MODULUS OF ELASTICITY UNDER CYCLIC DEFORMATION

It is necessary to establish the constitutive model in order to design effective SMA devices and working elements. For uniaxial loading conditions, a simple rate-form constitutive relation from phenomenological points of view has been proposed by Tanaka and co-workers to describe the complex deformation behavior of SMA [9,10]. Tanaka's constitutive equations are as follows:

$$\dot{\sigma} = D\dot{\varepsilon} + \Theta\dot{T} + \Omega\dot{\xi} \tag{1}$$

$$\xi = \Xi(\sigma, T) \tag{2}$$

where σ, ε and T represent the stress, strain and temperature, respectively. The coefficients D and Θ represent the modulus of elasticity and the thermoelastic constant, respectively. Ω is coefficient of the transformation strain due to the MT. ξ represents the volume fraction of the martensitic phase, thus the volume fraction of the parent phase is 1-ξ. For martensitic transformation, the transformation kinetics (2) is expressed by

$$\frac{\dot{\xi}}{1-\xi} = b_M c_M \dot{T} - b_M \dot{\sigma} \geq 0 \tag{3}$$

and, for the reverse transformation,

$$\frac{\dot{\xi}}{\xi} = b_A c_A \dot{T} - b_A \dot{\sigma} \geq 0 \tag{4}$$

where b_M, b_A, c_M and c_A are material constants which can be determined by a series of simple experiments.

The modulus of elasticity D varies with the maximum strain ε_0 under the conditions of cyclic deformation, especially internal loop. Because the parent phase and the M-phase exist together in the progress of SIM transformation, the rate between two phases has an effect on D. The modulus of elasticity of the parent phase and the M-phase are expressed by D_A and D_M, respectively. In the uniaxial tension, the interface between the parent phase and the M-phase moves along axial direction, and the volume fractions of two phases change with movement of the interface. If the volume fraction of the M-phase is m in a unit length, the volume fraction of the parent phase is 1-m. Under the action of stress increment $\Delta\sigma$, the strain increment $\Delta\varepsilon$ is $m\Delta\sigma / D_M$ for the M-phase and is $(1\text{-}m)\,\Delta\sigma / D_A$ for the parent phase. Therefor, the total strain

increment $\Delta\varepsilon$ in the unit length can be written as

$$\Delta\varepsilon = \frac{m \cdot \Delta\sigma}{D_M} + \frac{(1-m) \cdot \Delta\sigma}{D_A} \tag{5}$$

According to Eq. (5), the modulus of elasticity D is expressed as follows:

$$D = \frac{\Delta\sigma}{\Delta\varepsilon} = \frac{D_A D_M}{mD_A + (1-m)D_M} \tag{6}$$

As easily obtained from Eq.6(b), $D=D_A$ if $m=0$ and $D=D_M$ if $m=1$. The MT strain $\Delta\varepsilon_M$ is determined by $\Delta\varepsilon_M = \varepsilon_{Mf} - \varepsilon_{Ms}$, where ε_{Mf} and ε_{Ms} represent the MT completion strain and start strain, respectively. Let us assume that the volume fraction of the M-phase is proportional to the MT strain. If the maximum strain ε_0 is in the region of MT during cyclic loading, the MT strain is $\varepsilon_0 - \varepsilon_{Ms}$. Then the volume fraction of the M-phase m in the unit length can be obtained by following equation:

$$m = \frac{\varepsilon_0 - \varepsilon_{Ms}}{\varepsilon_{Mf} - \varepsilon_{Ms}} \tag{7}$$

In order to determine the material constants in the above-mentioned equations, tensile tests were performed at various ambient temperatures for a TiNi SMA wire. The values of the material constants obtained by these tests are shown in Table 1. The subscripts M and A for each coefficient denote the martensitic phase and parent phase or the MT and the reverse transformation, respectively.

In the present study, the established constitutive equations are applied to describe the deformation with decreasing maximum strains ε_0. The stress-strain curves obtained by cyclic loading and unloading test under strain rate of 1%/min at 343K are shown in Fig.9. A thick line in Fig.9 shows the results calculated from the above-mentioned constitutive equations. Comparing the calculated results with the experiment data, it can be found that SE behavior is expressed well for the internal loop with various maximum strains. The slope of line during unloading from an unloading start point to a start point of the reverse transformation increases with decrease in the maximum strain, that is, the modulus of elasticity of the material increases with decrease in the maximum strain.

TABLE 1 Material constants

D_M GPa	D_A GPa	b_M 1/MPa	b_A 1/MPa	c_M MPa/K	c_A MPa/K	Ω MPa
18.7	45.0	-0.132	0.132	6.125	5.01	-2371.5

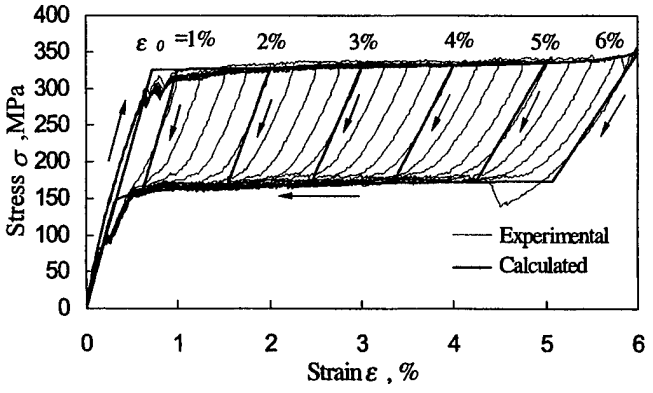


Figure 9. Stress-strain curves with various maximum strains

5 CONCLUSIONS

The superelastic properties of TiNi SMA under various loading conditions were investigated. Based on a mixed rule with the function of transformation strain, the modulus of elasticity during the internal loop was expressed and used to describe SE behavior of TiNi SMA. The results are summarized as follows:

(1) For full cyclic loading and unloading, if strain rate and temperature are high, the clear transformation plateau does not appear.

(2) The transformation stress decreases markedly in the early cycles but approaches a certain saturated value afterward. The amount of decrease in the transformation stress is almost proportional to residual strain.

(3) After mechanical training, the material exhibits two-way deformation behavior during heating and cooling under no load. The two-way deformation is induced due to the R-phase transformation.

(4) For cyclic partial loading and unloading after mechanical training with cyclic deformation, the transformation stress does not depend on the maximum strain and the minimum strain at low temperature. The starting and completing stresses of the phase transformation become unclear at high temperature.

(5) With respect to internal cyclic deformation, the modulus of elasticity is expressed by the mixed rule with the function of transformation strain. The results calculated with the proposed mixed rule are basically consistent with the experimental results for partial unloading.

ACKNOWLEDGMENTS

The experimental work of this study was carried out with the assistance of the students of Aichi Institute of Technology, to whom the authors wish to express their gratitude. The authors also wish to extend thanks to the Scientific Foundation of the Japanese Ministry of Education, Science, Sports and Culture for financial support.

REFERENCES

[1] Funakubo, H., 1987. *Shape Memory Alloy*. New York, USA: Gordon and Breach Science Publisher, pp.176-178.

[2] Miyazaki, S., Ohmi, Y., Otsuka, K. and Suzuki, Y., 1982. "Characteristics of deformation and transformation pseudoelasticity in Ti-Ni alloys," *J. de Pysique*, 15(C4), pp.255-260.

[3] Lin, P.H., Tobushi, H., Tanaka, K., Hattori, T. and Makita, M., 1994. "Pseudoelastic behaviour of TiNi shape memory alloy subjecred to strain variations", *J. Intell. Mater. Syst. Struct.*, 5, pp.694-701

[4] Shaw, J. A. and Kyriakides, S. 1995. "Thermomechanical aspects of NiTi," *J. Mechanics Phisics Solids*, 43(8), pp.1243-1281.

[5] Tobushi, H., Shimeno, Y., Hachisuka, T. and Tanaka, K., 1998. "Influence of strain rate on superelastic properties of TiNi shape memory alloy," *Int. Mechanics Mater.*, 30, pp.141-150.

[6] Wu, K., Yang, F., Pu, Z. and Shi, J., 1996. "The effect of strain rate on detwinning and superelatic behavior of NiTi shape memory alloys," *J. Intelligent Material System and Structures*, 7, pp.138-144.

[7] Tobushi, H., Tanaka, K., Kimura, K., Hori, T. And Sawada, T., 1992. "Stress-strain-temperature relationship associated with the R-phase transformation in TiNi shape memory alloy," *JSME Int. J.*, 35(3), pp.278-284.

[8] Miyazaki, S., 1990. "Thermal and stress cycling effect and fatigue properties of Ni-Ti alloys," in Engineering Aspects of Shape Memory Alloys, Duerig, T. W., Melton, K. N., Stockel, D. and Wayman, C. M, eds. London, Butterworth-Heinmann, pp.393-413.

[9] Tanaka, K., Kobayashi, S. and Sato, Y., 1986. "Thermomechanics of transformation pseudoelasticity and shape memory effect in alloys," *Int. J. Plasticity*, 2, pp.59-72.

[10] Tanaka, K 1986. "A thermomechanical sketch of shape memory effect: one-dimensional tensile behavior," *Res Mechanica*, 18, pp.251-263.

STRESS-INDUCED MARTENSITIC TRANSFORMATION BEHAVIOR AND LATERAL STRAIN OF TiNi SHAPE MEMORY ALLOY

Hisaaki Tobushi, Kayo Okumura, Masato Endo, Kazuyuki Takata

ABSTRACT

The behavior of the interface between two phases and the lateral to longitudinal strain ratio due to the stress-induced martensitic transformation (SIMT) were investigated in the regions of superelasticity (SE) in a TiNi shape-memory alloy wire through the tensile test. The interface between a parent phase and a martensitic phase which appears due to SIMT during the loading process and its reverse transformation during unloading starts at both ends in the gripping parts of the wire and propagates towards the central part. When the two interfaces meet, SIMT completes. The lateral to longitudinal strain ratio due to SIMT and its reverse transformation is 0.43~0.46. Poisson's ratio in a parent phase a martensitic phase is 0.33~0.34.

1. INTRODUCTION

In shape memory alloy (SMA), strain of about 6% is recovered by heating which is called shape memory effect (SME) or by unloading which is called superelasticity (SE). Strain appears due to the stress-induced martensitic transformation (SIMT) during the loading process in both cases, and disappears due to the reverse transformation by heating or by unloading.

In SIMT, it is observed that the interface between a martensitic (M) phase and a parent, i.e. an austenitic (A) phase which appears due to the action of stress moves during deformation [1-4]. The constitutive modes which describes the deformation properties of SMA is necessary in order to design SMA elements. It is necessary for the construction of the constitutive model to understand the above-mentioned behavior of the interface.

In order to use the function of SMA more effectively, the application to composite materials has attracted attention. In the case of application of SMA to composite materials, because the compatibility of the interface between matrix and fiber is important and strain induced due to SIMT is large, the amount of lateral strain to longitudinal strain becomes important. For these purposes, in the previous paper [5],

Hisaaki Tobushi, Kayo Okumura and Masato Endo, Aichi Institute of Technology, 1247 Yachigusa, Yagusa-cho, Toyota 470-0392, Japan

Kazuyuki Takata, Elastomix Co., Ltd., Shinkawa 1-17-25, Chuo-ku, Tokyo 104-0033, Japan

the authors investigated the behavior of the interface between the M-phase and the parent phase due to SIMT in the region of SME on a TiNi SMA wire and the lateral to longitudinal strain ratio.

In the present paper, by the tensile test of TiNi SMA wires, the variations of total axial strain of the specimen, local axial strain and local lateral strain were investigated. Based on the experimental results, it was clarified that the interface between the M-phase and the parent phase due to SIMT progressed or shrunk, the local lateral strain and local longitudinal strain varied according to the movement of the interface, and the lateral to longitudinal strain ratio was 0.43~0.46.

2. EXPERIMENTAL METHOD

2.1 Materials and specimen

The material was a TiNi SMA wire with diameter of 0.75mm. The reverse-transformation finish temperature A_f of the specimen was about 273K. Because the experiment was performed at room temperature, the initial state of the material was an austenite phase.

2.2 Experimental apparatus

An SMA-properties testing machine was used for the tensile tests. The specimen and set up of the testing part are shown in Fig.1. As seen in Fig.1, the eleven marked lines were drawn at equal distances l=20mm on the specimen. The gauge positions

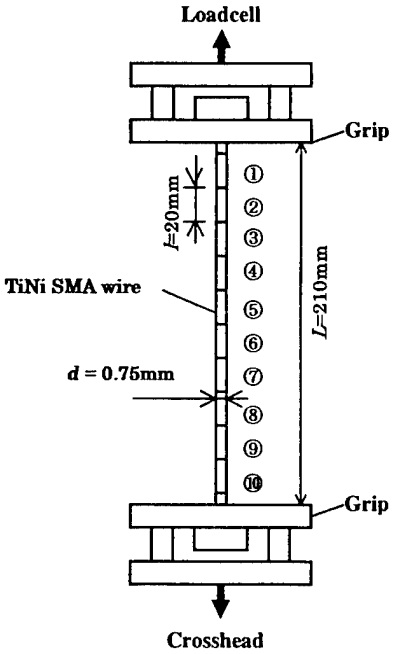


Figure.1 Set up of testing part

between the marked lines were arranged downward in order as ①~⑩ from an upper part. Diameter was measured at the gauge positions ①~⑩ through a micrometer. Taking a photograph of the specimen through a digital camera and enlarging an image on a display of a personal computer, each gauge length and diameter were measured. Total elongation was measured through displacement of a crosshead of the tensile machine.

2.3 Experimental procedure

The SE test was carried out to investigate the superelastic behavior at room temperature. Strain rate of total elongation during loading and unloading was 0.5%/min. Suspending the crosshead at the prescribed total elongation, gauge length and diameter at ①~⑩ were measured. The maximum strain was 7%.

3. EXPERIMENTAL RESULTS AND DISCUSSION

In dealing with the experiment date, stress and strain were treated in terms of nominal stress and nominal strain, respectively. Labels ①~⑩ used in the following figures correspond to the gauge positions ①~⑩ shown in Fig.1.

3.1 Behavior of SIMT

3.1.1 STRESS-STRAIN CURVE

The stress-strain curve obtained by the test is shown in Fig.2. Total axial strain $\Delta L/L$ represents the ratio of displacement ΔL of the crosshead to length L between grips. As seen in Fig.2, the stress-strain curve shows a large hysteresis loop. In the loading process, SIMT starts at point M_S with strain of 1.5% and finishes at point M_F with strain of 6.3%. In the unloading process, the reverse transformation starts at point A_S and finishes at point A_F.

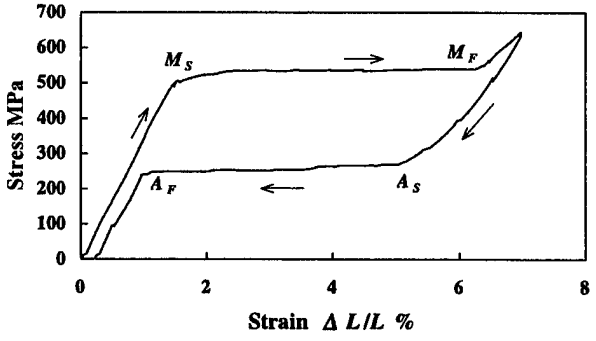


Figure. 2 Stress-strain curve in the SE

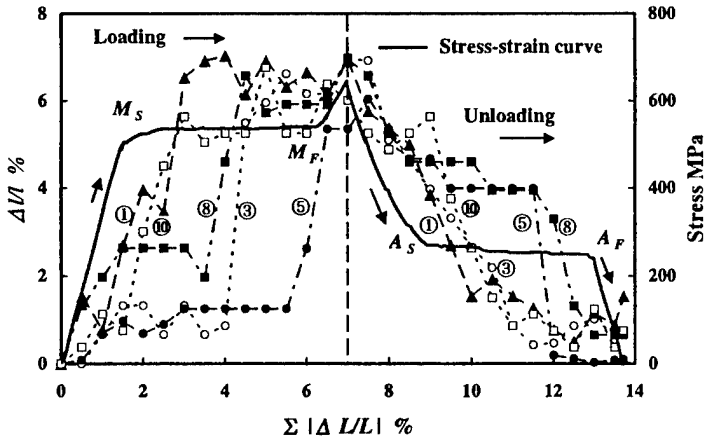


Figure. 3 Relationship between local axial strain and accumulated total axial strain in the SE test

3.1.2 RELATIONSHIP BETWEEN LOCAL AXIAL STRAIN AND TOTAL AXIAL STRAIN

The relationship between local axial strain $\Delta l/l$ and accumulated total axial strain $\Sigma\,|\Delta L/L|$ obtained by the test is shown in Fig.3. Local axial strain represents the ratio of the amount of variation Δl to gauge length l of the positions ①～⑩ shown in Fig.1. Accumulated total axial strain $\Sigma\,|\Delta L/L|$ represents the sum of absolute value of amount of variation in total axial strain during loading and unloading. The stress-strain curve is also shown by the solid line in Fig.3. The unloading curve of the stress-strain curve shown in Fig.2 is returned for the position of maximum strain, 7%. As seen in Fig.3, local axial strain $\Delta l/l$ at the end position ① in the specimen increases markedly at total axial strain $\Sigma\,|\Delta L/L| = 1.5\%$ and $\Delta l/l$ at another end ⑩ increases at $\Sigma\,|\Delta L/L| = 2\%$ by about 4.5%. The position of the variation in $\Delta l/l$ thereafter moves in turn from both ends of the specimen to central part. The increase in $\Delta l/l$ completes in the central part ⑤ at $\Sigma\,|\Delta L/L| = 6\%$ and thereafter the whole specimen becomes the elastic upswing region of the M-phase. The amount of variation in $\Delta l/l$ is almost the same at all positions ①～⑩. In the unloading process, $\Delta l/l$ decreases by about 4% in both ends of the specimen ① and ⑩ at the vicinity of $\Sigma\,|\Delta L/L| = 9\%$ where the reverse transformation starts. The variation in $\Delta l/l$ progresses in turn in the similar manner as the loading process. At $\Sigma\,|\Delta L/L| = 12.5\%$ where the reverse transformation finishes, $\Delta l/l$ decreases at the position ⑧.

3.1.3 RELATIONSHIP BETWEEN LOCAL LATERAL STRAIN AND TOTAL AXIAL STRAIN

The relationship between local lateral strain $-\Delta d/d$ and accumulated total axial strain $\Sigma\,|\Delta L/L|$ obtained by the test is shown in Fig.4. The stress-strain curve is also shown in Fig.4.

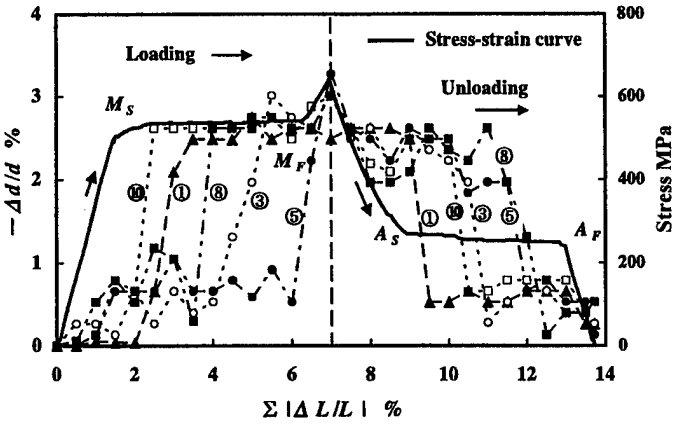


Figure. 4 Relationship between local lateral strain and accumulated total axial strain in the SE test

As seen in Fig.4, $-\Delta\, d/d$ increases abruptly by about 2% from both ends of the specimen ① and ⑩ at $\Sigma|\Delta L/L| = 2\%$. The position where $-\Delta\, d/d$ increases markedly moves in turn to the center of the specimen. For every position, the amount of increase in $-\Delta\, d/d$ is the same. The variation in $-\Delta\, d/d$ finishes in the central part of the specimen ⑤ at $\Sigma|\Delta L/L| = 6.3\%$ corresponding to the SIMT finish point M_F and the whole specimen becomes the elastic region of the M-phase. After abrupt increase in $-\Delta\, d/d$ for each position, the value of $-\Delta\, d/d$ keeps constant till the point M_F. In the unloading process, $-\Delta\, d/d$ decreases at the end of the specimen ① by about 2% at $\Sigma|\Delta L/L| = 9\%$ where the reverse transformation starts. In another end ⑩, $-\Delta\, d/d$ decreases at $\Sigma|\Delta L/L| = 10\%$. The variation in $-\Delta\, d/d$ follows in turn. In the position ⑧, $-\Delta\, d/d$ decreases at $\Sigma|\Delta L/L| = 12.5\%$ which corresponds to the finish point A_F of the reverse transformation.

3.1.4 PROGRESSING PROCESS OF SIMT AND REVERSE TRANSFORMATION

As observed in Figs.2~4, the abrupt variation in local axial strain $\Delta l/l$ and local lateral strain $-\Delta\, d/d$ due to SIMT appears at the end of the specimen and progresses to central part in turn. In the present section, based on both behaviors, the movement of the interface between the induced phase (M-phase) and the parent phase and the progressing process of SIMT will be discussed. The relationship between the gauge position where $\Delta l/l$ and $-\Delta\, d/d$ changed markedly due to SIMT and the reverse transformation and accumulated total axial strain is shown in Fig.5. The relationship observed for local axial strain is shown by label ○ and that for local lateral strain by ●.

As seen in Fig.5, abrupt changes in $\Delta l/l$ and $-\Delta\, d/d$ occur at both ends of the specimen ① and ⑩ and thereafter progress in turn to the central part of the specimen. If an extensometer is used to measure displacement in the SE tensile test of a TiNi SMA wire, an overshoot appears at the SIMT start point M_S and thereafter

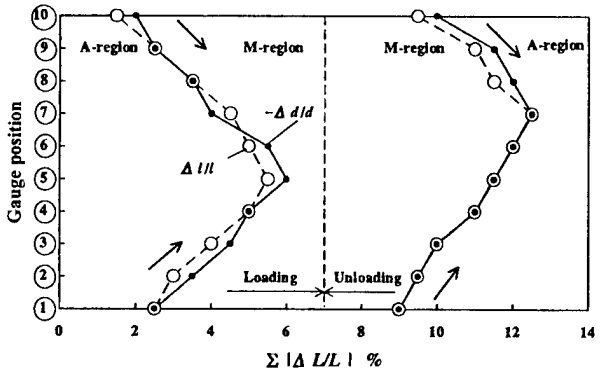


Figure. 5 Relationship between gauge position where $\Delta l/l$ and $-\Delta\, d/d$ changed markedly and accumulated total axial strain in the SE test

SIMT progresses under the stress plateau which is lower than a peak stress. On the contrary, if displacement is controlled through a crosshead without using an extensometer, because some slippage occurs in the gripping part, an overshoot does not appear at the point M_S and large residual strain appears after unloading [6]. Based on these facts, it is observed that stress which is necessary to nucleate the M-phase at the SIMT start point M_S is higher than stress which is necessary to move the interface between the M-phase and the parent phase. This behavior is similar to yielding phenomenon of mild steel. That is, yielding starts at an upper yielding point and *Luder*'s band propagates in the yielding plateau. If a wire with uniform cross section is in tension, stress concentration occurs in the gripping part and stress increases in this part. Therefore the M-phase nucleates in the gripping part and thereafter propagates. Thus abrupt changes in $\Delta l/l$ and $-\Delta\, d/d$ appear at both ends ① and ⑩ and propagates in turn. The variation in $\Delta l/l$ and $-\Delta\, d/d$ appear at almost the same elongation. The interfaces propagate in this way from both ends and combine in the central part, resulting in completion of SIMT.

Similarly in the reverse transformation, the parent phase nucleates at both ends ① and ⑩ and the interfaces propagate toward the central part. In the gripping part where stress concentration occurs, stress does not distribute uniformly on the cross section and stress in the central part on the cross section of a wire is lower than a mean value. Therefore in the unloading process, the parent phase may nucleate due to lower stress than average stress in the central element at the gripping part. This corresponds to the fact that an undershoot appears at the start point A_S of the reverse transformation in the unloading process if an extensometer is used which is similar to an overshoot at the point M_S in the loading process.

The above-mentioned behavior of SIMT is schematically shown in Fig.6. In Fig.6, a SMA wire is subjected to tension in the vertical direction, and the variation in the martensitic (M) phase and the parent (austenitic, A) phase and the variation in elongation and diameter are shown. In the early stage of loading, elastic deformation of the parent phase appears till the SIMT start point M_S and SIMT appears from both ends above the point M_S, resulting in axial elongation and decrease in diameter in the part subjected to SIMT. Elastic deformation of the M-phase appears above the SIMT finish

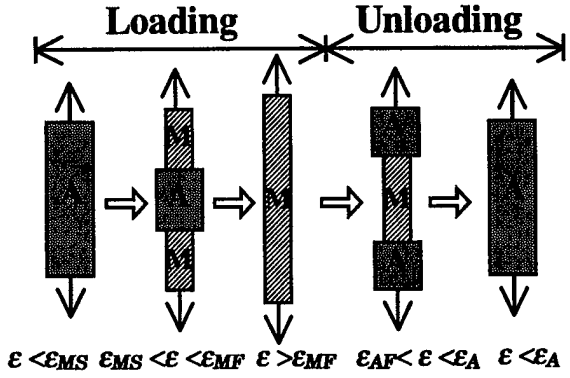


Figure. 6 Deformation pattern due to SIMT during loading and unloading in the SE test, A: austenitic phase, M: martensitic phase

point M_F. In the unloading process, the parent phase appears from both ends after the start point of the reverse transformation A_S, resulting in axial contraction and increase in the diameter in the part subjected to the reverse-transformation. Elastic deformation of the parent phase appears after the finish point of the reverse transformation A_F. The movement of the interface due to SIMT under tensile deformation is similar to the behavior of *Luder*'s band in mild steel, the observed result through an optical microscope in single crystal of Cu-based SMA [1] and the observed result due to variation in local elongation and temperature in TiNi SMA [6-8]. The above-mentioned behavior of the interface is important for consideration of the constitutive equation of SMA and is necessary to be reflected. Because the relationship shown in Fig.5 is expressed almost by a straight line, volume fraction of the M-phase is proportional to transformed strain if the progress of SIMT is expressed by volume fraction of the M-phase[7].

3. 2 Lateral to longitudinal strain ratio

In the case of uniaxial tensile deformation the ratio of lateral strain to longitudinal strain is a constant value in the range of elastic deformation and is known as Poisson's ratio. In the present study the lateral to longitudinal strain ratio is defined by a ratio $\nu = |\Delta\varepsilon'/\Delta\varepsilon|$ where $\Delta\varepsilon$ represents axial strain increment and $\Delta\varepsilon'$ lateral strain increment, respectively. The value of ν associated with SIMT will be discussed as follows.

The value of ν was determined by an average value of the ratios of local-axial strain increment to local-axial strain increment at each gauge position. First, the value of ν associated with SMIT will be shown. The value of ν for loading (Figs.3 and 4) in the SE test is 0.43. The value of ν associated with the reverse transformation in the unloading process is 0.46. The value of ν associated with SIMT is close to 0.5 which is the case of incompressibility. This occurs based on the fact that deformation associated with SIMT appears due to detwinned shear deformation.

Second, the value of ν for elastic deformation will be shown. The value of ν for elastic deformation of the parent phase during the loading process till the point M_S in the SE test is 0.34. Elastic deformation of the M-phase appears during the unloading process till the point A_S in the SE test, and the value of ν is 0.33%.

4 CONCLUSIONS

The tensile test of TiNi SMA wires was carried out, and the behavior of the interface due to SIMT in the regions of SE and the lateral to longitudinal strain ratio were discussed. The results obtained are summarized as follows.

(1) With respect to SE deformation, the interfaces between the parent phase and the M-phase appear due to SIMT in the loading process and the reverse transformation in the unloading process. The interface occur in the gripping part of the wire and propagate to the central part. SIMT and the reverse transformation complete when two interfaces combine.

(2) The lateral to longitudinal strain ratio associated with SIMT and the reverse transformation is 0.43～0.46.

References

1. H. Funakubo ed., Shape Memory Alloys, (1987), pp.39-41, Gordon and Breach Science, New York.
2. P. H. Leo, T. W. Shield and O. P. Bruno, "Transient Heat Transfer Effects on the Pseudoelastic Behavior of Shape-Memory Wires", Acta Metall. Mater., Vol.41, No.8 (1993), pp.2477-2485.
3. J. A. Shaw and S. Kyriakides, "Thermomechanical Aspects of NiTi", J. Mech. Phys. Solids, Vol.43, No.8, (1995), pp.1243-1281.
4. S. P. Gadaj, W. K. Nowacki amd H. Tobushi, "Temperature Evolution during Tensile Test of TiNi Shape Memory Alloy", Arch. Mech., Vol.51, No.6, (1999), pp.649-663.
5. T. Hachisuka, H. Tobushi, T. Hashimoto and Y. Shimeno, "Tensile Deformation and Lateral Strain of a TiNi Shape-Memory Alloy Wire", Trans. JSME, Vol.64, No.628, Ser. A(1998), pp.2970-2974.
6. P. H. Lin, H. Tobushi, K. Tanaka, T. Hattori and A. Ikai, "Influence of Strain Rate on Deformation Properties of TiNi Shape Memory Alloy", JSME Inter, J., Vol.39 No.1, Ser.A,(1996), pp.117-123.
7. K. Tanaka, S. Kobayashi and Y. Sato, "Thermomechanics of Transformation Pseudoelasticity and Shape Memory Effect in Alloys", Inter. J. Plasticity, Vol.2, (1986), pp.59-72.

THERMOMECHANICAL PROPERTIES OF POLYURETHANE-SHAPE MEMORY POLYMER FOAM

Hisaaki Tobushi, Kayo Okumura, Masato Endo, Syunichi Hayashi

ABSTRACT

The thermomechanical properties of polyurethane-shape memory polymer foam were investigated by the compressive tests. The results are summarized as follows. (1) The material contracts uniformly in the axial direction with the ratio of lateral strain to axial strain 0.4 in the early stage but about 0.15 thereafter. (2) The deformation resistance is large at low temperature and at high strain rate. (3) In the case of thermomechanical loading, strain is recovered at temperatures in the vicinity of Tg. The rate of strain recovery is 99%. The rate of strain fixity is 100%.

1. INTRODUCTION

The mechanical properties of shape-memory polymer (SMP) are different above and below the glass transition temperature T_g. The shape fixity and shape recovery exist due to the glass transition [1-3]. In application of SMPs, the shape fixity and shape recovery are used in the fields of technology, medical treatment, aerospace engineering, etc. The polyurethane-SMP foam has not only those characteristics but also impact relaxation property and heat insulating property. Therefore the applications of SMP foams are expected in the wide fields.

In the present study, in order to investigate the thermomechanical properties of polyurethane-SMP foam, the basic deformation property, shape fixity and shape recovery were examined by the compressive tests. In the experiments, the influence of temperature and strain rate on deformation property was investigated. The shape fixity and shape recovery were also investigated through the loading-unloading and heating-cooling paths. The results show that both the shape fixity and shape recovery are excellent.

Hisaaki Tobushi, Kayo Okumura and Masato Endo, Aichi Institute of Technology, 1247 Yachigusa, Yagusa-cho, Toyota 470-0032, Japan
Shunichi Hayashi, Mitsubishi Heavy Industries, Ltd., 1 Takamichi, Iwatsuka-cho, Nakamura-ku, Nagoya 453-8515, Japan

2. EXPERIMENTAL METHOD

2.1 Materials and specimen

The material used in the experiment was SMP foam of polyurethane of the polyether polyole series (Diary MFNo.21; produced by Mitsubishi Heavy Industries, Ltd.). The foams were made by chemical foaming. The expansion ratio was about 30. The foams were produced as slabstock. The specimen was cut off into a cube with length of the side 20mm. The glass transition temperature T_g was about 328K.

2.2 Experimental apparatus

A shape-memory material testing machine was used and the thermomechanical tests with loading-unloading and heating-cooling were performed.

Temperature was measured through a thermocouple of diameter 0.1mm, which was set at the bottom of the specimen. Displacement and load were measured through the displacement of a crosshead of the machine and a load-cell, respectively. The photograph of the compressed deformation state was taken through a digital camera and the state was measured on the display of a computer. During compression, two flat plates from both sides pressed the cubic specimen vertically. The Teflon sheets were set on the both contact faces between the upper or lower plates and the cubic specimen, respectively. The Teflon sheet reduced the frictional resistance on the contact face.

2.3 Experimental procedure

In the experiment, the following two kinds of tests were carried out.

(1) Compressive test

The specimen was compressed through the loading and unloading processes under a constant strain rate $\dot{\varepsilon}$ at a constant temperature T. The test was carried out at the temperature range between $T_g \pm 30$K and at $\dot{\varepsilon}$ =2.5～250%/min.

(2) Thermomechanical cycling test

The three-dimensional stress-strain-temperature diagram showing the loading path in the thermomechanical cycling test is shown in Fig.1. First ① maximum strain $-\varepsilon_m$ was

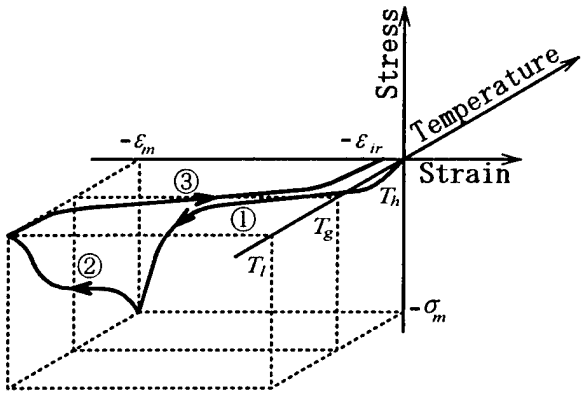


Figure1. Three-dimensional stress-strain-temperature diagram showing the loading path in compressive thermomechanical cycling test

applied at high temperature T_h above T_g. Second ② maintaining $-\varepsilon_m$, the specimen was cooled to low temperature T_l below T_g. Last ③ it was heated from T_l to T_h under no-load condition. The thermomechanical paths ① to ③ were repeated 10 times.
The experimental conditions were as follows: T_h=T_g+30K, T_l=T_g-30K, strain rate $\dot{\varepsilon}$ =25%/min, ε_m=75, 78 and 85%.

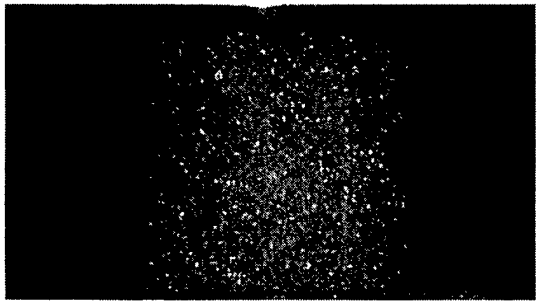
3. RESULTS AND DISCUSSION

In dealing with the experimental data, stress and strain were treated in terms of nominal stress and nominal strain, respectively.

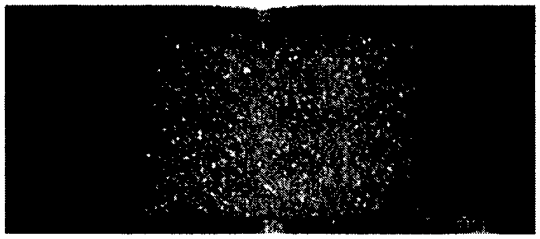
3.1 Compressive Deformation Properties

The deformation states of the cubic SMP foam compressed at room temperature are shown in Fig.2. Figure2 (a), (b) and (c) are photographs before the test, at compressive strain ε_m of 40% and at ε_m=80%, respectively. As seen in Fig.2, the cubic foam is compressed uniformly in the axial direction. This means that friction between both the upper or lower edge surfaces and the compressive plates is negligibly small.

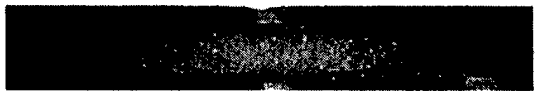
The relationship between axial compressive strain ε and lateral strain ε' showing the lateral expansion is shown in Fig.3. In Fig.3, the experimental results at strain rate of



(a) initial state (ε=0)



(b) ε=40%



(c) ε=80%

Figure 2. Photographs of SMP foam under compression

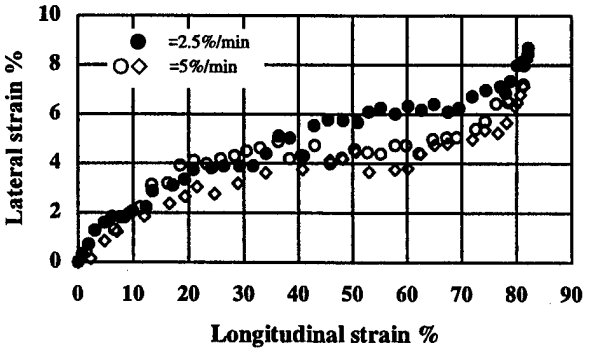


Figure 3. Relationship between lateral strain and longitudinal strain under compression

2.5 and 5%/min are shown. The ratio $|\varepsilon'/\varepsilon|$ is known as Poisson's ratio for Hookean elastic body. As seen in Fig.3, lateral strain increases markedly in the early stage, increases gradually at a constant rate thereafter and increases markedly when ε becomes larger than 70%. These inclinations are observed for every strain rate. The ratio $|\varepsilon'/\varepsilon|$ is 0.4 in the initial state through an origin. This value is close to the incompressive condition expressed by $|\varepsilon'/\varepsilon|=0.5$. In this stage, cells of the foam expand laterally corresponding to increase in axial strain. After the initial stage, the ratio $|\varepsilon'/\varepsilon|$ is about 0.15 and the rate of increase in lateral displacement due to the expansion of the foam is small. Therefore buckling of cells occurs and cells are folded like bellows. If axial strain becomes larger than 70%, the rate of increase in lateral strain increases due to post-buckling deformation of cells.

3.2 Stress-Strain Relationship

The stress-strain curves obtained by the compressive tests at temperatures T_g and $T_g \pm 30$K under constant strain rate $\dot{\varepsilon}$ are shown in Fig.4. As seen in Fig.4, in every case, the slope of the curve is steep in the initial stage of loading, gentle with showing stress plateau after a yield point and becomes steep above 60% of strain. In the initial stage, elastic deformation of the foam appears. After a yield point, large deformation occurs due to buckling of cells of the foam, resulting in stress plateau. After the stress plateau, post-buckling deformation of cells occurs, resulting in increase in deformation resistance. The lower the temperature, the larger the deformation resistance is. If temperature is higher than T_g, strain is perfectly recovered by unloading. In the case of high temperature, the stress-strain curve shows a hysteresis loop. The area surrounded by the hysteresis loop represents the dissipated energy density. As seen in Fig.4, the larger the strain rate $\dot{\varepsilon}$, the higher the stress in the loading process is, the larger the width of the hysteresis loop is, and the larger the area surrounded by the hysteresis loop is. Therefore the property of impact absorption is superior for high strain rate. The influence of $\dot{\varepsilon}$ on the stress-strain curves is most significant in the case of T_g. Therefore the influence of $\dot{\varepsilon}$ on the property of impact absorption is large at T_g.

3.3 Temperature Dependence of Modulus of Elasticity and Yield Stress

The compressive tests under strain rate of 10%/min were carried out at a constant temperature at intervals of 10K. The dependence of modulus of elasticity E and yield stress σ_y on temperature T obtained by the compressive tests are shown in Fig.5 and Fig.6, respectively. E was obtained from the slope of the initial stress-strain curve through the origin. Approximating the stress-strain curve with two straight lines, σ_y was determined from an intersection of the two lines. One line was the initial straight line through the origin and another was the straight-line approximating stress plateau after a yield point. As seen in Fig.5 and Fig.6, both E and σ_y are large at low temperature and small at high temperature. Both E and σ_y decreases markedly in the transition temperature region around T_g. The temperature dependence of E and σ_y appears due to the glass transition of the polymer which constructs the foam. Molecular chains move easily at high temperature but move hardly at low temperature. Due to the mechanical

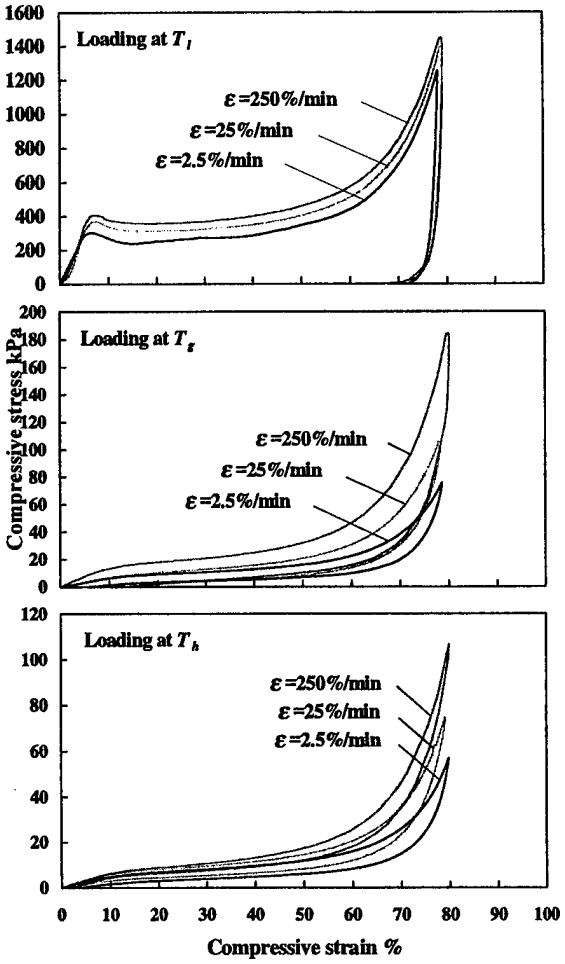


Figure 4. Stress-strain curves under compression for various strain rates ε at various temperatures T

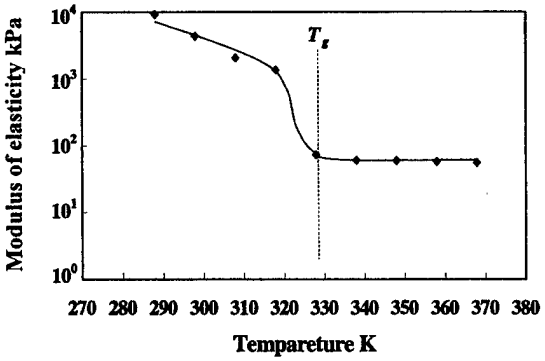


Figure 5. Modulus of elasticity in the initial elastic region at each temperature

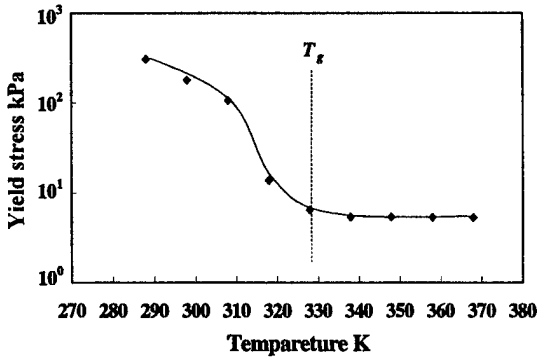


Figure 6. Yield stress at each temperature

properties of the glass transition, deformation resistance is small at high temperature but large at low temperature. Therefore the above-mentioned temperature dependence of E and σ_y appears.

3.4 Shape Fixity and Shape Recovery

3.4.1 STRESS-STRAIN RELATIONSHIP

The stress-strain curves obtained by the thermomechanical cycling tests are shown in Fig.7. N denotes the number of cycles. As seen in Fig.7, maximum stress in the loading process ① is a little large in N=1 and changes little thereafter. The cyclic deformation properties may be caused as follows. In the initial loading, incomplete cells may be destroyed but their variations may be small thereafter. Strain increases under stress plateau during the strain region between 10% and 60%. The increase in strain during

this region may correspond to buckling of cells. If strain increases above 60%, stress increases markedly. In the final region, deformation resistance becomes very large because post-buckling cells are deformed. In the cooling process ②, stress diminishes. Therefore maximum strain is fixed in its state and the rate of strain fixity is 100%.

3.4.2 STRESS-TEMPERATURE RELATIONSHIP

The stress-temperature curves obtained by the thermomechanical cycling tests are shown in Fig.8. As seen in Fig.8, stress decreases during the cooling process ②. In the initial stage of the process ②, stress decreases due to stress relaxation at high temperature. In the middle stage of the process ②, stress decreases gradually due to thermal contraction caused by decrease in temperature. Because the crosshead of the testing machine is held during the process in the tests and the compressed SMP foam contracted furthermore due to decrease in temperature, stress decreases. In the latter stage of the process ②, stress decreases markedly. As observed in Fig.5, modulus of elasticity is very large at temperatures below T_g. Therefore the variation in thermal stress due to thermal contraction caused by decrease in temperature becomes large, resulting in large decrease in stress. The stress-temperature curves do not change under cyclic loading.

3.4.3 STRAIN-TEMPERATURE RELATIONSHIP

The strain-temperature curves obtained by the thermomechanical cycling tests are shown in Fig.9. Strain decreases at temperatures in the vicinity of T_g during the heating process ③. In the initial stage of the process ③ at low temperature in the vicinity of T_l, strain is constant at ε_m because the microBrownian motion of soft segments of SMP is frozen. If it is heated to high temperature, strain is recovered because the micro-Brownian motion becomes active above T_g. The strain-temperature curves do not change under cyclic deformation. The rate of strain recovery is 99%.

3.4.4 INFLUENCE OF MAXIMUM STRAIN ON STRAIN RECOVERY

The strain-temperature curves for various maximum strains ε_m in N=1 obtained by the thermomechanical cycling tests are shown in Fig.10. As seen in Fig.10, the temperature at which strain is recovered markedly in the vicinity of T_g during the process ③ moves to lower temperature as ε_m becomes large. If maximum strain ε_m is large, internal stress induced in the material increases. The internal stress activates the recovery of strain. Therefore because the action of internal stress is added to thermal energy, strain is recovered at lower temperature in the case of large ε_m.

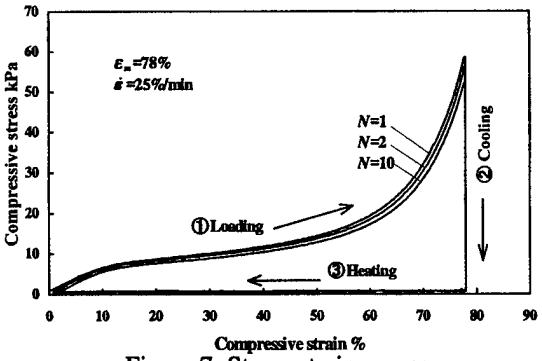


Figure 7. Stress-strain curves

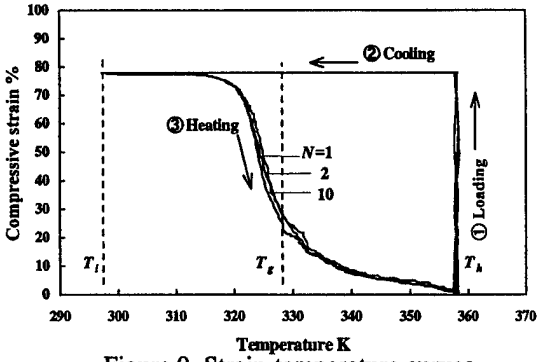


Figure 9. Strain-temperature curves

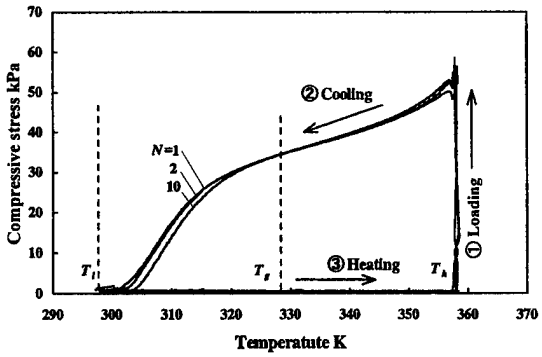


Figure 8. Stress-temperature

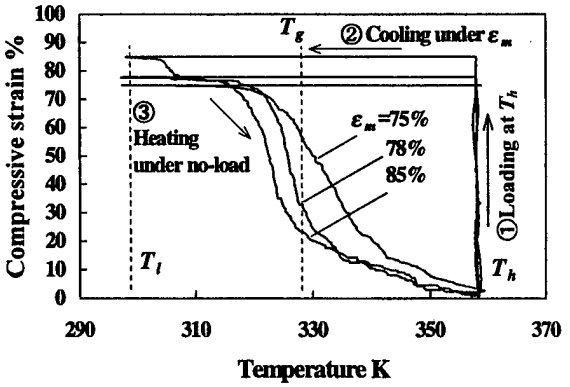


Figure 10. Strain recovery during the heating process under no-load for various maximum strains

4. CONCLUSIONS

The thermomechanical properties of polyurethane-SMP foam were investigated by the compressive test. The results are summarized as follows.

(1) The material contracts uniformly in the axial direction throughout the compressive process. The ratio of lateral strain to axial strain is 0.4 in the early stage but is about 0.15 thereafter.

(2) The deformation resistance is large at low temperature and at high strain rate. At temperatures above the glass transition temperature T_g, strain is recovered by unloading and the stress-strain curves show the hysteresis loops.

(3) In the case of thermomechanical loading, strain is recovered at temperatures in the vicinity of T_g. The rate of strain recovery is 99%. The rate of strain fixity is 100%.

(4) The shape-memory polymer foam has good performance for large elements of machines and structures.

REFERENCES

1. S.Hayashi, "Properties and Applications of Polyurethane Series Shape Memory Polymer", Inter. Progress in Urethanes, 6, 90 (1993)

2. H.Tobushi, H.Hara, E.Yamada and S.Hayashi, "Thermomechanical Properties in a Thin Film of Shape Memory Polymer of Polyurethane Series", Smart Mater. Struct., 5,483 (1996)

3. H.Tobushi, T.Hashimoto, N.Ito, S.Hayashi and E. Yamada, "Shape Fixity and Shape Recovery in a Film of Shape Memory Polymer of Polyurethane Series", J. Intell. Mater. Syst. Struct. 9,127 (1998)

TWO-WAY SHAPE MEMORY BEHAVIOR OBTAINED BY COMBINED LOADING TRAINING

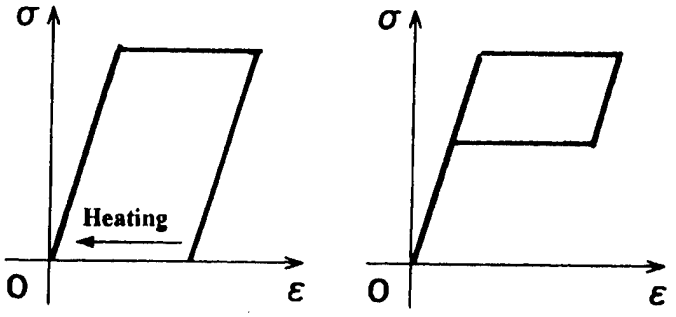
Masataka Tokuda, Souichi Sugino, Tadashi Inaba

Abstract

The two-way shape memory effect obtained by combined loading training is investigated experimentally by applying the combined loads of axial force and torque to the thin-walled tubular specimen of Cu-based Shape Memory alloy. In this paper, some unique two-way behavior are shown and discussed.

Introduction

Shape memory alloy (SMA) has two fundamental well–known properties, that is, one-way shape memory property and pseudo-elastic property as shown in Fig.1. That is, the inelastic deformation induced by the external force is erased by heating (shape memory phenomenon : Fig.1(a)), or disappeared only by the unloading at the higher temperature atmosphere (pseudoelastic phenomenon: Fig.1(b). When we want to use the SMA as the sensor/actuator, we have to apply some external load. For example, when the SMA wire (or spring) is connected with some weight, the SMA wire (or spring) shows the cyclic elongation-contraction (actuating) behavior by the change of temperature as shown in Fig.2(a) and (b). Figure 2(c) shows the prototype of SMA actuator using the external force induced by the additional spring. This kind of SMA actuators have been widely used in



(a) Shape Memory Effect **(b) Pseudoelastic Effect**

Fig.1 Fundamental properties of SMA

Department of Mechanical Engineering, Mie University, Kamihama 1515, Tsu 514-8507, Japan

the industrial/domestic applications, for examples, the sensor-actuators for the air conditioner, the hot-shower regulator, the coffee-maker, the rice-cooking bowl, and so on. In this case, the actuator is a combination of several components, and thus the actuator can not be so small. Now, we can arrive at an idea of simple SMA actuator without any external force. The actuating behavior of SMA without the external bias stress is called as TWO-WAY shape memory behavior [1-6]. The process is as follows: The actuator shown in Fig. 2(d) is principally equivalent to the SMA actuator shown in Fig. 2(c). Moreover, the actuator shown in Fig. 2(d) can be converted to the composite materials form as shown in Fig. 2(f). That is, the external stress for the actuating actions of SMA can be given by the internal (residual) stress. The internal (residual stress) is known to be created easily and effectively by the thermo-mechanical cyclic loading, in the engineering polycrystalline materials because these materials are non-homogeneous from the semi-microscopic point of view (that is, heterogeneous). The cyclic loading to produce the internal stress for the two-way shape memory effect is the TRAINING.

Figure 3 shows schematically the stress-temperature martensite phase transformation diagram of SMA. As found from this diagram, numerous possibilities for the cyclic thermo-mechanical loading training can be imagined, for examples, cyclic stress changes at the several constant temperatures (I, II, III, IV), cyclic temperature changes at the several constant stress state (V), or the simultaneous cyclic changes of stress and temperature. Which training is the most effective? The answer has not given yet. The systematic experimental and theoretical study may be necessary.

The authors' interest in this research area is related with the multi-axial loading [9-11] as follows: Stress is not the scalar variable, but 2-rank tensor whose independent components are 6. Here, the authors now propose a new training technique for the 2-way shape memory effect. That is, the cyclic complex (multi-axial) load training may produce the complex internal (residual) stress in the SMA. It means that the complex 2-way shape memory behavior can be obtained by the cyclic complex load training. The trained material may show the two- or three-dimensional actuating movement under the thermal cyclic changes without any external stress. In the authors' laboratory, the preliminary but

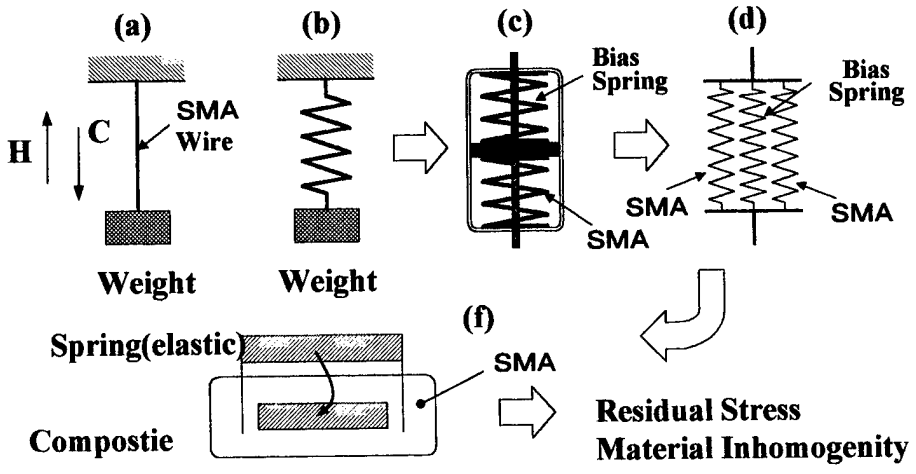


Fig.2 SMA actuator assisted by bias-load

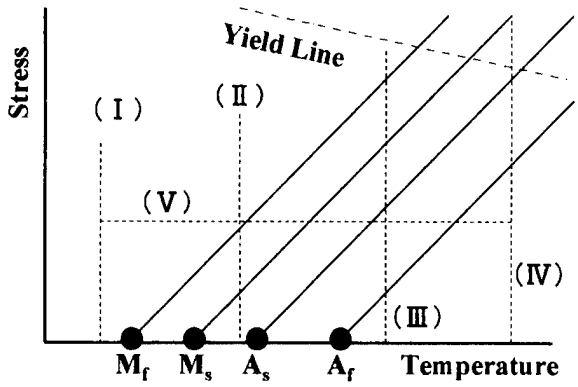


Fig.3 Stress-temperature diagram of martensite phase transformation

systematic experiments were performed. In the following sections, the detail of experiments and their results are shown and discussed.

Experimental method

The material used in the experiment is Cu-based shape memory alloy whose chemical constituent is Cu-10wt%Al-5wt%Mn-5wt%Zn. The heat treatment is T=650℃ heating for two hours following rapid cooling by the ice-water. The characteristic temperatures measured by DSC technique are Ms=-30℃, Mf=-55℃, As=-35℃, Af=-15℃. The geometry of specimen is the thin-walled tube whose inner and outer diameters are 5mm and 8mm, respectively, as shown in Fig.4. The multi-axial loading tests were performed, applying the combined loads of axial force and torque to the thin-walled tube specimen. Figure 5 shows the picture of multi-axial loading apparatus (Shimadzu Autograph AG10TS) which can apply the axial force and torque to the thin-wall tube specimen, simultaneously and automatically. Figure 6 shows the tensile stress σ - strain ε relations at the temperature T=20℃ and –40℃. As found from the figure, this material shows the pseudo-elastic behavior at T=20℃ and the shape memory behavior at T=-40 ℃. Figure 7 shows one example of experimental results under multi-axial loading conditions. Figure 7(a) shows the thermo-mechanical (proportional) loading path. In this figure, 1-2 is the proportional loading of axial stress σ and τ , 2-3-4 is the thermal cycle under the constant stress state (σ , $C_1\tau$)=(280MPa, 24oMPa), and 4-5 is the proportional unloading. Figure 7(b) shows the strain response in the strain space (ε , $C_2\gamma$), where ε and γ are the axial strain and shear strain of thin-walled tube, respectively. The coefficients C_1 and C_2 are the material constants related with the equivalent stress σ_{EQ} and equivalent strain ε_{EQ} respectively, defined as follows:

$$\sigma_{EQ}=\sqrt{[\sigma^2+(C_1\tau)^2]},\quad \varepsilon_{EQ}=\sqrt{[\varepsilon^2+(C_2\gamma)^2]}$$

The stress-strain relations for the proportional loading of axial stress σ and shear stress τ coincide very well with each other. In this material, C_1=1.2, and C_2=0.5 [9-11]. If the material is so-called Mises type, C1=$\sqrt{(3)}$ and C2=1/$\sqrt{(3)}$. As found from the figure, the strain response 2-3-4 corresponds to the temperature cycle 2-3-4 with the constant (bias) stress. That is, this material deforms proportionally and cyclically with the change of

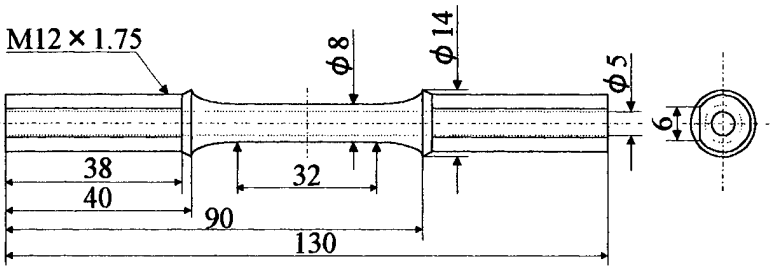


Fig.4 Geometry of specimen



Fig.5 Photo of complex loading apparatus

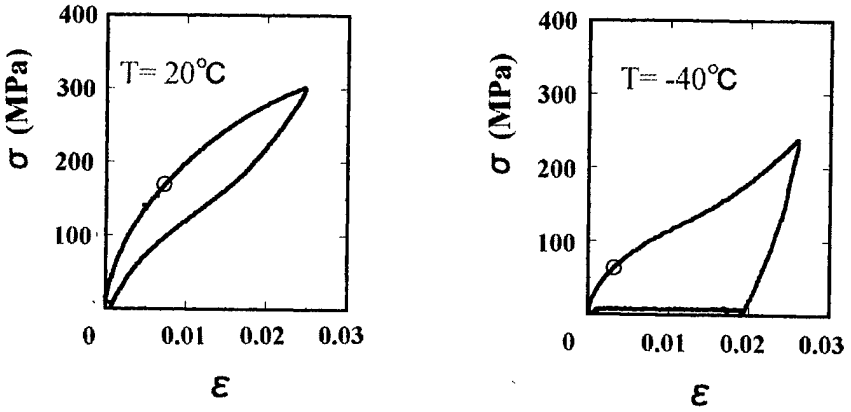


Fig.6 Fundamental properties of Cu-based SMA

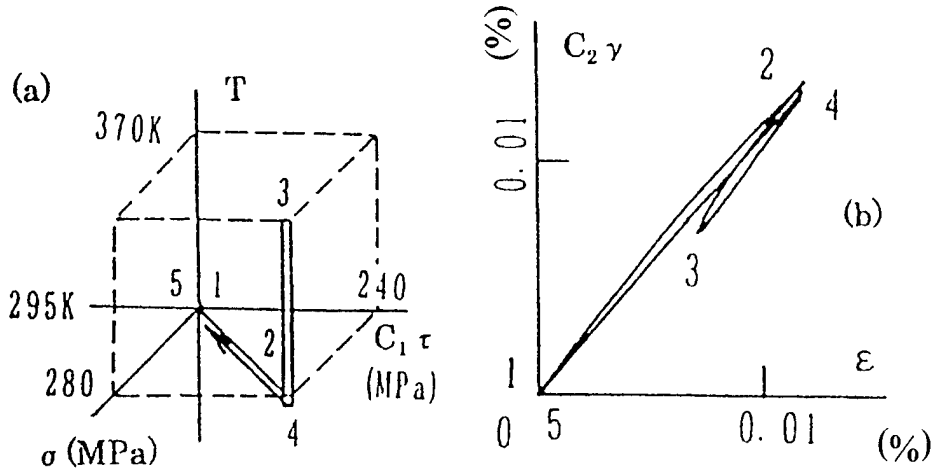


Fig.7 Pseudoelastic behavior of SMA subjected to proportional load

temperature under the combined bias stress. Judging from the experimental result, it may be expected that such proportional deformation (the two-dimensional actuating performances) without any bias stress can be obtained by the proportional cyclic training. This experimental result gave us the strong motivation of the present research work.

Experimental results

Figure 8 shows the experimental results obtained by the simple torsion experiments. Figure 8(a) shows the stress-strain relation obtained during the training whose cycle number is 5 times between $C_1\tau = 0$ and 410MPa. Figure 8(b) shows the 2-way behavior obtained by the training whose stress amplitudes are 345MPa and 410MPa. As found from this figure, the specimen subjected to the simple torsion training shows the cyclic torsion deformation by the cyclic change of temperature without any bias stress. Figure 9 shows the experimental results obtained by the proportional cyclic training. Figure 9(a) shows the stress-strain relation during the training. For the training, 5 times loading-unloading between stress states (σ 、$C_1\tau$)=(305MPa, 258MPa) and (0, 0) was employed. Figure 9(b) shows the two-way behavior obtained by the training. As found from the figure, the thin-walled tube specimen shows the cyclic and proportional deformation only by the change of temperature, without any bias stress, Figure10 shows one example of experimental results obtained by the complex loading training. Figure 10(a) shows the complex load training path, that is, 0-1 is the torsion loading, 1-2 is the axial stress loading while keeping the shear stress constant, 2-1 is the unloading of axial stress, and 1-0 is the unloading of shear stress. The number of training cycles is 5. Figure 10(b) shows the stress-strain response during the 5 times training. Figure 10(c) shows the obtained 2-way behavior. As found from the figure, there is a slight phase difference between the axial strain and shear strain during the change of temperature. Also, the axial strain is much larger than the shear strain. This difference may be explained by the path dependency of shape memory alloy. Figure 11 shows another example of complex load training. Figure 11(a) shows the training path, Figure 11(b) shows the strain response during the training, and Figure 11(b) shows the 2-way memory deformation. As found from the figure, the

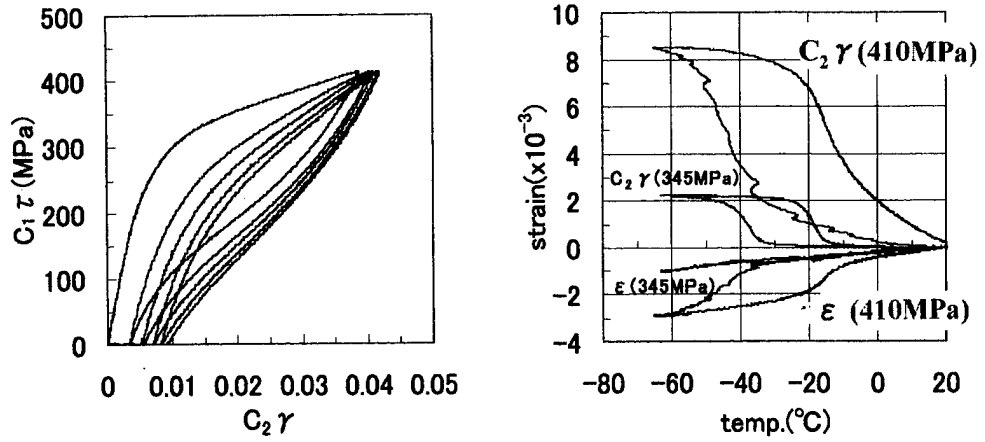


Fig.8 Two-way shape memory behavior obtained by the simple torsion training

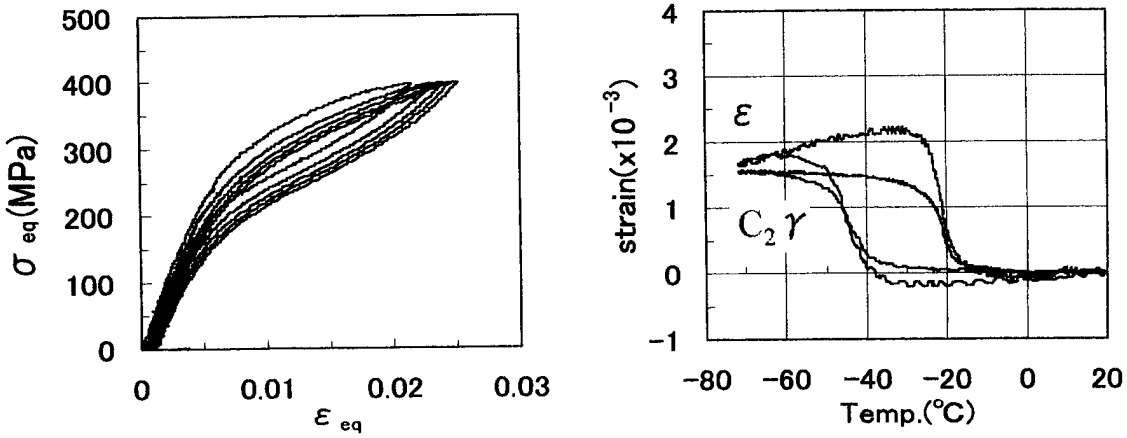


Fig.9 Two-way shape memory behavior obtained by the proportional load training

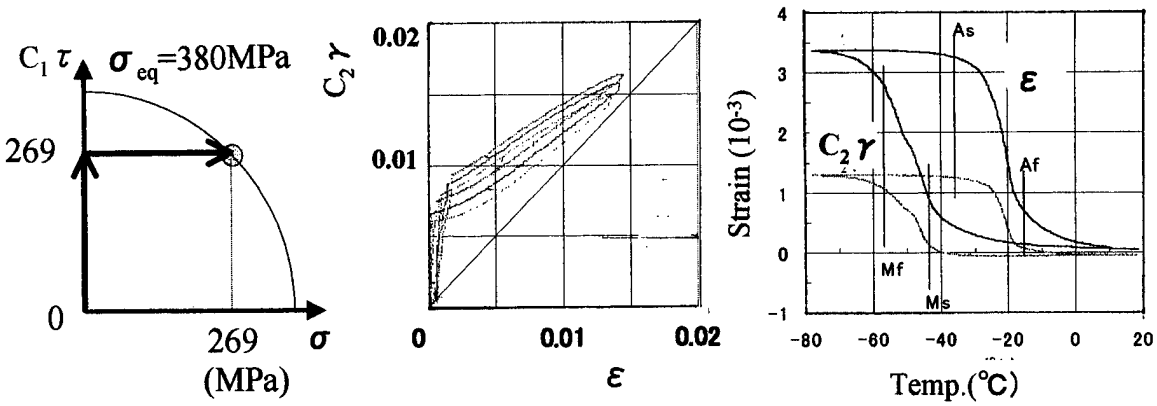


Fig.10 Two-way shape memory behavior obtained by the complex load training (I)

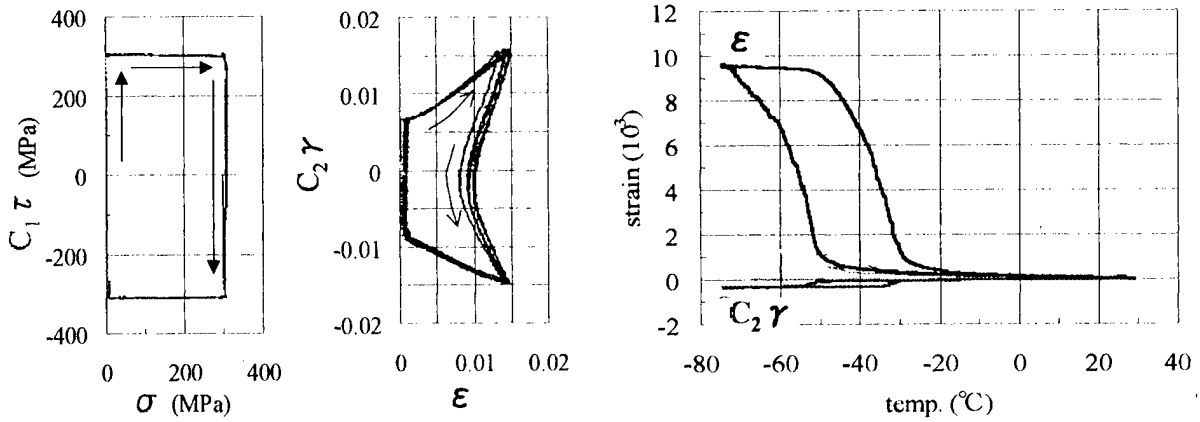


Fig.11 Two-way shape memory behavior obtained by the complex load training (II)

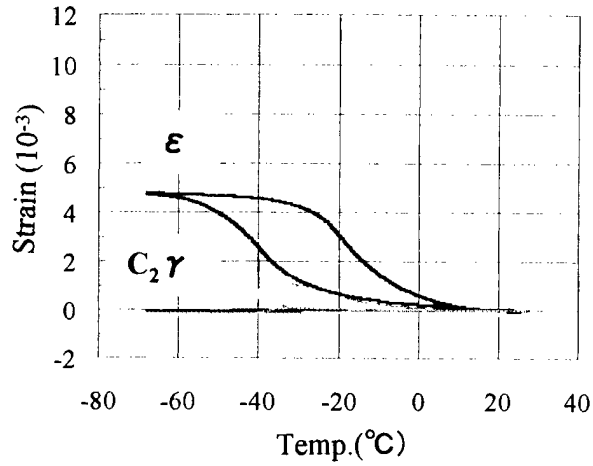


Fig.12 Two-way shape memory behavior obtained by the simple tension

shear strain is quite small. Figure 12 shows the two-way axial strain obtained by the simple tensile training whose stress amplitude is 300MPa which is the same as the amplitude used in the experiments shown in Fig.11. As found from Fig.11(b) and Fig.12, the obtained two-way axial strain obtained by the complex load training is much larger than the two-way strain obtained by the uni-axial tensile training whose cyclic amplitude is the same. That is, the training of shear stress component increases the 2-way shape memory axial strain.

Conclusions

The experimental results shown here suggested us quite interesting new possibilities of 2-way shape memory effect by using the combined stress training. The further systematic experiments are expected, and the theoretical discussion is necessary especially for the residual stress obtained by the complex loading training. The microscopic discussion may be very important, especially for the interaction between the martensite phase transformation and the movement of dislocation. The complex 2-way actuation will

develop the application area of shape memory alloy, especially in the field of micro-actuator for the smart (intelligent) structures.

References

1. Lexcellent, C., S.Leclercq, B.Gabry, and G.Bourbon. 2000. "The two way shape memory effect of shape memory alloy: an experimental study and a phenomenological model", International Journal of Plasticity, 16, pp.1155-1168
2. Kato,H., R.Stalmans, and J.Van Humbeeck. 1998. "Two-way Shape Memory Effect Induced by Tension Training in Cu013.4Al-4.0Ni(mass%) Alloy Single Crystals", Materials Transaction, JIM, 39(3), pp.378-386
3. Guilemany, J.M., J.Fernandez, and R.Franch. 1998. "On the stabilization of martensite during direct quenching and training of some Cu-Zn-Al-Zr spring", Intermetallic , 6, pp.15-19
4. Gil, F.J. and J.A.Planell. 1998. "Shape memory alloys for medical applications", Proc.Instn Mech Engrs, 212(Part II), pp.473-488
5. Zhang, J.X., Y.X.Liu, W.Cai and L.C.Zhao. 1997. "The mechanism of two-way shape memory efffect in a Cu-Zn-Al alloy", Materials letters, 33, pp.211-214
6. Bo, Z., and D Part III: evolution of plastic strains and two-way shape memory effect", International Journal of Engineering.C.Lagoudas. 1999. "Thermomechanical modeling of polycrystalline SMAs under cyclic loading, Sciences, 37, pp.1175-1203
7. Cingolani, E., J.Van Humbeeck, and M.Ahlers, 1999., "Stabilization and Two-way Shape Memory Effect in Cu-Al-Ni Single Crystals", Metallurgical and Materials Transactions A, 30A, pp.493-499
8. Gyobu, A., Y.Kawahara, T.Saburi and H.Horikawa, 1999., "Martenistic Transformation and Two-way Shape Memory Effect of Sputter-deposited Ni-Rich Ti-Ni Alloy Films
9. Tokuda, M., P.Sittner, M.Takakura, and M.Ye, 1995, "Experimental Study on Performances in Cu-based Shape Memory Alloy under Multi-axial Loading Conditions", Materials Science Research International, 1(4), pp.260-265,
10. Sittner, P., Y.Hara and M.Tokuda, 1995, "Experimental Study on the Thermoelastic Martensitic Transformation in Shape Memory Alloy Polycrystal induced by Combined External Force", Metallurgical and Materials Transactions A, 26A, pp.2923-2935
11. Tokuda, M., M.Ye, M.Takakura, and P. Sittner, 1999, "Thermomechanical behavior of shape memory alloy under complex loading conditions", International journal of Plasticity, 15, pp.223-239

Signal Processing and Composites

WAVELET DAMAGE DETECTION ALGORITHM FOR SMART STRUCTURES

Katharine J. Jones[1]

Abstract

A wavelet damage detection algorithm is described which combines active detection with Fiber Bragg Grating (FBG) sensors and passive detection with wavelet-based fault detection.

1 INTRODUCTION

Health monitoring of large scale structures has significance in many fields: in aerospace structures[1], in ships[2] and civil structures[3]. It can predict structural damage, reduce lifecycle costs and allow greater operational availiability. Use of composite-embedded optical fiber sensors has gone in the space of a few years from laboratories[4,5], to use in tunnel surveillance[6], bridges[7] and ships[8,9,10]. Also structural health monitoring by means of scanning X-ray microscopy has achieved an understanding of damage modes in composites[11,12]. Damage detection algorithms have been proposed for investigating the structural integrity of systems[13]. A new field which is uniquely suitable for damage detection is wavelets[14]. The author applied wavelet image processing to crack detection in a composite board with embedded optical fibers[15].

[1]Katharine J. Jones, Department of Mathematics, Rice University, 6100 Main St., Houston, TX 77005, USA.

2 APPROACH

An automated inspection system for aerospace structures needs either an active inspection probe or a passive system which can record and quantify impacts [1].

2.1 ACTIVE DETECTION

Fiber optics have become the nervous system for smart structures [5]. Fiber Bragg Gratings (FBG) [3] are presently the most widely used fiber optic sensors for bridges and other civil structures. Strain is encoded in a wavelength induced shift in the reflected signal. It is possible to identify damage or deterioration by placing sensors in critical high stress locations. E Udd and coworkers [7] attached 28 FBG sensors on a bridge and were able to differentiate between several types of vehicles and a pedestrian.

The most impressive application of optical fiber sensors in the hull of a ship has been reported by the University of Tokyo and NTT [9,10]. A fiber optic distributed sensor (Brillouin optical time domain refractometer) was installed on both circular and longitudinal axes of the Asura/Idaten, the Japanese entry in the America's Cup 2000. Since yacht structure designs push the strength of the materials to the limit, it is important to detect highly stressed regions which might cause catastrophic fracture.

2.2 PASSIVE DETECTION

Traditionally, the Fourier transform is used to extract the characteristic features of sampled signals. However, wavelet theory has emerged as a better tool, especially for singularity detection and pattern recognition[14]. The author[15] reported applying wavelet signal and image processing to a digital scan of a photographic image of composite-embedded optical fibers. The composite panels were from a series of papers published by the author and coworkers[16,17] on composite-embedded avionics data links. Noise reduction of the digitized image achieved improved resolution and allowed identificationof features of 50-100 micron dimensions.

3 WAVELET DAMAGE DETECTION ALGORITHM

3.1 Basic idea of the algorithm

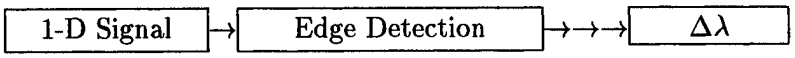
Our goal is to apply wavelet signal and image processing to two types of data for the purpose of locating damage:
(a) 1-D Fiber Bragg Grating (FBG) sensor data showing pulse displacement or

signal distortion as a function of strain.
(b) 2-D Image processing of the surface of a composite-embedded fiber optic board to locate cracks or damage.

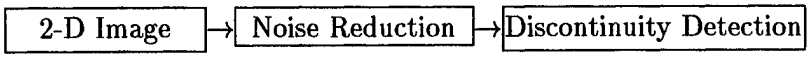
It has to be conceded that both (a) and (b) can be indicators of damage, though (a) comes from discrete sensors while (b) is a continuous xy plane. Also, (a) can be axial or tranverse. It is quite possible that that (a) will show distortion without cracks being detected in (b). Moreover, when cracks are detected in (b) and coincide with signal distortion in (a), the change is irreversible.

3.2 Implementation of algorithm

(a) 1-D Fiber Bragg Sensor Data.



(b) 2-D Image Data.



4 RESULTS

4.1 Wavelet signal processing of Fiber Bragg Grating sensor data

Implementation of 1-D wavelet signal processing is depicted in Figure 1. Figure 1(a) is a Matlab plot of FBG sensor reflection spectra[20]. Matlab plots were made from the paper by N. Takeda et al. since this data is specifically calibrated for changes in tensile strain. Figure 1(b) is the second peak from 1(a). Figure 1(c) shows application of discontinuity detection (db8) to 1(b). Figure 1(d) is a Matlab Waterfall plot of discontinuity detection of all the peaks in 1(a): a peak followed by a dip. The change in FBG sensor reflection spectra involves both displacement and distortion of the signal. The wavelet filter db8 detects second order discontinuities or peaks[22].

4.2 Wavelet image processing of 2-D image data

Implementation of 2-D wavelet image processing is depicted in Figure 2. Figure 2(a) shows the DeNoised image of the composite board with embedded optical fibers[15,16]. The crack is made visible because the optical fiber has input from a HeNe laser. The

crack is at column 50, row 110. Figure 2 (b) is a Matlab Waterfall plot of a series of consecutive rows. The center peak is the laser emission from the crack. Figure 2 (c) is a single row where the center peak is the cross section of the crack. Figure 2 (d) illustrates wavelet edge detection using the Haar wavelet at scale 1. The dip followed by the peak is the crack position. Other useful wavelets are db4 for first derivative discontinuitiy detection and db6 or db8 for second derivative discontinuity detection[22].

5 CONCLUSIONS AND DISCUSSION

Wavelet signal processing has been applied to both active FBG sensor data and passive image data for fault detection. The ultimate (though not yet achieved) goal is to use a common algorithm to make sensor data confirm image processing data. In Figure 1, discontinuity detection can track the displacement (but not the distortion) of FBG reflection spectra. In Figure 2, the position, as well as the size, of a crack can be determined using Haar wavelets. The change in spectra for critical damage or the crack size for irreversible damage needs to be experimentally defined. Also, the physical positions should coincide. Wavelets are called a "digital microscope" and provide a means to magnify singularities for both 1-D signals and 2-D images.

Two dynamic fields, Smart structures and wavelet signal and image processing have been combined to confirm sensor data, provide early detection of damage and increase fault detection sensitivity. This method of using a common form of information processing to find coincidence between active and passive detection could be extended to other sensors and materials. Also, a real time damage detection method would find application in many fields.

6 REFERENCES

1. W. J. Staszewski et al., Damage detection in composite materials using optical fibers - Recent advances in signal processing, SPIE Vol. 3985, *Smart Structures and Integrated Systems*, 3985-29, 2000.

2. T. G. Giallorenzi, Optical technology in Naval applications, *OPN*, April 2000, pp. 24-36.

3. E. J. Friebele, Fiber Bragg grating strain sensors: Present and future applications in smart structures, *OPN*, August 1998, pp. 33-37.

4. R. O. Claus et al., Performance of optical fiber sensors embedded in polymer matrix composites for fifteen years, SPIE Vol. 3330, *Sensory Phenomena and Measurement Instrumentation for Smart Structures and Materials*, pp. 8-11, 1998.

5. E. Udd, Early efforts to initiate the field of fiber optic smart structures at McDonnell Douglas, SPIE Vol. 3330, *Sensory Phenomena and Measurement Instrumentation for Smart Structures and Materials*, pp. 12-18, 1998.
6. P. M. Nellen, Optical fiber Bragg gratings for tunnel surveillance, SPIE Vol. 3986, *Sensory Phenomena and Measurement Instrumentation for Smart Structures and Materials*, pp. 263-270, 2000.
7. E. Udd et al., Multidimensional strain field mearuements using fiber grating sensors, SPIE Vol. 3986, *Sensory Phenomena and Measurement Instrumentation for Smart Structures and Materials*, pp. 254-262, 2000.
8. K. Pran et al., Instrumentation of a high-speed surface effect ship for structural response characterization during sea trials, SPIE Vol. 3986, *Sensory Phenomena and Measurement Instrumentation for Smart Structures and Materials*, pp. 372-379, 2000.
9. H. Murayama et al., Structural health monitoring of IACC yachts using fiber optic distributed strain sensors: a technical challenge for America's cup 2000, SPIE Vol. 3986, *Sensory Phenomena and Measurement Instrumentation for Smart Structures and Materials*, pp. 312-323, 2000.
10. A. Shimoda et al., Development of integrated damage detection system for international America's cup class yacht structures using fiber optic distributed sensor, SPIE Vol. 3986, *Sensory Phenomena and Measurement Instrumentation for Smart Structures and Materials*, pp. 324-329, 2000.
11. N. Takeda et al., The application of a ply-refinement technique to the analysis of microscopic deformation in interlaminar-toughened laminates with transverse cracks, *Composites Science and Tech.* 60(2000): 231-240.
12. N. Takeda and S. Ogihara, In situ observation and probabilistic prediction of microscopic failure processes in CFRP cross-ply laminates, *Composite Science and Tech.* 52(2000): 183-195.
13. A. W. Otiene et al., Damage detection using modal strain energy and laser vibrometer measurements, SPIE Vol. 3985, *Smart Structures and Integrated Systems*, 2000.
14. Y. J. Wu et al., Limited sample wavelet network and its application for damage detection composites, *Opt. Eng.* 39(4): 1002-1008, 2000.
15. K. J. Jones, Wavelet edge detection to be used with composite embedded fiber optic sensors, SPIE Vol. 3986, *Sensory Phenomena and Measurement Instrumentation for Smart Structures and Materials*, pp. 397-406, 2000.
16. R. E. Morgan, S. L. Ehlers, J. M. MacKenzie and K. J. Jones, An active evanescent coupler for smart processing, SPIE Vol. 1918, *Smart Structures and Materials '93: Smart Sensing, Processing, and Instrumentation*, pp. 2, 1993.
17. R. E. Morgan, S. L. Ehlers, and K. J. Jones, Composite-embedded fiber optic

data links and related material/connector issues, SPIE Vol. 1588, *Fiber Optic Smart Structures and Skins IV*, pp. 189-197, 1991.
18. H. Lamela et al., Temperature measurements in fiber optic interferometric multichannel automated instrumentation system, SPIE Vol. 3670, *Sensory Phenomena and Measurement Instrumentation for Smart Structures and Materials*, pp. 26-33, 1999.
19. S. Lloret et al., Optical set-up development for monitoring of structural dynamic behavior using SOFO sensors, SPIE Vol. 3986, *Sensory Phenomena and Measurement Instrumentation for Smart Structure and Materials*, pp. 199- 205, 2000.
20. Y. Okabe, S. Yashiro, T. Kosaka and N. Takeda, Detection of tranverse cracks in composites by using embedded FBG sensors, SPIE Vol. 3986, *Sensory Phenomena and Measurement Instrumentation for Smart Structures and Materials*, pp. 199-205, 2000.
21. S. Mallat, *A Wavelet Tour of Signal Processing*, Academic Press, 1998.
22. G. Strang and T. Nguyen, *Wavelets and Filter Banks*, Wellesley - Cambridge, 1996, 389-390.
23. K. J. Jones, Wavelet Image Processing: Assessment of Spatial and Spectral Resolution of Landsat Images, SPIE Vol. 4056, *Wavelet Applications VII*, pp. 137-147, 2000.

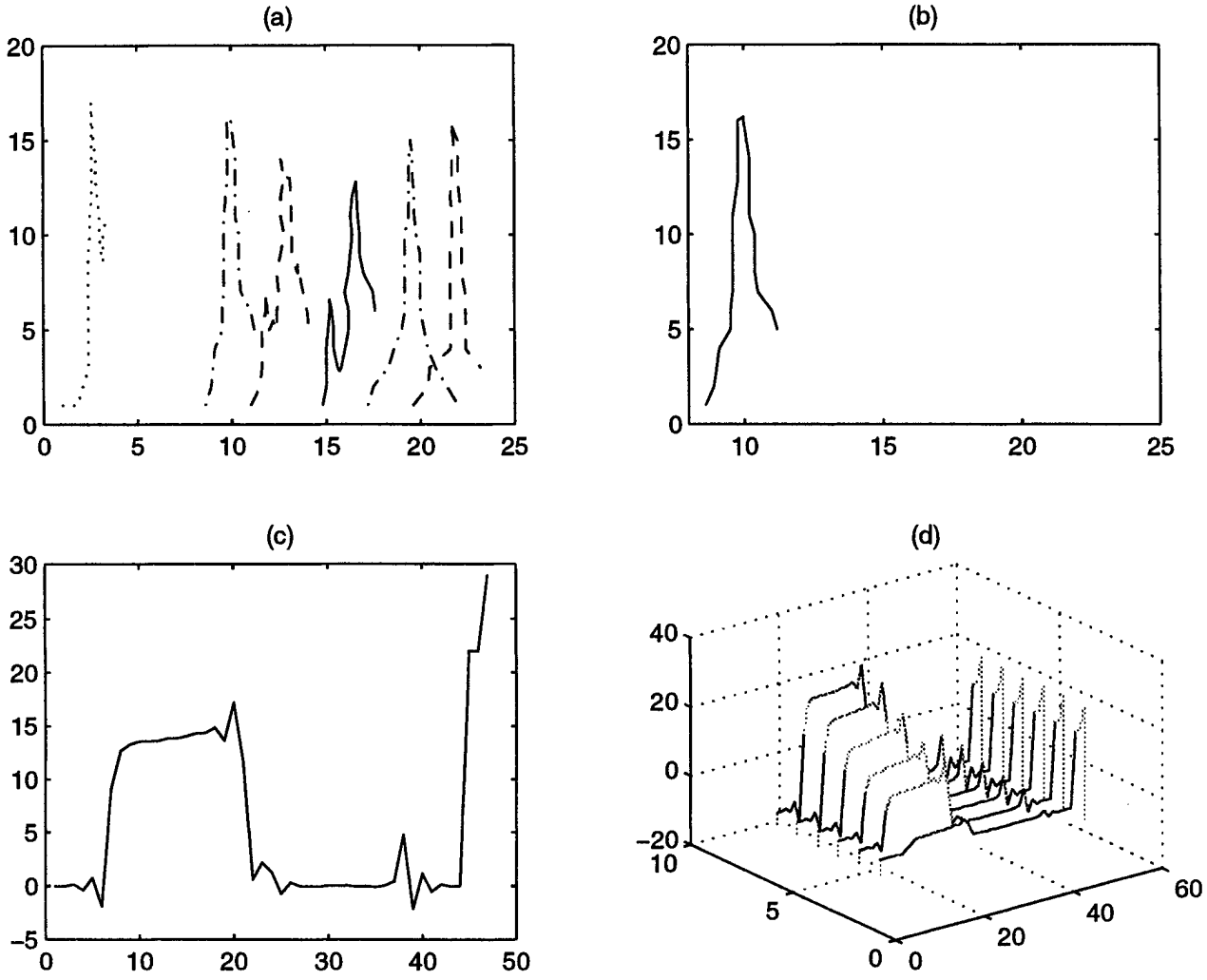


Figure 1: 1-D Signal Processing. (a) Matlab plot of FBG sensor reflection spectra[20]. (b) Single peak from (a). (c) Wavelet discontinuity detection of peak from (a). (d) Waterfall plot of wavelet discontinuity detection of reflection spectra peaks from (a): maximum followed by minimum indicate spectra peaks using db8[22].

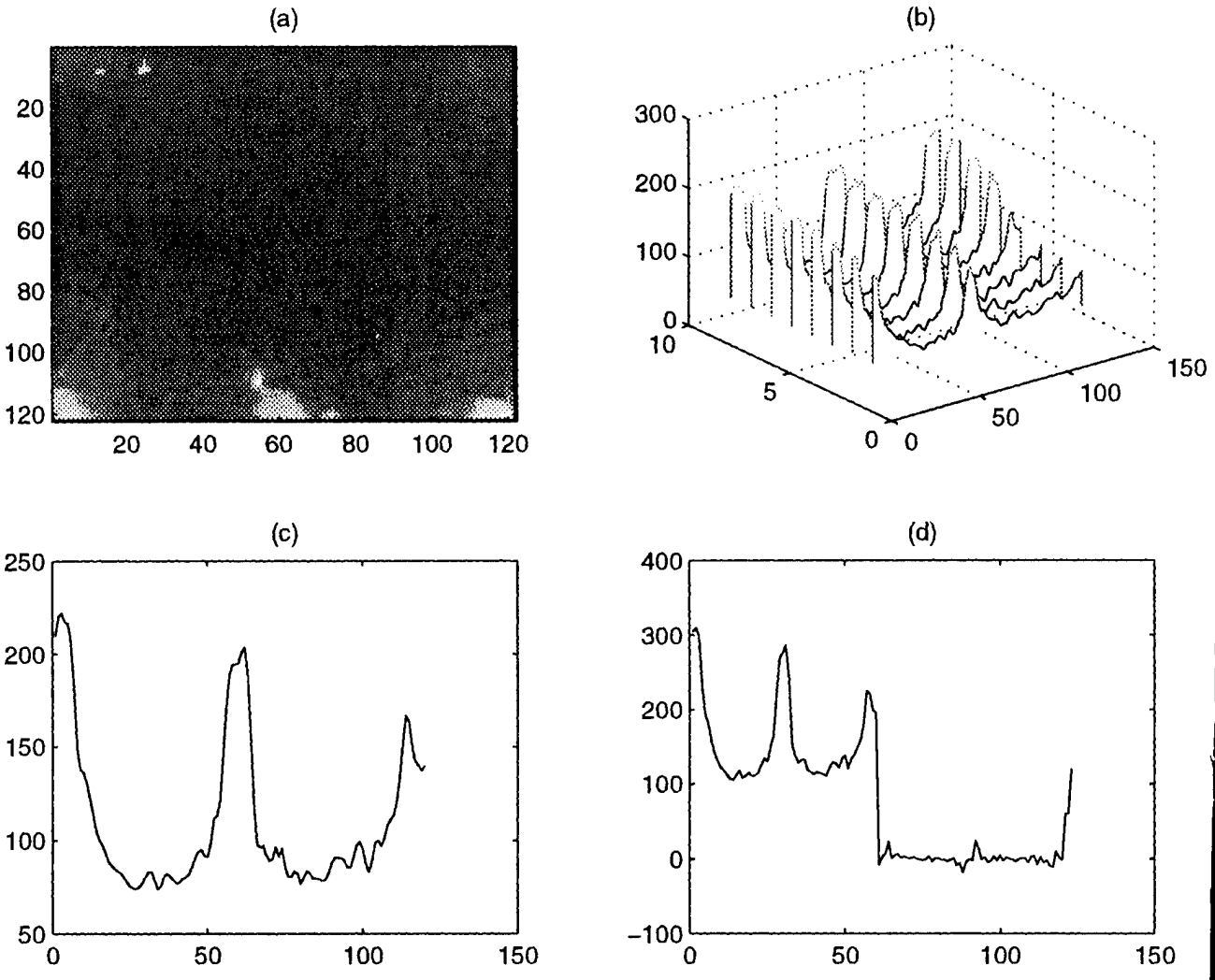


Figure 2: 2-D Image Processing. (a) DeNoised image of composite board with embedded optical fibers: crack is at column 50, row 110. (b) Waterfall plot of 1-D plots of crack (center peak). (c) 1-D plot of 4th row. (d) Edge detection of crack peak using 'Haar' wavelet at scale 1: dip followed by peak.

REAL-TIME ESTIMATION OF MULTI-MODAL FREQUENCIES FOR SMART STRUCTURES

Keun-Ho Rew, Sunmin Kim, In Lee, Youngjin Park

ABSTRACT

In this paper, various real-time estimation methods of multi-modal frequencies are realized in real-time and compared through numerical and experimental tests. The Bairstow method is introduced to decouple a characteristic equation for the estimation of multi-modal frequencies, and shows the computational efficiency. For a simple numerical test, two sinusoids of the same amplitudes mixed with various amount of white noises are considered, and the test results show that the AR(Auto Regressive) and ARMA(AR and Moving Average) methods are not suitable in noisy environments. In the view of computational efficiency, the ARMA method is inefficient, while the CNF(Cascade Notch Filter) methods are very effective. Experimental tests are devised to impose the severe conditions of drastically different amplitudes and of considerable changes of natural frequencies. From the experimental results, the AR method exhibits a remarkable performance. From the numerical and experimental results, the CNF methods are recommended when the computational efficiency is critical and the estimation condition is simple, while the AR method with the Bairstow method is recommended if the test environments are not noisy and there are more than two modes with different amplitudes.

INTRODUCTION

The frequency estimation problem has been an interesting issue since Fourier developed his transformation method in 1822. Since the 1970's, many algorithms have been developed for the on-line estimation of multi-modal frequencies in the fields of radar, communications, and adaptive signal processing [1-3]. The on-line information of natural frequencies can be applied to adaptive noise controllers [4-5], or to the adaptive vibration controller of time-varying structures [6], such as deployable space structures and the robot manipulator dealing with time-varying payloads. Because the local failure and delamination of composite structures tend to reduce natural frequencies, the on-line detection of the natural frequencies is also important in health monitoring. However, the multi-modal frequency estimation within each time step is not so manageable because of a heavy computational burden. Therefore, fast

Keun-Ho Rew, Sunmin Kim, In Lee, Youngjin Park, Dept. of Mechanical Engineering, Korea Advanced Institute of Science and Technology (KAIST), Taejon, Korea.

and reliable algorithms have been investigated for real-time frequency estimation.

Chaplin and Smith [7] patented an electronic circuit containing phased-locked-loops for the frequency estimation. For parametric methods, Nehorai [8] suggested and showed the advantages of the constrained-pole-zero structure and used the RML(Recursive Maximum Likelihood) method for parameter estimation. Tranvassor-Romano and Bellanger [9] developed the LinANF(Linearized Adaptive Notch Filter) method. Kim and Park [5] have developed an on-line multi-tonal noise estimation method, the CNF(cascade notch filer) method, and used to generate reference signal. Rew and Lee [6] applied the AR(Auto Regressive) method to the adaptive PPF vibration control.

The Bairstow method is adopted as a root finding method in this analysis, which enhances the computational efficiency drastically, and is compared with several frequency estimation methods through simple numerical and severe experimental tests. Various methods are investigated as follows: AR, ARMA(AR and Moving Average), RML, LinANF, EachCNF(Each-error-updated CNF), and LastCNF(Last-error-updated CNF). The above methods are named after the predetermined structures or parameter estimation method and the abbreviations are used for the sake of simplicity.

THEORIES ON FREQUENCY ESTIMATION METHODS

The frequency estimation methods are based on the adaptive signal processing theory. In general, the estimation of multi-modal frequencies is defined as the problem of finding frequencies, $f_i(n)$, of sinusoids mixed with white noises, $\xi(n)$ as the following equation.

$$x(n) = \sum_{i=1}^{p} U_i \sin(2\pi f_i(n) n T_s + \phi_i) + \xi(n) \tag{1}$$

AR, ARMA methods

These methods are composed of two steps. Firstly, we estimate the coefficients of a linear transfer function without inversing matrices by the RLS(Recursive Least Squares) method, which gives good convergence from arbitrary initial estimation. Secondly, we find roots of the characteristic equation by decoupling the characteristic equation into each mode through the Bairstow method.

If a system is modeled to have p modes, the characteristic equation of the system can be described as order of $2p$. A transfer function of an arbitrary structure can be described in the even order discrete form as follows:

$$H(z^{-1}) = \frac{B(z^{-1})}{A(z^{-1})} = \frac{b_1 z^{-1} + b_2 z^{-2} + \cdots + b_{2p} z^{-2p}}{1 + a_1 z^{-1} + a_2 z^{-2} + \cdots + a_{2p} z^{-2p}}, \tag{2}$$

where p is the number of vibrating mode, z^{-1} is a shifting operator, and $A(z^{-1})$ and $B(z^{-1})$ are called an AR part and an MA part, respectively.

The AR method estimates only AR coefficients neglecting MA. On the other hand, the ARMA method estimates MA coefficients as well as AR ones. Though the MA part is not used in the frequency detection, the MA part is helpful to estimate frequencies with robustness to noise as shown later.

The RLS method is used to obtain the coefficients of the AR and ARMA models with the cost function of weighted error squares, where λ is called a forgetting factor to weigh relative importance between the past and present error squares.

In order to obtain natural frequencies from the coupled characteristic equation, $A(z^{-1})$, the equation must be factorized into 2nd order equations. Only iterative algorithms can factorize the characteristic equation that has more than two modes. With the Bairstow method, we can factorize the AR part as the products of second order equations as follows:

$$A(z^{-1}) = z^{-2p}\prod_{i=1}^{p}(z^2 + p_i z^1 + q_i) = 0\,. \tag{3}$$

Then, the natural frequencies can be obtained from the following equation.

$$\hat{f}_i = \frac{1}{2\pi T_s} angle(Z_i \mid A(z^{-1}) = 0) = \frac{1}{2\pi T_s}[\cos^{-1}(-p_i / 2\sqrt{q_i})], \quad i = 1, 2, \cdots, p, \tag{4}$$

where T_s is a sampling time.

Finally, the obtained natural frequencies are sorted by magnitudes using a simple straight insertion algorithm [10]. Table I shows that the computational burden of the Bairstow method is quite less than that of the eigenvalue method, which has often been used in the previous approaches.

RML method

The RML method using the structure of constrained poles and zeros was suggested by Nehorai [8], who showed that the performance of the RML method is better than the ARMA method for pure sinusoidal signals. The structure can be written as follows:

$$N(z^{-1}) = \frac{A(z^{-1})}{A(\rho z^{-1})} = \frac{1 + a_1 z^{-1} + a_2 z^{-2} + \cdots + a_{2p} z^{-2p}}{1 + \rho a_1 z^{-1} + \rho^2 a_2 z^{-2} + \cdots + \rho^{2p} a_{2p} z^{-2p}},$$

$$a_{2p} = 1, \quad a_i = a_{2p-i}, \quad i = 1, 2, \cdots, p, \tag{5}$$

where ρ, called a pole contraction factor, is a positive real number close to but smaller than 1.0 and is related to the bandwidth of the notch. Note that the locations of zeros and poles are directly related as follows:

$$P_i = \rho^{-1} Z_i, \quad i = 1, 2, \cdots, p, \tag{6}$$

where P_i is the ith pole and Z_i is the ith zero of $N(z^{-1})$.

Then, the RML method uses the RLS scheme to estimate the parameters. λ and ρ are exponentially increased for a fast convergence and an accurate estimation from arbitrary initial parameters as follows:

$$\rho(n+1) = \rho_s \rho(n) + (1 - \rho_s)\rho_s, \quad \rho(0) = \rho_i, \tag{7.a}$$

$$\lambda(n+1) = \lambda_s \lambda(n) + (1 - \lambda_s)\lambda_s, \quad \lambda(0) = \lambda_i, \tag{7.b}$$

where ρ_s and λ_s are tuning variables, and ρ_i and λ_i are the initial values, respectively.

LinANF method

The LinANF method is famous for computational efficiency, fast tracking capability, and low threshold SNR(Signal to Noise Ratio). Kim and Park [5] compared the RML method and the LinANF method in view of the convergence speed, noise robustness aspect and computational load, and concluded that the LinANF method is more effective.

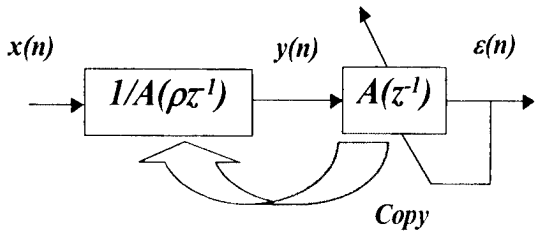


Figure 1. Structure of LinANF method.

The LinANF method also adopts the structure of constrained poles and zeros, but the estimation procedure is slightly different. The basic concept of this algorithm is to separate the numerator and the denominator of the ANF(Adaptive Notch Filter) and to update only the numerator and copy the coefficients to the denominator(Figure 1).

CNF methods

The CNF method for the multi-tonal noise control is proposed in Ref. [5] to reduce the computational burden. This method is originated from the following simple idea. The 2nd order notch filters connected in series as many as target sinusoids, p, can notch p sinusoids. If the parameters of notch filters are adapted properly, then the notched signal will be nearly zero; otherwise they would be adapted iteratively until the notch filter deducts the appropriate sinusoid. This repeat of adaptation makes the parameters converge to true ones. The CNF methods require quite small computational burden compared with the others.

The CNF methods consist of the EachCNF and the LastCNF method [5], depending on the error updating methods(Figures 2-3). The EachCNF method has p sections that notch each tonal signal with each error, though all sections of the LastCNF method are updated with the last error as Figure 2-3. This last error update allows the LastCNF method to avoid frequency conflicts each other. In the CNF methods, neither matrix calculation nor root-finding scheme is needed.

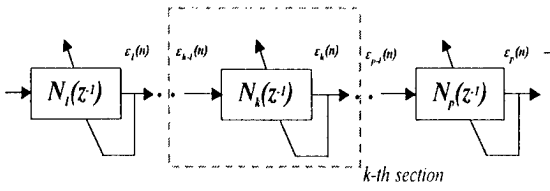


Figure 2. Structure of EachCNF method.

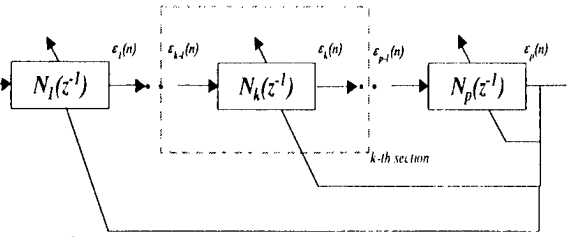


Figure 3. Structure of LastCNF method.

Other methods

There are several methods that were not mentioned above such as the eigenspace method, the Pisarenko method, the MUSIC(MUltiple SIgnal Classification) method and the ESPRIT(Estimation of Signal Parameters via Rotational Invariance Technique) method [2-3], etc.

NUMERICAL COMPARISON OF PERFORMANCES

For typical performance test, six methods were simulated for two sinusoids mixed with a white noise having equal amplitudes and time-varying frequencies. SNR and *Err* are defined

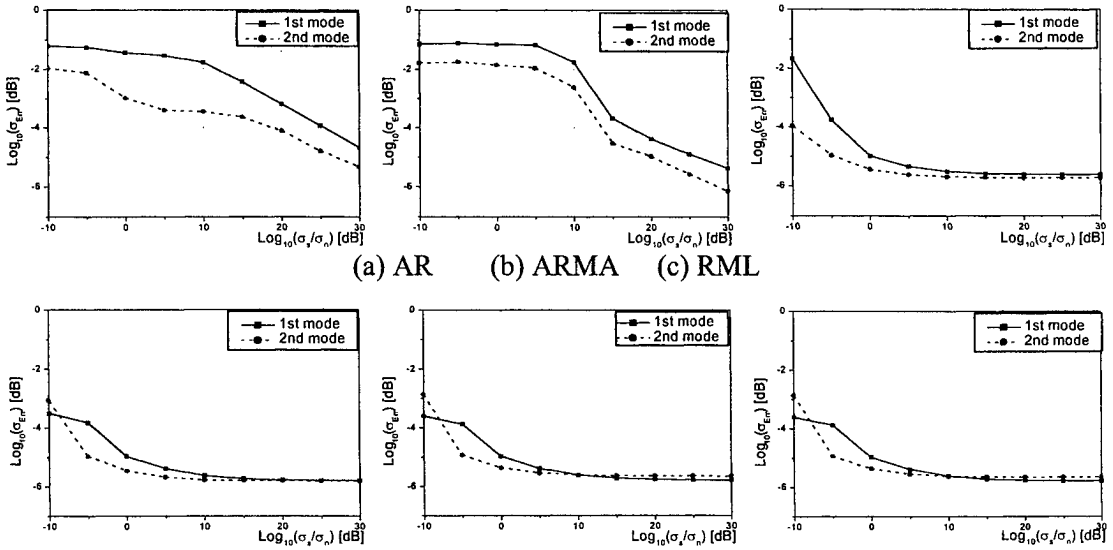
as follows:

$$SNR \triangleq 10Log_{10}(\sigma_S / \sigma_N), \tag{8.a}$$

$$Err \triangleq f_i - \hat{f}_i, \tag{8.b}$$

where σ_S and σ_N are the variances of signal and noise, respectively. *Err* is defined as a discrepancy between the true frequency and the estimated frequency. The estimation errors with respect to SNR were given in Figure 4. As the noise increases, *Err* increases, and the graph tends to move from right down to left up. At this time, *Err* increases drastically at a certain point. The x-axis value at this point is called the threshold SNR.

The robustness to noises of the AR and ARMA methods are not so good as the other methods(Figure 4 and Table I). This result implies that the AR and ARMA methods are not suitable for noisy environments.

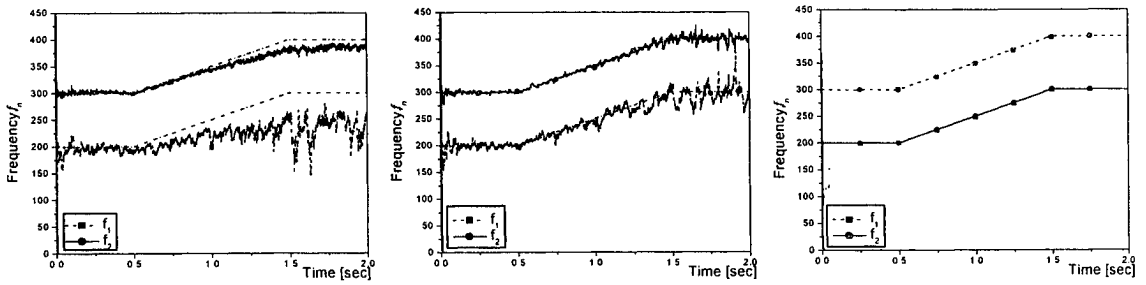


(a) AR (b) ARMA (c) RML

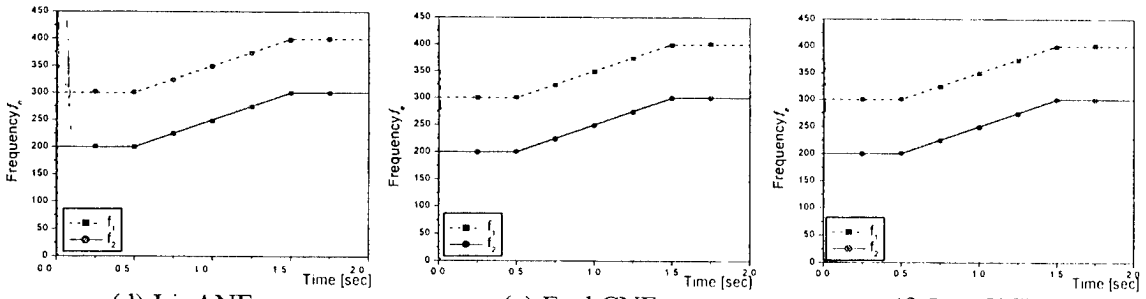
(d) LinANF (e) EachCNF (f) LastCNF

Figure 4. Variance of estimation error with respect to SNR.

Figure 5 shows the tracking capability of the 6 methods. The 1st and 2nd frequencies vary from 200 to 300 Hz and from 300 to 400 Hz, respectively. The parameters used in the simulations are introduced in Table II.



(a) AR (b) ARMA (c) RML



(d) LinANF (e) EachCNF (f) LastCNF

Figure 5. Frequency estimation when SNR = 15 dB.

The computational burden is compared in Table I. In the case that the computational burden is critical, the ARMA method is unsuitable, and the CNF methods are strongly recommended.

EXPERIMENTAL COMPARISON OF PERFORMANCES

The frequency estimation algorithms must be applied not only to a simple case as previous studies, but also to a severe case, which is more realistic. Experimental tests are devised to confirm the feasibility of real-time computations, and to impose strict conditions considering drastically different amplitudes and considerable changes of natural frequencies. These conditions have not been considered seriously in the previous researches.

A wing-like composite plate is manufactured(Figure 6). The Stacking sequence of the specimen is $[90_3/0_2]_S$. PZT and PVDF stand for the piezo-ceramic actuator and piezo-film sensor, respectively. Magnetic masses are attached to the wing-like specimen at the leading edge(Figure 6). Each of the added masses amounts to 1.62 *gram*, and three added masses approximately weigh 12.0 % of the specimen. For simplicity, the cases Fx and Fabc are named after the position of added masses. Off-line frequency responses show that the amplitudes of the first three modes have the amplitude ratio of 7.08 : 1.00 : 2.10 in the Fx case, respectively. The added masses make the first three natural frequencies decrease as much as 7.8 %, 13.5 %, and 10.1 %, respectively.

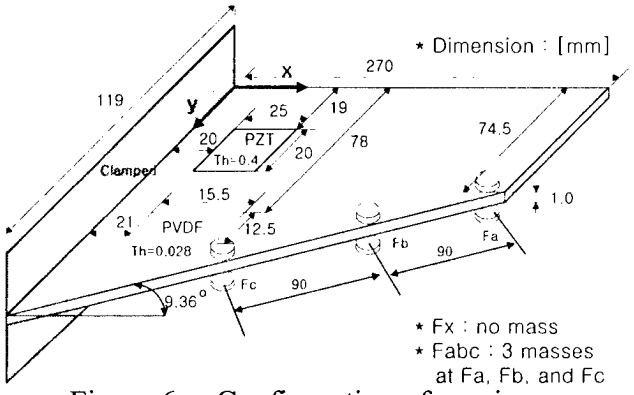
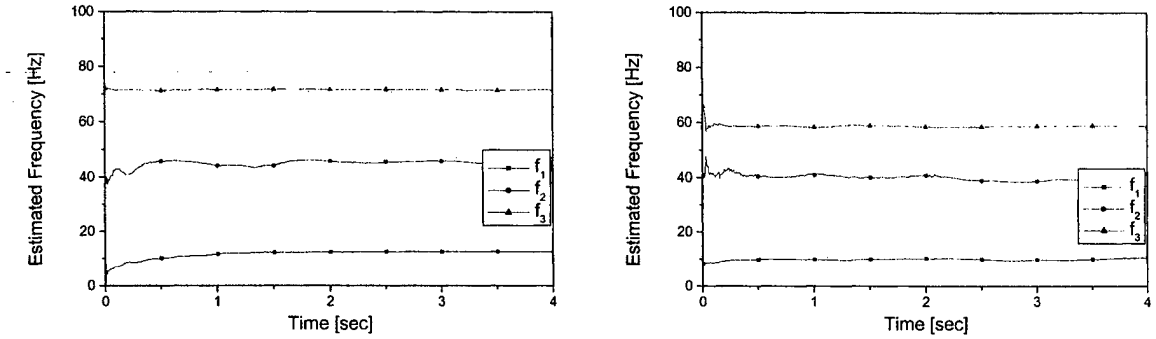


Figure 6. Configuration of specimen.

A charge amplifier converts the generated charge signal to electric voltage signal, and the converted signal is fed into the DSP controller. Then, the estimation signal is calculated using the above methods. The source module of the FFT analyzer generates an external disturbance

that is a banded white signal. This disturbance signal is applied to the piezoelectric actuator after 500 times voltage amplification. The time step of frequency estimation, T_s, is selected as 5.0 *msec.*

The estimation of the 1st and the 3rd modes using the AR method is relatively precise, but the 2nd mode frequency is somewhat incorrect because the 2nd mode contributes small amount in the total vibration(Figure 7). As noted in Figure 7, the 3rd mode frequency is converged quickly, whereas the 1st mode converges slowly. This originates from the fact that vibration signal of a faster mode contains much information in the same number of data. Added masses make the natural frequencies decrease as mentioned above. Those characteristics can be seen in Figure 7(b). It can be observed that the changes of the frequencies do not deteriorate the estimation performance.



(a) Fx case (b) Fabc case

Figure 7. Frequency estimation using AR method for each case.

As Regalia [3] pointed out through a numerical example, it is more difficult to detect natural frequencies from the vibration signal of structures having quite different amplitudes, than to detect the frequency of pure two sinusoids with similar amplitudes. The other methods do not perform well under severe experimental tests. This is due to the effect resulted from the damping of the system. Methods using ANF are updated without considering the damping of a system, while the AR and ARMA methods consider the damping effect.

CONCLUSIONS

In this paper, various real-time estimation methods of multi-modal frequencies are realized and compared through numerical and experimental tests. The following several methods are introduced and examined: AR, ARMA, RML, LinANF, EachCNF, and LastCNF. We introduced the Bairstow method to decouple the characteristic equation and revealed the computational efficiency quantitatively.

From the simple numerical test results, the AR and ARMA methods are not recommended in noisy environments. The results reveal that the ARMA method is inefficient in the view of computational efficiency; however, the EachCNF and LastCNF methods are fairly effective. The LinANF and RML methods have averages performances. For the severe experimental tests, we estimated in real-time the natural frequencies of a wing-like composite plate with a piezoelectric sensor and an actuator. By adding masses, the natural frequencies of the specimens are changed. The frequency estimation performance of the AR method is better than the other methods in the case of the frequency changes.

From the results, we recommend the CNF methods when the computational efficiency is critical and the estimation condition is simple and the AR method with the Bairstow method if the test environments are not noisy and there are more than two modes with different amplitudes.

ACKNOWLEDGEMENT

This study has been supported by the Korean Ministry of Science and Technology. The authors gratefully acknowledge the National Research Laboratory program.

REFRENCES

1. Goodwin, G.C., and Sin, K.S., Goodwin, G.C., and Sin, K.S., *Adaptive Filtering Prediction and Control*, 2nd ed., Prentice-Hall Inc., 1984.
2. Proakis, J.G., and Manolakis, D.G., *Digital Signal Processing*, 3rd ed., Prentice-Hall Inc., 1996.
3. Regalia, P.A., *Adaptive IIR Filtering in Signal Processing and Control*, Marcel Denkker Inc., 1995, Ch.10.
4. Hansen, C.H., and Snyder, S.D., *Active control of noise and vibration*, E&FN SPON, 1997, pp. 374-543.
5. Kim, S., and Park, Y., "Active Control of Multi-tonal Noise with Reference Generator Based on On-line Frequency Estimation," *Journal of Sound & Vibration*, Vol. 227, No. 3, 1999, pp. 647-666.
6. Rew, K.H., Han, J.H., and Lee, I., "Adaptive Multi-modal Vibration Control of Wing-like Composite Structure Using Adaptive Positive Position Feedback," AIAA 2000-1422, *41st Structures, Structural Dynamics, and Material Conference*, Atlanta, 2000.
7. Chaplin, G.R.B, and Smith, R.A., *US Patent 4,566,118*, "Method of and Apparatus for Canceling Vibrations from a Source of Repetitive Vibrations," 1986.
8. Nehorai, A., "A Minimal Parameter Adaptive Notch Filter with Constrained Poles and Zeros," *IEEE Trans. on ASSP*, Vol. ASSP-33. No. 4, 1985, pp. 983-996.
9. Tranvassor-Romano, J.M., and Bellanger, M., "Fast Least Squares Adaptive Notch Filtering," *IEEE Transactions on Acoustics, Speech, and Signal Processing*, Vol. 36, No. 9, 1988, pp. 1536-1540.
10. Press, W.H., et al, *Numerical Recipes in C*, 2nd ed., The Cambridge Press, 1988.

TABLE I. COMPUTATIONAL BURDEN AND THRESHOLD SNR.

Methods	Computational burden [FLOPS]	Root finding method	Threshold SNR [dB]
AR	867/1819	B/E	15
ARMA	2313	B	15
RML	778	B	5
LinANF	657	B	0
LastCNF	78	N	0
EachCNF	101	N	0

* FLOPS: Floating Point OPerationS
B : the Bairstow method
E : the eigenvalue method
N : not used

TABLE II. PARAMETERS USED IN TESTS.

	Mode	Frequency [Hz]	Amplitude
Numerical test	1st	200→300	1.0→1.0
	2nd	300→400	1.0→1.0
	Mode	Frequency [Hz]	Amplitude
Experimental test [A]	1st	12.75→11.75	7.08→2.83
	2nd	48.0→41.5	1.00→1.00
	3rd	71.75→64.5	2.10→1.31

* sampling time of numerical test : 1 msec.
sampling time of experimental test: 5 msec
[A] Fx→Fabc

SIMULTANEOUS MONITORING OF IMPACT LOCATIONS AND DAMAGES USING NEURAL NETWORKS AND WAVELET ANALYSIS

Dae-Un Sung, Chun-Gon Kim, Chang-Sun Hong

ABSTRACT

Low-velocity impact is a major concern in the design of structures made of advanced laminated composites, because it can cause extensive delaminations inside composites that can severely degrade the load-carrying capability. It is necessary to develop the impact monitoring techniques providing on-line diagnostics of smart composite structures susceptible to impacts. In this paper, we report on the simultaneous monitoring of impact locations and damage states. Up to now, the impact problems of composite laminate were classified into two main directions. One was the impact identification and the other was the detection of impact damages such as delaminations. This study focuses on the integrated approach for both two objects by PZT sensors. We discuss the procedures of impact location detection in which the generated acoustic signals are detected using PZT by the improved neural network paradigms. Simultaneously, the sensor output is processed with the Wavelet Transform (WT) to monitor the Acoustic Emission (AE) waves by the occurrence of damages and the result is compared with that of the undamaged case.

INTRODUCTION

Due to recent advances in sensor technology, a new concept of damage diagnostics for monitoring the integrity of in-service structures has been proposed. This concept is generally known as a health monitoring of smart structures. The health monitoring system must estimate structural health by using all of the information provided by the various sensor measurements. The impact monitoring process especially involves in the tracking of impact. The event and location of an impact load can be identified by the propagating acoustic waves. Simultaneously with the impact identification, the diagnostics of impact damages can be carried out to determine whether the incipient damage is initiated or not from the information of the AE waves.

Recently, Chang et al. [1] proposed the techniques for the reconstruction of force history and the determination of impact location by minimizing the difference between modeled response and actual response from built-in piezoceramic sensors. The response comparator

Korea Advance Institute of Science and Technology (KAIST), 373-1 Kusong-Dong Yusong-Gu, Taejon, 305-701, KOREA.

using an optimization algorithm was applied to compare the responses. However, these techniques are in many cases a time consuming process. Moreover, the response of real complex structures cannot be the same as the modeled response, because the result of this analytical method can be more influenced by boundary conditions, noises, and vibrating conditions of structures. An alternate approach to identify the impact location of a composite structure is to use a neural network [2]. These approaches used several kinds of information as the input data such as the differential signal arrival times of propagating acoustic waves and the integrated real and imaginary parts of the FFT of four strain signals. In this study, neural network paradigms are used for an inverse problem solver. This method may be easily applied when a specific equation or algorithm is not applicable, but when adequate knowledge or data exists to derive a knowledge-based solution.

The Active sensing diagnosis (ASD) was proposed to detect impact damage in in-service composite structures using piezoceramic sensors and actuators to generate and receive diagnostic waves by Chang [3]. The passive sensing diagnosis (PSD) without actuators may be simpler and more lightweight than the ASD system. Recently, the PSD method using the time-frequency analysis has been issued. The WT method can provide the time-frequency localization from sensor signals. The WT itself is a more intuitive decomposition of the data since it provides simultaneous time-frequency localization at multiple resolutions. Being a more flexible method of time-frequency decomposition, wavelets can describe signal characteristics in a much more precise manner and result in more accurate feature extraction. Several researches show that the WT can be a powerful tool for condition monitoring and fault diagnosis by using its ability to "zoom in" on short lived high frequency phenomena for the analysis of transients [4-5]. Though the WT has been applied to the diagnostics of transient vibration signals of machinery, this has been rarely used for damage diagnostic application to composite laminates.

This paper mainly focuses on the integrated approach for both two objects by PZT sensor system. This paper proposed the simultaneous impact monitoring techniques to identify the impact location and to detect the impact damage using the propagation property of acoustic waves and the AE waves. This paper proposed that the PSD method using the WT could be applied to monitor the AE signals due to damage initiation of composite laminates during the low velocity impact. The fundamental researches have been carried out to identify the impact location of composite laminates and the laminates with a circular hole. Then, we investigated the time-frequency characterization of the AE signals in the case of matrix cracks and delaminations respectively.

FUNDAMENTAL APPROACHES

The fundamental researches have been carried out to identify the impact location of composite laminates. Moreover, the time-frequency characteristics of impact damages have been investigated by the WT. The propagating acoustic waves due to impacts have a complex non-linear property on the wave velocities of composite laminates. The neural network using the Levenberg-Marquardt (LM) algorithm with the generalization methods was used for the identification of the impact location using the arrival time differences of acoustic waves. It was found that the AE waves generated by impact damages are undistinguishable from each damage mode and the amount of damage by the conventional analysis methods in time or frequency domain. The Fourier transform decomposes a signal into its various frequency

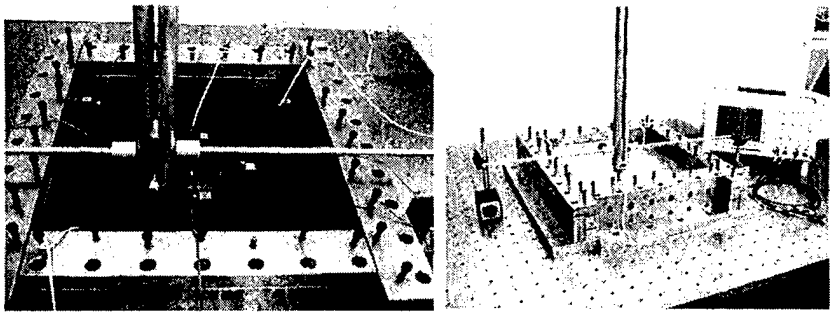


Figure1. The experimental setups for the low-velocity impact test.

components. Because it uses the sinusoidal basis functions that are localized in frequency only, it loses the transient feature of the signal. Therefore, it is necessary to implement the time-frequency analysis for diagnostics of a transient signal such as that induced by damage. The WT can be a powerful tool for condition monitoring and fault diagnosis by using its ability to "zoom in" on short-lived high frequency phenomena for the analysis of transients. The WT can decompose the AE waves in time and wavelet scale domain and catch the differences of these waves. It makes possible to distinguish the damage modes and size by the decomposed wavelet details. The experimental setups are shown in Figure 1.

Impact Identification by Neural Networks

The acoustic wave velocity is dependent on the material property, the wave frequency and

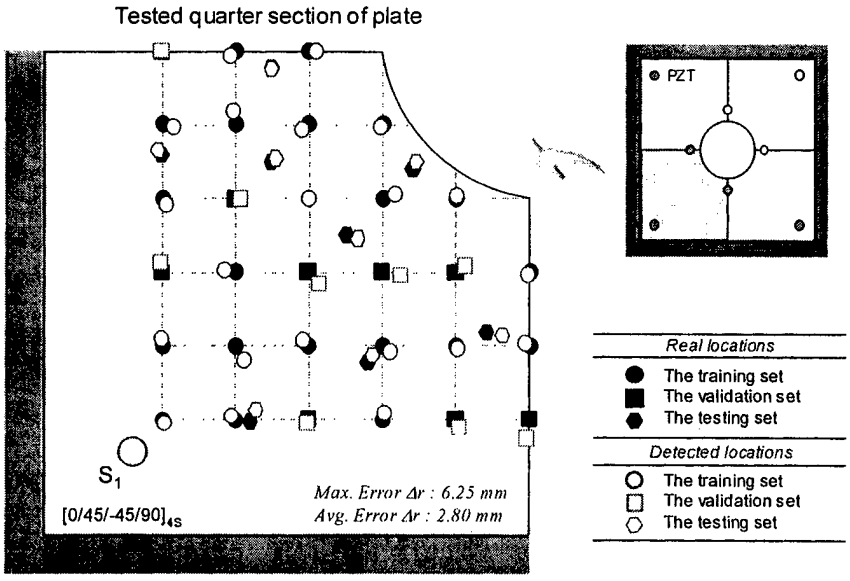


Figure 2. The results of the detection of impact locations of $[0/45/-45/90]_{4S}$ laminates with a circular hole.

the type of waves. In the case of composite laminates, the acoustic wave velocity varies with the direction of propagation because the wave propagates faster along fiber rather than matrix. Neural networks can be applied to make a nonlinear modeling for the differential arrival time of acoustic waves at a certain location of impacts. One inherent advantage in using neural networks is that their performance is independent of a particular system's complexities; the physics of boundary conditions and the velocity of acoustic waves, etc. It was discovered that the backpropagation Multi-Layer Perceptron (MLP) was adequate for the impact location detection. In this paper, the LM algorithm for nonlinear least squares was incorporated into the backpropagation algorithm for training the MLP. The algorithm was tested on many function approximation problems, and was compared with a conjugate gradient algorithm and a variable learning rate algorithm. In general, on networks that contain up to a few hundred weights the LM algorithm will have the fastest convergence. Another problem that occurs during the neural network training is called overfitting. The error on the training set is driven to a very small value, but when new data is presented to the network the error is large. The network has memorized the training examples but it has not learned to generalize to new situations. We used two methods for improving generalization: regularization and early stopping methods. This predicted the location of impact under the error of 6.25 *mm* in radial direction on a 330 *mm*×330 *mm* $[0/45/-45/90]_{4S}$ Graphite/Epoxy laminates with a circular hole, as shown in Figure 2. The influence of boundary condition on the accuracy of impact location was also studied.

Impact Damage Characterization

This research provides the real-time in-service damage monitoring techniques using the time-frequency analysis of PZT sensor signals. PZT sensors were utilized to monitor the impact events. These can be used as wide-band transducers of low-frequency vibrations and high-frequency acoustic emission waves. We chose PZT sensors suitable for detecting the frequency range from 20 *kHz* to 360 *kHz* that is known as the general frequency range of the

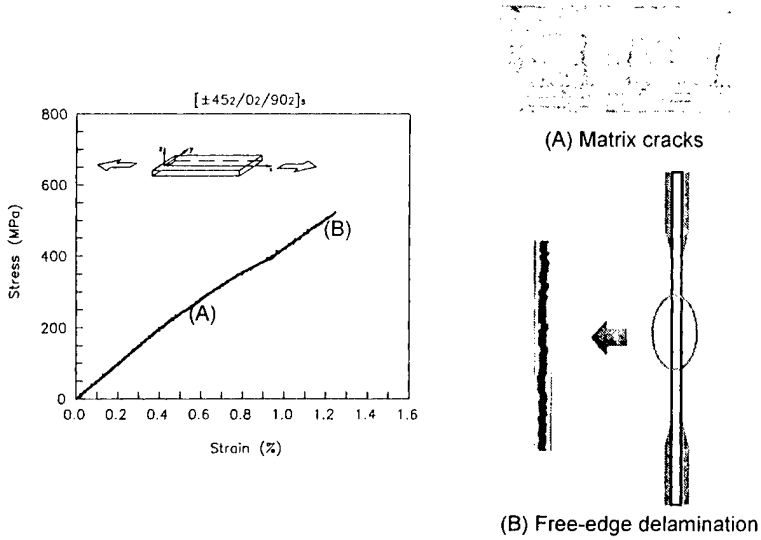


Figure 3. The evolution of matrix cracks and free-edge delaminations in tension of $[\pm 45_2/0_2/90_2]_S$ beam.

AE during the initiation of damage such as delaminations in composites laminates. These techniques present the simultaneous monitoring of damage at the time of impact events. Time-frequency analysis can be implemented by the STFT and the WT. The STFT cannot be a local spectral density because of the continuing nature of harmonic waves. Moreover, it is impossible to achieve high resolution in time and frequency simultaneously.

The WT decomposes a signal into a set of basis functions that are localized in both time and frequency. Each wavelet function $\Psi_{a,b}(t)$ is a stretched or narrowed version of a prototype wavelet $\Psi(t)$,

$$\Psi_{a,b}(t) = \frac{1}{\sqrt{a}}\Psi\left(\frac{t-b}{a}\right) \tag{1}$$

where $a \in R^+$ and $b \in R$ are scale and shift parameters, respectively.
The Continuous Wavelet Transform (CWT) is defined as follow,

$$\begin{aligned} W_{\Psi x}(a,b) &= \frac{1}{\sqrt{a}}\int_{-\infty}^{+\infty} x(t)\Psi^*\left(\frac{t-b}{a}\right)dt \\ &= \left\langle \Psi_{a,b}(t), x(t)\right\rangle \end{aligned} \tag{2}$$

That is, we measure the similarity between the signal $x(t)$ and the shifts, scales of an elementary function. Because the wavelet basis function is localized in both time and frequency, it can act as multi-scale band-pass filters when convoluted with the signal data. From the Discrete Wavelet Transform (DWT), a signal can be represented by its approximations and details. The approximations are the low frequency components of the signal decomposed by the high-scaled wavelet basis function. The details are the high frequency components of the signal decomposed by the low-scaled wavelet basis function. By

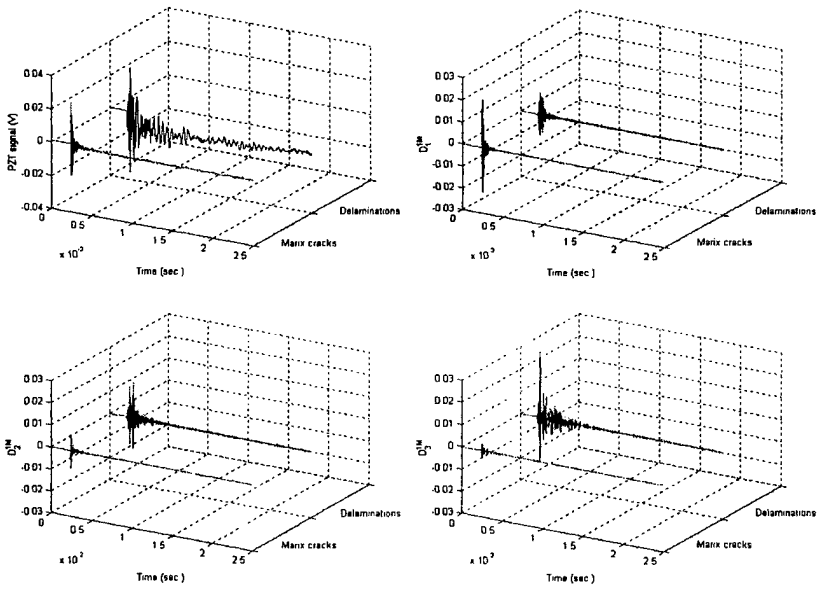


Figure 4. The comparison of details $D_1^{1M} \sim D_3^{1M}$ of PZT signals of matrix cracks and free-edge delaminations by DWT.

selecting different dyadic scales, a signal can be broken into many lower-resolution components, referred as the wavelet decomposition tree. The high frequency AE waves of PZT signals can be decomposed into several details ' D_j '.

The characteristics of the PZT signals due to matrix cracks and the evolution of free-edge delamination were analyzed by the WT. Tension tests were performed to investigate the AE waves due to matrix cracks and free-edge delaminations using $[\pm 45_2/0_2/90_2]_S$ Gr/Ep specimens. The stress-strain curve and the picture of damage modes are shown in Figure 3. The differences of transient characteristics of the AE waves due to matrix cracks and delaminations can be identified by the time-frequency analysis. The WT can be used to characterize damage modes by measuring the transient decomposed signals of a certain scale level of wavelets. The results are shown in Figure 4. The details are indicated by D_1^{1M} of which the subscript represents the level of decomposition and the superscript represents the sampling frequency. The details D_1^{1M}, D_2^{1M} and D_3^{1M} represent approximately 300~400 *kHz*, 140~240 *kHz*, 80~100 *kHz* signal range respectively from the calculation of approximate frequencies. Therefore, these details can represent the characteristic frequencies of AE signals. As the selection of wavelet functions, these details can show detailed characteristics that could not be represented by the harmonic function based analysis. Figure 3 shows that the AE signals due to matrix cracks are dominantly composed of the detail D_1^{1M}. However, the AE signals due to delaminations are mainly composed of D_2^{1M} and D_3^{1M}. These trends coincide with the frequency characteristics. From these results, delaminations known as the primary damage mode of low velocity impact can be detected by observing the details D_2^{1M} and D_3^{1M}.

SIMULTANEOUS IMPACT MONITORING

From the results of basic researches, these procedures were implemented to the

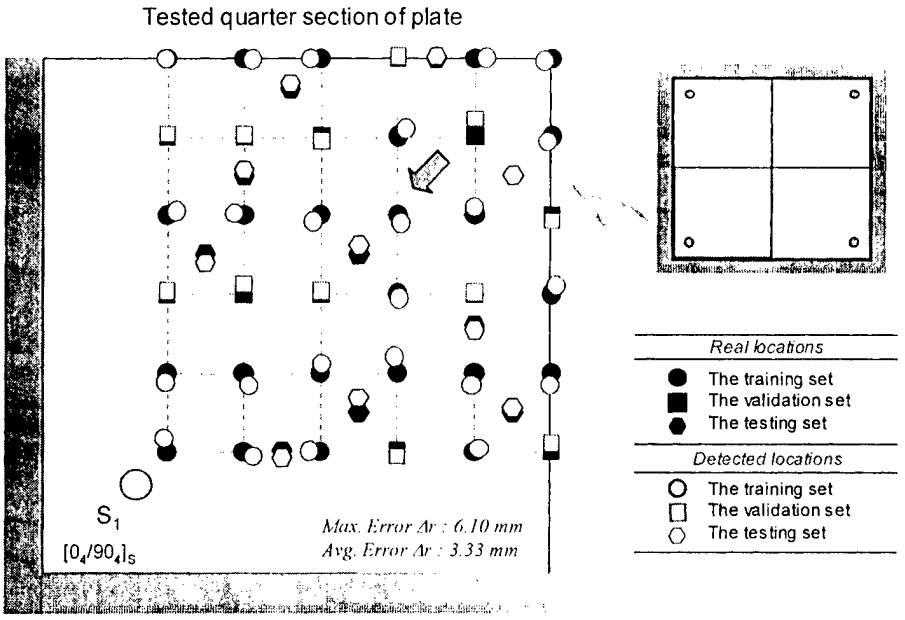


Figure 5. The results of the detection of impact locations of $[0_4/90_4]_S$ laminates.

simultaneous impact monitoring of 330 *mm*×330 *mm* $[0_4/90_4]_S$ Graphite/Epoxy laminates. Firstly, the same neural network paradigm was trained using the arrival time differences of acoustic waves. The energy of impact was fixed to 0.3 *J*. In this case, the acoustic wave velocity much varies with the direction of propagation than the case of quasi-isotropic laminates, because the wave propagates faster along fiber rather than matrix. This non-linear property produced much more error of detection than the case of quasi-isotropic laminates. Figure 5 shows the results of the identification of impact locations. After training of neural network, the drop-weight type impact test was carried out to simulate the low-velocity impact. The arrow in Figure 5 represents the test impact position. The impact energy was chosen to generate delaminations. First, the laminated plate was subjected to 8.0 *J* impact. After impact, delaminations having the dimension of about 40 *mm*×20 *mm* were measured by the C-Scan. Second, after 10.8 *J* impact, the size of delaminations was about 60 *mm*×25 *mm*.

Results of Impact Monitoring

The trained neural network could identify the impact location. The error of detected location was 7.64 *mm* in radial direction. The much more error was produced in the higher energy level of impact. Because the neural networks trained by the fixed 0.3 *J* impact, the much higher energy makes another leading waves slightly different from small energy impact. This affected the accuracy of detection. Simultaneously, the PZT signals were analyzed to decompose the AE waves along time domain by the WT. Figure 6 shows the wavelet details D_1^{IM}~D_3^{IM}. This figure shows that the AE signals of impact damages are dominantly composed of the detail D_1^{IM}. We can detect the occurrence of delaminations. Moreover, we can estimate the time of damage evolution by the WT. We can estimate the matrix cracks was

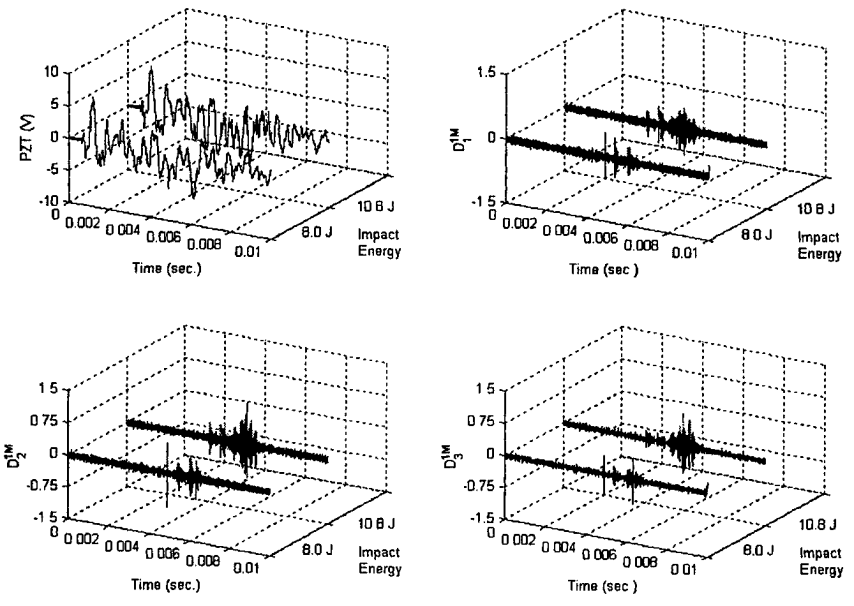


Figure 6. The comparison of details D_1^{IM}~ D_3^{IM} of PZT signals of 8.0 *J* and 10.8 *J* impacts by DWT.

generated at the same time. The higher amplitudes of the details D_1^{IM}~D_3^{IM} were observed in the 10.8 J case than the 8.0 J case that makes the smaller size of delaminations. These make it possible to monitor the damage state by measuring the interested detail components by adjusting the scale level. Because the voltage resolution of Digital Storage Oscilloscope is 120 mV in the ±4 V, the one-bit noises prevent the PZT signals under 120 mV. The data acquisition board having the higher voltage resolution should be used in the future experimentation. This would help to have a clear detail signals.

CONCLUSION

In this research, we have presented the impact monitoring techniques to detect the location of impact, to determine the occurrence of damage and to estimate the qualitative severity of damage simultaneously. The neural network using the LM algorithm with the generalization methods predicted the location of impact with the accuracy of about 5 *mm* error in radial direction. We also have presented the PSD using the time-frequency analysis like the WT on the determination of the occurrence of damage and the estimation of damage. It can be carried out simultaneously with the detection of impact locations using the same PZT sensor. We can confirm that the WT can be the better monitoring tool for the analysis of the transient signals like damage-induced signals. This makes it possible to examine the interested multi-band frequency range by adjusting the wavelet functions. These results show the possibilities of simultaneous monitoring of impact locations and damages. Future works include the impact monitoring of a stiffened composite plate and real-time data acquisition and processing programming.

ACKNOWLEDGES

This study has been supported by the Ministry of Science and Technology through National Research Laboratory programs. The authors gratefully acknowledge the support as the National Research Laboratory program.

REFERENCES

1. K. Choi and F.K. Chang. 1996. "Identification of Impact Force and Location Using Distributed Sensors," *AIAA Journal*, 34 (1), pp. 136-142.
2. R.T Jones, J.S. Sirkis and E.J. Frebele. 1997. "Detection of Impact Location and Magnitude for Isotropic Plates Using Neural Networks," *Journal of Intelligent Material Systems and Structures*, 7 (1), pp. 90-99.
3. F.K. Chang. 1995. "Built-in Damage Diagnostics for Composite Structures," *Proceedings of ICCM-10*, V, pp. 283-289.
4. G.A. Harrison, I. Koren, M. Lewis and F.J. Taylor. 1998. "Application of wavelet and Wigner analysis to gas turbine vibration signal processing," *Proceedings of SPIE on Wavelet Application*, 3391, pp. 490-501.
5. J.W. Wang and P.D. McFadden. 1996. "Application of Wavelets to Gearbox Vibration Signals for Fault Detection," *Journal of Sound and Vibration*, 192, pp. 927-939.
6. D.U. Sung, J.H. Oh, C.G. Kim and C.S. Hong. 2000. "Impact Monitoring of Smart Composite Laminates Using Neural Networks and Wavelet Analysis," *Journal of Intelligent Material Systems and Structures*, accepted.

SPECIFIC DAMPING CAPACITY OF MULTIPHASE UNIDIRECTIONAL HYBRID FIBER COMPOSITES

Vijayan Baburaj,[1] Yuji Matsuzaki,[2] Nae Florin Andrei,[2] Tadashige Ikeda[2]

ABSTRACT

Modeling and analysis on the specific damping capacity (SDC) of a unidirectional hybrid fiber composite lamina have been presented in this work.In an attempt to refine the SDC analysis for the case of hybrid composites a new unit cell has been identified. Idealization of the proposed unit cell introduces a fiber-matrix interphase into the hybrid composite damping model. Explicit lamina level SDC equations are derived using the strain energy method. The validity and the advantages of the present method have also been demonstrated by performing numerical simulations for conventional as well as shape memory alloy (SMA) hybrid fiber composites.

INTRODUCTION

Adaptive structures and technologies are considered to be one of the fast growing R& D areas that originated in the field of aerospace and gradually started diverging to other engineering fields also. Practical realization of the next generation technologies in a more cost effective way is a challenging task to the scientific and engineering community of today. Towards this goal, the role of adaptive composite material system as a promising candidate is very vital and expected to serve as the basic building blocks of the future adaptive structural systems. In order to derive the unlimited benefits of this new class of material system, several of its fundamental behaviours right from the architecture to modeling, analysis, and synthesis are to be well understood. Material damping has been identified as one of the important topics of adaptive composites in perspective of vibration control, noise reduction and fatigue endurance of structural systems subjected to dynamic loading environment.

A comprehensive study on material damping analysis of advanced fiber reinforced polymer composites right from the lamina level to laminated beams, plates, sandwich laminates and woven fibrous composites levels had been reported by Adams [1]. In metals, alloys, and metal matrix composites the inherent damping of the constituent materials combined with the

[1]Micro System Engineering Department, Nagoya University, Chikusa-ku, Nagoya 464-8603, Japan.
[2]Aerospace Engineering Department, Nagoya University, Chikusa-ku, Nagoya 464-8603, Japan

various effects of secondary phases are the main sources of material damping [2]. Similarly, short fiber reinforced polymer matrix composites also exhibit good material damping characteristics and further they have additional degrees of freedom, such as the fiber length and orientation, thus having more scope for optimum tailoring of damping and elastic properties [3,4]. However due to the advantages derived by the polymer matrix continuous fibre reinforced composite as a suitable host material to the emerging smart material systems motivates us to study the specific damping capacity (SDC) of such materials. Much research attention had been paid in understanding the mechanics of material damping of polymer matrix continuous fiber reinforced composites both analytically and experimentally [5-10].

The micromechanics of material damping is considered to be an emerging area looking for more research attention in a view point of adaptive materials and structures. A unified micromechanics damping theory was presented by Saravanos and Chamis [11] for unidirectional and off-axis fiber composites by deriving the damping coefficients corresponding to all the six directions of a composite lamina . Because of the simplicity of this model [11] combined with a satisfactory comparison with the available, but limited, experimental results they extended the scope of their theory further to damping of composite laminates [12]. Another new area of application of this micromechanics damping theory [11] is on passive damping analysis of smart hybrid composites [13,14] including the constitutive modeling of shape memory alloy composites [15,16].

In the case of conventional continuous fiber reinforced composites under an assumption of homogeneous fiber-matrix mixing, a simple square packing arrays of fibers reasonably represents the average value of randomly distributed fibers [11]. Therefore, a unit cell identified as a circular section surrounded by a square matrix segment may be simple enough to calculate the damping properties along the axial direction of fiber by assuming the Voigt condition (isostrain) for the normally used cylindrical fibers in a composite lamina. However the stress distribution in the matrix and fiber is not uniform along the transverse direction of the fiber mainly because of the curvature of the fiber and therefore they assumed the circular section as an equivalent square section [11]. This simplification resulted to have rectangular segments of fiber-matix material domains and SDC equations were derived by using combinations of Voigt /Reuss (isostress) conditions.

In the present work we propose to refine the assumption of Ref. [11] by idealizing the circular cross section of the fiber into two square sections of an inscribing and a circumscribing squares as discussed in the next section. This assumption retains the simplicity of the analytical modeling that enables to use mechanics of material approach to derive the SDC of the lamina along the remaining directions other than that of the normal fiber direction. The validity and the merit of the present method have also been demonstrated by performing numerical simulation. Structural constraints such as high stiffness requirement often need to use high modulus and therefore low damping fibers in composites. Therefore, unidirectional polymer matrix fiber composites generally exhibit very poor axial damping properties in comparison with the transverse and shear directions [11]. To improve the axial direction damping, hybrid fiber composite is considered to be one of the promising candidates [13] and this aspect has also been discussed in this paper through a numerical simulation of shape memory alloy (SMA) hybrid fiber composites.

ANALYTICAL MODELING

Material damping capacity can be defined as a measure of relative energy dissipation with respect to the maximum stored strain energy when the material is undergoing a cyclic dynamic loading. This measure of energy dissipation is generally expressed in different ways and in the present modeling, we employ, a non dimensional quantity, namely, specific damping capacity (SDC) to denote such relative energy dissipation. SDC is therefore defined as the ratio of the dissipated energy to the maximum stored energy from the beginning of the loading to the maximum during one complete cycle and is expressed as shown below [1]:

$$\psi = \frac{\delta U}{U} \tag{1}$$

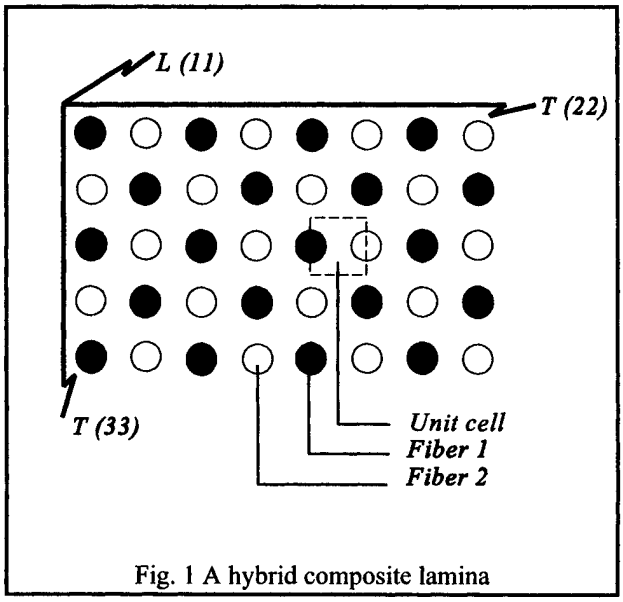


Fig. 1 A hybrid composite lamina

Present micromechanical modeling is for a unidirectional fiber reinforced composite containing cylindrical fibers of two different materials having the same diameter embedded in a common matrix material. A homogeneous mixing and simple square fiber packing are assumed. An idealized lamina configuration of such a hybrid composite and its unit cell is depicted in Figure 1.The geometrical details of unit cell in terms of fiber volume fraction are given in Figure 2. Saravanos and Chamis [11] idealized the circular fiber section into an eqivalentent square section and hence expressed the side of this equivalent square as $\sqrt{k_f}$, for a square cell of unit dimensions. Here, k_f is the fiber volume fraction. In the present work we propose to refine this by idealizing the circular cross section of the fiber into two square sections of an inscribing and a circumscribing squares as shown in Figure 2. This assumption retains the simplicity of the analytical modeling that enables to use mechanics of material approach to derive the SDC of the lamina along the remaining directions other than that of the normal fiber direction. Therefore, the dimensions of these circumscribing and inscribing squares can be expressed in terms of the fiber volume fraction as,

$$d = \sqrt{\frac{4k_f}{\pi}} \tag{2}$$

$$a = \sqrt{\frac{2k_f}{\pi}} \tag{3}$$

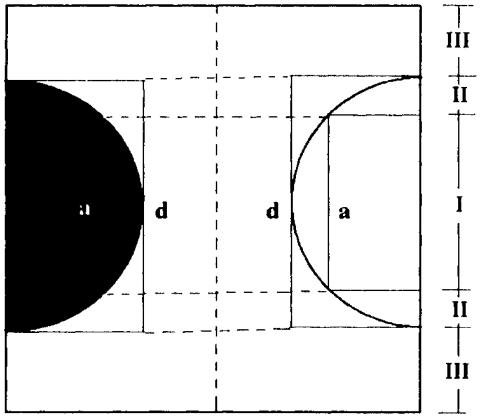


Fig.2 Idealized unit cell configuration

ANALYTICAL EQUATIONS

The unit cell consists of different fiber/matrix segments of different material phases and therefore a damping analysis is performed by using strain energy method within the framework of the mechanics of material approach. By making use of the classical definition of specific damping capacity [1], the stored strain energy and the dissipated energy of the multi-phase composite along any lamina direction, *ij*, can be expressed as shown in Equations (4) and (5) respectively.

$$U_{lij} = \frac{1}{2}\sum_{p=1}^{5}\int_{V_p}\sigma_{pij}\epsilon_{pij}dV_p \tag{4}$$

$$\delta U_{lij} = \frac{1}{2}\sum_{p=1}^{5}\int_{V_p}\psi_{pij}\sigma_{pij}\epsilon_{pij}dV_p \tag{5}$$

Symbols *V, l, p*, ψ, ϵ, and σ denote for volume, lamina, phase, SDC, strain and stress respectively. An isostrain assumption between the fiber-interphase and interphase-matrix segments has been made to derive the lamina SDC along the axial direction (*11*) of fiber and is

given by Equation (6).

$$\psi_{111} = \sum_{p=1}^{5} \frac{\psi_{p11} k_p E_{p11}}{E_{111}} \tag{6}$$

where, $E_{111} = \sum_{p=1}^{5} E_{p11} k_p$ and k volume fraction that can be calculated from the geometry of the unit cell and must be subjected to the condition, $\sum_{p=1}^{5} k_p = 1$.

Derivation of lamina level SDC along the remaining directions, namely, normal transverse to fiber (22, 33), inplane shear (12) and transverse shear (23, 31) can be derived by following the equivalent section method proposed by Saravanos and Chamis [11] for the case of unidirectional fiber composite lamina. As shown in Figure 2, the present unit cell consists of basically three segments all connected in parallel. In this, segment I can be considered as an assembly of five subsegments consisting of two fiber areas, two interphase areas and one matrix area all are connected in series. Therefore, the SDC and Young's modulus of segment I are derived by assuming an isostress condition throughout all the five constituent subsegments.

$$\psi_{22}^{I} = E_{22}^{I} \sum_{p=1}^{5} \frac{\psi_{p22} v_p}{E_{p22}} \tag{7}$$

$$\frac{1}{E_{22}^{I}} = \sum_{p=1}^{5} \frac{v_p}{E_{p22}} \tag{8}$$

Similarly, segment II consists of three subsegments namely the two different interphases and the common matrix area all are connected in series and therefore could be treated in the same way as above.

$$\psi_{22}^{II} = E_{22}^{II} \sum_{p=3}^{5} \frac{\psi_{p22} v_p}{E_{p22}} \tag{9}$$

$$\frac{1}{E_{22}^{II}} = \sum_{p=3}^{5} \frac{v_p}{E_{p22}} \tag{10}$$

Finally, segment III is matrix and is in parallel with segments I and II. Therefore, the resultant SDC along the transverse direction (*22*) of the lamina can be derived assuming an isostrain condition for all the three segments and the equations are given below.

$$\psi_{l22} = \frac{1}{E_{l22}} \left[a \psi_{22}^{I} E_{22}^{I} + (d-a) \psi_{22}^{II} E_{22}^{II} + (1-d) \psi_m E_m \right] \tag{11}$$

$$E_{l22} = a E_{22}^{I} + (d-a) E_{22}^{II} + (1-d) E_m \tag{12}$$

The transversely isotropic fibers embedded unidirectionally in an isotropic matrix generally result to have a composite with transversely isotropic properties. Therefore, the two transverse normal directions (*22* and *33*) must have the same mechanical and damping properties and can be expressed as,

$$\psi_{l33} = \psi_{l22} \tag{13}$$

$$E_{l33} = E_{l22} \tag{14}$$

In order to derive the inplane SDC and shear modulus along direction *12*, all the assumptions and procedures that followed to derive the transverse normal SDC and modulus of elasticity remain to be valid and applicable here also. Hence the inplane shear SDC and shear modulus of segmentI can be derived as shown by Equations (15) and (16) respectively.

$$\psi_{12}^{I} = G_{12}^{I} \sum_{p=1}^{5} \frac{\psi_{p12} v_p}{G_{p12}} \tag{15}$$

$$\frac{1}{G_{12}^{I}} = \sum_{p=1}^{5} \frac{v_p}{G_{p12}} \tag{16}$$

Similar equations for inplane SDC and shear modulus of segment II are given as,

$$\psi_{12}^{II} = G_{12}^{II} \sum_{p=3}^{5} \frac{\psi_{p12} v_p}{G_{p12}} \tag{17}$$

$$\frac{1}{G_{12}^{II}} = \sum_{p=3}^{5} \frac{v_p}{G_{p12}} \tag{18}$$

Finally, the resultant lamina level inplane shear SDC and shear modulus are derived as expressed by equations (19) and (20) respectively.

$$\psi_{l12} = \frac{1}{G_{l12}} \left[a\psi_{12}^{I} G_{12}^{I} + (d-a)\psi_{12}^{II} G_{12}^{II} + (1-d)\psi_{ms} G_{m} \right] \tag{19}$$

$$G_{l12} = aG_{12}^{I} + (d-a)G_{12}^{II} + (1-d)G_{m} \tag{20}$$

Again, as mentioned in the case of transverse normal SDC and modulus of elasticity, one of the interlaminar shear SDCs (ψ_{l31}) and interlaminar shear moduli (G_{l31}) are respectively equal to the inplane shear SDCand shear modulus due to the transverse isotropy of the lamina.

$$\psi_{l31} = \psi_{l12} \tag{21}$$

$$G_{l31} = G_{l12} \tag{22}$$

The remaining out of plane interlaminar shear SDC (ψ_{l23}) and the corresponding shear modulus (G_{l23}) can also be derived in a similar manner that we followed for the derivation of the inplane shear SDC and shear modulus.

RESULTS AND DISCUSSION

Aim of the present numerical study is to understand on the passive damping characteristics of SMA hybrid composite. As mentioned in the introductory section, our special interest now is on the fiber axial direction damping and its improvement by hybridizing SMA fibers to another advanced fiber both are embedded in a common matrix. In the present numerical simulation two hybrid composite materials are considered. The first hybrid composite consists of High Modulus Surface treated graphite fibers (HM-S) and NI-TI fibers as reinforcements embedded in an Intermediate Modulus Low Strength (IMLS), polyester, matrix. Instead of HM-S fibers, E-GLASS fibers are considered as the reinforcement for the second hybrid composite whereas the remaining constituent materials are the same as that of the first hybrid composite. Commercially available NI-TI fibers are the SMA material used here and its experimental values of Young's modulus and SDC are evaluated for isothermal loading/unloading conditions on specimens having 100 μ diameter and an austenite finish temperature (A_f)of 273 °K. Present numerical simulation is therefore restricted only to temperatures between A_f and the martensitic start temperature (M_s). Mechanical and damping properties of the remaining fibers and matrix materials are available in Ref. [11].

Numerical simulation results of HM-S/IMLS composite and HM-S, NI-TI/IMLS hybrid compsosie for the variation longitudinal normal SDC with respect to fiber volume fraction are shown by the continuous and broken curves respectively in Figure 3. This lamina level fiber axial direction SDC values were normalized by the normal SDC value of the matrix material. SDC of

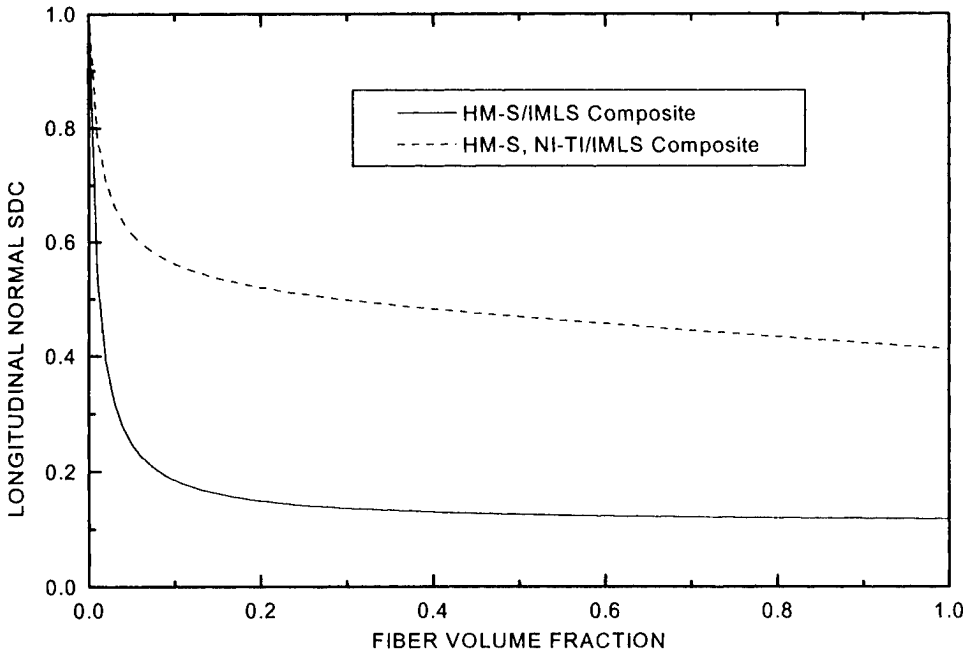


Fig. 3 Longitudinal Normal Specific Damping Capacity

HM-S/IMLS composite was computed as a special case of the present hybrid composite unit cell and the results obtained represent the corresponding literature values [11, 13]. As the material damping property of HM-S fibers is about an order less than that of the matrix material, the lamina SDC along the fiber dominant direction remains lower over the practically used fiber volume fraction as expected. Since the lamina SDC along the remaining normal and shear directions are governed by the matrix material, these values will be higher for almost the entire range of fiber volume fraction. However, it is very essential to have an improved fiber direction damping property in order to have a better overall damping property at the lamina level. This can be achieved by hybridizing NI-TI fibers into conventional composite and the result is shown in Figure 3. It is found that SDC enhancement of over 270% is possible over a wide range of fiber volume fraction by hybridizing NI-TI fibers into HM-S/IMLS composite. Because of the inverse relationship between the stiffness and damping properties of materials, a corresponding reduction of lamina level Young's modulus along the fiber direction due to such hybridization has been expected and this is demonstrated in Figure 4. It is found that about 40% stiffness reduction occurs through the entire range of fiber volume fraction. In the next numerical simulation E-GLASS/IMLS composite and E-GLASS, NI-TI/IMLS hybrid composite were considered to study the fiber direction SDC and Young's modulus. The continuous and broken curves shown in Figure 5 represent the fiber direction SDC for E-GLASS/IMLS composite and E-GLASS, NI-TI/IMLS hybrid composite respectively. It is found that SDC enhancement of about 95% to 125% is possible for a range of fiber volume fraction of practical interest, that is, between 0.40 and 0.60 in the case of E-GLASS, NI-TI/IMLS hybrid composite. Figure 6 shows the corresponding variation of fiber direction Young's modulus of E-GLASS/IMLS composite and E-GLASS, NI-

TI/IMLS hybrid composite. The lamina level fiber direction stiffness reduction due to hybridization of NI-TI fibers in this case is found to be insignificantly lower than that found for HM-S/IMLS composite.

SUMMARY AND CONCLUSION

Specific damping capacity evaluation of a unidirectional hybrid composite containing cylindrical fibers of two different materials having the same diameter in a common matrix material with a homogeneous mixing has been carried out. In an attempt to refine the SDC analysis for the case of hybrid composites a new unit cell has been identified and lamina level SDC equations have been derived. Numerical simulations were also carried out to study the effects of hybridizing NI-TI fibers into conventional fiber composite in a view point of lamina level SDC improvement along the axial fiber direction. It has also been shown that significant improvement of axial damping is possible with NI-TI hybrid composite, however, the selection of host composite has a significant role in governing the lamina level stiffness along the axial direction. The pseudoelastic transformation of SMA fibers has not been considered in the present work, however, this task is planned as an extension of this for our future work.

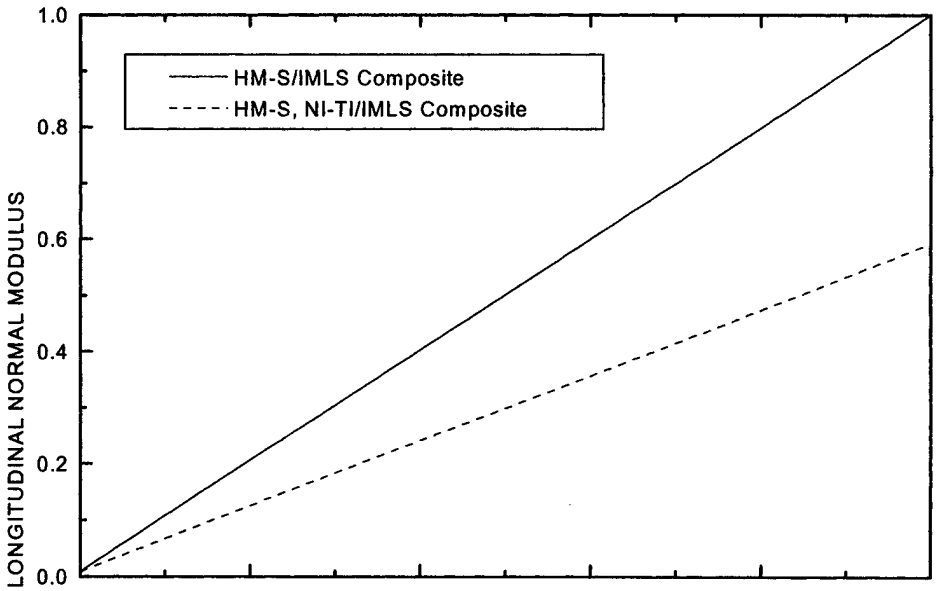


Fig.4 Longitudinal Normal Modulus of Elasticity

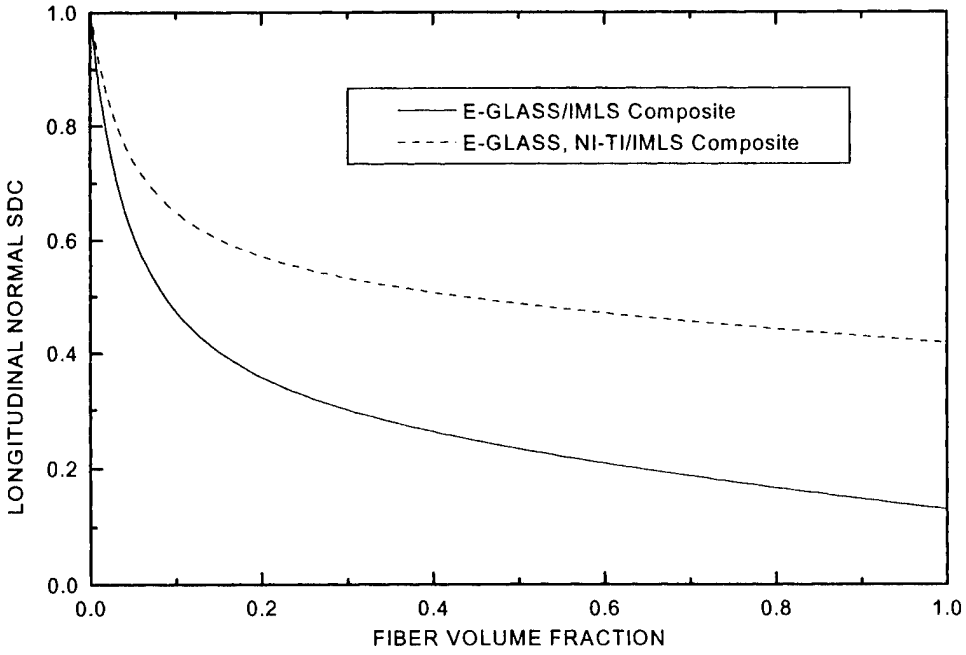


Fig. 5 Longitudinal Normal Specific Damping Capacity

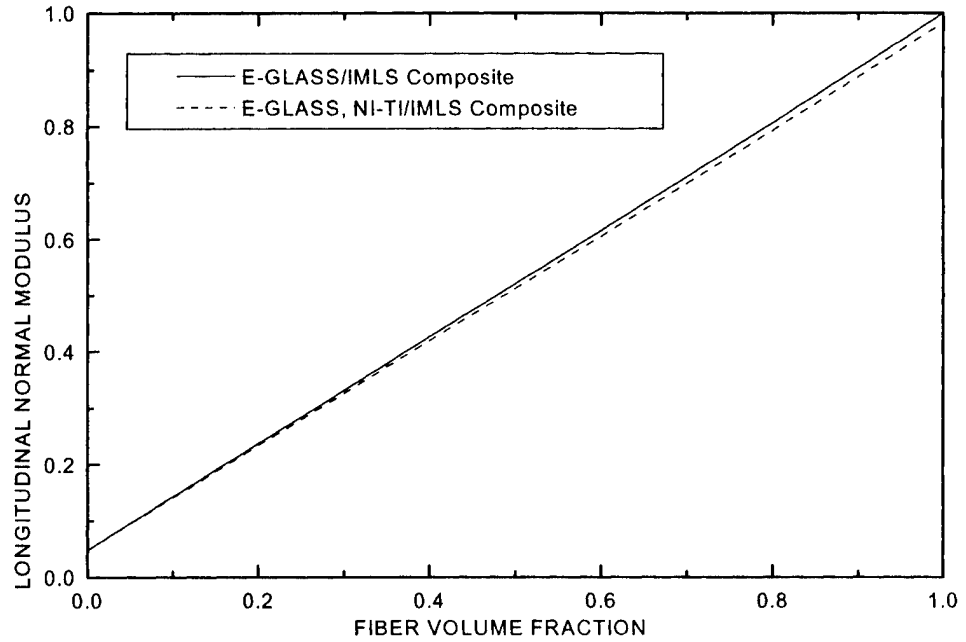


Fig. 6 Longitudinal Modulus of Elasticity

REFERENCES

1. Adams, R. D.1987. "Damping properties analysis of composites," *Engineered Materials Handbook, Vol 1 Composites* Metals Park, Ohio: ASM International pp.206-17.
2. Zhang, J., J. R. Perez , R. C. Wong, and E. J. Lavernia. 1994. "Effects of secondary phases on the damping behaviour of metals, alloys and metal matrix composites," *Matls. Sci. and Eng.* R13 No.8 pp.325-390.
3. Sun, C. T., S. K. Chaturvedi, and R. F. Gibson. 1985. " Internal damping of short-fiber reinforced polymer matrix composites," *Compu. Struct.* 20 pp.391-400.
4. Suarez, S. A., R. F. Gibson, C. T. Sun, and S. K. Chaturvedi. 1986. "The influence of fiber length and fiber orientation on damping and stiffness of polymer composite materials," *Experi. Mech.* 26 pp.175-184.
5. Schultz, A. B., and S. W. Tsai. 1968. "Dynamic moduli and damping ratios of fiber reinforced composites," *J. of Compo. Matls.* 2 pp.368-379.
6. Schultz, A. B., and S. W. Tsai. 1969. "Measurements of complex dynamic moduli for laminated fiber reinforced composites," *J. of Compo. Matls.* 3 pp.434-443.
7. Adams, R. D., M. A. O. Fox, R. J. L. Flood, R. J. Friend, and R. L. Hewitt. 1969. "The dynamic properties of unidirectional carbon and glass fiber reinforced plastics in torsion and flexure," *J. of Compo. Matls.* 3 pp.594-603.
8. Adams, R. D., and D. G. C. Bacon. 1973. "Measurement of the flexural damping capacity and dynamic Young's modulus of metals and reinforced plastics," *J. of Phys., D: Appl. Phys.* 6 pp. 27-41.
9. Adams, R. D., and D. G. C. Bacon. 1973. "Effect of fibre orientation and laminate geometry on the dynamic properties of CFRP," *J. of Compo. Matls.* 7 pp.402-428.
10. Ni, R. G., and R. D. Adams. 1984. "A rational method for obtaining the dynamic mechanical properties of laminae for predicting the stiffness and damping of laminated plates and beams," *Composites* 15 pp.193-199.
11. Saravanos, D. A., and C. C. Chamis. 1990. "Unified micromechanics of damping for unidirectional and off-axis fiber composites," *J. of Compo. Tech. & Resea.* 12 pp.31-40.
12. Saravanos, D. A., and C. C. Chamis. 1990. "Mechanics of damping for fiber composite laminates including hygrothermal effects," *A.I.A.A. J.* 28 pp.1813-1819.
13.Baburaj, V., and Y. Matsuzaki. 1994. "Material damping analysis of a smart hybrid composite lamina," *J. of Intell. Matls. Sys. Struct.* 5 pp.647-653.
14. Baburaj , V., and Y. Matsuzaki. 1996. "Material damping analysis of smart hybrid composite laminated plate structures," *J. of Intell. Matls. Sys. Struct.* 7 pp.427-432.
15. Baburaj, V., M. Kawai, K. Kinoshita, and T. Koga. 1996. "An Accurate Prediction of Specific Damping Capacity of TiNi SMA Composite through a Three-Dimensional Constitutive Model," *J. of Intell. Matls. Sys. and Struct.* 7 pp.145-149.
16. Birman, V., D. A. Saravanos, and D. A. Hopkins.1996. "Micromechanics of Composites with Shape Memory Alloy Fibers in Uniform Thermal Fields," *A.I.A.A.J.*, 34, pp.1905-1912.

OPTIMAL SENSOR LOCATION FOR DAMAGE DETECTION USING MUTUAL INFORMATION

Wan M. Said, Wieslaw J. Staszewski

ABSTRACT

The paper is concerned with determining the optimal sensor location for impact detection in composite structures. The problem is solved using combinatorial optimisation and information theory. The study involves the use of the Genetic Algorithm optimisation approach with mutual information as a fitness function. The mutual information assesses the information content of sensor data and estimates arbitrary dependences between features obtained from different sensor locations. The information assessment is made on the sensor's ability to detect the amplitude of impacts. The method is validated using a simple impact test experiment on a composite plate. The study shows the potential of the method for the optimal sensor location problem in structural health monitoring.

INTRODUCTION

Health monitoring of systems and structures is important for the increase in safety and the reduction of ownership costs of structures. There exists a number of sensor technologies and different methods of damage detection in structures. It appears that intelligent signal processing is one of the key elements of any structural health monitoring system. Apart from feature extraction and selection algorithms, pattern recognition or data fusion, the location and assessment of damage requires appropriate location of distributed sensors.

The problem of sensor location requires the application of different optimisation techniques. Many early optimisation methods, so called *ad hoc* methods, are based on rough and ready ideas without much use of theoretical background. Classical deterministic optimisation techniques can be classified into unconstrained and constrained optimisation. Simple deterministic techniques, for example gradient based methods, are sufficient for a local search, but for optimisation with several local minima they become inefficient. Constrained optimisation has a great degree of complexity, especially when nonlinear programming is used. More recently, new non-deterministic optimisation methods have been proposed. These are: neural networks [1], Genetic Algorithm (GA) [2-3], evolution

Department of Mechanical Engineering, Sheffield University, Mappin Street, Sheffield S1 3JD, UK; e-mail: w.j.staszewski@sheffield.ac.uk

strategies [4], simulated annealing [5], tabu search [6-7] and different hybrids of the above techniques as reported in [8-9].

The problem of determining the optimal type, number and location of sensors in engineering structures has found considerable attention in the literature. There exist three major areas of application: control engineering, system/modal identification and damage detection. A relatively small amount of applied experimental research has been done in the are of optimal sensor location for damage detection. The heuristic [10] and combined neural networks/genetic [11] algorithms have been used to detect structural faults in an isotropic and homogeneous plate. The combined genetic/neural approach [12] has been applied for optimal sensor location in the impact damage detection problem. This work has been extended to fail-safe sensor distributions [13-15] i.e. those whose sub-distributions also have a low probability of error. A new approach based on mutual information has been proposed for optimal location of sensors on a composite panel [16]. In contrast to optimisation techniques, mutual information assesses the informativeness of sensors and select sensor locations by eliminating sensors with low information content.

The aim of this paper is to combine the optimisation procedure based on the GA with the informativeness or ranking of sensors based on the mutual information approach. The procedure is suitable not only for sensor location but also for sensor selection problem. This problem is particularly important if a small number of sensors is required for damage detection in order to reduce costs for instrumentation and data processing.

The structure of the paper is as follows; for the sake of completeness Sections 2 and 3 briefly introduce the GA and mutual information; a simple impact detection composite test rig used in the study is described in Section 4; the optimal sensor distribution methodology and results are discussed in Section 5 and finally, the paper is concluded in Section 6.

GENETIC ALGORITHMS

GAs are search procedures based on the mechanisms of natural selection and genetics. These procedures use random selection algorithms to do a highly exploitative search through a parameter space. The parameter space consists of chromosomes which are coded as finite-length strings over some type of alphabet (genes). The first step before the GA is to generate, at random, an initial population of possible solutions. The number of chromosomes in a population depends on several parameters including the size of each individual chromosome and the size of the solution space. Having generated an initial population of chromosomes, chromosomes representing best solutions are chosen. To do this, a fitness function, which operates on encoded chromosomes, is used to provide best solutions in the population. The simple GA used involved the following operations:

- *reproduction* - an artificial version of natural selection; a process in which individual fittest genes are copied to the next generation with probability proportional to their fitness;
- *crossover* - a method of combination between pairs of genes in which the randomly chosen substrings from each gene are switched;
- *mutation* - an operation involving random switching of gene binary digits;

- *new blood* - new entirely random genes which form perturbations into the populations in order to prevent a population from stagnating;
- *elite* - a process in which the best solutions in a populations are copied automatically into the next population to prevent the loss of the fittest genetic material;

All these operations form an iterative process through new generations which is continued until the population is dominated by a few relatively fit genes.

MUTUAL INFORMATION

Mutual information is a measure which assesses the information content of random variables [17]. For a given set C of classes described by a set F of features, mutual information can be defined as

$$I(C,F) = H(C) - H(C|F) \tag{1}$$

where the entropy $H(C)$ and conditional entropy $H(C|F)$ are given by

$$H(C) = -\sum_{C} P(C) log P(C) \tag{2}$$

and

$$H(C|F) = -\sum_{F} P(F) \left(\sum_{C} P(C|F) log P(C|F) \right) \tag{3}$$

respectively. Here $P(C)$ is the probability of classes C and $P(C|F)$ is the conditional probability of classes C given the feature input vector F. The entropies given in above equations measure the uncertainty of the output classes C. Mutual information estimates arbitrary dependences between random variables and is capable of evaluating even non-linear relationships between features and classes.

OPTIMAL SENSOR LOCATION METHODOLOGY

The optimal sensor location problem studied here is to select a subset of K sensors from the initial set of N sensors that is maximally informative about a possible damage condition in the analysed structure. All possible sensor location positions on the structures are described using binary coding, i.e. using 0 and 1 numbers. In this coding, each chromosome consists of a fixed number of genes which represent sensor locations. For example the chromosome 10001010 represents a solution in which sensors are placed at positions 1, 5 and 8 on the analysed structure.

An initial population of chromsomes is formed to obtain an initial set of possible solutions. For each chromosome, representing a sensor configuration, a fitness values based on mutual information can be computed as

$$M = \sum_{i=1}^{N} I(C,F) - \frac{\beta}{N} \sum_{i=1}^{N} I(F,F) \tag{4}$$

Here, C forms the output class vector whereas F forms the feature vector. The first part of Equation (4) estimates the overall mutual information for all chosen sensors and features with respect to the output class C, while the second par measures the redundancies of the total mutual information. The parameter β is used to regulate the relative importance between features. If β is equal to zero, the overall mutual information with the output class is considered for each sensor without eliminating redundances that exist in the analysed sensors. As β increases, this value is discounted by a quantity proportional to the total mutual information between the selected sensors with respect to each other. In practice, the value of β between 0.5 and 1 is appropriate for use in many classification/optimisation problems [18]. The value of M indicates the fitness of any given chromosome with N number of sensors. It estimates the total amount of information content from the selected sensors. The GA is then run to maximise the value of M. The solution represents the optimal sensor location with respect to the output class C.

EXPERIMENTAL EXAMPLE

The optimal sensor location methodology was illustrated using a simple impact damage detection problem in which optimal locations of sensors have to be chosen to obtain the best information about the amplitude level of impact force on a composite panel.

Experimental Test Rig

The structure under investigation consisted of a rectangular $530mm \times 300mm$ composite plate and four aluminium channels (Figure 1). The top flanges of the channels were attached to the plate by a line of rivets, the bottom flanges were fixed rigidly with screws to a pneumatic measuring table. This box structure was intended to simulate the skin panel of an aircraft.

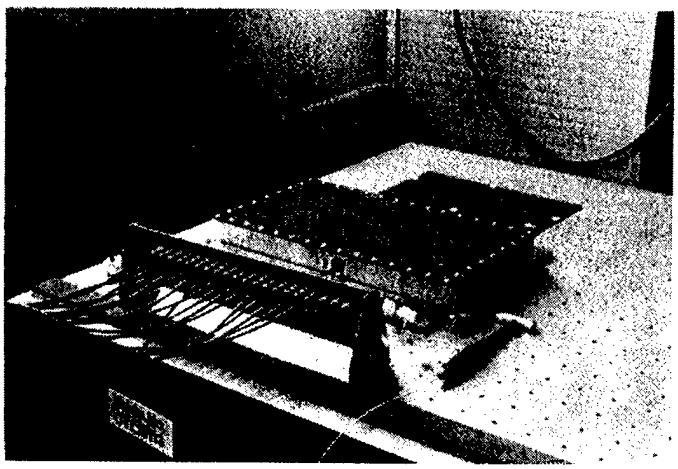


Figure 1: Experimental impact test rig.

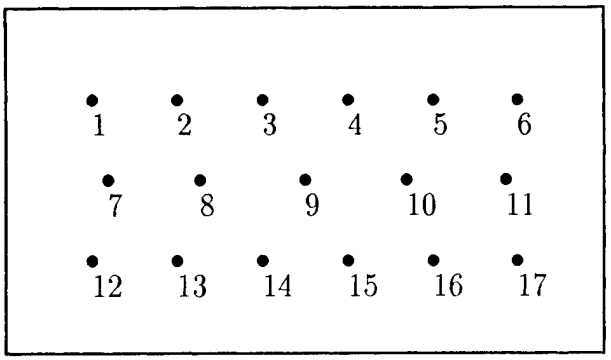


Figure 2: Sensor positions on the composite plate.

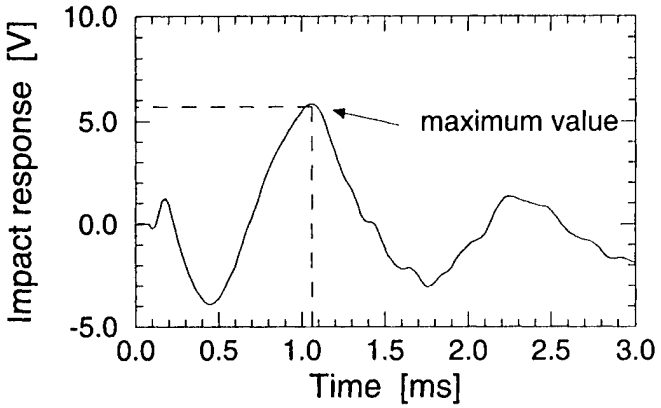


Figure 3: Example of the impact response from sensor no 12.

The composite plate was instrumented with 17 piezoceramic sensors (*PZT Sonox P5*, $15mm \times 15mm$) fixed on the lower surface of the plate, the impacts being performed on the upper surface. The piezoceramics were used as strain sensors. Figure 2 shows the total distribution of sensors used. The impacts were applied using a *PCB* instrumented hammer. The levels of force applied were kept below the threshold causing the damage. The strain data were recorded using a *DIFA SCADAS II* 24 channel measuring system run by the *LMS 3.4.04* data acquisition software.

Results and Discussion

Altogether, 176 impacts were performed in the experiment. For each impact, 8192 samples were recorded at a frequency of $25kHz$. Figure 3 shows an example of the strain data recorded. The fitness function for the GA was calculated from Equation (4). The class vector C was formed from the impact force amplitudes acquired by the PCB hammer. The feature vector F was formed from the magnitudes of maximum sensor response after impacts. The values of probabilities $P(C)$, $P(C)$ and $P(C|F)$ were estimated using histograms, i.e. by counting the number of cases with values of the variables belonging to

a given set of intervals. The six best sensor configurations were studied to provide a simple solution and formulate a realistic problem. The GA parameters used in the study were: number of generations - 500 number of chromosomes per population - 50, probability of crossover - 0.8, probability of mutation - 0.05, number of elite chromosome - 3, number of new blood chromosomes - 5. The GA was run for different values of parameter β in Equation (4). This parameter simply controls the effect of redundances between chosen sensors. Table 1 gives the summary of the results. Here, "*" indicate selected sensors. The results show that for $\beta > 0.7$ the optimal sensor positions are: 1,6,7,12,16 and 17. The optimal sensor configuration for the studied problem is shown in Figure 5.

Parameter	Sensors																
β	1	2	3	4	5	6	7	8	9	10	11	12	13	14	15	16	17
0.0							*			*	*	*		*	*		
0.1							*			*	*	*		*	*		
0.2			*				*				*	*		*	*		
0.3			*				*				*	*		*	*		
0.4							*				*	*		*	*		*
0.5	*					*	*					*		*	*		*
0.6	*						*					*		*		*	*
0.7	*					*	*					*				*	*
0.8	*					*	*					*				*	*
0.9	*					*	*					*				*	*
1.0	*					*	*					*				*	*

Table 1: Summary of the optimal sensor location results.

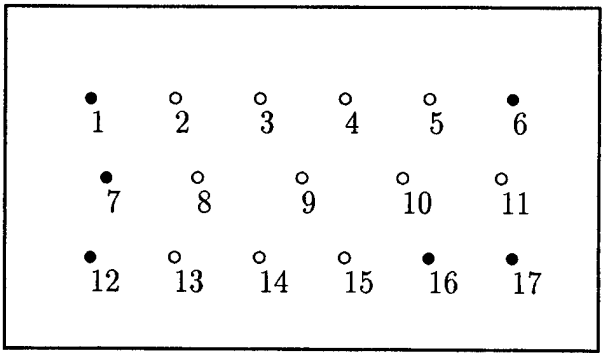


Figure 4: Optimal sensor positions on the composite plate.

The sensors selected by the method are located very close to the boundaries (shorter aluminium channels). This in no surprise; the practice shows that the most difficult region for the amplitude impact detection is always close to the boundaries where the deflection

under impacts remains small compared to the central area of the plate. Therefore in order to obtain the best information about the force amplitude of impacts located at different positions, the sensors need to be located close to the boundaries. The study also shows that sensors 7 and 12 have the greatest contribution to the overall information about the impact force amplitude.

CONCLUSIONS

The problem of finding optimal sensor locations for impact detection in a composite plate has been addressed in this paper. The analysis has involved the use of an optimisation procedure based on the GA with the fitness value based on mutual information. The results show the potential of the method for optimal sensor location for damage detection. In contrast to other approaches, e.g. neural networks, the method presented is independent of the learning process. The case studied here is relatively simple, however the methodology presented is not restricted to simple geometries and structures and also applicable to other sensor optimisation areas. It is assumed that the method should prove valuable in more complex engineering problems. Further work needs to be found to validate the methodology using other methods.

ACKNOWLEDGEMENTS

The authors would like to express their gratitude to Mr. Jack Clarke and Mr. Jim Hodgson for their technical support with the experimental test rig. The impact test rig was manufactured as a part of a university contract for the BAe Systems, Military Aircraft Division.

REFERENCES

1. Hopfield, J.J. and Tank, D.W. 1985, "Neural Computation of Decisions in Optimization Problems", *Biological Cybernetics*, 52, pp. 141-152.

2. Holland, J.H. 1975, *Adaptation in Natural and Artificial Systems*, University of Michigan Press, Ann Arbori.

3. Goldberg, D.E. 1989, *Genetic Algorithms in Search, Optimization, and Machine Learning*, Adison-Wesley Publishing Co., Inc., Reading, Massachusetts.

4. Shwefel, H.P. 1981, *Numerical Optimization for Computer Models*, Wiley, Chichester.

5. Aarts, E.H.L. and Korst, J.H.M. 1988, *Simulated Annealing and Boltzman Machines*, Wiley, Chichester.

6. Glover, F. 1989, "Tabu Search. Part I", *ORSA J. Computing*, 1, pp. 190-206.

7. Glover, F. 1989, "Tabu Search. Part II", *ORSA J. Computing*, 1, pp. 4-32.

8. Mahfoud, S.W. and Goldberg, D.E. 1995, "Parallel Recombinative Simulated Annealing: A Genetic Algorithm", *Parallel Computing*, 21, pp. 1-28.

9. Yip, P.C.P. and Pao, Y.H. 1995, "Combinatorial optimization with use of guided evolutionary simulated annealing", *IEEE Trans. on Neural Networks*, 6, pp. 290-295.

10. Worden, K. and Tomlinson, G.R. 1993, "Fault Detection and Sensor Location Using Neural Networks, technical report, *Dynamics and Control Research Group, Department of Engineering, University of Manchester*, UK.

11. Worden, K., Burrows, A.P. and Tomlinson, G.R. 1995, "A Combined Neural and Genetic Approach to Sensor Placement", in: *Proceedings of the 13th International Modal Analysis Conference, IMAC-95*, Nashville, Tennessee, 13-16 February.

12. Staszewski, W.J., Worden, K. and Tomlinson, G.R. 1996, "Optimal Sensor Placement for Neural Network Fault Diagnosis", in: *Proceedings of the Second International Conference on Adaptive Computing in Engineering Design and Control*, Plymouth, England, 26-28 March, pp. 92-99.

13. Side, S., Staszewski, W.J. and Worden, K. 1997, "Fail-Safe Sensor Distribution for Damage Detection", in: *Proceedings of the International Workshop on Damage Assessment Using Advanced Signal Processing Procedures - DAMAS 97*, Sheffield, UK, 30 June - 2 July, pp. 135-146.

14. Staszewski, W.J., Worden, K., Wardle, R. and Tomlinson, G.R. 1998, "An Experimental Study of Fail-Safe Sensor Distribution for Impact Detection in Composite Materials", in: *Proceedings of the 4th European Conference on Smart Structures and Materials*, Harrogate, UK, 6-8 July, pp. 465-473.

15. Staszewski, W.J., Worden, K., Wardle, R. and Tomlinson, G.R. 2000, "Fail-Safe Sensor Distributions for Impact Detection in Composite", *Smart Materials & Structures*, 9(3), pp. 298-303.

16. Wong, C.S. and Staszewski, W.J. 1998, "Mutual Information Approach to Sensor Location for Impact Damage Detection of Composite Structures", in: *Proceedings of the International Conference on Noise and Vibration Engineering, ISMA 23*, Leuven, Belgium, 16-18 September, pp. 1417-1422.

17. Shannon, C.E. and Weaver, W. 1949, *The Mathematical Theory of Communication*, University of Illinois Press, Urbana, IL.

18. Battiti, R. 1994, "Using Mutual Information for Selecting Features in Supervised Neural Net Learning, *IEEE Transactions on Neural Networks*, 5(4), pp. 537-550.

General

BRIEF OVERVIEW OF THE PHYSICAL BASIS FOR THE "ACTIVE MATERIALS" CONCEPT

P. F. Gobin, M. Salvia, J. C. Baboux, L. Goujon

ABSTRACT

During the last decade constant improvements have been made in materials and structures design and control. But now, some performance objectives cannot be achieved using classical technologies and require to use the 'smart materials concept'. So, this paper aims to perform a brief review of the physical basis of the 'active' materials behaviour.

INTRODUCTION

The idea of 'smart' materials and structures evolved in the early 1980's as the potentially viable solution to the problem posed by the next generation of -particularly military- aircraft. At the same time, the concept of 'intelligent ' and even 'wise' materials was pioneered with the purpose of establishing a new area in materials science, which would take into account the relationship between materials, the natural environment, and society.[1]

The "smartness" or 'intelligence' can be defined at three levels, each of them defining a field of research, technology development and potential applications:

- a material or a structure is said to be "sensitive" when it includes sensors providing information concerning the material itself or its environment.
- a material will be "adaptable" if integrated actuators (or "active" materials) can modify its characteristics. Such a material or structure will be adaptable only by the way of an externally determined action.
- The combination of these two above mentioned properties results in an "adaptive" or "really smart" material which collects data related to the changes in its environment or in its own evolution or damage. It processes these collected data, and reacts through its 'actuators' action. However the techniques for appropriate response functions have until now rarely been addressed.

The question is now : how works one actuator necessary to develop adaptive or smart materials?. In fact when this type of material is submitted to an optical, mechanical, electrical,..., eventually biochemical prompting, it generates a similar or different effect (Table 1). This table gives a general view (but, of course, non exhaustive) of such interphenomena coupling, symmetric or not, with a few examples of materials able to achieve them. The key point for the development of adaptive or smart materials and systems usable for structural or functional applications is evidently the improvement of the coupling transfer-functions.. Moreover it is important for the designers of future systems to know the current level, the trends and the limits of the actuation properties as well as the using conditions linked to the physico-chemical characteristics for each type of materials. So recognising the

PF Gobin, JC Baboux, L Goujon, GEMPPM UMR 5510 INSA de Lyon 69621 Villeurbanne France
M Salvia, Laboratoire IFOS UMR 5621 Ecole Centrale de Lyon 69131 Ecully France

TABLE I: Aspects of interphenomena coupling [2]

Action Effects	Optical	Mechanical	Electric magnetic	Chemical	Thermal	Biochemical
Optical	Photochromic Non linear optics materials Photoreactive and fluorescent mat.	Mechanochromic paints	Electrochromic materials Liquid crystals Non linear optics Electroluminescent Cathodoluminescent		Thermochromic (VO_2)	
Mechanical	photostriction	Polymers with negative Poisson modulus	Ferro-piezoelectric Magnetostrictives Electrorheol. fluids	Conducting polymer Artificial muscle	Shape memory alloy Reversible reticulation	
Electric magnetic	Pyroelectrics photoconductors	Ferro-piezoelectrics Piezo resistives	Conductors and semiconductors		Materials with insulator-conductor trans.	
Chemical	Photoreticulation photodegradation	mechanochemistry		Degradable polymers Delivery systems	Modif. of the diffusion coefficient thermo-dereticulation	Enzymes
Thermal			Non linearly resisting materials (ZnO)			
Biochemical	photoliberation	Systems with controlled delivery	Systems with controlled delivery		Degradable polymers	Biodegradable polymers

need of a basic approach of the actuation concept the present paper sets out to perform a brief review of the physical basis of active materials behaviour . With the exception of shape memory alloys, this review is mainly focused on the electromechanical coupling and on the solid-state actuators.

ELECTROACTIVE MATERIALS

For one anisotropic, homogeneous solid, under isothermal conditions and without magnetic field, the components of the elastic strain tensor are given by the following expression:

$$\varepsilon_{ij} = s_{ijkl}\,\sigma_{kl} + d_{ijk}.E_k + M_{klij}.E_k E_l + \text{higher order terms} \qquad (1)$$

where the applied electric field **E** is (as the polarisation **P**) a one rank tensor ; σ and ε (respectively stress and strain) are two rank tensors and **d** and **M** (respectively piezoelectric and electrostrictive coefficients), are respectively third and four rank tensors. The symmetry of the crystals determine the possible values of these tensors and two types of materials can exist:

-the eleven centrosymmetric point groups for which the components of the piezoelectric tensor (and all odd-rank tensors) are equal to zero.

-the remaining 20 noncentrosymmetric point groups, which are potentially piezoelectric. Among them 10 are polar and possess spontaneous electrical polarisation as well as pyroelectric effect.

For the first type of materials the electrostrictive effect described by an even rank tensor is not limited by the symmetry and is in fact present in all materials even those which are amorphous.

Piezoelectric materials

Most inorganic piezoelectric actuators are based on the lead titanate zirconate (PZT) with the perovskite structure. For these ferroelectrics materials a large spontaneous polarisation appears at the Curie temperature due to a displacive transformation with atomic displacements of about 0.01nm. This phase change results in a complex structure of ferroelectric domains in randomly axed grains of the polycrystalline ceramic. Therefore the poling process is required to partly align the polar vectors of the domains conferring to the polycrystalline sample the global symmetry (6mm) and inducing the piezoelectricity. Poling occurs under intense electric fields at elevated temperatures near the ferroelectric Curie point where the domains are easily aligned. This poling process is markedly aided by the nearness of a morphotropic phase boundary (MPB) between tetragonal (titanium rich) and rhomboedral (zirconium rich) phases. For these compositions there are 14 possible poling directions over a wide temperature range. This can explain partly why the piezoelectric coefficients are largest near this morphotropic boundary [3]. Typical values are d_{33} = 400 pC/N and $\varepsilon_{MAX} = 1.5.10^{-3}$.

The PVF_2 corresponding to the $(-CH_2\ CF_2\ -)_n$ polymer, is the typical example of an organic semi-crystalline piezoelectric material. The electronegativity of the fluor atoms confers to the CF_2 group one important dipole moment. Among the four possible crystalline phases, the orthorhombic β phase, directly obtained by crystallisation from the melt with the copolymer P(VF_2 /TrFE), presents the best ferroelectric properties. It is the reason why this statistic copolymer is the most widely used. It is interesting to note that if the piezoelectric constant d of PVDF is smaller than that of the PZT ceramics (20 pC/N), the piezolectric constant g which indicates the voltage per applied unit stress, is on the contrary larger by an order of magnitude (160.10^{-6} V/N). So the PVDF is particularly well suited for sensor applications. [4]

Electrostrictive materials

In the conventional materials as well as for many ferroelectrics, the electrostrictive effect is too small for potential applications as actuators. However equation (1) expressed for a zero stress indicates that the electrostrictive strain is equal to QP^2 where Q is a set of electrostrictive coefficient, $P = \kappa \varepsilon_0 E$ the induced polarisation, κ the dielectric constant and ε_0 the permittivity of free space. Thus materials with a very large dielectric constant can exhibit large electrostrictive strain, even though their electrostrictive coefficients are relatively small. It is the case for some ceramics with a complex distribution of the B_1 and B_2 cations in the B sites of the $A(B_1B_2)O_3$ perovskite structure. For instance the lead magnesium niobate (PMN) and its solid solutions with the lead titanate (PT) are probably the most studied. All compositions on the PMN rich side of a morphotropic phase boundary (at 35 mole% PT) exhibit a diffuse phase transition without a well defined Curie temperature and a very high dielectric constant peak dropping off rapidly with the frequency. In this type of 'relaxors' the diffuse phase transition would be linked to a chemical disorder responsible for the formation of nanodomains having different Curie temperatures. Such chemical fluctuations have been evidenced on a PMN by EDX spectroscopy nanoanalyses [5]. Some nanonodules (10 nm) enriched with lead and magnesium are embedded in the paraelectric matrix. Consequently some polar nanoregions seems coexist with the paraelectric matrix in a wide range of temperature, but the matrix keeps on average the cubic structure.

Moreover it seems possible to induce a phase transition under an electric bias field by percolation of the nanodomains of rhomboedric symmetry. But, in spite of many theoretical approaches, our knowledge of this complex behaviour very dependent of the chemical composition has to be improved.

Finally it is interesting to note first, that the non linearity between strain and electric field can be in this case used to tune the apparent piezoelectric coefficient by electric polarisation of a few MV/m and second that the development of electrostrictive ceramics single crystals allows to obtain reversible strains higher than 1 % [6].

Concerning the organic materials, a new class of electrostrictive polymers was recently developed by using the ferroelectric copolymers of polyvinylidene fluoride and trifluoroethylene P(VDF-TrFE) [7]. After electron irradiation the copolymers exhibit important dielectric constant and high electrostrictive strain levels (4 % at a biased electric field of 150 MV/m measured at 1Hz). Moreover, both the strain and the polarisation hysteresis are negligibly small. The reasons of this evolution are probably linked to the breakup of the coherent macro-polar regions into micropolar regions which reduces the energy barrier of switching the polarisation direction from to another.

Diffusion based electroactive polymers

The actuation mechanism is based in the case of the majority of polymers actuators on the diffusion of ionic species either in or out of a polymer network. The different types can be characterised as gels, conductive polymers, or ionic polymer-metal based composites (IPMC).

Gels are crosslinked polymer networks in a solvent. A gel actuator is activated by different forms of stimuli (pH, heat, light, electric potential) which can cause ions to move into or out of the polymer structure , thus leading it to swell or contract . This phenomenon is associated to very large volume changes (till 1000). The amount of volume change that can be generated in a gel is evidently related to his crosslink density. Gels with a low crosslinking density display large volume change, but the low crosslinking produces a low-modulus material. So the gels actuators have three drawbacks : *(i),* the actuation mechanism is based on ion diffusion with a low speed of reaction, *(ii),* the amount of work that can be generated is low due to the low-modulus, and *(iii),* these systems require aqueous solutions for operation.

Conducting polymers are similar in principle to the gels in that ion diffusion causes the dimensional change in the material, but the size of the actuator can be small, thereby reducing the response time. Moreover, conducting polymers are stiffer than gel actuators and a significant amount of work can be generated in this case. Conduction in these polymers is based on inserting a dopant species into the polymer network. Furthermore by applying an electric potential to the polymer dopant insertion and deinsertion can occur. This displacement of ions in and out of the polymer network leads to dimensional change and actuation. Evidently as in the previous system, conducting polymers require an anode, a cathode and an electrolyte for operation. Fortunately the electrolyte can be solid and the electrodes fabricated out of the conducting polymer, making the actuator component chemically and mechanically compatible.

Ionic membrane polymers or IPMC also rely on transport of ions with the same limitation in the response time. These systems are realised with one ion conducting membrane material, such as Nafion or Flemion plated with metal electrodes (Au, Pt,) [8]. By applying an electric field to this membrane, ions moving from one electrode to the other can drag water molecules through narrow hydrophilic channels in the resin. The difference in water content in the membrane swells or shrinks the membrane near the electrodes. For instance the swollen cathode and the shrunk anode deflect the composite to anode. These materials can be sealed because the ions are moving only within the membrane and the response time can be improved by controlling the diffusion length. These IPMC actuators are slightly stiffer than gel actuators but the components demonstrated to date are very soft and have limitations in work performing capability.

Carbon nanotubes

Just behind the extensive research on C_{60} fullerene came the discovery of the carbon nanotubes . First reported in 1991, their structures consist of rolled-up graphite sheets. Various degrees of helicity can exist, and it is predicted that these fibres can behave as either semi-conductors or conductors, depending on the tube diameter or degree of helicity.

Recently Baughman and al [9] have demonstrated that carbon nanotubes can function as actuators akin to artificial muscles. Two films of bundled single-walled nanotubes are stuck to a double–sided Scotch tape and immersed into a one mole NaCl electrolyte. A dc voltage of only a few volts is applied between the two strips and charge transfer occurs ; the injection of positive charges leads to an expansion of the tubes causing the strip to bend because of quantum chemical and electrostatic effect (not totally understood). Such bundled structures of nanotubes could be, in the future, used in the field of robotics and synthetics actuators. Nevertheless strength limitations involve the large-scale production of defect-free aligned nanotubes.

Classical polymer films

A new type of 'electrostrictive' actuation has been demonstrated on classical polymer films (silicone, polyurethane..) without taking in account the polarisation effect. When a voltage difference is applied on an elastomeric polymer film sandwiched between two compliant electrodes the polymer is squeezed in thickness and stretched in length and width by the electrostatic forces generated between free charges.

MAGNETOSTRICTIVE ACTUATORS

Magnetostriction phenomenon has been discovered by Joule in 1842. He observed that an iron rod lengthens under the effect of a magnetic field directed following its axis... This is important for actuator device application because electrical (magnetic) energy can be converted into mechanical (elastic) energy via magnetostrictive materials. This magnetostrictive effect is also reversible and change in stress applied to a material generates magnetic energy (Villari effect)

The relative deformation associated to the Joule effect is a square function of the magnetic induction but as in the case of electrostrictive materials a reversible and quasi linear effect can be obtained by a static polarisation.

Very large strains are often needed to deliver the large displacements required for smart system components and one of the shortcomings of the 3d transition metals is their low saturation strains (5.10^{-5}). Rare-earth are characterised by their 4f electron charge clouds which impart a non spherical shape to the atoms. This shape evolves in a regular way through the lanthanide series as electrons are added. Erbium Samarium and Thalium are 'egg-shaped'- , Terbium and Dysprosium resemble more to flattened oblate ellipsoids. This high anisotropy combined with strong spin orbit coupling leads to large magnetostriction (λ_{Σ}= 1.1 10^{-3}) with saturation strains of two orders higher than Nickel (3.4 10^{-5}), Cobalt and Iron , but at a cryogenic temperature because their very low Curie temperature. However the presence of iron in the rare-earth- Fe alloys increases the Curie temperature. Thus $TbFe_2$ and $SmFe_2$ exhibit important magnetostriction respectively positive and negative at ambient temperature, but their strong anisotropy disturbs the field rotation process. So in order to get a low anisotropy two rare-earth-Fe alloys having the same magnetostriction sign but opposed anisotropy have been combined and the best alloy allowing to control the shape change with small applield field is known as Terfenol-D with the composition Tb_{1-x} Dy_x Fe_2 (with generally x = 0.7). Finally it is interesting to note that this best composition of the terfenol

magnetostrictor is not very far from the magnetic phase boundary between rhomboedral and tetragonal phases

Moreover the use of magnetostrictive particles embedded in composite host materials has been thesubject of several recent publications.

SHAPE MEMORY MATERIALS

Shape memory alloys

The shape memory alloys undergo by cooling martensitic transformations similar to those observed on a lot of metallic, ceramic and even partially crystalline polymer materials, and in particular on steels. But in the case of the commonly used SMA's (Cu-Zn-Al or Nickel Titanium) this first order transition is reversible with a small thermal hysteresis linked to a negligible volume variation. Two important characteristics of martensite phase are the absence of long-range diffusion and the appearance of a shape change. The shape memory alloys typically transform from a partially ordered cubic austenitic phase to a martensitic low temperature state. This martensite easily deforms under stress by domain –wall displacements and when reheated goes back to the original shape of the high temperature structure : this is the one-way shape memory effect. It is also possible to obtain a reversible two way shape memory effect between high and low temperature shape by temperature cycling under applied stress or strain. This 'training' introduces in the austenite some bundles of dislocations homogeneously distributed which direct the growth of the martensite domains. Moreover mechanical stresses can also cause phase change as well as the temperature, inducing the well know super elastic effect linked to the austenite martensite transition.

Magnetic shape memory alloys

A drawback of the shape memory alloys is their slow response due to their thermal control mainly in cooling. A new mechanism based on the magnetic-field-induced reorientation of the twin structure of a magnetic shape memory alloy has been suggested by Ullakko [10]. Effectively the magnetic control of the shape memory effect would lead to much more rapid response of the actuator than the thermal control. Magnetic field controls the reorientation of the twin variants in an analogous way as the twin variants are controlled by the stress in classical shape memory alloys. When they are subjected to one externally applied magnetic field, the twins in a favourable orientation grow at the expense of the others. This results in a shape change of the magnetic shape memory alloy. Ullakko et al. reported a 0.2% reversible strain in Ni_2-Mn-Ga. This strain has been improved in the case of the Fe-Pd alloy with a 1.3% free strain on a material in a stress-cooled state.

Shape memory ceramics

The change in the spontaneous strain accompanying a phase transition can theoretically be expected to be much larger than that associated to the polarisation reorientation in the ferroelectric phase. It the reason why some antiferroelectrics lead titanate stannate based systems (PNZST) able to switch from an antiferroelectric state to a ferroelectric one have been proposed. The induced strain reaches up to 0.4% (longitudinal effect) which is much larger than the one expected in classical piezostrictors. This field induced transition exhibits a shape memory effect for appropriate compositions. The material memorises its ferroelectric state even under zero-field conditions although it can be erased with the application of a small

reverse bias field. It is important to note that this shape memory ceramic does not require a continuous electric field application but only a pulse drive, thereby saving a lot of energy [4].

TUNABLE MATERIALS: ELECTRO AND MAGNETO–RHEOLOGICAL SYSTEMS

Electro and magnetorheological fluids are not actuators *stricto sensu*. Nevertheless it is possible to tune within a millisecond time their rheological properties, yield stress and apparent viscosity, by using one electric or magnetic field. Currently no model can completely describe the behaviour of the ER fluids . However a Bingham plastic model can often provide a sufficient accurate description to be used for the designing of ER material devices. Although no consensus regarding the mechanism for the observed ER effect has been reached, it is generally accepted that the phenomenon originates from particles polarisation induced by the electric field. The observed changes in mechanical properties are the result of the formation and breakdown of one induced particle chain network. Nevertheless materials that exhibit more than 3 kPa in dynamic yield stress, less than 0.35 Pa.s in zero field viscosity, and stability over a reasonable temperature range are currently available.

The same type of comments can be made concerning the magnetorheological fluids, but the higher values of the yield stress(until 30 kPa in a 500 kA/m magnetic field) should facilitate their development. Finally it is interesting to note the occurrence of homogeneous liquid crystals polymers based functional fluids. This kind of non yield effect material could be particularly attractive for vibration control devices.

By extension of this concept of tunable fluid it is also possible to realise elastomer based functional materials loaded with magnetic particles before crosslinking. During the cure, a magnetic field induces the formation of a particle chain network with colinear dipoles parallel to the applied field. The crosslinking process locks the embedded particles chains in place and the stress-strain curve of the composite depends of the applied magnetic field. So this processing results in a material with a 'field dependent' apparent modulus. It seems possible to use such materials for different devices as a tuned vibration absorber or a stiffness tunable suspension.

CONCLUSIONS: TOWARDS IMPROVED AND NEW MATERIALS

The improvement of the small strain capabilities as well as the hysteresis behaviour of the piezoelectric ceramics is the subject of a lot of research . One interesting way is represented by the single crystals materials. Park and Shrout [6] reported first strain levels up to 1.5% for single rhombohedral crystals of relaxor perovskite PZN-PT with a reduced strain hysteresis. These outstanding properties only occur for specific orientations <001> of the electric field with respect to the crystal axes and the anisotropy in response is really large. The application of this concept of 'cristallographic engineering' to other ferroelectric crystals in order to enhance their piezoelectric performance is now in progress.

Driving the shape memory effect with other 'fields' than temperature is also an interesting research direction. The advantage consists mainly in the reduction of the response time. As in the case of the electroactive ceramics the elaboration of single crystals of magnetic shape memory alloys is the best way to improve the strain capabilities The theoretical maximum limiting the achievable strain is the value of the transformation strain, that is 6.6%.

Since the research on giant magnetostrictive materials started , most of the work has been conducted about bulk alloys of RE-Fe in order to obtain textured polycrystals or even single crystals. But the research and development for thin films has recently been increased and can open new fields of research and applications.

The potential of the classical electrorheological fluids for practical application is limited by the problems of particle precipitation and instability outside a rather narrow temperature range. This lead to renewed interest in homogeneous ER fluids since the discovery in the early 1990's of an extremely large ER effect in certain liquid-crystalline polymer fluids. Two structural mechanisms, one high aspect ratio of liquid-crystalline molecules , and a sufficient interaction between adjacent liquid-crystalline domains, were considered as a possible basis for obtaining a large ER effect. In the case of the poly (γ benzoyl L- glutamate) (PBLG), the increase in shear stress at 25°C by application of a dc 2kV/mm electric field is about 3 kPa [11]. This effect is enough large but polymeric fluids are in fact able of more than 10 kPa and present advantages over particles dispersed ER fluids particularly in torque control and vibration damping.

For EAP, actuation properties have been demonstrated at a small scale and in limited cases. In fact the fundamental mechanisms providing the actuation are, specially for IPMC, not fully understood. However, in spite of a severe limitation in their response time and in force generation linked to their low modulus, many applications could be reached as microrobotic actuators or even 'artificial muscles'.

REFERENCES

1.Beck G. and Gobin P.F. 1992."The research on intelligent materials developed in relation with the CNRS of France." *Journal of the Society of non tradiitional technology*, n°2-3, pp 27-54

2.Sillon B., J.C. Dubois, P.F.Gobin, M. Pineri, M. Sixou and M. Vert. 1997. "Matériaux actifs et systèmes adaptatifs" . *Cahiers de synthèse du CNRS en Science et Génie des Matériaux.* pp 65-106

2.Damjanovic D. and R.E. Newnham. 1992. " Electrostrictive and piezoelectric materials for actuator applications" . *J. Intell. Matls. Sys. & Struct.* (3). pp 190-208

4.Uchino K. 1999. " Piezoelectric actuators and ultrasonic motors". Kluwer Academic Publisher.

5.Lattard E. 1996. "Elaboration de céramiques massives (1-x)$PbMg_{1/3}Nb_{2/3}O_3$–x$PbTiO_3$ avec x=0,05 et 0,1. Des carctérisations structurales au comportement électromécanique". Thèse Université de Limoges

6.Park S.E.and T.R. Shrout. 1997 "Ultrahigh strain and piezoelectric behavior in relaxor ferroelectric single crystals", J. Appl. Phys., vol 4, n°82, pp 1804-1811

7.Ting R.Y. 2000. "New electrostrictive PVDF copolymers for large-strain applications" . Fifth ECSSM SPIE Vol. 4073 (P.F. Gobin, C.M. Friend Editors) pp 48-58

8.Kim J.K. M. Shahinpoor and Razani A. 2000 "Preparation of IPMCs for use in fuel cells,electrolysis,and hydrogene sensors". Smart Structures and Materials SPIE Vol.3987. pp 311-320

9.Baughman R.H. & al 1999: " Carbon nanotube actuators", *Science*, May, vol 284. pp1340-1344.

10.Kari Ullako 1996: Large strocke and high strength actuator materials for adaptive structures . *Third ICIM/ECSSM' 96.* SPIE Volume 2779 (P.F. Gobin, J. Tatibouet Editors). pp 505-510

11.Inoue A. & al. 1998: " ER fluids based on liquid crystalline polymers". *MRS bulletin* Vol. 23 n°8.pp 43-49.

STUDY ON ADAPTIVE CONTROL STRATEGIES FOR SMART STRUCTURE VIBRATION SUPPRESSION

Kougen Ma, Jörg Melcher, Hans Peter Monner

ABSTRACT

This paper focuses on adaptive control strategies for smart structure vibration suppression. It deals with following topics: the introduction of adaptive feedforward control scheme, adaptive algorithms and comparison, the choice of so-called reference signals, adaptive control with on-line identification and its extension to MIMO case, adaptive hybrid control, and adaptive inverse control using MX filters. For each aspect, simulations and experimental examples are pointed out. Comparison and discussions are also made to explain their properties.

INTRODUCTION

Smart structure technologies deal with sophisticated aspects that cover sensory units, actuation units, control units and others to realize some prescribed functions. It has vast potential in the fields of aerospace, civil engineering, shipping, automobile, precise instruments and machines, etc. For example, smart wings can provide more lift or/and better aeroelastic dynamic performance by driving integrated actuators to change the curvature of a profile or the angles of leading-edge and lagging-edge of an airfoil. Smart rotors have less vibration load and longer fatigue-life. Generally speaking, smart structures deal with multi-disciplines, such as mechanics, physics, mechanical engineering, control and signal processing, computer, etc.

Smart structures can behave in time-variant, always different dynamic and static, and non-linear characteristics. To control such kind of structures is a challenging task. Conventional active controller design methods, e.g. eigen-structure assignment, optimal control, require accurate mathematical models. But accurate models are almost impossible for smart structures, because of the above behaviors and simplifications in modeling process, manufacture error, the wear of parts in running, and the change of working surrounding. In this case, adaptive control may be an attractive alternative.

Institute of Structural Mechanics, German Aerospace Center (DLR)
Lilienthalplatz 7, 38108,Braunschweig, Germany

Adaptive control can be divided into two parts: adaptive feedback control and adaptive feedforward control. In general, adaptive feedback control, such as model reference adaptive control, may be used to control free vibration. Its controller is usually designed in state space. Some experiments have proven its validity [1]. Adaptive feedforward control was originally used for noise control [2-4] and then extended to vibration control. Now it has been studied in large space structure control [5], civil structure vibration under seismic excitation [6], helicopter vibration control [7], wing flutter suppression [8], smart structure vibration control [9,10], and automobile vibration reduction [11]. It bases on adaptive filtering theory. Its recursive capability makes it very suitable for realizing in digital signal processors (DSP). And the rapid development of digital signal processors accelerates its application. Compared with adaptive feedback control, an evident feature of adaptive feedforward control is a so-called reference signal.

This paper focuses on the control strategies of smart structure vibration suppression. It deals with many aspects of adaptive feedforward control. Following the introduce of the general adaptive feedforward control scheme, various adaptive algorithms are presented and compared, then the choice of reference signals is discussed. Thirdly, some extensions of general adaptive feedforward control are outlined, such as adaptive control with on-line identification, adaptive hybrid control, MIMO adaptive control with on-line identification and adaptive inverse control using MX filters. The last summarizes the paper. In each part, simulations and experimental examples are pointed out. Comparison and discussions are also made.

ADAPTIVE FEEDFORWARD CONTROL: ALGORITHMS AND COMPARISON

The basic principle of adaptive feedforward control is drawn in Figure1. In the figure, H_1 and H_2 are called the impulse response functions of primary path and secondary path respectively. They depend on the controlled structure. $\hat{H}_2$ is the estimation of H_2. f is a disturbance which causes structure vibration. x is a reference signal. d, called uncontrolled or desired response, and s are the responses caused by the disturbance and adaptive controller, respectively, i.e., $d = H_1 * f$ and $s = H_2 * u$, u is the output of the controller. e is called controlled response or error, W is the weights of the controller.

Assuming that H_1, H_2 and W can be described by finite impulse filters (FIR) with the lengthes M, L and P, respectively, then

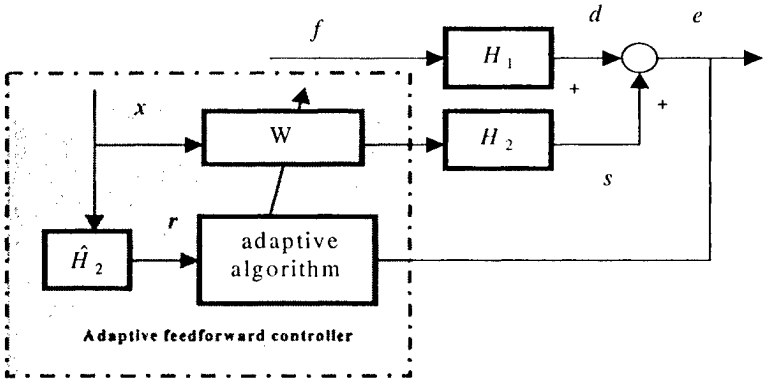


Figure 1 Adaptive feedforward control

$$e(j) = d(j) + s(j) = d(j) + \sum_{k=1}^{L} h_2(k)u(j-k+1)$$

$$= d(j) + \sum_{n=1}^{P} w_j(n)r_j(n) \tag{1}$$

where

$$r_j(n) = \sum_{k=1}^{L} h_2(k)x(j-k-n+2) \tag{2}$$

is called filter-x signal. In fact, for calculating $r_j(n)$, $h_2(k)$ has to be estimated, i.e. $h_2(k)$ in Equation (2) must therefore be replaced by $\hat{h}_2(k)$.

The adaptation is to search an optimal weight W to drive the error e to zero.

In adaptive feedforward vibration control, controllers are usually in the type of the FIR filter. The choices of the reference signal, the order of the filter and adaptive filtering algorithm are main technical points.

There are many adaptive filtering algorithms, e.g. Least Mean Square (LMS) algorithm, Recursive Least Square (RLS) algorithm and Fast Transversal Filtering algorithm (FTF). The choice of algorithms is an important task. It depends on the controlled structure, disturbance, the complexity of algorithms, the characteristics of algorithms and hardwares. LMS algorithm has small calculation, but normal LMS algorithm converges slowly. RLS algorithm has a little more calculation than that in LMS algorithm for a low order filter, but it can produces a faster convergence.

Here a new algorithm, named gradient-based least square (GLS) [11], is presented which possesses the strongpoint of both LMS and RLS algorithms. From the cost function of view, normally LMS only considers the error at a sample step, but RLS considers the error in several sample steps. The consideration of RLS algorithm can show the trend of the error, and lead adaptive algorithm to optimization in a good way. But the calculation of the inverse matrix of input correlation is required in RLS algorithm, it makes the algorithm complex.

The new algorithm GLS conserves the simple recursive process of LMS algorithm, but replaces the cost function of LMS algorithm with that of RLS algorithm. The calculation complexity of GLS algorithm is nearly same as that of LMS algorithm, but it has fast convergent rate. Table I lists the algorithms of LMS and GLS. Table II shows the computational complexities of LMS, GLS, RLS and FTF algorithms.

GLS, LMS and RLS algorithms are compared through a mechanical structure integrated with piezo-electric patchs. The vibration of the structure is caused by a harmonic excitation at frequency 277Hz. The length of the controller is 4, sampling rate 3000Hz. Convergent factors are optimized in each case. The response and weight are shown in Figure 2. It reveals

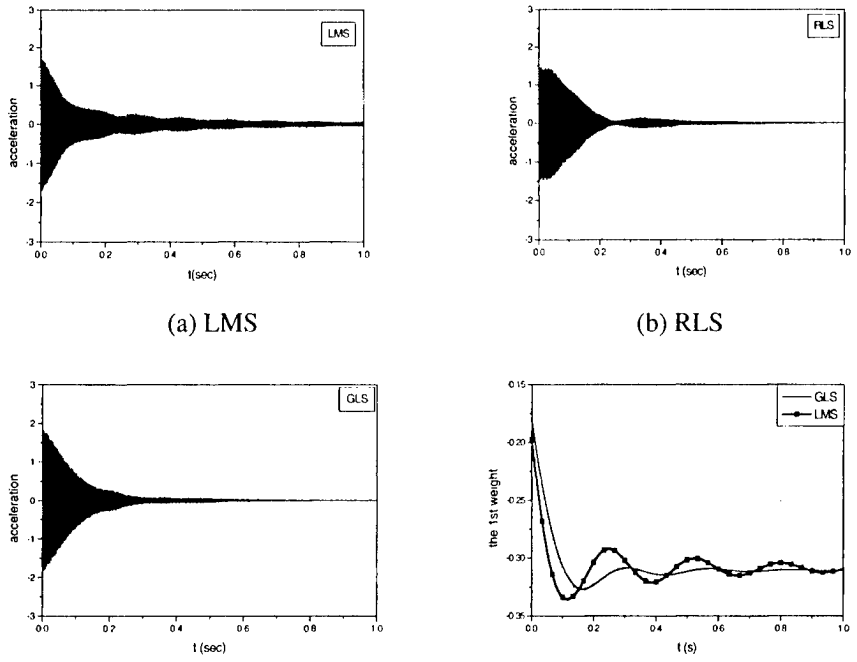
TABLE I. RECURSIVE PROCESS OF LMS AND GLS

Type of algorithms	LMS	GLS
Cost function	$J = \mathrm{E}[e^2(k)]$	$J(n) = \sum_{k=0}^{n} \lambda^{n-k} e^{2}(k)$
Recursive algorithm	$w_{k+1}(n) = w_k(n) - 2\mu e(k) r_k(n)$	$w_{k+1}(n) = w_k(n) - \mu \sum_{i=0}^{n} 2\lambda^{n-i} e(i) r_k(i)$

TABLE II. COMPARISON OF COMPUTATIONAL COMPLEXITIES

algorithm	number of operations per iteration		
	multiplications	divisions	addition/subtractions
LMS	$2m+1$	0	$2m$
GLS	$2m+1$	0	$2m+1$
RLS	$2m^2+7m+5$	m^2+4m+3	$2m^2+6m+4$
FTF	$7m+12$	4	$6m+3$

* m is the length of the adaptive filter



(a) LMS (b) RLS

(c) GLS (d) the first weight

Figure 2. The response and weight of LMS, RLS and GLS algorithms

that GLS algorithm can provide nearly same convergent rate as that in RLS algorithm. Figure 2(d) proves that the GLS algorithm is much faster than LMS algorithm.

THE CHOICE OF SO-CALLED REFERENCE SIGNALS

Besides adaptive algorithms, another very important point is the choice of so-called reference signas. Generally speaking, reference signals must correlate with the uncontrolled response of structures. Here four kinds of choices are discussed. The first one is the disturbance that causes structure vibration. It is the best reference signal, because the disturbance strongly correlates with uncontrolled responses. Unfortunately, it is hard to obtain the disturbance in many situations. The second one is a so-called virtual signal, which contains the characteristics of the disturbance [12]. For example, for rotor vibration control, rotating rate can be measured easily, the containing predominant frequencies of uncontrolled response spectra are the rotating rate and its harmonic. In this case, a virtual signal can be constructed using the measured rotating rate. The third one is to use estimated uncontrolled responses by an internal model [7]. The fourth choice comes from a sensor that is located on

controlled structures directly [11]. In these choices, the first is direct and efficient. The second is also very good in some cases. The last two choices would be used with care, because they may cause unstable.

ADAPTIVE CONTROL WITH ON-LINE IDENTIFICATION

From Figure1, it can be found that the impulse response of the secondary path plays the important role in adaptive feedforward control. It directly affects adaptive algorithms and further the performance of whole system. It may causes system unstable, if it is not so precise. Usually, an off-line estimation is used. The estimated impulse response does not change any more during the adaptation of the algorithm. If the controlled plant changes its dynamic characteristics during the controller running, the controller can not assure the performance, even causes the system unstable. In this case, an adaptive feedforward control with on-line identification is required. It can not only adapt the controller but also identify the impulse response of the secondary path in each sample step, and update the impulse response of the secondary path step by step.

Figure 3 depicts the diagram of the method. The reference signal, error, and control signal are the inputs of the identification block, the output of this block is the impulse response of the secondary path. The control block works as usual.

This method has been extended to MIMO case. In MIMO case, the cost function is the sum of the square of each sensor output. Figures 4 and 5 show the identification error and the cost function of a free-free structure with 4 accelerometers and 2 proof-mass actuators. The excitation signal is harmonic at frequency 20 Hz. The initial values in its identification and

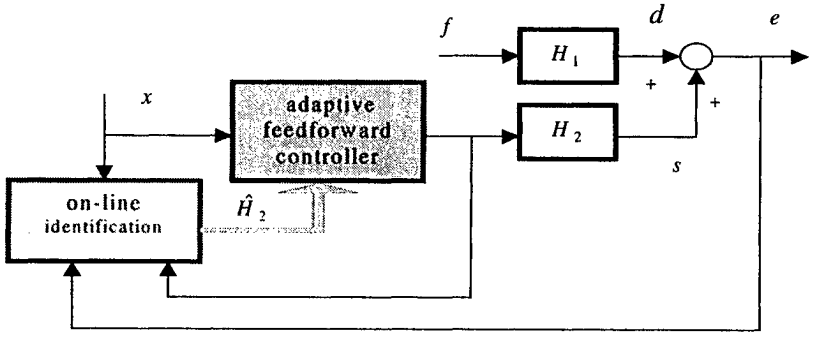


Figure 3 Adaptive control with on-line identification

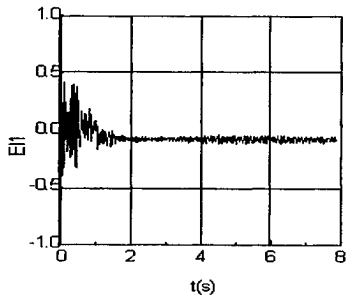


Figure 4 Identification error

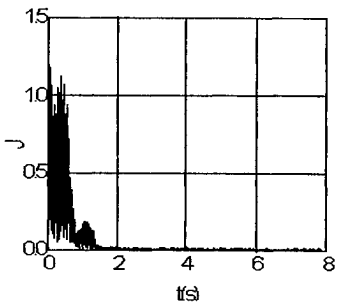


Figure 5 The cost function

control blocks are zeros. Figure 4 expresses that the secondary path is identified perfectly. The very evident vibration reduction can be observed in Figure 5.

HYBRID ADAPTIVE CONTROL

As mentioned above, the impulse response of the secondary path is very important in adaptive feedforward control, and normally it is in the type of FIR filter. If the controlled structure has very low damping, the order of the FIR filter must be large enough to describe the dynamic feature of the structure, further, the calculation of the filtered-x signal costs long time. In addition, the low damped structure is very sensitive to the change of excitation frequencies, etc. To improve the performance of adaptive feedforward control, a combined feedback and feedforward controller, named hybrid adaptive control [9,10], has been developed, as shown in Figure 6.

In hybrid adaptive control, the feedback controller is mainly used for increasing the damping of a controlled structure and decreasing vibration level. The adaptive feedforward

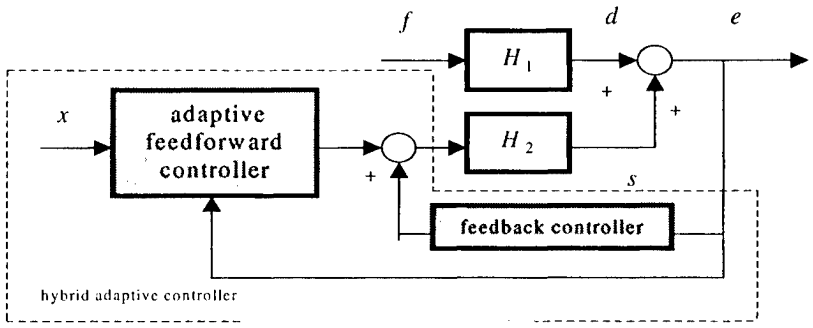
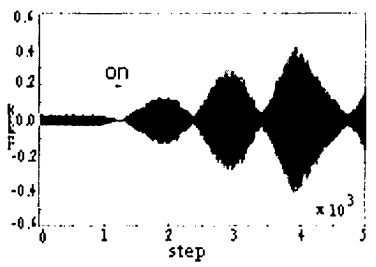
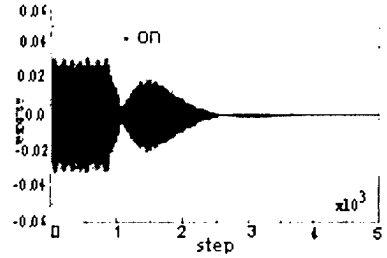


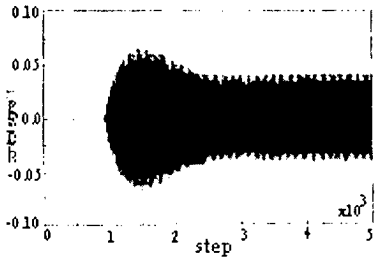
Figure 6 Hybrid adaptive control



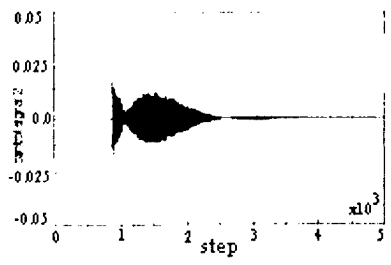
(a) vibration level (only feedforward control)



(b) vibration level (hybrid control)



(c) feedforward part of the control



(d) feedback part of the control

Figure 7 The results of a plate with two piezo-sheets

controller is responsible for reducing vibration level and driving the controller to optimization. This control method can raise the adaptive rate and robustness of the control system. Figure 7 shows the results of a plat with two piezo-electric patchs. The plate is placed in a closed box and excited by acoustic with the frequency of 187 Hz. The frequency is the one of resonant frequencies of the plate. Figure 7(a) gives the response of adaptive feedforward control, expresses an unstable control process. Figure 7(b) shows the response of hybrid adaptive control. Figure 7(c) and (d) are the feedforward and feedback parts of the hybrid controller output. It can be found that the feedback part of the controller plays great role in the beginning of the control action.

ADAPTIVE INVERSE CONTROL USING MX FILTER

MX filter [13], as shown in Figure 8, is a second-order filter, which has a cross-coupled structure and modal section-parallel configuration. It has been used for simulating dynamic behavior of structures [9,10] and on-line modeling of time-varying structures with the LMS algorithm [13-15], and inverse modeling.

To apply MX filter to structure control means that the FIR controller in Figure 1 would be replaced by a single section or multi-section MX filter, then the MX-LMS algorithm [14] is employed to achieve adaptation.

Figure 9 shows the amplitude via frequency curves of a complex structural system. In the figure, H_1 and H_2 are respect to the primary path and the secondary path, respectively, W_{opt} is the optimal controller derived from H_1 and H_2. The used MX filter has 4 sections. It can be

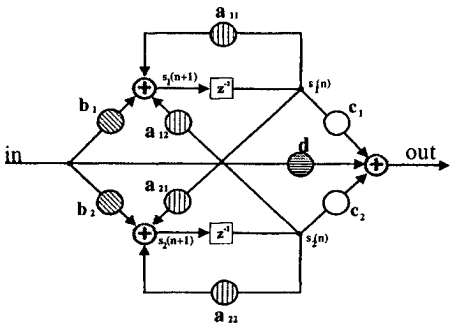


Figure 8 A section of MX filter

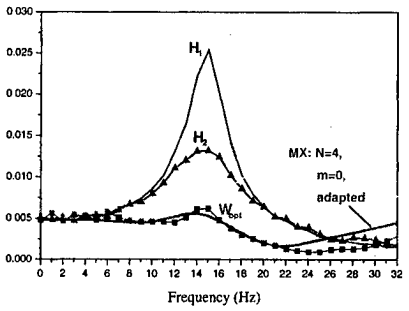


Figure 9 An example

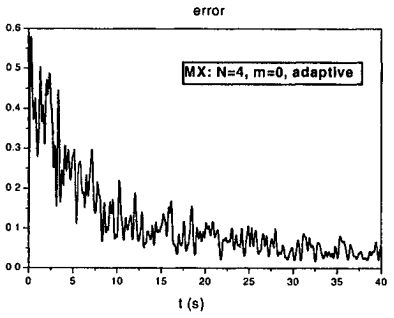


Figure 10 Error

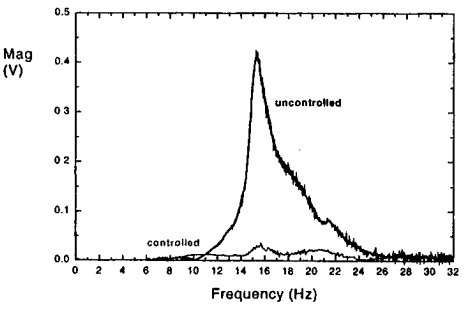


Figure 11 The response spectra

seen that the MX filter (controller) and the optimal controller are nearly same in the frequency range from 0 to 22Hz. Figures 10 and 11 demonstrate the evident vibration suppression.

CONCLUSIONS

This paper focuses on adaptive control strategies of smart structure vibration suppression. It deals with following topics: adaptive algorithms and comparison, the choice of the so-called reference signal, adaptive control with on-line identification, hybrid adaptive control, MIMO adaptive control with on-line identification and adaptive inverse control using the MX filter. Each method has its own peculiarity and application. To determine a method and adaptive algorithm depend on many factors, for example, characteristics of controlled structure, computer hardware and software, etc. The combine of control system configurations and adaptive algorithms can create various methods, and makes adaptive control of structure vibration vivid. In the future, besides the research of control configuration, to search simple and fast adaptive algorithm would be very important, especially for smart structure vibration reduction.

REFERENCES

1. Bar-Kana, I. and Howard, K. 1993. " Simple Adaptive Control of Large Flexible Space Structures ", *IEEE Transactions on Aerospace and Electronic Systems*, 29, pp.1137-1149.
2. Widrow, B., Glover, J.R., McCool, J.M., Kaunitz, J., Williams, C.S., Hearn, R.H., Zeidler, J.R., Dong, E. and Goodlin, R.C., 1975, " Adaptive Noise Canceling: Principles and Application, " Proceedings of the IEEE, 63, pp.1692-1716.
3. Nelson, P.A. and Elliott, S.J., 1992. *Active Control of Sound.* Academic, London.
4. Russell, H.T., Rixardo, A.B. and Steven, A.L., 1996, Time-averaged Active Controller for Turbofan Engine Fan Noise Reduction, " *Journal of Aircraft*, 33, pp.524-531.
5. Melcher, J. and Wimmel, R., 1991. " Modern Adaptive Real-time Controllers for Actively Reacting Flexible Structures, " *Journal of Intelligent Material Systems and Structures*, 2, pp.328-346.
6. Burdisso, R.A., Suarez, E. and Fuller,C.R. 1994. "Feasibility Study of Adaptive Control of Structures under Seismic Excitation, " *ASCE Journal of Engineering Mechanics*, 120, pp.580-591.
7. Ma, K.G. and Gu, Z.Q. 1997. " Adaptive control for structural response of helicopters," *Acta Aeronautica et Astronautica Sinica,* 18(3), pp.359-362
8. Roy, I.D. and Eversman, W., 1996. " Adaptive Flutter Suppression of an Unswept Wing," *Journal of Aircraft*, 33, pp.775-783
9. Ma, K.G. and Melcher, J. 1998. "On real-time model and hybrid adaptive control of smart rotor blades," *Acta Aeronautica et Astronautica Sinica*, 19(5) ,pp.525-530
10. Ma, K.G. and Melcher, J. 1997. " Hybrid adaptive control of smart rotor blades," Proc. of 23rd European Rotorcraft Forum, Dresden ,Germany, pp.52.1-52.8
11. Ma, K.G. and Melcher, J. 1999. "The comparison of different control strategies for reducing vehicle vibration," German Aerospace Center, IB 131-99/41, pp.1-28
12. Ma, K.G., Gu, Z.Q., Peng F. J. and Chen X. 1997. "On experiments of adaptive control for structure vibration," Proc. of ASME 16th Biennial Conference on Mechanical Vibration and Noise & 1997 ASME Design Technical Conferences, paper number DETC97/VIB-3939, Sacramento, CA
13. Melcher, J. 1992. "Adaptive on-line system identification of aerospace structures using MX filters," IFAC symposium on aerospace control, pp.135-140
14. Melcher, J. 1994. "MX filter: A new tool for performance tests of adaptive structural systems," *Journal of Intelligent Material Systems and Structures,* 5, pp.854-861
15. Ma, K.G. and Melcher, J. 1999. "The eigen-parameter identification of structures using CMX-LMS algorithm," German Aerospace Center, IB 131-99/40, pp.1-23

RECENT PROGRESS ON THE DEVELOPMENT OF A SMART ROTOR SYSTEM

Inderjit Chopra

ABSTRACT

This paper reviews the status of smart structures technology development for application to rotorcraft systems. Though a large component of research is focused to the minimization of helicopter vibration, the methodology is equally applicable to other problems such as aeromechanical stability augmentation, handling qualities enhancement, stall alleviation, reduction of interior/exterior acoustic signatures, minimization of blade dynamic stresses and rotor head health monitoring. More than any other system, the structural, mechanical and aerodynamic complexity and the interdisciplinary nature of rotorcraft offer many opportunities for the application of smart structures technologies with the potential for substantial payoffs in system effectiveness. Primarily, two types of smart rotor concepts are under development: trailing-edge flaps actuated with smart actuators, and controllable twist blades with embedded piezoceramic actuators. For flap actuation, actuators range from piezo-bimorphs, piezo/electrostrictive stacks and piezo/magneto-strictive-induced composite-coupled actuation. Most smart actuators are moderate force and extremely small displacement devices and hence some form of mechanical amplification of induced displacement is needed to achieve desired flap deflections. Because of compactness and weight considerations, the stroke amplification of these devices has been a key barrier for application to rotor blades. Most of the current smart rotor models under development have adopted the Froude scaling, but future developments are tending towards the Mach-scale and full-scale designs. The state-of-art on modeling of actuators is improving rapidly. Shape memory alloys (SMA) show potential of providing large induced strains (up to 6%), but are limited to low frequency (less than 1 Hz) applications such as tab adjustment for rotor tracking. Also, it is quite difficult to achieve fine-tune actuation control with SMA. Data base of smart actuators' characteristics under different loads, frequency and temperature are non-existent. For in-flight tracking of rotor SMA-actuated tab, it is important to incorporate adaptive control strategy and a locking mechanism. Comprehensive rotor analyses covering smart materials actuators are in development at this time. This paper will identify key barriers for applications of smart structure technology to rotorcraft systems and point out the need for future research in this area. The research in the application of smart structures technology to rotorcraft systems is in its early phase and activities need to be expanded before this promising technology can be

Alfred Gessow Professor & Director, Alfred Gessow Rotorcraft Center,
Department of Aerospace Engineering, University of Maryland, College Park, MD 20742, USA

exploited in a competitive manner.

INTRODUCTION

Helicopters are susceptible to high vibratory loads, excessive noise levels, aeromechanical instabilities, poor flight stability characteristics, and high dynamic stresses. Compared to fixed-wing aircraft, helicopters suffer from high operating cost, poor ride quality, low fatigue life of structural components, inferior handling qualities and a restricted flight envelope. To reduce these problems to an acceptable level, numerous passive and active devices, and many ad hoc design fixes, are resorted to with resultant weight penalties and reduced payloads. The primary source for all these problems is the nonsteady and complex aerodynamic environment in which the rotor must operate and the complex coupled structural and mechanical system comprised by the rotor, body, transmission system and engine. To counter some of these deficiencies, and also to further expand the flight capabilities of military and civilian helicopters, many new design modifications and devices are being contemplated. These appear to show incremental and modest gains in terms of performance improvement and reduction in operating costs. If the objective is to achieve *'a jet smooth ride'* with helicopters at a comparable operating cost, for example, one has to try revolutionary ideas. One innovative idea that appears to show the potential for a significant gain in performance improvement at a small penalty is to apply the technology of smart structures to rotorcraft. For such an application, numerous light-weight sensors and actuators are embedded or surface-mounted at different stations on the blades, and optimal distributed forces applied with the help of modern control theory.

At this time, smart structures technology is in its early stage of development, and its applications to various physical systems are evolving to actively control vibration, noise, aeromechanical stability (damping), shape and stress distribution. This paper will review the state-of-the-art on the application of smart structures technology to rotor systems.

Smart Structures

A smart structure involves distributed actuators and sensors, and one or more microprocessors that analyze the responses from the sensors and use distributed-parameter control theory to command the actuators to induce localized strains/displacements to minimize response or loads at selected stations. A smart structure has the capability to respond to a changing external environment (such as loads and shape change) as well as to a changing internal environment (such as damage or failure). It incorporates actuators that allow the alteration of system characteristics (such as stiffness or damping) as well as of system response (such as strain or shape) in a controlled manner [1]. Many types of actuators and sensors are being considered, such as piezoelectric materials, shape memory alloys, electrostrictive materials, magnetostrictive materials, electro-rheological/magneto-rheological fluids and fiber optics. Typically, these can be integrated with main load-carrying structures by surface bonding or embedding without causing any significant changes in the structural stiffness of the system. Among these, piezoelectrics are the most common. They undergo strain (elongation) when an electric field is applied across them and produce voltage when strain is induced, and thus can be used both as actuators and sensors. These materials, however, generate very low strains but over a wide range of actuation frequency. The most

widely used piezoceramics (such as lead zirconate titanate: PZT) are in the form of thin sheets which can be readily embedded or attached to composite structures [2,3].

Among other materials, shape memory alloys (SMA) are gaining rapid recognition as actuators because of the possibility of achieving large excitation forces and displacements. These alloys undergo phase transformation at a specific temperature. When plastically deformed at a low temperature, these alloys recover to their original undeformed condition if the temperature is raised above the transformation temperature. This process is reversible. The most common SMA material is Nitinol (nickel titanium alloy) and is available in the form of wires of different diameters. Though heating can be carried out internally (electrically), response is very slow (about 1 Hz). The thermo-mechanical behavior of SMA depends upon the internal crystalline structure (phase), temperature, stress, strain rate, and history of the material. The material resides in the austenite phase at higher temperatures and the Young's modulus of SMA in this phase is much higher (3-5 times) than the modulus in the martensite phase (at low temperatures) [4,5].

Electrostrictive materials are similar to piezoelectric materials, with slightly better strain capability, but are very sensitive to temperature [6]. Magnetostrictive materials such as Terfenol-D elongate when exposed to a magnetic field. These materials generate low strains and moderate forces over a wide frequency range. Because of coil and magnetic return path, these actuators are often bulky [7]. Fiber optics are becoming popular as sensors because they can be easily embedded in composite structures with a negligible effect on the structural integrity and also have the potential of multi-plexing [8]. Piezoelectric and electrostrictive materials are also available in the form of 'stacks' where many layers of materials and electrodes are assembled together. These stacks generate large forces but small displacements, in the direction normal to the top and bottom surface [9]. Also, piezoceramics in form of bimorphs or bending actuators are available commercially where two layers of these materials are stacked with a thin shim (typically of brass) between them. If an electric field is applied such that one of the piezo layers expands while the other one contracts, a pure bending action results [10].

Potential Applications to Rotorcraft

The multidisciplinary nature of rotorcraft offers many opportunities for the applications of smart structures technologies with the potential for very substantial payoffs in system effectiveness. The rotor is the key subsystem, setting the current limits on vehicle performance, handling qualities and reliability. The flow field on the rotor disk is extremely complex and may involve transonic flow on the advancing blade tips, dynamic stall and reversed flow on the retreating side of the disk, highly yawed flows on the front and rear part of disk, and blade-vortex interactions. The primary source of helicopter vibration is the main rotor that transmits large vibratory forces and moments to the fuselage. For an N-bladed rotor, the N/rev, N-1/rev and N+1/rev vibratory blade loads (in rotating frame) are transmitted to the body through the hub as dominating N/rev vibratory forces and moments. In contrast to traditional passive devices, active vibration control is achieved through excitation of blade pitch at higher harmonics of the rotational speed, thereby canceling vibratory forces at their source. Blade feathering/twist on the order of 1 to 2 degrees is required to suppress vibrations. Higher Harmonic Control (HHC) systems incorporate excitation of the swashplate at N/rev with servo actuators, and have been widely investigated as a viable concept to suppress vibration through numerical simulations, rotor model tests in wind tunnels and in flight tests

[11-14]. Although this active system has been proven to be quite effective in reducing vibration and may incur a lower weight penalty (up to 1-2% of gross weight) than passive systems (weight penalty of 3%), a number of significant drawbacks exist. The power requirements of the servo-actuators needed to excite the swashplate become substantial at extreme flight conditions, where vibrations are likely to be highest. Also, excitation frequencies of conventional swashplates are restricted to multiples of N/rev. It is well known that other harmonics are important to minimize blade stresses and to improve rotor performance. The limitations of HHC have spurred research on Individual Blade Control (IBC) systems that control pitch of each blade independently with servo-actuators mounted in the rotating frame [15-17]. Although blades can be excited at any desired combination of frequencies, there is a mechanical complexity of hydraulic sliprings. Again, the weight penalty of this system may not be less than an HHC system. To overcome many of these problems associated with existing active control devices, there has been growing interest recently in the application of smart structures technology to rotor systems in order to reduce vibration and noise level as well as to improve rotor performance.

Because the rotor is a flexible structure, changes in shape, mechanical properties and stress/strain fields can be imposed upon it. These in turn will alter the vibratory modes, aeroelastic interactions, aerodynamic properties, and dynamic stresses of the rotor. Smart structures technologies will enable these imposed changes to be tailored to conditions sensed in the rotor itself. Furthermore, because the smart actuators and sensors can be distributed over each individual rotor blade, control can be imposed over a much larger bandwidth than with current swashplate-based controls, which are limited to N/rev for an N-bladed rotor. This opens up a hitherto unavailable domain for vibration control, aeromechanical stability augmentation, handling qualities enhancement, stall alleviation, and acoustic suppression. The use of smart structures also offers the prospect of in-flight tracking of main rotor blades and sensing structural damage in the rotor, drive-train and other critical components. The pilot can then be alerted to take suitable action. A further very promising application of smart structures is to actively control the interior noise of a rotorcraft [18]. Structure-borne noise can be minimized by actively controlling the response of airframe panels. A source of high frequency interior noise can be drive-train system (gearbox meshing tonal frequencies). Actively tuning transmission strut systems with smart actuators may minimize noise in cabin (high frequency noise cancellation) [19].

State of the Art

Recently, there has been an increase in smart structures research activities, covering a wide range of applications to aerospace, automotive, civil, marine, machine tools and medical fields. Much of the earlier work is focused on the application of piezoelectric technology to space related systems, such as the control of vibration of large space structures [20], and for stable bases for precision pointing in space (telescope, mirrors, etc., see Ref. [21]). Also, there are applications to the field of fixed-wing aircraft, such as controlling wing twist and camber for wing divergence and flutter suppression [22-27], increasing panel flutter boundary [28] and controlling structure-borne noise [29]. Recently, there have been growing research activities on the use of smart structures for rotorcraft applications to actively control vibration and external/internal noise, augment damping and improve rotor performance (see a special issue in *Smart Materials & Structures,* (February 1996) and review articles [30-31]).

Much of the work in this field has focused on building dynamically-scaled smart rotor models [30]. Two types of Froude-scale models have been built: controllable twist models incorporating embedded specially-shaped piezoelectric elements, and trailing-edge flap models actuated by piezoceramic and magnetostrictive actuators. These rotor models were tested in a vacuum chamber, on a hover stand and in a wind tunnel. For both types of models, the performance of the actuation systems degraded dramatically at higher rotational speeds because of higher dynamic pressure, centrifugal force and frictional moments. For trailing-edge flap models, one requires a compact torsional actuation technique and several approaches have been examined to drive the flap. These include piezoceramic elements, piezo-bimorphs, piezostacks and magnetostrictictive actuators in conjunction with either a mechanical amplification arrangement or twist-inducing tailored composite coupling. A mechanical leverage system incorporates moving hinges and often suffers from slippage and frictional moments at joints. On the other hand, tailored extension-twist or bending-twist composite coupling may eliminate moving hinges and also may be able to use the full length of the blade for housing, but often suffer from structural efficiency. For controllable twist models, banks of piezoceramic elements are embedded under the skin at ±45 deg relative to the blade span axis respectively on the top and bottom surfaces; an in-phase activation induces a pure twist in the blade. To induce a sufficient blade twist for active control of vibration or noise, a large number of distributed piezoceramic elements are required that incur a significant weight penalty and an increase in blade stiffness from its baseline value. This scheme affords actuation redundancy and involves no moving hinges, but imposes structural integrity issues. At this stage, even though both type of models have not achieved the desired level of flap deflection or blade twist, they show potential for further improvements.

Straub [32] carried out a feasibility study of using smart structures technology for primary as well as active control of a full-scale vehicle. For this study, the AH-64 helicopter was selected. It was concluded that the concept of twist and camber control using embedded actuators is not practical with the available smart materials. Servoflap control system using on-blade smart material actuators appeared conceptually feasible for primary and active controls [33]. There are other studies that discuss various applications of smart structures technology to rotorcraft systems [34], including collective pitch control with SMA actuation [35], dynamic stall delay with piezostack actuated leading-edge flaps [36, 37], damping augmentation with electro-rheological and magneto-rheological dampers [38], active transmission mounts with smart actuators to control vibration and noise [39], vibration minimization with active control of structural response (ACSR system) using distributed smart actuators in airframe [40] and active/passive constrained layer damping control of flexbeams [41].

So far there has been limited research towards the development of analytical tools for a smart rotor. Currently most methods are focused to predict the static and dynamic response of non-rotating anisotropic beams that too limited to bending and extension of beams using paired piezo-actuation (via identical actuators bonded to the top and bottom surfaces of the beam) [42, 43]. Continued research in this area is expanding these theories to include the coupled torsion/bending/extension of beams with single or multiple piezo elements not aligned along the beam axis and bonded on one or both surfaces of the beam [44, 45]. Recently, there has been some effort [46] to develop a coupled actuator-flap-rotor dynamic analysis, but it is far from a comprehensive smart rotor analysis.

The objective of this paper is to assess the status of smart structures technology developments for application to the rotor systems. Though a large part of this research is

focused on vibration minimization, these developments are equally applicable to other problems. In this paper four different topics are covered: trailing-edge flap concept, controllable blade twist concept, shape memory alloys actuation concept and analytical modeling of smart rotors.

TRAILING EDGE FLAPS

Trailing-Edge Flaps Actuated with Piezo Birmorphs

This section discusses the development of a scaled rotor model with piezo-bimorphs (piezo-benders) actuated trailing edge flaps. The flaps are located near the tip of the blade (Fig. 1). A piezo-bimorph is a bending actuator and consists of piezoceramic (PZT) sheets that are bonded on both sides of a very thin brass shim with an electrically conducting adhesive coating. When the bimorph is clamped at one end, and equal but opposite fields are applied to the PZT sheets, a pure bending of the bimorph occurs. The resulting small tip displacement of the bimorph is amplified using a mechanical leverage or flexure system to provide the actuation stroke for the flap (Figs. 2). The piezo-bimorph is a compact actuation device and generates a small actuation force.

References [46-52] present the development of a six foot diameter, two-bladed, 1/8-th Froude scale bearingless rotor (ITR-Boeing simulation) model with flaps actuated with piezo-benders. Blades were constructed out of rigid foam, covered with fiber-glass prepreg fabric, embedded with a spar made of unidirectional glass-epoxy prepreg. The spar was located near the quarter chord to carry blade centrifugal loads in rotation. To minimize the possibility of aeroelastic instability in rotation, the sectional center of gravity of blades was placed at the quarter-chord by adding tantalum weights near the leading edge. The blade used NACA0012 airfoil sections and was 3.0 inch in chord length. The trailing edge flap consisted of 4.38 inch length, 0.6 inch wide (20% chord) plain flap located at the trailing edge.

Samak [47] first demonstrated the feasibility of using piezo-bimorphs to actuate trailing edge flaps of a rotor model. Commercially available two-layered bimorphs (G-1195) were used to actuate the flaps. The trailing edge flap was actuated by three 1.5 inch long, 1.0 inch wide and .021 inch thick piezoelectric bender elements. These bimorph elements were rigidly anchored to the blade spar so that they formed 1.0 inch long cantilever beams. When actuated, these bimorphs bend upward or downward depending on the applied voltage field and produce force when they are restrained at the tip. The bender elements were connected to the flap through a common hinge. A system of mechanical hinges and linkages were used to amplify the bending of the elements at the tip to cause larger flap rotation (Fig. 2). This flap rotation was measured using a Hall Effect sensor with the flux-inducing permanent magnet mounted along the flap hinge line, which rotates with the flap. A two-bladed rotor model was tested on the hover stand. There was enough oscillatory flap amplitude (±7 deg) in a non-rotating condition, but the amplitude precipitously decreased with higher RPM. At the scaled operating speed of 900 RPM, maximum flap amplitude of ±1 deg was achieved. This fell far short of the targeted amplitude of about ±6 deg at N/rev (where N is number of blades) to suppress vibration completely.

Efforts were then focused to increase oscillatory flap deflection at the operating rotational speed. A major drawback of a two-layered piezo-bimorphs was its inability to generate a high actuation force. To actuate a flap in a rotating environment, sufficient actuation force is needed to overcome aerodynamic, centrifugal and frictional hinge moment. Walz [10]

formulated a simple rotor analysis using quasisteady aerodynamics and carried out parametric studies to match the flap moment requirements with the capability of actuators. It was shown that the actuation force of a two-layered bimorph is not sufficient to generate the required flap authority. Four-layered bimorph actuators were built in-house in order to increase their actuation force. Also, modifications to the mechanical leverage arrangement between actuators and flap were incorporated including a rod-cusp arrangement (Fig. 2). In spite of several modifications and improvements to the flap actuation system, the desired increase in flap performance was not realized. Ben-Zeev [48] built new rotor blades with several modifications to actuation system and tested them in the 10 ft diameter vacuum chamber to isolate the effects of centrifugal loading on the actuator-flap performance. A beam model of the piezo bimorph including propeller moment effect (due to rotation) was formulated. The cause of the reduced flap deflections at a higher rotation speed was attributed to the frictional force at the flap hinge. The introduction of a thrust bearing was found to dramatically improve flap performance at higher rotational speeds (±5 deg at 800 RPM in the vacuum chamber and ±2 deg at 750 RPM on the hover stand). Again, on the hover stand, there was a severe degradation of flap performance at the operating speed (900 RPM).

Koratkar [49] developed an improved analytical model of the coupled bimorph-flap dynamics including time-domain unsteady aerodynamics (Hariharan-Leishman [50]), and centrifugal, inertial and frictional forces. The linkage arm length associated with mechanical amplification mechanism was selected in order to maximize flap performance in the rotating environment. Through systematic testing of a 2-bladed rotor model in the vacuum chamber, the slippage of the bimorph under high centrifugal loads was discovered to be the culprit for performance degradation at high rotational speeds. An improved clamping of bimorph actuator (Fig. 3) showed a dramatic improvement of flap performance. In hover, flap deflections of ±4 to ±8 degrees were achieved for 1/rev to 5/rev excitation at 900 RPM (Figs. 4 and 5). This flap activation resulted in a 10% variation of steady rotor thrust at a collective pitch of 6 degrees. Systematic validation of analytical model was carried out using test data from a series of bench tests, vacuum chamber tests, and hover tests. Using this analysis, a feasibility study of a Mach-scaled rotor model with piezo-bimorph actuated flaps was carried out. Also, it was shown that a higher voltage can be applied in the polarization direction than that against this direction thereby extending the peak-to-peak excitation field. This study showed that flap deflections of ±6 degrees at 4/rev excitation could be obtained at the Mach-scaled operating speed of 2150 RPM using a 8-layer tapered piezo-bimorph in conjunction with a bias voltage (unequal voltage to top and bottom sheets) (Figs. 6-8).

Subsequently, a four-blade Mach scaled rotor model of diameter 6 feet with piezoelectric bender actuated flap was built [46, 51] (Fig. 9). From analysis, it became quite clear that an 8-layered tapered actuator with a bias voltage is needed to obtain the desired actuation authority. This model was designed for Mach scaled hub of Bell-412 model. Model rotor test in the vacuum chamber showed a marked degradation of performance at 2000 RPM. A maximum flap deflection of ±3.2 degree was achieved at 95 Vrms with 3:1 AC bias at 10 Hz; less than half of the predicted value (Fig. 10). This degradation was traced to frictional force at the blade-flap interface. Subsequently, a micro-thrust bearing was specially mounted on the flap shaft to reduce this frictional force and it resulted in flap deflections of over ±8 degrees at 2000 RPM in the vacuum chamber. This model was tested on hover stand (Fig. 11) and it achieved ±6 to ±10 degree flap deflections at a RPM of 1850 and an over 10% oscillatory thrust (Fig. 12).

A 4-bladed Mach-scaled rotor model was tested in the Glenn L. Martin wind tunnel using the Bell-412 hub in both open- and closed-loop studies [52] (Fig. 13). In open-loop tests, flap deflections of ±4 to ±5 degrees were achieved at 1800 RPM over a wide range of advance ratios and collective settings. Preliminary closed loop tests conducted using a neural-network based adaptive controller demonstrated the control authority of actuation system by minimizing the 4/rev vertical hub shear by 40% with one activated flap. In another test, a large 1/rev flapwise bending moment near the blade root was actively minimized by 90%. It is planned to expand the close-loop tests in the wind tunnel.

Spnagler and Hall [53] and Prechtl and Hall [54] built wing models with piezobimorph-driven flaps respectively incorporating mechanical hinges and flexural amplification mechanisms. It was shown that the efficiency of the bimorph actuator could be improved by tapering its thickness with length, and the frictional losses at hinges and backlash could be minimized through the use of a flexural amplification mechanism. Flap deflections of 11.5 degrees were demonstrated in a non-rotating environment. Fulton and Ormiston [55] built a 7.5 ft diameter two-bladed Froude-scaled rotor model with a plane trailing-edge flap actuated with piezo-bimorphs and tested on hover stand. A maximum of ±5 deg. of flap deflection at 760 RPM was achieved. Subsequently, this rotor model was tested in the wind tunnel to investigate the effectiveness of on-blade elevon control to reduce vibratory loads [56]. The open loop tests successfully demonstrated the effectiveness of flaps to minimize 3, 4, and 5/rev blade vibratory bending moments at representative advance ratios.

Normally, plane trailing-edge flaps are integrated into the blade profile and often characterized as "lift flaps." For these, oscillatory flap generates primarily oscillatory lift on the section along with a small component of oscillatory moment. On the other hand, servo flaps are auxiliary airfoil sections, located outside of main blade profile and are often characterized as "moment flaps." It is perceived that an oscillatory motion of flap generates primarily oscillatory moment. Koratkar [51] carried out a study to investigate the effectiveness of these two types of flaps. It was found that twist generated due to the moment action of plain trailing-edge flap was substantial (.2 deg at 1/rev to .65 at 4/rev) and hence should be included to check flap effectiveness. Fulton and Ormiston [55] showed that at a high dynamic pressure, this moment action could cause control reversal.

To build a full-scale rotor using this concept, a design study was conducted to achieve a trailing-edge flap deflection of ±4 degrees. Fig. 14 shows actuator size for three different rotor scales. This shows that it is possible to build a full-scale system using a 40-layered bimorph, but at a considerable weight penalty. Overall, the concept appears suited for scaled rotor models and especially to check the effectiveness of adaptive control strategies to minimize vibration with trailing-edge flaps.

Trailing Edge Flap Actuated with Piezo Stacks

In a piezo stack actuator, a large number of thin piezoceramic sheets are bonded together by means of conducting adhesives (Fig. 15). Voltage is applied through electrodes attached lengthwise on opposite sides of stack. The displacement of the device in the direction normal to its plane is given as:

$$\delta = n\, d_{33}\, v \tag{1}$$

where δ is displacement, n is number of piezo sheets, V is applied voltage and d_{33} is piezoelectric constant. The value of d_{33} is positive and is normally about 2 to 3 times of the value of d_{31} (peizo constant to define strain in the plane of sheet). With an electric field, each sheet expands in the thickness direction thus causing stack elongation. Bond layer thickness between sheets reduces the effective deflection. It is important to note that for a given piezoceramic material, a higher value of transverse displacement (stroke) can be obtained by using a large number of piezoceramic sheets and by reducing the bond thickness.

Piezoceramic stack actuators are high force and low displacement devices and it is possible to trade force for displacement by mechanical means. Samak [6] explored this possibility of using piezostack actuator with mechanical leverage amplification (Fig. 16) to actuate a 'flaperon' consisting of a small movable surface hinged at 10% chord of wing model with a span and chord of 12 inch. The objective of this flaperon was to improve stall characteristics of the airfoil by energizing the flow near its leading edge. The free displacement of the chosen piezostack was 0.72 mil at 150 volts. A mechanical amplification of 25 was used. However, because of mechanical losses and slippage at knife edges, the free displacement of the device was found to be 5 mils as compared to the calculated value of 18 mils. Samak [6] also built a leading-edge droop actuation using an electrostictive stack actuator in conjunction with mechanical amplification. Again, like piezo-stack actuation, this device could not achieve the desired amplification of stroke. It was quite clear that the amplification system needed to be refined before the potential of these devices could be realized in full-scale applications.

Spencer [52] employed two piezostacks and L-arm amplification (Fig. 17) to actuate a trailing edge flap in a wing model of chord 8 inch and span 10 inch. A single plane flap of chord 1.6 inch and span 4 inch was built. Two piezostacks bonded together back to back yielded a free displacement of 1.5 mils which was amplified 10 times. The measured value of free displacement was 11 mils as against the calculated value of 15 mils. Thus the mechanical losses in this device were less dominant. The linear motion of the actuator was converted to rotary motion for flap actuation using a hinge offset mechanism. This wing model was tested in an open-jet tunnel, and the performance of the flap degraded at high dynamic pressures. No-velocity flap amplitude of ± 3.5 degree was reduced to ± 1.5 degree at a forward speed of 118 ft/sec. Even though the measured values of flap deflections at high dynamic pressures were less than one-half of the predicted values, this showed the room for improvement of the amplification system.

Chandra[58] improved the actuation system of the trailing-edge flap in a wing model using a high performance piezo-stack actuator with integrated mechanical amplification (flexure and no hinges, Fig. 18). The composite wing model was of 8 inch in chord and 16 inch in span (Fig. 19). Measured free displacement and block force of this actuator were respectively 28 mils and 16 lbs at 1000 volts excitation. The flap deflection was measured using a Hall effect sensor, and a maximum of 6.5 degrees of free flap deflection was achieved. As predicted, a 30% reduction of flap deflection at a free stream velocity of 95 ft/sec in an open-jet wind tunnel was noticed (Fig. 20). Angle of attack of 10 degree did not change flap deflection. To simulate the full-scale aerodynamic forces for a typical rotor blade, the performance of several commercially available actuators was examined for flap actuation. The calculated results show the feasibility of a full-scale flap actuated with a piezo-stack actuator to minimize vibration (Fig. 21).

Lee [9,59] carried out systematic testing of eleven different piezostack actuators to evaluate their characteristics that include maximum free strain, maximum block force, elastic

TABLE I. COMPARATIVE TEST EVALUATION OF COMMERCIALLY AVAILABLE PIEZOSTACK ACTUATORS

Part/material No.	Operating voltage V	Maximum Strain *μ-strain*	Block force (BF) *lbs.*	Normalized Block force ksi	Strain-force index	Energy Density *ft-lb/slug*
MM 8M (70018)	360	254	128	1.05	0.133	1.27
MM 5H (70023-1)	200	449	101	0.83	0.180	1.80
MM 4S (70023-2)	360	497	143	1.17	0.291	2.78
PI P-804.10	100	1035	1133	7.31	3.783	36.72
PI PAH-018.102	1000	1358	1505	9.71	6.593	62.95
XI RE0410L	100	468	95	5.16	1.207	11.52
XI PZ0410L	100	910	70	3.58	1.629	15.55
EDO 100P-1 (98)	800	838	154	2.00	0.838	8.00
EDO 100P-1 (69)	800	472	50	0.66	0.156	1.49
SU 15C (H5D)	150	940	266	7.48	3.516	33.57
SU 15C (5D)	150	1110	274	7.70	4.274	40.80

modulus, operating voltage and shape/compactness. Tests were carried out first with static excitation and preload (0-10 ksi) and then followed by dynamic excitation. Because the piezostacks were different in shape and size, a strain-force index consisting of a product of free strain and normalized block force as well as an energy density index were used for comparison. Based on these indexes, two actuators respectively built by two different companies showed superior static performance (Table I). Further dynamic tests showed that the first category of stacks resulted in constant actuation envelope for all ranges of preloads while the second category stacks tended to increase envelope with preloads. The first category stacks with higher stiffness as well as dynamic characteristics were selected. Using five of these stack actuators, a double-lever (L-L) amplification device was built to actuate a full-scale trailing-edge flap (Fig. 23) [59-60]. The design goal was to obtain flap deflection of $\pm 5^{o}$ at the nominal speed for the Boeing MD-900 Explorer helicopter. A model wing section of chord 12" and span 12" and with a flap of span of 4" and chord 3" was built (Fig. 24). The first prototype of the amplification device was tested in the vacuum chamber and an amplification factor of about 19 was achieved for a 600g of centrifugal loading. Further design refinements were introduced to build the second version of this actuator that achieved a peak actuation force of 18 lbs and a stroke of 43 mils for a 710g of centrifugal loading in the vacuum chamber (Fig. 25). For the spin test, a coil spring was mounted at the outer lever to simulate aerodynamic loading. At 1000 RPM, no major degradation in peak-to-peak output displacement was observed for up to 6/rev excitation. Subsequently, this model was tested systematically in the open-jet wind tunnel to check its performance under different aerodynamic loading. The flap was actuated using a push rod arrangement and it achieved peak-to-peak flap deflections of 4 to 20 deg. depending on excitation frequency at a speed of 120 ft/sec (Fig. 26) [61]. One drawback of this actuator was its single directional actuation. Restoring spring was used to make it bi-directional, but it degraded at high dynamic forces. As a result of it, a bi-directional actuator with L-L amplification mechanism is being built. This concept consists of two unidirectional L-L amplification mechanisms in a parallel arrangement that can offer high force and high displacement capability without compromising its compactness.

Straub et al [62-65] are developing a stack-actuated trailing-edge flap for the MD-900 Explorer rotor system (5-bladed, 34 ft bearingless rotor) to actively control its vibration, noise and aerodynamic performance. Based on the energy output (stroke and force) for a prescribed

volume, the piezo-ceramic/lead magnesium niobate stack was initially selected (low-voltage, co-fired PMN:PZ stack developed by Xinetics). The required large deflection is accomplished using a bi-axial arrangement of two long stack columns operating in push-pull mode in conjunction with L-shaped lever and flexural mount [Fig. 27]. The flap length is 18% radius and it is centered at the 87% radial position. A detailed design was carried out to meet the severe operating environment (665g steady load, 90g oscillatory, -60 to 160°F). The flap was expected to undergo ± 4 deg at 40 Hz with an actuation force of 112 lbs. The stack actuator however did not realize the projected potential. Flap sizing and aerodynamic optimization to minimize actuation power were discussed in Ref [64]. Recently, a series of enhancements were made to the design of the actuation system including high energy density piezostacks [65]. The performance of this bi-axial actuator was demonstrated through testing in a spin chamber under 814g steady and 29g vibratory loading. Selected configuration consisted of a 25% flap chord, a span of 18% radius and an aerodynamic balance of 40%. Prechtl and Hall [66] designed a discrete trailing edge servo-flap actuator called X-frame actuator [Fig. 28] and tested the prototype (150% of model scale) on the bench top test. The actuator consists of two active piezostacks and two criss-cross frames and amplification is achieved via shallow angle arrangement. The X-frame achieves a higher mass efficiency but requires larger frame dimensions than that of lever amplification mechanism. A 1/6th Mach scale rotor model of CH-47D (Chinook) incorporating a trailing-edge flap actuated by X-frame actuators was built and tested on a hover stand [66]. This flap extends aft of the main blade chord. At the operating speed (tip Mach .63) and collective pitch of 8 deg., oscillatory flap deflections of ±2.4 deg. were achieved with an excitation of ±1 KV. The X-frame actuator has been selected for the MD900 Explorer active flap of a full-scale system. To obtain bi-directional functionality, dual X-frame actuators are being built. The proposed flap has 18% span, 25% chord and 40% hinge offset and is located at 83% radial position. The full-scale rotor system with trailing-edge flap actuated with X-frame actuators is under fabrication and is planned for testing on the whirl tower, followed by testing in the 40x80 ft wind tunnel at NASA Ames and finally by flight testing. Janker and et al [36, 68-69] developed a piezostack-based actuator for trailing-edge flap. Amplification device consists of a shallow angle flexure mechanism that is wrapped around the stacks. The performance of this actuator was demonstrated through testing of wing-section in the wind tunnel. It is estimated that an actuator with block force of 2000 N and free displacement of 1mm will be adequate to achieve a target flap deflection of ±8 deg. for an EC-135 helicopter. It planned to investigate this actuator on a rotor model in the wind tunnel.

Shaner [37, 70] carried out design and development of piezostacks-actuated leading-edge flap. Stroke amplification was achieved through a single lever. Bench-top tests were performed to evaluate its performance. Even though the current prototype did not achieve the desired stroke output, potential problems were identified and future testing of wing section in the wind tunnel is planned. Janker and et al [36] also examining peizostack-based actuator for leading-edge droop control for delaying dynamic stall.

Overall, the actuation of flaps with piezostacks appears feasible for full-scale applications. Even though it may not be cost effective to apply this actuation mechanism to minimize vibration and exterior noise with currently available smart materials technology, but there is an enormous potential with future large stroke actuators.

Trailing Edge Flap Actuated with Magnetostrictive Actuators and Extension-Torsion Coupled Composite Tube

For a full-scale trailing edge flap system, the force requirement of actuators becomes substantial. At the same time, the blade can also accommodate larger size actuators. An alternate concept of using extension-torsion coupled composite tube in conjunction with magnetostrictive actuator was investigated to cause twisting of the trailing edge flap [7]. Figure 29 shows a schematic of this concept. The extension-torsion composite coupled tube was subjected to an axial force generated by a magnetostrictive actuator that induces twisting of the tube. An extension-torsion composite beam was built by wrapping angle plies resulting in an anti-symmetric ply lay-up with respect to the beam axis.

A thin-walled beam analysis developed in Ref. [71] was specialized to predict the induced twist of an extension-torsion coupled composite cylindrical tube due to axial force. The essence of this analysis is that two-dimensional stress and displacement fields associated with any local plate segment of the tube are reduced to the global one-dimensional beam displacements and forces (Vlasov theory). Non-classical effects such as cross-section warping, transverse shear and warping restraint at edges were included. The objective was to determine the design of the composite tube that best utilizes the prescribed force and displacement characteristics of the magnetostrictive actuator to generate maximum torsional motion. To understand the influence of ply lay-up, number of plies and tube diameter on the induced twist, extensive parametric studies were carried out. Three different composite materials, graphite-epoxy, kevlar-epoxy, and glass-epoxy were examined. Figure 30 shows that for a prescribed axial force, the maximum induced twist occurs for kevlar-epoxy tube with a ply angle of approximately 30 deg. Then an optimization study was carried out to calculate the best tube design keeping in view first ply failure and buckling instability.

The magnetostrictive actuator was selected because of its large actuation force as compared to electrostrictive and piezoelectric stacks. For the present study, a commercial available magnetostrictive actuator (100/6-MP Etrema) was chosen. In order to utilize the extension-torsion coupling characteristics of the composite tube, the magnetostrictive actuator must be attached to the tube in such a way that both twist and axial strain is permitted freely. Figure 31 shows the schematic of the tube and actuator assembly. A series of tests were performed to check the performance of this torsional actuation device for different loading.

To validate the analysis, extension-twist kevlar-epoxy tubes of different ply lay-ups were fabricated using an autoclave molding technique. These tubes were first tested under static mechanical loads and then tested under manetostrictive actuation. Tip twist was measured using a laser optical system. The $[11]_2$ tube generated the maximum twist of 0.2 degree and there was a good correlation between measured and predicted twist values (Fig. 32). Also, alternate actuator concepts for these tubes, specifically piezoelectric and electrostrictive stacks, were examined. A piezoelectric stack was found to induce much larger force and twist (approximately 3 times that created by magnetostrictive actuator system). It was shown that ten $[11]_4$ kevlar-epoxy tube/piezoelectric stack systems of 20 inch length in series would generate approximately ± 5.2 degrees of flap deflection. Such a system can be implemented in a full-scale rotor to actively control vibration.

Because of poor overall structural efficiency of extension-twist coupled tubes, this type of actuation system appears less meritorious than other actuation systems.

Trailing Edge Flaps Actuated with Piezoceramic Actuators and Tailored Bending-Torsion Coupled Composite Beam

This section presents the development of a dynamically scaled rotor model with torsional actuation via a piezo-induced bending-torsion coupled composite. A novel spanwise variation in ply lay-up of the beam and phasing of surface-mounted piezoceramic actuators is used to convert the bending-torsion coupled beam into a pure twist actuator [72-76]. This twist actuator is used to actuate either a trailing edge flap (Fig. 33) or an all-movable blade tip or induced blade twist (Fig. 34). The beam is divided into a number of spanwise segments with reversed bending-torsion couplings for each successive segment. Over each beam segment, identical piezoceramic actuators are bonded on the top and bottom surfaces resulting in an equivalent bimorph unit (Fig. 35). Again, the polarity is reversed for successive piezo elements. This composite beam is located spanwise within the blade profile at about quarter-chord. The beam is clamped in an anchor at the root of the blade and has a radial bearing at the outboard end. An excitation generates a sinusoidal spanwise bending where as the induced twist is additive in the spanwise direction (Fig. 36).

For the trailing edge flap configuration, the flap is an integral element of the outboard end of the beam (Fig. 33). As the tip of the beam twists relative to the root end (cantilevered), the flap rotates too. For movable tip configuration, the blade tip segment is attached to the outboard end of the beam via a rigid adapter and a radial bearing (Fig. 34). As the tip of the beam twists, the blade tip is torsionally deflected. For the induced blade twist configuration, the outboard end of the beam is locked to the end-rib of the blade. Thus, as the tip of the composite beam twists, it will induce twist in the entire blade.

A two-bladed rotor model (dia 6ft) was tested on the hover stand using a bearingless rotor rig to evaluate the performance of this actuation system at various rotational speeds and collective settings. The actuation mechanism was excited at various frequencies and RMS voltages. First, the trailing-edge flap concept (span 3% radius and chord 20%) located at 90% radial position was tested systematically. In Fig. 37, the flap deflection is plotted vs. rotor speed for different excitation voltages. The excitation frequency is set at 40 Hz and collective is zero. As shown, the flap deflection does not decrease with rotational speed. Because of a large actuation force, the flap deflection stays constant with rotational speed. It was also shown that the effect of collective setting on flap deflection was negligible. The peak-to-peak flap deflection of 4 degrees was obtained at the operating speed of 900 RPM. From the results, it is quite clear that a larger flap can be driven with this bending-torsion device.

To follow on, two movable-tip rotor models respectively with 5% and 10% tip span were manufactured and tested systematically in a two-bladed configuration. Initially, the controllable twist configuration was tested on the hover stand at various excitation frequencies and collective settings. A non-rotating blade tip amplitude of .65 degree at 75 Hz was reduced to .5 degree at a RPM of 875 (Fig. 38). Then, hover testing was carried out on movable-tip configurations. At a RPM of 875 and a collective pitch of 8 degree, oscillatory tip pitch amplitudes of about ±2 degree were obtained at 2, 3, 4, 5/rev excitation with a corresponding dynamic thrust of about 7.5% of steady value [73]. Subsequently, a coupled actuator and elastic blade aeroelastic analysis was developed to predict the performance of an active-tip rotor [74]. The hover test data obtained from the Froude-scale rotor model were used to validate analysis. Predictions of active blade pitch deflections and vertical root shear were within 20% of measured values.

Subsequently, a 4-bladed Mach-scale rotor model with 10% tip was built for testing at an RPM of about 2000 in hover using Bell 412 hub [75, 76] (Fig. 39). For an actuation of 125 V_{rms}, the measured blade tip deflection at the first four harmonics was between ±1.2 and ±1.6 deg (Fig. 40). At 2000 RPM and 5/rev excitation, a large tip response is due to resonance amplification. Again, there was no degradation of tip response with rotor speed and aerodynamic thrust authority was in the range of 10% to 30%. The performance of blade tip deteriorated at high collective pitch because of locking of shaft in the bearing. Redesign of blade tip shaft assembly was suggested for future improvement of this concept. In a parallel study, active tip rotor was re-configured to test it in an active twist mode. The blade tips were taped down to prevent relative twisting between the tip and main blade section and actuation of beam resulted in twisting of complete blade. Even though the rotor was not designed for active twist mode, a significant tip twist was observed; 0.78 deg in non-rotating condition to 0.83 deg at 2000 RPM. Closed-loop tests were conducted using a neural-network based adaptive controller to minimize background vibratory blade loads [76]. The algorithm used a combined Kalman filter and a single hidden layer neural network to learn the system dynamics and minimize the desired vibration objective function online in real time. A large 1/rev vertical hub load as a result of blade dissimilarity was minimized by 90% using this controller. In another test, the controller was asked to minimize the simulated vibratory root flap bending and rotor thrust (target amplitudes) and it successfully minimized these by 80 to 95%.

Analyses and tests so far have demonstrated the feasibility of such a solid state torsional actuation device for active control of vibration and acoustics. It will be important to develop a comprehensive coupled rotor analysis including modeling smart actuator, validate it with measured test data and then carry out parametric studies to investigate the potential of this concept for a full-scale system. This innovative concept shows potential for control of vibration and noise for a full-scale system especially as a partial reduction auxiliary device.

CONTROLLABLE TWIST BLADE WITH EMBEDDED PIEZOCERAMIC ACTUATORS

This section presents the development of a dynamically scaled rotor model where blade twist is controlled using distributed embedded piezoceramic actuators [77-81]. Specially-cut piezoelectric actuators are attached under the skin at an orientation so that a pure twisting of blade occurs when the same potential is applied to both top and bottom actuators.

The smart rotor model was built with a six-foot diameter, 1/8-th Froude scale, four-bladed bearingless rotor (Boeing-ITR). The blade was constructed by laminating 10 mil pre-preg fiberglass cloth plies around a foam core, which was cured in a NACA 0012 airfoil mold (Fig. 41). The overall blade length was 26.58 inches from tip to root and the chord was 3.0 inches.

Structural integrity was achieved through a mahogany wood root section and a continuous longitudinal 10 mil fiberglass spar with ply angles of [0/90] degrees, which was embedded at the quarter chord location. Bringing the airfoil section center of gravity at quarter-chord by placing tantalum weights near the leading edge reduced inertial coupling between the flap and pitch modes. To activate blade motion independently in bending and torsion and to sense blade deformations, specially shaped 11.5 mil thick for single-layer piezoceramic actuators, and 23 mil for dual-layer actuators, were embedded under the fiberglass skin in banks of five discrete elements at angles of ±45 degree respectively on the top and bottom surfaces of the blade. Wires extend from each bank to the root of the blade, allowing for independent actuation of each bank. The piezoceramic actuators (PZT-5H, Morgan-Matroc) used for this

study were cut to dimensions of 2.0 inches in length and 0.25 inch in width to minimize transverse actuation. The dual-layer actuators were manufactured by bonding two single-layer actuators using a high temperature cyanoacrylate (CA) adhesive. Total number of actuators per blade range from 24 (single-layer, 1.5 inch apart) to 120 (dual-layer, .75 inch apart). A twist distribution along the blade span was achieved through an in-phase excitation of the top and bottom actuators at equal potentials, while a pure bending distribution is achieved through an out-of-phase excitation.

The structural properties of the piezoceramic blade were experimentally determined by measuring the spanwise bending and twist distributions along the blade. A laser beam was reflected off mirrors mounted at the elastic axis along the span of the blade and several tip loading were used to determine average values for the structural stiffness. The measured flapwise and chordwise bending stiffness were within 25% of target values, whereas the measured torsional stiffness was over 40% of the desired Froude-scale value for some blade configurations. Keeping in view the complexity of the fabrication process, the overall range of variation of stiffness was within an acceptable level. Generally, a close spacing of actuators increased the stiffness.

To assess the effect of bond thickness on actuator performance, simple blade specimens were built and tested under a static field [79]. The bond thickness was varied from 0.0025 inch (close to perfect bond condition) to 0.02 inch (not too abnormal) and the orientation of actuators was varied from 0° (aligned with beam axis) to 65°. Also, uniform strain beam theory for embedded skewed actuators including effect of bond layer was developed and compared with test data. The effect of reducing the bond thickness can be seen in Fig. 42. The maximal torsional and bending deflections increased by 60 and 90% respectively when the bond thickness was reduced from 0.020 to 0.0025 inch. A minimal bond layer thickness results in the most efficient shear transfer, which in turn results in maximum torsional and bending response. An optimum blade twist actuation will result for perfectly bonded actuators oriented at skew angles of ±45 degrees.

The effect of spacing between actuators was investigated by a series of blade test specimens with spacing ranging from 0.1 inch to 2.0 inch [79]. Test results showed that increasing the actuator spacing reduced the structural stiffness of the blades, as well as the nonlinear interference effects. A simple block force beam model was formulated for two overlapping skewed actuators and satisfactorily validated with test data. The nonlinear interference effect was observed to have reduced the twist by up to 38% when the spacing was reduced from 1.5 to 0.1 inch. If the overlapping between two adjacent actuators is reduced to zero, the interference effect is non-existent.

To assess the effectiveness of the embedded actuators in the rotating environment, the blades were tested first, in a two-bladed bearingless rotor configuration on a hover tower, and later on as a four-bladed configuration in the Glenn L. Martin wind tunnel [80]. Single and dual-layer rotor configurations were tested for varying electric field for different excitation frequency and tip twist was measured using two micro-accelerometers placed at the blade tip. Tip twist of the order of .4 degree at 4/rev was obtained in both hover and forward flight (μ=0.33) (Figs. 43). The change in oscillatory thrust, torque, pitching moment and rolling moment were measured using a rotating frame balance (Fig. 44). A maximum increase in oscillatory rotor thrust, torque, pitching moment and rolling moment (as percentage of nominal steady-state values) of 11, 13, 6 and 10%, respectively was measured for the dual-actuator configuration.

Although the oscillatory twist amplitudes attained in the forward flight experiments were less than the target value (1-2 degree of tip twist for complete vibration suppression), it showed the potential for partial vibration suppression. A feasibility study was carried out to apply this methodology on a typical full-scale rotor system (UH-60) to minimize vibration. Using today's commercially-available actuators, it is possible to build a full-scale controllable-twist blade with embedded multi-layered piezoceramic actuators that can completely suppress vibration, but at a considerable weight penalty (16% of blade weight) [81]. However, this scheme of actuation shows potential for a partial active control of vibration and acoustics.

Hagood et al [82-85] built a controllable-twist blade by embedding distributed piezoelectric fibers in a composite blade (Fig. 45). By laying piezo fibers at ±45° to the blade axis, and actuating the piezo material along the fiber direction using an interdigitated electrode pattern, it induces blade twist. The actuation of the active fiber composites induces shear stresses in the spar, resulting in a linear twist along the length of the spar. Using this active fiber composite (AFC), a 1/6th Mach-scaled rotor model of the Chinook CH-47D was constructed with a weight penalty of 20% of blade weight to cause a ±2° of blade tip twist. A high excitation voltage of 1.7 KV is needed to achieve desired twist. The model was tested on their hover stand and a maximum of tip twist of .4° was achieved [85]. Low tip twist was attributed to actuator electrical failures and manufacturing defects. However, it demonstrated the feasibility of this concept for a Mach scale rotor system. Again, this technology shows potential for full-scale applications provided compact high-voltage slipring is developed and structural integrity of a blade with fibers is improved.

SHAPE MEMORY ALLOY ACTUATORS

Shape memory alloys (SMA) such as Nitinols can undergo large plastic deformation via extension, bending or twisting at room temperature and then recover the deformation (i.e., recover to original shape) upon heat activation. Large strains, on the order of 6% can be recovered with a moderate increase in temperature (say to 120°F). Mechanically restrained SMA wires can develop large tensile recovery force due to the shape memory effect. Also, there is a dramatic increase in modulus of elasticity of SMA at a high temperature. These characteristics can be exploited in different applications. Even though SMA actuators can result in high strains and high forces, frequency range is very small (less than 1 Hz) that restricts these actuators to mostly static applications.

There are four transition temperatures associated with SMA materials [4]. These are martensite start, M_S, martensite finish, M_f, austenite start, A_S, and austenite finish, A_f temperatures. In the heating cycle, for temperature below A_S, the material is in the 100% martensite phase, where as for temperatures above A_f, the material is in 100% austenite phase. In the cooling cycle, for temperatures above M_S, the material is in 100% austenite phase, where as for temperature below M_f, the material is in 100% martensite phase. At any other temperature, the SMA's is in mixed phase, partly matensite and partly austenite. The state of SMA is characterized by the volume fraction of the martensite phase ξ that depends on temperature, stress and initial state of material.

Using shape memory effects, there is the potential of designing a variable speed rotor, trailing-edge tab adjustment for in-flight tracking of the main rotor, supercritical tail-rotor shaft and collective pitch control system (without swashplate). To accomplish these goals,

understanding of constitutive models of SMA and development of analysis and fabrication of thin-walled composite beams with embedded SMA wires is important.

Even though several constitutive models of SMA are developed to characterize its thermo-mechanical behavior, these are not validated systematically for different load conditions. These models are based on thermomechanics, or a combination of thermo-mechanics and SMA phenomenology, and/or statistical mechanics. One of the earliest models was developed by Tanake [86] that is based on thermo-mechanics. In this model, the second law of thermodynamics is written in terms of the Helmholtz free energy. This model assumes that stress (σ), strain (ε), temperature (T) and the martensite volume fraction (ξ) are the only state variables needed to characterize shape memory alloys. The stress consists of three parts, the mechanical stress, the thermoelastic stress, and the stress due to phase transformation. The constitution equation is as follows:

$$(\sigma - \sigma_o) = E(\xi)(\varepsilon - \varepsilon_o) + \Theta(T - T_o) + \Omega(\xi)(\xi - \xi_o) \tag{2}$$

where subscript 'o' represents the initial condition of SMA. Note that the Young's modulus (E) and the phase transformation coefficient (Ω) are function of the martensite volume fraction. Tanake used an exponential expression to describe the martensite volume fraction in terms of temperature and stress. Liang and Rogers [87] developed a constitutive model similar to Tanaka's model, except that they used a cosine function to represent the matensite volume fraction. Brinson [88] modified these two models by dividing the matensite volume fraction into two parts, stress-induced martensite and temperature-induced martensite. Also, the coefficients of the constitutive model are assumed to be non-linear and are resolved about the initial matensite state. Boyd and Lagoudas [89] utilized the Gibbs free energy instead of the Helmholtz free energy to obtain the constitutive model. The martensite volume fraction is derived from the dissipation potential, and by satisfying the second law of thermodynamics.

The stress-strain curve for an SMA consists of three regions: (1) elastic region where no transformation occurs, (2) transformation region where stress-induced matensite forms, and (3) yield region where permanent deformations occur (Fig. 46). The material constitutive models vary considerably in three regions. So far, only a few limited validation studies have been carried out to evaluate these constitutive models. Epps [4] carried out systematic testing of a 20 mil Nitinol wire to obtain its thermo-mechanical characteristics including stress-strain (fixed temperature) and strain-temperature (fixed stress) curves, and then evaluated above four constitutive models using these test data. Figures 47 shows the measured and calculated stress-strain curves at 100°F and 140°F respectively representing mixed mode (both martensite and austenite phases exist) and austenite phases. It was concluded that all models correlate well with test data as long as the constants for the constitutive models are derived properly from the test data. Especially the model developed by Brinson showed a clear distinction between temperature-induced and stress-induced matensite volume fractions. Prahlad [5] carried out a systematic quasistatic testing of NiTi wire at constant temperature, constant stress and constant strain to determine the extent of variation of properties depending on the path of testing. It was pointed out that the state of material is not unique at points along the transformation, and is a function on not only the state variables but also the history, path of loading, strain rates, loading pattern and boundary condition. This behavior is likely to be critical to the application of SMA in devices involving dynamic loading.

Rogers, Liang and Jia [90-91] analytically studied the behavior of shape memory alloy reinforced composite plates. They demonstrated the structural control characteristics and

authority with the SMA reinforcement for four different plate problems; plate bending, free vibration, buckling analysis, and acoustic transmission loss through the plate. It was shown that the first bending frequency of a simply supported composite plate increased by about 100% at activation for 10% SMA reinforcement (by volume). Rogers and Barker [92] presented an experimental study of active strain energy tuning of composite beams with embedded SMA. The beam and the SMA wires were independently clamped. They showed the fundamental bending frequency of a clamped-clamped graphite/epoxy beam increased by about 200% with 15% nitinol volume fraction. These early studies showed the potential of controlling static and dynamic characteristics of beams and plates using embedded SMA fibers. However, no correlation of test results with predictions was made. Baz, Imam and McCoy [93] conducted a study on the active vibration control of flexible beams with SMA wires mechanically constrained on the exterior of the beam. The recovery force due to heat activation was used to change the dynamic characteristics of the beam. In another study, Baz et al [94] inserted SMA wires into a flexible beam with sleeves to control its buckling and vibration behavior. SMA wires were clamped separately. They showed that the buckling load of fiberglass composite beam could be increased three fold upon heat activation. Epps and Chandra[95] embedded SMA wires with sleeves into solid graphite-epoxy composite beam and showed a 22% increase in the first bending natural frequency with a 2% nitinol volume fraction (Fig. 48). Vibration analysis of a composite beam with SMA wires was developed by assuming separately constrained SMA wires as an elastic foundation for the main beam. The spring constant of elastic foundation depends on the recovery force in the SMA wires. Finite element analysis showed good correlation of fundamental frequency with test data for different temperatures. A numerical study by Epps and Chandra[96] showed that embedded SMA wires with sleeves can be used for active tuning of composite shafts. For example, 25 SMA wires of 20 mil diameter embedded into a graphite-epoxy beam of 30 inch length, 1 inch width and 62 mil thickness increase its first bending frequency by 276% on heat activation.

There are two important considerations for embedding SMA fibers in composite beam [96]. The first one is that the matrix of composite material should withstand the prestrain of the SMA fibers. This requirement does not permit the use of normal composite materials and calls for the use of materials with superior interlaminar shear strain at failure. IM7-8552 from Hercules appears to show the potential of satisfying this requirement. The second consideration is that the SMA fibers must be constrained during the manufacturing, so that these do not return to their original position at curing temperatures which are higher than the phase transformation temperature of the SMA. In order to avoid this problem of curing at high temperature, three approaches have been followed. In the first approach, composite solid beams with SMA wires were built using room temperature curing adhesive with glass-epoxy sheets. This does not need the device to constrain the SMA fibers as the phase transformation temperature of SMA (158°F) is above the curing temperature (70°F) of the adhesive. In the second approach, graphite-epoxy beams with fused silica tubes filled with 'dummy' steel wires were fabricated using an autoclave molding technique. In order to assure a good bond between the tubes and the graphite-epoxy material, a film adhesive was used. After curing the composite beam, the steel wires were replaced with pre-strained SMA wires. In the third approach, each one of the pre-strained SMA wires is held fixed between two ends during the curing process. After the curing cycle completed, the end restraints were released.

Currently, research activities are growing towards application of SMA to aerospace systems. One potential application is to adjust trailing-edge trim-tab of a helicopter rotor for in-flight tracking. Liang et al [97] investigated the usage of pre-twisted SMA rod to torsionally

deflect the blade tab. Two concepts were examined respectively using one-way and two-way memory actuators. In the first concept, one SMA rod was used as actuator while second one as a restoring spring (differential bias). In the second concept, one SMA rod in conjunction with locking arrangement is used. Kudva and et al [25-26] examined the induced wing twist and camber control using SMA actuators in a Mach-scaled fixed-wing model. Tests of this wing model in the Transonic Dynamics wind tunnel at Langley showed potential of this device for aeroelatic control of aircraft. Hanagud and Roglin [35] demonstrated the collective control in a flying-model rotor using SMA actuators.

A study [98] was undertaken to develop a SMA-actuated trailing-edge tab (length 4% radius) for the MD-900 rotor system (5-bladed bearingless rotor) for in-flight blade tracking. This tab was located at 72% radial position and was expected to be driven by a SMA torsional actuator (developed by Memry). A locking mechanism was developed to keep the tab in position without power to the actuator. It was designed to undergo ±7.5 deg in steps of 0.25 deg. Maximum torsional actuation moments expected were 5 in-lb during forward flight and 9 in-lb during maneuvers. It was proposed to test this full-scale rotor on the whirl tower, followed by testing in the wind tunnel and flight testing.

Epps [99-102] built a wing model of span and chord of 1 foot with a trailing-edge tab of span 4 inch and chord 2.4 inch to investigate the concept of in-flight tracking of rotor blades using shape memory alloy actuators (Fig. 49). 2 to 5 nitinol wires of diameter 0.015 inch with an initial prestrain of about 3% were clamped at one side to the spar located at quarter-chord and at other side to the hinge tube attached to the tab, respectively on its top and bottom surfaces (Fig. 50). To deflect the tab downward, the bottom wires are heated (using internal resistance) while the top wires remain at room temperature. To deflect the tab back to its original position or upward, the upper wires are heat-activated, while the lower set remains at room temperature. To lock the tab at a desired angle (in power-off condition), a gear-locking mechanism consisting of spur gears, pulling solenoid, restoring spring and pawl was built. A displacement feedback controller was developed to fine tune the tab deflection in about 10 seconds. This wing section was tested in the open-jet wind tunnel and tab deflections of the order of 20 degrees were obtained at a speed of 120 ft/sec (Fig. 51). This concept appears to show the potential for further full-scale development.

MODELING OF BLADES WITH SMART ACTUATORS

To fully exploit the application of smart structures technology in the rotor system, it is necessary to develop analytical tools to model blades with induced strain actuation. Two types of analytical models are needed respectively to represent controllable twist blades and trailing-edge flap blades. For both type of rotors, simple constitutive relations of smart actuators under different loadings are required. For the comprehensive aeroelastic analysis of a rotor system, it becomes essential to treat the blade as one-dimensional beam undergoing extension, bending and torsion deformation. For such an analysis, key elements are: modeling of a beam with surface-mounted or embedded actuators, modeling of actuators with axial force and restraint, unsteady aerodynamics especially pertaining to flaps, and integration of dynamics into rotor analysis.

Crawley and de Luis [42] formulated a uniform strain bending model of a beam with strain-induced piezo-actuation. A pair of piezoceramic actuators aligned along the beam axis was assumed, and the shear lag effects of the adhesive layer between the piezoceramic actuators and the beam were included. Predicted response of the first two bending modes of a

cantilevered beam was verified experimentally. Crawley and Anderson [43] formulated a Bernoulli-Euler model and compared it with uniform strain model, detailed finite element model and experiment. It was shown that for thin beams, Bernoulli-Euler model is more accurate than uniform strain model. Chandra and Chopra [103] developed a formulation for coupled composite thin-walled beams with distributed actuators and then validated analysis with experimental data. Analysis was based on Vlasov theory where two-dimensional stress and displacement fields associated with any local plate segment of the beam are condensed to one-dimensional generalized forces and moments. Correlation with experimental data from a cantilevered graphite-epoxy beam with surface mounted piezoelectric actuators (Fig. 52) showed that the inclusion of chordwise bending is essential to accurately predict a beam's coupled response (Fig. 53).

These analytical models [42, 43, 103] are developed for a pair of piezoceramic actuators, one on each surface aligned along the beam axis. If the same voltage is applied to both piezoceramics, it will result in pure extension for an isotropic beam, and if opposite voltage is applied it will result in pure bending. If the piezoceramic actuator is attached at an arbitrary orientation with respect to the beam axis, it will cause extension, bending and torsional deformation. Park et al [44-45] formulated one-dimensional analytical model of a beam actuated by single piezoceramic actuators surface-mounted at an arbitrary orientation with respect to the beam axis (Fig. 54). Both uniform strain and Bernoulli-Euler models were developed and shear lag effects due to a finite thickness of adhesive layer between the piezoceramic and beam were included. The actuator was assumed to be a line element and only permitted to induce strain in its lengthwise direction. Analysis is also applicable to distributed actuators on both top and bottom surfaces. Experimental tests on response of cantilevered beams with piezoceramic actuators were carried out to evaluate the accuracy and limitations of the models. The bending and coupled bending and extension models showed acceptable correlation with static test results whereas the combined extension, bending and torsion model showed poor correlation especially at high actuator orientation angles. Consequently, the coupled model was modified to include effects of section warping. It improved prediction of torsional response somewhat, but it is still not satisfactory for larger orientation angle of actuator with respect to beam axis (Fig. 55). Detailed strain measurements indicated that transverse actuation is not negligible for all actuator orientations and needs to be included to refine the analysis. Modeling of a beam with

Recently, there have been several efforts to develop comprehensive aeroelastic analyses for rotors with trailing-edge flaps. Current analyses however assume prescribed flap deflections and hence neglect the dynamics of actuators. Milgram [104, 105], for example, developed a comprehensive finite element rotor analysis for plain trailing-edge flaps including indicial-based flap unsteady aerodynamics [106] and a pseudo-implicit free wake model [107]. Extensive validation studies were conducted by comparing vibratory hub loads with experimental wind tunnel data (MDHC Active Flap Rotor test in TDT wind tunnel) and predictions from another comprehensive analysis (modified CAMRAD-JA). Correlations were generally fair and showed room for improvement. Subsequently, parametric studies were conducted on a four-bladed Sikorsky S-76 rotor to examine the effect of flap size, flap location and controller on the minimization of vibratory loads [108, 109]. It was shown that a small size flap (length about 10% radius and chord about 20%) located around 75% radial position requires least actuation power. Milot and Friedmann [110, 111] developed a comprehensive aeroelastic analysis for a rotor with servo-flaps and carried out extensive parametric studies that include flap sizing and placement, actuation power and blade torsional

stiffness. The flap location was determined to be an important design parameter. Myrtle and Friedman [112, 113] modified their rotor analysis with an improved unsteady aerodynamic model for airfoil/flap based on a rational function approximation approach. Straub and Hasan [114] modified the comprehensive rotorcraft code CAMRAD/JA to account for account for flapped rotor and carried out conceptual sizing and design of trailing edge flaps for an active vibration control for the MD-900 helicopter. The selected flap configuration consists of a chord ratio (flap chord/blade chord) of 25%, length of 18% radius and an aerodynamic balance of 40%.

For an accurate prediction of the behavior of rotor blades with smart material acutators, it is important to include the dynamics of actuators into rotor analyses. Recently, Koratkar [46] formulated a coupled actuator-flap-rotor model in hover. This finite element linear analysis includes piezoelectric bender actuator, blade undergoing flapwise bending and torsion, and plane trailing-edge flap. Vibratory blade response due to oscillatory field showed that the effect of coupling due to trailing-edge flap dynamics is about 10% on flap amplitude. Straub and Charles [115] carried out coupled blade/flap/actuator dynamic analysis of a bearingless rotor using a multi-body, high fidelity comprehensive code CAMRAD II. Predicted results were correlated with MDART test data as well as with CAMRAD/JA results. It was shown that simplified efficient analyses (such as CAMRAD/JA) neglecting actuator dynamics are adequate to predict rotor response, conduct concept development studies and formulate control algorithms, where as detailed coupled analyses (such CAMRAD II) including actuator dynamics are necessary for prediction of blade loads and system stability. Shen [116] developed a coupled blade/flap/actuator analysis including flap and actuator dynamics and predicted results for a bearingless rotor were correlated with test data as well as with predictions from other comprehensive codes. Inclusion of actuator dynamics resulted in larger flap control angles (10% increase) as well as more actuation power (30% increase). This study showed that the coupling effect of actuator dynamics is important for the evaluation of the performance of flap, especially for a torsionally soft actuator.

CONCLUSIONS

This paper reviewed developments in smart structures technology for application to rotor systems. Two types of scaled rotors are under development: trailing-edge flap models actuated by piezoceramic or magnetostrictive actuators, and controllable twist models incorporating specially-shaped piezoceramic elements or fibers. These models were tested in a vacuum chamber, on a hover stand and in a wind tunnel to examine their potential to minimize. For both types of rotor models, the performance of the system degraded dramatically at higher rotational speeds because of higher dynamic pressure, centrifugal field and frictional moments. Shape memory alloys actuators can undergo large strokes at a very low frequency (less than 1 Hz) and are being envisaged for several applications that include in-flight rotor tracking and variable speed rotors. Analytical tools to model a smart rotor undergoing bending, extension and torsion are under development. The following conclusions are drawn:

Trailing-Edge Flap Actuated with Piezo Bimorphs

For a Froude-scaled rotor model in hover, a flap actuated by a piezo-bimorph was able to deflect about ±6 deg at 4/rev at the operating speed of 900 RPM. To achieve the target flap deflection of ±6 deg for a Mach-scaled rotor model (2000 RPM), an 8-layered tapered

bimorph was incorporated. This model was tested in both open and closed loop studies and successfully achieved the desired flap authority at several flight conditions. Overall, this actuation system is compact and appears suited for scaled rotor models, especially to check effectiveness of adaptive control strategies. For full-scale applications, it becomes necessary to build multi-layered actuators (say 40 layers), and more importantly to develop a refined frictionless amplification system.

Trailing-Edge Flap Actuated with Piezo Stacks

A multi-piezostacks actuated flap in a fixed-wing model achieved ±5 to ±10 degree depending on excitation frequency at a free stream velocity of 120 ft/sec. Also, it was tested successfully in a vacuum spin chamber for a centrifugal loading of 710g, with no degradation of flap response with rotational speed (up to 1000 RPM) and excitation frequency (up to 6/rev). To achieve reliable flap deflection in a full-scale system, it is important to build a compact bi-directional actuator system of moderate to large force and high stroke capability. The major challenge is to build a compact stroke-amplification system. Overall, this actuation system shows the most potential for a full-scale system.

Trailing-Edge Flap Actuated with Magnetostrictive Actuators and Extension-Torsion Coupled Composite Tube

To implement the trailing-edge flap concept on a full-scale vehicle, a kevlar-epoxy extension-torsion coupled tube with a magnetostrictive actuator was designed to achieve the desired actuation force and displacement. A piezoelectric stack actuator was found to be better than a magnetostrictive actuator. Ten $[11]_4$ kevlar-epoxy/piezo-stack systems of 20 inch length each in series (placed spanwise) would generate ±5.2 deg of flap deflection. Because of poor structural efficiency of extension-twist coupled structures and with available stack actuators, this actuation system is less meritorious than other actuation systems.

Trailing-Edge Flap Actuated with Piezoceramic Actuators and Tailored Bending-Torsion Coupled Composite Tube

This novel actuation system was demonstrated to actuate a trailing-edge flap or an all-movable tip or complete blade twist. For a Froude-scaled model, a flap deflection of ±2 deg at 4/rev was obtained at the operating speed of 875 RPM and there was no degradation of flap amplitude with RPM or with collective setting. For controllable twist configurations, a tip twist of .4 deg at 4/rev was obtained at 875 RPM. For an all-movable 10% tip, a 4-bladed Mach-scaled rotor was successfully tested in hover (RPM = 2000), resulting in tip deflection of ±1.2 to ±1.6 degree (depending on frequency of excitation) with thrust authority of 10% to 30%. From a closed-loop adaptive test, it was demonstrated that this smart tip was capable of minimizing simulated flap bending and rotor thrust by 80% to 95%. This device can be easily accommodated in a blade spar and appears to show the potential to control vibration and acoustics as a partial reduction device in a full-scale system.

Controllable Twist Blade with Embedded Piezoceramic Actuators

At an operating speed of 900 RPM in hover, a maximum tip twist of .4 deg at 4/rev was achieved using dual-layer piezoceramics embedded at ±45 deg on the top and bottom surfaces.

At an advance ratio of .33, an oscillatory rotor thrust of 11% of nominal steady state value was achieved in a wind tunnel. Using today's actuators technology, it is possible to build a full-scale controllable twist rotor, but at a considerable weight penalty (16% of blade weight). This approach shows the potential for partial vibration suppression

Shape Memory Alloy Actuators

The constitutive models of SMA developed by different researchers correlate well with test data as long as the constants the material constants for models are derived properly form test data. Building composite shafts or beams with embedded SMA is a challenge, and needs focused effort. A SMA wire-actuated tab showed deflections of the order of 20 degrees at a forward speed of 120 ft/sec. For in-flight tracking with tab, it is important to incorporate adaptive control strategy and a locking mechanism.

Modeling of Blades with Smart Actuators

Validation of newly formulated one-dimensional beam models undergoing bending, extension and torsional deformation with experimental data showed an acceptable correlation for bending response and a poor correlation for torsional response. This beam model needs further refinements to include transverse actuation. Comprehensive aeroelastic analyses for rotors with trailing-edge flaps are under development and need to include the dynamics of smart actuators.

ACKNOWLEDGMENTS

Most of these research activities were supported by the Army Research Office under the grants URI: DAAL 03-92-G-0121 and MURI: DAAH-04-96-10334 with Dr. Gary Anderson and Dr. Tom Doligalski as Technical Monitors. Author acknowledges many useful discussions and enthusiastic input from Dr. Friedrich Straub (Boeing-Mesa), Dr. Norman Wereley (UM), Dr. Ramesh Chandra (UM), Darryll Pines (UM) and many graduate students (Peter Chen, Andy Bernhard, Nikhil Koratkar, Jeanette Epps, Taeoh Lee, Jayant Sirohi, Harsha Prahlad, Mike Spencer, Mark Shaner and Judah Milgram).

REFERENCES

1. Chopra, I., "State-of-the-Art of Smart Structures and Integrated Systems," *Proceedings of the 1996 SPIE's North American Symposium on Smart Structures and Materials,* San Diego, CA, February 1996.
2. Sirohi, J. and Chopra, I., "Fundamental Behavior of Piezoceramic Sheet Actuators," *Proceedings of the 1998 SPIE's North American Symposium on Smart Structures and Materials,* San Diego, CA, March 1998.
3. Sirohi, J. and Chopra, I., "Fundamental Understanding of Piezoelectric Strain Sensors," *Proceedings of the 1999 SPIE's North American Symposium on Smart Structures and Materials,* Newport Beach, CA, March 1999.
4. Epps, J. J. and Chopra, I.,"Compartive Evaluation of Shape Memory Alloy Constitutive Models with Test Data," *Proceedings of the 38th AIAA /ASME/ASCE/AHS/ASC Structures, Structural Dynamics and Materials Conference and Adaptive Structures Forum,* Kissimmee, FL, April 1997.
5. Prahlad, H. and Chopra, I., "Experimental Characterization of Ni-Ti Shape Memory Alloy Wires under Complex Loading Conditions," *Proceedings of the 1999 SPIE's North American Symposium on Smart Structures and Materials,* Newport Beach, CA, March 1999.

6. Samak, D. K. and Chopra, I., "Design of High Force, High Displacement Actuators for Helicopters Rotors" *Smart Materials & Structures*, Vol. 5, No. 1, February 1996, pp. 58-67.
7. Bothwell, C. M., Chandra, R. and Chopra, I., "Torsional Actuation with Extension-Torsional Composite Coupling and Magnetostrictive Actuators," *AIAA Journal,* Vol. 33, No. 4, April 1995, pp. 723-729.
8. Udd, E., "Fiber Optic Sensors: An Introduction for Engineers and Scientists," John Wiley and Sons, New York, 1991.
9. Lee, T. and Chopra, I., "Design and Static Testing of a Trailing-Edge Flap Actuator with Piezostack for a Rotor Blade," *Proceedings of the 1998 SPIE's North American Symposium on Smart Structures and Materials,* San Diego, CA, March 1998.
10. Walz, C. and Chopra, I., "Design and Testing of a Helicopter Rotor Model with Smart Trailing Edge Flaps," *Proceedings of the 35th AIAA /ASME/ASCE/AHS/ASC Structures, Structural Dynamics and Materials Conference and Adaptive Structures Forum,* Hilton Head, SC, April 1994.
11. Chopra, I. and McCloud, J. C., "A Numerical Simulation Study to Open-Loop, Closed-Loop and Adaptive Multicyclic Control Systems," *Journal of the American Helicopter Society,* Vol. 28, No. 1, January 1983, pp. 63-77.
12. Nguyen, K. and Chopra, I., "Application of Higher Harmonic Control to Rotors Operating at High Speed and Thrust," *Journal of the American Helicopter Society,* Vol. 35, No. 3, July 1990, pp. 78-89.
13. Shaw, J., Albion, N., Hanker, E. J. and Teal, R. S.,"Higher-Harmonic Control: Wind Tunnel Demonstration of Fully Effective Vibratory Hub Forces Suppression," *Journal of the American Helicopter Society,* Vol. 34, No. 1, January 1989, pp. 14-25.
14. Wood, E. R., Powers, R. W., Cline, C. H. and Hammond, C. E., " On Developing and Flight Testing a Higher Harmonic Control System," *Journal of the American Helicopter Society,* Vol. 30, No. 1, January 1985, pp. 3-20.
15. Ham, N. D., "Helicopter Individual-Blade Control Research at MIT 1977-1985," *Vertica,* Vol. 11, No. 1/2, 1987, pp. 109-122
16. Richter, P. and Blaas, A., "Full Scale Wind Tunnel Investigation of an Individual Blade Control System for the BO 105 Hingeless Rotor," Proceeding of the 19th European Rotorcraft Forum, Cernobbio (Como), September 1993
17. Jaclin, S. A., Blaas, A., Teves, D. and Kube, R., "Reduction of Helicopter BVI Noise, Vibration, and Power Consumption Through Individual Blade Control," *Proceedings of the 51st Annual Forum of the American Helicopter Society,* Fort Worth, TX, May 1995.
18. Balachandran, B., Sampath, A. and Park, J., "Active Control of Interior Noise in Three-Dimensional Enclosure," *Smart Materials & Structures,* Vol. 5, No. 1, February 1995, pp 89-97.
19. Gembler, W., Schweitzer, H., Maier, R., Pucher M., Janker, P. and Hermle, F., "Smart Struts – The Solution for Helicopter Interior Noise Problem," Proceeding of the 25th European Rotorcraft Forum, Rome, Italy, September 1999.
20. Crawley, E. F., "Intelligent Structures for Aerospace: A Technology Overview and Assessment," *AIAA Journal,* Vol. 32, No. 8, August 1994, pp. 1689-1699.
21. Wada, B.K., Fanson, J.L., and Crawley, E.F., "Adaptive Structures," *Journal of Intelligent Material Systems and Structurs,* Vol. 1, No. 2, April 1990, pp. 157-174.
22. Ehlers, S. M., and Weisshaar, T. A., "Static Aeroelastic Control of an Adaptive Lifting Surface," *Journal of Aircraft,* Vol. 30, No. 4, July-August 1993, pp. 534-540.
23. Lazarus, K. B., Crawley, E. F. and Bohlmann, J. D., "Static Aeroelastic Control Using Strain Actuated Adaptive Structures," *Journal of Intelligent Material Systems and Structurs,* Vol. 2, No. 3, July 1991, pp. 386-410.
24. Lin, C. Y., Crawley, E. F. and Heeg, J., "Open- and Closed-Loop Results of a Strain-Actuated Active Aeroelastic Wing," *Journal of Aircraft,* Vol. 33, No. 5, September - October 1996, pp. 987-994.
25. Kudva, J., Appa, K., Martin, C., Jardine, P. and Sendeckyi, " Design, Fabrication and Testing of the DARPA/WL "Smart Wing" Wind Tunnel Model," *38th AIAA/ASME/ASCE/AHS/ASC Structures, Structural Dynamics, and Materials* Conference, Kissimmee, Florida, April 1997.
26. Kudva, J. and et al, "Overview of the DARPA/AFRL/NASA Smart Wing Program," *Proceedings of the 1999 SPIE's North American Symposium on Smart Structures and Materials,* Newport Beach, CA, March 1999.
27. Becker, J. and Schroder, "Advanced Aircraft Structures Program: An Overview," *Proceedings of the 1999 SPIE's North American Symposium on Smart Structures and Materials,* Newport Beach, CA, March 1999.

28. Frampton, K. D., Clark, R. L. and Dowell, E. H., "Active Control of Panel Flutter with Piezoelectric Transducers," Journal of Aircraft, Vol. 33, No. 4, July-August 1996, pp. 768-774.
29. Fuller, C. R., Hansen, C. H. and Snyder, S. D., "Experiments on Active Control of Sound Radiation from a Panel Using a Piezoceramic Actuator," *Journal of the Acoustical Society of America,* Vol. 91, No. 6, 1992, pp. 3313-3320.
30. Chopra, I., "Development of a Smart Rotor," Proceeding of the 19th European Rotorcraft Forum, Cernobbio Como, Italy, September 1993.
31. Loewy, R. G., "Recent Developments in Smart Structures with Aeronautical Applications," *Proceedings of the 37th Israel Annual Conference on Aerospace Sciences,* Tel Aviv, Israel, February 1996.
32. Straub, F. K., "A Feasibility Study of Using Smart Materials for Rotor Control" *Smart Materials & Structures,* Vol. 5, No. 1, February 1995, pp 1-10.
33. Straub, F. K. and Merkley, D. J., "Design of a Servo-Flap Rotor for Reduced Control Loads, *Smart Materials & Structures,* Vol. 5, No. 1, February 1995, pp 68-75.
34. Strehlow, H., and Rapp, H., "Smart Materials for Helicopter Rotor Active Control" *Proceedings of AGARD/SMP Specialists Meeting on Smart Structures for Aircraft and Spacecraft,* Lindau, Germany, Oct. 1992.
35. Roglin, R. L. and Hanagud, S. V., "A Helicopter with Adaptive Rotor Blades for Collective Control," *Smart Materials & Structures,* Vol. 5, No. 1, February 1995, pp 1-10.
36. Janker, P., Kloppel, V., Hermle, T., Lorkowski, T., Storm, S., Christmann, M. and Wettemann, "Development and Evaluation of a Hybrid Piezoelectric Actuator for Advanced Flap Control Technology," Proceeding of the 25th European Rotorcraft Forum, Rome, Italy, September 1999.
37. Shaner, M. C. and Chopra, I., "Design and Testing of a Piezostacke Actuated Leading-Edge Flap," *Proceedings of the 1999 SPIE's North American Symposium on Smart Structures and Materials,* Newport Beach, CA, March 1999
38. Kamath, G., Wereley, N. and Jolly, M., "Analysis and Testing of a Model-Scale Magnetorheological Fluid Helicopter Lag Damper," *Proceedings of the 53rd Annual Forum of the American Helicopter Society,* Virginia Beach, VA, May 1997.
39. Pelinescu, I. and Balachandran, B., "Active Control of Vibration Transmission Through Struts," *Proceedings of the 1999 SPIE's North American Symposium on Smart Structures and Materials,* Newport Beach, CA, March 1999.
40. Park, H. and Chopra, I., "Active Control of Airframe Structural Response with Distributed Smart Actuators," Presented at the 4th ARO Smart Structures Workshop, Penn State, August 1999.
41. Wereley, N., "Active and Passive Damping Control of Helicopter Systems," *Proceedings of the 1999 SPIE's North American Symposium on Smart Structures and Materials,* Newport Beach, CA, March 1999.
42. Crawley, E.F., and de Luis, J., "Use of Piezoelectric Actuators as Elements of Intelligent Structures," *AIAA Journal,* Vol. 25, No. 10, Oct. 1987, pp. 1373-1385.
43. Crawley, E. F., and Anderson, E. H., "Detailed Modeling of Piezoceramic Actuation of Beams," *Journal of Intelligent Material Systems and Structures,* Vol. 1, No. 1, Jan. 1990, pp. 4-25.
44. Park, C., Walz, C and Chopra, I., " Bending and Torsion Models of Beams with Induced-Strain Actuators," *Smart Materials & Structures,* Vol. 5, No. 1, February 1995, pp 98-113.
45. Park, C. and Chopra, I., " Modeling of Piezoceramic Actuation of Beams in Torsion," *AIAA Journal,* Vol. 34, No. 12, December 1996, pp 2582-2589.
46. Koratkar, N. and Chopra, I., "Analysis and Testing of Mach Scaled Rotor Model with Piezoelectric Bender Actuated Trailing-Edge Flaps for Helicopter Vibration Control,"*Proceedings of the 38th AIAA /ASME/ASCE/AHS/ASC Structures, Structural Dynamics and Materials Conference and Adaptive Structures Forum,* St. Louis, MO, April 1999.
47. Samak, D. K., and Chopra, I., "A Feasibility Study to Build a Smart Rotor: Trailing Edge Flap Actuation" *Proceedings of the 1993 SPIE's North American Symposium on Smart Structures and Materials,* Albuquerque, NM, February 1993.
48. Ben-Zeev, O. and Chopra, I., "Advances in the Development of an Intelligent Helicopter Rotor Employing Smart Trailing-Edge Flaps," *Smart Materials & Structures*, Vol. 5, No. 1, February 1996, pp. 11-25.
49. Koratkar, N. A., and Chopra, I., "Analysis and Testing of a Froude Scaled Helicopter Rotor with Piezoelectric Bender Actuated Trailing Edge Flaps," *Journal of Intelligent Material Systems and Structures,* Vol. 8, July 1997, pp. 555-570.
50. Hariharan, N. and Leishman, J. G., "Unsteady Aerodynamics of Flapped Airfoil in Subsonic Flow by Indicial Concepts," *Journal of Aircraft,* Vol. 33, No. 5, Sept.-Oct., 1996, pp. 855-868.

51. Koratkar, N. A., and Chopra, I., "Design, Fabrication and Testing of a Mach Scaled Rotor Model with Trailing-Edge Flaps," *Proceedings of the 55th Annual Forum of the American Helicopter Society,* Montreal, Canada, May 1999.
52. Koratkar, N. A. and Chopra, "Wind Tunnel Testing of a Mach-Scaled Rotor Model with Trailing-Edge Flaps," *Proceedings of the 56th Annual Forum of the American Helicopter Society,* Virginia Beach, VA, May 2000.
53. Spangler, R.L., and Hall, S.R., "Piezoelectric Actuators for Helicopter Rotor Control," *Proceedings of the 31st AIAA /ASME/ASCE/AHS/ASC Structures, Structural Dynamics and Materials Conference,* Long Beach, CA, April 1990.
54. Hall, S.R. and Prechtl, E. F., "Development of a Piezoelectric Servoflap for Helicopter Rotor Control," *Smart Materials & Structures*, Vol. 5, No. 1, February 1996, pp. 26-34.
55. Fulton, M. V. and Ormiston, R. A., "Hover Testing of a Small-Scale Rotor with On-Blade Elevons" *Proceedings of the 53rd Annual Forum of the American Helicopter Society,* Virginia Beach, VA, May 1997.
56. Fulton, M. V. and Ormiston, R. A., "Small-Scale Rotor Experiments with On-Blade Elevons to Reduce Blade Vibratory Loads in Forward Flight," *Proceedings of the 54th Annual Forum of the American Helicopter Society,* Washington, DC, May 1998.
57. Spencer, B. and Chopra, I., "Advances in the Development of an Intelligent Helicopter Rotor Employing Smart Trailing-Edge Flaps," *Proceedings of the 1996 SPIE's North American Symposium on Smart Structures and Materials,* San Diego, CA, February 1996.
58. Chandra, R. and Chopra, I. "Actuation of Trailing Edge Flap in Wing Model Using Piezostack Device," *Proceedings of the 38th AIAA /ASME/ASCE/AHS/ASC Structures, Structural Dynamics and Materials Conference and Adaptive Structures Forum,* Kissimmee, FL, April 1997.
59. Lee, T. and Chopra, I., "Design and Spin Testing of an Active Trailing Edge Flap Actuated Piezostacks," Proceedings of the *AIAA /ASME/ASCE/AHS/ASC Structures, Structural Dynamics and Materials Conference and Exhibit,* St. Louis, MO, April 1999.
60. Lee, T. and Chopra, I., "Development and Validation of a Refined Piezostack-Actuated Trailing Edge Flap Actuator for a Helicopter Rotor," *Proceedings of the 1999 SPIE's North American Symposium on Smart Structures and Materials,* Newport Beach, CA, March 1999.
61. Lee, T., "High Displacement Piezoelectric Trailing-Edge Flap Mechanism for Helicopter Rotors," Ph.D. Dissertation, University of Maryland, College Park, MD, December 1999.
62. Straub, F. K. and King, R. J., "Application of Smart Materials to Control of a Helicopter Rotor," *Proceedings of the 1996 SPIE's North American Symposium on Smart Structures and Materials,* San Diego, CA, February 1996.
63. Straub, F. K., Ealey, M. A. and Schetky, L. M., "Application of Smart Materials to Helicopter Rotor Active Control,"*Proceedings of the 1997 SPIE's North American Symposium on Smart Structures and Materials,* San Diego, CA, March 1997.
64. Straub, F. K. and Hassan, A. A., "Aeromechanic Considerations in the Design of a Rotor with Smart Material Actuated Trailing Edge Flaps," *Proceedings of the 52nd Annual Forum of the American Helicopter Society,* Washington D.C., June 1996
65. Straub, F. K., Ngo, H. T., Anand, V. and Domzalski, D. B., "Development of a Piezoelectric Actuator for Trailing Edge Flap Control of Rotor Blades," *Proceedings of the 1999 SPIE's North American Symposium on Smart Structures and Materials,* Newport Beach, CA, March 1999.
66. Prechtl, E. F. and Hall, S. R., "Design of a High-Efficiency Discrete Servo-Flap Actuator for Helicopter Rotor Control," *Proceedings of the 1997 SPIE's North American Symposium on Smart Structures and Materials,* San Diego, CA, March 1997.
67. Hall, S. R. and Prechtl, E. F., "Preliminary Testing of a Mach-Scaled Active Rotor Blade with a Trailing Edge Servo-Flap,"*Proceedings of the 1999 SPIE's North American Symposium on Smart Structures and Materials,* Newport Beach, CA, March 1999.
68. Schimke, D., Janker, P., Blaas, A., Kube, R. and Kessler, C. "Individual Blade Control by Servo-Flap and Blade Root Control A Collaborative Research and Development Programme," Proceedings of the European Rotorcraft Forum, Dresden, Germany, September 1997.
69. Schimke P., Janker, V., Wendt, V. and Junker, B., "Wind Tunnel Evaluation of a Full Scale Piezoelectric Flap Control Unit, Proceedings of the European Rotorcraft Forum, Marseille, France, September 1998.
70. Shaner, M., "Active Blade Leading-Edge Droop with Piezostacks for High Speed Noise Suppression," MS Thesis, University of Maryland, College Park, January 2000.

71. Chandra, R. and Chopra, I., "Structural Response of Composite Beams and Blades with Elastic Couplings," *Composite Engineering,* Vol. 2, No. 5, 1992, pp. 347-374.
72. Bernhard, A., Chopra, I., "Trailing Edge Flap Activated by a Piezo-Induced Bending-Torsion Coupled Beam", Journal of the American Helcopter Society, Vol. 44, No. 1, January 1999, pp. 3-15.
73. Bernhard, A., Chopra, I., "Development of a Smart Moving Blade Tip Activated by a Piezo-Induced Bending-Torsion Coupled Beam", *Proceedings of the 1996 SPIE's North American Symposium on Smart Structures and Materials,* San Diego, CA, February 1996.
74. Bernhard, A., Chopra, I., "Development of a Smart Moving Blade Tip by a Piezo-Induced Bending-Torsion Coupled Beam", *Proceedings of the 53rd Annual Forum of the American Helicopter Society,* Virginia Beach, VA, May 1997.
75. Bernhard, A., Chopra, I., "Mach-Scale Design of a Rotor-Model with Active Blade Tip", *Proceedings of the 55th Annual Forum of the American Helicopter Society,* Montreal, Canada, May 1999.
76. Bernhard, A., "Smart Helicopter Rotor with Active Blade Tips (SABT)," Ph. D. Dissertation, Aerospace Engineering, University of Maryland, March 2000.
77. Chen, P. C., and Chopra, I., "A Feasibility Study Build a Smart Rotor: Induced-Strain Actuation of Airfoil Twisting Using Piezoelectric Crystals" *Proceedings of the 1993 SPIE's North American Symposium on Smart Structures and Materials,* Albuquerque, NM, February 1993.
78. Chen, P. C. and Chopra, I., "Induced Strain Actuation of Composite Beams and Rotor Blades with Embedded Piezoceramic Elements," *Smart Materials & Structures*, Vol. 5, No. 1, February 1996, pp. 35-48.
79. Chen, P. C. and Chopra, I., "Hover Testing of Smart Rotor with Induced-Strain Actuation of Blade Twist," AIAA Journal, Vol. 35, No. 1, January 1997, pp. 6-16.
80. Chen, P. C. and Chopra, I., "Wind Tunnel Test of a Smart Rotor with Individaul Blade Twist Control," Journal of Intelligent Material Systems and Structures, Vol. 8, No. 5, May 1997, pp. 414-425.
81. Chen, P. C., "Development of a Smart Rotor with Induced-Strain Actuation of Blade Twist," Ph. D. Dissertation, Aerospace Engineering, University of Maryland, 1996.
82. Rodgers, J. P. and Hagood, N. W., "Design and Manufacture of an Integral Twist-Actuated Rotor Blade,"*Proceedings of the 38th AIAA /ASME/ASCE/AHS/ASC Structures, Structural Dynamics and Materials Conference and Adaptive Structures Forum,* Kissimmee, FL, April 1997.
83. Derham, R. C. and Hagood, N. W., "Rotor Design Using Smart Materials to Actively Twist Blades,"*Proceedings of the 52nd Annual Forum of the American Helicopter Society,* Washington, DC, June 1996.
84. Rogers, J. P. and Hagood, N. W., "Preliminary Mach-Scale Hover Testing of an Integral Twist-Actuated Rotor Blade,"*Proceedings of the 1997 SPIE's North American Symposium on Smart Structures and Materials,* San Diego, CA, March 1997.
85. Rogers, J. P. and Hagood, N. W., "Development of an Integral Twist-Actuated Rotor Blade for Individual Blade Control,"*MIT AMSL 98-6* , October 1998.
86. Tanaka, K., "A Thermomechanical Sketch of Shape Memory Effect: One-dimensional Tensile Behavior," *Res. Mechanica*, Vol. 18, p. 251-263, 1986.
87. Liang, C., and Rogers, C. A., "One-Dimensional Thermomechanical Constitutive Relations for Shape Memory Material," *Journal of Intelligent Materials and Structures*, Vol. 1, April 1990, pp. 207-234.
88. Brinson, L. C., "One Dimensional Constitutive Behavior of Shape Memory Alloys: Thermo-mechanical Derivation with Non-Constant Material Functions," *Journal of Intelligent Material Systems and Structures* Vol. 4, No. 2, p. 229-242, 1993.
89. Boyd, J. G., and Lagoudas, D. C., "A thermodynamic Constitutive Model for the Shape Memory Materials. Part I. The Monolithic Shape Memory Alloys," *International Journal of Plasticity*, Vol. 12, No. 6, 1996, pp. 805-842.
90. Rogers, C. A., Liang, C., and Jia, J., "Behavior of Shape Memory Alloy Reinforced Composite Plates, Part I: Model Formulations and Control Concepts,"*Proceedings of the 30th AIAA/ASME/ASCE/AHS/ASC Structures, Structural Dynamics and Materials Conference,* Washington D.C., April 1989.
91. Rogers, C. A., Liang, C., and Jia, J., "Behavior of Shape Memory Alloy Reinforced Composite Plates, Part II: Results,"*Proceedings of the 30th AIAA/ASME/ASCE/AHS/ASC Structures, Structural Dynamics and Materials Conference,* Washington D.C., April 1989.
92. Rogers, C. A., and Barker, D. K., "Experimental Studies of Active Strain Energy Tuning of Adaptive Composites,"*Proceedings of the 31st AIAA/ASME/ASCE/AHS/ASC Structures, Structural Dynamics and Materials Conference,* Washington D.C., April 1990.

93. Baz, A., Imam, K., McCoy, J., "Active Vibration Control of Flexible Beams Using Shape Memory Actuators," *Journal of Sound and Vibration*, Vol. 140 (3), 1990, pp. 437-456.
94. Baz, A. and Ro, S., " Thermo-Dynamic Characteristics of Nitinol-Reinforced Composite Beams," *Composite Engineering*, Vol. 2, No. 5-7, 1992, pp. 527-542.
95. Epps, J. J., and Chandra, R., "Shape Memory Alloy Actuation for Active Tuning of Composite Beams," *Proceedings of the 1995 SPIE's North American Symposium on Smart Structures and Materials*, San Diego, CA, February 1995.
96. Epps, J. J., and Chandra, R., "Shape Memory Alloy Actuation for Active Tuning of Composite Shafts," *Proceedings of the 1996 SPIE's North American Symposium on Smart Structures and Materials*, San Diego, CA, February 1996.
97. Liang, C., Schroeder, S. and Davidson, F. M., "Application of Torsion Shape Memory Alloy Actuators for Active Rotor Blade Control: Oportunities and Limitations," *Proceedings of the 1996 SPIE's North American Symposium on Smart Structures and Materials*, San Diego, CA, February 1996.
98. Straub, F. K., Ealey, M. A., and Schetky, L.McD., "Application of Smart Materials to Helicopter Active Control," *Proceedings of the 1997 SPIE's North American Symposium on Smart Structures and Materials*, San Diego, CA, March 1997.
99. Epps, J. J. and Chopra, I., "Shape Memory Alloy Actuators for In-Flight Tracking of Helicopter Rotor Blades," *Proceedings of the 1998 SPIE's North American Symposium on Smart Structures and Materials*, San Diego, CA, March 1998.
100. Epps, J. J. and Chopra, I., "In-Flight Tracking of Helicopter Rotor Blades Using Shape Memory Alloy Actuators," *Proceedings of the 40th AIAA /ASME/ASCE/AHS/ASC Structures, Structural Dynamics and Materials Conference and Adaptive Structures Forum*, St. Louis, MO, April 1999.
101. Epps, J. J. and Chopra, I., "Methodology of In-Flight Tracking of Helicopter Rotor Blades Using Shape Memory Alloy Actuators," *Proceedings of the 55th Annual Forum of the American Helicopter Society*, Virginia Beach, VA, May 1999.
102. Epps, J. J., "In-Flight Tracking of Helicopter Rotor Blades with Tabs actuated with Shape Memory Alloy Actuators," Ph. D. Dissertation, Aerospace Engineering, University of Maryland, Feb. 2000.
103. Chandra, R. and Chopra, I., "Structural Modeling of Composite Beams with Induced Strain Actuation," *AIAA Journal*, Vol. 31, No. 9, Sept. 1993, pp. 1692-1701.
104. Milgram, J. and Chopra, I., "A Comprehensive Rotorcraft Aeroelastic Analysis with Trailing-Edge Flaps: Validation with Experimental Data, *Proceedings of the 52nd Annual Forum of the American Helicopter Society*, Washington D.C., June 1996.
105. Milgram, J., Chopra, I. and Straub, F., "Rotors with Trailing Edge Flaps: Analysis and Comparison with Experimental Data," *Journal of the American Helicopter Society*, Vol. 43, No. 4, October 1998, pp. 319-332.
106. Hariharan, N. and Leishman, J. G., "Unsteady Aerodynamics of a Flapped Airfoil in Subsonic Flow by Indicial Concepts," Journal of Aircraft, Vol. 33, No. 5, Sept.-Oct. 1996, pp. 855-868.
107. Bagai, A. and Leishman, J. G., "Rotor Free-Wake Modeling Using a Pseudo-Implicit Technique – Including Comparisons with Experimental Data," *Journal of the American Helicopter Society*, Vol. 40, No. 3, July 1995, pp.
108. Milgram, J. and Chopra, I. "A Parametric Design Study for Actively Controlled Trailing Edge Flaps," *Journal of the American Helicopter Society*, Vol. 43, No. 2, April 1998, pp. 110-119.
109. Milgran, J., "A Comprehensive Aeroelastic Analysis of Helicopter Main Rotors with Trailing Edge Flaps for Vibration Reduction," Ph. D. Dissertation, Aerospace Engineering, University of Maryland, 1997.
110. Millott, T. A. and Friedmann, P. P., "The Practical Implementation of an Actively Controlled Flap to Reduce Vibration in Helicopter Rotors," *Proceedings of the 49th Annual Forum of the American Helicopter Society*, St. Louis, MO, May 1993.
111. Millott, T. A. and Friedmann, P. P., "Vibration Reduction in Hingeless Rotors Using an Actively Controlled Trailing Edge Flap: Implementation and Time Domain Simulation," *Proceedings of the 35th AIAA /ASME/ASCE/AHS/ASC Structures, Structural Dynamics and Materials Conference and Adaptive Structures Forum*, Hilton Head, SC, April 1994.
112. Myrtle, T. F. and Friedmann, P. P., "Vibration Reduction in Rotorcraft Using Actively Controlled Trailing Edge Flaps and Issues Related to Practical Implementation," *Proceedings of the 54th Annual Forum of the American Helicopter Society*, St. Louis, Washington, D. C., May 1998.
113. Myrtle, T. F. and Friedmann, P. P., "New Comprehensive Time Domain Unsteady Aerodynamics for Flapped Airfoils and Its Application to Rotor Vibration Reduction Using Active Control," *Proceedings of the 53rd Annual Forum of the American Helicopter Society*, Virginia Beach, VA, May 1997.

114. Straub, F. K. and Hasan, A. A., "Aeromechanic Consideration in the Design of a Rotor with Smart Material Actuated Trailing Edge Flaps," *Proceedings of the 52nd Annual Forum of the American Helicopter Society,* Washington D. C., June 1996.
115. Straub, F. K. and Charles, B. D., "Comprehensive Modeling of Rotors with Trailing Edge Flaps," *Proceedings of the 55th Annual Forum of the American Helicopter Society,* Montreal, Canada, May 1999.
116. Shen, J. and Chopra, I., "Aeroelastic Modeling of Trailing-Edge Flaps with Smart Material Actuators," ," *Proceedings of the 41st AIAA /ASME/ASCE/AHS/ASC Structures, Structural Dynamics and Materials Conference and Adaptive Structures Forum,* Atlanta, GA, April 2000.

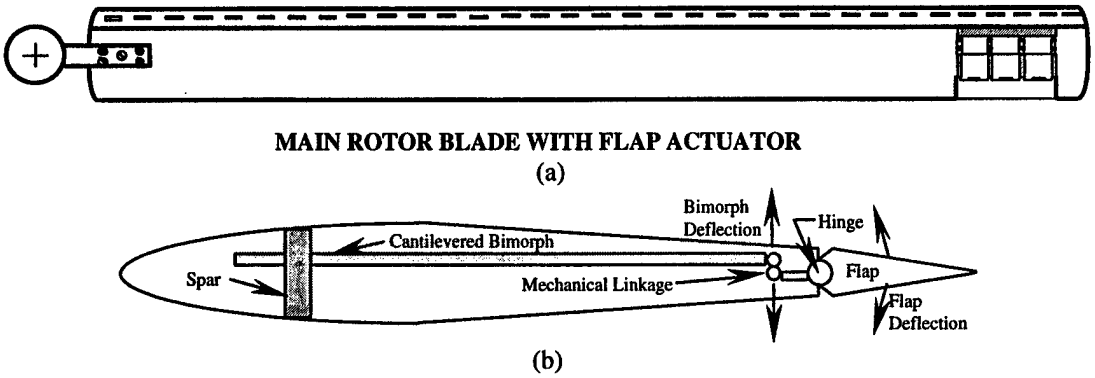


Figure 1. Actuator layout in blade section

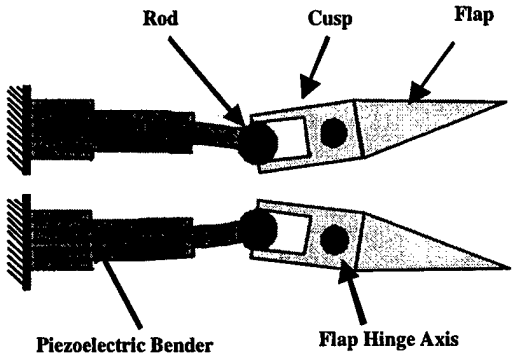


Figure 2. Piezo-bimorph flap actuation system

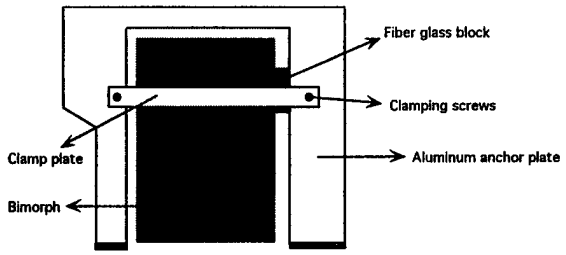


Figure 3. Bimorph clamping arrangement

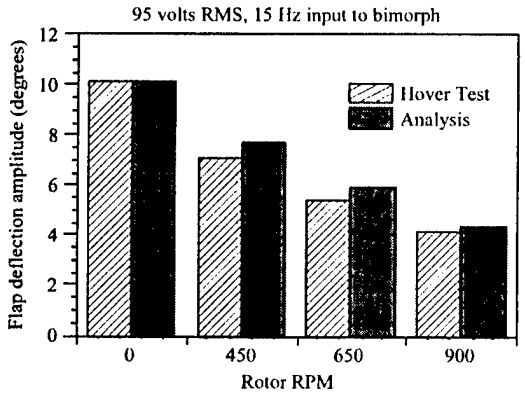


Figure 4. Froude scaled rotor model in hover: RPM sweep with 1/rev excitation [45]

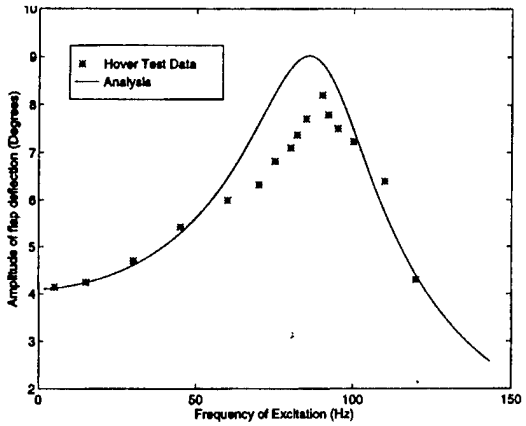


Figure 5. Froude scaled rotor model in hover: frequency sweep at 900 RPM [45]

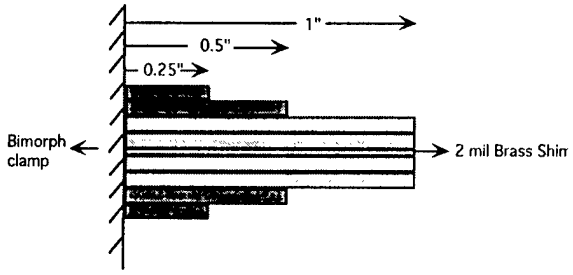


Figure 6. 8-layered, one inch wide, tapered Piezo-Bimorph (each PZT layer is 7.5 mils thick) [45]

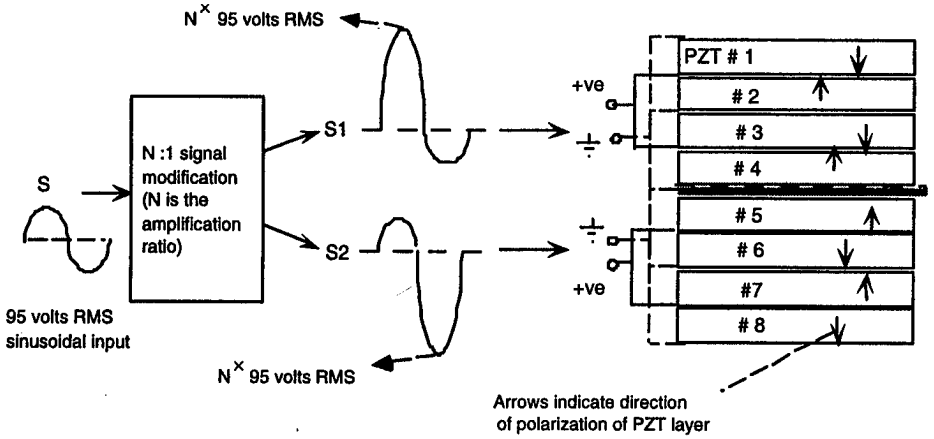


Figure 7. AC bias circuit

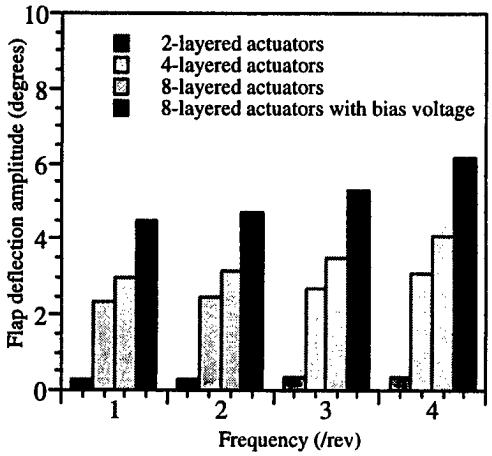


Figure 8. Comparison of actuator configurations for Mach scaled rotor [45]

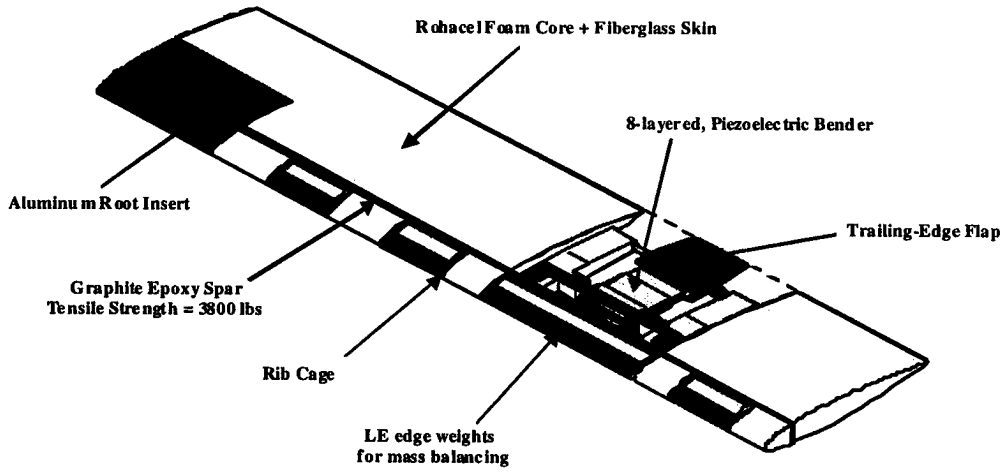


Figure 9. Mach scaled blade layout

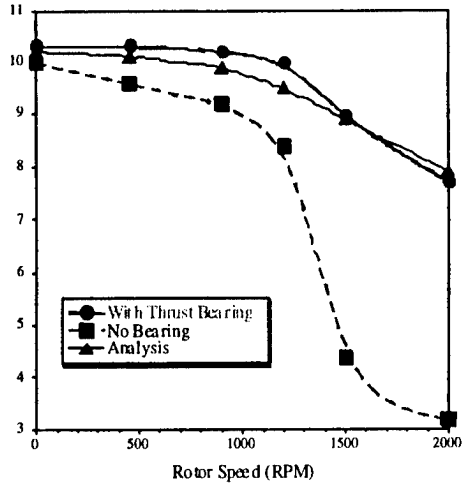


Figure 10. Mach scaled rotor test in vacuum chamber: with and without thrust bearing and correlation with predictions [51]

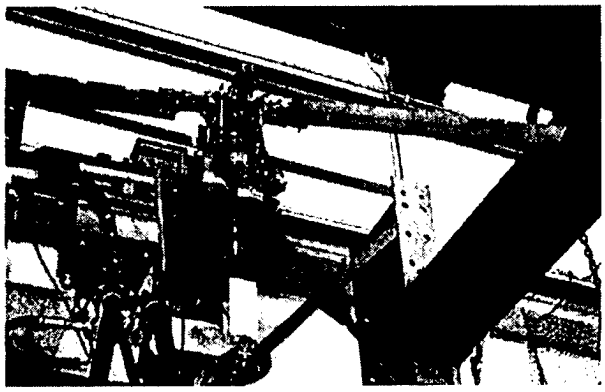
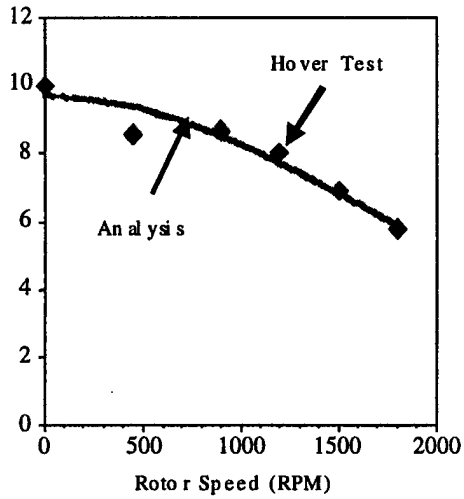
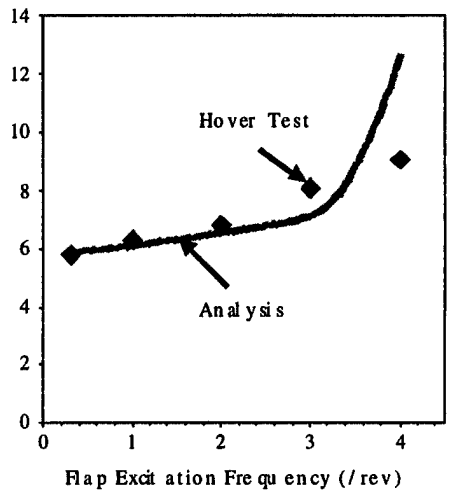


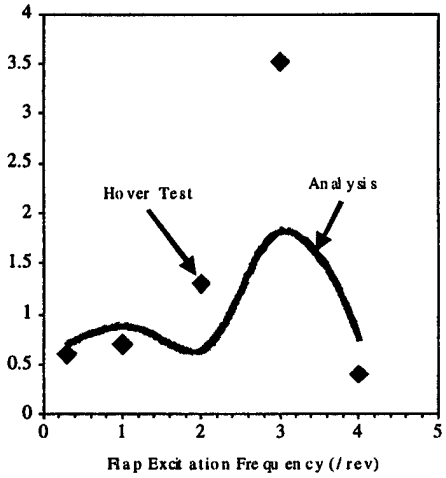
Figure 11. Model rotor test on a hover stand



(a) RPM sweep with 1/rev excitation



(b) Frequency sweep at 1850 RPM



(c) Oscillatory rotor thrust due to 1/rev excitation

Figure 12. Mach scaled rotor test in hover: at 1850 RPM [52]

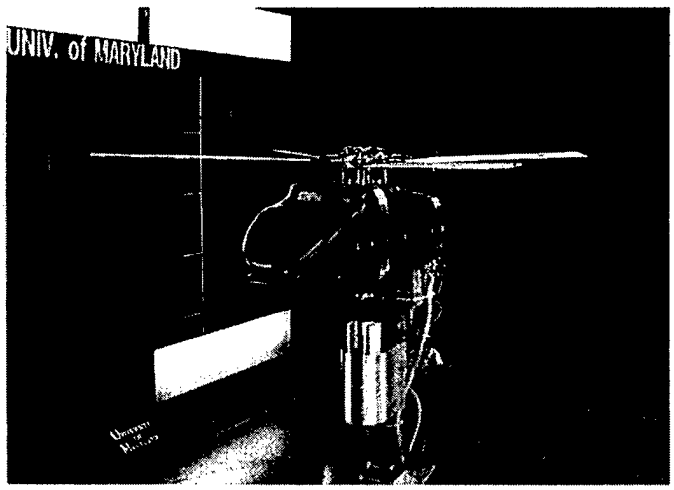
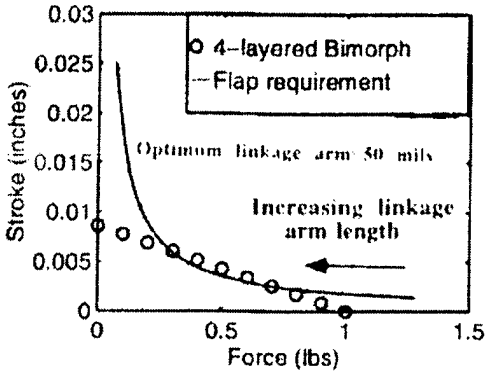
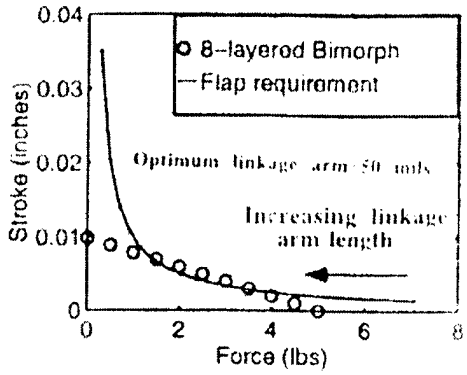


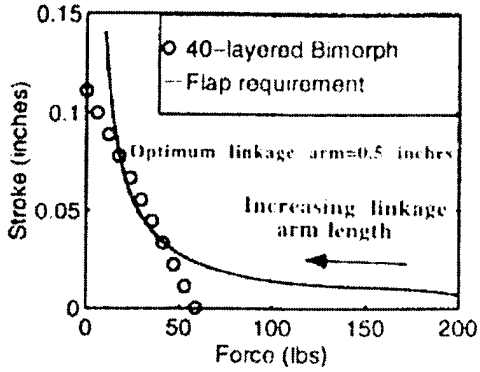
Figure 13. Mech-scaled rotor model in the Glenn L. Martin wind tunnel



a) Froude scale



(b) Mach scale



(c) Full scale : S-76 rotor

Figure 14. Actuator capability (14.5 Vrms/mil) vs flap requirements (8 degrees peak to peak deflection) for a 5% span, 20% chord flap located at 75% radius

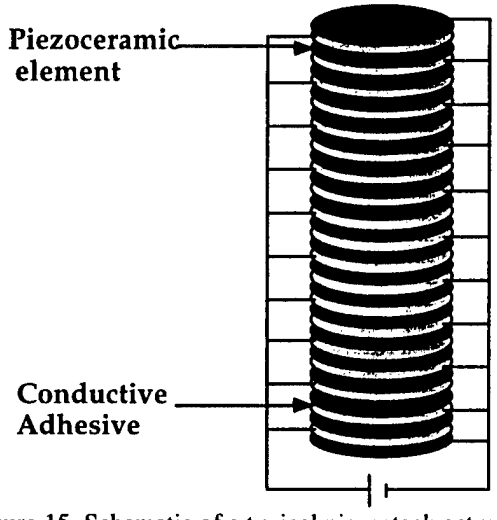


Figure 15. Schematic of a typical piezostack actuator

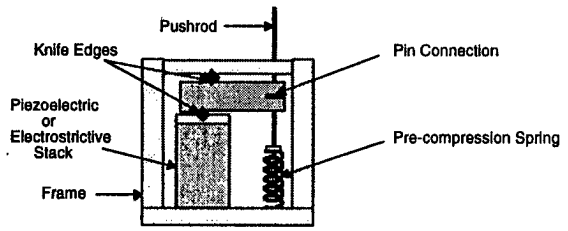


Figure 16. Mechanical leverage amplification system [6].

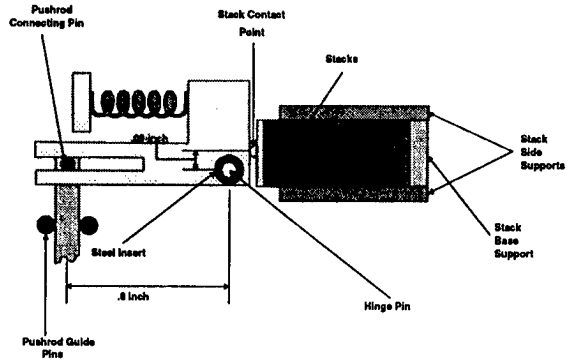


Figure 17. Stacks and L-Arm Arrangement [57]

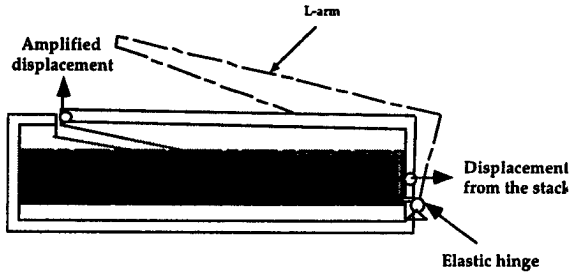


Figure 18. Piezostack Actuator with Integrated Mechanical Amplification

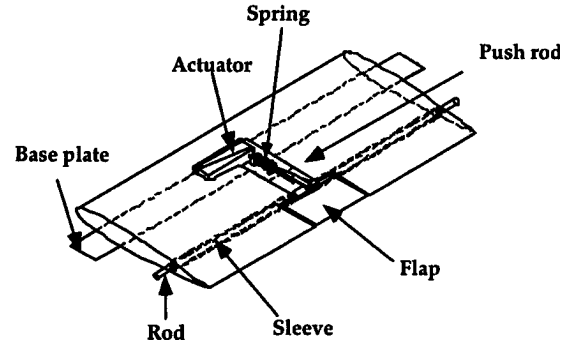


Figure 19. Schematic of wing model with flap actuated with piezo stack and flexural amplification [58]

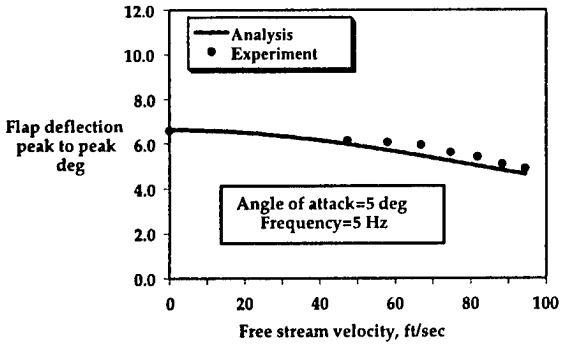


Figure 20. Flap deflection at 5 Hz frequency, 5 deg angle of attack [58]

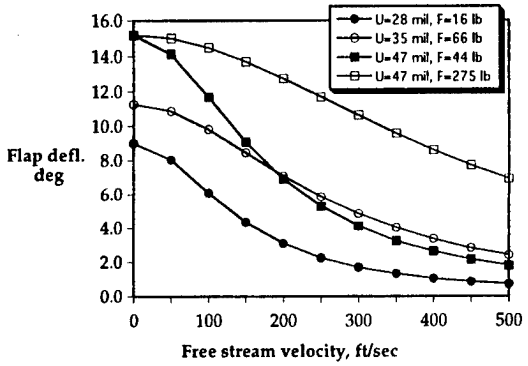


Figure 21. Predicted flap amplitude at different speeds with four different piezostack actuators [58]



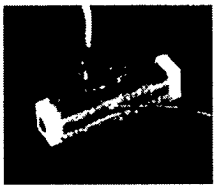
EDO



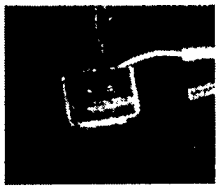
Morgan Matroc (MM)



Physik Instrumente (PI)

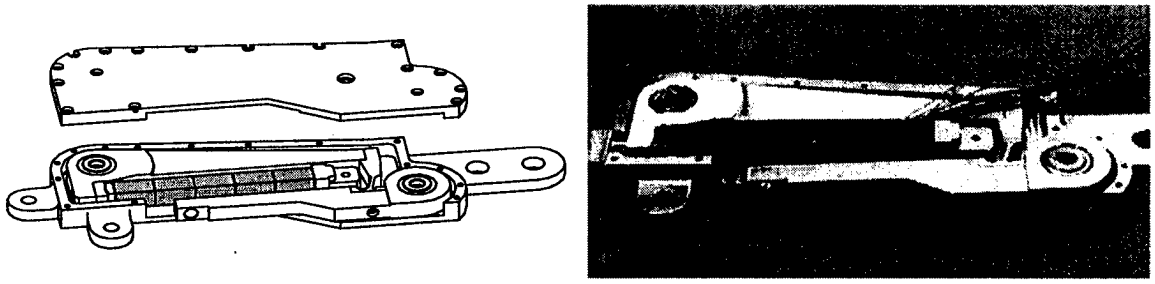


Sumitomo (SU)



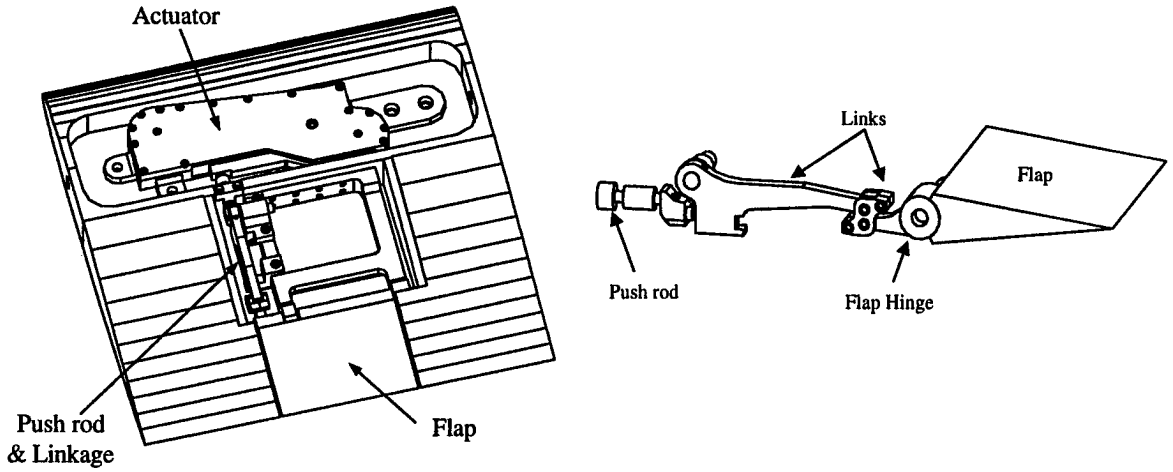
Xinetics (XI)

Figure 22. Piezostack actuators



(a) Actuator lay-out (b) Fabricated actuator

Figure 23. Flap actuator with L-L amplification mechanism [60]



(a) Wing lay-out (b) Flap/actuator push-rod attachment

Figure 24. Model wing section with trailing-edge flap actuated with piezostacks in conjunction with L-L amplification mechanism [60]

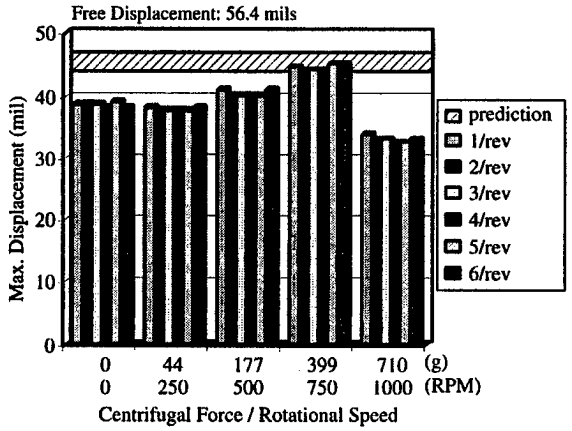


Figure 25. Vacuum spin testing of L-L actuator: actuator stroke vs. CF loading (90Vpp excitation) [59]

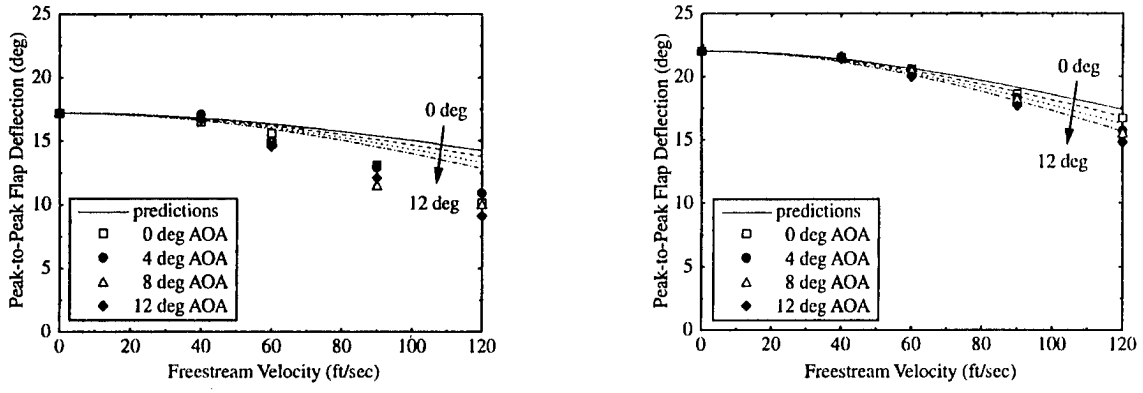


Figure 26. Peak-to-peak flap deflection vs. freestream velocity for the excitation frequencies of: (a) 1/rev (6.53Hz) and (b) 2/rev (13.1Hz) (90Vpp excitation) [61]

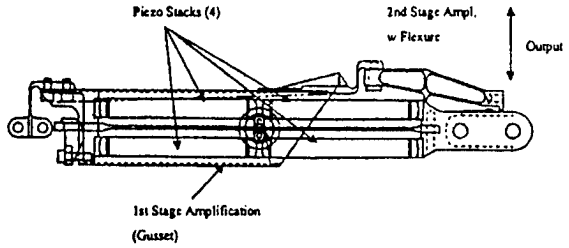


Figure 27. Bi-axial piezostack flap actuator schematic [65]

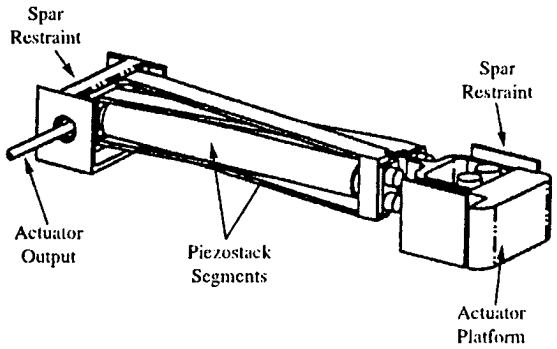


Figure 28. X-Frame actuator schematic [67]

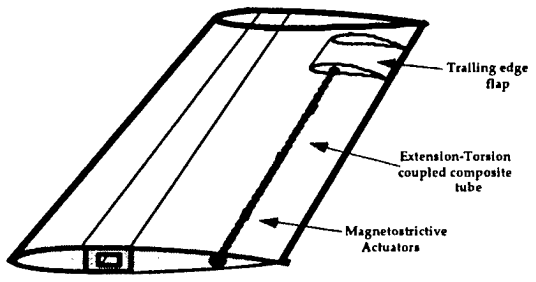


Figure 29. Schematic of rotor blade trailing edge flap actuated by extension-torsion coupled composite tube and magnetostrictive actuators [7]

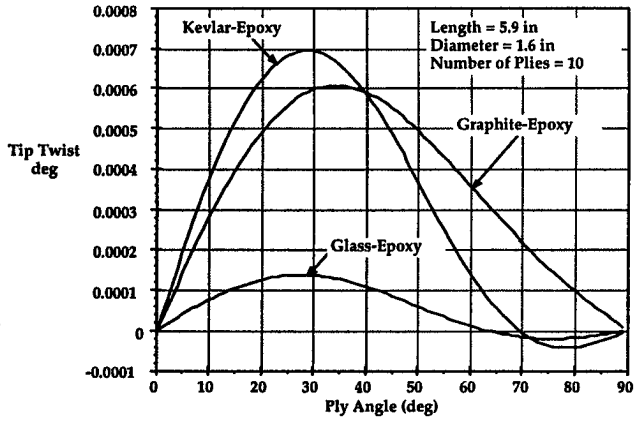


Figure 30. Induced Twist vs. ply angle for extension-torsion composite tube for a Prescribed Axial Load [7]

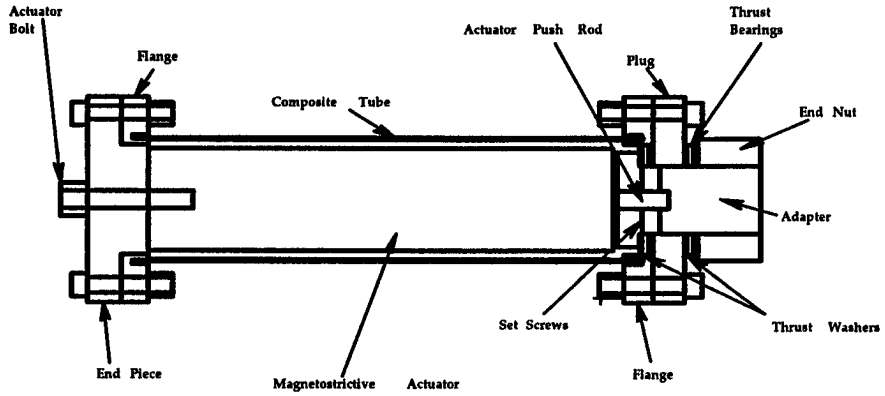


Figure 31. Schematic of composite tube and actuator assembly [7]

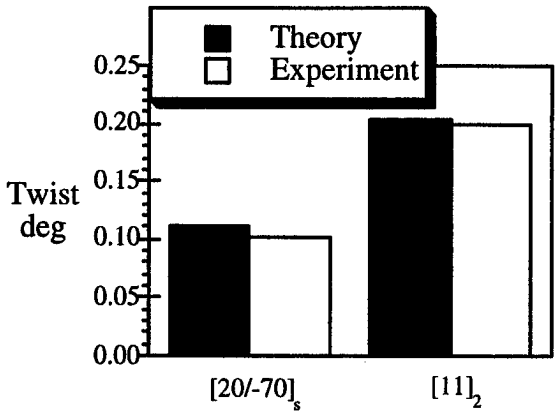


Figure 32 (a). Tip Twist of Kevlar-Epoxy Tube with xtension-Torsion & Manetostrictive Actuator [7]

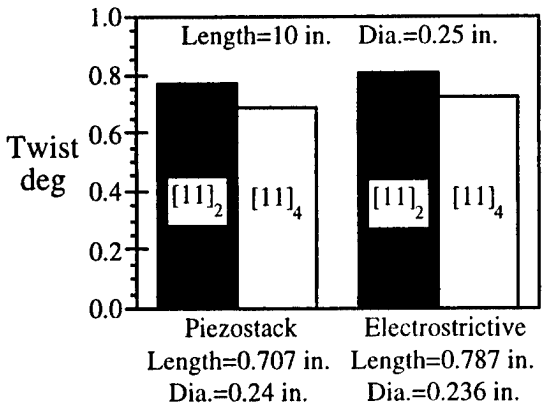


Figure 32 (b). Tip Twist of Kevlar-Epoxy Tube with Piezoelectric and Electrostrictive Stacks [7]

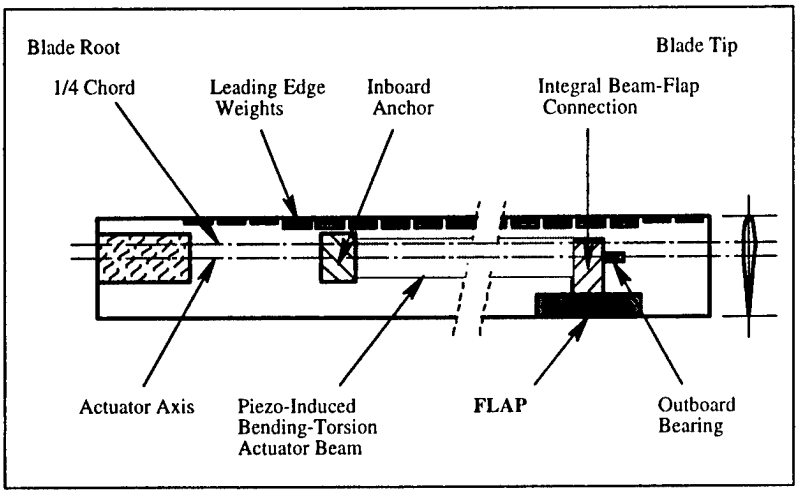


Figure 33. Trailing-Edge Flap Actuated with Bending-Torsion Actuator

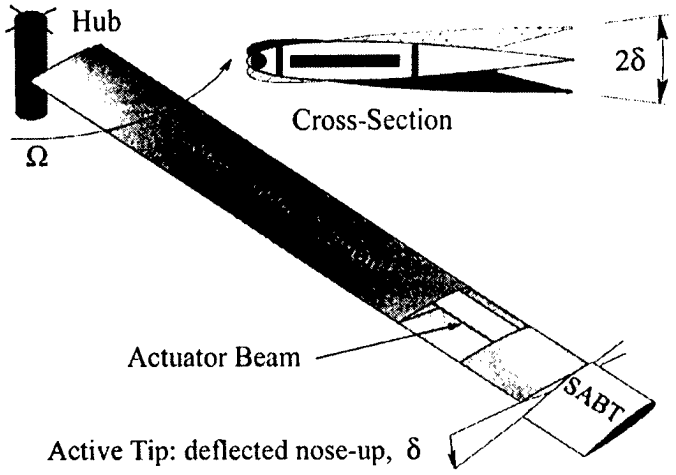


Figure 34. Blade tip actuated with bending-torsion actuator [73]

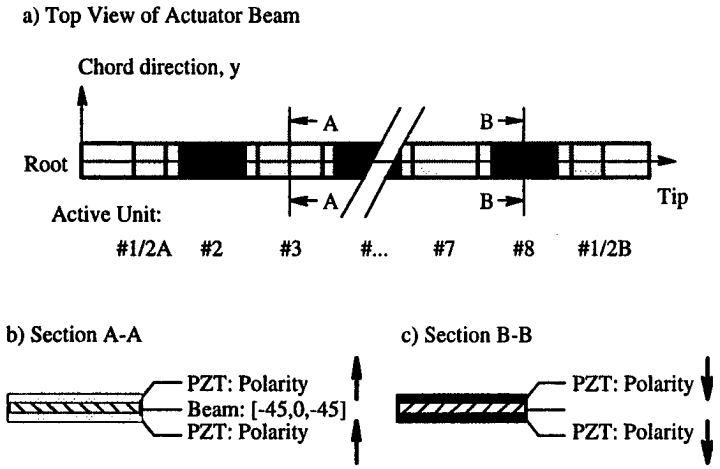


Figure 35. Composite Bending-Torsion Beam [72]

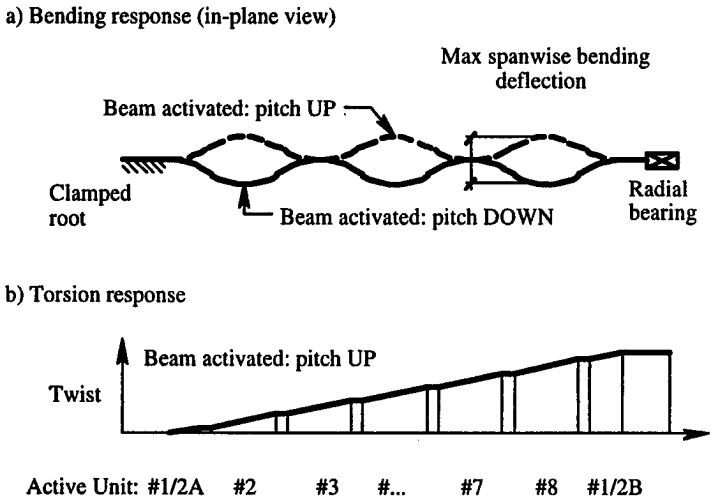


Figure 36. Schematic of Actuator Beam Mechanics [72]

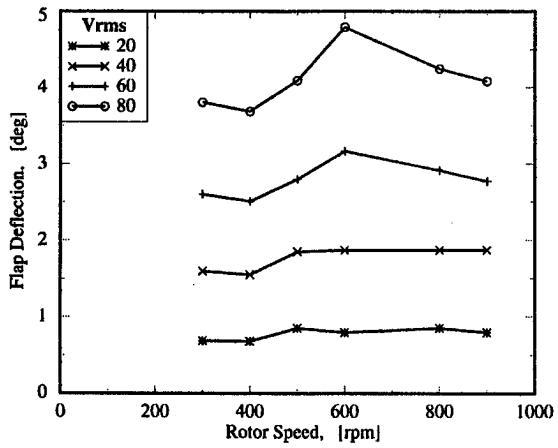


Figure 37. Hover Test Results: Trailing-Edge Flap, Peak-to-Peak Flap Deflection, Zero Collective, Excitation Frequency = 40 Hz [72]

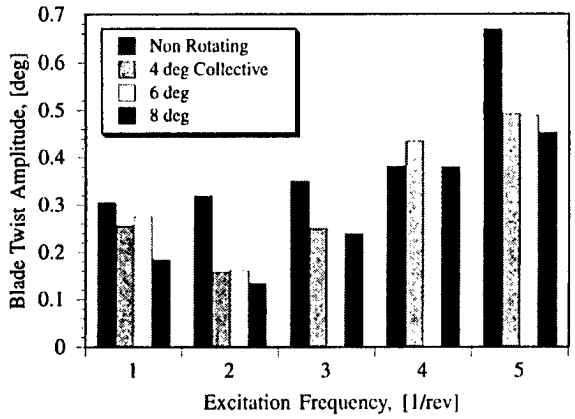


Figure 38. Hover Test Results, Blade Tip Twist at 875 RPM, Excitation 100 Volts RMS (Clamped Actuator Beam to Blade Tip) [73]

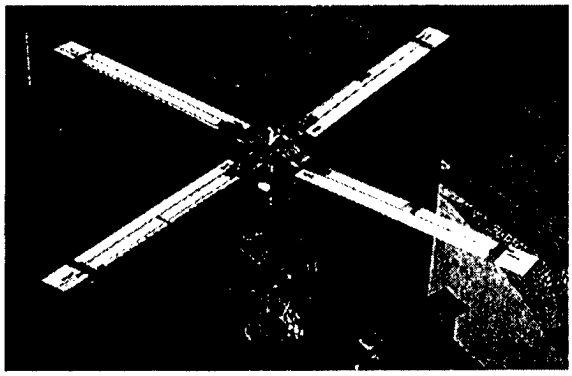


Figure 39. Active blade tip rotor on the hover test stand, diameter 6 feet, tip Mach .47, RPM 2000, blade tip 10%R, Bell 412 hub.

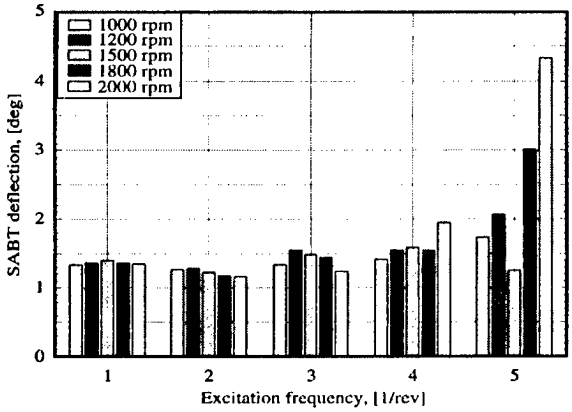


Figure 40. Active blade tip rotor test in hover: Oscillatory tip amplitude with RPM sweep at 100 V_{rms} and 2 deg collective

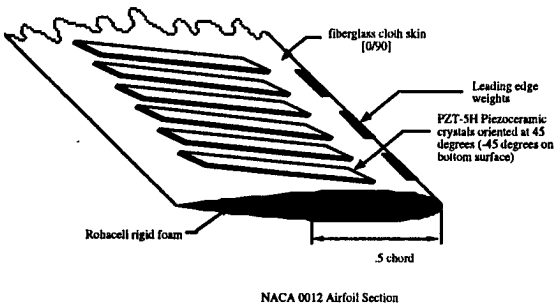
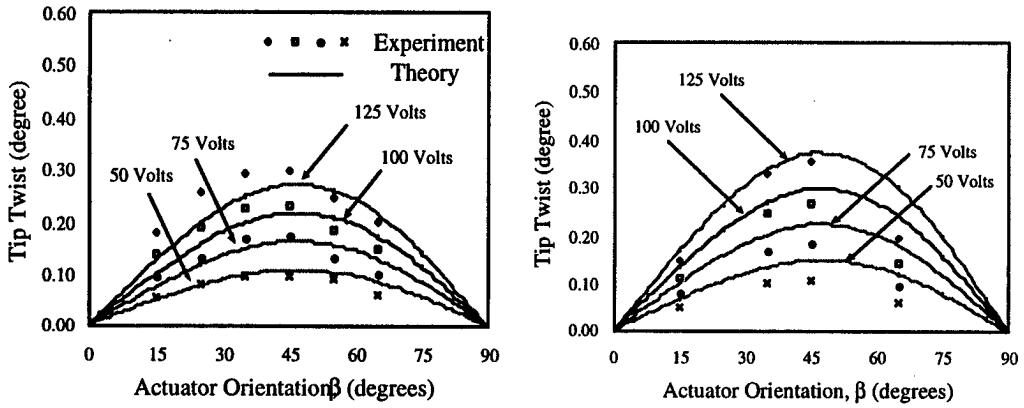
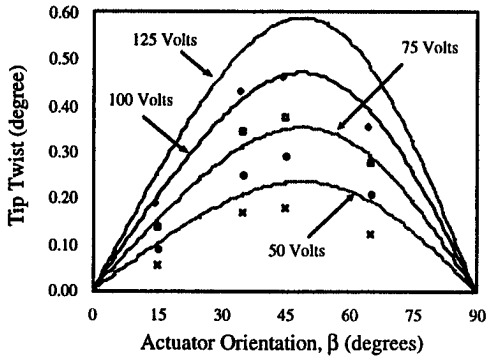


Figure 41. Piezoceramic Blade Cross Section Details



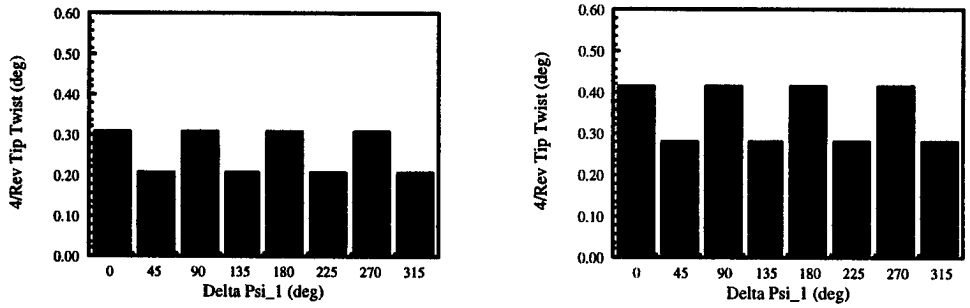
(a) Bond Thickness .020 inch

(b) Bond Thickness .010 inch



(c) Bond Thickness .0025 inch

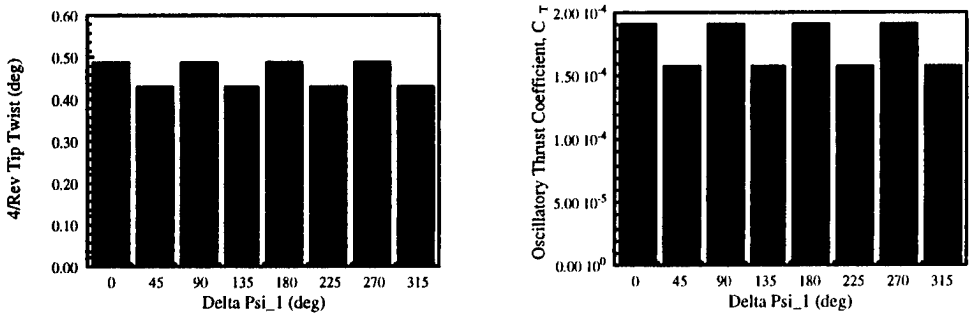
Figure 42. Effect of Bond Thickness and Actuator Orientation on Cantilevered Beam Tip Twist [79]



(a) Single-Layer Actuators

(b) Dual-Layer Actuators

Figure 43. Blade Response at 4/rev Excitation at 100 Volts RMS in a wind tunnel test at an advance ratio μ=0.33 [80]



(a) Blade Response at Tip (b) Oscillatory Rotor Thrust

Figure 44. Dual-Layer Actuators Blade Response at 4/rev Excitation at 150 Volts RMS in a wind tunnel

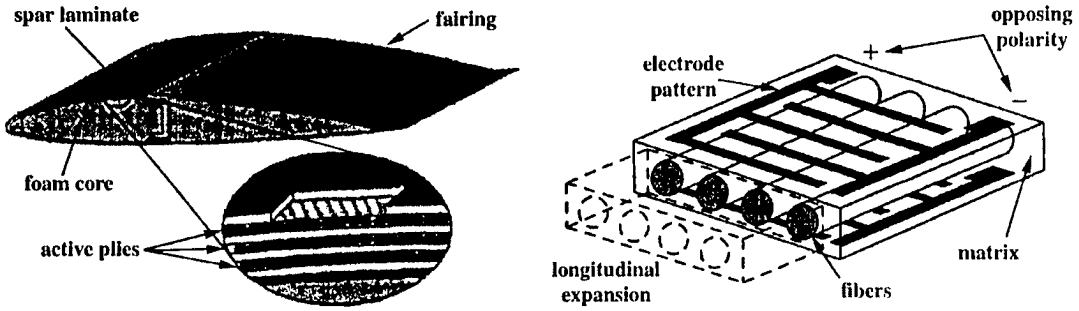


Figure 45. Active twist blade incorporating active piezo fibers

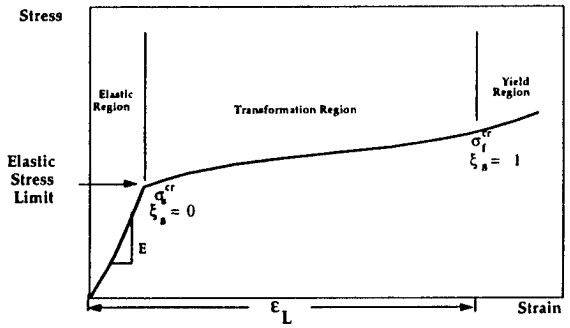
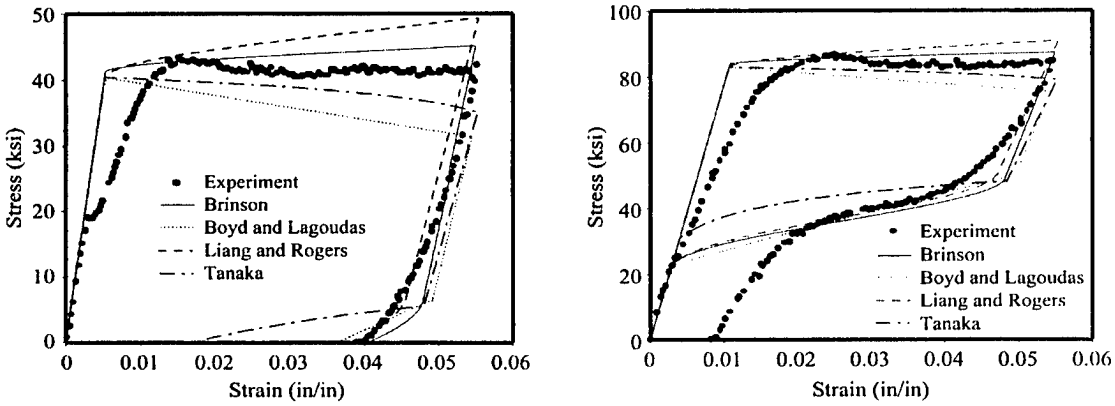


Figure 46. Schematic diagram of stress-strain characteristics of SMA



(a) 100°F Temperature (b) 140°F Temperature

Figure 47. Stress-Strain Curves of 20 mil Nitinol Wire [4]

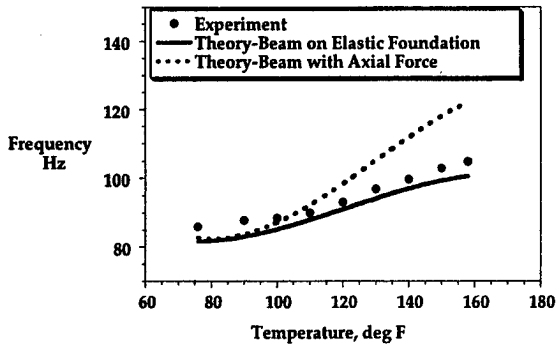


Figure 48. Fundamental Frequency of Clamped-Clamped Graphite-Epoxy Beam Activated by One 20 mil Dia SMA Wire, Beam Dimensions: length = 18 in., width = 0.25 in., thickness = 0.068 in. [96]

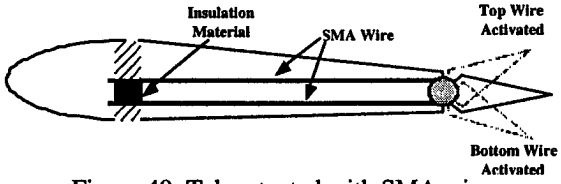


Figure 49. Tab actuated with SMA wires

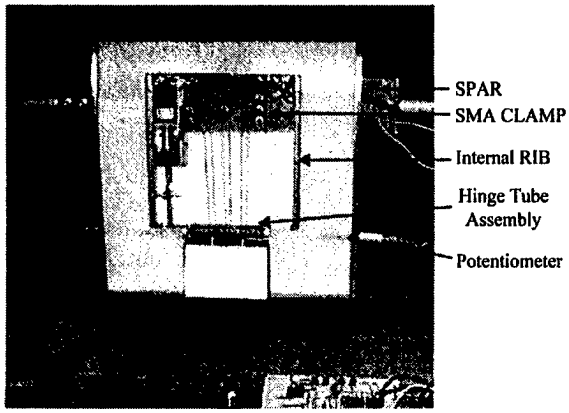


Figure 50. Blade section with tab actuated with 3 SMA wires

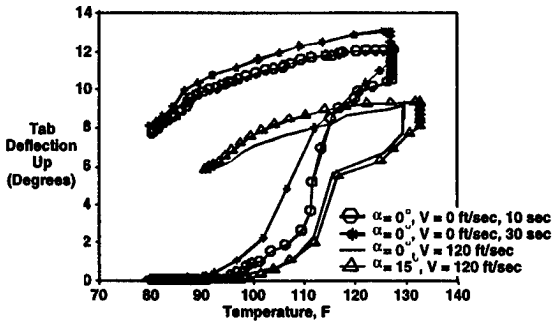


Figure 51. Comparison of bench-top and open-jet wind tunnel test results for tab deflection at different temperatures [102]

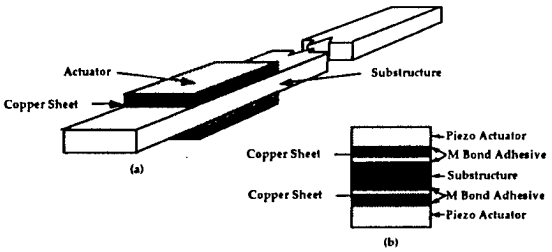


Figure 52. Solid Beam with Piezoelectric Actuators

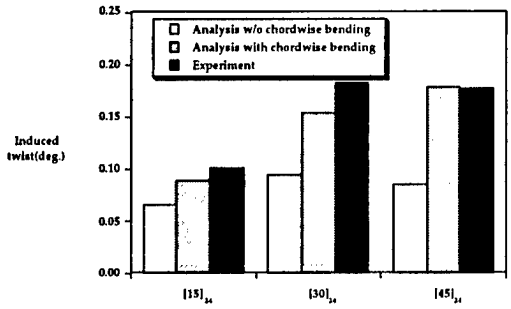


Figure 53. Induced twist of graphite-epoxy solid beams under piezoactuation, free actuator strain=240 microstrain [103]

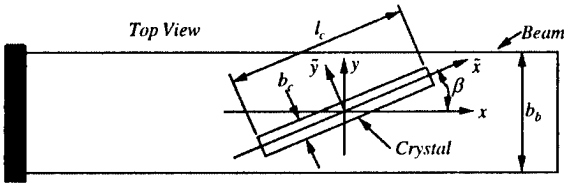


Figure 54. Piezo element skewed from beam axis

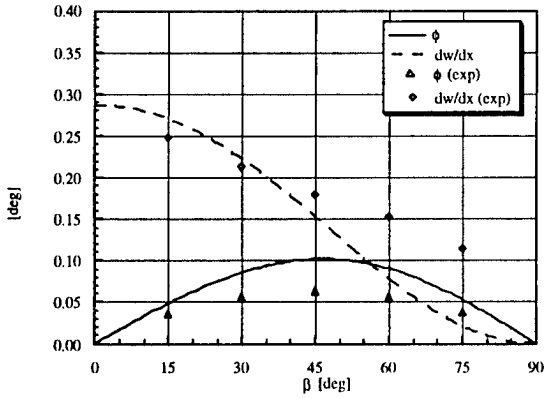


Figure 55. Bending slope and twist results of a Cantilevered Beam (Tip) [45]

Author Index

Abe, M., 285
Adachi, K., 100
Ando, N., 261
Andrei, N. F., 417
Awakua, Y., 100

Baboux, J. C., 439
Baburaj, V., 417
Benjeddou, A., 158
Bernard, J. E., 208
Boller, C., 336

Chapuis, G., 319
Chen, K. C., 81
Cho, J. Y., 43
Cho, K.-D., 73
Chonan, S., 185
Chopra, I., 455

Dimock, G. A., 61

Endo, M., 200, 367, 375

Fischer, G., 89
Funami, K., 344
Furuya, H., 150

Gandhi, F., 319
Garcia, E., 89
Gobin, P. F., 439
Gong, J.-M., 359
Gorge, V., 158
Goujon, L., 439
Grohmann, B., 3

Han, J.-H., 127
Hanahara, K., 227
Hayashi, S., 375
Hayashi, T., 50
Hegewald, T., 309
Higuchi, K., 251
Hong, C.-S., 293, 409
Hsu, Y. H., 169, 177
Hwang, J.-S., 43

Ichinose, H., 185
Ichinose, N., 243
Ikeda, T., 336, 344, 417
Inaba, T., 382
Inman, D. J., 285, 309
Ishimura, K., 251
Iwatsubo, T., 100

Jeng, Y. S., 81
Jiang, Z. W., 185
Jones, K. J., 393

Kang, H.-K., 293
Kawamata, A., 301
Kim, C.-G., 293, 409
Kim, D.-H., 73
Kim, S., 401
Kim, S. J., 10, 43
Kishimoto, S., 108
Kobori, A., 150
Konstanzer, P., 3, 336
Kröplin, B., 3

Lee, C. K., 81, 169, 177
Lee, I., 73, 401
Lee, S., 43
Lee, S.-W. R., 142
Lesieutre, G. A., 208
Liao, W. H., 277

Ma, K., 447
Matsuzaki, Y., 336, 344, 417
Melcher, J., 447
Michaelis, B., 119
Monner, H. P., 447
Muramatsu, E., 134
Murotsu, Y., 219

Nagayasu, K., 50
Naito, H., 344
Nakamura, H., 50
Naomi, A., 35
Natori, M. C., 251
Nishigaki, T., 200
Nishimoto, S., 219
Numagami, K., 185

Oda, Y., 235
Ogisu, T., 261
Ohayon, R., 158
Okabe, T., 261
Oki, K., 35
Okubo, H., 134
Okumura, K., 359, 367, 375
Ozawa, S., 150

Park, G., 285
Park, J.-H., 127
Park, Y., 401

Qiu, J., 127, 351

Rahman, M. A., 351
Regelbrugge, M. E., 193
Rew, K.-H., 401
Ryu, C.-Y., 293

Said, W. M., 428
Sakamoto, H., 251
Salvia, M., 439
Sanda, T., 301
Sater, J., 89
Sato, J., 344
Senda, K., 219
Shin, W.-H., 73
Shinya, N., 108
Staszewski, W. J., 428
Sugino, S., 382
Sung, D.-U., 409

Tada, Y., 19, 27, 227, 235
Tai, Y., 134
Takahashi, H., 50
Takaki, J., 261
Takata, K., 359, 367
Takeda, N., 261, 269, 301
Tanaka, M., 35, 185, 243
Tani, J., 127, 351
Tobushi, H., 359, 367, 375
Todoh, M., 35
Tokuda, M., 382
Tokutake, H., 134
Tsutsui, H., 301

Uchida, N., 50

Wang, D. H., 277
Wereley, N. M., 61
Wong, H. L., 142

Yamazaki, J., 27
Yeh, C. S., 81
Yuasa, H., 19
Yun, C. Y., 10

Zhang, W., 119